

NASA TM X- 55742

FINAL REPORT 1966 SESSION OF THE GODDARD SUMMER WORKSHOP

N 67-22741

(ACCESSION NUMBER)

496

(PAGES)

TM-X-55742

(NASA CR OR TMX OR AD NUMBER)

FACILITY FORM 602

N 67-22775

(THRU)

1

(CODE)

34

(CATEGORY)

JUNE 15 TO SEPTEMBER 15, 1966

NASA

———— GODDARD SPACE FLIGHT CENTER ————
GREENBELT, MARYLAND

FINAL REPORT
1966 SESSION OF THE GODDARD
SUMMER WORKSHOP

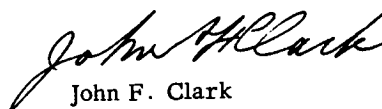
June 15 to September 15, 1966

Goddard Space Flight Center
Greenbelt, Maryland

FOREWORD

The Goddard Summer Workshop has, with the 1966 session, completed its fifth year. During the five years the Workshop has continued to grow in effectiveness in generating information of immediate interest, in acquainting university faculty members with NASA interests and problems, and in offering new challenging concepts to the participating graduate students.

The participants in the Goddard Summer Workshop are university faculty members, graduate students, and members of the Goddard staff, who work together in teams organized in specific problem areas. The accomplishments have included not only direct inputs for Goddard programs but in the universities some course material, research projects, and thesis concepts have been generated. Participants have authored several scientific and technical publications based on their Summer Workshop results.



John F. Clark
Director

PREFACE

This document contains the collected papers written by participants in the 1966 Goddard Summer Workshop during the 12-week session. The form and scope of the individual papers vary with the nature and status of the problem, but in each case the paper represents a contribution of the author within the limited time of this summer session.

The Goddard Summer Workshop session of 1966 was divided into five groups, each engaged in a different problem area. A Goddard division chief was responsible for the program and operation of each group. In three of the groups there was also a principal investigator, a senior professor who assisted the division chief in establishing the program, coordinated the work in the group, and acted as advisor in the group. The groups were:

Group A-Information Systems

Division Chief-Dr. R. A. Stampfl
Systems Division

Principal Investigator-Dr. Monsour Javid
City University of New York

(1)

Group B-Structural Dynamics

Division Chief-Dr. R. J. Coates
Advanced Development Division

Principal Investigator-Dr. Yu Chen
Rutgers, The State University of New Jersey

(2)

Group C-Magnetic Fields and Plasma Studies

Division Chief-Mr. J. C. New
Test and Evaluation Division

Principal Investigator-Dr. Donald L. Waidelich
University of Missouri

(3)

Group D-Atmospheric Studies

Division Chief-Mr. N. W. Spencer
Laboratory for Atmospheric and Biological Sciences

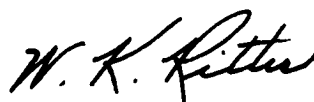
(4)

Group E-Radiation Simulation Problems

Division Chief-Mr. J. C. New
Test and Evaluation Division

(5)

The papers are presented in sections corresponding to the subject area groups.



W. K. RITTER
Director, Summer Workshop

UNIVERSITY WORKSHOP PARTICIPANTS

FACULTY MEMBERS

CALLAHAN, William, Dr.—Lecturer in Physics, Weston College
CHEN, Yu, Dr.—Professor of Engineering Mechanics, Rutgers, The State University, New Jersey
DALRYMPLE, Jean, Dr.—Associate Professor of Mechanics, Michigan Technological University
JAVID, Monsour, Dr.—Associate Professor of Electrical Engineering, City College of New York
KAHN, Robert E., Dr.—Assistant Professor Electrical Engineering, Massachusetts Institute of Technology
KANEFSKY, Morton, Dr.—Assistant Professor of Electrical Engineering, Yale University
KELLY, Robert—Instructor Electrical Engineering, University of Rhode Island
KINNIER, John, Dr.—Assistant Professor of Physics, Boston College
McELANEY, James, Dr.—Assistant Professor of Physics, Fairfield University
MOHR, Eugene I., Dr.—Professor of Physics, Columbia Union College
WAIDELICH, Donald L., Dr.—Professor of Electrical Engineering, University of Missouri
WILLIAMS, Thomas R., Dr.—Associate Professor of Electrical Engineering, Princeton University

GRADUATE STUDENTS

CROWELL, John—Physics, Johns Hopkins University
EICHMANN, George—Electrical Engineering, City College of New York
FEUSTEL, Edward—Electrical Engineering, Princeton University
FITZGERALD, James F.—Electrical Engineering, University of Massachusetts
HENRY, Donald—Physics, Johns Hopkins University
JOYCE, Glenn, Dr.—Physics, University of Missouri
MORRISON, John C.—Physics, Johns Hopkins University
MUNN, Dale—Physics, University of Missouri
MURPHY, James D.—Physics, Georgetown University
REED, Edward—Physics, Johns Hopkins University
SCHOEN, Paul—Physics, Johns Hopkins University
SMITH, Michael—Physics, Johns Hopkins University
SOBOTKIN, Fred—Electrical Engineering, City College of New York

COOPERATING PARTICIPANTS

CHU, Y., Dr.—Assistant Professor, University of Maryland
DAVISSON, Lee D., Dr.—Assistant Professor, Princeton University
TORIDIS, Theodore, Dr.—Assistant Professor, George Washington University

SUMMER WORKSHOP 1966

Program Outline and Team Participants

PROJECT A: Information Systems

Problem Topics

- A-1 Bit-plane encoding
- A-2 The fan method of data compression
- A-3 Application of the concept of energy compression ratio to run length coding
- A-4 Channel error effects on a binary sequence time encoding system
- A-5 Counting with maximal length shift registers
- A-6 Reliability of a confidence level procedure for error probability of a bank of correlators
- A-7 Non-parametric signal detectors
- A-8 Phase-locked loops in space communications
- A-9 Use of formal language for processing satellite experimental data
- A-10 Mimic language applications for space investigations
- A-11 Radiation through a uniaxial anisotropic plasma

TEAM A

Academic Personnel

Dr. M. Javid
Principal Investigator
Dr. Y. Chu*
Dr. Lee D. Davisson*
Dr. M. Kanefsky
Dr. R. Kahn
Dr. T. Williams
Mr. E. Feustel
Mr. R. Kelley
Mr. D. Munn
Mr. F. Sobotkin

Goddard Personnel

Dr. R. A. Stampfl
Staff Advisor
Mr. Cyrus J. Creveling
Dr. Thomas J. Lynch
Dr. R. W. Rochelle
Mr. C. H. Ehrmann
Mr. A. L. Hedrich
Mr. J. M. Bridger

*Consultants

PRECEDING PAGE BLANK NOT FILMED.

PROJECT A: INFORMATION SYSTEMS

CONTENTS

	<u>Page</u>	
DATA COMPRESSION USING BIT-PLANE ENCODING	1	✓
M. Kanefsky		
THE FAN METHOD OF DATA COMPRESSION	23	✓
L. D. Davisson		
THE CONCEPT OF ENERGY COMPRESSION RATIO AND ITS APPLICATION TO RUN LENGTH CODING.....	31	✓
L. D. Davisson		
THE EFFECT OF CHANNEL ERRORS ON A SAMPLE COMPRESSION SYSTEM EMPLOYING BINARY SEQUENCE TIME ENCODING	45	✓
R. Kelley		
COUNTING WITH MAXIMAL LENGTH SHIFT REGISTERS	65	✓
R. Kahn		
INVESTIGATION OF THE RELIABILITY OF A PROPOSED CONFIDENCE LEVEL PROCEDURE FOR ERROR-PROBABILITY OF A BANK OF CORRELATORS.....	75	✓
D. Munn		
NON-PARAMETRIC SIGNAL DETECTION.....	83	✓
E. Feustel		
A NOTE ON PHASE-LOCKED LOOPS IN SPACE COMMUNICATION	111	✓
T. R. Williams		
USE OF A FORMAL LANGUAGE TO DESCRIBE ON-BOARD AND GROUND STATION PROCESSING OF SATELLITE EXPERIMENTS.....	121	✓
F. Sobotkin		
APPLICATION OF MIMIC LANGUAGE AT GSFC.....	135	✓
Y. Chu		
RADIATION FROM A DIPOLE ANTENNA IMMERSED IN A HALF-SPACE OF UNIAXIAL ANISOTROPIC PLASMA	225	✓
M. Javid		

PRECEDING PAGE BLANK NOT FILMED.

INTRODUCTORY REMARKS ON PROJECT A
INFORMATION SYSTEMS

R. A. Stampfl

The group of papers reporting the results of studies related to information systems deals with selected subjects according to the author's inclination and specialty and are arranged in no particular sequence. Neither the full range of interesting subjects nor the available time permitted exhaustive treatment of the discipline. The variety of problems investigated, including computer language and design, source encoding and data compression, instrument design and antenna radiation, attests to this fact. One paper defining Energy Compression Ratio as a figure of merit offers the possibility to compare the quality of various data compression methods and is deserving of special mention.

The importance of information system studies to progress in deep ~~space communication~~ capability is widely appreciated. Nevertheless, it should be re-emphasized that the capability of collecting and distributing large quantities of data with the earth orbiting satellite is not enough if the same techniques do not permit their economic exploitation to the benefit of mankind.

The reader will easily recognize many subjects as continuations of work started last year, a further indication of the need to extend this work, both during conception at the universities where the ideas were formed and at the Center where the investigations were pursued.

DATA COMPRESSION USING BIT PLANE ENCODING

Morton Kanefsky*

INTRODUCTION

N 67-22742

An efficient and versatile data compression scheme known as bit-plane encoding has been suggested by Barker and Schwartz (References 1 and 2). This technique requires temporary storage of a block of telemetry data in a buffer memory. Since it is standard practice for a "word" to be stored vertically in memory, the least significant digits of all the words in the block lie on the same horizontal plane. The bit-plane procedure is to encode and transmit the binary data in each of the planes sequentially. It is clear that when the data contains a high degree of dependency the "most significant" or "highest order" bit planes should contain long "runs" of zeros or ones. Thus, these planes can be significantly compressed by some type of run-length encoding. Furthermore, efficient quantization (a form of compression) can be achieved by truncating the number of planes. The power of this technique can be best understood by example.

EXAMPLE

Consider a continuous uniformly distributed process that, when sampled, can be regarded as a Markov process with a normal transition probability density. The width ($\pm 2\sigma$) of the transition probability density is 12.5 percent of the peak-to-peak value of the process and the degree of quantization determines the transition matrix. The assumption of a uniform distribution results in equally likely levels for equal-spaced quantization. Given the degree of quantization one can easily determine the entropy of the source, and hence the maximum possible amount of data compression. This limit on the data compression is plotted in Figure A-1 as a function of the degree of quantization. Furthermore, for a given source code, one can determine the "prediction probabilities" for the binary, Markov data in each of the bit planes. In this report it is assumed that the source code is a Gray code. The primary reason for this assumption is that a Gray code results in more efficient bit-plane compression than a standard PCM code since a change of one level always corresponds to a change of only one bit. No attempt has been made to find an "optimum" source code for bit-plane compression. It is easy to determine the entropy of the individual bit-planes, having found the prediction probabilities, and hence to determine the maximum possible amount of data compression using the bit-plane technique (with a Gray source code). This limit on the bit-plane compression is also shown in Figure A-1.

Observe that it costs very little to concentrate on compressing the bit-planes separately rather than compressing the process in its entirety. The assumptions that are sufficient for this result to be true in general are: 1. The data are a first-order Markov Process, and 2. The levels are equally likely. The second assumption is probably unnecessary.

A third curve in Figure A-1 is the net "energy compression" for a particular implementation of the bit-plane technique which will be described in detail later. The notation of energy compression has been suggested by Davisson** as a means for taking into consideration the effect of errors due to noise in comparing data compression schemes. The energy compression is the factor by

*Yale University, New Haven, Conn.

**Davisson, L.D., "Information Systems," 1966 Goddard Summer Workshop Report.

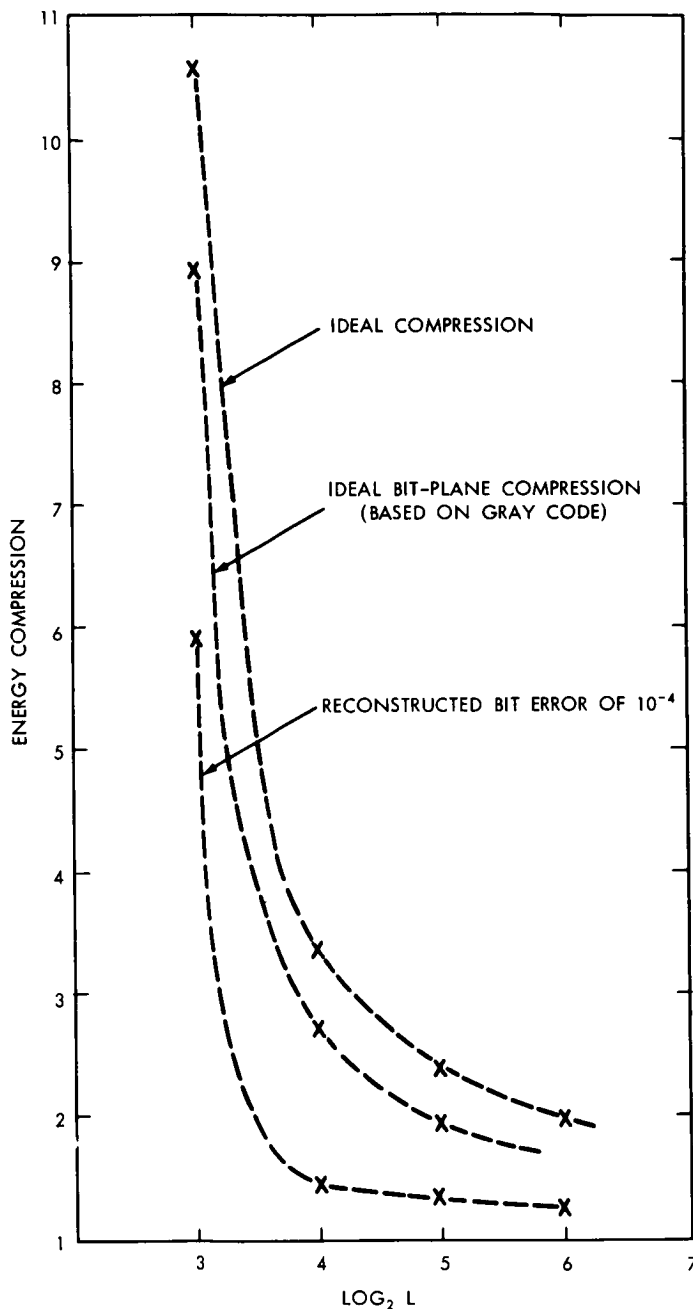


Figure A-1—Energy compression for a Markov process with a normal transition probability density whose width (± 2) is 12.5% of the truncated peak-to-peak value of the process. The L levels are assumed to be equally likely.

which the total energy is reduced for a given reconstructed bit error rate. The energy per bit of transmitted data must be larger for compressed data than for uncompressed data in order to achieve the same reconstructed bit error rate. The calculation of this curve will be explained later. The gap between the net energy compression curve and the maximum amount of data compression is not an indication of the efficiency of the particular compression scheme considered. Unfortunately "Information Theory" does not indicate the maximum compression attainable for a given error criterion on the reconstructed data.

The maximum possible data compression for the individual bit-planes is shown in Figure A-2 as a function of the prediction probability. In addition, Figure A-2 contains curves indicating the data compression attainable by three different run-length type encoding schemes which will be described in detail later. Observe that for binary, Markov data, simple ad-hoc compression schemes do a very efficient job. It follows that the bit-plane technique yields efficient data compression for Markov processes with simple ad-hoc schemes for compressing the binary planes. Other ad-hoc schemes, such as "zero-order hold," in order to be relatively efficient, require the equally likely levels assumption in addition to restricted classes of probability transition matrices.

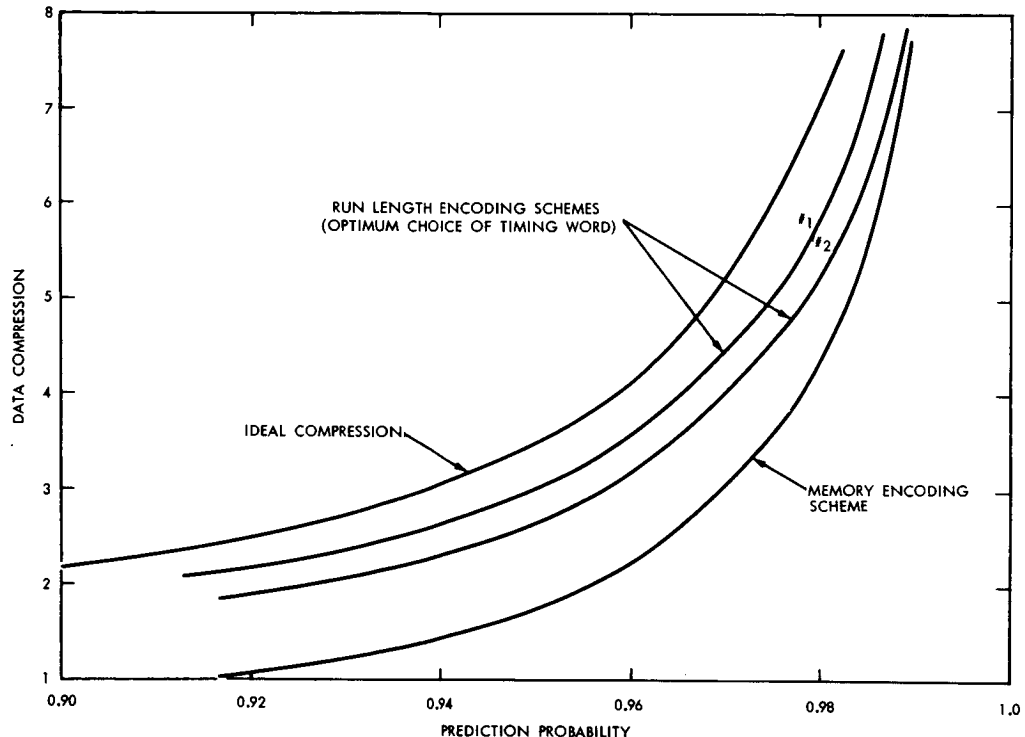


Figure A-2—Data compression scheme for binary Markov sources.

Let us now assume that we wish to quantize the process of this example into 16 levels. Suppose, however, that the energy of the process is slowly nonstationary, and that the dynamic range for which we require 4 bit accuracy is 16 to 1. For equally spaced quantization we require 8 bits for each sample. However for logarithmic quantization we require only 4 bits per sample to achieve 9 percent accuracy over the entire dynamic range (Reference 4). An approximately equivalent scheme that truncates the 8 bit equally-spaced word requires 5 bits to transmit the first four significant bits (Reference 5). It can be determined that the average entropy of the source (8 bit words) is of the order of 4 bits depending of course on the form of the nonstationarity. It is clear that, for this example, the quantization procedure is most important and should precede, but not necessarily preclude, any source encoding scheme for compression.

Consider using a bit-plane procedure that transmits only the first 4 non-zero planes. This technique requires transmitting, in addition to the 4 planes, some plane identification bits to indicate the number of all-zero planes and the place of truncation. This procedure, the organization for which will be indicated shortly, requires 4.1 bits per word on the average. Thus the net saving in bits is comparable to that of logarithmic quantization. One can now, however, profitably compress

three of the four significant planes by source coding. The resultant "effective" number of bits per word is remarkably constant over the entire dynamic range and is equal to 2.75 bits. The effective number of bits is defined as the product of the average number of bits times the increase in the energy per bit required to achieve a reconstructed bit error rate that is equivalent to the uncompressed bit error rate. For this example, a bit error rate of 10^{-4} has been assumed. Thus the net energy has been reduced by an additional factor of 1.45. Observe that this additional reduction is consistent with the data in Figure A-1. The versatility of bit plane encoding is reasonably clear from this example.

A peculiarity of the bit-plane technique is that the reconstructed data is bound to have a different error probability for each of its bits since it is unlikely that any practical implementation will make the energy per bit a function of its plane. If, however, we assume that the data will be channel encoded in addition to source encoded, this peculiarity becomes distinctly advantageous. We can, for example, make some of the most significant planes immune to single errors at very little overall cost in bandwidth since these planes should be highly compressed. More generally, we should be able to employ channel encoding in such a way as to effectively minimize some error criterion for the reconstructed data, given a fixed increase in bandwidth. The effects of channel encoding will be considered briefly later in this report.

ORGANIZATION OF THE BIT PLANE TECHNIQUE

There are four types of planes that we must distinguish. First there are those planes for which all the bits have the same value (class A planes). Class B planes are those in which the number of runs is small enough to be profitably compressed. Class C planes are those for which it is not profitable to compress and for which the original source code is transmitted intact. Finally there are those planes which we omit as a result of our quantization procedure. In addition to identifying these planes it is convenient to include the value of the first bit for both the class A and class B planes with the plane identification bits. This plane identification can be accomplished with 3 bits. However, it will be assumed that 4 bits are used for single error detecting. For example,

Type A	00	$\begin{cases} 00 \\ 11 \end{cases}$	Type C	1010
Type B	11	$\begin{cases} 00 \\ 11 \end{cases}$	Omit	0101

In the analysis it will be assumed that the plane identification is transmitted without error. Additional bits can be employed as necessary.

In order to distinguish the plane identification bits from the data, a timing word is needed to indicate the end of the plane (or equivalently, the final run). The encoding schemes considered in this report also use timing words, e.g., run length. Plane synchronization can be accomplished by allowing a t bit timing word to represent $(2^t - 1)$ words with the remaining word set aside to indicate the end of the plane. Single errors in the end of plane word can usually be identified by context, particularly for the preferred encoding scheme. It will be assumed in the analysis that this end-of-plane word is also transmitted without error. For reasonably sized buffer memories one can always repeat the end-of-plane word or add error correcting bits at very small cost.

The bit plane system is implemented in the following way.* A block diagram is shown in Figure A-3 which includes a memory, preceded by a "monitor" and followed by a "code box." The memory is sequentially loaded by parallel written sample words. A simple binary decision device

*This description of the implementation as well as Figure A-3 is essentially that of References 1 and 2.

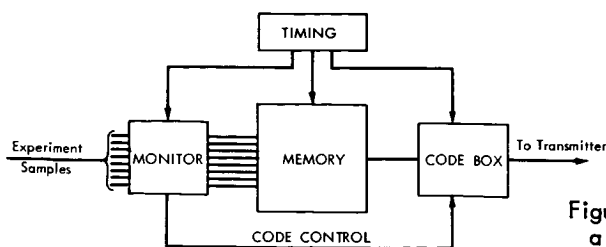


Figure A-3—The schematic of the organization of a bit-plane encoded data processing memory.

monitors each bit line as the memory is loaded. The decision is based on the number of changes in the value of the bit being written. If there are no changes, the plane is class A. If the number of changes is less than some threshold, the plane is class B; otherwise it is class C. Following readout of the monitor, which establishes plane identification, the memory is serially read along the bit planes starting with the first class B plane. Before the plane is read, however, the corresponding identification word in the monitor sets the code box to the appropriate mode, either run-length counter, for example, or parallel-accessed register to take the bits as they come directly. The code box can then be read in parallel into a buffer memory prior to transmission.

So far, the type of source encoding to be used for the class B planes has not been considered. In fact, it would appear advantageous to consider more than one kind of class B plane depending on the count of the monitor. It will be seen that this is not the case. Three types of run encoding will now be analyzed and the resultant energy compression per bit plane will be calculated as a function of the prediction probability. It will be seen that "memory" or "end of run" encoding is clearly preferable and furthermore, "optimum" memory size will be indicated. When this is accomplished it will become a straightforward matter to calculate the net energy compression for any given Markov source.

RUN STATISTICS FOR BINARY MARKOV DATA

All of the encoding schemes considered utilize the run properties of the data and hence some pertinent statistics are common to them all. Let p be the prediction probability for a sequence of binary digits; that is p is the probability that any sample has the same value as the preceeding sample. The probability that there are m changes in a sequence of N bits is given by the binomial distribution:

$$P_r(m \text{ changes}) = \binom{N-1}{m} (1-p)^m p^{N-m-1}. \quad (1)$$

The number of runs (n) is of course $(m+1)$, and the average number of runs (\bar{n}) can be calculated in a straight forward manner resulting in:

$$\bar{n} = N(1-p) + p. \quad (2)$$

The probability that a run is of length r is given by:

$$P_r(\text{run length } r) = \begin{cases} p^{r-1} (1-p) & ; \quad r < N \\ p^{N-1} & ; \quad r = N. \end{cases} \quad (3)$$

This result can be established by first recognizing that it is correct for the initial run and then observing that all of the runs must have the same distribution by symmetry. The average run length calculated from Equation (3) of course turns out to be N/\bar{n} .

For some of the run length schemes considered it is preferable to use a run length word of less than $\log_2 N$ bits. These schemes break up the longer runs and hence increase the number of runs. Let us assume a maximum allowable run length of T ($T = 2^t - 1$) where t is the number of bits in the run word). The probability that a run length is greater than T is obtained from Equation (3) where

$$P_r(r > T) = p^T \quad (4)$$

Given n untruncated runs, it is clear that the expected number of truncated runs is

$$\bar{n}_t = n[1 + p^T + p^{2T} + \dots + p^{mT}], \quad (5)$$

where m is the largest integer such that $mT < N - n$. It follows that the average number of truncated runs is essentially given by (provided $\bar{n} < N$)

$$\bar{n}_t \cong [N(1 - p) + p] \frac{1 - p^{[N/T]T}}{1 - p^T}, \quad (6)$$

where $[x]$ is the smallest integer greater than or equal to x .

In the bit plane procedure, regardless of the compression scheme, the last run is indicated by the end of plane word (This automatically implies the length of the run whereas the run length implies the end of the plane only in the absence of errors). This end of plane word is however not transmitted for type A planes which occur with probability p^{N-1} . It is convenient to define an average "effective" number of runs by

$$\bar{n}^1 = (\bar{n} - 1) + (1 - p^{N-1}) = \bar{n} - p^{N-1}, \quad (7)$$

with this definition the average number of bits used for timing purposes only becomes $\bar{n}'t$.

COMPRESSION SCHEMES FOR BINARY DATA

The first scheme considered is a form of run length encoding which, for all the schemes considered here, most closely approximates the entropy of the source. This scheme transmits timing information only, except when the timing word achieves its maximum which occurs with probability p^{T-1} . In the latter event a single bit is added which indicates the value of the next run. This bit is of course necessary to distinguish between transitions and continuations. The total number of bits required per plane has the average value

$$\bar{B} = \bar{n}'_t (t + p^{T-1}) + 4, \quad (8)$$

where the four extra bits are of course the plane identification bits. The net data compression (D_c) for this first run length scheme is accurately approximated by

$$D_{cr11} \simeq \left\{ [N(1-p) + p] \frac{1 - p^{\lceil N/T \rceil T}}{1 - p^T} - p^{N-1} \right\} \frac{t + p^{T-1}}{N} + \frac{4}{N}. \quad (9)$$

Equation (9) is plotted in Figure A-2 as a function of p for $N = 500$ where t is optimized for each value of p .

A difficulty with this scheme that is perhaps more important than the implementation complexity is the possibility of losing synchronization. If, as a result of channel errors, a non-maximal run length is mistaken for a maximum length run or vice versa, synchronization will be lost. A less efficient scheme, from a data compression view point, that avoids this difficulty is one which transmits the value of the next run regardless of the size of the run. The net data compression for this second run length scheme is of course

$$D_{cr12} \simeq \left\{ [N(1-p) + p] \frac{1 - p^{\lceil N/T \rceil T}}{1 - p^T} - p^{N-1} \right\} \frac{t + 1}{N} + \frac{4}{N}, \quad (10)$$

which is also plotted in Figure A-2. The small cost in data compression will be at least partially compensated for by the reduction in the error rate for the reconstructed data.

The final compression scheme considered in this report is known as "memory" or "end of run" encoding. In this scheme one indicates the location in memory of the transitions (or equivalently, the cumulative run length). Memory encoding requires a timing word of $\log_2 N$ bits and does not involve truncated runs. It is less efficient than the run length schemes, from a data compression viewpoint, as a consequence of these long timing words. Memory encoding is easier to implement, however, since one needs to transmit only timing information and since the timing word length is fixed. More important, the error rate for the reconstructed data is significantly lower for memory encoding since the errors are localized (a run-length error introduces errors over the entire remaining portion of the bit plane). It will turn out that from an energy compression viewpoint as well as an implementation viewpoint, memory encoding is preferable to run length encoding for reconstructed bit error rates of the order of 10^{-4} . The net data compression for memory encoding is

$$D_{cm} = \frac{N(1-p) + p - p^{N-1}}{N} t + \frac{4}{N}, \quad (11)$$

where $t \geq \log_2 N$. It is obviously convenient to make N a power of 2 and for the curve in Figure A-2 it is assumed that $N = 512$ ($t = 9$). An additional result from the energy compression analysis is that a buffer memory of the order of 128 bits is the preferred size.

ENERGY COMPRESSION FOR BINARY DATA

Let us assume a channel that is binary symmetric as a result of additive gaussian noise. The bit error rate (e_b) is related to the signal-to-noise ratio per bit (S/N) by

$$S/N = Q^2(1 - e_b), \quad (12)$$

where $Q(\cdot)$ is the inverse of the normalized gaussian cumulative distribution function. Let $R(\epsilon)$ be the error probability in the reconstructed data, or equivalently, the uncompressed bit error rate. The energy compression for binary Markov data becomes

$$E_c = \frac{Q^2 [1 - e_b]}{Q^2 [1 - P_r(\epsilon)]} \frac{1}{D_c}. \quad (13)$$

It remains for an error analysis to be performed in order to find the transmitted bit error rate (e_b) required to achieve a given bit error rate in the reconstruction data $[P_r(\epsilon)]$.

ERROR ANALYSIS FOR RUN LENGTH ENCODING

It follows from the rules of conditional probabilities that

$$P_r(\epsilon) = \sum_j P_r(\epsilon/j \text{ bit errors in transmitted data}) P_r(j), \quad (14)$$

where $P_r(j)$ is the probability of j bit errors in the transmitted data. Let t' be the number of bits associated with each timing word ($t' \geq t$), then

$$P_r(j) = \frac{t'(\bar{n}_t - 1)}{j} e_b^j (1 - e_b)^{t'(\bar{n}_t - 1) - j}. \quad (15)$$

Recall that the last run length word is not a timing word but an end of plane word that is assumed to be transmitted without error. For practical bit error rates ($e_b \leq 10^{-4}$) and practical memory sizes the probability of more than one error is much less than the probability of a single error. Since the energy compression is very insensitive to small changes in the error probability, a simplifying assumption which results in a completely negligible error is

$$P_r(\epsilon) \cong P_r(\epsilon/\text{a single bit error in transmitted data}) t'(\bar{n}_t - 1) e_b. \quad (16)$$

It is convenient to consider the second run length scheme first since loss of synchronization errors do not occur. Furthermore one need only consider the effect of errors in the timing words since errors in the data values can usually be detected and if not are localized to one run. It is easy to show that errors in the data values are entirely negligible relative to errors in the timing words. The problem has been reduced to finding the error probability in the reconstructed data when given a single error in the timing data. A further reduction is to condition the error probability on a single timing error in a run preceeding the run in which the given sample lies. This simplifies the analysis since the probability that a single timing error preceeds the run of a randomly selected sample given a single timing error is just equal to one half (see appendix, Lemma 1). Thus,

$$P_r(\epsilon) \cong P_r(\epsilon/\text{shift}) \cdot \frac{1}{2} t(\bar{n}_t - 1) e_b, \quad (17)$$

where $P_r(\epsilon/\text{shift})$ is the error probability of an arbitrary sample in the reconstructed data given that the entire run in which the sample lies has been shifted by k positions where k is some power of 2 less than or equal to $T/2$.

It is now convenient to expand the conditional probability $P_r(\epsilon/\text{shift})$ in the following way

$$P_r(\epsilon/\text{shift}) = \sum_r \sum_i \sum_k P_r(\epsilon_j \text{ rs}(k), \text{ss}(i), \text{rl}(r)/\text{shift}), \quad (18)$$

where the event $rs(k)$ corresponds to a shift in the run of k positions, the event $ss(i)$ corresponds to a shift in the sample in question by i positions beyond the original run, and the event $rl(r)$ corresponds to the run in which the sample lies being of length r . From the rules of conditional probability and the fact that the run length is independent of the shift error, we obtain

$$P_r(\epsilon, rs(k), ss(i), rl(r)/\text{shift}) = P_r(\epsilon/ss(i)) \times P_r(ss(i)/rl(r), rs(k)) \cdot P_r(rs(k)/\text{shift}) \cdot P_r(rl(r)). \quad (19)$$

Now $P_r(rl(r))$ is given by Equation (3). Also

$$P_r(rs(k)/\text{shift}) = \begin{cases} 1/t & \text{for } k = 1, 2, 4, 8, \dots, T/2 \\ 0 & \text{otherwise} \end{cases} \quad (20)$$

Furthermore

$$P_r(ss(i)/rl(r), rs(k)) = \begin{cases} 1/r & \text{if } i \leq k \leq r+i-1 \\ 0 & \text{otherwise} \end{cases} \quad (21)$$

Hence Equation (18) becomes

$$P_r(\epsilon/\text{shift}) = \sum_{r=1}^T \frac{1}{r} p^{r-1} (1-p) \sum_{i=1}^{T/2} P_r[\epsilon/ss(i)] \sum_{k=i}^{r+i-1} P_r(rs(k)/\text{shift}). \quad (22)$$

Now it is shown in the appendix (Lemma 2) that

$$P_r[\epsilon/ss(i)] = \frac{1}{2} [1 + (2p-1)^{i-1}] [1 - 2p^T] + p^T. \quad (23)$$

Observe that for untruncated runs this decreases monotonically from 1 to $1/2$ with increasing i , which agrees with intuition.

It is now straightforward to calculate $P_r(\epsilon/\text{shift})$ as a function of p from equations (20), (22), and (23) using digital techniques. One can then solve for $P_r(\epsilon)$ as a function of p from equations (6) and (17). As a result of the approximation, $P_r(\epsilon)$ is taken to be proportional to e_b . It is therefore straightforward to determine the energy per bit required to achieve a given bit error rate in the reconstructed data.

The energy compression for the second run length encoding scheme can now be calculated from Equation (13). The results are plotted in Figure A-4 for different length timing words and an assumed reconstructed bit error rate of 10^{-4} . Observe that if one wished to pick a fixed length timing word which gives reasonable energy compression for any arbitrary prediction probability, this timing word would probably be long relative to the size of the buffer memory. This is an indication that memory encoding could be relatively efficient.

For the first run length scheme there are two sources of error other than shift errors that are far more costly, but which are less likely to occur. First if one of the data samples used to distinguish between transitions and continuations is in error (relatively unlikely), then the rest of the block is in error with probability near unity (the next maximum length run will correct the

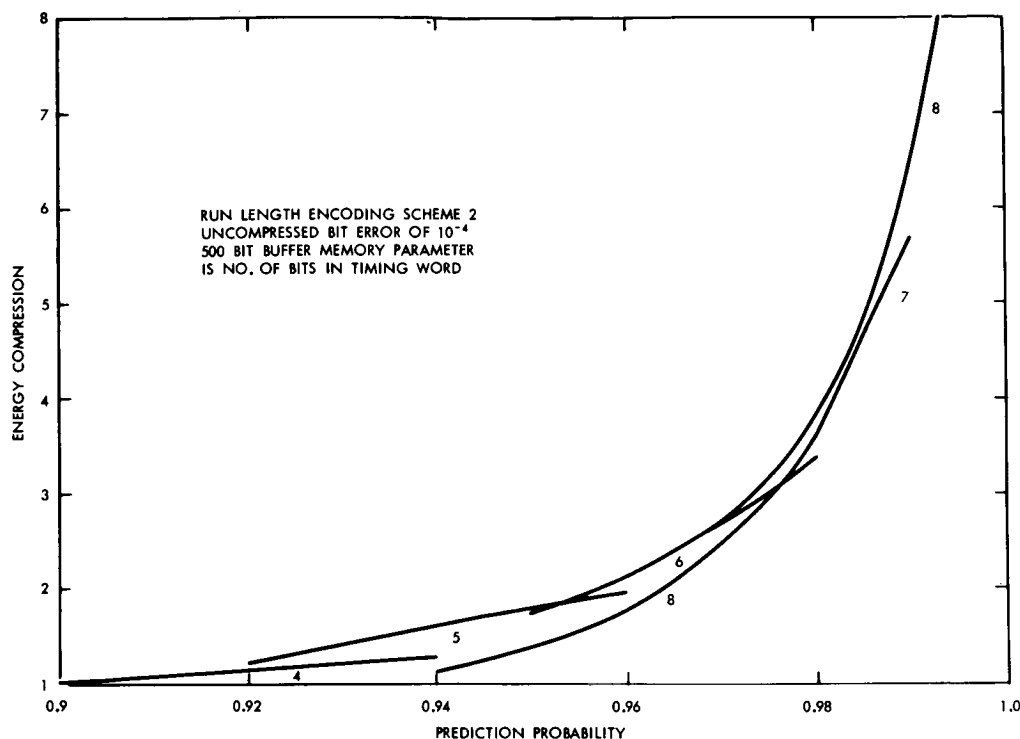


Figure A-4—Energy compression ratio for Markov binary data.

error). For this analysis it is sufficiently accurate to assume that the rest of the block is in error with probability one when this error occurs. Second, if one of the timing bits in the maximum length word is in error or if the error is such as to make a non-maximum length word appear as a maximum length word, then synchronization is lost and the remaining samples are in error with probability one half. These errors can be taken into consideration by rewriting Equation (17) as

$$P_r(\epsilon) \simeq P_r(\epsilon/\text{single prev. bit error}) \frac{1}{2} (t + p^{T-1}) (\bar{n}_\epsilon - 1) e_b, \quad (24)$$

where

$$P_r(\epsilon/\text{single prev. bit error}) = P_r(\text{error in data sample}) + \frac{1}{2} P_r(\text{losing sync}) + [1 - P_r(\text{losing sync}) - P_r(\text{error in data sample})] P_r(\epsilon/\text{shift}), \quad (25)$$

where $P_r(\epsilon/\text{shift})$ has been evaluated for the second run length scheme. It is reasonably straightforward to determine that

$$P_r(\text{error in data sample}) = \frac{1}{t+1} p^{T-1}, \quad (26)$$

and

$$P_r(\text{losing sync}) = p^{T-1} \left\{ \frac{t}{t+1} + \frac{1}{t} \sum_{n=0}^{t-1} p^{-2^n} \right\} \quad (27)$$

The previous analysis neglects the possibility that synchronization may have been lost in a previous bit plane. Let S be the probability of an undetected loss of synchronization in a previous plane. A more accurate expression for the error probability would be

$$P'_r(\epsilon) = \frac{1}{2} S + (1 - S) P_r(\epsilon). \quad (28)$$

This expression is difficult to work with even if one assumes that all synchronization losses go undetected since S depends on the number of previous planes and on the prediction probabilities of these planes. Fortunately, this corrected error probability is not significantly larger than that of Equation (24) and the difference should be hardly noticeable from an energy compression point of view.

The energy compression for the first run length encoding scheme is plotted in Figure A-5 where the probability of an undetected loss of synchronization in a previous plane has been ignored. Even though the error probability for the first scheme is somewhat larger than that of the second, it is still better as regards a comparison of energy compression. This is an indication of the insensitivity of energy compression to the error probability. For memory encoding, however, the error probability is significantly reduced and this effect shows up in the energy compression.

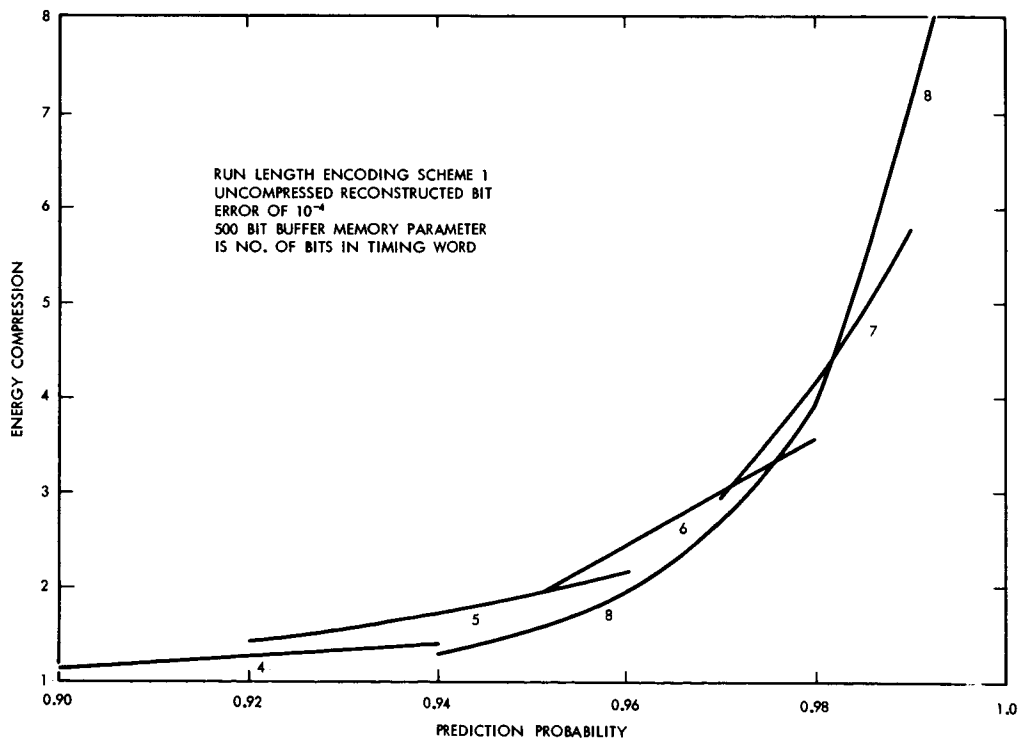


Figure A-5—Energy compression ratio for Markov binary data.

ERROR ANALYSIS FOR MEMORY ENCODING

In memory or end of run encoding there are three types of timing errors that we must distinguish. These three events are defined by

$E_1(k) = \text{shift of } k \text{ positions and } r_0 > k,$

$E_2(k) = \text{shift of } k \text{ positions and } r_0 + r_1 \leq k,$

$E_3(k) = \text{shift of } k \text{ positions and } r_0 \leq k < r_0 + r_1,$

where r_0 is the length of the run whose end of run timing word is in error and r_1 is the length of the pertinent adjacent run. The distinction between these events can perhaps be best understood by example.

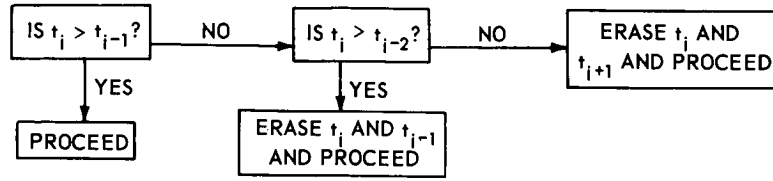
Run no.	1	2	3	4
End of run	6	18	30	42
PCM code	0000110	0010010	0011110	0101010
$E_1(8)$	6	26	30	42
$E_2(32)$	6	50	30	42
$E_3(16)$	6	18	14	42

Observe that for event one the memory locations remain monotonically increasing and hence the error is undetected. For event two it is clear that run number 2 is in error and some error correcting procedure at the receiver is indicated. For event three, either run number 2 or run number 3 is in error and some detection algorithm is also indicated. For this example an "optimum" detection algorithm (based on single errors) would correct events 2 or 3, however it should be clear that this is not always possible.

It is immediately obvious that an error analysis must depend on the detection algorithm used. After examining many examples, an optimum strategy for correcting single error for a PCM source code becomes apparent. One first enumerates all of the single bit changes that return the memory locations to a strictly monotone sequence. Given that event two has occurred, the middle bit in the sequence of ordered possible bit changes is changed. When the middle bit is undefined, either one of the two middle bits can be changed. Given that event three has occurred, the smallest possible bit change is chosen. This detection algorithm is somewhat difficult to implement and, considering the insensitivity of the energy compression to small changes in the reconstructed error probability, it would appear advantageous to consider simpler algorithms.

Possibly the simplest detection algorithm suggests itself by considering event three more closely. Given event three, the probability that there exists only one possible bit change capable of restoring the monotonicity of the end of run words (as in the example) is really quite small. If we exclude this possibility, a detection algorithm that turns out to be completely equivalent to the optimum algorithm for event three is to remove the two timing words in question. This algorithm results in a single run being in error (the average run length is conditioned on event three occurring and is smaller than the unconditioned average run length). This algorithm which is nearly optimal for event three is relatively inefficient for event two but nevertheless results in only one conditioned run being in error. It will be seen that the cost in energy compression of this simple algorithm relative to some optimal algorithm is minimal. A precise description of this algorithm is given by the following flow diagram where t_j represents the j^{th} timing word:

Detection Algorithm



Assuming this simple detection algorithm; let $\bar{N}_i(p)$ be the product of the average number of samples that are in error given event i has occurred times the probability of event i occurring. It follows that the average number of samples in error $\bar{N}_T(p)$ is given by

$$\bar{N}_T(p) = \sum_{i=1}^3 \bar{N}_i(p). \quad (29)$$

An approximation for the reconstructed error probability that involves the same assumptions as Equation 16 (single error analysis) is

$$P_r(\epsilon) \simeq \frac{\bar{N}_T(p)}{N} t(\bar{n} - 1) e_b, \quad (30)$$

where for memory encoding $t = \log_2 N$ and the runs are not truncated. The $\bar{N}_i(p)$ are given by the following set of equations:

$$\bar{N}_1(p) = \sum_k P_r[E_1(k)] \bar{r}_1(k), \quad (31)$$

$$\bar{N}_2(p) = \sum_k P_r[E_2(k)] \bar{r}_2(k), \quad (32)$$

and

$$\bar{N}_3(p) = \sum_k P_r[E_3(k)] \bar{r}_3(k) \quad (33)$$

where $k = 1, 2, 4, 8, \dots, N/2$ and $\bar{r}_i(k)$ is the average run length given a timing shift of k positions and the fact that event i has occurred.

Using the run length distribution of Equation (3) it is easily obtained that

$$P_r[E_1(k)] = \frac{1}{t} P_r(r_0 > k) = \frac{1}{t} p^k. \quad (34)$$

It follows from equations (31) and (34) that

$$\bar{N}_1(p) = \frac{1}{t} \sum_k k p^k. \quad (35)$$

Furthermore

$$P_r [E_2(k)] = \frac{1}{t} P_r (r_0 + r_1 \leq k) = \frac{1}{t} [1 - p^k - kp^{k-1} (1 - p)], \quad (36)$$

and

$$P_r [E_3(k)] = 1 - P_r [E_1(k)] - P_r [E_2(k)] = \frac{1}{t} kp^{k-1} (1 - p). \quad (37)$$

The conditioned average run length $\bar{r}_2(k)$ is given by

$$\bar{r}_2(k) = \sum_{r=1}^k r P_r (r_0 = r/r_0 + r_1 \leq k). \quad (38)$$

From the rules of conditional probability

$$P_r (r_0 = r/r_0 + r_1 \leq k) P_r (r_0 + r_1 \leq k) = P_r (r_0 = r) P_r (r_1 \leq k - r/r_0 = r) = r p^{r-1} (1 - p) [1 - p^{k-r}]. \quad (39)$$

Combining equations (32), (36), (38), and (39) one obtains

$$\bar{N}_2(p) = \frac{1}{t} \sum_k \sum_{r=1}^{k-1} r p^{r-1} (1 - p) [1 - p^{k-r}], \quad (40)$$

which can be written as (see appendix, Lemma 3)

$$\bar{N}_2(p) = \frac{1}{t} \sum_k \left\{ \frac{1 - p^k}{1 - p} - kp^{k-1} \left[1 + \frac{1}{2} (k - 1) (1 - p) \right] \right\}. \quad (41)$$

The conditional average run length $\bar{r}_3(k)$ is given by

$$\bar{r}_3(k) = \sum_{r=1}^k r P_r (r_0 = r/r_0 < k) = \sum_{r=1}^k r p^{r-1} (1 - p) / (1 - p^k). \quad (42)$$

This reduces simply to (see appendix, Lemma 4)

$$\bar{r}_3(k) = \frac{1}{1 - p} - \frac{kp^{k-1}}{1 - p^k}. \quad (43)$$

Combining equations (33), (37), and (43) one obtains

$$\bar{N}_3(p) = \frac{1}{t} \sum_k kp^{k-1} (1 - p) \left[\frac{1}{1 - p} - \frac{kp^k}{1 - p^k} \right]. \quad (44)$$

The $\overline{N}_i(p)$ can now be calculated from equations (35), (41), and (44) digitally and the reconstructed error probability can be determined from equations (29) and (30).

The energy compression ratio for memory encoding is plotted in Figure A-6 for a 512 bit buffer memory and a reconstructed bit error rate of 10^{-4} where the simple detection algorithm has been assumed. In addition to this curve an approximate unachievable upper bound on the energy compression is shown. This curve is calculated by setting $\overline{N}_2(p)$ to zero. The small difference between the energy compression for the simple algorithm and for some "optimal" algorithm shrinks as the size of the buffer memory decreases. This can be observed from Figure A-7 where a 128 bit buffer memory is assumed.

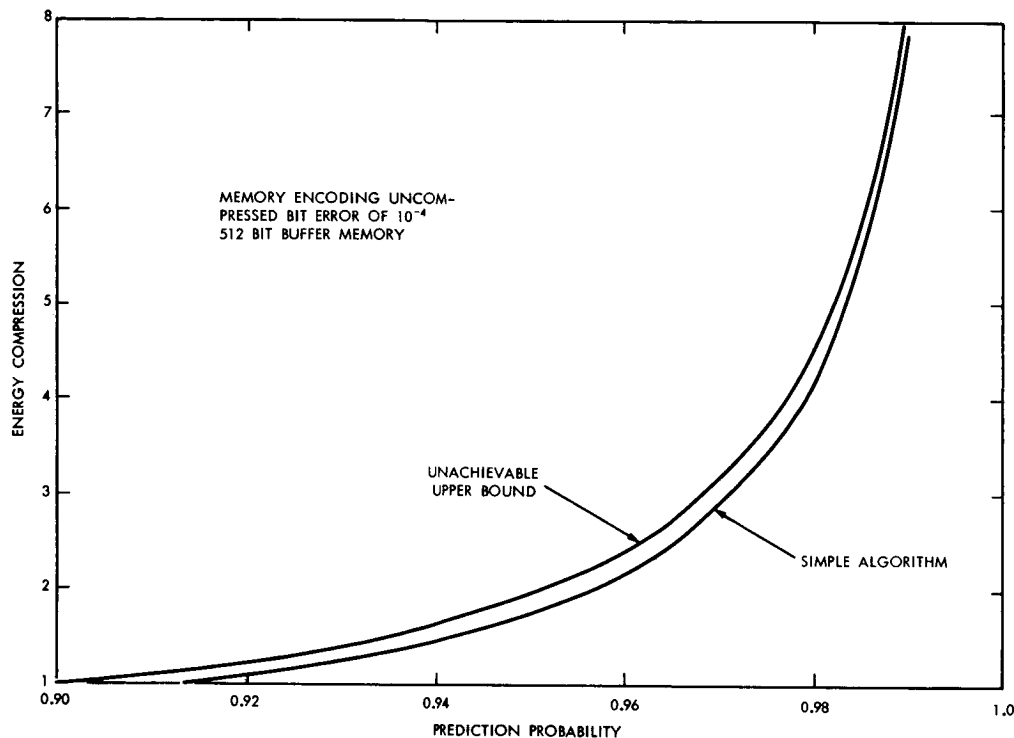


Figure A-6—Energy compression ratio for Markov binary data.

Observe from Figures A-6 and A-7 that the energy compression is larger for the smaller buffer memory. This is a result of a smaller error probability with only a negligible increase in the data compression. This effect continues only as long as the number of plane identification bits is a small fraction of the total number of bits. The energy compression for different sized buffer memories is shown in Figure A-8. It will be clear from the next section that for 4 bit plane identification relatively small memories are preferred. However, the size of the buffer memory does not substantially effect the energy compression.

Finally a comparison of the various compression schemes is given in Figure A-9. It is observed that memory encoding is at least as efficient for energy compression as run length encoding schemes using an optimum choice of timing words when the reconstructed bit error is 10^{-4} . It is definitely preferable to run length schemes that use a fixed timing word. For smaller bit error rates, the energy compression approaches the data compression and memory encoding compares slightly less favorably, however, considering the implementation simplicity there is little doubt that memory encoding is preferable regardless of the signal-to-noise ratio.

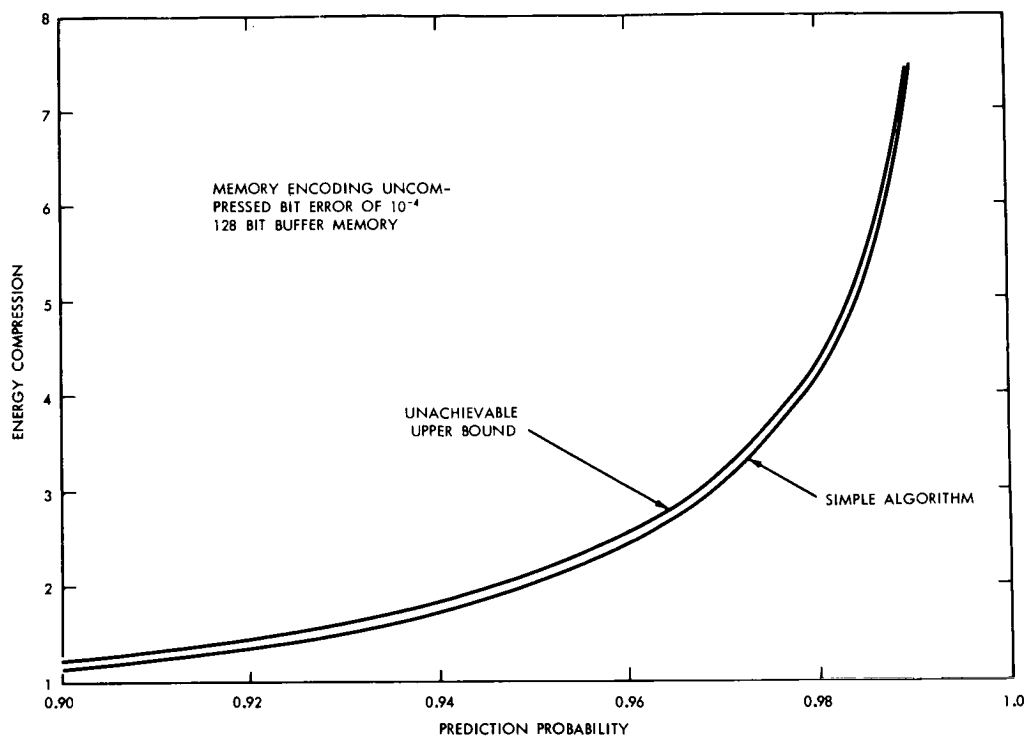


Figure A-7—Energy compression ratio for Markov binary data.

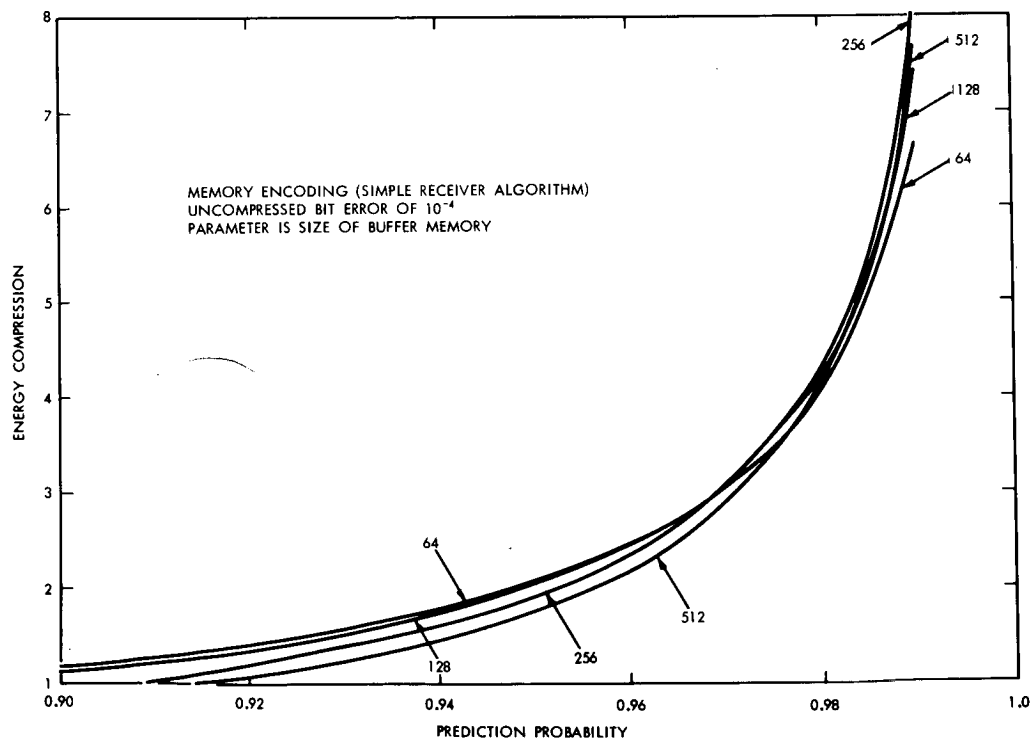


Figure A-8—Energy compression ratio for Markov binary data.

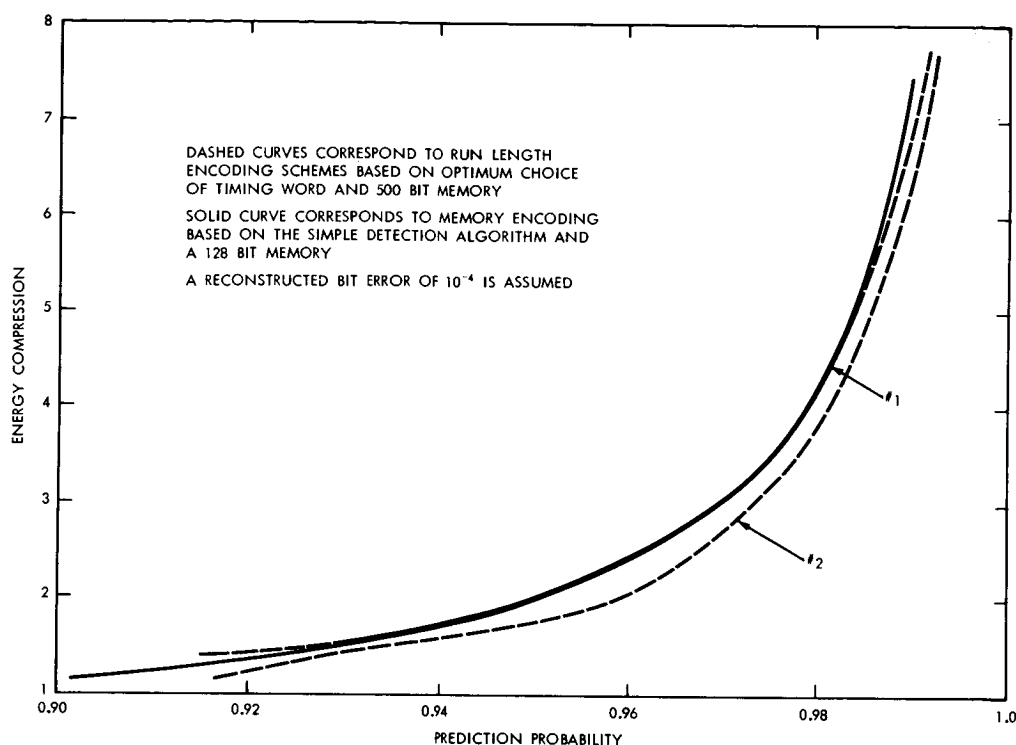


Figure A-9—Energy compression ratio for binary Markov sources.

NET ENERGY COMPRESSION FOR MARKOV PROCESSES

The over-all or net energy compression for any first order Markov process is given by

$$E_{cn}^{-1} = \frac{1}{\log_2 L} \sum_{i=1}^{\log_2 L} E_{ci}^{-1}, \quad (45)$$

where E_{ci} is the energy compression for the i^{th} bit plane and L is the total number of quantization intervals. As a result of the inverse property, the net energy compression is relatively insensitive to changes in the energy compression of the highest order planes. It follows (see Figure A-8) that small buffer memories (≥ 64 words) are preferable to large memories for good net energy compression.

The remaining step in calculating the net energy compression is to determine the prediction probabilities of the individual bit planes from the statistical model of the Markov source. This is purely a bookkeeping problem, however tedious, for a given source code. The simplest source model is one with equally likely levels and with the same symmetrical transition matrix for each of the levels. (The probabilities of transitions off the end are added to the probability of transferring to the end sample). Assuming a Gray code, useful formulas for determining the prediction probability of the i^{th} plane (p_i) as a function of the transition probabilities ($p(j)$ = prob of a change of j levels) are

$$p_i = 1 - \frac{2}{2^i} \sum_{j=1}^J jP(j), \quad (46)$$

for

$$i \geq 3 \text{ and } i \geq 1 + \log_2 3,$$

and

$$p_i = 1 - \frac{3}{4} p(1) - \left(\frac{6}{4} - \frac{1}{L}\right) p(2) - \left(\frac{7}{4} - \frac{3}{L}\right) p_3, \quad (47)$$

for

$$i = 1, 2.$$

The restricted range of validity of these formulas causes no problems for almost all cases of interest since either the transition matrix can be truncated to fit the formulas with negligible error or the prediction probabilities are too low to allow profitable compression ($p_i < 0.9$). The analysis of the example considered in this report can now be carried out in a straightforward manner.

EFFECT OF CHANNEL ENCODING

Channel encoding can be thought of as a means for energy reduction by increasing rather than decreasing the bandwidth. If, as in the case of some space telemetry systems, there is essentially unlimited bandwidth, then channel encoding can be used with or without data compression and the effect is merely to reduce the bit error rate for fixed signal-to-noise ratio. When bandwidth becomes an important design parameter, both bandwidth reduction as well as energy reduction have to be considered when comparing different compression schemes. One useful comparison might be energy compression for a fixed reduction in bandwidth. Those schemes that have a relatively large bandwidth reduction could then increase their energy compression by channel encoding.

Consider for example the use of an optimal Group Code (Reference 6) that converts seven bit data into an eleven bit word, (This particular code is chosen merely because 7 bit timing words have been assumed in the example). This code increases the bandwidth by a factor of 1.57 which is slightly more than the reduction obtained in bandwidth of the example by bit-plane compression. The resultant bandwidth is therefore slightly larger than the original bandwidth of the source. The additional energy reduction is given by

$$E_r = \frac{7}{11} \frac{S/N}{(S/N)',} \quad (48)$$

where

$$51 [1 - \Phi(\sqrt{(S/N)'})]^2 \cong 7 [1 - \Phi(\sqrt{S/N})], \quad (49)$$

where $\Phi(\cdot)$ is the normalized gaussian cumulative distribution function. Equation (49) follows from the fact that the optimum (7, 11) group code corrects all the single errors and 4 of the 55 possible double errors (Reference 6). In the example it has been assumed that the signal-to-noise ratio per bit for uncompressed planes is 13.831 ($e_b = 10^{-4}$). For the compressed planes the signal-to-noise ratio per bit should be slightly higher to achieve the same reconstructed bit error rate, however, the additional energy compression due to channel coding will be evaluated by setting $(S/N)'$ equal to 13.831. This increases the energy compression by a factor of 1.226. This additional energy compression increases as the bit error rate decreases. It seems that channel encoding using parity check techniques is not extremely powerful for energy compression and hence an energy compression comparison which ignores channel encoding for data compression schemes giving approximately the same bandwidth reduction is not unreasonable.

One possible use of channel encoding is to encode only those planes that have been compressed. This results in a much smaller increase in bandwidth and also in a smaller reconstructed bit error rate for the most significant planes than that of the uncompressed planes for a fixed signal-to-noise ratio per bit. This effect is desirable for most error criterion other than probability of error (say mean square error). As indicated previously, it should be possible, using the bit-plane technique, to employ channel encoding in such a way as to effectively minimize some error criterion for the reconstructed data (given a fixed increase in bandwidth).

REFERENCES

1. Schwartz, J.W., "Bit plane encoding of spacecraft data memories" (unpublished - submitted to the Transactions of the IEEE Space Electronics and Telemetry group).
2. Schwartz, J.W., "Data processing in scientific space probes" Ph.D. thesis, Yale University, 1964 (NASA NsG-138-61, Technical Note 5).
3. Davisson, L.D., "Information systems" Goddard Summer Workshop Report, 1966.
4. Cliff, R.A., "Coding an analog variable for constant percentage error" NASA TN D-2257, March, 1964.
5. Schaefer, D.H., "Logarithmic compression of binary numbers" Correspondence to the Proceedings of the IRE, V. 49 No. 7, July, 1961.
6. Slepian, D., "A class of binary signaling alphabets" The Bell System Technical Journal, V. 35, p. 203-234, January, 1956.

APPENDIX - PROOFS

Lemma 1. The probability that a randomly selected sample lies in a run which follows a timing error, given the occurrence of a single timing error, is one half.

Proof: Let n_t be the number of runs. The desired conditional probability is just

$$\frac{1}{n_t - 1} \left\{ \frac{N - r_1}{N} + \frac{N - r_1 - r_2}{N} + \dots + \frac{r_{n_t}}{N} \right\},$$

where r_i is the length of the i^{th} run. This follows since there are $n_t - 1$ timing words all containing the same number of bits. All of the run lengths are equally distributed and the average run length, given n_t runs, is clearly N/n_t . Hence averaging with respect to run lengths first yields

$$\frac{1}{n_t - 1} \sum_{j=1}^{n_t-1} (1 - j/n_t) = \frac{1}{2},$$

which is independent of the number of runs and gives the desired result.

Lemma 2. The probability that a binary Markov sample, which is i positions beyond a given run, has a different value than the samples in the given run is given by Equation (23).

Proof: The probability that the first sample following a run has a different value than the preceeding sample is just $1 - P_r(\text{run length} > T) = 1 - p^T$. The probability that the next sample is also different is just $p(1 - p^T) + (1 - p)p^T$. It follows, inductively, that the probability that the i^{th} sample following a run has a different value than the run $[P_r(i \text{ diff})]$ is given by

$$\begin{bmatrix} p & (1-p) \\ (1-p) & p \end{bmatrix}^{i-1} \begin{bmatrix} p^T \\ 1 - p^T \end{bmatrix} = \begin{bmatrix} 1 - P_r(i \text{ diff}) \\ P_r(i \text{ diff}) \end{bmatrix},$$

It is clear that $P_r(i \text{ diff})$ is equivalent to $P_r(\epsilon/ss(i))$, which is the conditional probability to be determined. One can now solve the preceeding equation in a straight forward manner resulting in Equation (23) of the text.

Lemma 3. The double sum expression of Equation (40) can be written as the single sum expression of Equation (41).

Proof: Equation (40) can be written as:

$$N_2(p) = \frac{1}{t} \sum_k \left\{ (1-p) \sum_{r=1}^{k-1} r p^{r-1} - p^{k-1} (1-p) \sum_{r=1}^{k-1} r \right\}.$$

Recognizing that

$$\sum_{r=1}^{k-1} r p^{r-1} = \frac{d}{dp} \left[\sum_{r=0}^{k-1} p^r \right]$$

and that

$$\sum_{r=0}^{k-1} p^r = \frac{1 - p^k}{1 - p}$$

it follows that

$$\sum_{r=1}^{k-1} r p^{r-1} = \frac{(1 - p)^r - r p^{r-1} (1 - p)}{(1 - p)^2}$$

Furthermore

$$\sum_{r=1}^{k-1} r = \frac{k(k-1)}{2}.$$

Equation (41) is obtained in a straightforward manner by combining these results.

Lemma 4. The average conditioned run length ($r_3(k)$) of Equation (42) reduces to Equation (43).

Proof: The proof follows trivially from the results of lemma 3 where it was shown that

$$\sum_{r=1}^{k-1} r p^{r-1} = \frac{(1 - p)^r - r p^{r-1} (1 - p)}{(1 - p)^2}.$$

THE FAN METHOD OF DATA COMPRESSION

Lee D. Davisson* 7

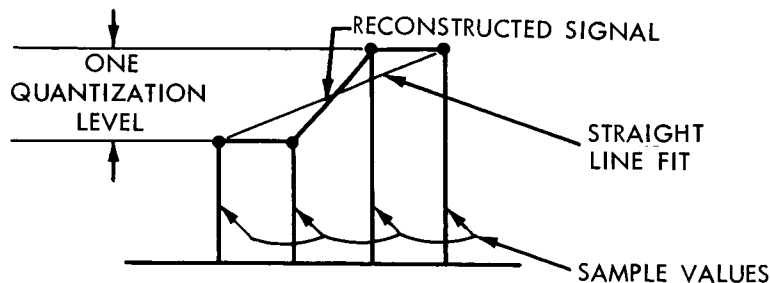
N 67-22743

One method which has been suggested for data compression relies on the approximation of the source time series by straight line segments. Starting from some initial point the line which minimizes the maximum error magnitude between the line and the data over the length of the line is found as a function of the distance from the starting time. The longest line for which the maximum error is below a given threshold is found and used to approximate the data. This procedure may be performed on the source data or on the sampled and quantized data. The encoded message contains information about the length of the line and its starting and ending points. The starting point may be fixed in the scheme as the final end point of the previous interval. In this case the code word length is reduced at the expense of decreased flexibility (i.e., degrees of freedom) in the interpolation scheme which may or may not result in a net compression ratio decrease. A scheme of the general class just described is called a "fan" method (Reference 1).

Because of the fixed nature of the method it may or may not closely approximate the "optimum" (i.e., a transmission rate close to the source entropy). As will be seen here, its capability relative to another method such as straight run length encoding (zero order hold), where the number of consecutive samples at a given level is transmitted, depends on the data source distribution. It will be shown that for the specific fan method chosen the scheme is inferior to run length coding for data of the TV type. It is suspected that an adaptive method of an "appropriate" type should always do at least as well.

Specifically, the fan method analyzed here is as follows:

1. The data is sampled and quantized.
2. No error is acceptable in the reconstructed data. If the line fitting the data does not go through one of the quantization levels, the data is reconstructed by rounding off to the nearest level as illustrated below:



If the line is half way between levels, the higher level is chosen, i.e., $2.5 \rightarrow 3$. Thus no error results between the reconstructed and original quantized values.

3. The starting point for a given line is the same as the final endpoint of the previous line.

*Princeton University, Princeton, N.J.

4. The message is encoded as a level-run length pair. The level is the final endpoint of the line, one of L levels, and the timing word is one of T possible "runs" between line endpoints.

5. The data is stationary.

ANALYSIS

In order to find the compression ratio for the fan method, the probability distribution of the line run lengths for a given data probability distribution is required. Supposed the $(g+1)$ st line segment has as its initial endpoint the level j and as its final endpoint the level k located n samples away. The probability of this occurrence is denoted by $p_{f,q}(j, k, n)$, which is read the probability that the $(q+1)$ st line from the beginning goes from level j to level k in n steps. The reason for the dependence on q even though the data is stationary will be mentioned shortly. Suffice it to say that, in general, as $q \rightarrow \infty$, the probability approaches a steady state value

$$p_f(j, k, n)$$

The average run length in terms of this probability is given by

$$\bar{n} = \sum_{j,k,n} n p_f(j, k, n)$$

Then the compression ratio is

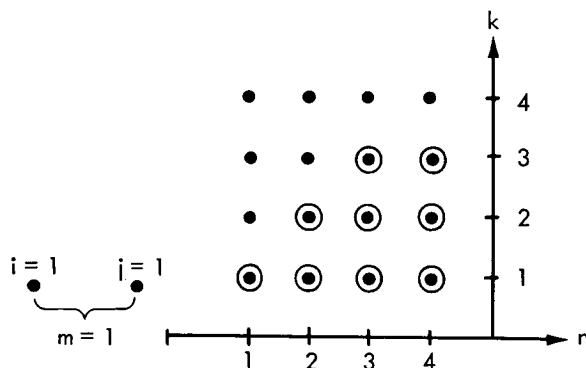
$$\frac{\log_2 T + \log_2 L}{\bar{n}}$$

It is important to note that, with the exception of the first line segment which has no predecessors, the probability $p_{f,q}(j, k, n)$ depends on the fan procedure as well as the data source probability distributions; thus the f subscript on the probability. That is, the probability of starting at level j and proceeding along a straight line to level k and no further in n steps is affected by the fact that the j^{th} level is the end point of the last line segment and thus that the preceding line segment could be extended no further. To illustrate this, consider the conditional probability of the event (j, k, n) given that the previous starting point was i and the previous run length was m , denoted by $p_f(j, k, n | i, j, m)$ which is read as "the probability of going from level j to level k in n steps given that the previous line was from level i to level j in m steps. Unlike the marginal probability, the conditional probability does not depend on q for reasons which will be seen shortly. Certain values of the conditional probability are zero independent of the data source distributions. For example:

$$p_f(1, 1, n | 1, 1, m) = 0 \text{ for } m < T.$$

This probability is zero because the occurrence of level 1 after $(1, 1, m)$ implies that the line connecting level 1 with level 1 in m steps could have been extended further, violating the fan conditions. Thus the effect of the fan procedure is to assign zero to certain values of the conditional probability

independent of the source statistics. To further illustrate this idea, in the following diagram for $L = T = 4$, those endpoints (values of (k, n)) which have probability zero are circled for $i = j = m = 1$:



Note that for every path from j to one of the encircled endpoints (k, n) , it is possible to make the line which starts at i longer. Let the set of points (k, n) where the conditional probability is zero for a given value (i, j, m) be denoted by S_{ijm} and the complement of this set, the remaining points, be denoted by S_{ijm}^c . Then in terms of the conditional probability of the data, $p_d(j, k, n, i, j, m)$, the desired fan conditional probability can be specified as:

$$p_f(j, k, n | i, j, m) = \begin{cases} 0 & \text{if } (k, n) \in S_{ijm} \\ \frac{p_d(j, k, n | i, j, m)}{P_d(S_{ijm}^c)} & \text{if } (k, n) \in S_{ijm}^c \end{cases} \quad (1)$$

where $P_d(S_{ijm}^c)$ is the data probability of occurrence of the set S_{ijm}^c given (i, j, m) has occurred:

$$P_d(S_{ijm}^c) = \sum_{(k, n) \in S_{ijm}^c} p_d(j, k, n | i, j, m) \quad (2)$$

Note that the data conditional probability does not depend on the fan procedure as contrasted with the "fan" conditional probability.

The conditional probabilities of Equation (1) can be calculated by straightforward (although, as will be seen, usually lengthy) calculations. It is clear then that the desired unconditional probabilities satisfy the equations

$$p_{fq}(j, k, n) = \sum_{i, j, m} p_f(j, k, n | i, j, m) p_{fq-1}(i, j, m) \quad (3)$$

$$j, k = 1, \dots, L$$

$$n = 1, \dots, T.$$

These equations can be solved for the probability desired as a function of the interval number q subject to the constraint that the initial value is determined only by the data, i.e.:

$$p_{f,0}(j, k, n) = p_d(j, k, n) \quad (4)$$

Let the fan conditional probability matrix be denoted by Π and the desired probability column vector be given by π_q . Then (3) can be put in the matrix form:

$$\pi_q = \Pi \pi_{q-1} \quad (5)$$

Proceeding recursively and using Equation (4), this becomes

$$\pi_q = \Pi^q \pi_0$$

As $t \rightarrow \infty$, it can be shown that under very general conditions* π_q approaches a limit π_∞ which is independent of π_0 and satisfies the equation:

$$\pi_\infty = \Pi \pi_0 \quad (6)$$

COMPUTER RESULTS

Unfortunately, it is not practical to solve Equation (6) directly. Note that the matrix Π contains $L^3 T^2$ elements. Typically for $L = 16$, $T = 16$, this is $16^5 \approx 10^6$ elements. However, a recursive solution based on Equation (5) is possible. Since $\pi_q \rightarrow \pi_\infty$, the compression ratio $C_q \rightarrow C_\infty$. Thus one need only calculate enough steps so that $|C_q - C_{q-1}|$ is less than some threshold.

Even with the recursive solution the computations are lengthy since $L^3 T^2$ probabilities must be recalculated after every step**. It is difficult to estimate precisely how many machine cycles are required to find each probability vector π_q due to the complexity of the logic required. Figure A-10 is a simplified computer flow diagram of a program developed to solve for the compression ratio for given source probability distributions.

One economy made in the programming was the bypass of most of the calculations when the data probability $p_d(i, j, m)$ is sufficiently small (i.e., $< \epsilon_1$). The following table gives representative running times on the IBM 7094 for the first order Markov process shown next to the table. $p(\cdot | \cdot)$ is the process one step transition probability.

<u>L</u>	<u>T</u>	<u>Time (min)</u>	<u>Markov process</u>
4	8	1	$p(i/j) = \begin{cases} 0; & i-j \geq 2 \\ p; & i=j \\ 1-p; & i=j+1 = 2 \text{ or } i=j-1 = T-1 \\ 1-p/2; & i=j \pm 1, 1 < j < T. \end{cases}$
4	16	2	
8	8	3	
8	16	10	
16	16	73	

*Roughly speaking the conditions are satisfied if all line sequences (j, k, n) of nonzero probability occur infinitely often in an infinite sequence of values. This is always true in practice. See (Reference 2) for a more precise statement.

**If disk storage were available, this requirement might be eliminated. However, the seek transfer time between disk and core then becomes significant.

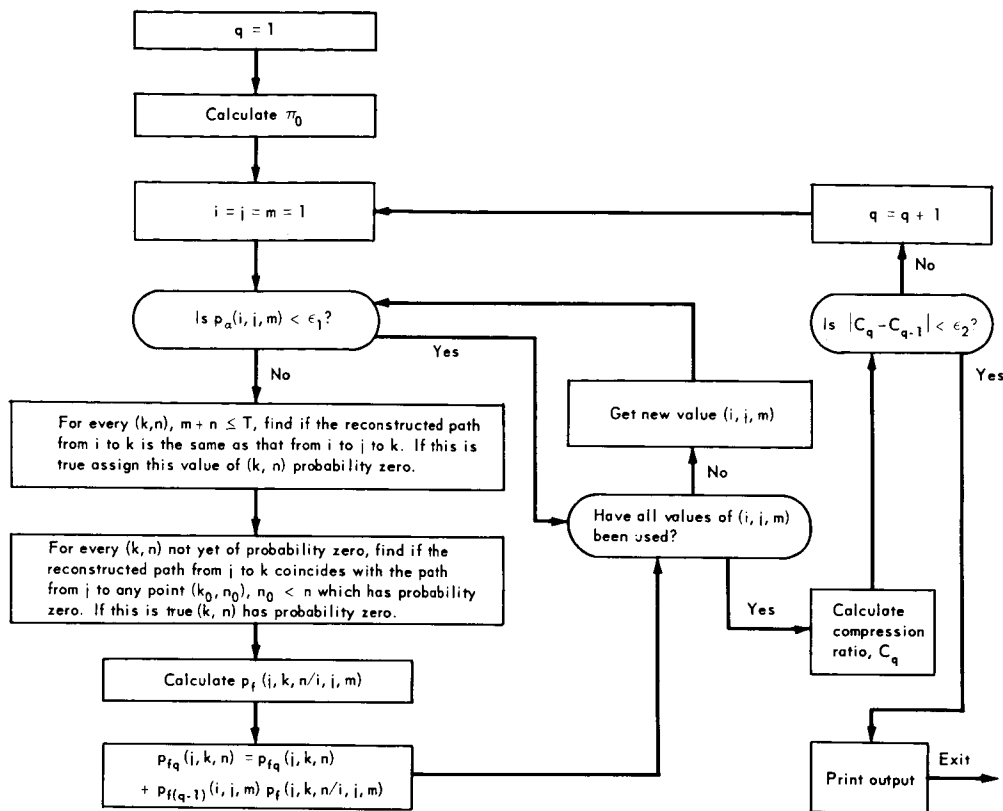


Figure A-10-Computer flow diagram.

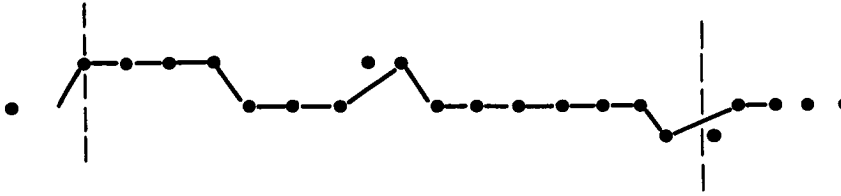
As suspected, the amount of running time goes up sharply with $L^3 T^2$. Because of this the numerical results given shortly are confined to $L = 8$.

The particular Markov process chosen for the example is a simplified model for TV data which has been found empirically to be approximately first order Markov with the highest transition probability being from the present level to the same level in one step. The rest of the probability weight is primarily on the neighboring levels.

The data generated by this model for "large" values of p , say $p > .7$, would be predominated by a sequence of straight level lines of average length given by:

$$(1-p) \sum_{n=0}^{\infty} np^n = \frac{1}{1-p},$$

with occasional rising and falling sequences of isolated points forming nonlevel lines. For these values of p the simple zero order hold or run length method of encoding can be expected to be superior to the fan method. The reason for this is illustrated by the following figure of a "typical" sequence generated by the above source:



Between the dashed lines the fan method requires 8 lines whereas simple run length coding requires only 5 messages.

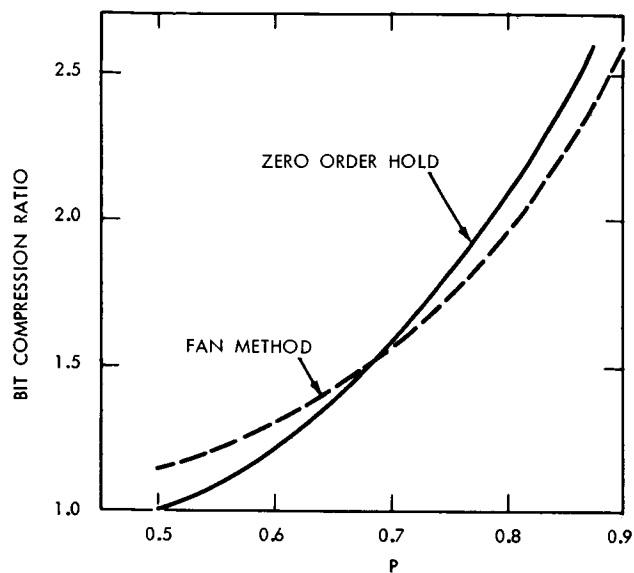
On the other hand, if p is "small," say less than 0.5, rising and falling sequences tend to dominate the data and the fan method is superior to the zero order hold predictor. Unfortunately, the advantage in this case is of no use since the resulting compression ratio over straight PCM encoding is small.

Figure A-11 bears out this reasoning. Figure A-11a is the bit compression ratio as a function of p for 8 quantization levels (3 level bits) and 8 timing words (3 run length bits) where Figure A-11b is for 8 levels and 16 run lengths. Note that for reasonable compression ratios one would favor the zero order hold system. In both cases the compression ratio curves cross at about $p = 0.7$. Thus one can tentatively conclude that for TV data at least, this fan method should not be used.

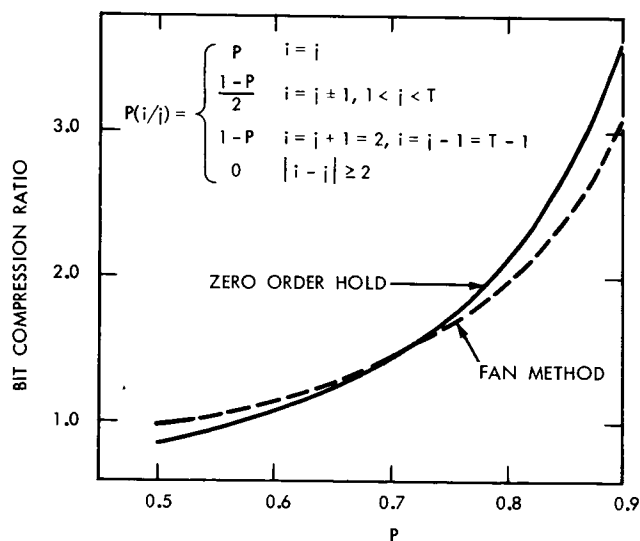
One cannot conclude, however, that this fan method is inferior for all kinds of data. For data which has statistical dependence beyond the previous sample, that conclusion is certainly not valid. Consider the following second order Markov process where the most probable level based on the immediate past is the extrapolation of the last 2 points if this is one of the L levels and the closest of the top or bottom levels if this is not so:

$$P(k | j, i) = \begin{cases} \begin{cases} k = 1, & 2j - i \leq 1 \\ 1 \leq k = 2j - i \leq T \\ k = T, & 2j - i \geq T \end{cases} & p_i \\ \frac{1-p}{2}; & k = 2j - i \pm 1, 1 < 2j - i < T \\ 1 - p; & k = 2j - i + 1 = 2 \text{ or } k = 2j - i - 1 = T - 1 \\ 0 & \text{elsewhere} \end{cases}$$

For these data there tends to be many non-level straight line-runs so that one would expect the fan method to have the advantage. Analytical results bear out this expectation. Figure A-12 presents the bit compression ratios for each system as a function of p for 8 quantizing levels and 8 and 16 run length words. Note that the fan method is indeed the better performer.

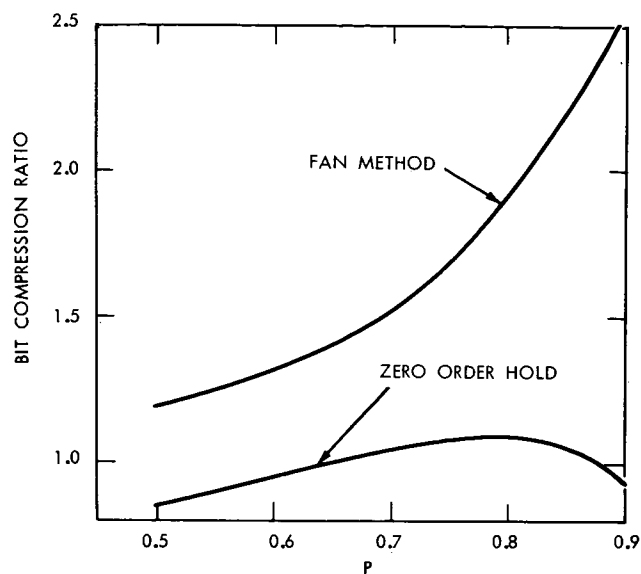


(a) $L = 8, T = 8$

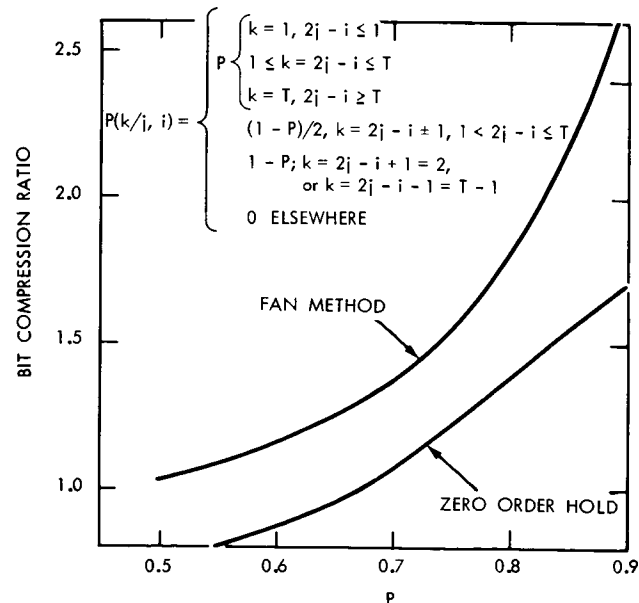


(b) $L = 8, T = 16$

Figure A-11—Compression ratio for the zero order hold and for methods for a first order Markov hold.



(a) $L = 8, T = 8$



(b) $L = 8, T = 16$

Figure A-12—Compression ratio for the zero order hold and fan methods for a second order Markov process.

CONCLUSIONS

The choice of a predictor should be based on the data distributions. Because of the lack of uniform superiority of predictors of a fixed nature, it is perhaps better to use some adaptive technique if an accurate data model is lacking.

REFERENCES

1. Gardenhire, L. W., "Redundancy reduction - the key to adaptive telemetry." 1964 National Telemetering Conference. Proceedings June 2-4, 1964, Los Angeles, Calif., New York, N.Y., The Institute of Electrical and Electronics Engineers. Paper No. 1-4.
2. Parzen, E., Modern Probability Theory and Its Applications. John Wiley & Sons, New York, N.Y.

OK

THE CONCEPT OF ENERGY COMPRESSION RATIO AND ITS APPLICATION TO RUN LENGTH CODING

L. D. Davisson* 7

N 67-22744

In many, if not most, digital communications applications, the sampling and hence transmission rate is set too high most of the time so that the periods of maximum data interest can be accommodated. It is a well known fact that this is the case for TV data and most telemetry data. This has aroused the interest of numerous people who have developed schemes for the removal of unnecessary or "redundant" data prior to transmission in an attempt to make the communication more efficient. Such systems are called data compression systems. Usually these schemes attempt to take advantage of the inherent predictability or smoothness of the data during inactive periods. Only those samples which can not be predicted or fit by a polynomial of some fixed degree, usually a straight line segment, are transmitted. Perhaps the simplest such system is the run length or zero order hold predictor method wherein a message is only transmitted when the quantization level of the data changes. At this time the level and the number of times it repeats, called the run length, are sent.

Many publications (References 1 through 10 to name a few) have appeared on data compression methods. Unfortunately there is yet no uniform standard by which to compare these methods and in almost every case there is insufficient data within the papers with which to apply such a standard. For example, in every instance, it is assumed that the compressed data are encoded and transmitted over a noiseless channel or at least that the noise has a negligible effect on the reconstructed data. The purpose of this paper is to propose certain criteria by which various compression schemes can be compared and to demonstrate the overwhelming importance of noise through typical system calculations. Specifically, the computations are applied to the run length coding scheme described above. By using the same analytical techniques, Kelly and Kanefsky have obtained results for other coding schemes of the same general class. Their results also appear within this Summer Workshop Report.

ENERGY COMPRESSION RATIO

In the literature, various figures of merit have been proposed for the evaluation of data compression systems. Perhaps the most common (and least meaningful) is the "element" or simply "data" compression ratio defined as the ratio of the sampling rate to the nonredundant or nonpredictable sample rate. This is not too useful because it neglects the effect of coding on the transmission rate. It is clear that the actual reduction in transmission rate must be somewhat smaller than that given by the element compression ratio because of the necessity of transmitting spacing or timing information for the transmitted samples in addition to the samples themselves. It is clear, then, that the actual reduction in transmission rate is smaller than the data compression ratio, the precise amount by which it is less being tied up with the method of coding. A second definition (see Reference 10) intended to remove the preceding objection is the "bit" compression ratio which is defined as the ratio of the bit transmission rate for uncompressed data to that for compressed data including coding. The major drawback to this definition is that the effect of channel errors on data quality is ignored. Unfortunately, the effect of the always present bit errors has differing effects on different compression schemes and, at least in general, for the same channel, data which is compressed transmitted and reconstructed is noisier than it would be if sent

*Princeton University, Princeton, N.J.

uncompressed. The reason for this is clear. The removal of some of the samples makes the correct reception of the remaining samples with their accompanying timing information more critical. In light of this, it seems unreasonable to compare two systems on the basis of bit rate alone.

Thus a new basis for the comparison of transmission systems is required. From the above considerations it seems reasonable to define the system energy compression ratio, the ratio of the average energy required to send a sample in an uncompressed communication system to that required in a proposed compression system for the same data quality. This ratio is a function of the bit error rate in the compression system. Clearly, as the error rate goes to zero the energy compression ratio approaches the bit compression ratio. On this basis it is possible to determine the exact value of a given scheme relative to another scheme. The measure of data quality can be chosen as the average value of any desired cost function although usually the mean square error or sample probability of error is chosen.

It will be shown in succeeding sections that the effect of channel errors can be quite significant, resulting in an energy compression ratio which is markedly below the bit compression ratio for typical error rates (i.e., around 10^{-5} bits/bit).

ENERGY COMPRESSION RATIO FOR RUN LENGTH CODING

To illustrate the above ideas, the energy compression ratio is calculated for a particular coding scheme under particular assumptions about the data and channel probability models. Specifically, these are:

1. The data is encoded in blocks of N samples (e.g., a TV line) for which there are no synchronization errors and the synchronization word is of negligible length compared with the block length. These restrictions will be removed in a future publication.
2. Within each block the data is run length encoded as a level-run word pair. The level word is one of L levels and the run length, the number of times the sample is repeated, is one of T values. Each value is PCM encoded.
3. The data is a first order Markov chain with a probability p , called the probability of prediction, of remaining at the same level independent of the level (which approximates the situation for TV data). The other transition probabilities can be chosen arbitrarily.
4. The channel is binary symmetric with error rate r bits/bit. Specifically the bits are coherently transmitted in white Gaussian noise. The latter requirement makes it possible to make energy calculations and could readily be modified.
5. The data quality measure is the average cost, where the cost of deciding level i , given level j to be the correct level, is given by an arbitrary matrix, s , with elements s_{ij} .

In this method errors are caused by timing errors up to the sample chosen or by a level word error or a combination of both. The details of the calculations based on the above 5 conditions are extremely involved and are therefore relegated to the appendix. Generally speaking, the method involves the calculation of the probability that h timing word errors have preceded a randomly selected sample times the average cost of h timing errors. This expression can be evaluated numerically starting with one error and summing until further errors contribute little to the average cost. (For the particular cost function which is the probability of error, ($s_{ij} = 0$, $s_{ij} = 1$, $i \neq j$), it is possible to get upper and lower bounds. These bounds approach each other as the accumulated effects of 1, 2, 3, ..., errors are accounted for. When the bounds are sufficiently close, the computations cease.) Then the channel bit error rate for the same average cost for uncompressed data transmission can be calculated. The ratio of the energies required per sample

for the compressed and uncompressed transmission systems is computed. This is the required energy compression ratio.

NUMERICAL RESULTS

To illustrate the nature of the energy compression ratio and the effect of timing errors on the received data, the probability of received sample error is used as the data cost function or quality measure ($s_{ii} = 0$, $s_{ij} = 1$, $i \neq j$). It will be seen that the probability of received sample error is many times greater in the compressed system than in the uncompressed system for the same bit error rate. The following system parameters are used as being "typical" (specifically, as being typical of TV data):

$$\begin{aligned} N &= \text{block length} = 500 \text{ (e.g. elements in a TV line)} \\ L &= \text{number of levels} = 16 \\ T &= \text{maximum run length} = 16 \\ p &= \text{probability of prediction} = 0.8 \text{ or } 0.9 \end{aligned} \quad (1)$$

The complete Markov transition probability matrix places all the probability weight on the same level and its neighbors. That is:

$$P_r(k|m) = \begin{cases} p & k = m \\ \frac{1-p}{2} & k = m \pm 1 \quad 1 < m < T \\ 1-p & k = m - 1 = T - 1 \text{ or } k = m + 1 = 2 \\ 0 & \text{elsewhere} \end{cases} \quad (2)$$

For the values of (1), the approximate solution of Equation (A-21) for the probability of error is

$$P_e = 146.9 \frac{r_T}{C_d} + r_2 \quad (3)$$

where $r_L = r_T$ is the level word error rate. Hence

$$P_e = \left(\frac{146.9}{C_d} + 1 \right) r_2 \quad (4)$$

Thus for the same error rate, the ratio of compressed sample error rate to uncompressed sample error rate, P_u , is

$$\frac{P_e}{P_u} = \frac{146.9}{C_d} + 1 \gg 1.$$

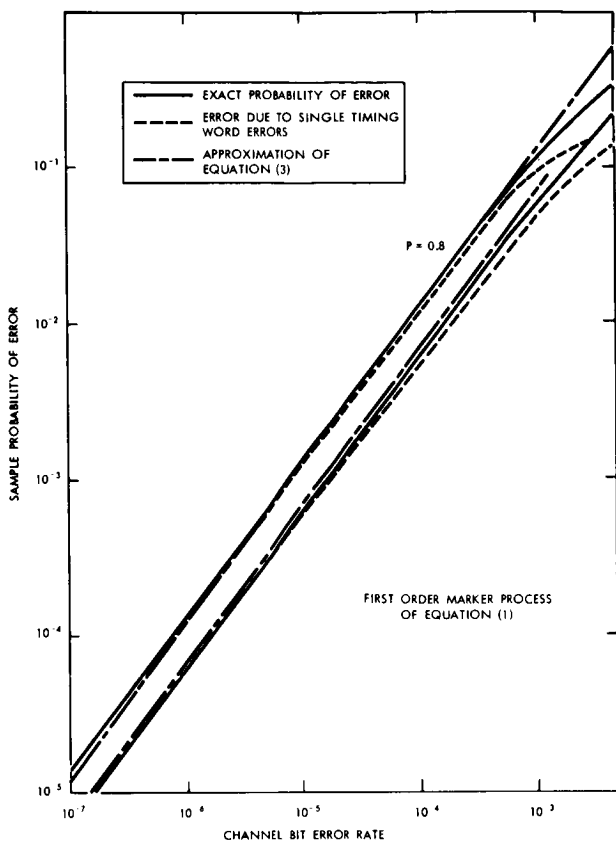


Figure A-13—Sample error rate vs. channel error rate, probability of prediction = P , number of levels, $L = 16$, max run length, $T = 16$, block length $N = 500$.

In fact for the values of $p = 0.8$ and 0.9 :

$$\frac{P_e}{P_u} = 32.2 \quad p = 0.8 \quad (5)$$

$$= 18.2 \quad p = 0.9$$

Figure A-13 presents the exact probability of error as a function of channel bit error rate together with the error due to single bit errors and the approximate solutions of Equation (4) (here $r_L \approx 4 \times$ channel bit error rate) and Equation (5). It is seen that for the region of usual interest, the errors are primarily due to single timing word errors and that the approximate solutions of Equations (4) and (5) is quite good. In any computations as complicated as these, errors are possible. Hence a simulation was performed with a 5 percent confidence interval at a level of confidence of 90 percent. Excellent agreement was found. From Equation (5) it is apparent that energy compression ratios that are much less than the bit compression ratio can be expected. Figure A-14 bears this out. Even for a channel bit error rate of 10^{-7} the energy compression ratio is not close to the bit compression ratio.

Placing equal energy in the timing and level bits is not the most efficient use of the average energy available as indicated by Equation (3). Figure A-15 is a plot of the

energy compression ratio as a function of the ratio of the timing word energy per bit and the level energy per bit for fixed average energy. Note that a significant improvement can be expected by doing this. An improvement that is on the order of 15 percent can apparently be gained.

FURTHER COMMENTS

Many problems remain to be investigated. For example, the synchronization problem was ignored. Without allowing energy for synchronization, the energy compression ratio could be made to approach the bit compression ratio by making N small. However, this is not reasonable since energy must be used in synchronization. The tradeoff point between synchronization energy and block length must be found. This in turn is tied up with an "optimum" synch word.

A second problem is the use of error correcting codes to improve the energy compression ratio. This can readily be done within the framework of the preceding sections.

The application to channels which are bandwidth constrained and to those channels with "memory" (e.g. telephone lines) need further investigation.

Finally the energy compression for non-Markov data can be investigated. It is clear that the above results can be modified to handle any prediction system where the prediction probability is constant and sample-to-sample independent. This remains to be accomplished.

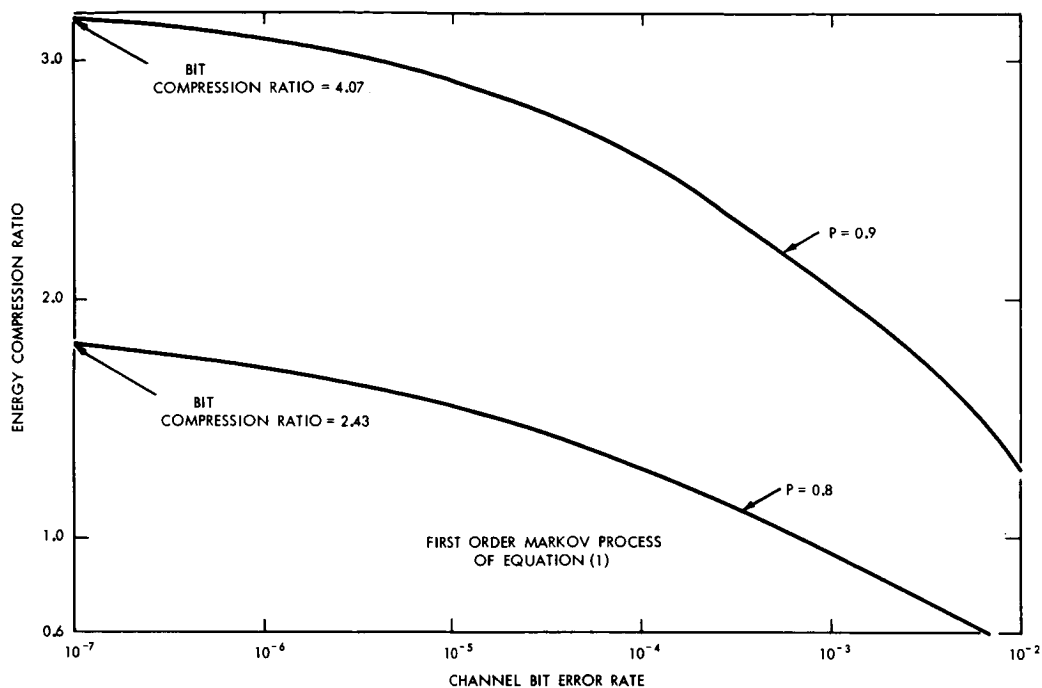


Figure A-14—Energy compression ratio as a function of bit error rate, probability of prediction = P ; number of levels, $L = 16$; max run length $T = 16$; block length, $N = 500$.

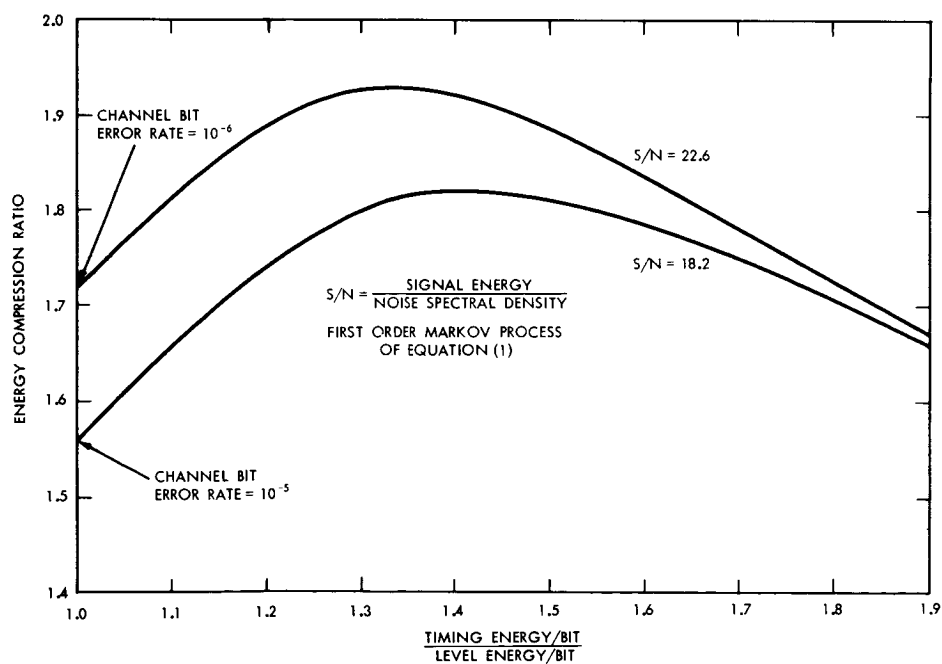


Figure A-15—Energy compression ratio V vs. ratio of timing and level energies per bit for fixed average energy, probability of prediction, $P = 0.8$; number of levels, $L = 16$; max run length, $T = 16$; block length, $N = 500$.

REFERENCES

1. Weber, D. R. and F. J. Wynhoff, "The concept of self-adaptive data compression." 1962 National Symposium on Space Electronics and Telemetry. PGSET Record. October 2-4, 1962, Miami Beach, Florida. New York, N.Y., The Institute of Radio Engineers, Paper No. 4.1.
2. Schomburg, R. A., "Computer simulation of a data compressor for aerospace telemetry systems." 1962 National Symposium on Space Electronics and Telemetry, PGSET Record. October 2-4, 1962, Miami Beach, Florida. New York, N.Y., The Institute of Radio Engineers. Paper No. 4.2.
3. Hulme, J. R. and R. A. Schomburg, "A data bandwidth compressor for space vehicle telemetry." 1962 National Telemetering Conference Proceedings. May 23-25, 1962, Washington, D.C., New York, N.Y., The Institute of Radio Engineers. Paper No. 3-2.
4. Sommer, R. C. and B. Harris, "Some recent advances in adaptive digital space telemetry systems." 1962 National Telemetering Conference Proceedings. May 23-25, 1962, Washington D.C., New York, N.Y., The Institute of Radio Engineers. Paper No. 10-5.
5. Medlin, J. E., "Buffer length requirements for a telemetry data compressor." 1962 National Telemetering Conference Proceedings. May 23-25, 1962, Washington, D.C., New York, N.Y., The Institute of Radio Engineers. Paper No. 14-5.
6. Gardenhire, L. W., "Redundancy reduction-the key to adaptive telemetry." 1964 National Telemetering Conference Proceedings. June 2-4, 1964, Los Angeles, California, New York, N.Y., The Institute of Electrical and Electronic Engineers. Paper No. 1-4.
7. Blasburg, H. and R. Van Blarckom, "Message compression." IRE Transactions on Space Electronics and Telemetry, SET-8: 228-238, September 1962.
8. Balakrishnan, A. V., "An adaptive non-linear data predictor." 1962 National Telemetering Conference Proceedings. May 23-25, 1962, Washington, D. C., New York, N.Y., The Institute of Radio Engineers. Paper No. 6-5.
9. Davisson, L. D., "A theory of adaptive data compression," Advances in Communication Systems, v. 2, Academic Press.
10. Davisson, L. D., "Data compression and its application to video signals," Final Report of the Goddard Summer Workshop Program, 1965.

APPENDIX

ANALYTICAL COMPUTATIONS

Note that timing errors accumulate with each succeeding transmission. That is, the j^{th} run is reconstructed starting at the end of the reconstructed $(j-1)$ st run. The analytical computations proceed by defining the contribution to the average cost, \bar{S}_h , which is due to the presence of h timing errors prior to a randomly chosen sample and then summing over h :

$$\begin{aligned}\bar{S} &= \text{average cost} \\ &= \sum_{h=0}^{\infty} \bar{S}_h\end{aligned}\tag{A-1}$$

\bar{S}_h is found by evaluating an appropriately chosen sequence of joint probabilities. The choice is governed solely by ease of computation and was found by a process of trial and error. For a different system of coding a different approach may be required. Specifically, if $\bar{S}(\Delta)$ is the average cost due to an accumulated timing error of Δ prior to a randomly chosen sample (which does not depend on h), then:

$$\bar{S}_h = \sum_{\Delta} \bar{S}(\Delta) \Pr(\Delta, h)\tag{A-2}$$

where $\Pr(\cdot)$ is used as a generic notation to denote the probability of the enclosed event or value occurring in (A-2)

$\Pr(\Delta, h)$ = probability that h timing errors have occurred prior to a randomly chosen sample resulting in an accumulated timing error of Δ .

The evaluation of $\bar{S}(\Delta)$ will be postponed for the moment. Turning to the evaluation of $\Pr(\Delta, h)$, a further expansion is made. Suppose a randomly selected sample is in the j^{th} transmitted run and t_i = value of the i^{th} run length (timing word) where an error has occurred. Then:

$$\Pr(\Delta, h) = \sum_{\{t_i\}} \Pr(\{t_i\}) \sum_{j=h+1}^{\infty} \Pr(\Delta | h, j, \{t_i\}) \Pr(h | j, \{t_i\}) \Pr(j | \{t_i\})\tag{A-3}$$

where $\Pr(\cdot|\cdot)$ denotes conditional probability and where the above probabilities are broken down in terms of j , the number of runs which have occurred up to and including the randomly selected sample and in terms of the h run lengths, $\{t_i; i \in 1, \dots, j-1\}$, the correct values of the h timing words where the errors have occurred. The probability of h timing errors prior to a sample in the j^{th} run obviously increases with j but is independent of the values $\{t_i\}$. In fact:

$$\Pr(h|j, \{t_i\}) = \binom{j-1}{h} r_T^h (1-r_T)^{j-h-1} \quad (\text{A-4})$$

where:

r_T = timing word error rate

$$= 1 - (1-r)^{\log_2 T}$$

r = channel error rate

T = number of possible encoded run lengths.

The probability that a randomly chosen sample is in the j^{th} run given $\{t_i\}$ is proportional to the length of the j^{th} run whose probability distribution is affected by its position in the data. Specifically

$$\Pr(j|\{t_i\}) = \sum_{\sigma_{j-h-1}=0}^{N-1} \sum_{t_j=1}^T \frac{t_j}{N} \Pr(t_j|\sigma_{j-h-1}, \{t_i\}) \Pr(\sigma_{j-h-1}) \quad (\text{A-5})$$

where the sum of the $j-h-1$ timing words preceding the j^{th} run and excluding the set $\{t_i\}$ is

$$\sigma_{j-h-1} = \sum_k' t_k$$

where the ' denotes summation over the aforesaid set.

The run lengths are independent random variables due to the first order Markov dependence of the data except for the last run in a block which is truncated. Their probability density is:

$$\begin{aligned} \Pr(t) &= p^{t-1} (1-p) & t < T \\ &= p^{T-1} & t = T \\ &= 0 & \text{otherwise.} \end{aligned}$$

The characteristic function of the run lengths is

$$\begin{aligned}\phi(e^{i\lambda}) &= \sum_{t=1}^T e^{it\lambda} P_r(t) \\ &= e^{i\lambda} \frac{1-p + p^{T-1}(e^{i(T-1)\lambda} - e^{iT\lambda})}{1-pe^{i\lambda}}\end{aligned}$$

In terms of this characteristic function:

$$\Pr(\sigma_{j-h-1} = n) = \frac{1}{2\pi} \int_{-\pi}^{\pi} e^{-in\lambda} \phi^{j-h-1}(e^{i\lambda}) d\lambda. \quad (\text{A-6})$$

The last run in a block of length N is truncated. This affects the conditional probability of t_j as shown by:

$$\begin{aligned}\Pr(t_j | \sigma_{j-h-1}, \{t_i\}) &= p^{t-1}(1-p); \quad t < T \text{ and } \sigma_{j-h-1} + \sum_{i=1}^h t_i < N \\ &= p^{t-1} \quad ; \quad t \leq T \text{ and } \sigma_{j-h-1} + \sum_{i=1}^h t_i = N \\ &= 0 \quad ; \quad \text{otherwise.}\end{aligned} \quad (\text{A-7})$$

It is now possible to write an expression for the summation over j of the product of equations (A-4) and (A-5) which appears in (A-3). Using (A-6) and (A-7):

$$\begin{aligned}\sum_{j=h+1}^{\infty} \Pr(h|j, \{t_i\}) \Pr(j|\{t_i\}) &= \sum_{j=h+1}^{\infty} \binom{j-1}{h} r_T^h (1-r_T)^{j-h-1} \frac{1}{2\pi} \int_{-\pi}^{\pi} \phi^{j-h-1}(e^{i\lambda}) \sum_{t_j=1}^T \frac{t_j}{N} \left[\Pr(t_j) \sum_{n=0}^{N-\sum_{i=1}^h t_i-1} e^{-in\lambda} + p^{t-1} e^{-i(N-\sum_{i=1}^h t_i)\lambda} \right] d\lambda \\ &= \frac{r_T^h}{2\pi N} \int_{-\pi}^{\pi} \frac{d\lambda}{[1-(1-r_T)\phi(e^{i\lambda})]^{h+1}} \sum_{t_j=1}^T t_j \left[\Pr(t_j) \sum_{n=0}^{N-\sum_{i=1}^h t_i-1} e^{-in\lambda} + p^{t-1} e^{-i(N-\sum_{i=1}^h t_i)\lambda} \right].\end{aligned} \quad (\text{A-8})$$

Now, it is convenient to rearrange a portion of the integrand slightly:

$$\frac{1}{[1 - (1 - r_T) \phi(e^{i\lambda})]^{h+1}} = \sum_{j=0}^{\infty} (1 - p e^{i\lambda})^{h+1} \binom{j+h}{h} e^{ij\lambda} [p + (1 - r_T)(1 - p) + p^{T-1}(e^{i(T-1)\lambda} - e^{iT\lambda})]. \quad (\text{A-9})$$

This summation is of the form:

$$\sum_{j=0}^{\infty} a_j e^{ij\lambda} \quad (\text{A-10})$$

The first N components of this sum (the only ones which contribute to the integral) can be evaluated numerically on a digital computer. The other term of the integral of Equation (A-8) can be put in the form:

$$\sum_{n=0}^N \beta_n e^{-in\lambda} \quad (\text{A-11})$$

This too can be evaluated numerically. Thus, using (A-10) and (A-11), Equation (A-8) becomes:

$$\sum_{j=h+1}^{\infty} \Pr(h|j, \{t_i\}) \Pr(j|\{t_i\}) = \frac{r_T^h}{N} \sum_{j=0}^N a_j \beta_j \quad (\text{A-12})$$

Returning now to Equation (A-3), the conditional probability of an error of magnitude Δ , $\Pr(\Delta|h, j, \{t_i\})$, remains to be evaluated. Clearly there is no dependence on j . The probability of an accumulated error, Δ , in the h timing words whose true values are given by the set $\{t_i\}$ is found by the h -fold convolution of the probabilities of the h (independent) timing errors. This is most conveniently represented in integral form as the inverse transform of the product of the characteristic functions of the timing errors. These characteristic functions are given by:

$$Q_i(v) = \sum_{\Delta = -t_i + 1}^{T - t_i} \Pr(t_i + \Delta \text{ received} | t_i) e^{iv\Delta}$$

The probability in the summand is determined by the number of bits that are different between the PCM encoded word t_i and the received word $t_i + \Delta$ (Hamming distance). If q is the Hamming distance, then the probability is

$$\frac{r^q (1 - r) \log_2 T - q}{r_T}$$

Thus:

$$\Pr(\Delta | h, j, \{t_i\}) = \frac{1}{2\pi} \int_{-\pi}^{\pi} e^{-iv\Delta} \prod_{i=1}^h Q_i(v) dv. \quad (\text{A-13})$$

Finally, using (A-12) and (A-13), equation (A-3) becomes

$$\Pr(\Delta, h) = \sum_{\{t_i\}} \frac{1}{2\pi} \int_{-\pi}^{\pi} e^{-iv\Delta} \prod_{i=1}^h Q_i(v) \Pr(t_i) dv \cdot \frac{r_T^h}{N} \sum_{j=0}^N \alpha_j \beta_j. \quad (\text{A-14})$$

Returning now to Equation (A-2), the remaining factor to be evaluated is $\overline{S(\Delta)}$ which can be written as

$$\overline{S(\Delta)} = \Pr(t_j) \Pr(i | \Delta, t_j) \Pr(k, n | \Delta, t_j, i) s_{kn} \quad (\text{A-15})$$

where

$\Pr(i | \Delta, t_j)$ = probability that the level reconstructed in place of the correct value for a randomly selected sample is located i samples away from the endpoint of the run whose length is t_j given Δ .

$\Pr(k, n | \Delta, t_j, i)$ = probability that the correct value is the k^{th} level but the value reconstructed is n given Δ , t_j and i

s_{kn} = the cost of deciding k is the correct level when in fact n is the true value.

The first of the above defined probabilities is given by the simple expression:

$$\begin{aligned} \Pr(i | \Delta, t_j) &= \frac{1}{t_j} \quad \text{if } |\Delta| - t_j + 1 \leq i \leq |\Delta| \\ &= 0 \quad \text{otherwise} \end{aligned} \quad (\text{A-16})$$

The remaining probability is determined by the transition matrix of the Markov process and the probability density of a level error. It is evaluated in a straightforward manner using as initial conditions the probabilities of the first sample outside of the interval of the t_j run. This is found through the use of the fact that if $\Delta < 0$, the probability that the first sample outside the interval equals the desired level is p^T (the probability that the preceding run is of length T and that the run continues into the t_j interval). If $\Delta > 0$ and $t_j < T$, the same probability equals zero. If $t_j = T$, and $\Delta > 0$, the probability equals p .

Equation (A-16) is substituted in (A-15) along with the results of the preceding paragraph to get $\overline{S(\Delta)}$. Finally in Equation (A-2), using (A-14):

$$\overline{S_h} = \sum_{\Delta} \overline{S(\Delta)} \sum_{\{t_i\}} \frac{1}{2\pi} \int_{-\pi}^{\pi} e^{-iv\Delta} \prod_{i=1}^h Q_i(v) \Pr(t_i) dv \cdot \frac{r_T^h}{N} \sum_{j=0}^N \alpha_j \beta_j. \quad (\text{A-17})$$

Now let

$$\sum_{\Delta} \overline{S(\Delta)} = W(v).$$

Then

$$\overline{S_h} = \frac{1}{2\pi} \int_{-\pi}^{\pi} W(v) \left[\sum_{\{t_i\}} \prod_i Q_i(v) \Pr(t_i) \right] dv \cdot \frac{r_h^h}{N} \sum_{j=0}^N \alpha_j \beta_j. \quad (A-18)$$

This is the equation which is numerically evaluated to obtain the exact average cost.

The data compression ratio is given by the average run length which is

$$C_d = \sum_{t=1}^T t \Pr(t) \\ = \frac{1 - p^T}{1 - p}.$$

The bit compression ratio is

$$C_b = C_d \frac{\log_2 L}{\log_2 L + \log_2 T}.$$

The energy compression ratio at bit error rate r in the compressed data is given by the ratio of the energy per bit, E_u , required in the uncompressed system for average cost \bar{S} to that required in the compressed system, E_c , times the bit compression ratio:

$$E = C_b \frac{E_u}{E_c}. \quad (A-19)$$

If r_u is the uncompressed bit error rate for cost \bar{S} and r is the compressed value, then for the assumed coherent white Gaussian channel:

$$\frac{E_u}{E_c} = \left[\frac{\Phi^{-1}(1 - r_u)}{\Phi^{-1}(1 - r)} \right]^2$$

where Φ is the cumulative Gaussian probability distribution.

An approximate solution for the average cost of (A-1) can be found when the timing word error rate times the block length is small, i.e., $r_T N \ll 1$. In this case the effects on the calculations of more than one timing word error can be neglected,

$$\bar{S} \approx \bar{S}_0 + \bar{S}_1 \quad (\text{A-20})$$

where \bar{S}_0 is the average cost due to a level error and no timing errors whereas \bar{S}_1 is the average cost due to a single timing word error. \bar{S}_0 is the same as the average cost in uncompressed data for error rate r . Suppose there are M transmitted level-run length pairs in the transmitted block of length N . (M is a random variable.) Then the probability of a single error preceeding a randomly chosen sample given M , is approximately

$$\sum_{j=2}^{\infty} \Pr(h=1 | j, t_1) \Pr(j | t_1) \approx \frac{M}{2} r_T.$$

The expected value of this quantity with respect to M is given by

$$\frac{N r_T}{2 C_d}.$$

Thus from (A-18) the following approximate expression is found

$$\bar{S} = \frac{N r_T}{2 C_d} \frac{1}{2\pi} \int_{-\pi}^{\pi} W(v) \sum_{t_1=1}^T Q_1(v) \Pr(t_1) dv + \bar{S}_0 \quad (\text{A-21})$$

This expression is evaluated with relatively few computations compared with the exact expression where most of the labor lies in the evaluation of Equations (A-10) and (A-11). An additional advantage is that, because the integral only needs to be evaluated once, (A-21) can easily be evaluated for a range of values of r_T whereas the exact expression can not.

THE EFFECT OF CHANNEL ERRORS ON A SAMPLE COMPRESSION SYSTEM EMPLOYING BINARY SEQUENCE TIME ENCODING

Robert B. Kelley* 7

N 67-22745

A sample compression system is a form of data processing which reduces the number of transmitted data samples and restores the data to original form after reception. That is, a sample compression system consists of an "encoder-decoder" pair. This reduction process is accomplished by taking advantage of "sample regularity" whenever present. What constitutes "sample regularity" depends upon the technique used to reduce the number of samples. For example, if an adaptive non-linear predictor, such as suggested by Balakrishnan (Reference 1) is used, then "sample regularity" implies only that the predictor based on the immediate past is applicable to the present and immediate future data. On the other hand, if non-adaptive "curve fitting" techniques are used such as mentioned by Weber (Reference 2), and others (References 3 through 11), then "sample regularity" implies that the data fit a specific family of curves.

Although the adaptive techniques could perform well for a larger class of data, an examination of the pertinent literature will show that the non-adaptive techniques have received the most attention. And fitting horizontal line segments seems to be the most popular of the curve fitting schemes—probably because of the extreme simplicity of mechanization.

To restore the non-transmitted samples, some kind of "timing" information is needed at the receiver to locate the transmitted samples in the original data sequence. Hence, timing must be transmitted in some form. In this paper, the case is considered where the timing information is encoded as a binary sequence, one bit for each original data sample.

In general, for a given signal to noise ratio, restored (sample) compressed data have a larger probability of sample error than if the same data samples were transmitted without compression. To obtain the same probability of sample error for these two modes of operation, a larger signal to noise ratio is required to compensate for the compression error effect. The object of this analysis is to determine the net savings of signal energy obtained by this sample compression scheme when the same block of data samples is transmitted with the same probability of sample error for both operating modes. The net energy savings per block of samples could be translated into a corresponding savings in time, bandwidth or average power level. For a fixed bandwidth case, with constant average power, the net energy savings is realized as a time savings and the larger signal to noise ratio is achieved through coding. The exact correspondence depends, of course, on the specific coding method employed.

DATA AND CHANNEL MODELS

The data samples are assumed to be a sequence of quantized time samples. For definiteness, M distinct quantum levels are assumed and the data is processed in blocks of fixed length; call the number of samples in a block, B . In this analysis, the data are modeled as a stochastic process which possesses nearest neighbor dependence; that is, the data will be modeled as a first-order Markov process. The transition probability matrix is taken to have the form:

*University of Rhode Island, Kingston, R.I.

$$\begin{bmatrix} p & p_{ij} \\ p_{ij} & p \end{bmatrix} \quad p_{ii} \doteq p, \forall i.$$

Thus, for each of the M quantum levels, the probability that the nearest neighbor is the same level as a given sample is equal to the same probability p . The other transition probabilities are completely arbitrary and may vary with each successive sample.

Looking at single frame television pictures (such as Nimbus and Tiros satellite cloud pictures), the Markov model has been empirically verified. The constancy of the main diagonal transition probabilities has been observed to be approximately true except for the extreme quantum levels.

The transmission channel is modeled as a (constant) binary symmetric channel with probability of bit error equal to r . The data levels are transformed into binary format (uncoded PCM) and transmitted along with the binary timing sequence through the same (time shared) channel.

The only source of error considered in this analysis is the channel since the object is to determine the effect of channel errors on the restored compressed data, and, from this, the net energy savings. In particular, error free block synchronization is assumed. Finally, because identical processing is performed on each block of B data samples, block-to-block dependences, if any exist, are not taken into account.

SAMPLE COMPRESSION AND BINARY SEQUENCE TIME ENCODING

Supposed that 4 quantum levels are used and therefore the data sample values are either 1, 2, 3, or 4. For a block length of 16, the original data samples might look like:

2 2 2 2 2 3 3 4 4 4 4 3 1 1 1 1

For this example, there are runs of length 5, 2, 4, 1, and 4 respectively. Sample compression is achieved by transmitting the quantum level for each run only once. The timing information needed at the receiver to restore the non-transmitted samples is the position of each run within the block of data.

With binary sequence time encoding, the position of each run is inferred from a binary sequence composed of one bit for each original sample. In this sequence, the last (or right hand) sample of a particular run is indicated by a 1. Thus, the binary timing sequence which corresponds to:

2 2 2 2 2 3 3 4 4 4 4 3 1 1 1 1

is

0 0 0 0 1 0 1 0 0 0 1 1 0 0 0 1

At the receiver, a 0 is interpreted as a repeat indication and a 1 as a call for a new (i.e., the next) quantum level. Suppose the transmitted data consists of the binary timing sequence followed by the uncoded PCM equivalent of the quantum levels

2 3 4 3 1

as shown below:

$$\underbrace{0\ 0\ 0\ 0\ 1\ 0\ 1\ 0\ 0\ 0\ 1\ 1\ 0\ 0\ 0\ 1}_{\text{timing sequence}}\ 1\ 0\ 1\ 1\ 0\ 0\ 1\ 1\ 0\ 1$$
(2)
(3)
(4)
(3)
(1)

The receiver identifies the timing sequence portion and each quantum level. The non-transmitted samples are restored by interpreting the binary timing sequence previously as explained. Thus, for the received sequence in this example, the receiver restored the data as:

RESTORED DATA: 2 2 2 2 2 | 3 3 | 4 4 4 4 | 3 | 1 1 1 1 |
 TIMING SEQUENCE: 0 0 0 0 1 | 0 1 | 0 0 0 1 | 1 | 0 0 0 1 |

Notice that the last bit of the binary timing sequence is always a 1. Hence, it would not be transmitted since the number of samples in a block is fixed, here $B = 16$.

Because the number of transmitted quantum levels, in this example 5, would in general vary from block to block of compressed data, some kind of block synchronization is required to signal the end of one block and the start of another. Using the example above, a block of compressed data might be transmitted using the format:

BLOCK SYNC	0	0	0	0	1	0	1	0	0	0	1	1	0	0	0	1	0	1	1	0	0	1	1	0	1
---------------	---	---	---	---	---	---	---	---	---	---	---	---	---	---	---	---	---	---	---	---	---	---	---	---	---

To assist the receiver in locating the block sync word and thereby maintaining synchronization, the number of 1 in the binary sequence might be counted. Also, the block sync word might be composed of forbidden quantum level code words. In any event, block synchronization should not be a significant problem. The "cost" of the block sync word in terms of additional bits and therefore additional energy is not included in the analysis which follows.

A sample compression system having the nature of the one analyzed in this paper might be represented by a block diagram as drawn in Figure A-16. The fitting tolerance ϵ may be an arbitrary number of quantum levels. (The assumed symmetry is not essential.) Since the fitting error is not caused by the transmission channel, the original data samples for purposes of this analysis are the noise-free version of the restored data.

If the fitting is accomplished by a piecewise constant quantum level approximation (analogous to a sampled-data zero-order hold device), then the corresponding transition probability matrix will have identically zero diagonals surrounding the non-zero main diagonal, reflecting the requirement that the quantum levels must change value by at least the fitting tolerance or stay the same.

BINARY SEQUENCE ERROR DECODING RULE

When there is a disagreement between the number of 1s in the received binary sequence and the number of received quantum levels (this number is always assumed to be correct), a decoding rule is needed to permit the non-transmitted data samples to be restored as previously indicated. That is, the binary sequence must either be modified so as

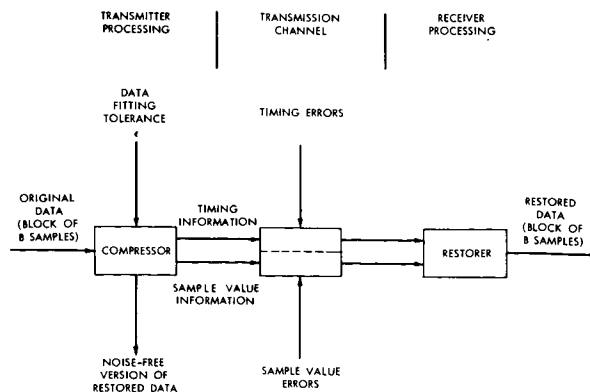


Figure A-16—Sample compression system model.

to use all the received quantum levels or the number of quantum levels must be changed to agree with the received binary sequence.

Since it is always true that the last data sample in the original block has the same quantum level as the last transmitted quantum level, the decoding rule employed in this analysis modifies the received binary sequence to maintain this condition. The rule is:

1. If there are excess 1s, change the terminal excess 1s to 0s.
2. If there are excess 0s, change the terminal excess 0s to 1s.

Suppose that the 15-bit binary sequence for the previous example was received with one bit in error, then depending on which bit was changed the received binary sequence might be:

0 → 1 error

0 0 0 0 1 1 1 0 0 0 1 1 0 0 0
 ↑
 error

and

1 → 0 error

0 0 0 0 1 0 0 0 0 0 1 1 0 0 0
 ↑
 error

For the first case, without the decoding rule, the restored data would be:

2 2 2 2 2 3 4 3 3 3 3 1 ? ? ? ?

Employing the decoding rule modifies the received binary sequence from

0 0 0 0 1 1 1 0 0 0 1 1 0 0 0

to

0 0 0 0 1 1 1 0 0 0 1 0 0 0 0

so that the restored data would now be:

2 2 2 2 2 3 4 3 3 3 3 1 1 1 1

For the second case, without the decoding rule, the restored data would be:

2 2 2 2 2 3 3 3 3 3 3 4 3 3 3 3 (quantum level of
1 left over)

The decoding rule modifies the received binary timing sequence from

0 0 0 0 1 0 0 0 0 0 1 1 0 0 0

to

0 0 0 0 1 0 0 0 0 0 1 1 0 0 1

so that the restored data would be:

2 2 2 2 2 3 3 3 3 3 3 4 3 3 3 1

These can be compared with the original data samples before compression:

2 2 2 2 2 3 3 4 4 4 4 3 1 1 1 1

NET ENERGY SAVINGS

The net energy savings (NES) is given in this analysis as the ratio of total signal energy with compression to that without compression to transmit the same block of data with the same probability of sample error. Denoting the signal power to noise spectral density per bit as SNR, the total signal energy is equal to the product of the number of bits transmitted and the SNR and a common constant of proportionality for both cases. Hence, defining the bit compression ratio in a consistent manner, this yields:

$$NES = \frac{SNR_c}{SNR_{nc}} \left\{ \begin{array}{l} \text{BIT} \\ \text{COMPRESSION} \\ \text{RATIO} \end{array} \right\}$$

where SNR_c = SNR with compression

and SNR_{nc} = SNR with no compression

Let the channel bit error probability for the compression system be r_c and for the non-compression system be r_{nc} . Denote the common probability of sample error by P_e and the number of bits in a quantum level word by μ . Assuming coherent detection, the bit error probability and the SNR are related by

$$r = \text{CERF} (SNR)$$

or

$$SNR = \text{CERF}^{-1} (r)$$

where

$$\text{CERF} (x) = \frac{1}{\sqrt{2\pi}} \int_x^{\infty} e^{-1/2 y^2} dy$$

For the non-compression system

$$r_{nc} = 1 - (1 - P_e)^{\frac{1}{\mu}}$$

Therefore

$$\frac{\text{SNR}_c}{\text{SNR}_{nc}} = \frac{\text{CERF}^{-1}(r_c)}{\text{CERF}^{-1}\left[1 - (1 - P_e) \frac{1}{\mu}\right]}$$

where P_e is a function of r_c and the sample compression system.

For the assumed data model, the average number of runs is equal to

$$B(1-p) + p.$$

Since the average number of quantum level words transmitted by the compression system is equal to the average number of runs, the bit compression ratio is given by

$$\frac{\mu [B(1-p) + p] + B - 1}{\mu B} = 1 - \left(1 - \frac{1}{B}\right) \left(p - \frac{1}{\mu}\right).$$

To evaluate the net energy savings then, the probability of sample error must be determined as a function of the channel bit error probability and the sample compression system employed. In the next section, bounds are obtained for the probability of sample error in terms of the data block length B , the main diagonal transition probability p , the number of bits in a sample value word μ , and the channel bit error probability r .

CHANNEL ERROR ANALYSIS

To determine the net energy savings obtained by using the sample compression system described above, it is necessary to find, as a function of the bit error probability r , the probability that a randomly selected receiver restored sample is in error. The probability of such a sample error can be viewed as the expected value of a zero-one random variable, ϵ , which is equal to zero if the selected receiver restored sample has the same quantum level as the noise-free version at the transmitter and is equal to one otherwise. Thus

$$P\{\text{SAMPLE ERROR}\} = E\{\epsilon\}$$

The joint distribution of all the random variables which affect the value of ϵ must be determined to perform the desired expectation. To establish the notation, suppose the randomly selected sample belongs to the k^{th} transmitter run.

Then, for the data block

$$\underbrace{\underbrace{m_1 m_1 \dots m_1}_{n_1} \dots \underbrace{m_{k-1} m_{k-1} \dots m_{k-1}}_{n_{k-1}} \underbrace{m_k m_k \dots m_k}_{n_k} \dots \underbrace{m_k m_k \dots m_k}_{n_k}}_t \quad \underbrace{\hspace{10em}}_n$$

The following symbols will be used:

$n = n_k$ = length of the k^{th} run

$t = \sum_{j=1}^{k-1} n_j$ = number of samples to the left of the k^{th} run

K = total number of runs in the block B

In the analysis which follows, bounds are obtained for $P\{\text{sample error}\}$ which depends on just these parameters: n, t, k, K . Treating them as random variables, the appropriate joint distribution is given as $P\{\xi, \text{transmission errors}, n, t, k, K\}$

Bounds on $P\{\xi | n, t, k, K\}$

Write the joint distribution as $P\{\xi, \text{transmission errors} | n, t, k, K\} \cdot P\{\tilde{n}, \tilde{t}, \tilde{k}, \tilde{K}\}$. Then a conditional probability can be defined as $P\{\xi | n, t, k, K\} = \sum P\{\xi, \text{transmission errors} | n, t, k, K\}$. Exact evaluation of this conditional probability requires a more complete specification of the data structure. However, enough structure has been assumed to permit the determination of upper and lower bounds.

Define the average (overall binary sequence bit errors) probabilities $C_0(n, t, k, K)$ and $C_1(n, t, k, K)$ as follows:

$$C_0(n, t, k, K) = \text{Prob} \left\{ \begin{array}{l} \text{selected sample is} \\ \text{in } k^{\text{th}} \text{ receiver} \\ \text{run} \end{array} \middle| n, t, k, K \right\}$$

$$C_1(n, t, k, K) = \text{Prob} \left\{ \begin{array}{l} \text{selected sample is} \\ \text{in } (k \pm 1)^{\text{st}} \text{ receiver} \\ \text{run} \end{array} \middle| n, t, k, K \right\}$$

Since the channel errors are independent, the sample value errors and the binary sequence bit errors are independent. If the number of bits in the quantum level word equals μ then

$$P\{\text{received quantum level error}\} = 1 - (1-r)^\mu \triangleq r_M$$

Similarly,

$$P\{\tau \text{ binary sequence bit errors}\} = \binom{B-1}{\tau} r^\tau (1-r)^{B-1-\tau}$$

Hence, for example,

$$\begin{aligned} &P\{\text{received quantum level error, } \tau \text{ binary sequence bit errors}\} \\ &= r_M \cdot \binom{B-1}{t} r^\tau (1-r)^{B-1-\tau} \end{aligned}$$

A lower bound is obtained, denoted by P_L , which in terms of the previously defined symbols is given by

$$P_L = r_M C_0 + (1 - r_M) C_1$$

By interpreting the terms, it can be verified that this is a lower bound.

The conditional probability of sample error is at least as large as the sum of the conditional probability of selecting a sample in the correct run and having the wrong quantum level plus the conditional probability of selecting a sample in an adjacent run and having that quantum level correct. Using a worse case assumption that the errors would exactly cancel in all other cases, a lower bound is clearly obtained.

Similarly, an upper bound is obtained, denoted by P_U , and is given as

$$P_U = r_M C_0 + (1 - C_0) [= 1 - (1 - r_M) C_0].$$

Again, it can be verified that this is an upper bound. The conditional probability is certainly larger than the sum of the conditional probability of selecting a sample in the correct run and having the wrong quantum level plus the conditional probability of selecting some other run. This last term represents a worse case assumption of no error cancellations ever occurring. (This upper bound is equivalent to a lower bound on the conditional probability of no error.)

For large values of signal to noise ratio and therefore small probabilities of bit error, only a few binary sequence errors contribute a significant amount to the average conditional probability of run selection. If at most one binary error is considered,

$$C_0 \approx (1 - r)^{B-1} \left[C_{00} + (B - 1) \frac{r}{1 - r} C_{01} \right]$$

and

$$C_1 \approx (B - 1) r (1 - r)^{B-2} C_{11}$$

where, taking the binary sequence error decoding rule into account, the probabilities C_{00} , C_{01} , C_{11} , are given by

0 BIT ERRORS

$$C_{00}(n, t, k, K) = 1$$

1 BIT ERROR

$$C_{01}(n, t, k, K) = \begin{cases} \frac{B - t - \frac{1}{2}(n + 1)}{B - 1}, & k \neq K \\ \frac{n(B - K) + K - 1}{n(B - 1)}, & k = K \end{cases}$$

$$C_{11}(n, t, k, K) = \begin{cases} \frac{t + \frac{1}{2}(n - 1)}{B - 1}, & k \neq K \\ \frac{(n - 1)(K - 1)}{n(B - 1)}, & k = K \end{cases}$$

The conditional probabilities of selecting particular runs are obtained by counting the number of samples in the pertinent runs assuming the appropriate number of binary sequence bit errors.

$C_{00}(n, t, k, K)$ is the conditional probability that a randomly selected sample in the k th transmitter run will be in the k th receiver run given no binary sequence bit errors and the values of n, t, k, K . This is obviously identically equal to one.

Given exactly one binary sequence bit error, the receiver runs can be displaced by no more than one run from their correct position. Hence

$$C_{01}(n, t, k, K) + C_{11}(n, t, k, K) = 1$$

That is, a randomly selected sample in the k th transmitter run will be in either the $k - 1$ st, k th, or $k + 1$ st receiver runs with probability one. Because of this property, the binary sequence error decoding rule affects only the last run; that is, for $k = K$, the decoding rule modifies the run partitions.

The transmitted binary sequence has the form:

$$\dots\dots\dots \begin{array}{c} 1 \\ t \end{array} \left| \begin{array}{c} 0 \dots 0 \ 1 \\ \leftarrow n \rightarrow \end{array} \right|_k \dots\dots\dots \begin{array}{c} () \\ B \end{array}$$

$C_{11}(n, t, k, K)$ is found by counting the number of ways a single binary sequence bit error can occur which results in exactly ν samples being in an adjacent run, that is, being in either the $k + 1$ st or $k - 1$ st run. When $k \neq K$, the counts are:

$$\begin{array}{ll} t \text{ ways,} & \text{for } \nu = n \\ 1 \text{ way,} & 1 \leq \nu \leq n - 1. \end{array}$$

Thus the average number of samples which are in an adjacent run as a result of a single binary sequence error is

$$nt + \sum_{\nu=1}^{n-1} \nu = nt + \frac{n}{2} (n - 1)$$

Therefore, the probability of selecting an adjacent run given a particular single bit error is

$$\frac{t + \frac{1}{2} (n - 1)}{B - 1} = C_{11}(n, t, k, K).$$

Taking the error decoding rule into account, when $k = K$, the counts are:

$$\begin{array}{ll} 0 \text{ ways,} & \text{for } \nu = n \\ K - 1 \text{ ways,} & \nu = n - 1 \\ 0 \text{ ways,} & 1 \leq \nu \leq n - 2. \end{array}$$

Thus, the probability of selecting the $K - 1$ st run given a particular single bit error is

$$\frac{(n - 1) (K - 1)}{n(B - 1)} = C_{11}(n, t, k, K)$$

Computation of Bounds

For moderate block lengths, the straight forward computation of the upper and lower bounds by taking the expectation with respect to the joint distribution

$$P\{n, t, k, K\}$$

can be extremely long. This is a result of the number of terms to be summed being on the order of the third power of the block length.

To shorten the computation time, observe that some of the expectation may be performed analytically. In particular, notice that both upper and lower bounds are linear functions of the conditional probabilities of selecting particular runs. Furthermore, it is evident that only one expectation is needed to compute the desired bounds. Namely, the conditional expectation

$$E\{C_{11} \mid 1 \text{ Bit error}\}$$

is all that must be determined since

$$E\{C_{01} \mid 1 \text{ Bit error}\} + E\{C_{11} \mid 1 \text{ Bit error}\} = 1$$

Recall that

$$(B-1) C_{11}(n, t, k, K) = \begin{cases} t + \frac{1}{2}(n-1), & k \neq K \\ \frac{n-1}{n}(K-1), & k = K \end{cases}$$

Employing an obvious change in notation, the desired expectation is given as

$$E\{C_{11}\} = E\{C_{11} \mid k = K\} \cdot P\{k = K\} + E\{C_{11} \mid k \neq K\} \cdot P\{k \neq K\}.$$

Therefore, we must determine the three quantities

$$P\{k = K\}, E\{C_{11} \mid k = K\}, E\{C_{11} \mid k \neq K\}$$

$$P\{k = k\}$$

This probability is found by first determining the joint distribution $P\{k, K\}$. Taking advantage of a partitioning point of view, it is easily seen that the random variable, $K-1$, has a binomial distribution with probability of the "successful event" equal to $1-p$. That is, for exactly K runs in a block B , there must be $K-1$ run terminations among the $B-1$ sample positions. Hence

$$P\{K\} = \binom{B-1}{K-1} (1-p)^{K-1} p^{B-K} \quad 1 \leq K \leq B.$$

Selecting the receiver restored sample at random is equivalent to selecting the transmitter run at random and then selecting the sample at random from that run. Thus

$$P\{k \mid K\} = \frac{1}{K} \quad 1 \leq k \leq K.$$

Therefore,

$$P\{k = K\} = \sum_{K=1}^B \sum_{K=1}^K \delta_{k,K} P\{k, K\} = \frac{1 - p^B}{B(1 - p)}$$

where

$$\delta_{k,K} = \begin{cases} 1, & k = K \\ 0, & k \neq K \end{cases}$$

is the Dirac delta function.

$$E\{C_{11} \mid k = K\}$$

The distribution of n , the run lengths, is clearly a truncated geometric distribution. Thus

$$P\{n\} = (1 - p) p^{n-1} (1 - \delta_{n,B}) + p^{B-1} \delta_{n,B} \quad 1 \leq n \leq B.$$

The conditional distribution of K , given n , is similar to that previously derived except that the conditioning requires $K-1$ run terminations among the $B-n$ sample positions. Hence

$$P\{K \mid n\} = \binom{B-n}{K-1} (1-p)^{K-1} p^{B-n-K+1} \quad 1 \leq K \leq B-n+1$$

and

$$E\{K - 1 \mid n\} = (B - n) (1 - p).$$

Therefore

$$(B - 1) E\{C_{11} \mid k = K\} = E\left\{\frac{n-1}{n} E\{K - 1 \mid n\}\right\} = p^B - p - (1 - p) \left[p^{B-1} - B \cdot 1 - \frac{(1-p)}{p} \sum_{1}^{B-1} \frac{p^n}{n} \right].$$

The last summation,

$$\sum_{1}^{B-1} \frac{p^n}{n},$$

can be evaluated by computer. For large values of B , this is approximately given by

$$\sum_1^{\infty} \frac{p^n}{n} = -\ln(1-p).$$

$$E\{\zeta_{11} | k \neq K\}$$

To evaluate this expectation, it is only necessary to determine $E\{\zeta | k \neq k\}$ and $E\{\eta | k \neq k\}$. Unfortunately, the conditional expectations turn out to be complicated. For the first expression, it is required to know the conditional joint distribution

$$P\{\zeta, \eta | k \neq K\} = \binom{B}{K} (1-p)^k p^{B-K} / [B(1-p) + p^B - 1] \quad \begin{matrix} 2 \leq K \leq B \\ 1 \leq K \leq K-1 \end{matrix}$$

$$E\{\zeta | k \neq K\}$$

The distribution of ζ is seen to be a doubly truncated negative binomial distribution. That is, ζ represents the number of sample positions such that a run terminates exactly at t . Hence, including both truncations due to $k = 1$ and $t = B - K + k - 1$,

$$\begin{aligned} P\{\zeta | k, K, k \neq K\} &= (1 - \delta_{k,K}) \delta_{k,1} \delta_{t,0} \\ &+ (1 - \delta_{k,K}) (1 - \delta_{k,1}) (1 - \delta_{t,B-K+k-1}) \binom{t-1}{k-2} (1-p)^{k-1} p^{t-k+1} \\ &+ (1 - \delta_{k,K}) (1 - \delta_{k,1}) \delta_{t,B-K+k-1} \left[1 - \sum_{t=k-1}^{B-K+k-2} \binom{t-1}{k-2} (1-p)^{k-1} p^{t-k+1} \right] \end{aligned}$$

Define $k-1 \leq t \leq B-K+k-1$

$$P\{\zeta = B-K+k-1\} = P_t$$

Then

$$\begin{aligned} E\{\zeta | k, K, k \neq K\} &= (1 - \delta_{k,K}) (1 - \delta_{k,1}) \left\{ (B-K+k-1) P_t \right. \\ &\quad \left. + \sum_{t=k-1}^{B-K+k-2} t \binom{t-1}{k-2} (1-p)^{k-1} p^{t-k+1} \right\} \end{aligned}$$

Therefore,

$$E\{t_k | k \neq K\} = \sum_{k=3}^B \frac{\binom{B}{K} (1-p)^k p^{B-K}}{B(1-p) + p^B - 1} \sum_{k=2}^{K-1} [E\{t_k | k, K, k \neq K\}]$$

This expression represents the main computational effort since the number of terms in the summation is on the order of B^3 .

$$E\{n | k \neq K\}$$

The distribution of n is a truncated geometric distribution as before except that the range depends on K . Thus

$$P\{n | K, k \neq K\} = (1 - \delta_{k,K}) (1 - \delta_{n, B-K+1}) (1-p) p^{n-1}$$

$$+ (1 - \delta_{k,K}) \delta_{n, B-K+1} p^{B-K} \quad 1 \leq n \leq B - K + 1$$

and

$$E\{n | K, k \neq K\} = (1 - \delta_{k,K}) \frac{1 - p^{B-K+1}}{1 - p}$$

Therefore,

$$E\{n | k \neq K\} = \frac{1}{1-p} \left\{ p \left[\sum_{k=2}^B (K-1) \binom{B}{K} (1-p)^K p^{2(B-K)} \right] \right. \\ \left. 1 - \frac{\quad}{B(1-p) + p^B - 1} \right\}$$

which, upon application of the Binomial theorem, yields

$$E\left\{\frac{n-1}{2} | k \neq K\right\} = \frac{p}{2(1-p)} \left\{ 1 - \frac{[(B+p)(1-p)-1][1-p(1-p)]^{B-1} - p^{2B}}{B(1-p) + p^B - 1} \right\}$$

These expressions can then be evaluated to determine

$$(B-1) E\{C_{n-1} | k \neq K\} = E\{t_k | k \neq K\} + E\left\{\frac{n-1}{2} | k \neq K\right\}$$

The upper and lower bounds on the probability of sample error can now be obtained for various values of the four parameters

$$B, p, r, \mu$$

from the quantities just derived.

APPROXIMATE EVALUATION OF BOUNDS

To evaluate the bounds on the probability of sample error, the number of terms in the summations is proportional to the cube of the block length. Hence for moderate block lengths the computation requires an inordinate amount of computer time. For example, to compute the bounds for a single value of p for block lengths of about 250 samples, approximately 75 minutes of 7094 time is required.

Since the computation problem occurs for large values of B , some analytical simplifications can be made to obtain approximate expressions which are easier to evaluate. As was indicated previously, the sum

$$\sum_{n=1}^{B-1} \frac{p^n}{n}$$

is approximately

$$\sum_{n=1}^{\infty} \frac{p^n}{n} = -\ln(1-p)$$

The approximation error is grossly overbounded by

$$\frac{p^B}{B(1-p)} \geq -\frac{1-p^B}{B(1-p)} \ln(1-p^B) \geq \sum_{n=B}^{\infty} \frac{p^n}{n}.$$

This approximation yields the analytical expression

$$(B-1) E\{C_{11} | k = K\} \cong (1-p) \left[B \left(1 + \frac{1-p}{p} \ln(1-p) \right) - p^{B-1} \right] - p + p^B.$$

Now, considering the expression for $E\{t_k | k, K, k \neq K\}$, when $B-K$ is sufficiently large, this is approximately

$$E\{\underline{t}|k, K, k \neq K\} \cong \sum_{t=k-1}^{\infty} t \binom{t-1}{k-2} (1-p)^{k-1} p^{t-k+1}$$

$$= \frac{k-1}{1-p}$$

Then

$$E\{\underline{t}|k = K\} \cong \frac{B(1-p)p + B^2(1-p)^2 - 3B(1-p) + 2 - p^B}{2(1-p)[B(1-p) + p^B - 1]}$$

The approximation error in this case is the expected value of

$$\sum_{t=B-K+1}^{\infty} t \binom{t-1}{k-2} (1-p)^{k-1} p^{t-k+1}.$$

This expectation is taken with respect to a binomial distribution which has a variance of the same order as the mean. Hence the condition on $B-K$ is satisfied less with increasing B as the region of high probability disperses. In other words, this approximation becomes poorer at a rate proportional to \sqrt{B} .

Using this approximation nevertheless yields the analytical expression

$$(B-1)E\{\underline{C}_{11}|k \neq K\} = E\{\underline{t}|k \neq K\} + E\left\{\frac{B-1}{2} \middle| k \neq K\right\}$$

$$\cong \frac{\{B(1-p)[B(1-p) + p - 3] + 2 - p^B - p[(B+p)(1-p) - 1][(1-p(1-p))^{B-1} + p^{2B}]\}}{2(1-p)[B(1-p) + p^B - 1]} + \frac{p}{2(1-p)}.$$

DISCUSSION OF RESULTS

The dependence of the sample error probability, P_e , on the channel bit error probability, r , is shown by the curves of the upper bounds plotted in Figure A-17 and Figure A-18. In Figure A-17 the exact upper bounds are plotted for, block length, $B = 64, 128$, and 256 . Notice that the curves are not too sensitive to the value of $p = 0.8$ and 0.9 and that doubling the block length doubles the sample error probability. The upper bounds for P_e obtained by approximation are plotted in Figure A-18. The approximation appears to overbound the exact upper bound by a factor of about $4/3$ for $B = 256$.

The relation of the net energy savings, NES, to the sample error probability, P_e , is given in the plots in Figures A-19, A-20, A-21, and A-22. The exact lower bounds on NES are shown in

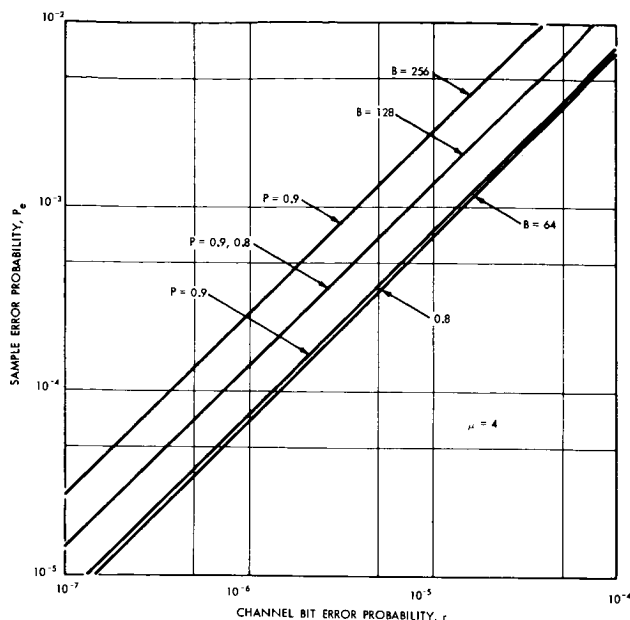


Figure A-17—Sample error probability exact upper bounds vs. channel bit error probability.

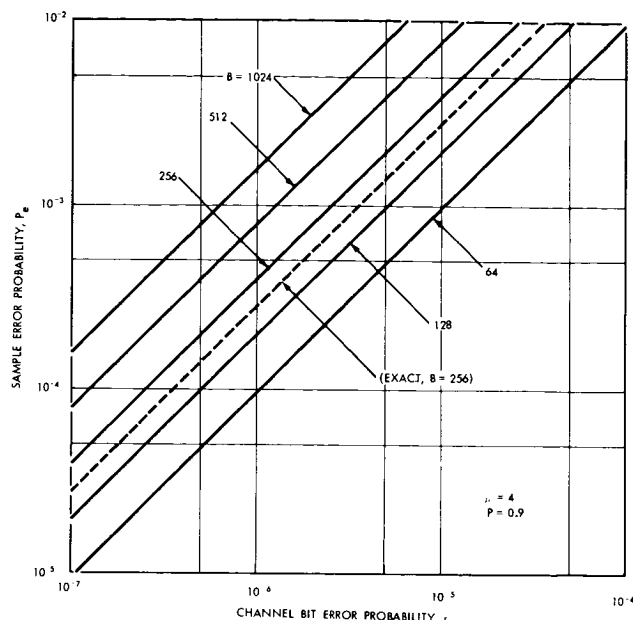


Figure A-18—Sample error probability approximate upper bounds vs. channel bit error probability.

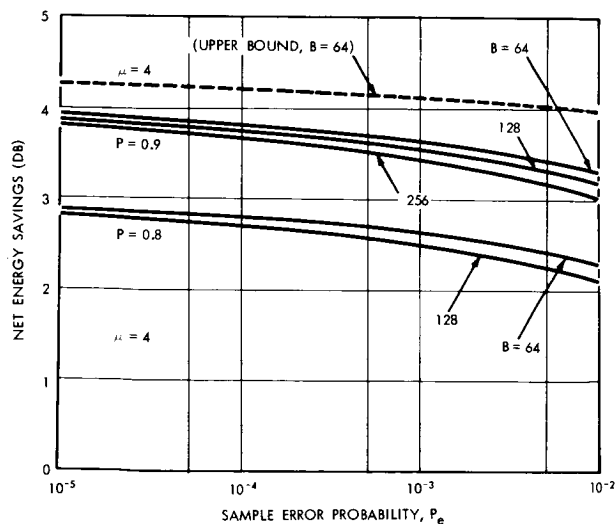


Figure A-19—Net energy savings exact lower bounds vs. sample error probability.

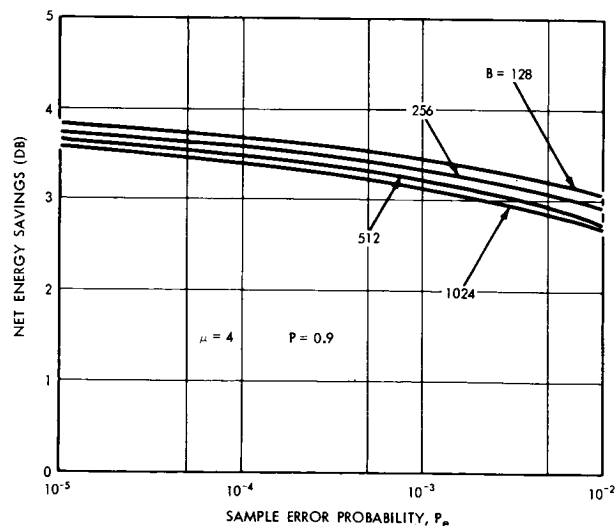


Figure A-20—Net energy savings approximate lower bounds vs. sample error probability showing dependence on block length.

Figure A-19 for the number of bits in a quantum level word, $\mu = 4$, and for $B = 64, 128$, and 256 . The upper bound for $B = 64$ and $p = 0.9$ is also plotted to show the narrow range of NES associated with all possible Markov sources which have constant main diagonal transition probabilities. It is significant to notice that for each value of p , the NES is decreased only about 0.1 db when the block length is doubled but is decreased by 1.0 db when p is changed from 0.9 to 0.8 . This indicates that the main contribution to net energy savings is the bit compression ratio. The amount of bit compression obtained is essentially constant for any given value of p since the asymptotic value has been essentially reached for $B \geq 64$. Shown in Figure A-20 is the same insensitivity to B obtained from the approximation.

The variation of net energy savings with p is shown in Figure A-21. The discrepancy noted before between the exact and approximate lower bounds is about 0.1 db. The interesting thing here is that the NES reaches a maximum of about 5 db.

Plotted in Figure A-22 is the effect of varying the number of quantum levels on the net energy savings. The NES obtained is increased with increasing μ . Comparing Figure A-21 and Figure A-22 shows the interesting parallel between adding one bit to μ and dividing the quantity $(1-p)$ by two. That is, there is almost a correspondence which might allow the extrapolation from the curves $\mu = 4$ and $p = 0.9$ to the set of curves plotted in either Figure A-21 or A-22 given the other set.

CONCLUSIONS AND COMMENTS

The scheme for time encoding which has been considered in this analysis does not lead to suitable amounts of net energy savings, as can be seen in Figure A-21, since the value for NES is always ± 1 db of 4 db when $0.8 \leq p \leq 0.99$ ($B = 256, \mu = 4$). Similar ranges for NES can be expected as B and μ are varied.

Hindsight indicates that this poor performance should have been expected from elementary considerations.

1. Poor bit compression. For $p > .7$, the number of extra bits transmitted by this scheme becomes significant.

2. Poor time error performance. A single timing bit error prior to a given run causes the entire selected run to be in error (neglecting error cancellation).

These two features serve to guarantee a smaller net energy savings for binary sequence time encoding than, say, run length encoding which has better bit compression (approaches the information theoretic entropy limit) and which has better time error performance. My feeling is that the first feature is the more significant of the two.

Future efforts along these lines should include an analysis of absolute time encoding where the end of each run is transmitted. Single time errors are delimited to effect at most three runs

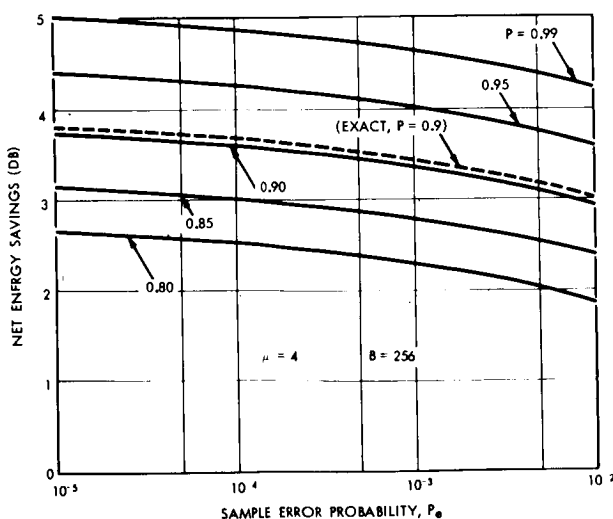


Figure A-21—Net energy savings approximate lower bounds vs. sample error probability showing dependence on the main diagonal transition probability.

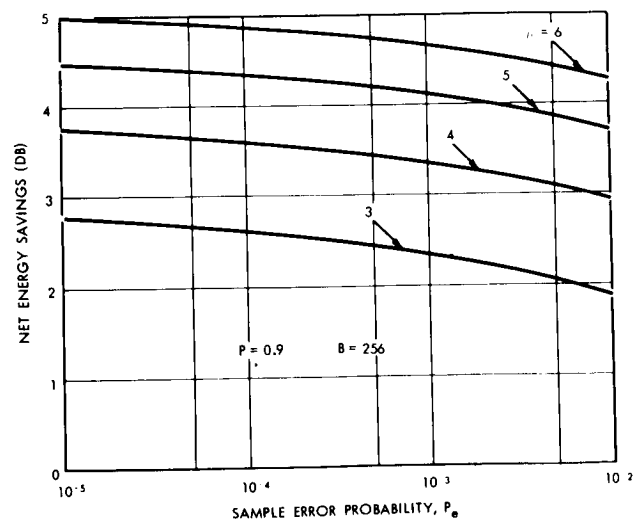


Figure A-22—Net energy savings approximate lower bounds vs. sample error probability showing dependence on number of quantum levels.

by the monotonicity of the absolute time words. This is to be compared with schemes which allow the errors to propagate to the end of the block of data. Since the bit compression is only somewhat poorer than run length encoding and the error performance is much better, this technique might prove to be competitive. Finally, in the case of pictorial, or other periodic, data, block to block processing might lead to significant improvements in NES.

ACKNOWLEDGMENT

The author would like to acknowledge the assistance given by L.D. Davisson in performing this work. Prior to starting on this analysis the author had the opportunity to study a preliminary version of the run length time encoding analysis by L.D. Davisson which appears elsewhere in this report. The method of attack used in the analysis presented herein is basically the same as that which L.D. Davisson employs in that paper.

REFERENCES

1. Balakrishnan, A. V., "An adaptive non-linear data predictor," 1962 Proc. Nat. Telem. Conf., The Institute of Radio Engineers, paper no. 6-5, Washington, D.C., New York, N.Y., May 23-25, 1962.
2. Weber, D. R., "A synopsis on data compression," 1965 Proc. Nat. Telem. Conf., The Institute of Electrical and Electronic Engineers, paper TA 1.1, Houston, Texas, New York, N.Y., April 13-15, 1965.
3. Massey, H. H., "An experimental telemetry data compressor," 1965 Proc. Nat. Telem. Conf., The Institute of Electrical and Electronic Engineers, paper TA 1.3, Houston, Texas, New York, N.Y., April 13-15, 1965.
4. Raga, G. L., "A unified approach to digital television compression," 1965 Proc. Nat. Telem. Conf., The Institute of Electrical and Electronic Engineers, paper TA 1.4, Houston, Texas, New York, N.Y., April 13-15, 1965.
5. Kortman, C. M., "Data compression and adaptive telemetry," 1965 Western Electronic Show and Convention. Technical Papers, Western Periodicals Co., paper no. 14.4, San Francisco, Calif., N. Hollywood, Calif., August 24-27, 1965.
6. Gardenhire, L. W., "Redundancy reduction—the key to adaptive telemetry," 1964 Proc. Nat. Telem. Conf., The Institute of Electrical and Electronic Engineers, paper no. 1-4, Los Angeles, Calif., New York, N.Y., June 2-4, 1964.
7. Berkowitz, M., "An adaptive data sampling system," 1963 Nat. Space Electron. Sym. Record, The Institute of Electrical and Electronic Engineers, paper no. 4.1, Miami Beach, Florida, New York, N.Y., October 1-4, 1963.
8. Lauler, L. J., "A system oriented PCM ground station incorporating data compression," 1963 Nat. Space Electron. Sym. Record, The Institute of Electrical and Electronic Engineers, paper no. 4.4, Miami Beach, Florida, New York, N.Y., October 1-4, 1963.
9. Hulme, J. R., and R. A. Schomburg, "A data bandwidth compressor for space vehicle telemetry," 1962 Proc. Nat. Telem. Conf., The Institute of Radio Engineers, paper no. 3-2, Washington, D.C., New York, N.Y., May 23-25, 1962.
10. Sommer, R.C., and B. Harris, "Some recent advances in adaptive digital space telemetry systems," 1962 Proc. Nat. Telem. Conf., The Institute of Radio Engineers, paper no. 10-5, Washington, D.C., New York, N.Y., May 23-25, 1962.

11. Medlin, J. E., "Buffer length requirements for a telemetry data compressor," 1962 Proc. Nat. Telem. Conf., The Institute of Radio Engineers, paper no. 14-5, Washington, D.C., New York, N.Y., May 23-25, 1962.
12. Weber, D. R. and F. J. Wynhoff, "The concept of self-adaptive data compression," 1962 Nat. Symp. on Space Electron. and Telem. PGSET Record. The Institute of Radio Engineers, paper no. 4.1, Miami Beach, Florida, New York, N.Y., October 2-4, 1962.
13. Schomburg, R. A., "Computer simulation of a data compressor for aerospace telemetry systems," 1962 Nat. Symp. on Space Electron. and Telem. PGSET Record. The Institute of Radio Engineers, paper no. 4.2., Miami Beach, Florida, New York, N.Y., October 2-4, 1962.

COUNTING WITH MAXIMAL LENGTH SHIFT REGISTERS

R. Kahn* 7

N 67-22746

Counters are used for a variety of purposes on board satellites and most often these counters are of the binary type. In certain cases it may be possible to reduce the amount of equipment and energy consumption by using a shift register in conjunction with a single modulo-two adder to form a counter. This report deals with a study of the theoretical background required for logical design of such a counter. In addition, it presents an efficient decoding algorithm for determination of the order number of the state of the register, given the state. This algorithm is specifically applied to a register of degree 7, however a basic part of it is general and it is conjectured that an ad-hoc pattern recognition scheme developed for 7-tuples and used in decoding may be generalized to apply to the state of registers of higher order.

An N-stage shift register is a storage device which can retain N bits of information and which can simultaneously shift each of the N bits one unit to the left. The last bit is usually discarded when a shift occurs.



The contents of the shift register may be denoted by the binary N-tuple $(x_{n-1}, x_{n-2}, \dots, x_0)$ where x_{n-1} is the binary digit in the leftmost storage unit and x_0 is the binary digit in the rightmost storage unit. When a left shift occurs, the following transformation takes place.

$$x_k \rightarrow x_{k+1} \quad k = 0, 1, \dots, n-2$$

This says that x_k becomes x_{k+1} or that x_k is shifted to the left one unit for each value of k . This leaves x_0 unassigned. If a new bit of information is assigned to x_0 which depends upon the information bits x_1, x_2, \dots, x_{n-1} then a sequence of N-tuples will be generated in the shift register memory. Each N-tuple in the sequence is obtained from the previous N-tuple by left shifting the digits and introducing the new information bit in the x_0 position.

Since it is possible for 2^N different N-tuples to occur in the shift register memory, it may be used for counting purposes by interrogating the particular state (N-tuple) of the register and determining what position in the sequence of N-tuples it occupies. For simplicity in instrumentation, the new information bit will be generated by taking a modulo-two sum of certain of the information digits x_1, x_2, \dots, x_{n-1} . The all zero N-tuple can be used only as a starting state. The maximum number of distinct non-zero shift register states is $2^N - 1$. A shift register which is instrumented to generate all of these states is called a maximal length shift register. The state s_0 is defined to be the state where $x_0 = 1$ and all other bits are zero. Thus we can count from zero up to $2^N - 1$ by identifying the count in one to one correspondence with a state, such as $s_0, s_1, s_2, \dots, s_{2^N-2}$. For reasonably small values of N , it is possible to count quite high.

*Massachusetts Institute of Technology, Cambridge, Massachusetts.

Three questions are considered here. How does one generate the new information bit? Can a sequence of $2^N - 1$ distinct states be obtained for any value of N ? How may one efficiently determine the count from the state of the register? The first two questions fall in an area which has been studied rather intensively. They lean quite heavily upon algebraic concepts. A start will be made on the last question.

Let each state $\underline{s} = (x_{N-1}, x_{N-2}, \dots, x_1, x_0)$ of the shift register be represented by the polynomial $x(t)$ of degree $N-1$

$$x(t) = x_{N-1} t^{N-1} + x_{N-2} t^{N-2} + \dots + x_0$$

Since all the non-zero states must be represented, every cyclic shift of a shift register state must also be a shift register state. We therefore start at some state, say $x(t) = 1$ which is s_0 , and successively generate all $2^N - 1$ non-zero states s_0, \dots, s_{2^N-2} .

Suppose S is a collection of states, each state represented by a polynomial with binary coefficients. This set of states forms a cyclic group under multiplication where multiplication of polynomials is defined modulo a primitive polynomial $f(t)$ of degree N . Different group representations, all of which are essentially identical in structure, result from the various choices for $f(t)$. Since $f(t)$ is primitive, the powers of t reduced modulo $f(t)$ generate all $2^N - 1$ states of S . Since $f(t)$ is primitive it has a root α whose powers exhaust all the non-zero linear combinations of powers of α of degree less than or equal to $N-1$ and α is said to be a primitive root. For example, the polynomial $t^2 + t + 1$ has for its roots neither zero or one. So if α is a root it must satisfy the equation $\alpha^2 = \alpha + 1$. The multiplication table for the linear combinations of roots is

	0	1	α	$1 + \alpha$
0	0	0	0	0
1	0	1	α	$1 + \alpha$
α	0	α	$1 + \alpha$	1
$1 + \alpha$	0	$1 + \alpha$	1	α

Both α and $1 + \alpha$ are primitive roots of $t^2 + t + 1$ and 0 and 1 occur from the linear combinations. Since α is a primitive element, its powers exhaust all the non-zero states. Thus the root α or the polynomial t may be thought of as generating the non-zero states. This provides the necessary theory for the understanding of the maximal length shift register operation.

Let $f(t)$ be a primitive polynomial and $x(t)$ be one n -tuple in the sequence of $2^N - 1$ n -tuples. The state following $x(t)$ is given by the remainder after dividing $tx(t)$ by $f(t)$, for if $x(t)$ corresponds to state t^k then $tx(t)$ corresponds to state t^{k+1} .

Example:

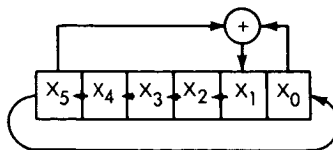
A table of some primitive polynomials is located in the back of Peterson (Reference 1). We will give an example for $N = 7$. The polynomial $t^7 + t^3 + 1$ is primitive. On dividing $x_6 t^7 + x_5 t^6 + \dots + x_0 t$ by $t^7 + t^3 + 1$ we get

$$x_4 t^5 + x_3 t^4 + x_2 t^3 + x_1 t^2 + (x_0 + x_5) t + x_5.$$

as the remainder. This says that the shift register should shift all digits one to the left bringing the left most digit to the x_0 position with the exception of the x_1 position, which should be the modulo two sum of x_0 and x_5 . The following is a list of the 63 successive distinct states of the shift register.

0	000001	32	001001
1	000010	33	010010
2	000100	34	100100
3	001000	35	001011
4	010000	36	010110
5	100000	37	101100
6	000011	38	011011
7	000110	39	110110
8	001100	40	101111
9	011000	41	011101
10	110000	42	111010
11	100011	43	110111
12	000101	44	101101
13	001010	45	011001
14	010100	46	110010
15	101000	47	100111
16	010011	48	001101
17	100110	49	011010
18	001111	50	110100
19	011110	51	101011
20	111100	52	010101
21	111011	53	101010
22	110101	54	010111
23	101001	55	101110
24	010001	56	011111
25	100010	57	111110
26	000111	58	111111
27	001110	59	111101
28	011100	60	111001
29	111000	61	110001
30	110011	62	100000
31	100101		

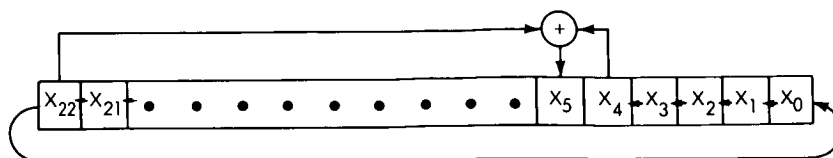
The shift register connections are illustrated below



The implementation requires only one modulo two adder because the primitive polynomial $f(t)$ has only one intermediate power of t between t^6 and t^9 , namely t^1 . If two or more such intermediate powers had been present, two or more modulo 2 adders would have been required. On glancing at the tables at the back of Peterson, it may be seen that a maximal length shift register with N stages and one Modulo 2 adder may be obtained when

$$N = 2, 3, 4, 5, 6, 7, 9, 10, 11, 15, 17, 18, 20, 21, 22, 23, 25, 28, 29, 31, 33 \dots$$

For example when $N = 23$ we have $f(t) = t^{23} + t^5 + 1$ as a primitive polynomial with only one intermediate term. The shift register configuration which implements $tx(t) \bmod t^{23} + t + 1$ is given by



The contents of the shift register are shifted left one unit, the left most bit is shifted into x_0 and x_5 is the modulo two sum of x_4 and x_{22} .

DECODING

If the shift register is used for counting purposes, the count must be rendered after reading the shift register contents. At a ground station, this could be accomplished by simulating a similar register on a computer and running through its states until one is obtained which matches the state of counter. However, this would involve large expenditures of computer time. For example, a maximal length shift register of length N , for which all counts are equally likely would require approximately 2^{N-1} shifts on the average. A method using less computer time would be more desirable.

All the sequences of N -tuples have the so-called shift and add property. If n and k are integers modulo $2^N - 1$ then $s_n + s_{n+k} = s_{n+f(k)}$, $n = 0, 1, \dots, 2^N - 2$ where $f(k)$ is one-to-one mapping of the integers mod $2^N - 1$ onto themselves. The specific form of the mapping depends upon the shift register connections or equivalently, the particular primitive polynomial. For the primitive polynomials $t^{23} + t^5 + 1$ the shift and add relationship $s_n + s_{n+5} = s_{n+23}$ may be used to avoid 18 of the 23 shifts between s_n and s_{n+23} . This decoding method would decrease the number of shifts by a factor of about $1/4$. It is guaranteed to eventually yield a sequence with a single one, regardless of which sequence is read out of the counter. For example, if after performing 14,295 shifts and 2859 additions, a sequence is obtained having a single one in the 16th position counting from the right, the original counter must have read $2^{23} - 2 + 16 - 2859 \times 23 = 8,322,865$. This method still requires an exponentially large number of shifts and additions.

It appears as if it ought to be possible to decode using an algebraically large number of operations. However, this would require geometric rather than arithmetic shifts from sequence to sequence. It is possible to shift from sequence s_n to sequence s_{2n} (or from sequence s_{2n} to sequence s_n) by appropriately rearranging modulo two sums of the entries in the N -tuple corresponding to state s_n . This is accomplished in the following manner. Multiplication is defined modulo the irreducible polynomial $f(t)$ of degree N . If s_n corresponds to the polynomial

$$x(t) = x_{N-1} t^{N-1} + x_{N-2} t^{N-2} + \dots + x_0$$

then s_{2n} corresponds to the polynomial $x^2(t) \bmod f(t)$. As an example, let $f(t) = t^7 + t^3 + 1$. If $x(t)$ is given by the equation

$$x(t) = x_6 t^6 + x_5 t^5 + x_4 t^4 + x_3 t^3 + x_2 t^2 + x_1 t + x_0$$

and corresponds to s_n , then s_{2n} corresponds to

$$x^2(t) \bmod (t^7 + t^3 + 1) = (x_3 + x_5) t^5 + x_6 t^5 + (x_2 + x_4 + x_6) t^4 \\ + x_5 t^3 + x_1 t^2 + (x_4 + x_6) t + x_0$$

The conversion of s_n to s_{2n} is accomplished by replacing the old entries x_k by new entries x_n^1 as follows.

$$\begin{aligned} \text{The new } x_0^1 &= \text{old } x_0 \\ \text{new } x_1^1 &= \text{old } x_4 + x_6 \\ \text{new } x_2^1 &= \text{old } x_1 \\ \text{new } x_3^1 &= \text{old } x_5 \\ \text{new } x_4^1 &= \text{old } x_2 + x_4 + x_6 \\ \text{new } x_5^1 &= \text{old } x_6 \\ \text{new } x_6^1 &= \text{old } x_3 + x_5 \end{aligned}$$

Conversely the conversion from s_{2n} to s_n is accomplished by replacing the old entries x_k by new entries x_k'' as follows:

$$\begin{aligned} \text{new } x_0'' &= \text{old } x_0 \\ \text{new } x_1'' &= \text{old } x_2 \\ \text{new } x_2'' &= \text{old } x_1 + x_4 \\ \text{new } x_3'' &= \text{old } x_3 + x_6 \\ \text{new } x_4'' &= \text{old } x_1 + x_5 \\ \text{new } x_5'' &= \text{old } x_3 \\ \text{new } x_6'' &= \text{old } x_5 \end{aligned}$$

If the counter contained a sequence corresponding to s_{2^k} then the halving procedure will eventually reduce the counter sequence to the sequence s_1 in $N - 1$ steps or fewer. For a sequence other than one of this form this procedure will not reduce to the s_1 sequence but will return to the original counter sequence in either N steps or fewer.

Every time a sequence corresponding to a state with an odd subscript s_{odd} is encountered, halving gives a new state whose subscript is larger. Only when halving s_{even} will this halving procedure give a state with a smaller subscript. If the even sequences s_{even} may be distinguished from the odd sequences s_{odd} , then the decoding may be accomplished with no more than $N - 1$ halvings.

The following ad-hoc procedure was found to be effective in distinguishing even and odd sequences for $N = 7$. It is fairly accurate. Count the number of ones in the sequence and let this number be k . The 7 positions where ones may occur are numbered

$$\begin{array}{ccccccc} 7 & 6 & 5 & 4 & 3 & 2 & 1 \\ \hline | & | & | & | & | & | & | \end{array}$$

If k equals

1. The sequence is even if the 1 is in an odd numbered position. Otherwise the sequence is odd.
2. The sequence is even if the middle zero (or the first 1 from the right if there is no middle zero) is in an even position. Otherwise the sequence is odd.
3. The sequence is even if the middle 1 is in an odd position. Otherwise the sequence is odd. The middle zero is defined to be present when the two ones are separated by an odd number of zeros. The middle zero is the center zero of this odd number of zeros.
4. If second and third ones are in consecutive positions, the sequence is
 - (a) even if the third 1 is in an even position
 - (b) odd if the third 1 is in an odd position.If second and third ones are not in consecutive positions, the sequence is
 - (a) even if the second 1 is in an even position
 - (b) otherwise the sequence is odd.
5. The sequence is even if the middle 1 is in an odd position. Otherwise the sequence is odd.
6. The sequence is even if the zero occurs in position 3,4,6, or 7.
7. Odd

Example: the counter contains 1101001

- (a) We guess this to be even because the second 1 is in position 4.
- (b) Halving gives us 1110001 which we guess to be even because the third 1 is in an even position.
- (c) Halving gives us 1011101 which we guess to be odd because the middle 1 is in position 4.
- (d) Shifting one count gives 0110011 which ought to be even, since the previous sequence was odd, and which the chart guesses is even anyway.
- (e) Halving gives us 1000001 which we guess to be even since the middle zero is in position 4.
- (f) Halving gives us 00010001 which we guess to be odd since the middle zero is in position 3.
- (g) Shifting one count gives 00100010 which the chart says is even anyway.
- (h) Halving gives us 0010000 which we recognize as the sequence s_4 . The original sequence must have been s_{108} (Since reversing the halving and shifting operations gives 4,8,7,14,28,27,54,108)

Example: The counter reads 0100101.

counter reads	0100101	- guess even
half	1010011	- guess odd (the guess is actually wrong!)
Shift	0101111	- guess even (so is this one!)
Halve	1101111	- guess odd
Shift	1010111	- guess even
Halve	0011011	- guess even
Halve	0111001	- guess odd
Shift	1110010	- guess even
Halve	1001001	- guess even
Halve	0100000	- sequence s_5

The original sequence was s_{44} or the 45th sequence.

It is apparent that every error in deciding between even and odd has the effect of negating all the previous work and requiring a new start. However, if the number of possible errors is small, the algorithm will still allow the count to be determined, but with more than $N-1$ halvings (but only an algebraic function of N). One method for detecting the possibility of error (using the chart to specify evenness and oddness) is to successively shift the sequence several times. Each shift produces a change from even to odd or odd to even and the guesses should reflect this series of changes. One shift will detect a single error and one could use a majority rule to make the decision if the possibility of two or three consecutive errors is not insignificant.

The next step would be to investigate the theoretical relationships between even and odd sequences and a generating primitive polynomial $f(t)$ of degree N . If precise theoretical discrimination between even and odd sequences, short of exhaustive tabulating procedures, is too difficult, one can look for recognition schemes. The chart for $N = 7$ is one example of such a pattern recognition scheme.

Another scheme, which is impractical because it requires storage of about $2^N/N$ sequences, uses the fact that successive doublings of a sequence will eventually generate the original sequence again in no more than $N + 1$ doublings. This defines a partition of sequences into equivalence classes, namely those sequences which can be reached from another by successive doublings are in the same equivalence class. For $N = 6$ there are 12 equivalence classes, the subscripts of which are listed below.

1, 2, 4, 8, 16, 32	13, 26, 52, 41, 19, 38
3, 6, 12, 24, 48, 33	15, 30, 60, 57, 51, 39
5, 10, 20, 40, 17, 34	21, 42
7, 14, 28, 56, 49, 35	23, 46, 29, 58, 53, 43
9, 18, 36	27, 54, 45
11, 22, 44, 25, 50, 37	31, 62, 61, 59, 55, 47

If one sequence from each of the equivalence classes were placed in storage and compared in turn with successive doublings of the counter sequence, a match would occur within N doublings.

An interesting set of graph like structures, which might have some use in the decoding of the counter sequence are generated when the shift and add property is incorporated in between the successive doublings. These graphs are illustrated below.

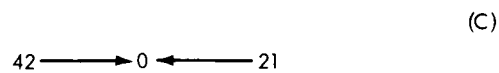
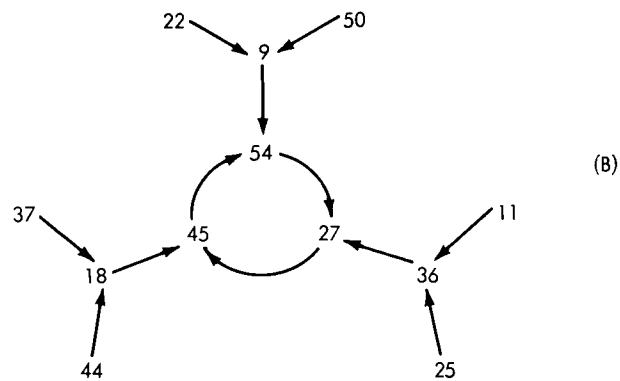
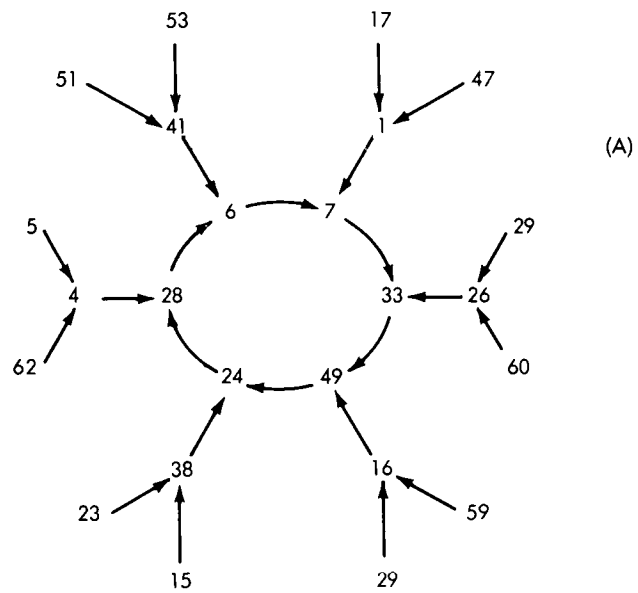


Figure A-23—Graphs generated when the shift and odd property is incorporated in between the successive doublings.

Suppose the counter sequence is s_{10} . If s_{20} is doubled and s_{40} is added to s_{20} the sequence s_{16} results. This is indicated on the graph by the arrow from 20 to 16. If s_{16} is doubled and s_{32} is added to s_{16} the sequence s_{49} results. Eventually a cyclic chain of sequences $s_7 - s_{33} - s_{49} - s_{24} - s_{28} - s_6 - s_7$ will result. If s_7 , say, is placed in storage it will be reached in 6 steps from s_{20} . When this occurs it is known that the original sequence was either s_{201} , s_{59} , or s_{26} . One way of determining which of these three was sent is to use the halving procedure from before or to shift the original sequence one or two times and use the graph again. There is also another graph identical to (A) but with each number doubled modulo 63. The graph itself has some interesting properties, such as the flow graph property with addition modulo 63. However, this graph structure is very much dependent upon the primitive polynomial $f(x)$ and may involve an exponentially large number of very simple graph structures. Furthermore, if it were to be useful in decoding it would have to be for values of N much larger than 6. Also it would be necessary to have a simple and efficient method of generating the basic graph structures.

INVESTIGATION OF THE RELIABILITY OF A PROPOSED CONFIDENCE LEVEL PROCEDURE FOR ERROR PROBABILITY OF A BANK OF CORRELATORS

D. A. Munn*

N 67-22747

At present one of the methods used for the detection of PFM signals transmitted by a satellite is to apply the signal to a bank of correlators resulting in a set of voltage outputs. The maximum likelihood decision rule in such a system is to select the frequency of the correlator with the largest output as the transmitted frequency. One method of obtaining a confidence measure on this decision is to obtain an estimate of the signal-to-noise ratio at the correlator's output. A formula used for this estimate is (Reference 1)

$$\text{SNR} = \frac{C_{\max}^2}{\frac{2}{M-1} \left(\sum_{i=1}^M C_i^2 - C_{\max}^2 \right)} \quad (1)$$

where

C_i = the output of the i^{th} correlator

C_{\max} = the largest of the correlator outputs

M = the number of linear correlators

This estimate of the signal-to-noise ratio may then be used with a probability of word error curve (see Reference 2) to obtain a confidence measure. The estimate of signal-to-noise ratio given by Equation (1) is reliable for values of SNR larger than 5 db. For lower values of SNR the results are less reliable.

An alternate procedure for obtaining a confidence level has been suggested by F. L. Ramsey (Reference 3) and it is stated that this suggested scheme results in reliable confidence levels for small values of SNR. The formula given for the confidence level L is

$$L = 1 - \left(\frac{C_{\text{next}}}{C_{\max}} \right)^{M-1} \quad (2)$$

where C_{\max} and M have the same meaning as in (1) and C_{next} is the output of the correlator having the next to the highest output.

It has been proposed to use the results of Equation (1) and Equation (2) to build a probability of correct decision computer in the data and synchronization portions of a phase coherent communication system. In this system the noise distribution at the output of the correlators is Gaussian.

The advantage of using Equation (2) to obtain a confidence measure is its simplicity, however, the reliability of this method has not been investigated. The present report gives the result of a computer simulation where a known amount of (RMS) noise is fed to $M - 1$ simulated "correlators" and the sum of known signal and noise is fed to the M^{th} simulated "correlator". Details of this simulation and results indicate that Equation (2) does not give a reliable confidence level for small signal-to-noise ratio.

*University of Missouri, Columbia, Missouri

COMPUTER SIMULATION

A uniform pseudorandom number generator was obtained (Reference 4) for use in generating Gaussian random numbers. The steps used to generate these pseudorandom Gaussian numbers are

$$y_i = \sum_{j=1}^{50} x_{i,j} \quad j = 1, 2, \dots, 200$$

$$\mu = \left(\sum_{j=1}^{200} y_j \right) / 200$$

$$\sigma^2 = \frac{\sum_{j=1}^{200} (y_j)^2}{200} - \mu^2$$

$$G_j = \frac{(y_j - \mu)}{\sigma}, \quad j = 1, 2, \dots, 200$$

where $x_{i,j}$ is a matrix of uniform random numbers with 200 rows of 50 random numbers in each row, and G_j is the resulting Gaussian random number. This method generates pseudorandom Gaussian numbers in groups of 200 that have a mean of 0 and a variance of 1.

The M simulated "correlator" outputs are formed by taking M Gaussian random numbers and adding a signal to the M^{th} . A subroutine is then used to determine the values of C_{max} and C_{next} . Let the correlator containing C_{max} be the k^{th} . The following intermediate values are calculated to determine L .

$$R = \frac{C_{\text{next}}}{C_{\text{max}}} \quad (3)$$

$$P = R^{(M-1)} \quad (4)$$

The number of correlators, the number of tests, and the signal are variables in the program. For each signal the error rate is calculated.

$$\text{error rate} = \frac{\text{number of tests where } k \neq M}{\text{total number of tests}}.$$

RESULTS

The reliability of a decision will depend on how much the value of L with a signal present differs from the value when no signal is present. The value of L is easily computed from

the ratio R and the presentation of results is more conveniently done in terms of R . For this reason the following sequence of tests was carried out.

1. A series of 16,000 tests with no signal was carried out for $M = 15$. Results of these tests are tabulated in Figure A-24. The value of the ratio R lies between 0 and 1. This interval is divided into 20 equal sub intervals and Figure A-24 shows the percentage of the time that the ratio R lies in any of these intervals. For example, in the absence of signal, 11.3 percent of the time the ratio R was in the interval 0.95 to 1.0, 11.4 percent of the time in the interval 0.90 to 0.95, etc. In fact 44.4 percent of the time, in the absence of signal, the ratio R is between 0.8 and 1.0. On the other end of the scale, in the absence of signal, 4.7 percent of the time the ratio R is between 0.0 and 0.4.

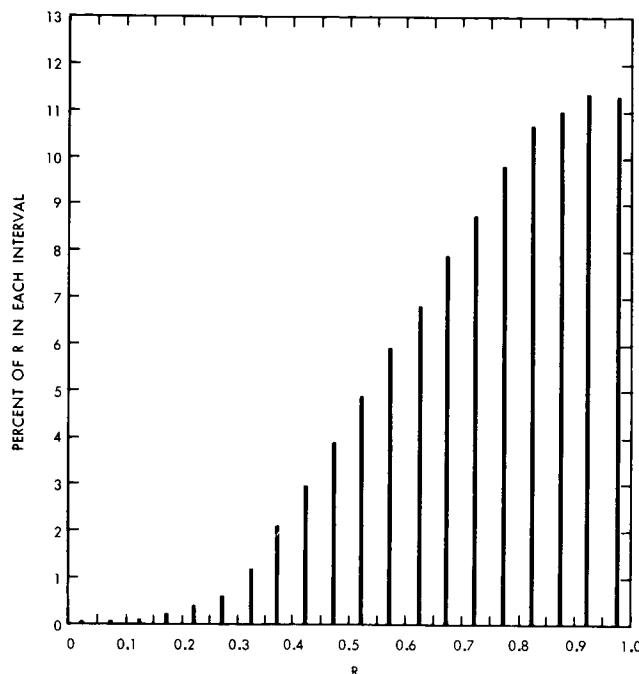


Figure A-24— $M = 15$, Random case, signal = 0, 16000 tests.

2. A series of 6000 tests with a signal of 3.0 (and noise variance of 1) was carried out for $M = 15$. With the signal present there are two cases: 1) Largest correlator output at the M^{th} correlator ($k = M$) and 2) Largest correlator output not at the M^{th} correlator ($k \neq M$).

With a signal of 3.0, 5234 tests out of 6000 indicated $k = M$ and the remaining 766 tests indicated $k \neq M$. This gives an error rate of 12.77 percent for the 6000 tests. The results of these tests are tabulated in Figure A-25. The interval between 0 and 1 is again divided into 20 equal sub intervals. In Figure A-24 the solid lines are based on the 5234 tests where $k = M$ and show the percentage of time that the ratio lies in any of the intervals, while the dashed lines are based on the 766 tests where $k \neq M$ and show the percentage of time that the ratio R lies in any of the intervals. For example, in the interval of 0.95 to 1.0 there were 17.6 percent of the 766 tests and 2.2 percent of the 5234 tests ($k = M$). Note that when there was a false alarm (signal indication with no signal present) 3.25 percent of the time the value of the ratio R was less than 0.5. This corresponds to a confidence level of greater than 0.9999 on the false alarm that a signal exists.

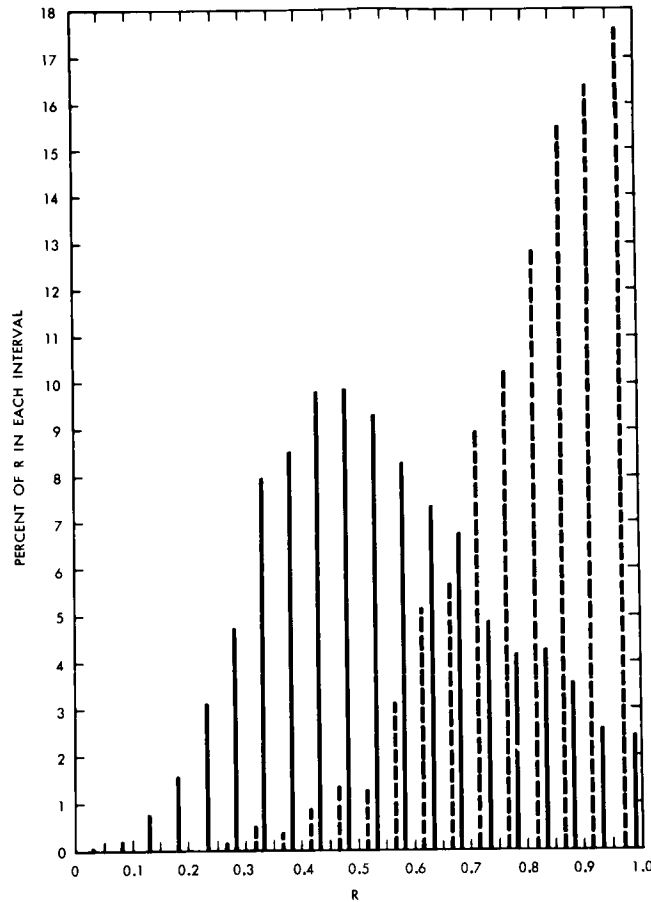


Figure A-25— $M = 15$, signal = 3.0; (SNR = 0.614 db)
solid link $k = M$; dashed line $k \neq M$; 6000 tests; error
rate, 0.1276.

3. Five more series of tests were carried out for $M = 15$. Information on this series of tests is tabulated below.

Table A-1

Figure	Number of Tests	Signal	Number of Cases $k = M$	Number of Cases $k \neq M$	Error Rate %	Comments
A-26	5000	3.5	4714	286	5.72	For $k = M$, 35.2% of time $R < 0.4^*$
A-27	5000	4.0	4903	97	1.94	For $k = M$, 44.4% of time $R < 0.4^*$
A-28	1000	4.5	9900	100	1.00	For $k = M$, 56.9% of time $R < 0.4^*$
A-29	1000	5.0	9979	21	0.21	For $k = M$, 57.2% of time $R < 0.4^*$
A-30	1000	6.0	1000	0	0.00	For $k = M$, 84.5% of time $R < 0.4^{**}$

*There were an insufficient number of tests for case where $k \neq M$.

**There were no cases for $k \neq M$.

CONCLUSIONS

When the ratio R is applied to a phase coherent communication system, the resulting confidence measure is not reliable at low signal-to-noise ratios. This conclusion is reached by comparing the results of the case with no signal present to the cases with signal present. Reliability in the confidence measure is based on how much the case with signal present at the M th correlator overlaps the case with no signal present, as illustrated (Figures A-24 through A-30). This overlap decreases with increasing values of signal indicating that, for larger signal-to-noise ratios, the ratio R may give a reliable confidence measure. With further work the ratio R may provide a simple test to give a confidence measure for use in a probability of correct decision computer.

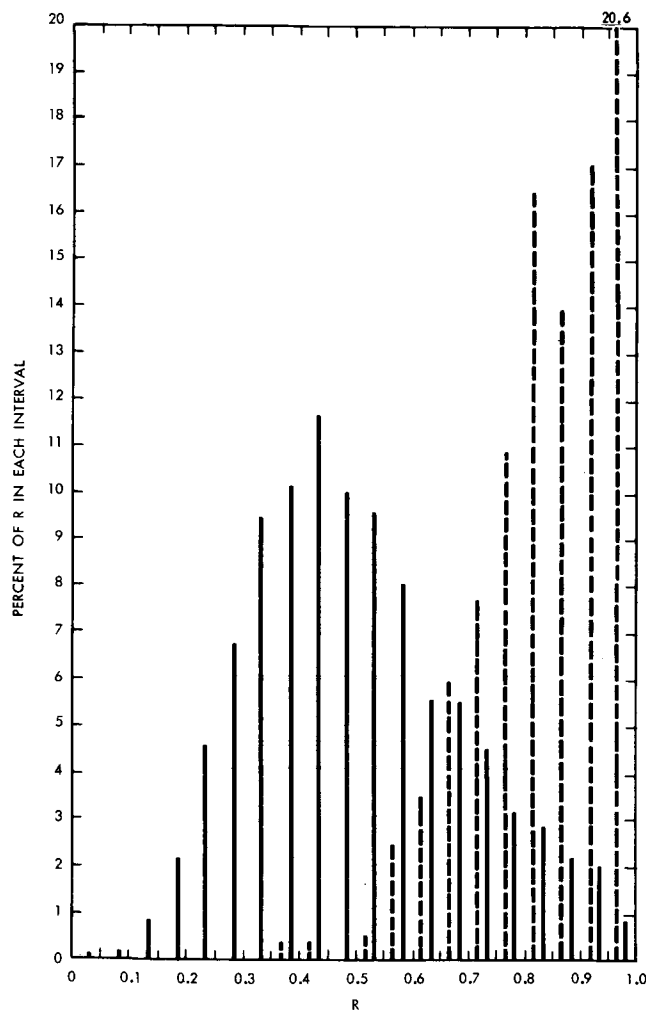


Figure A-26— $M = 15$; signal = 3.5; (SNR = 1.953 db)
solid line $k = M$; dashed line $k \neq M$; 5000 tests; error
rate = 0.0572.

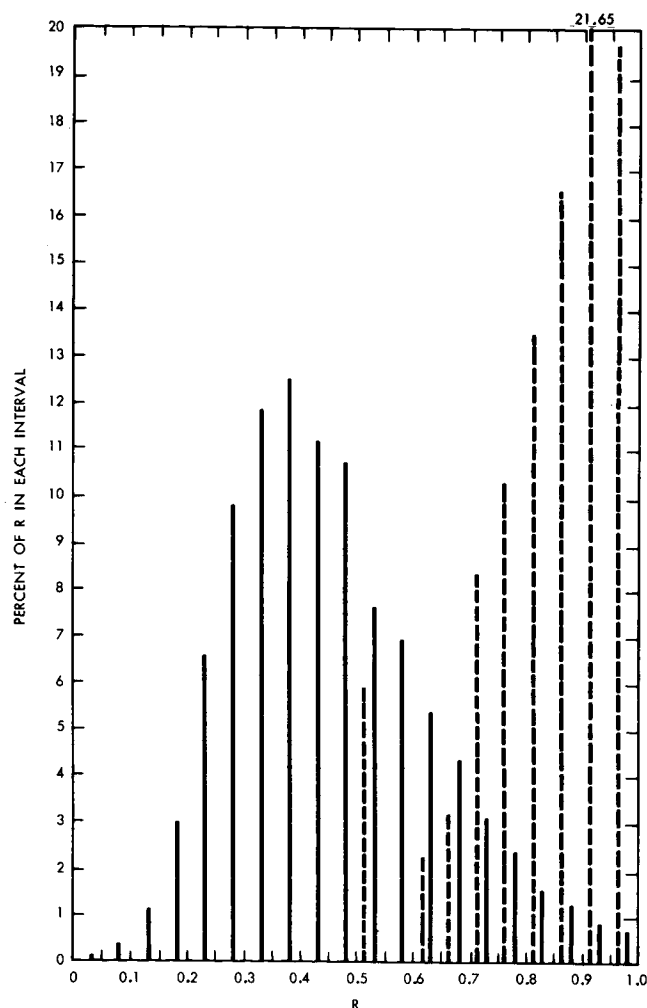


Figure A-27— $M = 15$; signal = 4.00; (SNR = 3.11 db)
solid line $k = M$; dashed line $k \neq M$; 5000 tests; error
rate = 0.0194.

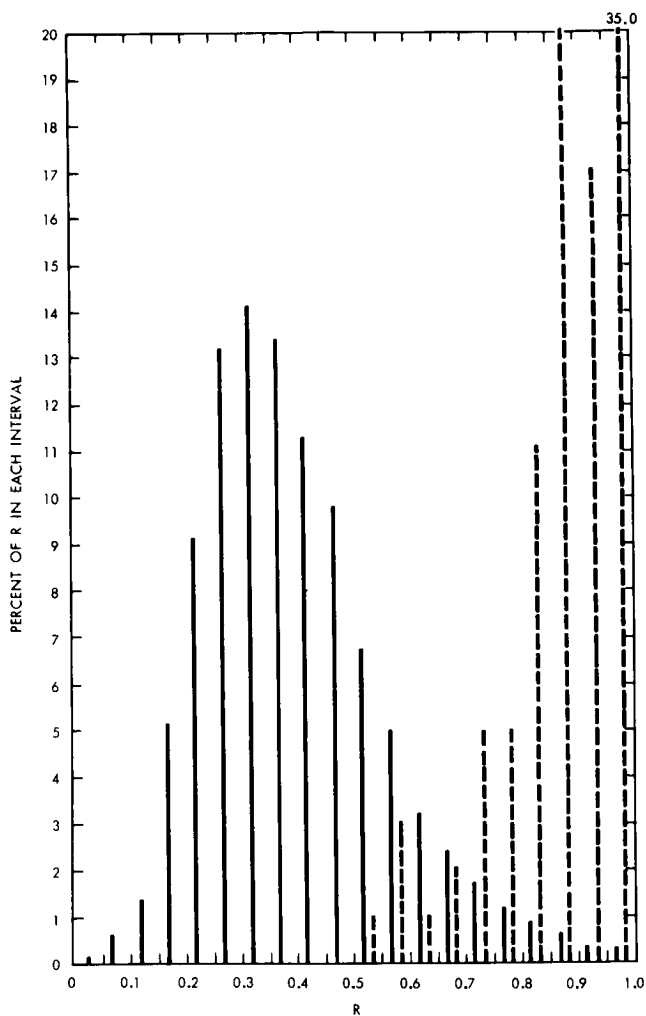


Figure A-28— $M = 15$; signal = 4.5; (SNR = 4.14 db)
solid line $k = M$; dashed line $k \neq M$; 10,000 tests;
error rate = 0.010.

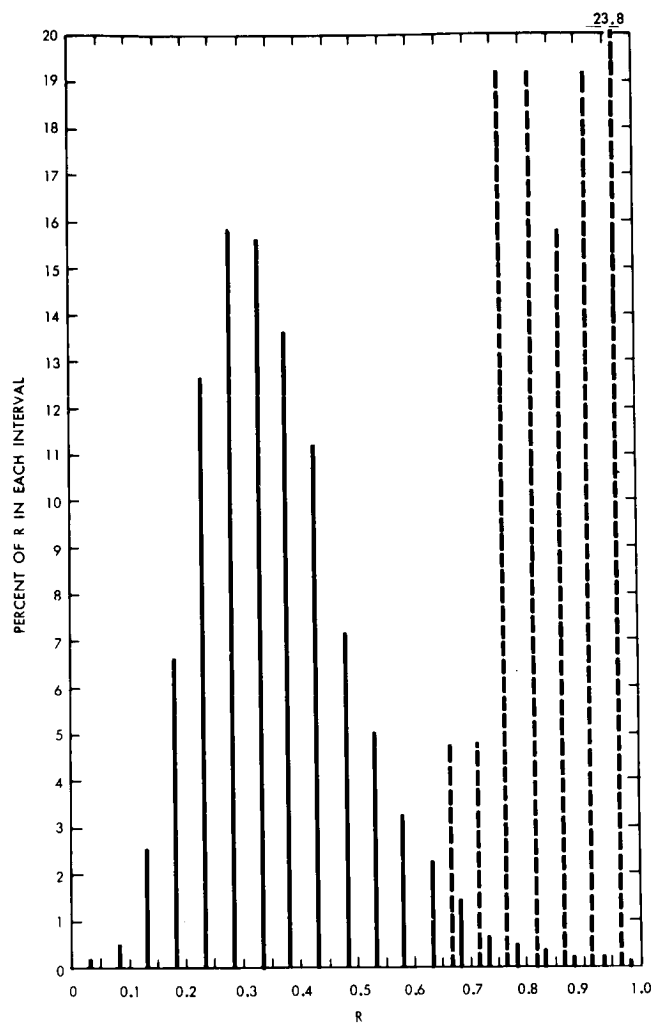


Figure A-29— $M = 15$; signal = 5.0; (SNR = 5.05 db)
solid line $k = M$; dashed line $k \neq M$; 10,000 tests;
error rate = 0.0021.

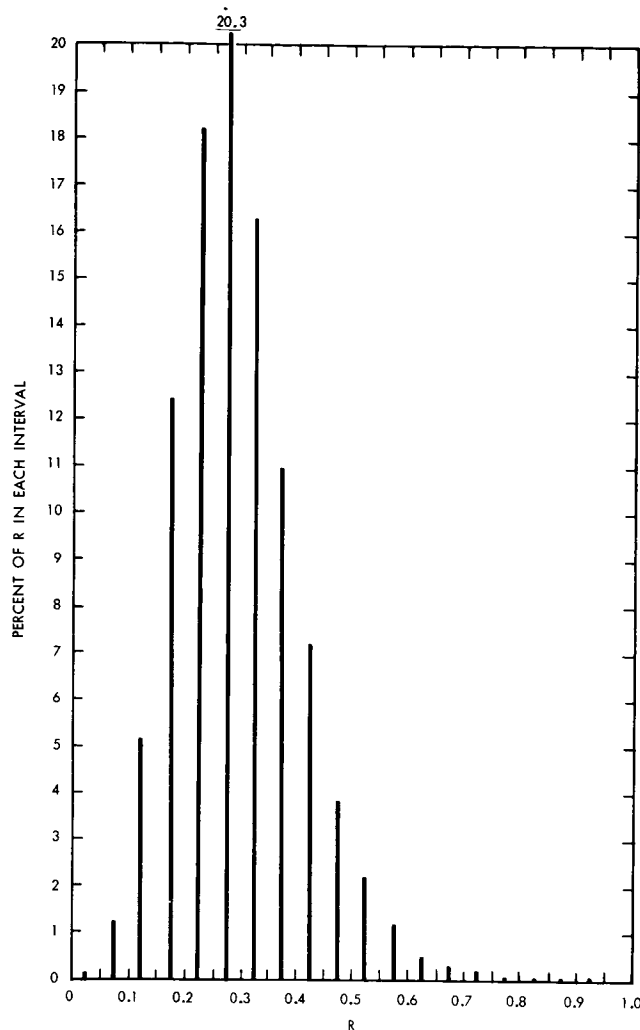


Figure A-30-M = 15; signal = 6.0; (SNR = 6.63 db)
k = M; 10,000 tests.

REFERENCES

1. Kerr, R.B., "On signal and noise level estimation in a coherent PCM channel," Duke University Research Contract No. NAS5-3815, Spacecraft Telemetry Systems Lab., Dept. of E.E., Duke University, 1965, also IEEE-AES-2, No. 4, 450-455.
2. Saliga, T.V. and Stronghill III, J.P., "Comparison of phase-coherent and non-phase-coherent coded communications," NASA Report TN-D-3079, March, 1966.
3. Ramsey, F.L., "A minimum confidence level for signal detection by a correlator bank," Goddard Summer Workshop Final Report (1965), NASA Report X-100-65-407, pages A97-A104.
4. Hutchinson, Davis W., "A new uniform pseudorandom number generator," Communications of the ACM V. 9, No. 6, p. 432, June, 1966.
5. Javid, M., "Confidence level of decision based on the output of correlators of a PFM system," Goddard Summer Workshop Final Report (1965), NASA Report X-100-65-407, pages A85-A88.

NON-PARAMETRIC SIGNAL DETECTION

E.A. Feustel*

N 67-22748

The topic studied in this report is based on the following binary decision problem. Given that, in an interval $(0, \tau)$, a sampled waveform $v(t)$ contains noise alone or noise and signal, decide whether or not the signal is present in this interval. If the form of the noise is known, the optimum solution has been found (Reference 1) for numerous decision criteria. The optimum realizations for the decision procedures are often difficult to achieve when the noise has non-stationary statistics or is of a non-Gaussian nature. In these cases practical considerations call for the use of sub-optimum techniques. One variety of these sub-optimum techniques is categorized as nonparametric (Reference 2). A special sub-class of nonparametric tests requires the calculation of rank statistics. This report is concerned with the effects of dependence of the observations on the resulting rank statistics.

Two criteria have been selected which determine the form of the decision rules. α is the probability of saying the signal is present when it is not. β is the probability of saying that the signal is present when it actually is. The tests considered are to minimize α , or to hold it below α_0 , a fixed level, while maximizing β . As might be expected there are many tests meeting the required criteria. This results in a need for further criteria which compare the effectiveness of the various decision rules. The criteria selected is known as the asymptotic relative efficiency (A.R.E.) of two tests with respect to one another. It compares the number of observations for the two tests, required for given α and β for small signal-to-noise ratios, under the assumption that the number for each is very large.

A well known test used for a decision is based on rank statistics. As previously used, this test requires independent observations. These observations are ranked on the basis of amplitude or magnitude and a function of the ranking is calculated and issued as the rank statistic associated with the group of observations. Typically, between one thousand and ten thousand observations are required and the work required for ranking these observations increases as $n \log n$ (minimum). Because of the requirement for independence and the large amount of work required to rank the observations, rank statistics are not usually useful in real time detection problems.

Recently a modification of rank statistics has been proposed which allows their use in real time decision procedures for very high observation rates. (Reference 3). This modification simplifies the calculation of rank statistics of independent observations. But, in practice, independent observations are rarely available, especially at reasonable sampling rates. The question thus arises: "How do the modified rank statistics perform if dependent observations are used?" This question has two phrasings. First, what is the effect on false alarm rate α and A.R.E. if independent observations are assumed when in truth the observations are dependent? Second, assuming that the correlation matrix of the data is known, how does the modified test compare with the test which was optimum for independent samples?

To determine the answer to these questions, the variance of the modified statistic and the optimum statistic must be found under the assumption of dependence. In addition, the incremental mean must be found (Reference 4). Because of the nonlinearity of the modified rank statistic, the variance is not easily determined. By restricting the class of noise processes to the class containing first order Markov processes of the continuous, stationary variety, some progress can be obtained.

*Princeton University, Princeton, N.J.

The generalized formula for the number of terms in each variance expression in question was found by induction from counts on experiments with small sample size. At the end of the workshop, a similar technique was being employed to determine analytic approximations to variance and incremental mean. A great deal of time was spent developing computer programs to aid in these determinations. Incidentally, an efficient test called Polarity Coincidence Wilcoxon, was developed for use in detecting pseudo-random signals. It has a relative efficiency of 190% with respect to the Polarity Coincidence Correlator. Work was begun on the use of nonparametric statistics in sequential analysis. Completed work appears in the appendices. Further research will be carried on at Princeton University this fall until the matters outlined above have been satisfactorily concluded.

THEORY

Consider the following problem of hypothesis testing.

$$H_0: \text{Hypothesis: } v(t_i) = n(t_i) \quad i = 1, 2 \dots N$$

$$H_1: \text{Alternative: } v(t_i) = n(t_i) + S(t_i) \quad i = 1, 2 \dots N$$

Where $n(t)$ is a random variable with continuous density function $dP(\mu)$. It is known that the optimum decision rule involves the calculation of the likelihood ratio:

$$\Lambda = \frac{dP(\mu/H_1)}{dP(\mu/H_0)}$$

and comparing this ratio to a threshold which has been determined a priori from decision criteria. In the case of the Neyman-Pearson criteria, the probability of false alarm α , the probability of saying H_1 when H_0 is true, and β the probability of saying H_1 when H_1 is true are specified. The Neyman-Pearson lemma guarantees optimality in the sense that for $\alpha \leq \alpha_0$, β is maximized.

If the optimum test is to be used, the form of the density $dP(\mu)$ must be known for H_0 and H_1 . If it is not and a test statistic is used improperly, detection efficiency is impeded. In Appendixes A through C, the optimum tests are computed with the sample mean test for Gaussian, Exponential, and Cauchy distributions. It is well to note the progressive failure of efficiency for the Sample Mean test.

A suboptimum test which yields better results is also illustrated. It is a member of a class of tests known as nonparametric tests. Nonparametric tests are less influenced by the form of the distribution $dP(\mu)$ and are useful when the distribution is compound or unknown. Many tests such as the one illustrated have been developed and a measure of test efficiency has come into use.

The measure is asymptotic relative efficiency, (A.R.E.). It indicates as a fraction the ratio of the average number of observations in test A to that of test B for a given α and β under the assumption of small signal to noise ratio and large sample size.

This measure indicates that, for three different kinds of hypothesis-alternative pairs, the Wilcoxon, Mann-Whitney, and Kendall τ nonparametric statistics are very efficient. These statistics are members of a family of statistics known as rank statistics. If the observations are ordered by some property such as magnitude, absolute magnitude, etc. and a numerical rank is assigned to each observation, the rank statistic is a sum of a non-linear functional operating on the rank each observation. This is denoted symbolically by:

$$S^N = \sum_{i=1}^N f(R(x_i))$$

where $R(x_i)$ is the rank of the i^{th} observation.

While these statistics have high efficiencies, they are rarely used in engineering practice. An examination of the Wilcoxon typical rank statistic will indicate why. The Wilcoxon statistic calculates the sum of the ranks of positive observations which have been ranked, smallest to largest, on the basis of absolute magnitude.

$$S^N = \sum_{i=1}^N f(R | x_i |)$$

$$S^N = \sum_{i=1}^N \sum_{j=1}^N u(x_i + x_j)$$

An example follows.

Suppose the following sequence is received: -1, +3, -7, +5, -4, -6, +10, +8. In absolute order these become: -1, +3, -4, +5, -6, -7, +8, +10. Summing the ranks of positive observations: +2 +4 +7 +8 = 21. This sum is compared to a threshold which has been determined by a priori consideration of requirements for α and β . If the number is greater than the threshold, H_1 is chosen as the probable cause; otherwise H_0 is chosen.

The average number of observations required for detection probabilities; $\alpha = 0.001$, $\beta = 0.8$, is measured in thousands, each of which must be ranked. The work involved in the ranking goes up as $n \log n$ and prohibits realtime application. In addition, it has been assumed that the sampled data consists of independent observations. This assumption is not realistic when the many natural low pass filters in a system are considered.

Recent work (Reference 2) has shown that all the work in ranking is not necessary. A trade-off of efficiency for ranking speed is available and advantageous. If the rank statistics are calculated on blocks of observations and the resultant numbers are summed over all blocks, it is found that the asymptotic properties change little if the block size is greater than ten. These new statistics are much easier to calculate and if a method such as the Wilcoxon is employed to process the blocks, the resulting statistic can be calculated in real time utilizing flip-chip hardware. Such a mixed statistic is of the form:

$$S_w^N = \sum_{i=1}^N \text{sgn}(x_i) R(|x_i|) = \sum_{i=1}^N \sum_{j=1}^N u(x_i + x_j)$$

where

$$u(a) = \begin{cases} 1 & a > 0 \\ 0 & a < 0 \end{cases}$$

Because of this newly available tool, a fresh look at dependent sample rank tests seems appropriate. This involves a calculation of incremental mean,

$$\frac{\partial E[S^N]}{\partial \mu} \bigg|_{\mu=0}$$

and variance, $\text{var}(S^N/H_0)$. If a Markov model of degree n is assumed, it becomes apparent that the calculation of variance is an insurmountable task for large n . In the Wilcoxon Mixed Statistic the following must be calculated:

$$E[(S_w^N/H_0)^2] = \sum_{i=0}^{p-1} \sum_{j=0}^{p-1} \sum_{k=i_m+1}^{(L+1)_m} \sum_{\ell=k}^{(i+1)_m} \sum_{q=i_m+1}^{(j+1)_m} \sum_{r=q}^{(j+1)_m} u(x_k + x_\ell) u(x_q + x_r)$$

It was decided to limit the investigation to first order Markov processes with Gaussian, Exponential, and Cauchy distributions on the underlying variables. If for example we have n underlying independent random variables $\{Y_i\}$, the dependent ones are: $\{x_i/x_i = y_i + \rho Y_{i-1}\}$

PROGRESS

This work has progressed steadily since the beginning of the summer workshop. The incremental means have been shown to be simple analytic expressions and are tabulated in Appendixes D through F. The variance has proven a somewhat more difficult problem. For example in the case of the Wilcoxon there are 27 different types of correlation that are possible. After these expressions had been determined, a Fortran program was designed to calculate the number of terms of each type for a block size m and block length p . By operating a number of runs with differing parameters, the algebraic equations in m and p for each term were deduced. A second type of Fortran program was written which calculates the variance of the Wilcoxon terms for Gaussian Markov processes up to twenty-fifth order. This was used to provide an indication of the effect of using more terms in the variance expression. In tables A-2, A-3, and A-4, the effects of increasing the Markov order are shown. Note that for small order correlation the effect is negligible.

A second phase was begun with the development of a program which causes the automatic calculation of variance for a first order Markov process of correlation ρ and variables m and p . Double precision arithmetic was utilized so that coefficient calculation could be performed. A SHARE subroutine is currently being employed to reduce the numbers obtained for the variance to analytic form in ρ , m , and n . All the foregoing has also been done for the Mann-Whitney, and Kendall rank test. Results should be forthcoming shortly.

Finally, a new statistic has been developed as a generalization of the Polarity Coincidence Correlator which performs almost 190% as efficiently for Gaussian inputs. Details for this development are included in Appendix G.

CONCLUSION

Considerable progress has been made toward an understanding of the effect of first order Markov dependence on rank statistics. While the study is not yet complete, it is expected that the results will lend encouragement to the use of mixed rank statistics in signal detection and communications systems where they have not previously been employed. A new test has been developed which relates the Polarity Coincidence Correlator to a more efficient test.

Table A-2
Variance of Mixed Wilcoxon Gaussian Input

m	p	Rho	Variance	Markov Order
10	3	0.	0.288749999999978D 03	25
10	3	0.500000000000000D-01	0.312105658378760D 03	1
10	3	0.500000000000000D-01	0.313224621749041D 03	2
10	3	0.500000000000000D-01	0.313278896300521D 03	3
10	3	0.500000000000000D-01	0.313281527982008D 03	4
10	3	0.500000000000000D-01	0.313281655467091D 03	5
10	3	0.500000000000000D-01	0.313281661636395D 03	6
10	3	0.500000000000000D-01	0.313281661934604D 03	7
10	3	0.500000000000000D-01	0.313281661944678D 03	8
10	3	0.500000000000000D-01	0.313281661945111D 03	9
10	3	0.500000000000000D-01	0.313281661945129D 03	10
10	3	0.250000000000000D-00	0.404603657968225D 03	1
10	3	0.250000000000000D-00	0.430859828937045D 03	2
10	3	0.250000000000000D-00	0.437147964695943D 03	3
10	3	0.250000000000000D-00	0.438674413276918D 03	4
10	3	0.250000000000000D-00	0.439045858642001D 03	5
10	3	0.250000000000000D-00	0.439136239627604D 03	6
10	3	0.250000000000000D-00	0.439158217464643D 03	7
10	3	0.250000000000000D-00	0.439163557357898D 03	8
10	3	0.250000000000000D-00	0.439164853201212D 03	9
10	3	0.250000000000000D-00	0.439165166817389D 03	10

Table A-3
Variance of Mixed Mann Whitney Gaussian Input

m	p	Rho	Variance	Markov Order
10	3	0.	0.524999999999934D 03	25
10	3	0.500000000000000D-01	0.571869271734086D 03	1
10	3	0.500000000000000D-01	0.574127193281210D 03	2
10	3	0.500000000000000D-01	0.574235920490215D 03	3
10	3	0.500000000000000D-01	0.574241148631275D 03	4
10	3	0.500000000000000D-01	0.574241399627740D 03	5
10	3	0.500000000000000D-01	0.574241411656958D 03	6
10	3	0.500000000000000D-01	0.574241412232274D 03	7
10	3	0.500000000000000D-01	0.574241412244982D 03	8
10	3	0.500000000000000D-01	0.574241412245489D 03	9
10	3	0.500000000000000D-01	0.574241412245507D 03	10
10	3	0.250000000000000D-00	0.761198694107417D 03	1
10	3	0.250000000000000D-00	0.817799620531049D 03	2
10	3	0.250000000000000D-00	0.831410355223006D 03	3
10	3	0.250000000000000D-00	0.834681509297296D 03	4
10	3	0.250000000000000D-00	0.835466588604710D 03	5
10	3	0.250000000000000D-00	0.835654690365099D 03	6
10	3	0.250000000000000D-00	0.835699674277845D 03	7
10	3	0.250000000000000D-00	0.835710409899442D 03	8
10	3	0.250000000000000D-00	0.835712966216963D 03	9
10	3	0.250000000000000D-00	0.835713573399426D 03	10

Table A-4
Variance of Mixed Kendall τ Gaussian Input

m	p	Rho	Variance	Markov Order
10	3	0.	0.937499999999922D 02	25
10	3	0.500000000000000D-01	0.940147890595990D 02	1
10	3	0.500000000000000D-01	0.940088579137069D 02	2
10	3	0.500000000000000D-01	0.940085785965303D 02	3
10	3	0.500000000000000D-01	0.940085668049355D 02	4
10	3	0.500000000000000D-01	0.940085663251770D 02	5
10	3	0.500000000000000D-01	0.940085663066784D 02	6
10	3	0.500000000000000D-01	0.940085663060282D 02	7
10	3	0.500000000000000D-01	0.940085663060090D 02	8
10	3	0.500000000000000D-01	0.940085663060086D 02	9
10	3	0.500000000000000D-01	0.940085663060085D 02	10
10	3	0.250000000000000D-00	0.100981637896153D 03	1
10	3	0.250000000000000D-00	0.100458879968806D 03	2
10	3	0.250000000000000D-00	0.100271052659572D 03	3
10	3	0.250000000000000D-00	0.100229666171645D 03	4
10	3	0.250000000000000D-00	0.100221316389987D 03	5
10	3	0.250000000000000D-00	0.100219734233924D 03	6
10	3	0.250000000000000D-00	0.100219462943411D 03	7
10	3	0.250000000000000D-00	0.100219424914857D 03	8
10	3	0.250000000000000D-00	0.100219421486065D 03	9
10	3	0.250000000000000D-00	0.100219420621855D 03	10

REFERENCES

1. Helstrom, Carl, Statistical Theory of Signal Detection, New York: Pergamon Press, 1960.
2. Kendall, M. G. and Stuart, A., The Advanced Theory of Statistics, Volume II, New York, Hafner Publishing Co., 1961.
3. Feustel, E. A. and Davisson, L. D., "The asymptotic relative efficiency of mixed statistics," In preparation.
4. Middleton, David, "Canonically optimum threshold detection" IEEE Transactions on Information Theory, V. IT-12 No. (2); April, 1966.

APPENDIX A

OPTIMUM GAUSSIAN DETECTION FOR INDEPENDENT SAMPLED DATA

$$\Lambda = \frac{p(\vec{x}/H_1)}{p(\vec{x}/H_0)}$$

$$= \frac{\frac{1}{(2\pi)^{N/2} \sigma^N} \exp \left[-\frac{1}{2} \sum_{i=1}^N \frac{(x_i - \mu)^2}{\sigma^2} \right]}{\frac{1}{(2\pi)^{N/2} \sigma^N} \exp \left(-\frac{1}{2} \sum_{i=1}^N \frac{x_i^2}{\sigma^2} \right)}$$

$$\ln \Lambda = \frac{1}{2} \left[\sum_{i=1}^N \left(\frac{2\mu x_i - \mu^2}{\sigma^2} \right) \right] \underset{H_0}{\overset{H_1}{>}} C$$

$$S_0^N = \frac{1}{N} \sum_{i=1}^N x_i \underset{H_0}{\overset{H_1}{>}} C_1$$

$$E(S_0^N/H_1) = \mu$$

$$\left. \frac{\partial E(S_0^N/H_1)}{\partial \mu} \right|_{\mu=0} = 1$$

$$\text{Var}(S_0^N/H_0) = \frac{\sigma^2}{N}$$

$$\varepsilon_0 = \frac{N}{\sigma^2}$$

MIXED STATISTIC DETECTION FOR INDEPENDENT GAUSS DISTRIBUTED SAMPLE DATA

$$\text{Wilcoxon: } S_W^N = \sum_{i=0}^{p-1} \sum_{j=im+1}^{m(i+1)} \sum_{k=j}^{m(i+1)} u(x_j + x_k)$$

$$u(x) = \begin{cases} 1 & x > 0 \\ 0 & x < 0 \end{cases}$$

$$E(S_W^N/H_1) = p \left\{ m E[u(x_i)] + \frac{m(m-1)}{2} E[u(x_i + x_j)] \right\}$$

$$\left. \frac{\partial E(S_W^N/H_1)}{\partial \mu} \right|_{\mu=0} = p \left[\frac{m}{\sqrt{2}\pi\sigma} + \frac{m(m-1)}{2} \frac{\sqrt{2}}{\sqrt{2}\pi\sigma} \right]$$

$$= p \frac{m(m-1+\sqrt{2})}{2\sqrt{\pi}\sigma} = \frac{N(m-1+\sqrt{2})}{2\sqrt{\pi}\sigma}$$

$$\text{Var}(S_W^N/H_0) = p \frac{m(2m+1)(m+1)}{24} = \frac{N(2m+1)(m+1)}{24}$$

$$\varepsilon_W = \frac{N^2(m-1+\sqrt{2})^2 24}{4\pi\sigma^2 N(2m+1)(m+1)} = \frac{6N(m-1+\sqrt{2})^2}{\pi(2m+1)(m+1)\sigma^2}$$

ASYMPTOTIC RELATIVE EFFICIENCY FOR INDEPENDENT
GAUSS DISTRIBUTED SAMPLED DATA

$$\text{A.R.E. (Mixed to Optimum)} = \frac{\xi_w}{\xi_0} = \frac{6N(m-1+\sqrt{2})^2 \sigma^2}{\pi(2m+1)(m+1)\sigma^2 N}$$

$$= \frac{6(m-1+\sqrt{2})^2}{\pi(2m+1)(m+1)}$$

$$= \frac{2}{\pi} \quad m = 1$$

$$\rightarrow \frac{3}{\pi} \quad m \rightarrow \infty$$

APPENDIX B

OPTIMUM EXPONENTIAL DETECTION WITH INDEPENDENT SAMPLED DATA

$$\Lambda = \frac{\frac{1}{(2b)^N} \exp - \sum_{i=1}^N \frac{|x_i - \mu|}{b}}{\frac{1}{(2b)^N} \exp - \sum_{i=1}^N \frac{|x_i|}{b}}$$

$$\ln \Lambda = \frac{1}{b} \sum_{i=1}^N (|x_i| - |x_i - \mu|)$$

$$S_0^N = \frac{1}{N} \sum_{i=1}^N (|x_i| - |x_i - N|)$$

$$\begin{aligned} E(S_0^N/H_0) &= \int_{-\infty}^{\infty} \frac{(|x_i| - |x_i - \mu|)}{2b} \exp - \frac{|x|}{b} dx \\ &= b(1 - e^{-\mu/b}) - N \end{aligned}$$

$$\begin{aligned} E(S_0^N/H_1) &= \int_{-\infty}^{\infty} \frac{(|x_i| - |x_i - N|)}{2b} \exp - \left(\frac{|x - N|}{2b} \right) dx \\ &= -b(1 - e^{-N/b}) + N = -E(S^N/H_0) \end{aligned}$$

$$\text{Var}(S_0^N/H_1) = E[(S^N/H_1)^2] - E^2(S^N/H_1)$$

$$= \frac{1}{N} \left[b^2 (3 + e^{-N/b}) (1 - e^{-\mu/b}) - \frac{4\mu}{b} e^{-N/b} \right]$$

$$\text{Var}(S_0^N/H_0) = \text{Var}(S^N/H_1).$$

$$K = E(S_0^N/H_1) - E(S_0^N/H_0) = z [\mu - b(1 - e^{-\mu/b})]$$

$$\varepsilon_0 = \frac{K^2}{\mu^2 \text{Var}} (S_0^N/H_0) = \frac{4N [(\mu^2 - 2\mu b + b^2) - (2b^2 + 2b\mu) e^{-\mu/b} - b^2 e^{-2\mu/b}]}{b^2 [(3 + e^{-\mu/b}) (1 - e^{-\mu/b}) - 4\mu/b e^{-\mu/b}]}$$

Expanding the numerator and denominator in a power series about $\mu = 0$ and disregarding second order terms:

$$\mathcal{E}_0 = \frac{\frac{\mu^4}{b^2}}{\frac{\mu^2}{N}} = \frac{N\mu^2}{b^2}$$

MIXED STATISTIC DETECTION FOR INDEPENDENT EXPONENTIALLY DISTRIBUTED SAMPLED DATA

For a Wilcoxon:

$$S_W^N = \sum_{i=0}^{p-1} \sum_{j=mi+1}^{m(i+1)} \sum_{k=j}^{m(i+1)} \mu (x_j + x_k)$$

$$E_{H_1} (S_W^N) = pm E [\mu (x_j)] + p \frac{m(m-1)}{2} E [\mu (x_i + x_j)]$$

$$\left. \frac{\partial E_{H_1} (S_W^N)}{\partial \mu} \right|_{\mu=0} = pm \left(\frac{1}{2b} \right) + \frac{pm(m-1)}{2} \left(\frac{1}{2b} \right)$$

$$= \frac{N(m+1)}{4b}$$

$$\text{Var} (S_W^N/H_0) = p \frac{m(2m+1)(m+1)}{24}$$

$$= \frac{N(2m+1)(m+1)}{24}$$

$$\mathcal{E}_W = \frac{N^2 (m+1)^2 \cdot 24}{16b^2 \cdot N(2m+1)(m+1)} = \frac{3N(m+1)}{2b^2(2m+1)}$$

SAMPLE MEAN DETECTION FOR INDEPENDENT EXPONENTIALLY DISTRIBUTED SAMPLE DATA

$$S^N = \frac{1}{N} \sum_{i=1}^N x_i$$

$$E_{H_1}(S^N) = \mu$$

$$\left. \frac{\partial E_{H_1}(S^N)}{\partial \mu} \right|_{\mu = 0} = 1$$

$$\text{Var}(S^N/H_0) = \frac{2b^2}{N}$$

$$\varepsilon_{SM} = \frac{N}{2b^2}$$

ASYMPTOTIC RELATIVE EFFICIENCIES OF EXPONENTIALLY DISTRIBUTED INDEPENDENT SAMPLED DATA

$$\text{A.R.E. (Wilcoxon to Sampled Mean)} = \frac{\varepsilon_w}{\varepsilon_{SM}} = \frac{\frac{3N(m+1)}{2(2m+1)}b^2}{\frac{N}{2b^2}}$$

$$= \frac{3(m+1)}{(2m+1)}$$

$$= 2 \quad m = 1$$

$$\rightarrow \frac{3}{2} \quad m \rightarrow \infty$$

$$\text{A.R.E. (Wilcoxon to Optimum)} = \frac{\varepsilon_w}{\varepsilon_o} = \frac{\frac{3N(m+1)}{2(2m+1)}b^2}{\frac{N}{b^2}}$$

$$= \frac{3(m+1)}{2(2m+1)}$$

$$= 1 \quad m = 1$$

$$\rightarrow \frac{3}{4} \quad m \rightarrow \infty$$

$$\text{A.R.E. [Sampled Mean to Optimum]} = .5$$

APPENDIX C

OPTIMUM DETECTION FOR INDEPENDENT CAUCHY SAMPLES

$$\Lambda = \frac{\prod_{i=1}^N \frac{1}{\pi b} \frac{1}{\left[1 + \left(\frac{x_i - a}{b}\right)^2\right]}}{\prod_{i=1}^N \frac{1}{\pi b} \frac{1}{\left[1 + \left(\frac{x_i}{b}\right)^2\right]}}$$

$$-\ln \Lambda = \sum_{i=1}^N \left[\frac{1 + \left(\frac{x_i - a}{b}\right)^2}{1 + \left(\frac{x_i}{b}\right)^2} \right]$$

$$= N - \sum_{i=1}^N \frac{2 a x_i - a^2}{b^2 \left[1 + \left(\frac{x_i}{b}\right)^2\right]}$$

$$\ln \Lambda = \sum_{i=1}^N \frac{2 a x_i - a^2}{b^2 \left[1 + \left(\frac{x_i}{b}\right)^2\right]} - N \underset{H_0}{\overset{H_1}{>}} C$$

$$S_0^N = \frac{1}{N} \sum_{i=1}^N \frac{2 a x_i - a^2}{\left[1 + \left(\frac{x_i}{b}\right)^2\right]}$$

$$E(S_0^N/H_0) = -\frac{a^2}{2}$$

$$E(S_0^N/H_1) = +\frac{a^2}{2}$$

$$\text{Var}(S_0^N/H_0) = \frac{a^2 b^2}{2N} + \frac{a^4}{8N} \approx \frac{a^2 b^2}{2N}$$

$$\text{Var } (S_0^N/H_1) = \frac{a^2 b^2}{2N}$$

$$\mathcal{E}_0 = \frac{1}{a^2} \cdot \frac{a^4}{\frac{a^2 b^2}{2N}} = \frac{2N}{b^2}$$

MIXED STATISTIC DETECTION FOR INDEPENDENT CAUCHY DISTRIBUTED SAMPLE DATA

Wilcoxon Detection: $S_W^N = \sum_{j=1}^p \sum_{R=(j-1)m+1}^{jm} \sum_{l=k}^{jm} u(x_k + x_l)$

$$E(S_W^N/H_1) = p \left\{ m E[u(x_j)] + \frac{m(m-1)}{2} E[u(x_k + x_l)/k \neq 1] \right\}$$

$$E[u(x_j)] = \frac{1}{2} + \frac{1}{\pi} \tan^{-1} \left(\frac{a}{b} \right)$$

$$E[u(x_j + x_k)/k \neq 1] = \int_{-\infty}^{\infty} \frac{\left[\frac{1}{2} + \frac{1}{\pi} \tan^{-1} \left(v + \frac{2a}{b} \right) \right]}{\pi [1 + v^2]} dv$$

$$\frac{\partial E[S_W^N/H_1]}{\partial a} = p \left[\frac{m}{\pi b} + \frac{m(m-1)}{2\pi b} \right]$$

$$= \frac{pm(m+1)}{2\pi b}$$

$$= \frac{N(m+1)}{\pi b}$$

$$\text{Var } [S_W^N/H_0] = \frac{pm(m+1)(2m+1)}{24} = \frac{N(m+1)(2m+1)}{24}$$

$$\mathcal{E}_W = \frac{N^2(m+1)^2 24}{4\pi^2 b^2 (m+1)(2m+1)N} = \frac{6(m+1)}{\pi^2 b^2 (2m+1)}$$

SAMPLE MEAN DETECTION OF INDEPENDENT CAUCHY DISTRIBUTED SAMPLED DATA

$$S^N = \frac{1}{N} \sum_{i=1}^N x_i$$

$$E_{H_1} (S^N) = a$$

$$\frac{\partial E_{H_1} (S^N/H_1)}{\partial a} \bigg|_{a=0} = 1$$

Var (S^N/H₀) is indeterminate

ASYMPTOTIC RELATIVE EFFICIENCY FOR INDEPENDENT CAUCHY DISTRIBUTED SAMPLED DATA

$$\text{A.R.E. (Mixed to Optimum)} = \frac{\frac{6(m+1)N}{\pi^2 b^2 (2m+1)}}{\frac{2N}{b^2}}$$

$$= \frac{3(m+1)}{\pi^2 (2m+1)}$$

$$= \frac{2}{\pi^2} \quad m = 1$$

$$= \frac{\frac{3}{2}}{\pi^2} \quad m \rightarrow \infty$$

APPENDIX D MIXED WILCOXON DEPENDENT SAMPLE ANALYSIS

Assume: $^2u_{ijk1} = u(x_i + x_j) u(x_k + x_1)$

$$^1u_{ij} = u(x_i + x_j)$$

where

$$u(a) = \begin{cases} 1 & a > 0 \\ 0 & a < 0 \end{cases}$$

and

$$R_{nm} = \begin{cases} 1 & n = m \\ \rho & n = m \pm 1 \\ 0 & \text{otherwise} \end{cases}$$

$$S_W^N = \sum_{i=0}^{p-1} \sum_{j=im+1}^{(i+1)m} \sum_{k=j}^{(i+1)m} ^1u_{ij}$$

$$E(S_W^N/H_1) = \sum_{i=0}^{p-1} \sum_{j=im+1}^{(i+1)m} \sum_{k=j}^{(i+1)m} E(^1u_{ij})$$

$$E(\cdot) = \int_0^\infty d p(x) = p_1 \quad i = j$$

$$E(\cdot) = \int_{-\infty}^\infty \int_{-x_1}^\infty p(x_1, x_2) dx_2 dx_1 = p_2 \quad i = j \pm 1$$

$$E(\cdot) = \int_{-\infty}^\infty \int_{-x_1}^\infty d p(x_1) d p(x_2) = p_3$$

Otherwise if $p(x)$ is Gaussian with mean μ and variance σ^2

$$p_1 = 1 - \Phi\left(-\frac{N}{\sigma}\right)$$

$$p_3 = 1 - \Phi\left(-\frac{\sqrt{2}N}{\sigma}\right)$$

$$p_2 = 1 - \int_{-\infty}^{\infty} \Phi \left(\frac{-y - 2N - \rho y}{\sigma (1 - \rho^2)^{1/2}} \right) \frac{1}{\sqrt{2\pi} \sigma} \exp - \frac{1}{2} \frac{y^2}{\sigma^2} dy$$

$$\left. \frac{\partial p_1}{\partial N} \right|_{N=0} = \frac{1}{\sqrt{2\pi} \sigma}$$

$$\left. \frac{\partial p_2}{\partial N} \right|_{N=0} = \frac{1}{\sqrt{\pi}} (1 + \rho)^{1/2} \sigma$$

$$\left. \frac{\partial p_3}{\partial N} \right|_{N=0} = \frac{1}{\sqrt{\pi}} \sigma$$

$$\left. \frac{\partial E [S_W^M]}{\partial \mu} \right|_{\mu=0} = \frac{Mp}{\sqrt{2\pi} \sigma} + \frac{p(m-1)}{(1+\rho)^{1/2} \sqrt{\pi} \sigma} + \frac{1}{\sqrt{\pi} \sigma} \frac{(m-1)(m-2)}{2}$$

for

$$|\rho| < .5$$

If the p blocks are dependent of one another, by induction one has that:

$$\begin{aligned} \text{Var } (S_W^N) = & \left\{ p(m-3)(m-4)(m-5)(m-6)/4 + \right. \\ & \left. (m-2)^2 \left[\frac{(m-1)^2}{4} p - 2 \right] (p-1) \right\} E^2 u_{1357} \\ & + \{ p(m-3)(m-4)(m-5) + (m-2)[(m-1)^2 p - 4](p-1) \} E^2 u_{1257} \\ & + \{ p(m-2)(m-3)(m-4) + (m-2)(p-1)[m(m-1)p - 4] \} E^2 u_{1157} \\ & + \{ p(m-3)(m-4) + (p-1)[(m-1)^2 p - 2] \} E^2 u_{1256} \\ & + \{ 2p(m-2)(m-3) + [2m(m-1)p - 4](p-1) \} E^2 u_{1156} \\ & + \{ p(m-1)(m-2) + [m^2 p - 2](p-1) \} E^2 u_{1155} \\ & + [2p(m-3)(m-4)(m-5) + 2(m-2)^2(p-1)] E^2 u_{1427} \\ & + [p(m-2)(m-3)(m-4)] E^2 u_{1417} \\ & + [4p(m-3)(m-4) + 4(m-2)(p-1)] E^2 u_{1317} \end{aligned}$$

$$\begin{aligned}
& + [2p(m-3)(m-4)] E^2 u_{1327} \\
& + [2p(m-3)(m-4)] E^2 u_{1425} \\
& + [4p(m-2)(m-3) + 4(m-2)(p-1)] E^2 u_{1125} \\
& + [4p(m-2)(m-3)] E^2 u_{1215} \\
& + [2p(m-1)(m-2)] E^2 u_{1114} \\
& + [p(m-1)(m-2)/2] E^2 u_{1313} \\
& + [2p(m-3) + 2(p-1)] E^2 u_{1234} \\
& + [2p(m-3)] (E^2 u_{3425} + E^2 u_{2435}) \\
& + 4p(m-2) E^2 u_{1213} \\
& + 2p(m-2) E^2 u_{1223} \\
& + [4p(m-2) + 4(p-1)] E^2 u_{2234} \\
& + 2p(m-2) E^2 u_{2213} \\
& + [2p(m-1) + 2(p-1)] E^2 u_{1122} \\
& + p(m-1) E^2 u_{1212} \\
& + 4p(m-1) E^2 u_{1113} \\
& + pm E^2 u_{1111} \\
& + 2p(m-2)(m-3) E^2 u_{1314} \\
& - \left\{ p \left[m E^1 u_{11} + (m-1) E^1 u_{12} + \frac{(m-1)(m-2)}{2} E^1 u_{13} \right] \right\}^2
\end{aligned}$$

where for gaussians

$$E^2 u_{ijkl} = \frac{1}{4} + \frac{1}{2\pi} \arcsin \left[\frac{R_{ik} + R_{il} + R_{jk} + R_{kl}}{(1 + R_{ij})^{1/2} (1 + R_{kl})^{1/2}} \right]$$

APPENDIX E MIXED MANN-WHITNEY DEPENDENT SAMPLE ANALYSIS

Assume:

$$^2u_{ijk1} = u(x_i - y_j) u(x_k - y_l)$$

$$^1u_{ij} = u(x_i - y_j)$$

where

$$u(x) = \begin{cases} 1 & x > 0 \\ 0 & \text{otherwise} \end{cases}$$

and

$$R_{nm} = \begin{cases} 1 & n = m \\ \rho & n = m \pm 1 \\ 0 & \text{otherwise} \end{cases}$$

$$S_{mw}^N = \sum_{i=1}^p \sum_{j=i(m-1)+1}^{im} \sum_{k=i(m-1)+1}^{im} u(x_j - y_k)$$

$$\begin{aligned} E_{H_1} [S_{mw}^N] &= \sum_{i=1}^p \sum_{j=i(m-1)+1}^{im} \sum_{k=i(m-1)+1}^{im} E \ ^1u_{jk} \\ &= \int_{-\infty}^{\infty} \int_{-\infty}^{\infty} d p_x(x) d p_y(y) \end{aligned}$$

for Gaussians:

$$= Nm \int_{-\infty}^{\infty} \left[1 - \Phi \left(\frac{y - \mu}{\sigma} \right) \right] \frac{1}{\sqrt{2\pi}\sigma} \exp - \frac{1}{2} \frac{y^2}{\sigma^2} dy$$

where

$$\Phi(x) = \int_{-\infty}^x \frac{1}{\sqrt{2\pi}} \exp\left(-\frac{1}{2} y^2\right) dy$$

$$\left. \frac{\partial E_{H_1}(S_{MW}^N)}{\partial \mu} \right|_{\mu=0} = \frac{Nm}{\sqrt{2} \sqrt{2\pi} \sigma}$$

For dependent blocks

$$\begin{aligned} \text{Var}(S_{M-W}^N/H_0) = & [(m-1)^2 (m-2)^2 p + (m^4 p - 4m^2 + 2)(p-1)] E^{2u}_{1357} \\ & + [4(m-1)^2 (m-2) p + 4(m^2 - 1)(p-1)] E^{2u}_{1859} \\ & + [4(m-1)^2 p + 2(p-1)] E^{2u}_{1829} \\ & + [2m(m-1)(m-2)p] E^{2u}_{1517} \\ & + [4m(m-1)p] E^{2u}_{1516} \\ & + m^2 p E^{2u}_{1212} - \frac{p^2 m^4}{4} \end{aligned}$$

APPENDIX F

MIXED KENDALL τ GAUSSIAN DEPENDENT SAMPLE ANALYSIS

Assume:

$$^4u_{ijkl} = u(x_i - x_j) u(x_k - x_l) \cdot u(y_i - y_j) u(y_k - y_l)$$

$$^2u_{ij} = u(x_i - x_j) u(y_i - y_j)$$

where

$$u(x) = \begin{cases} 1 & x > 0 \\ 0 & x < 0 \end{cases}$$

and

$$R_{nm} = \begin{cases} 1 & n = m \\ \rho & n = m \pm 1 \\ 0 & \text{otherwise} \end{cases}$$

$$S_{\tau}^N = \sum_{i=0}^{p-1} \sum_{j=m_i+1}^{m(i+1)} \sum_{k=j+1}^{m(i+1)} \frac{1}{2} (1 - \operatorname{sgn}(x_i - x_j) \operatorname{sgn}(y_i - y_j))$$

Find

$$E \left[\frac{1}{2} (1 - \operatorname{sgn}(x_i - x_j) \operatorname{sgn}(y_i - y_j)) \right]$$

Assume that x_i, x_j, y_i, y_j are Gaussian with zero mean and covariance:

$$\bar{R}(H_1) = \begin{vmatrix} 1 & \rho & \gamma & 0 \\ \rho & 1 & 0 & \gamma \\ \gamma & 0 & 1 & \rho \\ 0 & \gamma & \rho & 1 \end{vmatrix}$$

and

$$\bar{R}(H_0) = \begin{vmatrix} 1 & 0 & \gamma & 0 \\ 0 & 1 & 0 & \gamma \\ \gamma & 0 & 1 & 0 \\ 0 & \gamma & 0 & 1 \end{vmatrix}$$

After considerable manipulation:

$$\frac{\partial E [S_r^N]}{\partial \gamma} \bigg|_{\gamma=0} = p(m-1) \left(\frac{2(1+\rho^2)}{\pi(1+\rho)} \right) + \frac{p(m-1)(m-2)}{2} \cdot \left(\frac{2}{\pi} \right)$$

In calculating the variance we note that for this case

$$\begin{aligned} \text{Var}_{H_0} & \frac{1}{2} [1 - \text{sgn}(x_i - x_j) \text{sgn}(y_i - y_j)] \\ & = \frac{4}{(2\pi)^2} \arcsin^2(Q) \end{aligned}$$

where

$$Q = \frac{\cos[(x_i - x_j)(x_k - x_l)]}{\text{Var}^{1/2}(x_i - x_j) \text{Var}^{1/2}(x_k - x_l)}$$

let

$${}^2A_{ijkl} = \frac{4}{(2\pi)^2} \arcsin^2(Q)$$

then

$$\text{Var}_{H_0}(S_r^N) =$$

$$\begin{aligned} & \left\{ p(m-3)(m-4)(m-5)(m-6)/4 + (m-2)^2 \left[\frac{(m-1)^2}{4} p - 2 \right] (p-1) {}^2A_{1357} \right\} \\ & + \left\{ p(m-3)(m-4)(m-5) + (m-2)(p-1)[(m-1)^2 p - 4] \right\} {}^2A_{1257} \\ & + \left\{ p(m-3)(m-4) + (p-1)[(m-1)^2 p - 2] \right\} {}^2A_{1256} \\ & + [4p(m-3)(m-4)(m-5)/3] {}^2A_{1527} \\ & + [2p(m-3)(m-4)(m-5)/3 + 2(m-2)^2(p-1)] {}^2A_{1568} \\ & + [p(m-2)(m-3)(m-4)] \left(\frac{2}{3} {}^2A_{1417} + \frac{1}{3} {}^2A_{1558} \right) \\ & + [2p(m-3)(m-4)] {}^2A_{4537} \\ & + [2p(m-3)(m-4) + 4(m-2)(p-1)] {}^2A_{4513} \\ & + [2p(m-3)(m-4)] {}^2A_{1327} \\ & + [2p(m-3)(m-4)] {}^2A_{1425} \end{aligned}$$

$$+ [2p(m-2)(m-3)] ({}^2A_{1214} + {}^2A_{4514})$$

$$+ [p(m-1)(m-2)/2] {}^2A_{1313}$$

$$+ [2p(m-3) + 2(p-1)] {}^2A_{1234}$$

$$+ [2p(m-3)] ({}^2A_{1324} + {}^2A_{2314})$$

$$+ [4(m-2)p] {}^2A_{1213}$$

$$+ [2p(m-2)] {}^2A_{1223}$$

$$+ p(m-1) {}^2A_{1212}$$

$$+ 2p(m-2)(m-3) {}^2A_{1314}$$

APPENDIX G

A NEW MIXED STATISTIC: POLARITY COINCIDENCE WILCOXON

$$H_0: x_i = n_{1i} \quad y_i = n_{2i} \quad n_{1i}, n_{2i} \sim G(0, \sigma^2)$$

and n_{1i}, n_{2i} are independent

$$H_1: x_i = n_{1i} + \mu_i \quad y_i = n_{2i} + \mu_i$$

where n_{1i} and n_{2i} are as before and $\mu_i \sim G(0, \gamma^2)$ and μ_i is independent of all other variables

$$S_{pcw}^N = \sum_{i=0}^{p-1} \sum_{j=m_i+1}^{m(i+1)} \sum_{k=j}^{m(i+1)} u(x_j y_j + x_k y_k)$$

$$\left. \frac{\partial E_{H_1} [u(x_i y_i)]}{\partial \gamma^2} \right|_{\gamma^2=0} = \frac{1}{\pi \sigma^2}$$

$$\left. \frac{\partial E_{H_1} [u(x_i y_i + x_j y_j) / i \neq j]}{\partial \gamma^2} \right|_{\gamma^2=0} = \frac{\pi}{2 \pi \sigma^2}$$

$$\begin{aligned} \left. \frac{\partial E(S_{pcw}^N / H_1)}{\partial \gamma^2} \right|_{\gamma^2=0} &= p \left[\frac{m}{\pi \sigma^2} + \frac{m(m-1)}{\pi \sigma^2} \frac{\pi}{4} \right] \\ &= N \left[\frac{1 + \frac{\pi}{4}(m-1)}{\pi \sigma^2} \right] \end{aligned}$$

$$\text{Var}(S_{pcw}^N / H_0) = p \frac{m(m+1)(2m+1)}{24}$$

$$\varepsilon_{pcw} = \frac{24 N^2 \left[1 + \frac{\pi}{4}(m-1) \right]^2}{N(m+1)(2m+1) \pi^2 \sigma^4}$$

$$= \frac{24 N \left[1 + \frac{\pi}{4} (m - 1) \right]^2}{(m + 1) (2m + 1) \pi^2 \sigma^4}$$

$$A.R.E._1 = \frac{\varepsilon_{pcw}}{\varepsilon_{pcc}} = \frac{6 \left[1 + \frac{\pi}{4} (m - 1) \right]^2}{(m + 1) (2m + 1)}$$

$$A.R.E. = \begin{cases} 1 & m = 1 \\ 1.85 & m \rightarrow \infty \end{cases}$$

$$A.R.E._2 = \frac{\varepsilon_{pcw}}{\varepsilon_{cor}} = \frac{24 \left[1 + \frac{\pi}{4} (m - 1) \right]^2}{(m + 1) (2m + 1) \pi^2} = .75 \quad m \rightarrow \infty$$

$$A.R.E._3 = \frac{\varepsilon_{pcw}}{\varepsilon_{opt}} = \frac{12 \left[1 + \frac{\pi}{4} (m - 1) \right]^2}{(m + 1) (2m + 1) \pi^2} = .375 \quad m \rightarrow \infty$$

APPENDIX H OPTIMUM GAUSSIAN DETECTION FOR DEPENDENT SAMPLED DATA

$$\Lambda = \frac{\frac{1}{(2\pi)^{N/2}} ||R|| \exp -\frac{1}{2} (x - \mu)^T R^{-1} (x - \mu)}{\frac{1}{(2\pi)^{N/2}} ||R|| \exp -\frac{1}{2} (x)^T R^{-1} (x)}$$

$$= \exp -\frac{1}{2} (-\mu^T R^{-1} x - x^T R^{-1} \mu + \mu^T R^{-1} \mu)$$

let

$$R_y = x; y = R^{-1} x$$

$$\ln \Lambda = -\frac{1}{2} [-\mu^T y - y^T \mu + \mu^T R^{-1} \mu]$$

$$S_{opt}^N = \frac{1}{N} \sum_{i=1}^N y_i \begin{matrix} H_1 \\ > \\ < \\ H_0 \end{matrix} C$$

$$\frac{1}{N} E_{H_1} (y) = \frac{1}{N} E_{H_1} (R^{-1} x) = \frac{1}{N} R^{-1} \mu$$

$$\frac{1}{N} \frac{\partial}{\partial N} E_{H_1} (y) = \frac{1}{N} R^{-1} [1$$

$$\frac{\partial E(S_{opt}^N)}{\partial N} = \frac{1}{N} [1^T R^{-1} [1$$

$$\text{Var} (S_{opt}^N / H_0) = \frac{1}{N} \text{Var} H_0 ([1^T y)$$

$$= \frac{1}{N^2} E (\text{Trace} ([1^T y y^T [1)$$

$$= \frac{1}{N^2} \text{Trace} ([1^T R^{-1} [1)$$

$$\xi_{\text{opt}} = \frac{\left\{ \frac{\partial \mathbb{E}_{H_1} [S_{\text{opt}}^N]}{\partial \mu} \right\} \Big|_{\mu=0}}{\text{Var} (S_{\text{opt}}^N / H_0)} = [1^T R^{-1} [1$$

$$= \sum_{i=1}^N \sum_{j=1}^N R_{ij}^{-1}$$

A NOTE ON PHASE-LOCKED LOOPS IN SPACE COMMUNICATIONS

T. R. Williams

N 67-22749

ABSTRACT

Analogies for simple second-order phase locked loops are derived and discussed, and a simple method for graphical analysis is presented. It appears that the analogies and the method of graphical analysis can be usefully extended to cover more complex types of frequency-modulation receiving systems with feedback.

INTRODUCTION AND HISTORICAL BACKGROUND

Phase-locked loops (Reference 1) continue to be of importance in communication systems for satellites as well as in other areas. In spite of their widespread use, their operation is not well understood and the purpose of this note is to clarify the operation of such loops through the use of simple analogies.

We concentrate on second-order loops because of their practical importance. Second order phase-locked loops are usually described mathematically by an ordinary differential equation of the form:

$$\left(\frac{p^2}{\alpha} + p\right) \theta_x = \frac{KE_v}{2} \left(\frac{p}{\beta} + 1\right) T_b \sin(\theta - k\theta_x), \quad (1)$$

where $p = d/dt$; α , β , K , k , and E_v are non-negative constants; T_b and θ are often functions of time (θ and T_b are frequently called "inputs" and they are formed by non-linear operations on a "signal" and, possibly, a random "noise"); and θ_x is a function of time (θ_x , or its derivative, is usually referred to as the "output").

Such an equation can of course be solved either numerically or with a computer once the constants and T_b and θ are specified. In some cases of practical importance we might have especially simple values for some of the constants and the functions of time T_b and θ . For example, if the loop is tracking a constant-frequency sine wave in the absence of noise, T_b is a constant and θ varies linearly with time.

The foregoing equation is not restricted to space communication problems or to phase-locked loops, as it occurs in other areas as well. For example, a similar equation occurs in the theory of the synchronous electrical motor (Reference 2). Going back further, an equation similar to ours also occurs in the theory of a simple damped pendulum. This will be clarified in the following material.

Here, since Equation (1) is easily solved using a computer, we will concentrate on concepts and techniques which assist in thinking about and visualizing the behavior of phase-locked loops.

DERIVATION OF EQUATION (1)

Although equations similar to Equation (1) have been derived many times in the literature, we will, for completeness, include a derivation here. Our notation will differ somewhat from that usually employed for reasons of mathematical convenience (we use mainly the polar form to represent the noise and modulated carrier).

A block diagram of the simple phase-locked loop considered here is shown in Figure A-31.* The modulated carrier e_m is frequency-modulated by the signal $a(t) = a$:

$$e_m = E_m \cos(\omega_o t + \theta_a)$$

where

$$\dot{\theta}_a = \int_0^t a(\tau) d\tau$$

and E_m and ω_o are constants. The received wave form e_r is the sum of e_m and the noise $n(t) = n$, and this sum is applied to the box marked "BP."

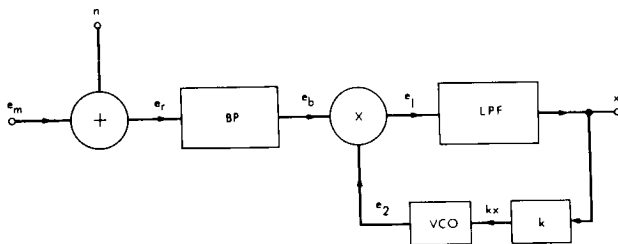


Figure A-31—Block diagram of a simple phase-locked loop.

In the following material assume that the noise has a power spectrum which is symmetrical about the carrier frequency ω_o and that the noise can be adequately represented by

$$n = N_o N \cos(\omega_o t + \theta_n)$$

where N and θ_n are the random envelope and phase of the noise and N_o is a constant equal to the rms noise (we assume that the mathematical expectation of N^2 is equal to 2 so that $N \cos(\omega_o t + \theta_n)$ has unit variance).

We represent the noise, the modulated carrier, and the received wave form as rotating vectors in Figure A-32, where all angles are measured with respect to the angle $\omega_o t$ and the vectors are shown at the instant $t = 0$.

The noise n and the carrier e_m are the projections of the noise and carrier vectors on the horizontal axis.

We have clearly

$$e_r = T \cos(\omega_o t + \theta)$$

where, from trigonometry,

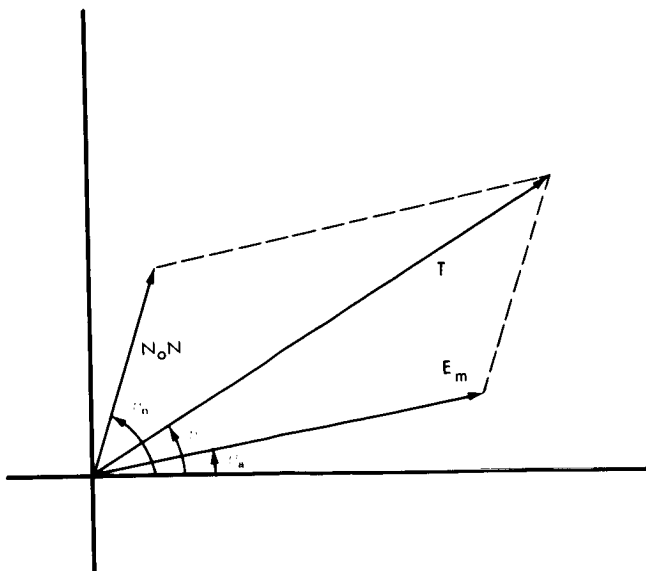


Figure A-32—Vector representation of noise, modulated carrier, and received waveform.

*Some of the material in this section closely parallels an unpublished technical memorandum by the author.

$$T = [E_m^2 + 2N_o N E_m \cos(\theta_n - \theta_a) + N_o^2 N^2]^{1/2}$$

and

$$\theta = \tan^{-1} \left[\frac{E_m \sin \theta_a + N_o N \sin \theta_n}{E_m \cos \theta_a + N_o N \cos \theta_n} \right].$$

Note that as $N_o \rightarrow 0$ we have $T = E_m$ and $\theta = \theta_a$.

We consider further two cases of practical importance: Either (1), the box marked BP will be assumed to be an ideal all-pass network in which case $e_b = e_r$; or (2), the box BP will be assumed to be an ideal bandpass limiter in which case

$$e_b = T_c \cos(\omega_o t + \theta)$$

where T_c is a positive constant. We can represent either case by letting

$$T_b = \begin{cases} T, & \text{Case 1} \\ T_c = \text{constant}, & \text{Case 2,} \end{cases} \quad (2)$$

and

$$e_b = T_b \cos(\omega_o t + \theta).$$

The box marked "k" in Figure A-31 represents an ideal attenuator or amplifier which multiplies x by a constant, k . We assume that k is non-negative.

We make the assumptions (which are usually made in most analyses) that the voltage-controlled oscillator (VCO) has negligible noise in its output and that it has no phase jitter. It would be most natural to assume that the VCO output has the form $E_v \cos(\omega_o t + k \theta_x)$. However, there will be approximately a 90° phase shift between the VCO output and e_b under the usual operating conditions, and, accordingly we assume that the voltage-controlled oscillator (VCO) produces an output voltage

$$e_2 = -E_v \sin(\omega_o t + k \theta_x)$$

where E_v is a non-negative constant and

$$\theta_x = \int_0^t x(\tau) d\tau. \quad (3)$$

The multiplier produces the product $e_1 = e_b e_2$ at its output and, dropping the double-frequency terms, we have

$$e_1 = \frac{E_v T_b}{2} \sin(\theta - k\theta_x). \quad (4)$$

The voltage e_1 is the input of the low pass filter (LPF) and x is the output, and once the transfer function of the filter is specified we can proceed.

At this point we note, as have many authors, that in the important case where the LPF is linear one can write an integral equation of the form

$$x(t) = \int_{-\infty}^{\infty} e_1(\tau) g(t - \tau) d\tau$$

relating x and e_1 , where g is the impulse response of the (possibly non-physically realizable) linear LPF. One can then, by using the series expansion for $\sin(\theta - k\theta_x)$ under the integral, produce many interesting and useful results. Since many studies of this type have been made we will not pursue the matter further, but will note that in many practical phase-locked loops the LPF is both linear and of a fairly simple form.

In all that follows we assume that the relationship between e_1 and x is a first-order, linear, time-invariant differential equation. Specifically:

$$\left(\frac{p}{\alpha} + 1\right) x = K \left(\frac{p}{\beta} + 1\right) e_1 \quad (5)$$

where α , β , and K are non-negative constants. Physically, K is the "low-frequency gain" of the filter. In the case where $\beta = \infty$ the filter is a simple low-pass filter with an "upper half-power frequency" equal to $\alpha/2\pi$. Filters of the type described by Equation (5) are commonly used in many phase-locked loops.

From Equation (5) on using Equation (4) for e_1 and Equation (3) for θ_x we obtain, of course, Equation (1).

MECHANICAL ANALOGS FOR PHASE-LOCKED LOOPS

Let us normalize the vectors shown in Figure A-32 by dividing all magnitudes by E_m , which represents the strength of the received carrier. We define

$$n_0 = \frac{N_0}{E_m}$$

and

$$T_0 = \frac{T}{E_m} \quad (6)$$

We clearly have

$$T_0 = [1 + 2 n_0 N \cos (\theta_n - \theta_a) + n_0^2 N^2]^{1/2}$$

and

$$\theta = \tan^{-1} \left[\frac{\sin \theta_a + n_0 N \sin \theta_n}{\cos \theta_a + n_0 N \cos \theta_n} \right]$$

Consider the mechanical system shown schematically in Figure A-33. The vector with its tip at A represents the (normalized) modulated carrier; the length of the vector is unity and its angle is θ_a . In a similar way the vectors with their tips at C and D represent the (normalized) noise and the (normalized) received waveform. Thus point D moves in two dimensions under the influence of the modulated carrier and the received waveform.

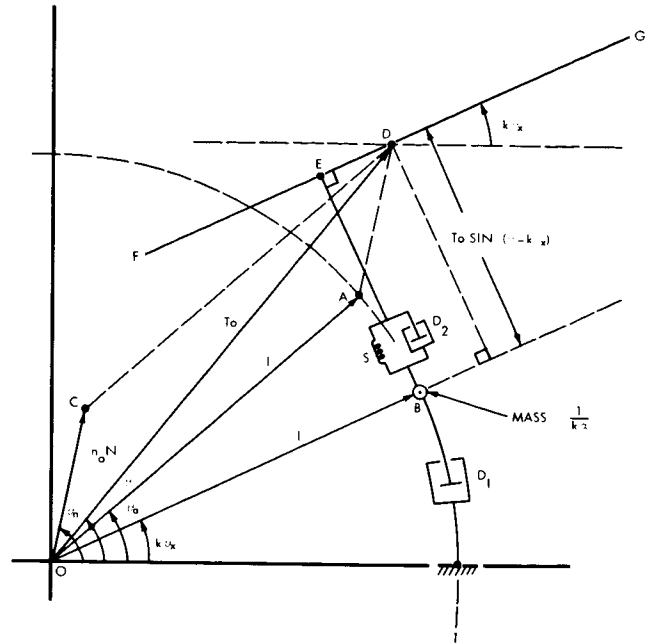


Figure A-33—Analog for the simple phase-locked loop without a band-pass limiter.

We represent the output by a vector of unit magnitude with an angle of $k\theta_x$. (Note that the loop output can be simply obtained by differentiating θ_x once.) At the tip of the output vector (point B) let there be a point mass of mass $1/k\alpha$.

Let there be a weightless rigid rod FG through point D and let this rod be maintained parallel to the output vector. Let point E slide with no friction along the rod FG and let there be connected between E and B a linear spring S of spring constant $KE_v E_m/2$, and a linear viscous damper D_2 with a damping co-efficient of $KE_v E_m/2\beta$. Finally let there be connected between point B and a fixed reference point a linear torsional viscous damper D_1 which exerts a force on point B equal to $-d\theta_x/dt$, i.e., the damping coefficient is $1/k$. (Note that the effect of the viscous damper D_1 could be obtained if the mass B were moving in a viscous fluid and a weightless vane were attached to the mass.)

On summing tangential forces on point B we get

$$-\left(\frac{1}{k\alpha} p^2 + \frac{1}{k} p\right) k \theta_x + \frac{KE_v E_m}{2} \left(\frac{p}{\beta} + 1\right) T_0 \sin (\theta - k \theta_x) = 0.$$

On noting that, from Equation (16), we have $T_0 = T/E_m$, we see that this equation is the same as Equation (1) for case 1, where the box BP contain an all-pass network (see Equation (2)). Thus we have a mechanical analog for case 1.

Case 2, where the box BP contains an ideal bandpass limiter, requires further consideration. Since the bandpass limiter removes amplitude fluctuations, we expect that the vector representing the output of the bandpass limiter must have a constant magnitude and an angle equal to θ , the angle of the input.

Consider Equation (1) and assume that T_b is independent of time. Clearly multiplication of T_b by a positive constant is equivalent to dividing both of the coefficients of the right hand side by

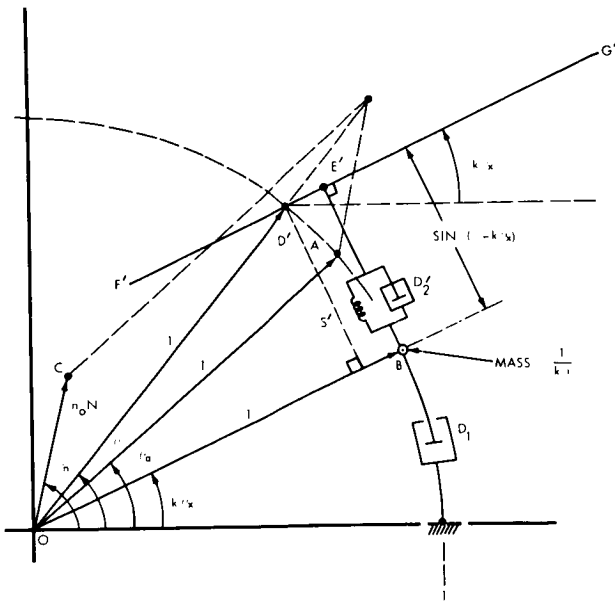


Figure A-34—Analog for the simple phase-locked loop with a band-pass limiter.

the same constant. Accordingly, in an analog, if we adjust the spring constant of S and the damping coefficient of D_2 by the same factor, we can choose the magnitude of T_b arbitrarily (it must be positive, of course, to be meaningful). This fact can also be established from physical reasoning with the analog. Accordingly, in the analog for Case 2, we can choose the length of T_b to have any convenient value and we choose

$$T_b = E_m \text{ (Case 2).} \quad (7)$$

It is now easy to see what the analog is in Case 2: it is similar to Figure A-3 except point D lies on the unit circle as shown in Figure A-34. Note that the spring S' and the damper D'_2 do not necessarily have the same coefficients as in Figure A-33. Accordingly, they are shown with primes in Figure A-34 and this must be remembered in comparing the operation of the two systems.

To show the analogy completely for Case 2, we sum tangential forces on B again and get

$$-\left(\frac{1}{k\alpha} p^2 + \frac{1}{k} p\right) k\theta_x + \frac{K' E_v E_m}{2} \left(\frac{p}{\beta} + 1\right) \sin(\theta - k\theta_x) = 0$$

where we have put a prime on K to denote the fact that S' and D'_2 might have different coefficients than before. On using Equation (7) and rearranging slightly we see that this is the same as Equation (1) again.

UTILITY OF THE ANALOGIES

The analogies can be employed usefully in a number of ways. For example, consider the situation when there is no noise ($n_0 = 0$). In both cases under consideration, point D coincides with point A (see Figures A-33 and A-34), and the systems are equivalent (which we expect, of course, since an ideal bandpass limiter will have no effect when there is no noise).

The ambiguity of the angle $k\theta_x$ in a phase-locked loop is also made clear. In either case if we leave all vectors but the one representing the output (B) fixed, and if we rotate the vector B through an integral multiple of 2π radians (forward or backwards) the forces on point B will be the same after the rotation as before (remember that our ideal "springs" and "dampers" do not have "stops"). Hence the angle $k\theta_x$ is determined, in general, only to within a multiple of 2π .

Consider the situation when there is no noise and the signal a is a step of height A_0 which starts at $t = 0$. The received waveform e_r is of the form $e_r = E_m \cos(\omega_0 t + A_0 t u(t))$ where $u(t)$ is the unit step at $t = 0$, and we are dealing with the case of a frequency "step" at $t = 0$. In either case 1 or 2 the analog is "at rest" at $t = 0$ ($\theta_x = \theta_a = 0$) and at $t = 0$ point A starts to rotate in the counter-clockwise direction with an angular speed of A_0 radians per second. If A_0 is small we intuitively expect point B to "follow" point A (lagging behind by some angle); if A_0 is larger we expect that damper D_1 will prevent point B from following A and the loop is then said to have lost

"lock" or to have become "unlocked." We can be more quantitative: Assume the final value of $k\theta_x$ as $t \rightarrow \infty$ is given by $A_0 t - \phi_0$ where ϕ_0 is a constant. On substituting this value for $k\theta_0$ into Equation (1) we readily find that such a solution can exist only if

$$A_0 \leq \frac{1}{2} k K E_v E_m.$$

Furthermore it is also apparent that ϕ_0 must be less than or equal to $\pi/2$.

The meaning of the term "lock" also is clear when noise is present. Assume that both the signal a and the noise n are small and bounded for all time. Then we expect that point B will "follow" point A, with some error of course, for all time. If the noise becomes large occasionally, as is often the case in practice, then $k\theta_x$ will "skip cycles" or change by a multiple of 2π occasionally, and when this occurs, the loop is said to have lost "lock."

SOLUTION OF EQUATION (1)

As noted previously, Equation (1) and similar equations can be solved by computer or numerically. Sometimes even a rough graphical solution will give information of engineering importance. In this section we present a method of graphical analysis which appears to be novel (at least in the communication theory literature on phase-locked loops which is available to the average communications engineer), and which possibly could be extended to cover systems more general than those described by Equation (1).

We define the new variables

$$x = \dot{\theta}_x \quad (8)$$

and

$$\sigma = \theta - k\theta_x, \quad (9)$$

where the dot signifies the time derivative, i.e., $\dot{\theta} = p\theta_x$. On substituting Equations (8) and (9) in Equation (1) we obtain

$$\left(\frac{p}{\alpha} + 1\right) x = \frac{K E_v}{2} \left(\frac{p}{\beta} + 1\right) T_b \sin \sigma. \quad (10)$$

These last three equations are, of course, equivalent to Equation (1), and they have been used to make phase-plane analyses in the x - σ plane in special cases (see References 3 and 4). One of the difficulties encountered in such analyses lies in the fact that the isoclines in the x - σ plane are not easy to plot and, accordingly, the graphical analysis is tedious and time consuming. This difficulty can be rectified in part if we make a further transformation of variables. We define

$$u = x - \frac{K E_v \alpha}{2\beta} T_b \sin \sigma. \quad (11)$$

Equation (10) can be written as

$$\frac{\dot{u}}{\alpha} = -x + \frac{K E_v}{2} T_b \sin \sigma. \quad (12)$$

Differentiating Equation (9) once and making use of (8) we have

$$\dot{\sigma} = \dot{\theta} - kx \quad (13)$$

Finally, on eliminating x from Equations (12) and (13) by means of (11), we have two equations:

$$\dot{u} = -\alpha u - \frac{KE_v \alpha}{2} \left(\frac{\alpha}{\beta} - 1 \right) T_b \sin \sigma$$

and

$$\dot{\sigma} = -ku - \frac{kKE_v \alpha}{2\beta} T_b \sin \sigma + \dot{\theta}.$$

Note that in the case where T_b and $\dot{\theta}$ are independent of time, which is of some practical importance, solution for phase trajectories in the u - σ or the σ - u plane will be simplified due to the fact that the isoclines will be simple sinusoids. The isoclines can therefore be rapidly found and graphical solution can proceed relatively quickly. (Note that once σ is known, θ_x can be found from Equation (9).) It appears that this method of solution could be easily applied to more general types of phase-locked loops (Reference 5).

CONCLUDING REMARKS

Finding analogies to problems does not solve the problems, and analogies can frequently be misleading. Nevertheless, analogies allow one to apply knowledge of one field to another and they often give quite valuable insight into a new problem.

Modern phase-locked loops are frequently more complex than the simple loops considered here: they not only use IF amplifiers (several in some cases) but they also use bandpass limiters within the feedback loop. When effects of the IF amplifier(s) and limiters are considered it appears that the theory of such loops is closely related to the theory of the FM demodulator with feedback (also called a frequency-compressive feedback demodulator). In fact it appears that one can define a general class of feedback systems which contains many of the modern phase-locked loops as well as the FM demodulator with feedback as special cases. The mathematical description of the general class requires at least a third-order differential equation and analysis is, accordingly, more difficult than for a simple second-order phase-locked loop. Once the differential equations are known, however, they can be simulated and solved, by a digital computer if necessary. Time and space prevents further comment and study here, but study of the general class appears to be a promising area for future research.

REFERENCES

1. Jaffe, R. and Rechtin, E., "Design and performance of phase-lock circuits capable of near-optimum performance over a wide range of input signal and noise levels," IRE Transactions on Information Theory, V. IT-1: pp. 66-67, March, 1955.
2. Minorsky, N., Introduction to Non-Linear Mechanics, CH. VII, Ann Arbor: J. W. Edwards, 1947.
3. Viterbi, A. J., "Acquisition and tracking behavior of phase-locked loops," JPL Ext. Pub. No. 673, Cal. Tech., Pasadena, California; July 1959.

4. Sanneman, R.W. and Rowbotham, J.R., "Unlock characteristics of the optimum type II phase-locked loop," IEEE Transactions on Aerospace and Navigation Electronics., ANE-11: 15-24, March, 1964.
5. Robinson, L.M., "Tanlock: a phase-lock loop of extended tracking capability," Proceedings 1962 IRE Conv. on Military Electronics, Los Angeles, California, February 7-9, 1962.

USE OF A FORMAL LANGUAGE TO DESCRIBE ON-BOARD AND GROUND STATION DATA HANDLING AND PROCESSING OF SATELLITE EXPERIMENTS

F. M. Sobotkin* 7

N 67-22750

INTRODUCTION

As space experiments on telemetry satellites grow in sophistication and in number, the orders of complexity of the required on-board system will increase as will the number of people involved with their design. Before attempting to simulate or construct a satellite system, a complete description for each experiment and its data handling and processing requirements must be specified. Therefore, a means for conveying these details of specification in a complete and non-ambiguous manner between experimenters, system designers, and programmers is needed.

In the present work, an attempt is made to show the feasibility of a non-ambiguous description, by describing two specific Goddard experiments using a "higher order" programming language. The Iverson language (Reference 1), with minor modifications and additions, was chosen to show that, due to the simplicity and descriptive power of the language, the data handling and logical processes for an experiment may be completely described. For the first experiment considered (EGO satellite micrometeorite experiment #4916), a brief higher order programming language description will be presented to illustrate the capability of the language for conveying the essential requirements of experiments. The second experiment's [Graduate Research Center of the Southwest (GRCSW) IMP experiment] description, which includes ground station processing, is written in much greater detail than would be required for simulation and implementation of data processing and handling equipment.

BACKGROUND

During the 1965 Goddard Summer Workshop program, Dr. Edward P. Stabler (Reference 2) studied the feasibility of using special purpose computers to process telemetry data and to control the experiments on small telemetry satellites. At present, data processing of sensed data to be transmitted and the control of each experiment is performed by the individual experimenter's package. Many such packages may be on a given satellite and the possibility of unnecessary duplication of equipment exists. Since, in the past, little on-board processing was performed, and the number of experiments per satellite has not been too large, no major problems have arisen. There is a trend towards increased use of on-board data processing, and as the experiments grow in sophistication and in number, a central data processor or centralized telemetry computer (CTM) may be desirable on future telemetry satellites. The computer would be time shared by the experiments to conserve space, weight, and hardware.

The proposed system is a stored program or micro-programmed computer, which can be thought of as a collection of storage elements, logic gates, and a switching network for inter-connecting the various pieces of hardware as required by the program. The unit is considered a universal computer because, by modifying the stored program, you in effect rewire the machine

*The City University of New York

for the problem at hand, offering great flexibility during design and making the computer adaptable for a wide variety of telemetry satellite systems.

The particular satellite investigated by Dr. Stabler was the IMP-F, which is a small satellite with few experiments and very little on-board processing; consequently, duplication of equipment is only minor. His conclusion was that the CTM would require the same space, weight, and power aboard the satellite as would the individual experimental packages. However, to perform the identical task assigned to the distributed data processing equipment, the CTM would only be on 10 percent of the time and be idle 90 percent of the time. Therefore, the CTM has available an unused stock of data processing capability. New data processing tasks can be performed on-board with only minor changes in weight and power.

Some possible additional computer tasks are:

1. Experiment conditioning and testing--Sample any or all of the experiments successively at very high rates, to establish confidence in the system and then reduce the rate to send just the information that is desired and needed.
2. Coding telemetry link.
3. Decode ground commands--It may be desirable to have very highly encoded commands to avoid having a miscommand which might wipe out the mission.
4. More on-board data processing--Eliminate transmission of superfluous information since the cost of data reduction is negligible compared to the savings in energy used for transmission (e.g., the conversion of an integer value of experimental data to floating point number prior to transmission. For IMP-F it costs 40 millijoules to transmit one bit to earth, but the energy required to convert a 20 bit integer to a 10 bit floating point number is about 0.2 millijoules using the CTM.)

An important result of Stabler's study was the need for an adequate notation or language for describing the logic processes (i.e., computing tasks, data collecting, and computer activities) performed in preparing the experimental data for telemetry. Two frequently used methods for describing processes are:

1. Natural language with reference to figures and block diagrams.
2. Logic block diagrams.

The first method suffers from the usual drawbacks of incompleteness (i.e., lack of both precision and conciseness), and tends to become complex and ambiguous very quickly. The second method is difficult to write and difficult to read.

Higher order programming languages have been devised that avoid these drawbacks and possess the following qualities:

1. Non-ambiguous, concise, precise, consistent over a wide area of applications, and economy of symbols.
2. Descriptive and analytic power which amply repay the effort required for its mastery.
3. Descriptive of actual register interaction.
4. Descriptive of simultaneous and sequential processes.
5. Highly expressive in binary representation and manipulation.

6. Capable of describing complicated systems (e.g., a formal description of the logic structure of IBM system 360 has been completely specified using Iverson's language).

Some of the advantages of a higher order programming language description are:

1. It is a useful aid in communication between experimenters, system designers, and programmers.
2. It permits simulation of experiments at a very early stage in design, providing valuable information on system characteristics (time on, power, response to real time inputs, and effects of modified input environments). This offers major assistance in debugging and reconfiguring design.
3. It can be used to adopt efficient data processes and formats for specific task at hand (i.e., determine only essential operations).
4. It lends itself to writing programs for computers on the ground.
5. It is sufficiently precise to proceed directly to logic diagrams and relatively straightforward sufficient to derive boolean equations, thereby eliminating both drudgery and error.
6. It supplies a readily understood permanent record of experiment for documentation.

Iverson's language, with minor modifications and additions, possesses the above qualities and advantages and will be used to describe two Goddard Space Flight Center experiments. First, a verbal description will be given so that the reader will have a basic idea of measurements and processes performed in the experiment. Secondly, a description of the higher order programming language will be given along with a partial explanation.

EGO SATELLITE MICROMETEORITE EXPERIMENT

Verbal Description*

The purpose of this experiment is to measure the mass, velocity, momentum, directionality, intensity, time, and spatial variations in the micrometeorite flux throughout the EGO orbit. Four nearly identical sensor tubes (0, 1, 2, 3) Figure A-35, are used in the experiment, with their openings in the $\pm X$, $\pm Y$, $\pm Z$ directions (body centered coordinates).

A micrometeorite entering the i^{th} tube ($i = 0, 1, 2, 3$) penetrates film A' producing a plasma cloud which is collected by A', creating a pulse A_i. This pulse is used to trigger a clock and also to identify the sensor tube penetrated (2 bit word ID). Upon striking the microphone plate M, the particle produces another plasma cloud and an M pulse. The cloud is collected at grid B producing a B pulse and simultaneously stopping the clock. The distance between A and M is accurately known and therefore the velocity of the particle is obtained by counting time pulses (clock). The B pulse gives information

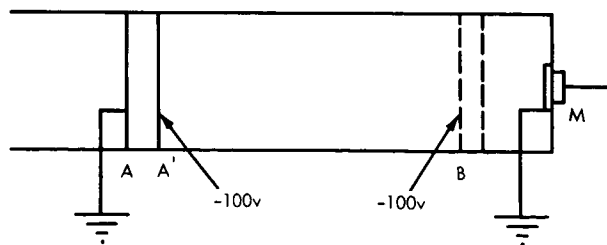


Figure A-35—Sensor tube (micrometeorite experiment)
two thin films A and A', grid B, microphone M.

*Space Technology Laboratories, Inc.; Inter-office Correspondence #8100.2-970 (April 1963).

concerning the kinetic energy of the particle and the output signal of the microphone (M pulse) is proportional to $\lambda + E$ momentum. Both a B and an M pulse must be obtained in order for data to be recorded; if either one is absent, no data are recorded. The B pulse and M pulse are each represented by a three bit word, while the number of clock pulses is represented by a 6 bit word. "The B, M, and clock signals all revert to zero whenever the signal exceeds the maximum level." This statement, as presented in the description obtained by the author, is open to different interpretations, which illustrates the ambiguity that a verbal description can possess. If this statement had been expressed in a formal language, there would be no ambiguity. Further on in the description, the experimenter states that "a series of 14 zeroes in the data output can mean a slow, high momentum particle entered tube zero," which would make you believe that he previously meant, only the signal that exceeds its maximum is reverted to zero. In this report, it will be assumed that all signals (B, M, and clock) are reset to zero if any of them exceeds maximum value (i.e., MAXB, MAXM, MAXC).

Data obtained in this experiment are stored in a 36 bit shift register until readout by the spacecraft telemetry system. The register includes complete information concerning two impacts (14 bits each) and an extra count (2 bits/sensor) which between telemetry readouts, is used to count hits occurring after the first two are recorded.

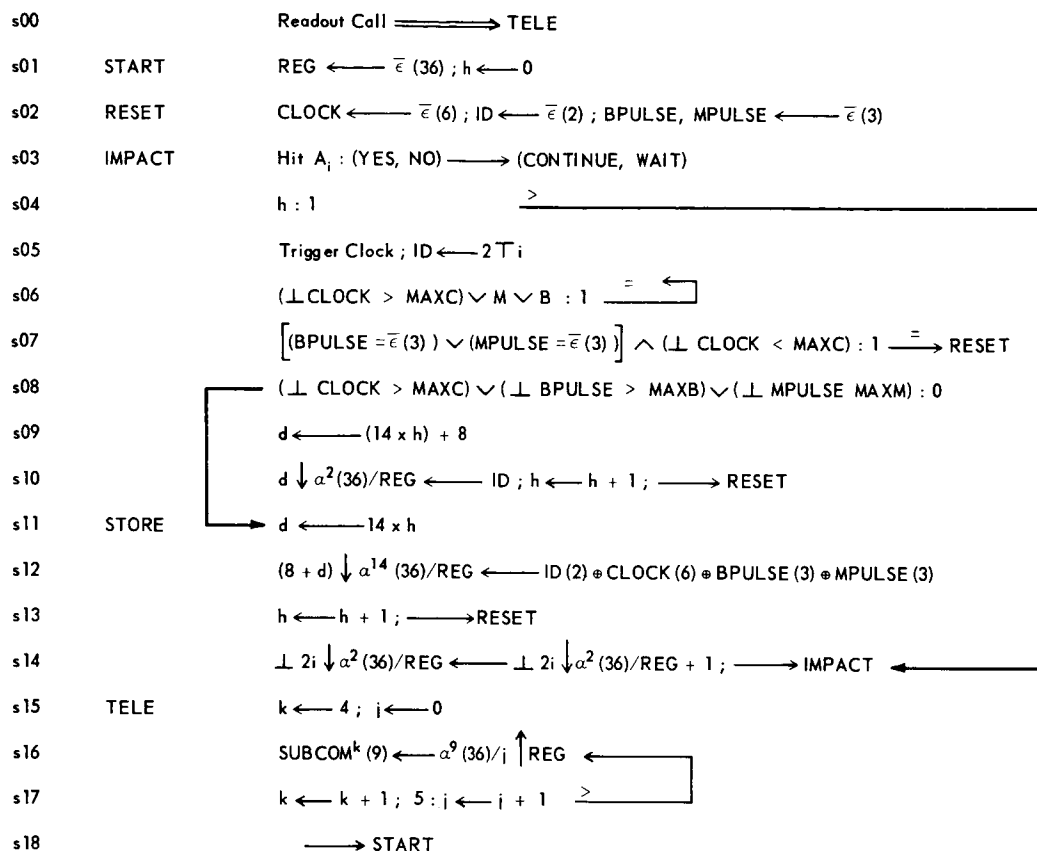
Table A-5
Bit Assignments Within the 36 Bit Shift Register (REG)

Iverson representation of bit locations	Bit numbers (leftmost bit is #1)
$\alpha^2(36)/\text{REG}$	1,2 Extra counts for Tube 0
$(2 \downarrow \alpha^2)/\text{REG}$	3,4 Extra counts for Tube 1
$(4 \downarrow \alpha^2)/\text{REG}$	5,6 Extra counts for Tube 2
$(6 \downarrow \alpha^2)/\text{REG}$	7,8 Extra counts for Tube 3
$(8 \downarrow \alpha^2)/\text{REG}$	9,10 Tube ID 1 st hit
$(10 \downarrow \alpha^6)/\text{REG}$	11-16 Clock pulses 1 st hit
$(16 \downarrow \alpha^3)/\text{REG}$	17-19 B pulse 1 st hit
$(19 \downarrow \alpha^3)/\text{REG}$	20-22 M pulse 1 st hit
$(22 \downarrow \alpha^2)/\text{REG}$	23,24 Tube ID 2 nd hit
$(24 \downarrow \alpha^6)/\text{REG}$	25-30 Clock pulses 2 nd hit
$(30 \downarrow \alpha^3)/\text{REG}$	31-33 B pulse 2 nd hit
$(33 \downarrow \alpha^3)/\text{REG}$	34-36 M pulse 2 nd hit

The experiment uses four adjacent digital words (4, 5, 6, and 7) in the experiment subcommutation for telemetry readout. No data are recorded between the start of readout of the first word (#4) and completion of the last (#7).

Higher Order Programming Language Description

The higher order programming language description of the above experiment (Program #1, illustrated in Figure A-36), is very brief and is presented to show its brevity to describe the data collecting, and preparation for telemetry of the experimental data.



Statement
Number

- s00 When call for data readout, there is an immediate branch to statement TELE (s15)
- s01 All 36 bits of register and variable h are set to zero. (h indicates the number of recorded impacts for the sequence, i.e., 1st impact h = 0, 2nd impact h = 1, etc.)
- s02 The bits of binary words CLOCK, ID, BPULSE and MPULSE are all set to zero.
- s03 Pause until particle penetrates film A of sensor tube. i denotes which tube is involved.
- s04 If h > 1, two impacts have already been recorded in this sequence and control branches to s14, where the base 2 value of extra counts for ith sensor is increased by 1, and then a branch to statement s03 (IMPACT). Otherwise if h ≤ 1, continue to statement s05.
- s05 The clock is triggered and ID is set equal to the 2 bit binary representation of the value i.
- s06 Wait for the value of CLOCK to exceed MAXC, or the presence of a BPULSE or MPULSE and then continue to s07
- s07 If CLOCK < MAXC, and either a BPULSE or MPULSE is recorded but not both, branch to RESET (s02) no data recorded for this impact. Otherwise continue to s08.
- s08 Determines if a signal (CLOCK, BPULSE or MPULSE) has exceeded its maximum value. If not exceeded, branch to STORE (s11), otherwise continue to s09.
- s09-10 Since a maximum value has been exceeded, the signals (CLOCK, BPULSE and MPULSE) are recorded as zeroes. ID is transferred to its appropriate register position, h is advanced by 1 and a branch to RESET (s02) takes place.
- s11-12-13 Words ID, CLOCK, BPULSE, and MPULSE for a completed measurement are stored in appropriate bit positions of the register, h increased by 1, and branch to RESET (s02). (⊕ denotes catenation)
- s15-16-17 Bits from register are transferred to appropriate subcommutator 9 bit digital word [SUBCOM^k(9)].
- s18 Branch to START (s01) and begin new sequence.

Figure A-36—Program #1 — higher order programming language description for EGO micrometeorite experiment.

Table A-6
Summary of Notation for Higher Order Programming Language (Reference 1)

$\alpha^j(n)$	"prefix vector of weight j", vector of dimension n, first j elements are 1's and all remaining elements are 0's. [e.g., $\alpha^3(7) = (1\ 1\ 1\ 0\ 0\ 0\ 0)$]
$\omega^j(n)$	"suffix vector" [e.g., $\omega^3(7) = (0\ 0\ 0\ 0\ 1\ 1\ 1)$]
$\iota^j(n)$	"interval vector" $\iota^j(n) = (j, j+1, j+2, \dots, j+n-1)$
$\epsilon(n)$	"full vector" consists of all 1's (e.g., $\epsilon(4) = (1\ 1\ 1\ 1)$)
$\bar{\epsilon}(n)$	consists of all 0's [e.g., $\bar{\epsilon}(4) = (0\ 0\ 0\ 0)$]
$k \downarrow$	denotes right circular rotation by k places.
$k \uparrow$	denotes left circular rotation by k places.
$k \downarrow \alpha^j(n)$	"infix vector" [e.g., $2 \downarrow \alpha^3(7) = (0\ 0\ 1\ 1\ 1\ 0\ 0)$]
u/a	"selection operation" (vectors u and a must be of same dimension) "u" is a logical vector composed of 1's and 0's. The resulting vector is formed by selecting components (a_i) of "a", corresponding to those components of "u" for which $u_i = 1$. [e.g., $u = (1\ 0\ 1\ 1\ 0\ 1)$, $a = (\text{R E P O R T})$ $u/a = (\text{R P O T})$] Therefore $2 \downarrow \alpha^3(7)/(R_6\ R_5\ R_4\ R_3\ R_2\ R_1\ R_0) = (R_4\ R_3\ R_2)$
$b \mid_j n$	denotes j^{th} -residue of n modulo b. (e.g., $3 \mid_0 10 = 1$)
$\perp x$	the base 2 value of x. [e.g., $\perp(1\ 0\ 1) = 5$]
$n \top x$	n bits base 2 representation of x. [$4 \top 5 = (0\ 1\ 0\ 1)$]
\oplus	denotes catenation
$(x \ R\ y)$	relational statement, - logical variable which is true (i.e., equal to 1) if and only if x stands in the relation R to y.
$x : y \ r \rightarrow s$	branch to statement s, if relationship x (r) y is satisfied
$x \rightarrow s$	immediate branch to statement on condition x. (independent of present program position)
$\rightarrow s$	unconditional branch to statement s.
$x \leftarrow y$	connect y to x.
$x \# y$	disconnect y from x.
$x \leftarrow y$	x is specified by y (or transfer y to x)

GRADUATE RESEARCH CENTER OF THE SOUTHWEST
(GRCSW) IMP EXPERIMENT

Verbal Description*

The major objective of this experiment is to study the degree of anisotropy of the low energy portion of the solar cosmic radiation and to determine the manner in which it varies with time and nuclear species. The experiment uses four detectors, Figure A-37, a photon counter and a pulse height analyzer (PHA) to obtain data about particles throughout the satellite orbit.

Each complete GRCSW sequence (cycle) represents 64 different measurements. For each telemetry sequence, Frame 03, channels 04 thru 15 inclusive, and Frame 11 channels 04 thru 15 inclusive, will contain the GRCSW data. Each of the above frames represents 96 bits of information and may be considered as one complete measurement. Consequently, GRCSW receives two measurements for every one spacecraft (or telemetry) sequence. The 96 bits of data per measurement are divided into 11 distinct units of information such that the first 90 bits represent nine data units (Data unit number $M = 1, \dots, 9$) of ten bits each and the last six bits represent two data units (Data unit numbers $M = 10, 11$) of three bits each. Data are read out by the spacecraft every 10.24 seconds. The experiment is gated off for 0.960 seconds (by Freeze Pulse FRP) of this time and therefore accumulation time is 9.280 seconds.

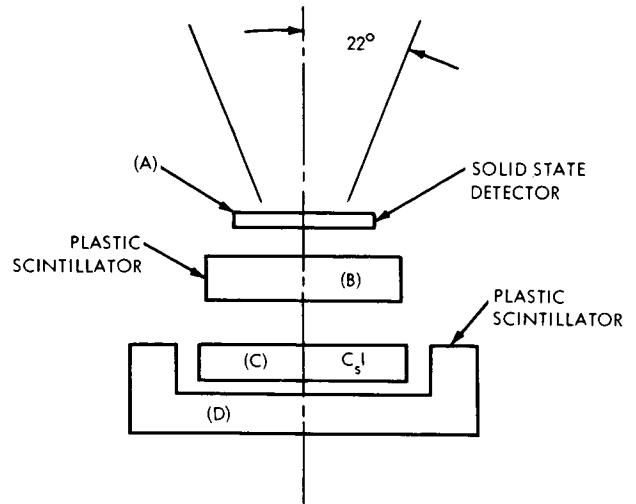


Figure A-37-GRCSW Four-detector telescope.

The 64 measurements can be divided into 8 groups ($k = 0, 1, \dots, 7$), of 8 measurements each ($L = 0, 1, \dots, 7$). Any GRCSW data unit may be defined in subscript nomenclature as:

DATA ($J, 8K + L, M$) where:

$J = 1, 2, \dots, \infty$ GRCSW cycle number

$8K + L = 0, 1, \dots, 63$ Measurement reference within a cycle

$M = 1, 2, \dots, 11$ Data unit within a measurement

As k varies, measurements for $L = 0, \dots, 6$ are invariant, but measurements for $L = 7$ are sub-commutated. The significance of each data unit is illustrated in Table A-7.

The four columns, (DETECTOR LOGIC, IPHA, SIG GEN, and Particle Type) apply only to $M = 1, \dots, 8$. DETECTOR LOGIC indicates the setup of the detector logical expression. IPHA indicates the source of input to the pulse height analyzer (PHA), SIG GEN indicates the source of output to be counted, and Particle Type, types the characteristics of the particles that will be counted.

Measurements $L = 0, \dots, 5$ are all cosmic ray anisotropy measurements where the sky is divided into 8 octants with data accumulated (i.e., particles counted) as the experiment Look angle sweeps through each of the octant sectors of rotational position. For $M = 9$, the number of particles

*GRSW IMP Experiment Data Organization; Southwest Center for Advanced Studies Specification #104012; Seconds 1-5,20 (Feb. 1966).

Table A-7
Summary of GRCSW Data Units Data (J, 8K + L, M)

DATA UNIT M																
		Ten Bits Each													Three Bits Each	
K	L	Detector Logic	IPHA	Sig. Gen.	Particle Type	1	2	3	4	5	6	7	8	9	10	11
0	- 7	0	$A\bar{B}_E$	$A\bar{B}$	Protons <10 Mev	Oct. 1	Oct. 2	Oct. 3	Oct. 4	Oct. 5	Oct. 6	Oct. 7	Oct. 8	DET A	Start	Stop
0	- 7	1	$B_p \bar{C}\bar{D}$	PHA (1 and 2)	Protons 10-30 Mev									DET B_E		
0	- 7	2	$B_p \bar{C}\bar{D}$	PHA (3 and 4)	Protons 30-63 Mev									DET C		
0	- 7	3	$B_p \bar{C}\bar{D}$	PHA (5 and 6)	Protons 63-120 Mev									DET D		
0	- 7	4	$B_p \bar{C}\bar{D}$	$BC\bar{D}$	Protons 120 Mev									P		
0	- 7	5	$B_p \bar{C}\bar{D}$	BC	All Particles									P		
0	- 7	6	$B_p \bar{C}\bar{D}$			PHA (1)	PHA (2)	PHA (3)	PHA (4)	PHA (5)	PHA (6)	PHA (7)	DET CD	P	Total No. of Octants	
0	7	$A\bar{B}_E$	A		1-10 Mev Protons									P	000 000	000
1	7	$B_E \bar{C}\bar{D}$	C		Electrons									P	000 000	001
2	7	$A\bar{B}_E$	A		Protons									P	000 000	010
3	7	$B_E \bar{C}\bar{D}$	C		Electrons									P	000 000	011
4	7	$A\bar{B}_E$	A		Protons									P	000 000	100
5	7	$B_E \bar{C}\bar{D}$	C		Electrons									P	000 000	101
6	7	AB_E	A		Protons									P	000 000	110
7	7	C Calibrate	C		DC Spectrum AM 241									P	000 000	111

counted are those seen by the detector listed. "Start" is the number of complete octants pasted through before the first Sun pulse (SP) and "Stop" is the number of complete octants pasted through after the last sun pulse before the freeze pulse FRP (call for readout). For $L = 6, 7$, data units $M = 1, \dots, 7$ indicate the number of events recorded in each of the seven channels of the PHA and are unrelated to rotational position. The combined values of DATA (J, $8K + 6, 10$) and DATA (J, $8K + 6, 11$) represents the total number of octants scanned for that measurement. Data units DATA (J, $8K + L, M$), $M = 1, \dots, 9$ (except P count) use their most significant bit $[R(M)]$, as a status bit. When particles are being counted, $R(M) = 0$. After 512 particle counts, $R(M) = 1$ and pulses from spacecraft signal C11 (100 hertz) are counted for the remainder of the measurement. During ground processing, the number of counts for the total accumulation time (9.28 seconds) can be determined. The P count is a measurement of the azimuth from which a cosmic photon (1.5 - 6 kev) has been observed and is obtained by counting C11 pulses from the time of impact to the time the next sun pulse, SP, is observed.

Many of the signals used in this experiment are generated in other locations on-board the satellite. Satellite signal a5 which is derived from the spacecraft sequence counter alternate between a positive and negative state. The duration of each state is equal to 16 spacecraft sequences. The satellite freeze pulse occurs every 10.24 seconds for a duration of 0.960 seconds ("1" state) during which time data are read out from the GRCSW experiment. As the spacecraft rotates, the optical aspect circuitry generates sun pulses s_p each time the sun is viewed. The rotational position of the craft is divided into 8 octants and the pulse OCTP is generated whenever the GRCSW detectors view a new octant. The base two value 1 of the 3 bit counter COCT, indicates the present octant position (1, 2...8) for the detectors.

Ground Processing

The following information is desired for each GRCSW measurement, and will be denoted by the values of M (Data unit numbers) ranging from 12 to 21.

M = 12	total number of complete spin periods
M = 13	experiment synchronization
M = 14	number of acquisitions for octant 1
M = 15	number of acquisitions for octant 2
M = 16	number of acquisitions for octant 3
M = 17	number of acquisitions for octant 4
M = 18	number of acquisitions for octant 5
M = 19	number of acquisitions for octant 6
M = 20	number of acquisitions for octant 7
M = 21	number of acquisitions for octant 8

After each completed GRCSW cycle, the following information is required:

SANIS (J, L, M) $L = 0, \dots, 5$; $M = 1, \dots, 8$

Sum of specific particle counts for individual octants over a complete cycle.

MANIS (J, L, M)

Mean count per octant.

SPROTH (J, M) $M = 1, \dots, 7$

Sum of particle counts for grouped, PHA channels with detector logic $B_p \bar{C} \bar{D}$

SPROTL (J, M) $M = 1, \dots, 7$

Sum of particle counts for individual PHA channels with detector logic $A \bar{B}_E$

SELECT (J, M) $M = 1, \dots, 7$

Sum of particle counts for individual PHA channels with detector logic $B_E \bar{C} \bar{D}$

SOCT (J, L, M) $M = 1, \dots, 8; L = 0, \dots, 5$

Sum of acquisitions for each octant

NX (J, L) $L = 0, \dots, 3$

Number of good measurement for detectors A, B, C, D [$N(J, 8K + L) = 1$ if good data, as determined by GSFC DCI.]

SX (J, L) $L = 0, \dots, 3$

Sum of counts from detectors A, B, C, D (only over good data, $N(J, 8K + L) = 1$)

MX (J, L) $L = 0, \dots, 3$

Mean of counts from A, B, C, D Per cycle.

Higher Order Programming Language Description of GRCSW Experiment

This description will be presented in four segments (Programs 2, 3, 4, 5 as illustrated in Figures A-38, A-39, A-40, and A-41, respectively). Program 2 includes the higher order programming language description of the data handling, logical processes, and preparation for telemetry on-board the satellite. As the experiment progresses, the interconnections of equipment for particular measurements are obtained from Program 3, the CONNECTING MEMORY (CM). Program 4 includes the initial ground processing as the data for each measurement is received at the ground station; after a completed GRCSW cycle has occurred, Program 5 illustrates the necessary processing, to terminate the data calculations for that cycle.

Before the experiment can proceed, its registers, counters (CT), and its data storage locations (DM) must be set to zero. (Program 2, 00-01) Measurements can not begin until the first FRP after the positive transition of a5 so that the experiment will be synchronized to the spacecraft clock (s02, 03, 04). Once synchronization has occurred, program 2 (s05) branches to program 3 (CM⁰), and connections of appropriate equipment can be made. CM⁰ connects detector A to counter CT¹, and the logical combination of $A \bar{B}_E$ to the signal line SIG, then returns to program 2 s06. After a new octant is entered, SIG is connected to CT⁰ and the starting octant position of the measurement is stored in R (s07); the ones complement of R, (\bar{R}), is then transferred to the first 3 bits of REG2 (s08). Statement s09 checks to see if a call has been made for telemetry and would branch to s19 if it is time for readout, otherwise s10 follows. If a new octant has been entered s10 branches to s13 where CT⁰ is stored in address $\bar{1}R$ (base two value of R) location of DM. The word R is then stored in the last 3 bits of REG2 just in case this is the last completed octant for the measurement. If a new octant had not been entered, s11 determines if the counter CT⁰ has exceeded 512 counts (i.e., most significant bit $R(M) = 1$) and has not already been connected to C11. Appropriate connections are made if needed. The same check is made for CT¹ by

$CM^0 \quad CT^1 \leftarrow DET(A) ; SIG \leftarrow DET(A \wedge \bar{B}_E) ; \rightarrow s06$
 $CM^1 \quad CT^1 \leftarrow DET(B) ; IPHA \leftarrow DET(B_P \wedge C \wedge \bar{D}, CLG) ; SIG \leftarrow OPHA(1 \vee 2) ; \rightarrow s06$
 $CM^2 \quad CT^1 \leftarrow DET(C) ; IPHA \leftarrow DET(B_P \wedge C \wedge \bar{D}, CLG) ; SIG \leftarrow OPHA(3 \vee 4) ; \rightarrow s06$
 $CM^3 \quad CT^1 \leftarrow DET(D) ; IPHA \leftarrow DET(B_P \wedge C \wedge \bar{D}, CLG) ; SIG \leftarrow OPHA(5 \vee 6) ; \rightarrow s06$
 $CM^4 \quad IPHAP \leftarrow DET(P) ; P \leftarrow OPHAP ; SIG \leftarrow DET(B_P \wedge C \wedge D) ; \rightarrow s20$
 $CM^5 \quad IPHAP \leftarrow DET(P) ; P \leftarrow OPHAP ; SIG \leftarrow DET(B_P \wedge C) ; \rightarrow s20$
 $CM^6 \quad IPHA \leftarrow DET(B_P \wedge C \wedge \bar{D}, CLG) ; CT^{t^0(7)} \leftarrow OPHA [t^1(7)] ; CT^7 \leftarrow DET(C \wedge D) ;$
 $IPHAP \leftarrow DET(P) ; P \leftarrow OPHAP ; \rightarrow s35$
 $CM^7 \quad IPHA \leftarrow DET(A \wedge \bar{B}_E, AHG) ; CT^{t^0(7)} \leftarrow OPHA [t^0(7)] ; CT^7 \leftarrow DET(C \wedge D) ;$
 $IPHAP \leftarrow DET(P) ; P \leftarrow OPHAP ; \rightarrow s46$
 $CM^8 \quad IPHA \leftarrow DET(B_E \wedge C \wedge \bar{D}, CHG) ; CT^{t^0(7)} \leftarrow OPHA [t^1(7)] ; CT^7 \leftarrow DET(C \wedge D) ;$
 $IPHAP \leftarrow DET(P) ; P \leftarrow OPHAP ; \rightarrow s46$
 $CM^9 \quad IPHA \leftarrow OCAL(AM^{241}, CHG) ; CT^{t^0(7)} \leftarrow OPHA [t^1(7)] ; CT^7 \leftarrow DET(C \wedge D) ;$
 $IPHAP \leftarrow DET(P) ; P \leftarrow OPHAP ; \rightarrow s46$

Figure A-39—Program #3 — connection memory (CM) GRCSW experiment.

s12. If a new octant had been entered, the new octant number is placed in R and the appropriate location of DM is determined and its stored value is transferred to the counter (after the data are stored (s13)); a check is made to see if the counter should be connected to SIG or C11. When FRP = 1, a branch is made to s19, where CT^1 is transferred to DM^8 , REG2 is transferred to DM^9 and program branches to TELE (t00). The value of L_0 is examined to determine which telemetry frame is used and then the appropriate components of DM are read into the telemetry channels (t03). The counters, DM and REG2, are zeroed. The address for the next branch to CM is calculated and transferred to.

The remainder of the program proceeds in a similar manner except for a few statements which will be explained.

CM^6 Detector logic is set to $B_P \bar{C} \bar{D}$ and then the output of C low gain connects to the input of the Pulse Height Analyzer (IPHA). The outputs of the PHA channels are connected to the indicated counters. [i.e., $OPHA(1) \rightarrow CT^0$, $OPHA(2) \rightarrow CT^1$, ..., $OPHA(7) \rightarrow CT^6$] Detector setup $C \wedge D$ connects to CT^7 . The photon measurement equipment is set by connecting detector P to input PHA (photon), and output OPHAP to the P line (i.e., $P = 1$ if desirable photon detected)

s28 CT^1 is disconnected from C11, P line is disconnected from OPHAP and then set to zero so that no further photon data is taken for that measurement.

Program 4 b12

Three bit binary word DATA (J, $8K + 7$, 11) is compared to the first 3 bits of the binary representation for the modulo 2^6 value of $(2 \times SEQ + 32 + HSEQ - 1)$. The k^{th} bit of DATA (J, $8K + L$, 13) is set equal to 1 or 0 depending on whether the above comparison was equal or not equal (SEQ = Spacecraft sequence number, $HSEQ = 1$ if GRCSW data is in frame 11 or 0 if data in frame 3).

```

b00    K ← 0
b01    L ← 0
b02    DATA(J, 8K + L, 12) ←  $\alpha^3 / \left[ \text{DATA}(J, 8K + 10) \oplus \text{DATA}(J, 8K + 6, 11) + T^2 \right.$ 
                                              $\left. - \text{DATA}(J, 8K + L, 10) - \text{DATA}(J, 8K + L, 11) \right]$ 
b03    M ← 14
b04    DATA(J, 8K + L, M) ← DATA(J, 8K + L, 12) +  $\left[ \text{DATA}(J, 8K + L, 10) > (20 - M) \right] + \left[ \text{DATA}(J, 8K + L, 11) < (M - 14) \right]$ 
b05    M ← M + 1 ; M:21
b06    M ← 1
b07    DATA(J, 8K + L, M)9 : 1
b08    DATA(J, 8K + L, M) ←  $512 \times F \times \left[ \frac{9.280}{9.280 - \text{DATA}(J, 8K + L, M) \times .01} \right]$ 
b09    M ← M + 1 ; M:9
b10    L : 7 = → b12
b11    L ← L + 1 ; L:5 (≤, >) → (b02, b06)
b12    DATA(J, 8K + L, 13)K ←  $\left[ \text{DATA}(J, 8K + 7, 11) = \alpha^3 / T^{26} \right]_0 (2 \times \text{SEQ}_Y 32 + \text{HSEQ} - 1)$ 
b13    K ← K + 1 ; K:7 (≤, >) → (b01, EXIT)

```

Figure A-40—Program #4 —GRCSW ground processing for each data measurement of Jth cycle.

CONCLUSIONS

The purpose of this project was to examine the feasibility of non-ambiguous descriptions for the data handling and logical processing of satellite experiments by using a formal language. The higher order programming language descriptions given in this report for two Goddard experiments establishes this feasibility by completely specifying the experiment's process in a manner which may directly be used for design and simulation of the systems involved.

This work may be extended by writing similar descriptions for all of the experiments on-board a particular satellite as a part of an over-all program. This program may then be used to design a CTM.

REFERENCES

1. Iverson, K. E., A Programming Language, John Wiley & Sons, 1962.
2. Stabler, E. P., "Telemetry computer studies," Final Report of the Goddard Summer Workshop Program in Analysis of Space Data and Measurement of Space Environments. (X 100-65-407) pages A1-A34, 1965.

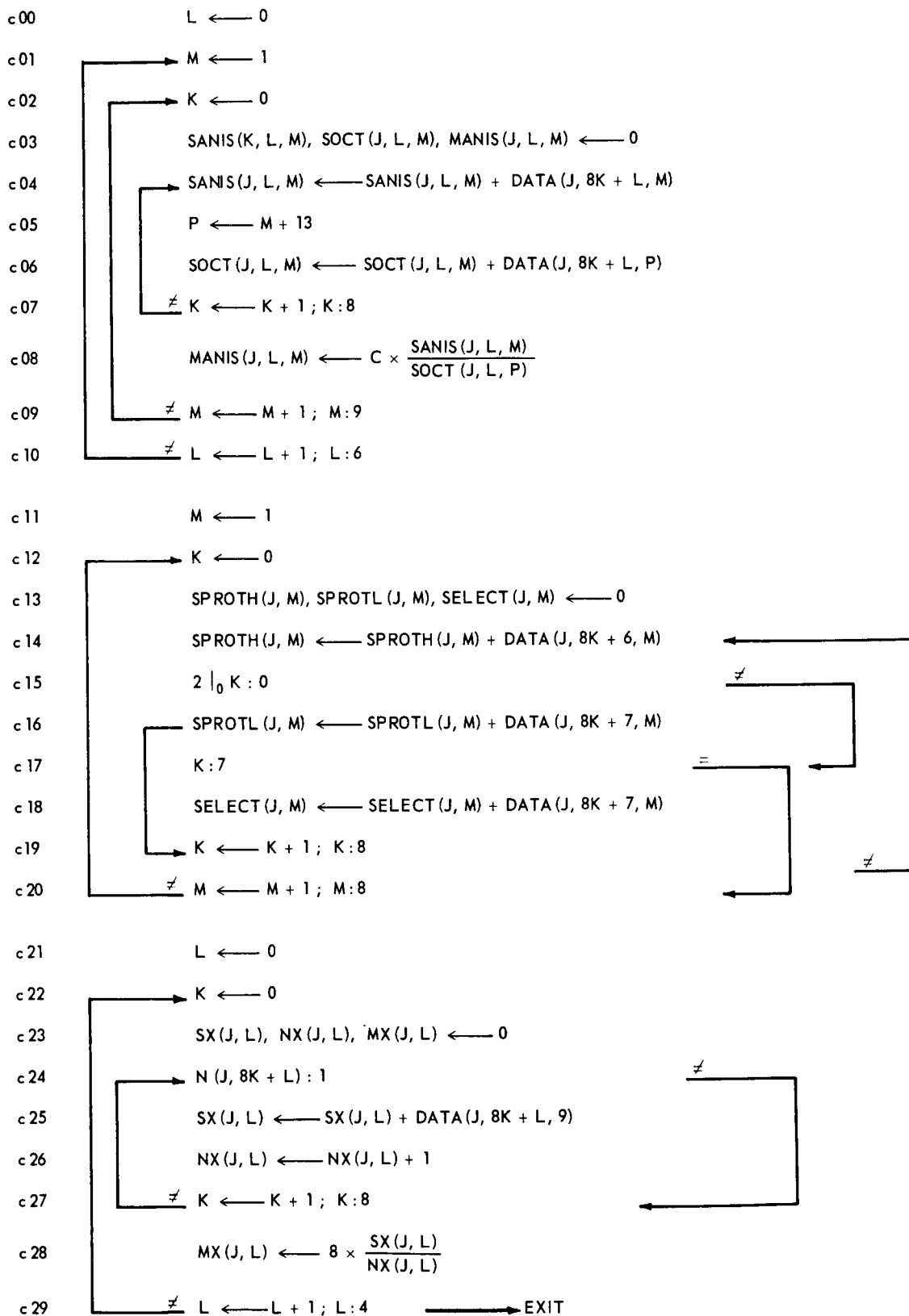


Figure A-41—Program #5 -GRCSW ground processing after each completed cycle.

APPLICATION OF MIMIC LANGUAGE AT GSFC

Yaohan Chu*

N 67-22751

INTRODUCTION

Goddard Space Flight Center of NASA is acquiring an integrated complex of IBM 360 computers for support of its scientific program. One important feature of the computer complex is the availability of terminals for on-line use of the computer in a conversational mode. The use of these terminals can distribute the computing power and provide rapid computer response to the programmers, engineers, and scientists located throughout the Center. Of all the available terminals, the graphical kind is perhaps the most sophisticated, as it can (among other things) provide a means for human participation in a computing process. An example is the human judgement and action highly desired at the end of each iteration when the computer is running a differential correction process for orbit determination.

The use of a graphical terminal highlights the problem of the language with which man and machine must communicate. An effective language can reduce the time which a user requires from the graphical terminal. A new programming language, called Mimic, has recently emerged. The problem-oriented Mimic language is different from the algorithmic Fortran language. It has been developed for solving differential equations and related computations. The learning time and relearning time are short. Thus, this language is of value to scientists and engineers for use with a graphical terminal.

SUMMER WORKSHOP

With the opportunity of the workshop held this summer at GSFC, this Mimic language was introduced to GSFC scientists, engineers, and programmers. The main purpose was to test this language with problems encountered at GSFC to determine its suitability. With the support of the Laboratory for Theoretical Studies, the Mimic processor was first incorporated into 7094/7040 DCS system, since the processor was written for IBM 7094 computers. It was later incorporated into the 7094's in Building 3.

The workshop consisted of half-day sessions for a week or less. Four sessions were conducted, in addition to several for small groups or individuals. A significant number of the participants had not previously used the digital computer directly. These new users programmed a sample problem of non-linear differential equation in one morning. Some received the correct result that day; others received it one or two days later after a few turnarounds.

With great simplicity in programming, the user can concentrate on analysis of the problem and meaningful interpretation of the result. Of course, the problems of singularity, convergence, and stability in the case of a mathematical model are still problems of the user. During the workshop, the user learned the rules of the language by learning more programs and by writing his own programs. An ardent beginner can learn to use a digital computer in one week.

*Goddard Space Flight Center

APPLICATION EXAMPLES

This report has a collection of 15 problems which were solved at GSFC. These problems were programmed with Mimic language, tested, and debugged. They represent some of the results, but more important, they can serve as programming examples to supplement the Mimic manual* which is the only document now available for Mimic programming.

These problems are edited for readability, uniformity, and usefulness as Mimic programming examples. For these reasons, each example consists of a problem description, presentation of the equations or block diagram which represents the model, as well as the values of constants, parameters and initial conditions for numerical computation. The Mimic program and a portion of the printout are then presented. Some examples include one or more plots of the result. In most examples, symbolic names in the equations and program are tabulated for easy reading.

In the subsequent examples, the attention of the reader is called to the unusual Mimic statements and programming techniques. In Example 1, the use of IMP statement is illustrated in Figure A-44. Example 2 illustrates a complex computation (not solving a differential equation), where the real and imaginary parts are computed separately. Example 3 shows a highly non-linear feedback control system (an interesting control problem now at GSFC). Example 4 shows the use of an FSW statement to precompute some constants; the result of this problem can be obtained either by solving a differential equation or by a straight transcendental computation. Example 6 shows a series of five programs of a relay servo system to illustrate the study of non-linear servos by readily obtaining phase-plane plots and transient responses as well as illustrating the use of IOR, FLF, and LSW statements. Examples 3 and 7 introduce the idea of using Mimic symbolic names directly in block diagrams for simplicity. Example 8 shows one comparison of the result obtained by Mimic and by Fortran using double precision arithmetic. Example 11 employs FSW statements to guard against possible discontinuities. Example 12 illustrates the use of FTR and PLO statements. Example 13 illustrates the use of decade values of DT; this has resulted in a concise printout for a log plot. Also notice the use of a logical control variable on one OUT statement so that certain particular values were printed out only once. Example 14 shows the simulation of friction in a control system. Both examples 13 and 14 show the use of the AND statement.

*Peterson, H.E., and Sanson F.J., Mimic - A Digital Simulation Program, SESCA Internal Memo. 65-12, Directorate of Computation, Wright-Patterson Air Force Base, Ohio, May, 1965.

THE TWO BODY PROBLEM OF CELESTIAL MECHANICS (EXAMPLE 1)

Y. Chu and L. H. Carpenter

Problem Description

The two-body problem is to determine the motion of two mass points which move under the influence of their mutual attractions in accordance with Newton's law of universal gravitation. The differential ϕ equation of motion of one mass with respect to the other is,

$$\frac{d^2 \vec{r}}{dt^2} = -\mu^2 \frac{\vec{r}}{r^3} \quad (1)$$

where

$$\mu^2 = k^2 (m_1 + m_2)$$

k = Gaussian constant

m_1 = mass of body 1

m_2 = mass of body 2

The solution of the equation of motion is known to be a conic section.

The differential equation can be solved numerically when m_1, m_2 , and the initial conditions of r and dr/dt are given.

For cases of elliptic motion, we have,

$$\mu^2 = n^2 a^3 \quad (2)$$

where

a = semi-major axis of the ellipse

$n = 2\pi/P$

P = period of the orbit.

Let us take x - y plane to be the plane of the ellipse with the origin at the focal point corresponding to the central body. Let the x axis be in the direction of the pericentron (the point on the ellipse closest to the origin). The equations for the coordinates of a point on the orbit are then,

$$x = a (\cos E - e) \quad (3)$$

$$y = a \sqrt{1 - e^2} \sin E \quad (4)$$

where

E = eccentricity

The eccentric anomaly is given by the solution of the Kepler's equation,

$$E - e \sin E = G \quad (5)$$

where G , the mean anomaly, is given by,

$$G = G_0 + nt \quad (6)$$

and G_0 is a constant.

To relate the initial conditions to the orbital elements, the equations for the coordinates are differentiated to give,

$$\frac{dx}{dt} = -n a \sin E / (1 - e \cos E) \quad (7)$$

$$\frac{dy}{dt} = n a \sqrt{1 - e^2} \cos E / (1 - e \cos E) \quad (8)$$

By choosing the initial time so that the body 2 is at the pericentron (i.e., $G_0 = 0$), we have for the initial conditions,

$$\begin{aligned} x(0) &= a(1 - e) \\ y(0) &= 0 \\ \dot{x}(0) &= 0 \\ \dot{y}(0) &= a n \sqrt{1 - e^2} / (1 - e) \end{aligned} \quad (9)$$

These formulas are used to give the initial conditions for the numerical solution which correspond to the elliptic formulas.

Orbit Computation by Numerical Integration

For the Mimic program, we choose the motion of the earth orbiting around the sun in the orbit plane. Equation (1) gives,

$$\frac{d^2 x}{dt^2} = -\mu^2 \frac{x}{r^3} \quad (10)$$

$$\frac{d^2 y}{dt^2} = -\mu^2 \frac{y}{r^3} \quad (11)$$

$$r = \sqrt{x^2 + y^2} \quad (12)$$

$$\mu^2 = n^2 a^3 \quad (13)$$

The following are the chosen constants,

$a = 1$ astronomical unit

$n = 1$ degree per mean solar day

$e = 0.02$

The initial conditions will be computed from Equation (9)

Table A-8
Equivalent Symbols

Program Symbols	Equation Symbols
ND	$= n$
N	$= n/57.3$
E	$= e$
XO, Y(O)	$= x(0), y(0)$
1DX0, IDY0	$= \dot{x}(0), \dot{y}(0)$
R	$= r$
MUSQ	$= \mu^2$
THE	$= \arctan (y/x)$
THED	$= \text{ditto in degrees}$
2DX, 2DY	$= \ddot{x}, \ddot{y}$
EE	$= E$
XEXACT, YEXACT	$= x, y \text{ from exact solution}$
G	$= G$
GO	$= G_0$
T	$= t$

The Mimic Program is shown in Figure A-42. For convenience of reading the program, equivalent symbols between the program and the equations are shown in Table A-8. Note that the computation is specified for 400 days. Both x and y positions and the polar r and θ coordinates are printed out at every two days (i.e. $DT = 2$). Figure A-43 shows a portion of the printout.

Orbit Computation from Elliptic Formulas

The above orbit can also be computed from the exact solution. In this case we use Equation (3) through (6). The same values of constants and initial conditions are chosen. The Mimic program is shown in Figure A-44. Equivalent symbols for this program are also shown in Table A-8. Note that the use of IMP statement is required in solving the transcendental Equation (5). As required in using the IMP function, a PAR statement for the unknown EE must be used to indicate a starting value (chosen to be 1 in this program). Figure A-45 shows a table from which a block diagram can be constructed for debugging purposes. This table is available in each run and will not be further shown. A portion of the result is shown in Figure A-46. This result agrees very well with that from the previous program of Figure A-42.

MIMIC SOURCE-LANGUAGE PROGRAM

TWO BODY PROBLEM---EARTH AROUND THE SUN

```

*
      CON(A,ND,E)
*
      DT      = 2.
      N       = ND/57.3
      B       = 1.-E
      C       = SQR(1.-E*E)
      XC      = A*B
      Y0      = 0.
      1DX0    = 0.
      1DY0    = A*N*C/B
*
      R       = SQR(X*X+Y*Y)
      THE     = ATN(Y,X)
      THED    = THE*57.3
      MUSQ    = N*N*A*A*A
      D       = MUSQ/(R*R*R)
*
      2DX     = -D*X
      1DX     = INT(2DX,1DX0)
      X       = INT(1DX,X0)
      2DY     = -D*Y
      1DY     = INT(2DY,1DY0)
      Y       = INT(1DY,Y0)
*
      FIN(T,400.)
      HDR(TIME,X,Y,R,THED)
      HDR
      OUT(T,X,Y,R,THED)
      END

```

SORT DIAGNOSTICS FOLLOW

Figure A-42-Mimic program.

TIME	X	Y	R	THED
0.	9.80000E-01	0.	9.80000E-01	0.
2.00000E 00	9.79366E-01	3.56015E-02	9.80013E-01	2.08203E 00
4.00000E 00	9.77464E-01	7.11570E-02	9.80051E-01	4.16395E 00
6.00000E 00	9.74297E-01	1.06620E-01	9.80114E-01	6.24566E 00
8.00000E 00	9.69870E-01	1.41946E-01	9.80203E-01	8.32705E 00
1.00000E 01	9.64189E-01	1.77088E-01	9.80316E-01	1.04080E 01
1.20000E 01	9.57260E-01	2.12000E-01	9.80455E-01	1.24884E 01
1.40000E 01	9.49595E-01	2.46639E-01	9.80618E-01	1.45682E 01
1.60000E 01	9.39703E-01	2.80960E-01	9.80806E-01	1.66472E 01
1.80000E 01	9.29098E-01	3.14917E-01	9.81018E-01	1.87254E 01
2.00000E 01	9.17295E-01	3.48468E-01	9.81254E-01	2.08027E 01
2.20000E 01	9.04308E-01	3.81570E-01	9.81514E-01	2.28789E 01
2.40000E 01	8.90157E-01	4.14181E-01	9.81797E-01	2.49539E 01
2.60000E 01	8.74860E-01	4.46258E-01	9.82103E-01	2.70277E 01
2.80000E 01	8.58438E-01	4.77761E-01	9.82431E-01	2.91001E 01
3.00000E 01	8.40913E-01	5.08651E-01	9.82782E-01	3.11712E 01
3.20000E 01	8.22308E-01	5.38888E-01	9.83154E-01	3.32407E 01
3.40000E 01	8.02650E-01	5.68434E-01	9.83547E-01	3.53086E 01
3.60000E 01	7.81964E-01	5.97252E-01	9.83960E-01	3.73748E 01
3.80000E 01	7.60279E-01	6.25307E-01	9.84394E-01	3.94392E 01
4.00000E 01	7.37622E-01	6.52563E-01	9.84847E-01	4.15017E 01
4.20000E 01	7.14025E-01	6.78987E-01	9.85319E-01	4.35624E 01
4.40000E 01	6.89518E-01	7.04546E-01	9.85809E-01	4.56210E 01
4.60000E 01	6.64135E-01	7.29209E-01	9.86317E-01	4.76775E 01
4.80000E 01	6.37908E-01	7.52947E-01	9.86841E-01	4.97319E 01
5.00000E 01	6.10873E-01	7.75730E-01	9.87382E-01	5.17840E 01
5.20000E 01	5.83065E-01	7.97532E-01	9.87938E-01	5.38339E 01
5.40000E 01	5.54520E-01	8.18326E-01	9.88509E-01	5.58815E 01
5.60000E 01	5.25276E-01	8.38088E-01	9.89094E-01	5.79266E 01
5.80000E 01	4.95371E-01	8.56795E-01	9.89692E-01	5.99693E 01
6.00000E 01	4.64843E-01	8.74426E-01	9.90302E-01	6.20095E 01
6.20000E 01	4.33732E-01	8.90959E-01	9.90925E-01	6.40472E 01
6.40000E 01	4.02078E-01	9.06377E-01	9.91558E-01	6.60823E 01
6.60000E 01	3.69922E-01	9.20663E-01	9.92201E-01	6.81148E 01
6.80000E 01	3.37304E-01	9.33800E-01	9.92853E-01	7.01446E 01
7.00000E 01	3.04266E-01	9.45776E-01	9.93514E-01	7.21718E 01
7.20000E 01	2.70851E-01	9.56576E-01	9.94182E-01	7.41962E 01
7.40000E 01	2.37100E-01	9.66191E-01	9.94857E-01	7.62179E 01
7.60000E 01	2.03055E-01	9.74610E-01	9.95538E-01	7.82368E 01
7.80000E 01	1.68760E-01	9.81826E-01	9.96224E-01	8.02530E 01
8.00000E 01	1.34256E-01	9.87832E-01	9.96914E-01	8.22664E 01
8.20000E 01	9.95879E-02	9.92624E-01	9.97607E-01	8.42770E 01
8.40000E 01	6.47974E-02	9.96198E-01	9.98303E-01	8.62848E 01
8.60000E 01	2.99275E-02	9.98552E-01	9.99000E-01	8.82898E 01
8.80000E 01	-4.97904E-03	9.99686E-01	9.99698E-01	9.02920E 01
9.00000E 01	-3.98795E-02	9.99601E-01	1.00040E 00	9.22914E 01

Figure A-43-Part of printout of result.

```

***MIMIC SOURCE-LANGUAGE PROGRAM***
TWO BODY PROBLEM - EARTH AROUND THE SUN - EXACT SOLUTION
*
  CON(A,ND,E,GO)
  PAR(E)
*
  DT      = 2.
  N       = ND*3.1416/180.
  C       = SQR(1.-E*E)
*
  XEACT   = A*(COS(E)-E)
  YEACT   = A*SIN(E)*C
  G       = GO+N*T
  EE      = IMP(E,E*SIN(E)*G)
*
  FIN(T,200.)
*
  HDR(TIME,XEACT,YEACT,EE,G)
  HDR
  OUT(T,XEACT,YEACT,EE,G)
  END
***SORT DIAGNOSTICS FOLLOW***

```

Figure A-44-Mimic program.

```

***FUNCTION-LANGUAGE PROGRAM GENERATED***

```

IFN	LCV	RESULT	FTN	A	B	C	D	E	F
1			CON	A	ND	E	GO		
2			PAR	EE					
3		DT	EQL	2.					
4		102	MPY	NC	3.1416				
5		N	DIV	102	180.				
6		104	MPY	E					
7		105	SUB	1.	104				
8		C	SQR	105					
9		107	COS	EE					
10		108	SUB	107	E				
11		XEACT	MPY	A	108				
12		110	SIN	EE					
13		YEACT	MPY	A	110	C			
14		G	MAC	N	T	GO			
15		115	EQL	110					
16		117	MAC	EE	115	G			
17		EE	IMP	EE	117				
18			T	200.					
19			FIN	T					
20			HDR	TIME	XEACT	YEACT	EE	G	
21			HDR						
22			OUT	T	XEACT	YEACT	EE	G	
23			END						

```

***FURTHER DIAGNOSTICS AND EXECUTION FOLLOW***

```

A	ND	E	GO
1.00000E 00	1.00000E 00	2.00000E-02	0.

Figure A-45-Table used in debugging process.

Figure A-46—Part of printout of result.

ANTENNA ARRAY RADIATION PATTERN COMPUTATION (EXAMPLE 2)

A. F. Durham

Problem Description

To provide increased radiation directivity in a desired direction, an antenna design may comprise many radiation elements of low directivity combined in an array. When the current intensities in each element of the array follow simple mathematical laws and the spacing between elements is uniform, simple expressions exist for the resulting radiation pattern of the antenna. Where this simple situation does not exist it is necessary to sum the contributions from each element of the array at the far-field point, and the solution is not amenable to simple calculation.

For a one dimensional array of N elements, the normalized radiation pattern of the array is given by,

$$E(\theta) = \frac{\sum_{n=1}^N I_n \exp(j 2 \pi (d_n/\lambda) \sin \theta)}{\sum_{n=1}^N I_n} \quad (14)$$

where

I_n is the current intensity in the n th element,

d_n is the spacing of the n th element from an arbitrary reference (such as the location of the first element)

θ is the angle from the normal to the plane of the array

and

λ is the wavelength of operation.

When each element of the array is an isotropic radiator, the computed radiation pattern $E(\theta)$ will be identical with the radiation pattern of the array. If the elements of the array have some directivity in the plane containing the array, then the computed radiation pattern $E(\theta)$ must be multiplied on a point by point basis with the normalized radiation pattern of the element in the plane of the array. The resulting product is the final radiation pattern of the array.

A Four-Element Binomial Array

As an example, a four-element binomial array with unequal element spacing shown in Figure A-47 is chosen. It is required to compute the radiation pattern of this array where the current intensities follow a binomial distribution, but the spacing between successive elements is entirely arbitrary. To be specific, the radiation pattern is given by,

$$E(\theta) = I_1 \exp[j 2 \pi (d_1/\lambda) \sin \theta] + I_2 \exp[j 2 \pi (d_2/\lambda) \sin \theta] \\ + I_3 \exp[j 2 \pi (d_3/\lambda) \sin \theta] + I_4 \exp[j 2 \pi (d_4/\lambda) \sin \theta] \quad (15)$$

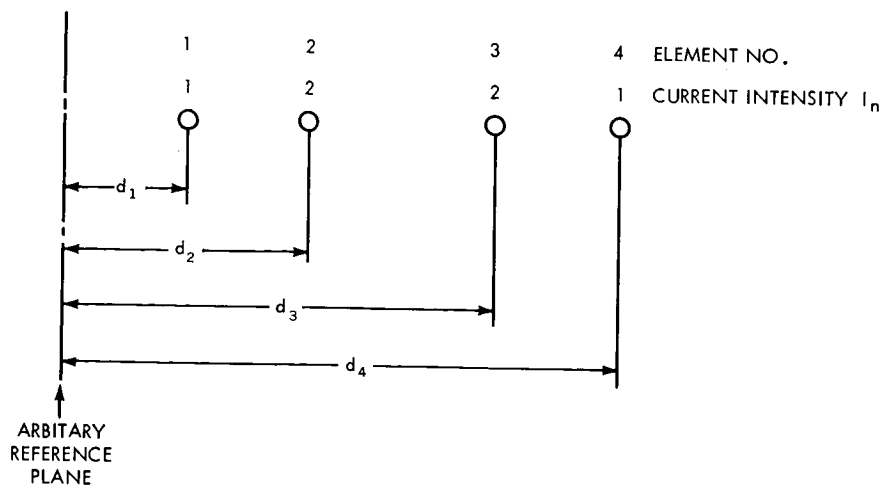


Figure A-47—Binomial array.

The real part R_1 of the $E(\theta)$ is,

$$R_1 = I_1 C_1 + I_2 C_2 + I_3 C_3 + I_4 C_4 \quad (16)$$

and the imaginary part is,

$$R_2 = I_1 S_1 + I_2 S_2 + I_3 S_3 + I_4 S_4 \quad (17)$$

where

$$C_i = \cos [2\pi (d_i/\lambda) \sin \theta] \quad (18)$$

and

$$S_i = \sin [2\pi (d_i/\lambda) \sin \theta] \quad (19)$$

and the magnitude of the $E(\theta)$ is,

$$R = \sqrt{R_1^2 + R_2^2} \quad (20)$$

The power in db is,

$$PWR = 20 \log_{10} R \quad (21)$$

The Mimic Program

Table A-9
Equivalent Symbols

Program Symbols	Equation Symbols
Ii	$= I_i$
Di	$= d_i/\lambda$
Ci	$= \cos (2 \pi (d_i/\lambda) \sin \theta)$
Si	$= \sin (2 \pi (d_i/\lambda) \sin \theta)$
PSI	$= \theta \text{ (radians)}$
T	$= \theta \text{ (degree)}$
L	$= \sin \theta$

The Mimic program for computing magnitude of the radiation and the power by using equations (14) through (21) and using the following constants and parameters,

$$I_1 = 1 \quad d_1/\lambda = 0$$

$$I_2 = 2 \quad d_2/\lambda = 1$$

$$I_3 = 2 \quad d_3/\lambda = 2$$

$$I_4 = 1 \quad d_4/\lambda = 3$$

is shown in Figure A-48. Equivalent symbols for the program are shown in Table A-9. The program is to compute the normalized pattern from θ equal to 0 degree to 180 degrees. A partial result is shown in Figure A-49. The result is plotted as a curve showing the radiation pattern in Figure A-50.

```

***MIMIC SOURCE-LANGUAGE PROGRAM***

4 ELEM BINOMIAL ARRAY UNEQUAL SPACE 525 AFD 12JUL66
*
      CON(I1,I2,I3,I4,DT)
      PAR(D1,D2,D3,D4)
*
      DTMIN = DTMAX
      DTMAX = 1.
*
      PSI = T*3.1416/180.
      L = SIN(PSI)
      P1 = 6.2832*D1*L
      P2 = 6.2832*D2*L
      P3 = 6.2832*D3*L
      P4 = 6.2832*D4*L
*
      C1 = COS(P1)
      C2 = COS(P2)
      C3 = COS(P3)
      C4 = COS(P4)
*
      S1 = SIN(P1)
      S2 = SIN(P2)
      S3 = SIN(P3)
      S4 = SIN(P4)
*
*REAL PART
      R1 = (I1*C1+I2*C2+I3*C3+I4*C4)/6.
*IMAGINARY PART
      R2 = (I1*S1+I2*S2+I3*S3+I4*S4)/6.
*MAGNITUDE
      R = SQR(R1*R1+R2*R2)
*POWER
      PWR = 20.*LOG(R,10.)
*
      FIN(T,180.)
      HDR(T,R,PWR)
      HDR
      OUT(T,R,PWR)
      END

```

SORT DIAGNOSTICS FOLLOW

Figure A-48—Mimic program.

D	D2	D3	D4
0.	1.00000E 00	2.00000E 00	3.00000E 00
T	R	PWR	
0.	10.00000E-01	-2.24285E-07	
1.00000E 00	9.94499E-01	-4.79124E-02	
2.00000E 00	9.78127E-01	-1.92091E-01	
3.00000E 00	9.51274E-01	-4.33886E-01	
4.00000E 00	9.14575E-01	-7.75617E-01	
5.00000E 00	8.68891E-01	-1.22070E 00	
6.00000E 00	8.15285E-01	-1.77581E 00	
7.00000E 00	7.54988E-01	-2.44120E 00	
8.00000E 00	6.89361E-01	-3.23106E 00	
9.00000E 00	6.19858E-01	-4.15416E 00	
1.00000E 01	5.47980E-01	-5.22470E 00	
1.10000E 01	4.75237E-01	-6.46180E 00	
1.20000E 01	4.03099E-01	-7.89177E 00	
1.30000E 01	3.32965E-01	-9.55204E 00	
1.40000E 01	2.65119E-01	-1.14985E 01	
1.50000E 01	2.03703E-01	-1.38200E 01	
1.60000E 01	1.46691E-01	-1.66719E 01	
1.70000E 01	9.58640E-02	-2.03669E 01	
1.80000E 01	5.18019E-02	-2.57131E 01	
1.90000E 01	1.48732E-02	-3.65519E 01	
2.00000E 01	1.47642E-02	-3.66158E 01	
2.10000E 01	3.71578E-02	-2.85990E 01	
2.20000E 01	5.25486E-02	-2.55888E 01	
2.30000E 01	6.13547E-02	-2.42430E 01	
2.40000E 01	6.41500E-02	-2.38561E 01	
2.50000E 01	6.16405E-02	-2.42027E 01	
2.60000E 01	5.46369E-02	-2.52503E 01	
2.70000E 01	4.40272E-02	-2.71256E 01	
2.80000E 01	3.07475E-02	-3.02438E 01	
2.90000E 01	1.57544E-02	-3.60520E 01	
3.00000E 01	2.19850E-02	-1.12771E 02	
3.10000E 01	1.56038E-02	-3.61354E 01	
3.20000E 01	3.01851E-02	-3.04042E 01	
3.30000E 01	4.29534E-02	-2.73401E 01	
3.40000E 01	5.32044E-02	-2.54811E 01	
3.50000E 01	6.03339E-02	-2.43888E 01	
3.60000E 01	6.58466E-02	-2.38972E 01	
3.70000E 01	6.83605E-02	-2.39636E 01	
3.80000E 01	5.86085E-02	-2.46408E 01	
3.90000E 01	4.94366E-02	-2.61190E 01	
4.00000E 01	3.57995E-02	-2.89225E 01	
4.10000E 01	1.77530E-02	-3.50146E 01	
4.20000E 01	4.55421E-03	-4.68317E 01	
4.30000E 01	3.18915E-02	-3.02032E 01	
4.40000E 01	5.09579E-02	-2.42994E 01	
4.50000E 01	9.43943E-02	-2.05011E 01	
4.60000E 01	1.30796E-01	-1.76681E 01	
4.70000E 01	1.69727E-01	-1.54050E 01	
4.80000E 01	2.10726E-01	-1.35256E 01	
4.90000E 01	2.53327E-01	-1.19264E 01	
5.00000E 01	2.97063E-01	-1.05430E 01	
5.10000E 01	3.41475E-01	-9.33283E 00	
5.20000E 01	3.86125E-01	-8.26545E 00	
5.30000E 01	4.30599E-01	-7.31853E 00	
5.40000E 01	4.74516E-01	-6.47499E 00	

Figure A-49—Partial result of Mimic program.

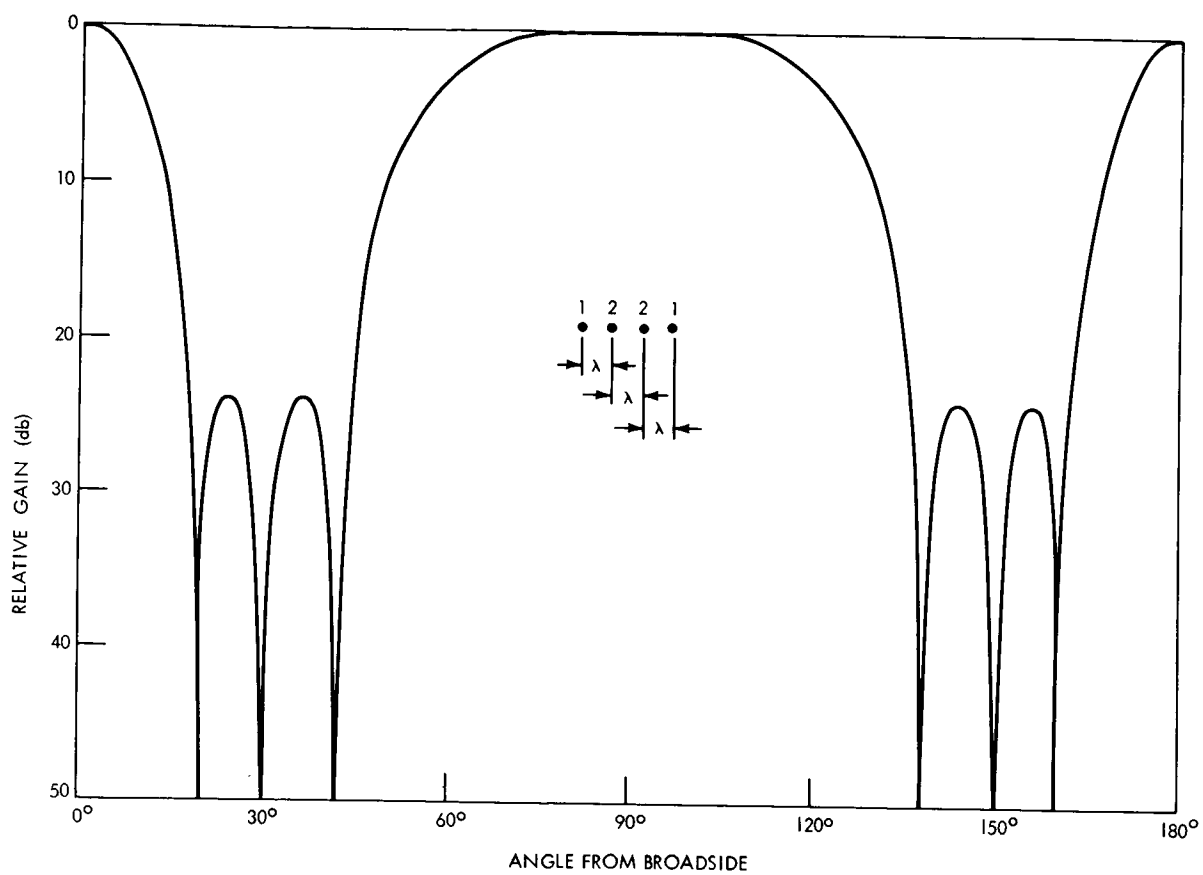


Figure A-50—Graph of result.

A SINGLE AXIS INITIAL ACQUISITION PROBLEM (EXAMPLE 3)

T. R. Buckler

Problem Description

The ATS-4 spacecraft will be required to acquire the earth while the spacecraft is in a stabilized condition. The spacecraft will be pointed at the sun when the sun is approximately 90 degrees from the earth. A command will be given which will cause the spacecraft to roll around the sun line. Since the spacecraft will be pointed at the sun while it is rotating around the earth there will be a maximum time the spacecraft can take to acquire the earth. This study concerns itself with the first phase of the acquisition; that is, pointing the spacecraft at the sun. The maximum time allotted for the spacecraft to acquire the sun is 15 minutes. The vehicle will be required to point to the sun to an accuracy of $\pm 2^\circ$. As a worst case single axis initial acquisition of the sun we will assume a 180° offset and an initial rate of zero degrees per second.

The sun paddles on the spacecraft are not rigid, and therefore exert a force on the spacecraft which will extend the time required to point the spacecraft at the sun.

The output from this program is the time required to acquire the sun to within $\pm 2^\circ$. The program will also show what effect the non-rigid paddles will have on the spacecraft's control system.

Model and Equations

The system that was simulated is shown in the block diagram of Figure A-51. The system includes a sun sensor, a pulse width modulator (PWM), a rate gyro and non-rigid paddles. The satellite dynamics are described by the equation

$$I \ddot{\theta} = T \quad (22)$$

where

I is the main body inertia

T is the torque applied

θ is the angular position of the spacecraft.

The non-rigid paddles are simulated using the following equations,

$$\frac{\gamma}{\theta} = \frac{-K_c}{I_p s^2 + Bs + K_c} \quad (23)$$

where

I_p = inertia of paddles

B = damping of paddles

K_c = paddle constant

$$T_p = K_c (\theta + \gamma) + B \dot{\gamma} \quad (24)$$

where T_p is the torque exerted on the spacecraft by the paddles.

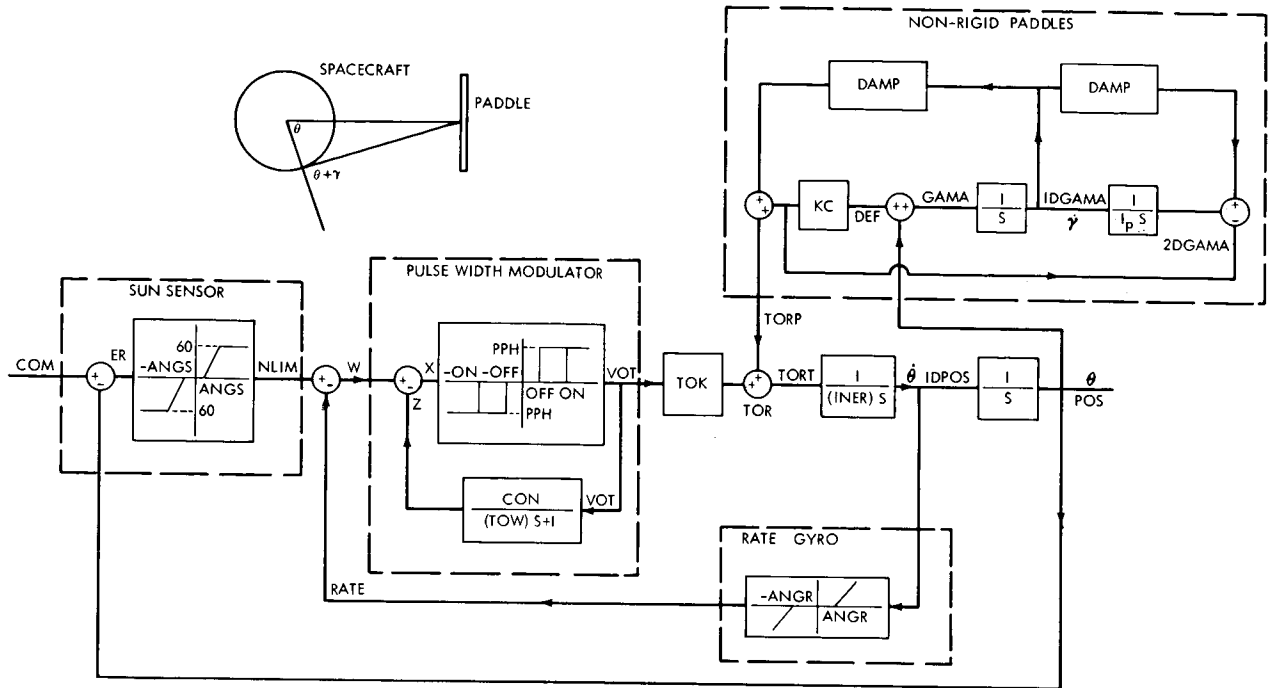


Figure A-51—Spacecraft control system (block diagram).

Constants, Parameters and Initial Conditions

(a) Constants

ON = Value of input to PWM which causes the jets to turn on = 1 volt

OFF = Value of input to PWM which causes the jets to turn off = .9 volt

PPH = Height of the pulses = 10 volts

CON = Gain of integrating loop in PWM = 1V/V

TON = Time constant in integrating loop = 150 seconds

INER = Inertia of spacecraft = 800 slug-ft²

KR = Gain of rate gyro = 3438 volts/radian

KS = Gain of sun sensor = 114.6 volts/radian

ANGR = Dead space of rate gyro = .0017452 radian

ANGS = Dead space of sun sensor = .0209424 radian

TOK = Gain of jet actuators = .0084 ft-lb/volt

(b) Parameters

NATFRE = Natural frequency of paddles = $\omega_n = \sqrt{K_c/I_p} = .5$

DAMRAT = Damping ratio of paddles = $\zeta = B/2\omega_n I_p = .06$

INERTP = Inertia of paddles - 1000 slug-ft²

(c) Initial Conditions

ICRATE = Initial condition on $\dot{\theta} = 0$ degrees/sec.

ICPOS = Initial condition on $\theta = -180$ degrees

The Mimic Program

The block diagram in Figure A-51 together with above equations, and the above values of constants, parameters, and initial conditions is used to prepare the Mimic program shown in Figure A-52. The result is shown in the sketch in Figure A-53. No table of equivalent symbols is provided here as the symbols in the program are used in the block diagram.

Results

The results of the study are shown in Figure A-53. The plot of theta vs time shows that the spacecraft acquires the sun line, from an initial offset of -180 degrees, to an accuracy of 2 degrees in 700 seconds. The paddle deflection does not have any noticeable effect on the spacecraft position.

MIMIC SOURCE-LANGUAGE PROGRAM

```

PITCH - SUN MODE - NON-RIDGED BODY
      CON(CON,OFF)
      CON(CON,TOW,PPH)
      CON(INER,KR,KS)
      CON(ANGR,ANGS,TOK)
      PAR(ICRATE,ICPOS)
      PAR(NATFRE,DAMRAT,INERTP)
CALCULATION OF SOLAR PADDLE PARAMETERS
      ICAL = FSW(T,FALSE,TRUE,FALSE)
      ICAL DAMP = 2.*DAMRAT*NATFRE*INERTP
      ICAL KC = NATFRE*NATFRE*INERTP
      COM = EQL(0.)
      ER = COM-POS
      M = DSP(ER,-ANGS,ANGS)
      N = KS*M
      NLIM = LIM(N,-60.,60.)
PULSE WIDTH MODULATOR
      W = NLIM-RATE
      U = INT((CON*VOT)-Z,0.)
      Z = U/TOW
      X = W-Z
      Y = ABS(X)
      I = FSW(Y-ON,FALSE,FALSE,TRUE)
      J = FSW(Y-OFF,TRUE,FALSE,FALSE)
      L = FLF(I,J,FALSE)
      VOTA = LSW(L,PPH,0.)
      VOT = FSW(X,-VOTA,0.,VOTA)
      TOR = TOK*VOT
      TORA = INT(TOR,0.)
      1DPOS = INT(TOR/INER,ICRATE)
      Q = DSP(1DPOS,-ANGR,ANGR)
      RATE = KR*Q
MODIFY POSITION OUTPUT TO STAY WITHIN ±180 DEGREES
      POST = INT(1DPOS,ICPOS)
      POSA = ABS(POST)
      R = FSW(POSA-3.14,FALSE,FALSE,TRUE)
      POS = LSW(R,-(POST/POSA)*(6.28-POSA),POST)
NON-RIDGED SOLAR PADDLES
      2DGAMA = (-KC*POS-KC*GAMA-DAMP*1DGAMA)/INERTP
      1DGAMA = INT(2DGAMA,0.)
      GAMA = INT(1DGAMA,-ICPOS)
      DEF = GAMA+POS
      TORP = (KC*DEF)+(DAMP*1DGAMA)
      TORT = TOR+TORP
      1DTHB = 1DPOS*57.3
      THETA = POS*57.3
      GAMAD = GAMA*57.3
      DEFC = DEF*57.3
      DT = 5.0
      DTMIN = .00001
      FIN(T,1200.)
      HDR(TIME,THETA,1DTHET)
      HDR(COM,ERROR,W)
      HDR(X,TORQUE,INTOR)
      HDR(GAMAD,TORP,TORT)
      OUT(T,THETA,1DTHE)
      OUT(COM,ER,W)
      OUT(X,TOR,INTOR)
      OUT(GAMAD,TORP,TORT)
      PLO(T,THETA,DEFC,TOR,TORP,1DTHE)
      END

```

Figure A-52-Mimic program.

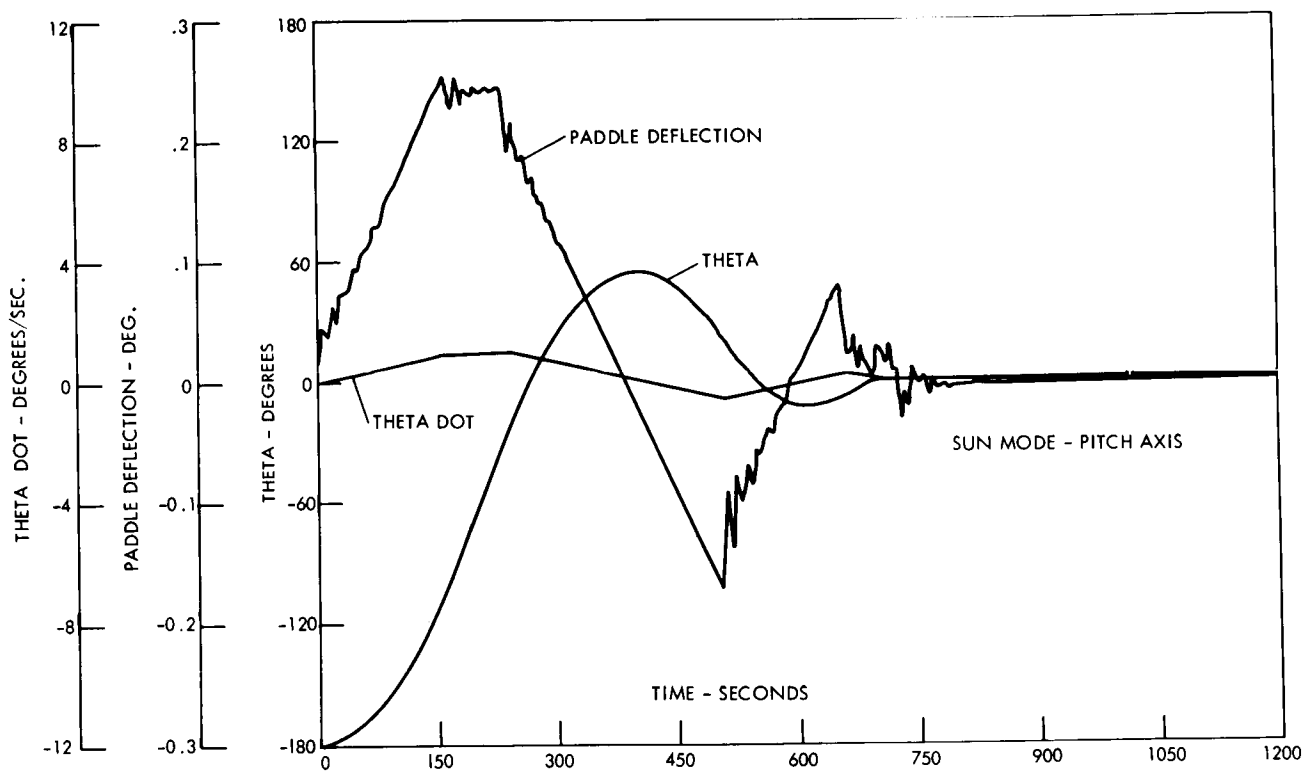


Figure A-53—Result of program.

DOPPLER FREQUENCY FROM A SATELLITE (EXAMPLE 4)

Howard I. Kingman, Jr.

Problem Description

A receiver used for satellite tracking application must have a very narrow bandwidth to extract the minute satellite beacon signal from its associated noise background. Since the satellite is moving, the received signal frequency is constantly changing due to the doppler effect. In order to maintain the signal in the receiver bandwidth, it is necessary to shift the local oscillator frequency by an amount equal to the doppler frequency shift. The doppler shift and rate of doppler shift determine the characteristics of the local oscillator and must be known in order to design a receiver. These doppler effects are the greatest where the satellite passes directly over the station, so this is the case considered here.

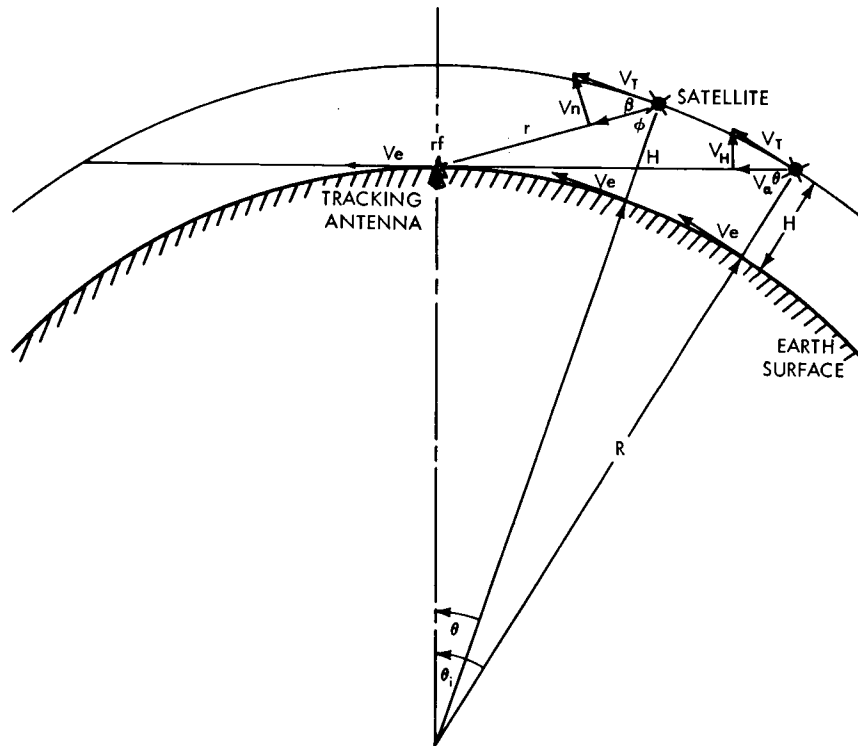


Figure A-54—Doppler shift analysis geometry.

Figure A-54 shows the geometry of the satellite, tracking station, and the earth where,

R = earth radius

r = slant range of the satellite

g_0 = earth gravitational pull at surface

H = height of the orbit

v_t = tangential velocity

v_r = radial velocity

v_e = tangential velocity of a point on the earth surface

α = orbit inclination w.r. to the equator

θ_i = contact angle

θ = the angle which is the variable

From the geometry, we have,

$$\theta_i = \theta(0) = \arctan \sqrt{H^2 + 2RH/R} \quad (25)$$

$$V_t = \sqrt{g_0 R^2 / (R + H)} = \text{constant} \quad (26)$$

$$\theta = V_t / (R + H) - \cos \alpha \cdot V_e \quad (27)$$

$$\theta = \theta_i - \dot{\theta} t \quad (28)$$

The doppler shift f_d , doppler rate f_{dr} , and received frequency f_{rec} are,

$$f_d = f_t V_r / c \quad (29)$$

$$f_{dr} = f_t (dV_r / dt) / c \quad (30)$$

$$f_{rec} = f_t + f_d \quad (31)$$

where

f_t = the transmitter frequency

c = velocity of light

Also from the geometry, the slant range r is,

$$r = \sqrt{4R(R + H) \sin^2(\theta/2) + H^2} \quad (32)$$

By differentiating r with respect to time t , we have,

$$V_r = \dot{r} = -V_t R \sin \theta / r \quad (33)$$

By differentiating V_r , we have,

$$dV_r / dt = \ddot{r} = -V_t^2 R \cos \theta / [(R + H) r] + V_t^2 R^2 \sin^2 \theta / r^3 \quad (34)$$

The initial conditions of the slant range and radial velocity are,

$$r(0) = \sqrt{H^2 + 2RH} \quad (35)$$

$$V_r(0) = \dot{r}(0) = V_t \cos \theta_i \quad (36)$$

Table A-10
Equivalent Symbols

Program Symbols	Equation Symbols
R	= R
H	= H
VT	= V_t
RNGE1	= r (integrated value)
RNGE2	= r (computed value)
RADVEL	= V_r (integrated value)
1DRN	= \dot{r} (computed value)
2DRN	= $r = dV_r/dt$
THE	= θ
THEDOT	= $\dot{\theta}$
INTHE	= θ_i
INTRNG	= $r(0)$
DOPFRQ	= f_d
DOPRTE	= f_{dr}
FT	= f_t
C	= c
INVEL	= $V_r(0)$
RI	= $R + H$
G	= g_0
RECFRQ	= f_{rec}
RE	= V_e

The Mimic Program

The mimic program is to compute doppler shift and doppler rate, slant range, radial velocity, and radial acceleration. Equations (25) through (36) are used for this computation. Although equations (32) and (33) are not needed, but they are employed to improve the accuracy. The values of the constants are:

$$c = 186,000 \text{ miles/sec}$$

$$R = 3963.34 \text{ miles}$$

$$g_0 = .0060983 \text{ miles/sec}^2$$

$$v_e = 7.27 \times 10^{-5} \text{ miles/sec}$$

and the values of the parameters are,

$$H = 150, \quad 2300, \quad 1100 \text{ miles}$$

$$f_t = 1700, \quad 108, \quad 283,000 \text{ mc}$$

$$\alpha = .49, \quad .49, \quad .49 \text{ radian}$$

These parameter values are for the Apollo spacecraft, the Vanguard satellite, and a laser experiment respectively.

The program is shown in Figure A-55. Notice that the logical control variable TEQQ controls the precomputation of constants. A portion of the result is shown in Figure A-56.

```

***MIMIC SOURCE-LANGUAGE PROGRAM***

SATELLITE DOPPLER PROGRAM BY HOWARD KINGMAN
*
      CON(DT,C,R,G,RE)
      PAR(H,FT,ALPHA)
*
PRECOMPUTE CONSTANTS
      TEQO   = FSW(T,FALSE,TRUE,FALSE)
      TEQO   R1   = SUM(R,H)
      TEQO   R1SQ  = MPY(R1,R1)
      TEQO   GRVITY = G*R*R/R1SQ
      TEQO   INTHE  = ATN(INTRNG/R)
      TEQO   INTRNG = SQR(H*H+2.*R*H)
      TEQO   VT     = SQR(GRVITY*R1)
      TEQO   THEDOT = VT/R1-COS(ALPHA)*RE
*
EQUATIONS
      THE    = INTHE-THEDOT*T
      1DRN   = -VT*R*SIN(THE)/RNGE2
      RNGE2  = SQR(4.*R*R1*SIN(THE/2.)*SIN(THE/2.)+H*H)
      DOPFRQ = -FT*1DRN/C
      RNCUBE = RNGE2*RNGE2*RNGE2
      R1RNGE = R1*RNGE2
      NUMAC  = VT*VT*R*R*SIN(THE)*SIN(THE)
      RNGE1  = INT(1DRN,INTRNG)
*
      2DRN   = -R*VT*VT*COS(THE)/R1RNGE+NUMAC/RNCUBE
      DOPRTE = FT*2DRN/C
      INVEL  = VT*COS(INTHE)
      RADVEL = INT(2DRN,INVEL)
      RECFRQ = FT+DOPFRQ
      NEGTHE = NEG(THE)
*
      FIN(NEGTHE,INTHE)
      HDR(TIME,DOPFRQ,DOPRTE,RANGE,RADVEL,RADACC)
      HDR(SECNDS,IN CPS, CPSS, MILES, MPS, MPSS)
      HDR
      OUT(T,DOPFRQ,DOPRTE,RNGE2,RADVEL,2DRN)
      END

***SORT DIAGNOSTICS FOLLOW***

```

Figure A-55-Mimic program.

H	TIME SECONDS	FT	ALPHA	DOPRTE CPSS	RANGE MILES	RADVEL MPS
1.50000E 02		1.70000E 09	4.90000E-01			
0.						
1.00000E 01		4.24983E 04	2.12802E-06		1.10068E 03	4.64981E 00
2.00000E 01		4.24955E 04	-5.88415E-01		1.05673E 03	4.64949E 00
3.00000E 01		4.24869E 04	-1.25832E 00		1.01278E 03	4.64849E 00
4.00000E 01		4.24714E 04	-2.02886E 00		9.68842E 02	4.64670E 00
5.00000E 01		4.24481E 04	-2.92425E 02		9.24925E 02	4.64401E 00
6.00000E 01		4.24156E 04	-3.97889E 00		8.81037E 02	4.64025E 00
7.00000E 01		4.23723E 04	-5.23390E 00		8.37188E 02	4.63523E 00
8.00000E 01		4.23159E 04	-6.74771E 00		7.93391E 02	4.62870E 00
9.00000E 01		4.22436E 04	-8.59899E 00		7.49660E 02	4.62034E 00
1.00000E 02		4.21519E 04	-1.08966E 01		7.06013E 02	4.60972E 00
1.10000E 02		4.20357E 04	-1.37935E 01		6.62473E 02	4.59628E 00
1.20000E 02		4.18885E 04	-1.75091E 01		6.19069E 02	4.57924E 00
1.30000E 02		4.17011E 04	-2.23644E 01		5.75836E 02	4.55755E 00
1.40000E 02		4.14606E 04	-2.88397E 01		5.32824E 02	4.52971E 00
1.50000E 02		4.11485E 04	-3.76715E 01		4.90096E 02	4.49358E 00
1.60000E 02		4.07374E 04	-5.00196E 01		4.47739E 02	4.44600E 00
1.70000E 02		4.01859E 04	-6.77626E 01		4.05875E 02	4.38218E 00
1.80000E 02		3.94296E 04	-9.40304E 01		3.64681E 02	4.29464E 00
1.90000E 02		3.83648E 04	-1.34175E 02		3.24417E 02	4.17140E 00
2.00000E 02		3.68205E 04	-1.97496E 02		2.85484E 02	3.99266E 00
2.10000E 02		3.45085E 04	-2.99982E 02		2.48513E 02	3.72507E 00
2.20000E 02		3.09466E 04	-4.66871E 02		2.14527E 02	3.31283E 00
2.30000E 02		2.53867E 04	-7.26305E 02		1.85183E 02	2.66931E 00
2.40000E 02		1.69491E 04	-1.06515E 03		1.63011E 02	1.69275E 00
2.50000E 02		5.45135E 03	-1.33485E 03		1.51203E 02	3.62002E-01
2.60000E 02		-7.32276E 03	-1.30898E 03		1.52193E 02	-1.11647E 00
2.70000E 02		-1.84197E 04	-1.01318E 03		1.65750E 02	-2.40083E 00
2.80000E 02		-2.63822E 04	-6.81062E 02		1.89192E 02	-3.32241E 00
2.90000E 02		-3.15856E 04	-4.36579E 02		2.19369E 02	-3.92465E 00
3.00000E 02		-3.49196E 04	-2.81265E 02		2.53888E 02	-4.31052E 00
3.10000E 02		-3.70917E 04	-1.86012E 02		2.91206E 02	-4.56193E 00
3.20000E 02		-3.85495E 04	-1.26977E 02		3.30371E 02	-4.73065E 00
3.30000E 02		-3.95593E 04	-8.93797E 01		3.70796E 02	-4.84753E 00
3.40000E 02		-4.02796E 04	-6.46594E 01		4.12104E 02	-4.93089E 00
3.50000E 02		-4.08066E 04	-4.78845E 01		4.54051E 02	-4.99189E 00
3.60000E 02		-4.12007E 04	-3.61602E 01		4.96471E 02	-5.03750E 00
3.70000E 02		-4.15006E 04	-2.77422E 01		5.39246E 02	-5.07222E 00
3.80000E 02		-4.17322E 04	-2.15485E 01		5.82295E 02	-5.09901E 00
3.90000E 02		-4.19129E 04	-1.68897E 01		6.25556E 02	-5.11993E 00
4.00000E 02		-4.20549E 04	-1.33140E 01		6.68983E 02	-5.13637E 00
4.00000E 02		-4.21670E 04	-1.05188E 01		7.12540E 02	-5.14934E 00

Figure A-56-Part of result.

COMPOSITION CHANGES IN THE SOLAR ATMOSPHERE DUE TO DIFFUSION (EXAMPLE 5) Minoru P. Nakada

Problem Description

This problem deals with changes in the composition of the solar atmosphere that may be produced by diffusion in the region where the temperature rises rapidly from some 6000°K at the surface to over 1,000,000°K at higher altitudes.

Only H^+ and He^{++} have been considered since they are most plentiful. Where the temperature is about 6000°K, the H to He ratio is about 10 to 1. A diffusion equation due to Chapman has been used. Diffusion is due to radial gradients in composition, pressure, and temperature. The composition term has one specie to move away from the region where it has a large concentration. The pressure term has heavier particles settling relative to lighter ones. The temperature gradient tends to move the more highly charged species toward the hotter region so that it acts in the opposite direction to the pressure gradient in this problem. The temperature gradient term is the more powerful. In the steady state, the diffusive processes due to pressure and temperature gradients are balanced by concentration gradients. Thus, given initial concentrations, the concentrations are evaluated as a function of altitude or temperature.

Mathematical Model

The equations which describe the diffusion are shown below,

$$\frac{d(\log_{10} u)}{dx} = G(u) + \Lambda(au - 1)/10^{1.5x} \quad (37)$$

where

$$\frac{d(\log_{10} u)}{dx} = \frac{\log_{10} e}{u} \frac{du}{dx}$$

$$G(u) = .516 \left(\frac{1+u}{2u+3} \right) - 1.64 \left(\frac{1+u}{u+4} \right) - \frac{1.13(1+u)(1+1.82u)}{(1+0.122u)(1+2.04u)} \quad (38)$$

and Λ and a are constants.

In the above, the dependent variable u represents the ratio of H^+ to He^{++} concentrations, and x is,

$$x = \log_{10} (T/T_0) \quad (39)$$

where T_0 is the temperature above which equations (37) and (38) are applicable. In the expression $G(u)$, the positive term is due to the pressure gradient and the negative terms due to the thermal gradient. The concentration gradient is the derivative term.

The problem is made somewhat more complex since a solar wind is given off by the solar atmosphere. This is accounted for in the term with Λ , where Λ is proportional to the solar wind flux. (a) gives the fraction of He^{++} in the solar wind.

A	SMALLA
0.	0.
X	U
0.	1.00000E 01
1.00000E-01	3.19309E 00
2.00000E-01	1.50972E 00
3.00000E-01	8.57967E-01
4.00000E-01	5.36004E-01
5.00000E-01	3.53421E-01
6.00000E-01	2.40857E-01
7.00000E-01	1.67669E-01
8.00000E-01	1.18382E-01
9.00000E-01	8.43936E-02
1.00000E 00	6.05680E-02
1.10000E 00	4.36742E-02
1.20000E 00	3.15980E-02
1.30000E 00	2.29159E-02
1.40000E 00	1.66480E-02
1.50000E 00	1.21095E-02
1.60000E 00	8.81624E-03
1.70000E 00	6.42279E-03

A	SMALLA
8.30000E 00	5.00000E-02
X	U
0.	1.00000E 01
1.00000E-01	1.09876E 00
2.00000E-01	2.33286E-01
3.00000E-01	7.38017E-02
4.00000E-01	3.00621E-02
5.00000E-01	1.45536E-02
6.00000E-01	7.94948E-03
7.00000E-01	4.72705E-03
8.00000E-01	2.98450E-03
9.00000E-01	1.96585E-03
1.00000E 00	1.33426E-03
1.10000E 00	9.24988E-04
1.20000E 00	6.50949E-04
1.30000E 00	4.62987E-04
1.40000E 00	3.31784E-04
1.50000E 00	2.39031E-04
1.60000E 00	1.72857E-04
1.70000E 00	1.25337E-04

Figure A-58-Part of result.

The result from this model seems to give a large change in the composition with temperature, and is contrary to most expectations.

The Mimic Program

It is required to solve Equation (37) for u from $x = 0$ to $x = 1.6$. The initial value of u is 10 when x is 0. It is expected that the values of u should go from 10 to smaller values but will probably not go below 10^{-5} . The computation is required for the following sets of values:

$A = 0, 8.3, 3.3, 1.2, 8.3, 3.3, 1.2$

$a = 0, .05, .05, .05, .1, .1, .1$

The program is shown in Figure A-57 and a portion of the result is shown in Figure A-58. Since the symbols are readily identifiable, no equivalent symbol table is provided.

```

***MIMIC SOURCE-LANGUAGE PROGRAM***

COMPOSITION CHANGE IN SOLAR ATMOSPHERE DUE TO DIFFUSION - Y.CHU
*
      PAR(A,SMALLA)
      E      = 2.7183
      F      = A*(SMALLA*U-1.)/EXP(1.5*T,10.)
      G      = H-I/J
      H      = .516*(1.+U)/(3.+2.*J)-1.64*(1.+U)/(U+4.)
      I      = 1.13*(1.+U)*(1.+1.82*U)
      J      = (1.+0.112*U)*(1.+2.04*U)
*
      IDU    = (G+F)*U/LOG(E,10.)
      U      = INT(IDU,10.)
*
      FIN(T,1.6)
      HDR(X,U)
      HDR
      OUT(T,U)
      END

***SORT DIAGNOSTICS FOLLOW***

```

Figure A-57—Mimic program.

SIMULATIONS OF RELAY SERVO SYSTEMS (EXAMPLE 6)

K. Dolan and W. Raskin

Problem Description

This problem illustrates the use of Mimic program in simulating non-linear servo systems. The examples chosen here are simple relay servos, which, excluding the relay, can be represented by a second-order differential equation. Five cases are considered,

- Linear servo (Figure A-59)
- Simple relay servo (Figure A-64)
- Simple relay servo with a dead space (Figure A-69)
- Relay servo with hysteresis (Figure A-74)
- Relay servo with dead space and hysteresis (Figure A-79).

For each of these cases, an initial displacement is chosen and the transient response is to be sought. The constants and parameters chosen for these five cases are shown in Table A-11.

Table A-11
Constants and Parameters

Name	(a)	(b)	(c)	(d)	(e)
A	2	2	2	2	2
B	.5	.5	.5	.5	.5
V	-	1	1	1	1
D	-	-	.2	.2	.2
H	-	-	-	-	.1
1DXO	0	0	0	0	0
XO	2	2	2	2	2
DT	.1	.1	.1	.1	.1

Linear Servo

The block diagram for the linear servo system is shown in Figure A-59. The gain from the amplifier is symbolically lumped with the constant A of the motor transfer function. The Mimic program is shown in Figure A-60 and the printout in Figure A-61. A plot showing the error response is shown in Figure A-62, and a phase-plane plot in Figure A-63. This case is included here for the sake of comparison with the remaining cases.

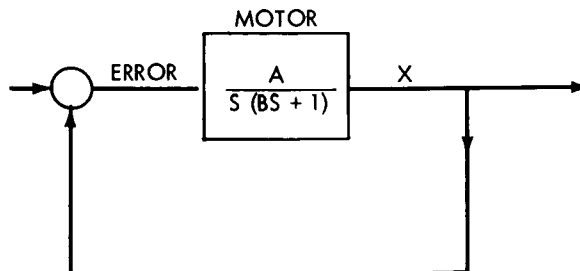


Figure A-59-Block diagram of system.

MIMIC SOURCE-LANGUAGE PROGRAM

KEN DCLAN
LINEAR SYSTEM

```
CON(DT,A,B)
PAR(1DX,XC)
2DX -1DX/B-X*A/B
1DX INT(2DX,1DXC)
X INT(1DX,XC)
FIN(T,5.)
FOR(TIME,X,XDOT,XDBDOT)
QUIT(T,X,1DX,2DX)
END
```

SORT DIAGNOSTICS FCLLCW

Figure A-60-Mimic program.

1DXC	XC	2DX	1DX	X	XDOT	XDBDOT
0.	2.00000E-00					
TIME	X			XDOT	XDBDOT	
C.	2.00000E-00	C.				
1.00000E-01	1.96266E-00	-7.20256E-01		-8.00000E-00		
2.00000E-01	1.86117E-00	-1.28393E-00		-6.41013E-00		
3.00000E-01	1.71083E-00	-1.69903E-00		-4.87684E-00		
4.00000E-01	1.52593E-00	-1.97749E-00		-3.44527E-00		
5.00000E-01	1.31940E-00	-2.13403E-00		-2.14872E-00		
6.00000E-01	1.10264E-00	-2.18508E-00		-1.00954E-00		
7.00000E-01	8.85325E-01	-2.14792E-00		-4.03903E-02		
8.00000E-01	6.75415E-01	-2.03989E-00		7.54545E-01		
9.00000E-01	4.79150E-01	-1.87773E-00		1.37812E-00		
1.00000E-00	3.01149E-01	-1.67712E-00		1.83886E-00		
1.10000E-00	1.44532E-01	-1.45227E-00		2.14964E-00		
1.20000E-00	1.10830E-02	-1.21571E-00		2.32641E-00		
1.30000E-00	-9.85764E-02	-9.78096E-01		2.38708E-00		
1.40000E-00	-1.84796E-01	-7.48216E-01		2.35050E-00		
1.50000E-00	-2.48709E-01	-5.32970E-01		2.23562E-00		
1.60000E-00	-2.92051E-01	-3.37484E-01		2.06078E-00		
1.70000E-00	-3.16983E-01	-1.65239E-01		1.84317E-00		
1.80000E-00	-3.25942E-01	-1.82465E-02		1.59841E-00		
1.90000E-00	-3.21499E-01	1.62760E-01		1.34026E-00		
2.00000E-00	-3.06245E-01	1.98119E-01		1.08048E-00		
2.10000E-00	-2.82691E-01	2.69034E-01		8.28743E-01		
2.20000E-00	-2.53192E-01	3.17373E-01		5.92696E-01		
2.30000E-00	-2.19891E-01	3.45482E-01		3.78021E-01		
2.40000E-00	-1.84681E-01	3.56012E-01		1.88601E-01		
2.50000E-00	-1.49181E-01	3.51769E-01		2.67018E-02		
2.60000E-00	-1.14725E-01	3.35585E-01		-1.06815E-01		
2.70000E-00	-8.23702E-02	3.10209E-01		-2.12269E-01		
2.80000E-00	-5.29036E-02	2.78224E-01		-2.90938E-01		
2.90000E-00	-2.68669E-02	2.41984E-01		-3.44834E-01		
3.00000E-00	-4.57902E-03	2.03569E-01		-3.76500E-01		
3.10000E-00	1.38342E-02	1.64762E-01		-3.88822E-01		
3.20000E-00	2.84098E-02	1.27036E-01		-3.84861E-01		
3.30000E-00	3.93168E-02	9.15589E-02		-3.67712E-01		
3.40000E-00	4.68260E-02	5.92040E-02		-3.40385E-01		
3.50000E-00	5.12820E-02	3.05749E-02		-3.05712E-01		
3.60000E-00	5.30773E-02	6.03054E-03		-2.66278E-01		
3.70000E-00	5.26294E-02	-1.42826E-02		-2.24379E-01		
3.80000E-00	5.03609E-02	-3.63974E-02		-1.81952E-01		
3.90000E-00	4.66840E-02	-4.24928E-02		-1.40649E-01		
4.00000E-00	4.19867E-02	-5.08603E-02		-1.01750E-01		
4.10000E-00	3.66238E-02	-5.58733E-02		-6.62262E-02		
4.20000E-00	3.09597E-02	-5.79586E-02		-3.47486E-02		
4.30000E-00	2.51145E-02	-5.75718E-02		-7.72140E-03		
4.40000E-00	1.94623E-02	-5.51748E-02		1.46856E-02		
4.50000E-00	1.41315E-02	-5.12186E-02		3.25003E-02		
4.60000E-00	9.25632E-03	-4.61289E-02		4.59114E-02		
4.70000E-00	4.93043E-03	-4.02950E-02		5.52325E-02		
4.80000E-00	1.21154E-03	-3.40626E-02		6.08683E-02		
4.90000E-00	-1.87879E-03	-2.77292E-02		6.32831E-02		
5.00000E-00	-4.34023E-03	-2.15419E-02		6.29736E-02		
				6.04447E-02		

Figure A-61-Printout of Mimic program.

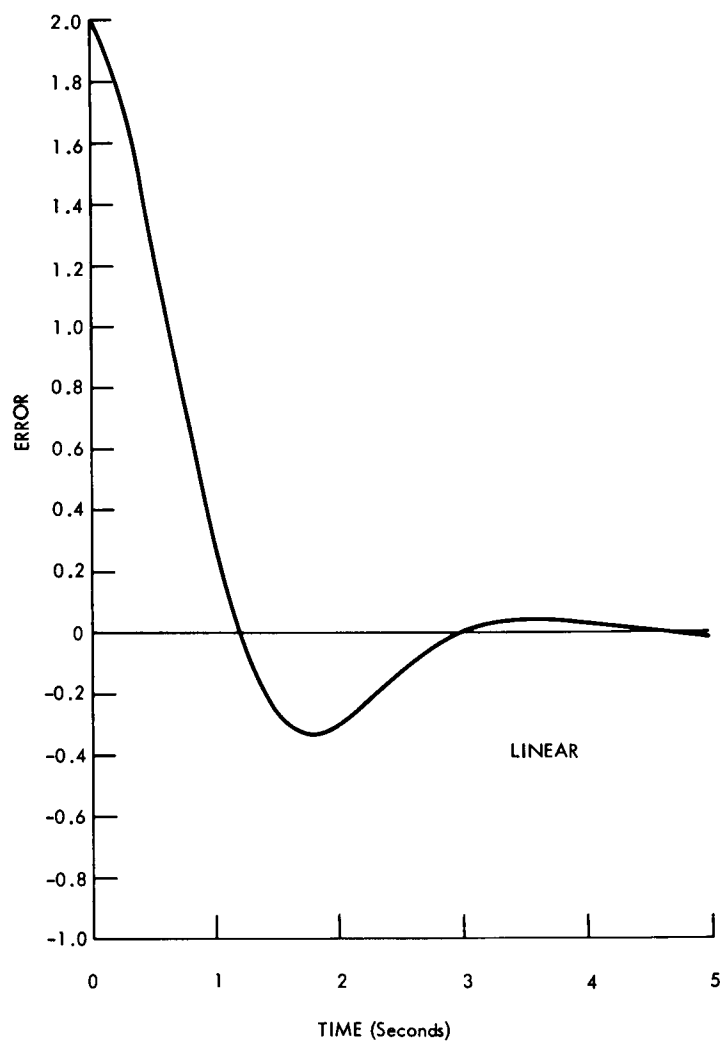


Figure A-62—Plot of error response.

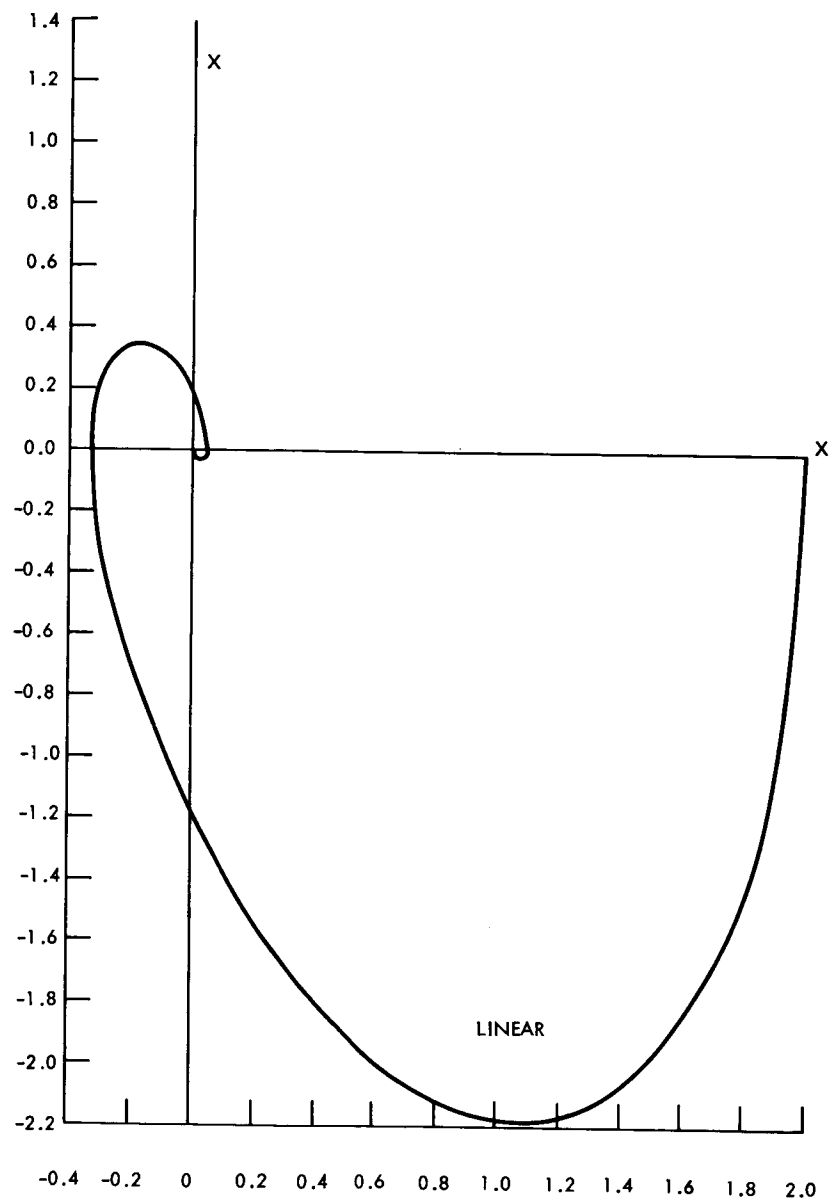


Figure A-63—Phase-plane plot.

Simple Relay Servo

In this case an on-off relay is inserted in the control loop as shown in the block diagram of Figure A-64. The Mimic program is shown in Figure A-65, and the printout in Figure A-66. The error response is plotted in Figure A-67 and the phase-plane plot in Figure A-68. The oscillatory response of simple relay servo is shown in both plots.

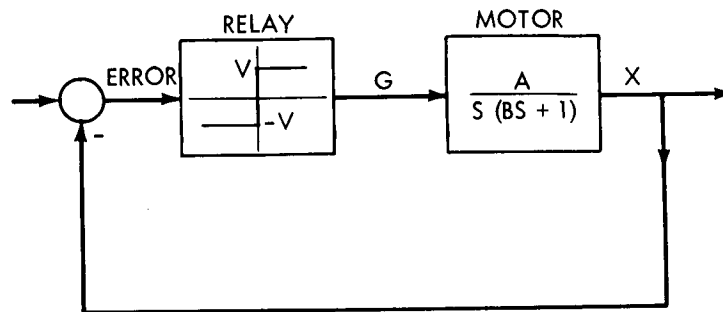


Figure A-64—Block diagram of servo.

MIMIC SOURCE-LANGUAGE PROGRAM

```

KEN DCLAN
SIMPLE RELAY PROBLEM
                                CON(V,DT,A,B,)
                                PAR(1DXC,X0)
E1      G      -V*A/B
E2      G      V*A/B
        2DX    -1DX/B+G
        1DX    INT(2DX,1DXC)
        X      INT(1DX,X0)
E1      FSW(-X,TRUE,FALSE,FALSE)
E2      NOT(E1)
        FIN(T,5.)
        HCR(TIME,X,XDOT,XDBDOT)
        OUT(T,X,1DX,2DX)
        END

```

SORT DIAGNOSTICS FOLLOW

Figure A-65 Mimic program.

10XC C.	X0 2.00000E 00		
TIME	X	XDOT	XDEDOT
C.	2.00000E 00	C.	-4.00000E 00
1.00000E-01	1.98127E 00	-3.62539E-01	-3.27492E 00
2.00000E-01	1.92968E 00	-6.59360E-01	-2.68128E 00
3.00000E-01	1.85119E 00	-9.02377E-01	-2.19525E 00
4.00000E-01	1.75067E 00	-1.10134E 00	-1.79732E 00
5.00000E-01	1.63212E 00	-1.26424E 00	-1.47152E 00
6.00000E-01	1.49881E 00	-1.39761E 00	-1.20478E 00
7.00000E-01	1.35340E 00	-1.50681E 00	-9.86388E-01
8.00000E-01	1.19810E 00	-1.59621E 00	-8.07586E-01
9.00000E-01	1.03470E 00	-1.66940E 00	-6.61196E-01
1.00000E 00	8.64665E-01	-1.72933E 00	-5.41341E-01
1.10000E 00	6.89197E-01	-1.77839E 00	-4.43213E-01
1.20000E 00	5.09282E-01	-1.81856E 00	-3.62872E-01
1.30000E 00	3.25726E-01	-1.85145E 00	-2.97094E-01
1.40000E 00	1.39190E-01	-1.87838E 00	-2.43240E-01
1.50000E 00	-4.70776E-02	-1.69581E 00	7.39162E 00
1.60000E 00	-1.82046E-01	-1.02587E 00	6.05175E 00
1.70000E 00	-2.56295E-01	-4.77376E-01	4.95475E 00
1.80000E 00	-2.80831E-01	-2.83036E-02	4.05661E 00
1.90000E 00	-2.64665E-01	3.39365E-01	3.32127E 00
2.00000E 00	-2.15176E-01	6.40387E-01	2.71923E 00
2.10000E 00	-1.38404E-01	8.86843E-01	2.22631E 00
2.20000E 00	-3.92950E-02	1.08862E 00	1.82275E 00
2.30000E 00	6.19480E-02	7.66729E-01	-5.53346E 00
2.40000E 00	1.12709E-01	2.65206E-01	-4.53041E 00
2.50000E 00	1.18016E-01	-1.45406E-01	-3.70919E 00
2.60000E 00	8.61060E-02	-4.81587E-01	-3.03683E 00
2.70000E 00	2.37268E-02	-7.56828E-01	-2.48634E 00
2.80000E 00	-4.48290E-02	-4.58901E-01	4.91780E 00
2.90000E 00	-6.76905E-02	-1.31779E-02	4.02636E 00
3.00000E 00	-5.51542E-02	3.51749E-01	3.29650E 00
3.10000E 00	4.55351E-04	6.45001E-01	-5.29000E 00
3.20000E 00	4.01840E-02	1.65543E-01	-4.33109E 00
3.30000E 00	3.64572E-02	-2.27003E-01	-3.54599E 00
3.40000E 00	-2.73764E-03	-5.06547E-01	5.01309E 00
3.50000E 00	-2.99176E-02	-5.21875E-02	4.10437E 00
3.60000E 00	-1.59169E-02	3.19811E-01	3.36038E 00
3.70000E 00	1.84649E-02	1.80076E-01	-4.36015E 00
3.80000E 00	1.60552E-02	-2.15105E-01	-3.56979E 00
3.90000E 00	-1.34343E-02	-1.76317E-01	4.35263E 00
4.00000E 00	-1.06835E-02	2.18182E-01	3.56364E 00
4.10000E 00	1.29124E-02	7.24309E-02	-4.14486E 00
4.20000E 00	7.46435E-04	-3.03237E-01	-3.39353E 00
4.30000E 00	-9.75194E-03	9.82883E-02	3.80342E 00
4.40000E 00	8.51993E-03	6.82604E-02	-4.13652E 00
4.50000E 00	-3.21916E-03	-1.94238E-01	4.38848E 00
4.60000E 00	-2.09312E-03	2.03510E-01	3.59298E 00
4.70000E 00	4.20394E-03	-1.33181E-01	-3.73364E 00
4.80000E 00	-4.48231E-03	9.41566E-02	3.81169E 00
4.90000E 00	4.00231E-03	0.37842E-02	-3.83243E 00
5.00000E 00	-3.04367E-03	9.88516E-02	3.80230E 00

Figure A-66-Printout of the program.

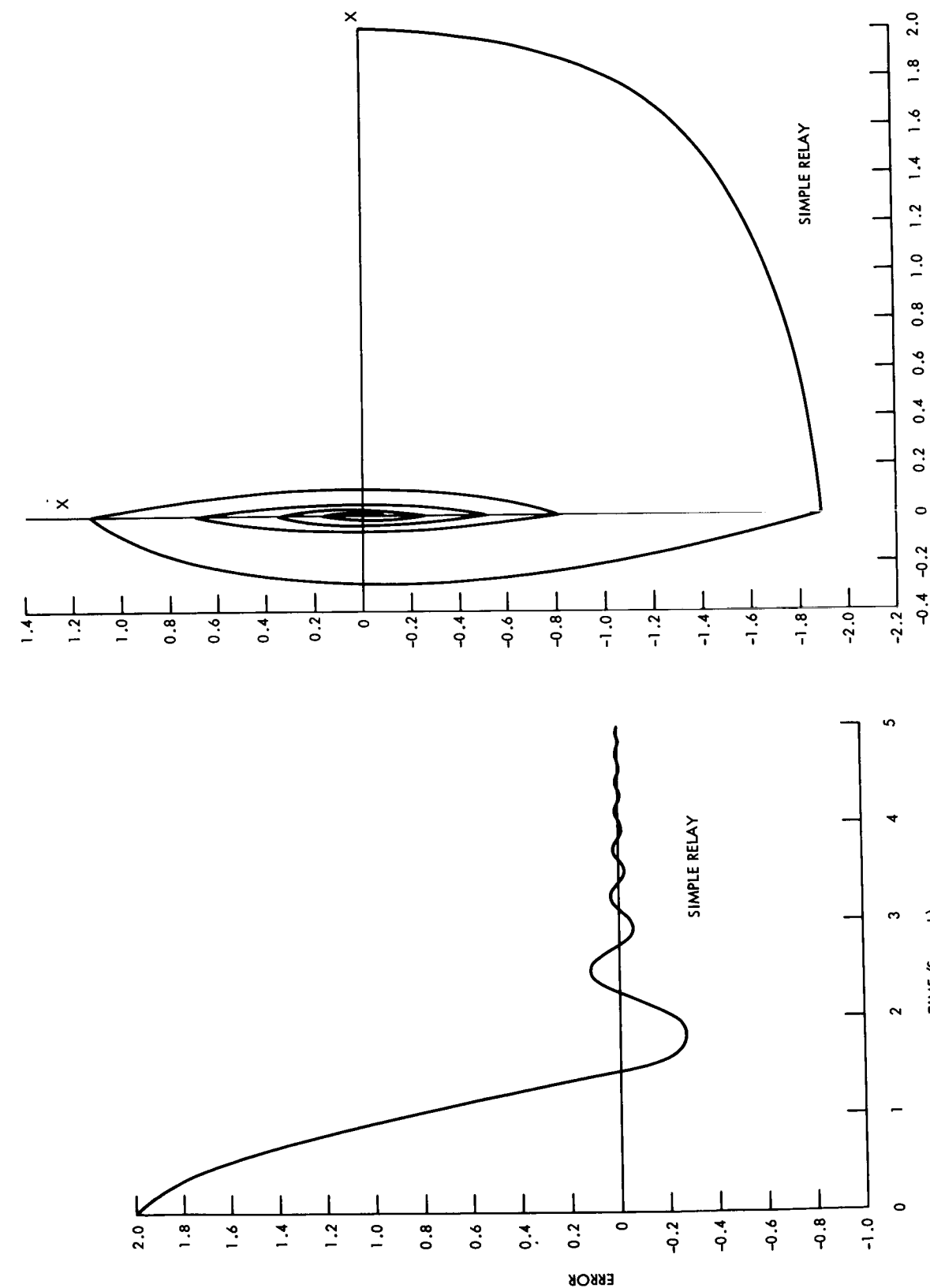


Figure A-68—Phase-plane plot.

Figure A-67—Graph of error response.

Simple Relay Servo with a Dead Space

In this case the on-off relay has a dead space when the input signal to the relay is small as shown in the block diagram of Figure A-69. The Mimic program is shown in Figure A-70 and the printout in Figure A-71, and the transient response plot and the phase-plane plot are shown in Figures A-72 and A-73 respectively.

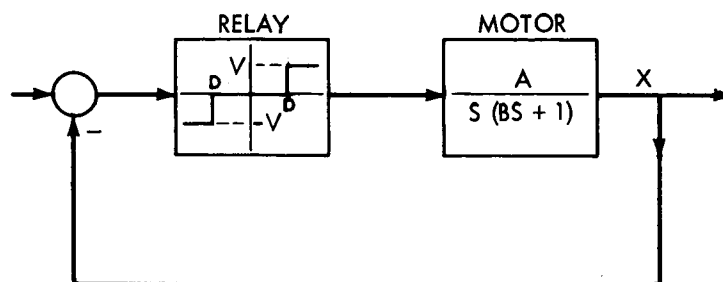


Figure A-69—Block diagram of servo.

MIMIC SOURCE-LANGUAGE PROGRAM

```
KEN COLAN
RELAY WITH DEAD SPOT
      CON(V,DT,A,B,D)
      PAR(1DXC,XC)
E1      G      V*A/B
E2      G      0.
E3      G      -V*A/B
      2DX      -1DX/B-G
      1DX      INT(2DX,1DX0)
      X        INT(1DX,X0)
E1      FSW(X-D,FALSE,FALSE,TRUE)
E3      FSW(X+D,TRUE,FALSE,FALSE)
      H        IOR(E1,E3)
      E2       NOT(H)
      FIN(T,5.)
      HDR(TIME,X,XDOT,XDBCOT)
      OUT(T,X,1DX,2DX)
      END
```

SORT DIAGNOSTICS FOLLOW

Figure A-70—Mimic program.

1DX0 0.	X0 2.00000E 00		
TIME	X	XDGT	XDBDGT
0.	2.00000E 00	0.	-4.00000E 00
1.00000E-01	1.98127E 00	-3.62539E-01	-3.27492E 00
2.00000E-01	1.92968E 00	-6.59360E-01	-2.68128E 00
3.00000E-01	1.85119E 00	-9.02377E-01	-2.19525E 00
4.00000E-01	1.75067E 00	-1.10134E 00	-1.79732E 00
5.00000E-01	1.63212E 00	-1.26424E 00	-1.47152E 00
6.00000E-01	1.49881E 00	-1.39761E 00	-1.20478E 00
7.00000E-01	1.35340E 00	-1.50681E 00	-9.86388E-01
8.00000E-01	1.19810E 00	-1.59621E 00	-8.07586E-01
9.00000E-01	1.03470E 00	-1.66940E 00	-6.61196E-01
1.00000E 00	8.64665E-01	-1.72933E 00	-5.41341E-01
1.10000E 00	6.89197E-01	-1.77839E 00	-4.43213E-01
1.20000E 00	5.09282E-01	-1.81856E 00	-3.62872E-01
1.30000E 00	3.25726E-01	-1.85145E 00	-2.97094E-01
1.40000E 00	1.41251E-01	-1.75269E 00	3.50539E 00
1.50000E 00	-1.76034E-02	-1.43498E 00	2.86997E 00
1.60000E 00	-1.47663E-01	-1.17487E 00	2.34973E 00
1.70000E 00	-2.48654E-01	-7.59541E-01	5.51908E 00
1.80000E 00	-2.98764E-01	-2.59321E-01	4.51864E 00
1.90000E 00	-3.03536E-01	1.50224E-01	3.69955E 00
2.00000E 00	-2.71190E-01	4.85532E-01	3.02894E 00
2.10000E 00	-2.08454E-01	7.60058E-01	2.47988E 00
2.20000E 00	-1.35808E-01	6.58396E-01	-1.31679E 00
2.30000E 00	-7.61344E-02	5.39049E-01	-1.07810E 00
2.40000E 00	-2.72779E-02	4.41336E-01	-8.82672E-01
2.50000E 00	1.27224E-02	3.61335E-01	-7.22670E-01
2.60000E 00	4.54719E-02	2.95836E-01	-5.91672E-01
2.70000E 00	7.22849E-02	2.42210E-01	-4.84420E-01
2.80000E 00	9.42375E-02	1.98305E-01	-3.96610E-01
2.90000E 00	1.12211E-01	1.62358E-01	-3.24717E-01
3.00000E 00	1.26926E-01	1.32928E-01	-2.65856E-01
3.10000E 00	1.38974E-01	1.08832E-01	-2.17664E-01
3.20000E 00	1.48638E-01	8.91041E-02	-1.78208E-01
3.30000E 00	1.56914E-01	7.29523E-02	-1.45905E-01
3.40000E 00	1.63526E-01	5.97283E-02	-1.19457E-01
3.50000E 00	1.68939E-01	4.89014E-02	-9.78028E-02
3.60000E 00	1.73371E-01	4.00371E-02	-8.00741E-02
3.70000E 00	1.77000E-01	3.27796E-02	-6.55592E-02
3.80000E 00	1.79971E-01	2.68377E-02	-5.36753E-02
3.90000E 00	1.82404E-01	2.19728E-02	-4.39456E-02
4.00000E 00	1.84395E-01	1.79898E-02	-3.59796E-02
4.10000E 00	1.86026E-01	1.47288E-02	-2.94576E-02
4.20000E 00	1.87367E-01	1.20589E-02	-2.41179E-02
4.30000E 00	1.88453E-01	9.87302E-03	-1.97460E-02
4.40000E 00	1.89348E-01	8.08334E-03	-1.61667E-02
4.50000E 00	1.90081E-01	6.61808E-03	-1.32362E-02
4.60000E 00	1.90681E-01	5.41843E-03	-1.08369E-02
4.70000E 00	1.91172E-01	4.43623E-03	-8.87246E-03
4.80000E 00	1.91574E-01	3.63208E-03	-7.26416E-03
4.90000E 00	1.91903E-01	2.97369E-03	-5.94739E-03
5.00000E 00	1.92173E-01	2.43465E-03	-4.86931E-03

Figure A-71-Printout.

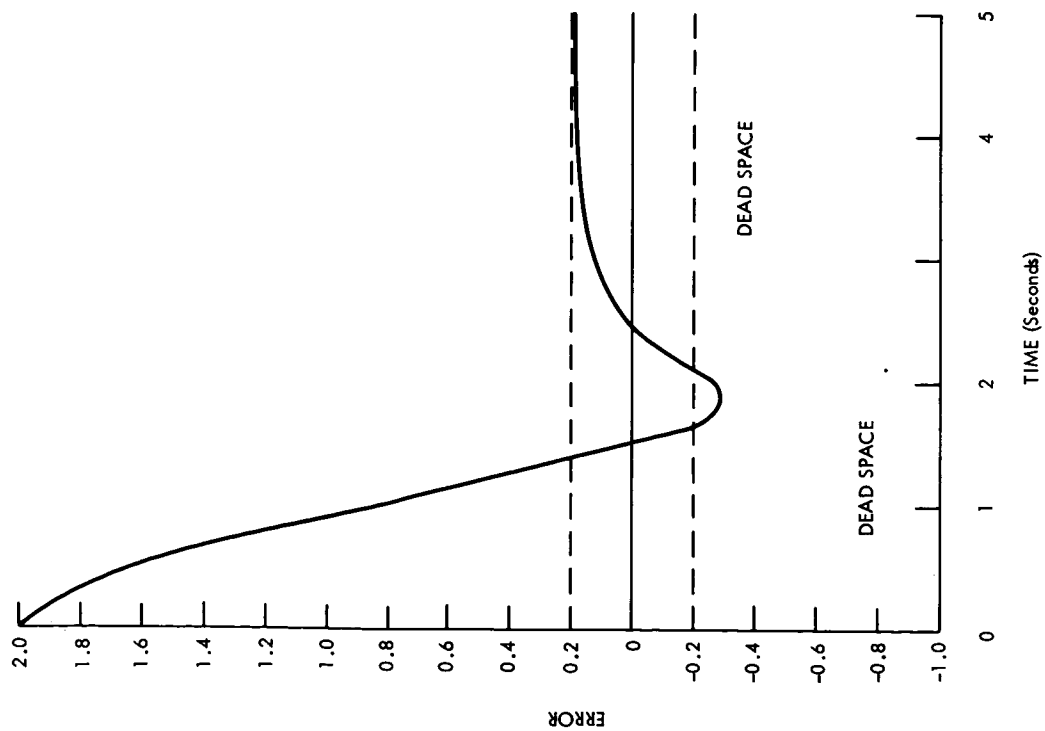


Figure A-72—Graph of transient response.

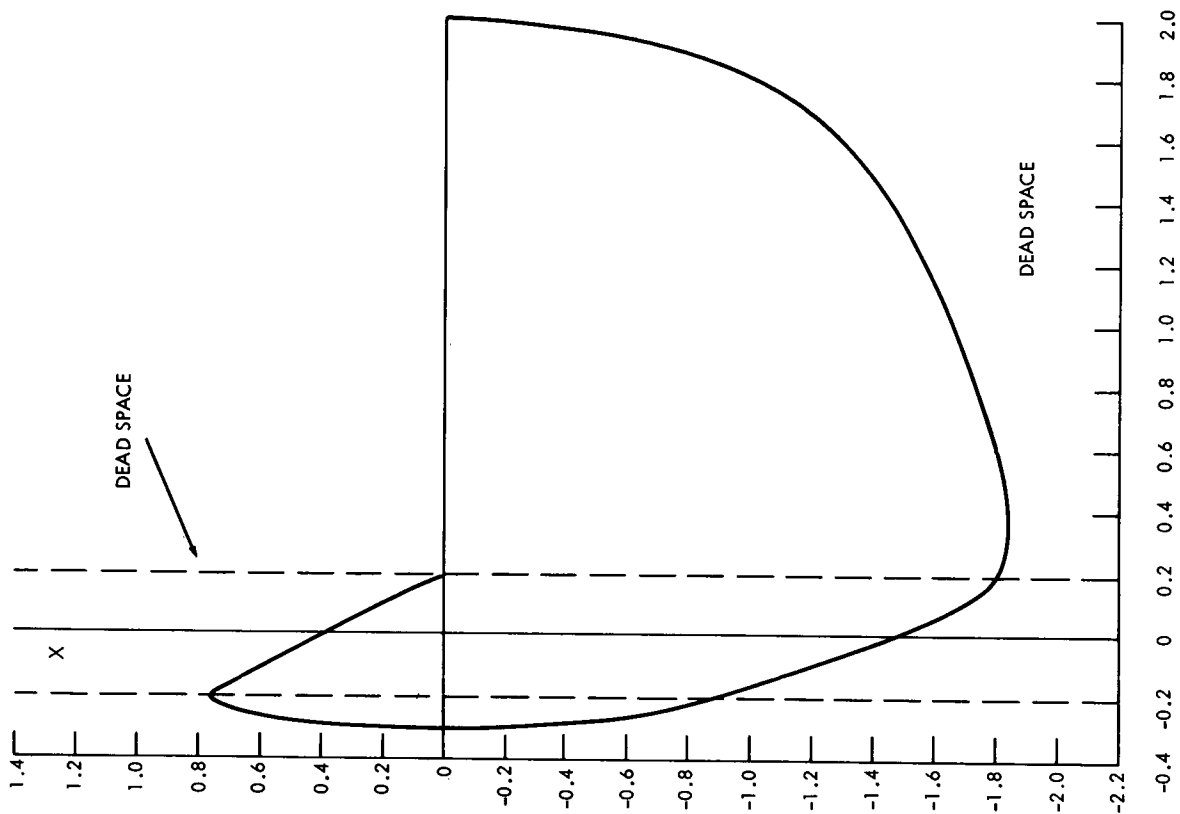


Figure A-73—Phase-plane plot.

Relay Servo with Hysteresis

In this servo, the relay has a rectangular hysteresis loop as shown in the block diagram of Figure A-74. The Mimic program is shown in Figure A-75 and the printout in Figure A-76. The plots are shown in Figures A-77 and A-78.

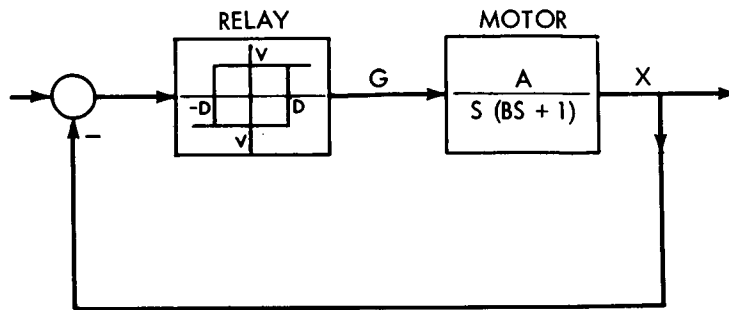


Figure A-74—Block diagram of relay servo.

MIMIC SOURCE-LANGUAGE PROGRAM

WFR
FYS RELAY

```
CON(V,DT,A,B,D)
PAR(1DX,XG)
E1 FSW(X+D,TRUE,FALSE,FALSE)
E2 FSW(X-D,FALSE,FALSE,TRUE)
C IOR(E1,E2)
H FLF(E2,C,FALSE)
G LSW(H,V*A/B,-V*A/B)
2DX -1DX/B-G
1DX INT(2DX,1DXQ)
X INT(1DX,XQ)
FIN(T,5.)
HDR(TIME,X,XDOT,XDBDOT)
OUT(T,X,1DX,2DX)
END
```

SORT DIAGNOSTICS FOLLOW

Figure A-75—Mimic program.

1DXG C.	XQ 2.00000E 00	X 2.00000E 00	XDOT C.	XDEDOCT 4.00000E 00
UNDRELOW AT 27167 IN MC				
UNDRELOW AT 27249 IN MC				
UNDRELOW AT 27263 IN MC				
UNDRELOW AT 27167 IN MC				
UNDRELOW AT 27212 IN MC				
1.00000E-01	1.98127E 00	-3.62538E-01	-3.27492E 00	
2.00000E-01	1.92968E 00	-6.59360E-01	-2.68128E 00	
3.00000E-01	1.85119E 00	-9.02377E-01	-2.19525E 00	
4.00000E-01	1.75067E 00	-1.10134E 00	-1.79732E 00	
5.00000E-01	1.63212E 00	-1.26424E 00	-1.47152E 00	
6.00000E-01	1.49880E 00	-1.39761E 00	-1.20478E 00	
7.00000E-01	1.35340E 00	-1.50681E 00	-9.86388E-01	
8.00000E-01	1.19810E 00	-1.59621E 00	-8.07586E-01	
9.00000E-01	1.03470E 00	-1.66940E 00	-6.61196E-01	
1.00000E 00	8.64664E-01	-1.72933E 00	-5.41341E-01	
1.10000E 00	6.89196E-01	-1.77839E 00	-4.43213E-01	
1.20000E 00	5.09281E-01	-1.81856E 00	-3.62872E-01	
1.30000E 00	3.25726E-01	-1.85145E 00	-2.97095E-01	
1.40000E 00	1.39189E-01	-1.87838E 00	-2.43240E-01	
1.50000E 00	-4.97878E-02	-1.90043E 00	-1.99149E-01	
1.60000E 00	-2.03312E-01	-1.19350E 00	6.38700E 00	
1.70000E 00	-2.92754E-01	-6.14615E-01	5.22923E 00	
1.80000E 00	-3.29729E-01	-1.40666E-01	4.28133E 00	
1.90000E 00	-3.23747E-01	2.47371E-01	3.50526E 00	
2.00000E 00	-2.82596E-01	5.65069E-01	2.86986E 00	
2.10000E 00	-2.12650E-01	8.25178E-01	2.34964E 00	
2.20000E 00	-1.19130E-01	1.03814E 00	1.92373E 00	
2.30000E 00	-6.30796E-03	1.21249E 00	1.57501E 00	
2.40000E 00	1.22317E-01	1.35524E 00	1.28951E 00	
2.50000E 00	2.26429E-01	7.47141E-01	-5.49428E 00	
2.60000E 00	2.75415E-01	2.49169E-01	-4.49834E 00	
2.70000E 00	2.79267E-01	-1.58536E-01	-3.68293E 00	
2.80000E 00	2.46168E-01	-4.92337E-01	-3.01533E 00	
2.90000E 00	1.82814E-01	-7.65630E-01	-2.46874E 00	
3.00000E 00	9.46910E-02	-9.89383E-01	-2.02123E 00	
3.10000E 00	-1.37122E-02	-1.17258E 00	-1.65485E 00	
3.20000E 00	-1.38719E-01	-1.32256E 00	-1.35487E 00	
3.30000E 00	-2.39869E-01	-7.20384E-01	5.44077E 00	
3.40000E 00	-2.86430E-01	-2.27262E-01	4.45452E 00	
3.50000E 00	-2.88297E-01	1.76472E-01	3.64706E 00	
3.60000E 00	-2.53572E-01	5.07021E-01	2.98596E 00	
3.70000E 00	-1.88888E-01	7.77653E-01	2.44469E 00	
3.80000E 00	-9.96747E-02	9.99227E-01	2.00155E 00	
3.90000E 00	9.62058E-03	1.18064E 00	1.63873E 00	
4.00000E 00	1.35358E-01	1.32916E 00	1.34168E 00	
4.10000E 00	2.37106E-01	7.25786E-01	-5.45157E 00	
4.20000E 00	2.84157E-01	2.31685E-01	-4.46337E 00	
4.30000E 00	2.86425E-01	-1.72851E-01	-3.65430E 00	
4.40000E 00	2.52028E-01	-5.04057E-01	-2.99189E 00	

Figure A-76-Printout.

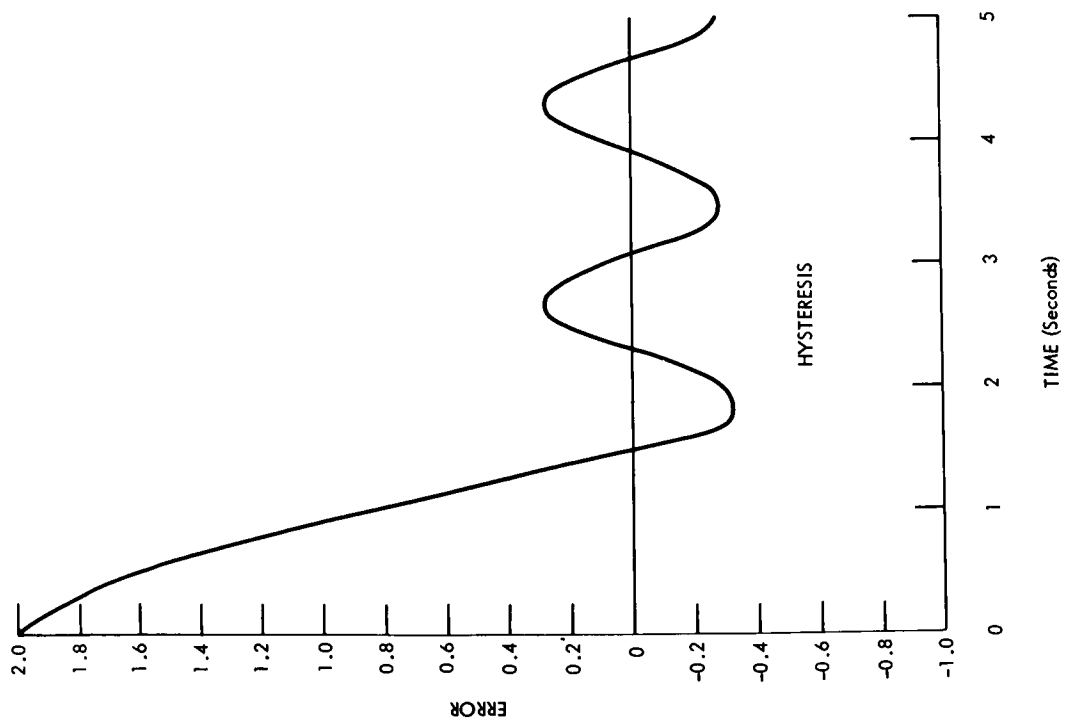


Figure A-77-Plot #1.

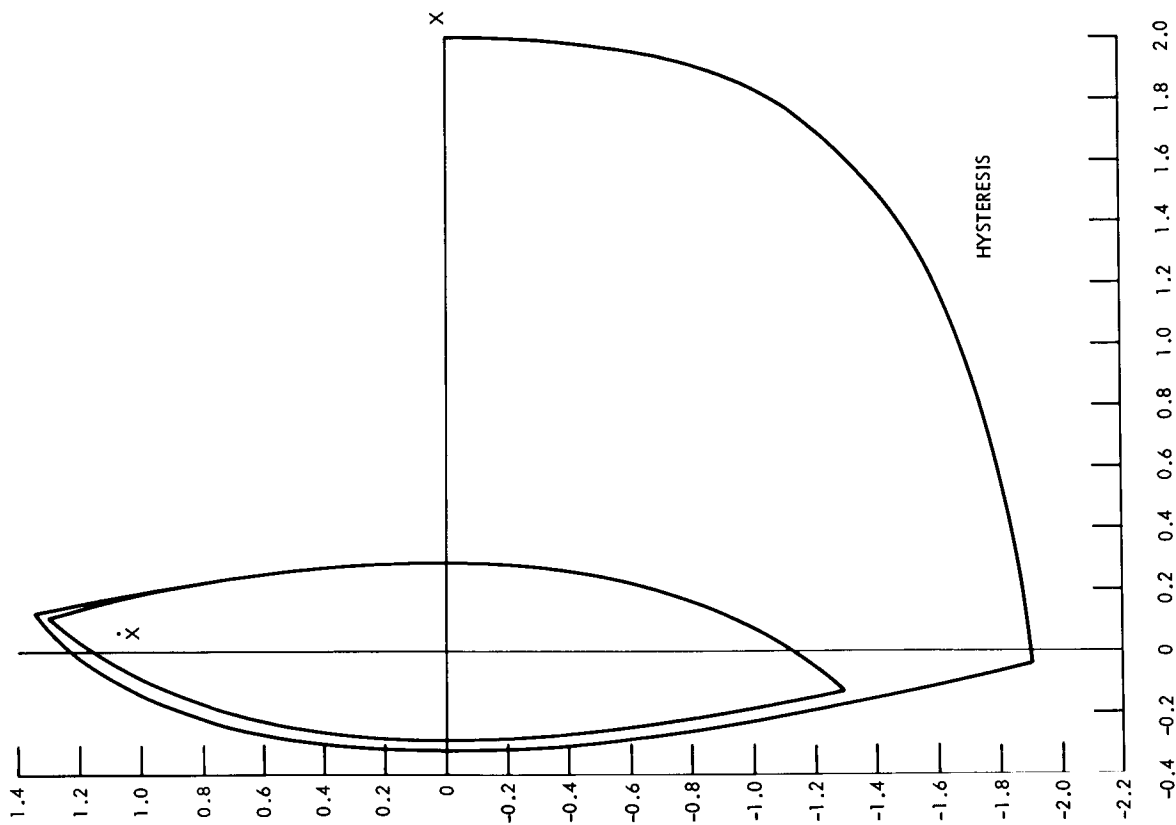


Figure A-78-Plot #2.

Relay Servo with Dead Space and Hysteresis

In this case, the relay has both a rectangular hysteresis loop and a dead space as shown in the block diagram of Figure A-79. The Mimic program is shown in Figure A-80, and the printout in Figure A-81. The plots are shown in Figures A-82 and A-83.

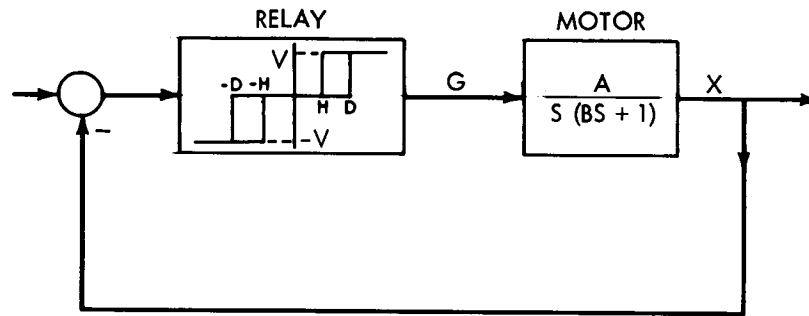


Figure A-79—Block diagram of relay servo.

MIMIC SOURCE-LANGUAGE PROGRAM

```

KEN COLAN
RELAY WITH DEADSPOT AND HYSTERESIS
CON(V,DT,A,B,D,H)
PAR(1DX,X0)
2DX      -1DX/B-G
1DX      INT(2DX,1DX0)
X        INT(1DX,X0)
S1       FSW(X-D,FALSE,FALSE,TRUE)
R1       FSW(X-H,TRUE,FALSE,FALSE)
L1       FLF(S1,R1,TRUE)
S2       FSW(X+D,TRUE,FALSE,FALSE)
R2       FSW(X+H,FALSE,FALSE,TRUE)
L2       FLF(S2,R2,TRUE)
E3       G      0.
E2       G      -V*A/B
E1       G      V*A/B
E2       LSW(L2,TRUE,FALSE)
E1       LSW(L1,TRUE,FALSE)
E3       NOT(E1,E2)
          FIN(T,5.)
          HDR(TIME,X,XDOT,XBDDOT)
          OUT(T,X,1DX,2DX)
          END

```

SORT DIAGNOSTICS FOLLOW

Figure A-80—Mimic program.

1DX0	X0		
0.	2.00000E 00		
TIME	X	XDCT	XDRDCT
0.	2.00000E 00	0.	-4.00000E 00
1.00000E-01	1.98127E 00	-3.62539E-01	-3.27492E 00
2.00000E-01	1.92968E 00	-6.59360E-01	-2.68128E 00
3.00000E-01	1.85119E 00	-9.02377E-01	-2.19525E 00
4.00000E-01	1.75067E 00	-1.10134E 00	-1.79732E 00
5.00000E-01	1.63212E 00	-1.26424E 00	-1.47152E 00
6.00000E-01	1.49261E 00	-1.39761E 00	-1.20478E 00
7.00000E-01	1.35340E 00	-1.50681E 00	-9.86388E-01
8.00000E-01	1.19810E 00	-1.59621E 00	-8.07586E-01
9.00000E-01	1.03470E 00	-1.66940E 00	-6.61196E-01
1.00000E 00	8.64665E-01	-1.72933E 00	-5.41341E-01
1.10000E 00	6.89197E-01	-1.77839E 00	-4.43213E-01
1.20000E 00	5.09282E-01	-1.81856E 00	-3.62872E-01
1.30000E 00	3.25726E-01	-1.85145E 00	-2.97094E-01
1.40000E 00	1.39190E-01	-1.87838E 00	-2.43240E-01
1.50000E 00	-3.10674E-02	-1.53799E 00	3.07597E 00
1.60000E 00	-1.70462E-01	-1.25920E 00	2.51839E 00
1.70000E 00	-2.65869E-01	-6.68504E-01	5.33701E 00
1.80000E 00	-3.07728E-01	-1.84786E-01	4.36957E 00
1.90000E 00	-3.05745E-01	2.11248E-01	3.57750E 00
2.00000E 00	-2.67868E-01	5.35494E-01	2.92901E 00
2.10000E 00	-2.00661E-01	8.00964E-01	2.39807E 00
2.20000E 00	-1.09278E-01	1.01831E 00	1.96338E 00
2.30000E 00	-1.69722E-02	8.33823E-01	-1.66765E 00
2.40000E 00	5.86010E-02	6.82676E-01	-1.36535E 00
2.50000E 00	1.20475E-01	5.58928E-01	-1.11786E 00
2.60000E 00	1.71133E-01	4.57612E-01	-9.15223E-01
2.70000E 00	1.93889E-01	1.22218E-02	-4.02444E 00
2.80000E 00	1.76266E-01	-3.52532E-01	-3.29494E 00
2.90000E 00	1.25584E-01	-6.51167E-01	-2.69767E 00
3.00000E 00	6.65544E-02	-5.33230E-01	1.06646E 00
3.10000E 00	1.82253E-02	-4.36572E-01	8.73144E-01
3.20000E 00	-2.13433E-02	-3.57435E-01	7.14870E-01
3.30000E 00	-5.37392E-02	-2.92643E-01	5.85286E-01
3.40000E 00	-8.02628E-02	-2.39596E-01	4.79191E-01
3.50000E 00	-1.01978E-01	-1.96164E-01	3.92329E-01
3.60000E 00	-1.19758E-01	-1.60606E-01	3.21212E-01
3.70000E 00	-1.34314E-01	-1.31493E-01	2.62986E-01
3.80000E 00	-1.46232E-01	-1.07657E-01	2.15315E-01
3.90000E 00	-1.55990E-01	-8.81423E-02	1.76285E-01
4.00000E 00	-1.63978E-01	-7.21648E-02	1.44330E-01
4.10000E 00	-1.70519E-01	-5.90836E-02	1.18167E-01
4.20000E 00	-1.75874E-01	-4.83735E-02	9.67471E-02
4.30000E 00	-1.80258E-01	-3.96049E-02	7.92098E-02
4.40000E 00	-1.83848E-01	-3.24257E-02	6.48515E-02
4.50000E 00	-1.86787E-01	-2.65480E-02	5.30959E-02
4.60000E 00	-1.89193E-01	-2.17356E-02	4.34712E-02
4.70000E 00	-1.91163E-01	-1.77956E-02	3.55912E-02
4.80000E 00	-1.92776E-01	-1.45698E-02	2.91396E-02
4.90000E 00	-1.94196E-01	-1.19288E-02	2.38575E-02
5.00000E 00	-1.95177E-01	-9.76644E-03	1.95329E-02

Figure A-81-Printout.

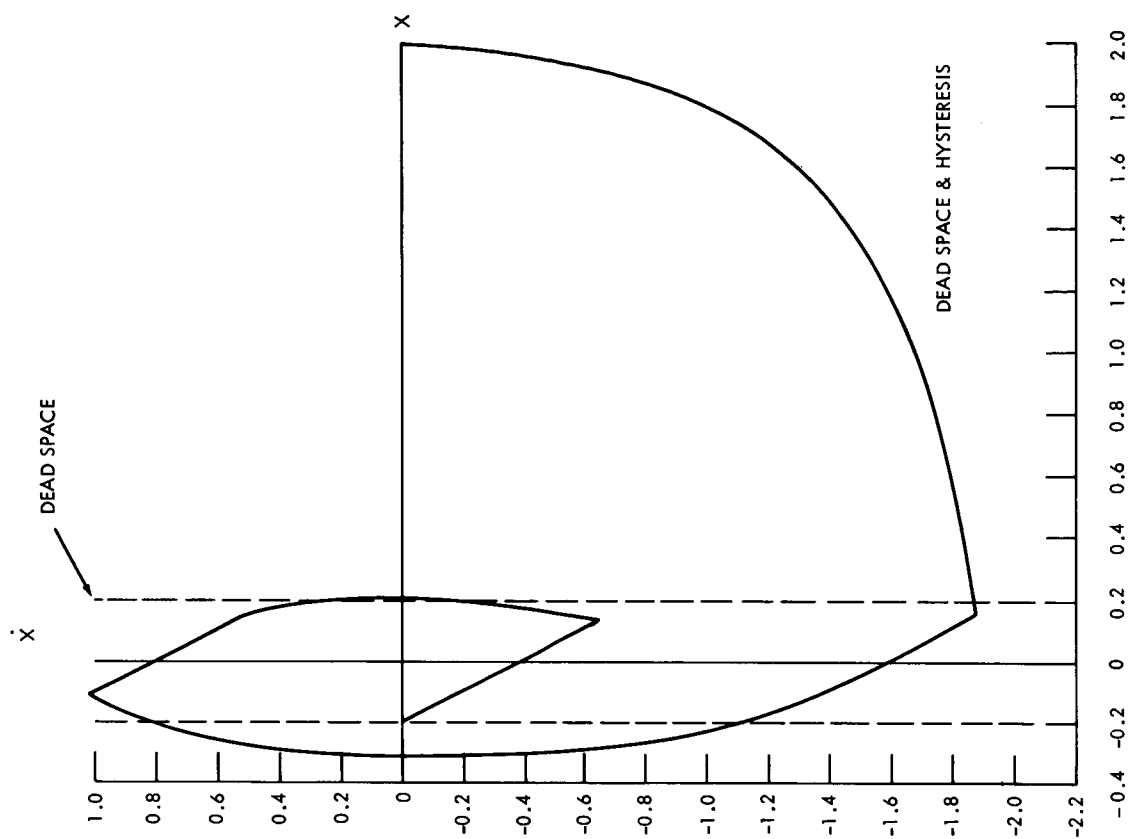


Figure A-83-Plot #2.

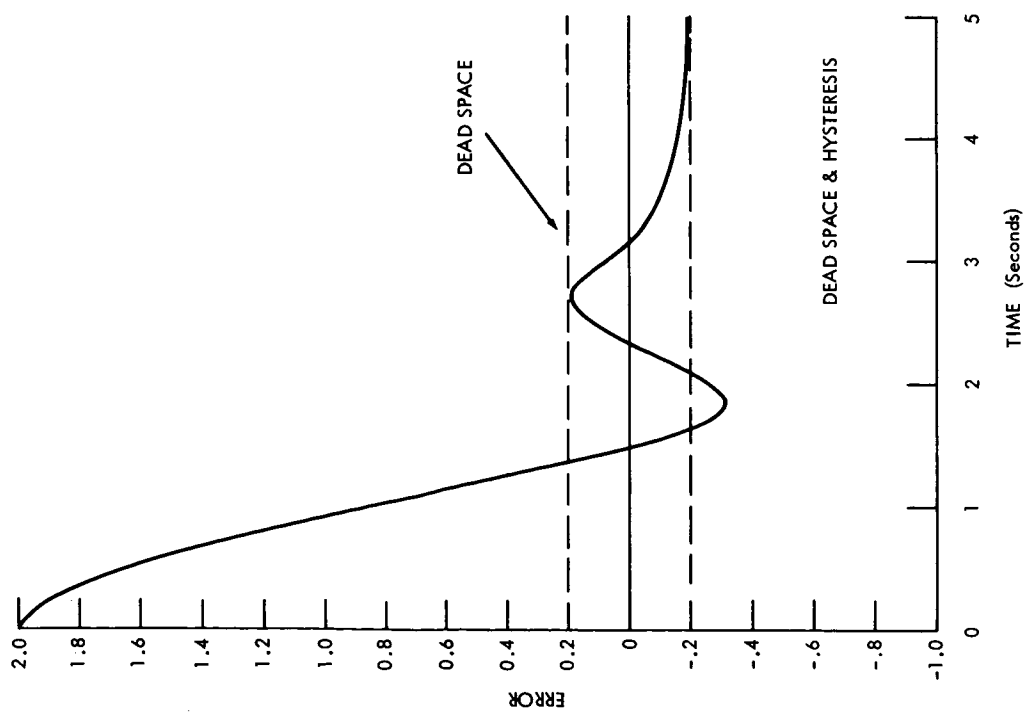


Figure A-82-Plot #1.

SIMULATION OF AEROBEE ATTITUDE CONTROL SYSTEM (EXAMPLE 7)

David J. Shrewsberry

Problem Description

It was desired to provide a simple means for simulating a "bang-bang" sounding rocket Attitude Control System (ACS) in order to study the effects of all types of parameter variations, control innovations, and varied operating conditions. The ACS of this study utilizes two free gyroscopes having two degrees of freedom as reference elements and three orthogonally oriented rate gyroscopes for rate feedback. The system controls the attitude of the rocket only in the coast phase of flight (after the engine has ceased burning). Cold-gas jets (or thrusters) which operate off the residual helium gas remaining in the rocket fuel tanks after combustion has ended provide the means for changing the angular orientation of the rocket. The mode of operation is such that when the combined position plus body rate electrical signal equals the valve controller trip voltage, a valve is energized, which causes the rocket to accelerate at a constant angular acceleration in a direction which would reduce the position error. Control continues throughout free flight in this manner. Pointing of the rocket or its instruments to targets in the sky is achieved by electrically torquing the gimbals of the free gyros, causing the gyro to precess, with the rocket following the gyro. Nominal static trip points at $\pm 1/8^\circ$. For simplicity, a single-axis simulation was performed. All symbols and variable names used below are the same as those used in the MIMIC program.

Network to be Simulated

Figure A-84 shows the signal mixing network which was simulated. VPOS and VRATE are the free gyro and rate gyro output voltages. They are low impedance sources; hence, they can be represented as generators. RP, RR, and RL are actual resistors. The values of the resistors control the mixing ratio of position error signal with respect to rate signal.

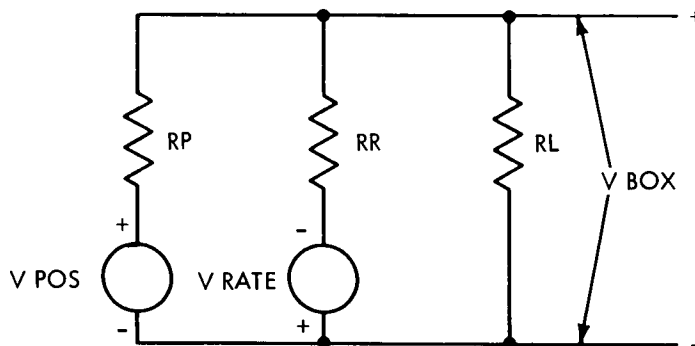


Figure A-84—Diagram of network.

$$V_{BOX} = \frac{V_{POS} \cdot \frac{RR \cdot RL}{RR + RL}}{RP + \frac{RR \cdot RL}{RR + RL}} + \frac{V_{RATE} \cdot \frac{RP \cdot RL}{RP + RL}}{RR + \frac{RP \cdot RL}{RP + RL}} \quad (41)$$

where $VPOS = \text{Free gyro output signal} = 11.9 \text{ volts} \times \sin (\text{THETA})$

and THETA free gyro error in deg.

$\text{VRATE} = \text{Rate gyro output signal} = .130 \text{ volts/degree/second}$

$$= .130 \cdot \text{THEDOT}$$

$\text{THEDOT} = \text{the body rate in deg/sec.}$

$VBOX$, the output of the mixing network controls the state of the valve controller (Figure A-85). When $VBOX$ is larger than $TRIP$, (the controller trip voltage) a valve is energized, producing an angular acceleration. A positive $VBOX$ produces negative acceleration and a negative $VBOX$ produces positive acceleration.

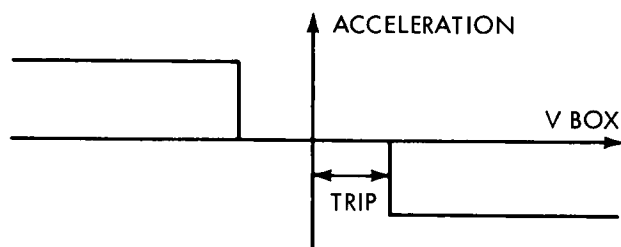


Figure A-85

Figure A-86 shows a simplified block diagram of the MIMIC program. The output of the valve controller is shown as torque in order to facilitate the ready inclusion of moment arm length and rocket moment of inertia as parameters. Acceleration is related to torque as follows,

$$T = I \text{FACT} \quad (42)$$

where $T = \text{applied torque (ft/lb)}$

$I = \text{moment of inertia (slug ft}^2\text{)}$

$\text{FACT} = \text{angular acceleration (rad/sec}^2\text{)}$

$$\text{additionally, } T = F \cdot M \quad (43)$$

where

$F = \text{Applied force (lb)} - (\text{which depends upon gas pressure and type of valve, a constant for this study})$

$M = \text{Moment arm to rocket center of gravity (ft)}$

By combining (41) and (42) we obtain

$$\text{FACT} = \frac{FM}{I} \quad (44)$$

as the expression for angular acceleration in the units of radians/sec² Figure A-86 shows that the angular rate THEDOT was obtained as the first integral of angular acceleration ALPHA and angular position and THETA was obtained as the second integral of ALPHA .

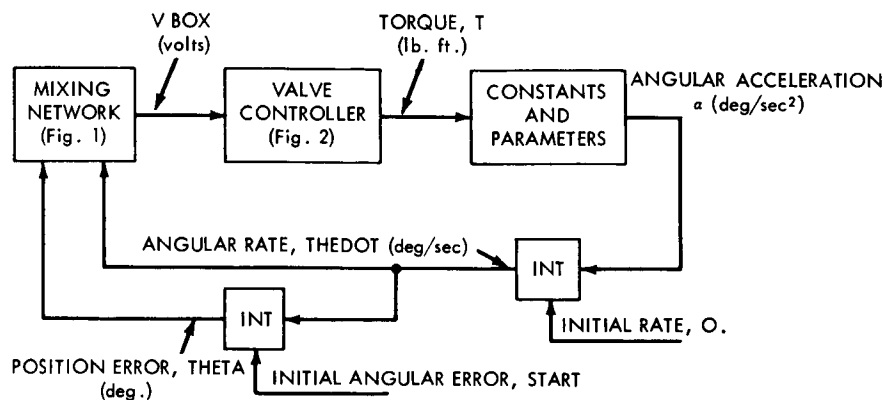


Figure A-86—Mimic program (simplified diagram).

Constants, Parameters, and Initial Conditions

The following constants and parameters were used:

RP = position mixing resistor = 33 kilohms

RR = rate mixing resistor = 33 kilohms

RL = controller input resistance = 25 kilohms

TRIP = valve controller trip voltage = .025 volts ($\approx 1/8^\circ$)

START = Initial angular error = 15°

F = thruster force = 4 lb

I = moment of inertia = 900 slug ft²

M = moment arm to rocket center of gravity = 12.5 ft.

The Mimic Program

The Mimic program is to simulate the equations (41) through (44) together with the above mentioned values of constants, parameters, and initial conditions. The program is shown in Figure A-87 and the result in Figure A-88. Since program symbolic names are the same as those names in the equation, no equivalent symbol table is needed.

```

***MIMIC SOURCE-LANGUAGE PROGRAM***

AEROBEE ATTITUDE CONTROL SYSTEM
  CON(RR,RP,RL,F)
  CON(DT)
  PAR(START,TRIP,I,H)

MIXING NETWORK
  TERM1 = DIV(RR*RL,RR+RL)
  V1    = DIV(VPOS*TERM1,RP+TERM1)
  TERM2 = DIV(RP*RL,RP+RL)
  V2    = DIV(VRATE*TERM2,RR+TERM2)
  VBOX  = ADD(V1,V2)

VALVE CONTROLLER USING LOGICAL FUNCTIONS
  CHECK1 = FSW(VBOX-TRIP,TRUE,TRUE,FALSE)
  VAR1   = 1.
CHECK1  VAR1 = 0.
  CHECK2 = FSW(VBOX+TRIP,FALSE,TRUE,TRUE)
  VAR2   = -1.
CHECK2  VAR2 = 0.
  ALPHA  = (VAR1+VAR2)*(-FACTOR)

FACTOR CONVERTS TORQUE TO ACCELERATION
  FACT = F*I/I

CONVERT FACT(RADIANS PER SECOND) TO DEGREES PER SECOND
  FACTOR = FACT*360.*7./44.
  THEDOT = INT(ALPHA,0.)
  THETA  = INT(THEDOT,START)
  VPOS   = 11.9*SIN(THETA/57.296)
  VRATE  = .130*THEDOT
  HDR(TIME,THETA,RATE,ALPHA)
  OUT(T,THETA,THEDOT,ALPHA)
  FIN(T,10.)
END

***SORT DIAGNOSTICS FOLLOW***

```

Figure A-87-Mimic program.

START	TRIP	I	E
1.50000E 01	2.50000E-02	9.00000E 02	1.25000E 01
TIME	THETA	RATE	ALPHA
0.	1.50000E 01	0.	-3.18182E 00
5.00000E-02	1.49960E 01	-1.59091E-01	-3.18182E 00
1.00000E-01	1.49841E 01	-3.18182E-01	-3.18182E 00
1.50000E-01	1.49642E 01	-4.77273E-01	-3.18182E 00
2.00000E-01	1.49364E 01	-6.36364E-01	-3.18182E 00
2.50000E-01	1.49006E 01	-7.95454E-01	-3.18182E 00
3.00000E-01	1.48568E 01	-9.54545E-01	-3.18182E 00
3.50000E-01	1.48051E 01	-1.11364E 00	-3.18182E 00
4.00000E-01	1.47455E 01	-1.27273E 00	-3.18182E 00
4.50000E-01	1.46778E 01	-1.43182E 00	-3.18182E 00
5.00000E-01	1.46023E 01	-1.59091E 00	-3.18182E 00
5.50000E-01	1.45187E 01	-1.75000E 00	-3.18182E 00
6.00000E-01	1.44273E 01	-1.90909E 00	-3.18182E 00
6.50000E-01	1.43278E 01	-2.06818E 00	-3.18182E 00
7.00000E-01	1.42205E 01	-2.22727E 00	-3.18182E 00
7.50000E-01	1.41051E 01	-2.38636E 00	-3.18182E 00
8.00000E-01	1.39818E 01	-2.54545E 00	-3.18182E 00
8.50000E-01	1.38506E 01	-2.70455E 00	-3.18182E 00
9.00000E-01	1.37114E 01	-2.86364E 00	-3.18182E 00
9.50000E-01	1.35642E 01	-3.02273E 00	-3.18182E 00
10.00000E-01	1.34091E 01	-3.18182E 00	-3.18182E 00
1.05000E 00	1.32460E 01	-3.34091E 00	-3.18182E 00
1.10000E 00	1.30750E 01	-3.50000E 00	-3.18182E 00
1.15000E 00	1.28960E 01	-3.65909E 00	-3.18182E 00
1.20000E 00	1.27091E 01	-3.81818E 00	-3.18182E 00
1.25000E 00	1.25142E 01	-3.97727E 00	-3.18182E 00
1.30000E 00	1.23114E 01	-4.13636E 00	-3.18182E 00
1.35000E 00	1.21006E 01	-4.29545E 00	-3.18182E 00
1.40000E 00	1.13818E 01	-4.45454E 00	-3.18182E 00
1.45000E 00	1.16551E 01	-4.61364E 00	-3.18182E 00
1.50000E 00	1.14205E 01	-4.77273E 00	-3.18182E 00
1.55000E 00	1.11778E 01	-4.93182E 00	-3.18182E 00
1.60000E 00	1.09273E 01	-5.09091E 00	-3.18182E 00
1.65000E 00	1.06687E 01	-5.25000E 00	-3.18182E 00
1.70000E 00	1.04023E 01	-5.40909E 00	-3.18182E 00
1.75000E 00	1.01278E 01	-5.56818E 00	-3.18182E 00
1.80000E 00	9.84545E 00	-5.72727E 00	-3.18182E 00
1.85000E 00	9.55511E 00	-5.88636E 00	-3.18182E 00
1.90000E 00	9.25681E 00	-6.04545E 00	-3.18182E 00
1.95000E 00	8.95056E 00	-6.20454E 00	-3.18182E 00
2.00000E 00	8.63636E 00	-6.36364E 00	-3.18182E 00
2.05000E 00	8.31420E 00	-6.52273E 00	-3.18182E 00
2.10000E 00	7.98408E 00	-6.68182E 00	-3.18182E 00
2.15000E 00	7.64602E 00	-6.84091E 00	-3.18182E 00
2.20000E 00	7.29999E 00	-7.00000E 00	-3.18182E 00
2.25000E 00	6.94602E 00	-7.15909E 00	-3.18182E 00
2.30000E 00	6.58408E 00	-7.31818E 00	-3.18182E 00
2.35000E 00	6.21420E 00	-7.47727E 00	-3.18182E 00
2.40000E 00	5.83636E 00	-7.63636E 00	-3.18182E 00
2.45000E 00	5.45056E 00	-7.79545E 00	-3.18182E 00
2.50000E 00	5.05859E 00	-7.84804E 00	-0.
2.55000E 00	4.66619E 00	-7.84804E 00	-0.
2.60000E 00	4.27533E 00	-7.74900E 00	3.18182E 00
2.65000E 00	3.89186E 00	-7.58990E 00	3.18182E 00
2.70000E 00	3.51634E 00	-7.43081E 00	3.18182E 00
2.75000E 00	3.14676E 00	-7.27172E 00	3.18182E 00

Figure A-88--Result of Mimic program.

THE LIBRATION OF MERCURY (EXAMPLE 8)

Han-Shou Liu

Problem Description

The analysis of the resonance-locked rotation of the planet Mercury under the influence of the planetary potential and the orbital eccentricity was recently reported.* As shown therein the equation of the planetary rotation about its polar axis has the form,

$$\Phi = f + \phi \quad (45)$$

where f is the true anomaly and ϕ , denoting the angle between the smallest of the moments of inertia with the radius vector, is the solution of the following differential equation,

$$\frac{d^2 \phi}{df^2} - \frac{2e \sin f}{1 + e \cos f} \left(\frac{d\phi}{df} + 1 \right) + \frac{3\lambda}{1 + \cos f} \cos \phi \sin \phi = 0 \quad (46)$$

where λ measures the difference between the two small moments of inertia and e is the orbital eccentricity.

The variable of function ϕ can be transformed from the true anomaly f to the mean anomaly M , in order to investigate the instantaneous physical librations of the planet Mercury. If E is the planet's eccentric anomaly, a well-known formula or orbital motion,

$$\tan \frac{E}{2} = \left(\frac{1 - e}{1 + e} \right)^{1/2} \tan \frac{f}{2} \quad (47)$$

constitutes the basis of the transformation. The mean anomaly can be calculated according to Kepler's equation,

$$M = E - e \sin E \quad (48)$$

Since the resonance condition is due to the angle,

$$N = \Phi - (3/2) M \quad (49)$$

about $\Phi - (3/2) M = 0$, the rotation of Mercury can remain locked-in motion when the rotational rates are within the range between an upper and a lower limit. This result as well as solutions of ϕ for various combinations of parameter λ and initial conditions for a period of 100 years were also reported.**

*Liu, Han-Shou and O'Keefe, John A. "Theory of Rotation for the Planet Mercury," Science, 1717 December 24, 1965.

**Liu, Han-Shou, "The Liberation of Mercury," J. Geophys. Res., 3099-3100, June 15, 1966.

The Mimic Program

Table A-12
Equivalent Symbols

Program Symbol	Equation Symbol
LPHI	$= \Phi$
PHI	$= \phi$
1DPHI	$= d\phi/df$
2DPHI	$= \frac{d^2 \phi}{df^2}$
1DPHIO	$= \frac{d\phi}{df} \text{ at } f = 0$
F	$= f \text{ in radian}$
FDEG	$= f \text{ in degree}$
E	$= e$
LAMDA	$= \lambda$
BIGE	$= E$
M	$= M$
N	$= N$

The Mimic program attempts to solve numerically equations (45) to (49). The following values are chosen for the constants and parameters,

$$\lambda = 5 \times 10^{-5}$$

$$e = 0.206$$

and

$$\text{at } f = 0, \frac{d\phi}{df} = -.03997, -.02723, -.043460$$

The program is shown in Figure A-89. Equivalent symbols are shown in Table A-12. Since the value of E obtained from Equation (47) by using an arctangent routine gives only principal value, an F is added in the equation for BIGE in the program. The computation is to last for about 300 revolutions.

A portion of the result is shown in Figure A-90, where the value of N demonstrates the stability of orientation for the planet Mercury at perihelion. Table A-13 shows the comparison between the values of N from the Mimic program and those from Liu; in the latter case, the initial value

MIMIC SOURCE-LANGUAGE PROGRAM

COMPUTATION OF RESONANCE-LOCKED ROTATION OF PLANET MERCURY

```

*
      CON(E,LAMDA)
      PAR(1DPHI)
*
      DT      = 6.2932
      DTMAX   = .31416
      F       = T
      FDEG    = F*180./3.1416
      LPHI    = PHI+F
*
      A       = 2.*E*SIN(F)/C
      B       = 3.*LAMDA*COS(PHI)*SIN(PHI)/C
      C       = 1.+E*COS(F)
*
      2DPHI   = A*(1DPHI+1.)-B
      1DPHI   = INT(2DPHI,1DPHI)
      PHI     = INT(1DPHI,1.)
*
      X       = SQRT((1.-E)/(1.+E))
      Y       = SIN(F/2.)/COS(F/2.)
      Z       = X*Y
      BIGE    = 2.*ATAN(Z)+F
      M       = BIGE-E*SIN(BIGE)
      N       = LPHI-1.5*M
*
      FIN(F,180.)
      FDR(F,FDEG,PHI,LPHI,M,N)
      FDR
      OUT(F,FDEG,PHI,LPHI,M,N)
      END

```

SCRT DIAGNOSTICS FOLLOW

Figure A-89-Mimic program.

Table A-13
Comparison of Results

F in revolution	N from Mimic	N from Liu
0	0	0
1	-6.21396E-02	-.62218933D-01
5	-3.05997E-01	-.30637823D+00
10	-5.85113E-01	-.58581506D+00
20	-1.00863E+00	-.10098216D+01
30	-1.26176E+00	-.12633649D+01
50	-1.47482E+00	-.14782922D+01
70	-1.52345E+00	-.15324656D+01
100	-1.43276E+00	-.14844301D+01
200	+1.41685E+00	+1.4714520D+01
300	-1.55447E+00	

1CPHI
-3.99700E-02

F	FDEG	PHI
0.	0.	0.
6.28321E 00	3.60000E 02	3.07947E 00
1.25664E 01	7.20000E 02	6.15918E 00
1.88496E 01	1.08000E 03	9.23936E 00
2.51328E 01	1.44000E 03	1.23202E 01
3.14160E 01	1.80000E 03	1.54021E 01
3.76992E 01	2.16000E 03	1.84850E 01
4.39824E 01	2.52000E 03	2.15690E 01
5.02656E 01	2.88000E 03	2.46548E 01
5.65488E 01	3.24000E 03	2.77421E 01
6.28320E 01	3.60000E 03	3.08310E 01
6.91152E 01	3.96000E 03	3.39217E 01
7.53984E 01	4.32000E 03	3.70143E 01
8.16816E 01	4.68000E 03	4.01087E 01
8.79648E 01	5.04000E 03	4.32151E 01
9.42480E 01	5.40000E 03	4.63134E 01
1.00531E 02	5.76000E 03	4.94037E 01
1.06814E 02	6.12000E 03	5.25059E 01
1.13098E 02	6.48000E 03	5.56099E 01
1.19381E 02	6.84000E 03	5.87158E 01
1.25664E 02	7.20000E 03	6.18236E 01
1.31947E 02	7.56000E 03	6.49337E 01

LPHI	M	N
0.	0.	0.
9.36267E 00	6.28321E 00	-6.21396E-02
1.87256E 01	1.25664E 01	-1.24040E-01
2.80890E 01	1.88496E 01	-1.85466E-01
3.74530E 01	2.51328E 01	-2.46190E-01
4.68181E 01	3.14160E 01	-3.05997E-01
5.61842E 01	3.76992E 01	-3.64694E-01
6.55516E 01	4.39824E 01	-4.22101E-01
7.49204E 01	5.02656E 01	-4.78059E-01
8.42909E 01	5.65489E 01	-5.32434E-01
9.36630E 01	6.28321E 01	-5.85113E-01
1.03037E 02	6.91153E 01	-6.36013E-01
1.12413E 02	7.53985E 01	-6.85063E-01
1.21790E 02	8.16817E 01	-7.32212E-01
1.31170E 02	8.79649E 01	-7.77433E-01
1.40551E 02	9.42481E 01	-8.20715E-01
1.49935E 02	1.00531E 02	-8.62064E-01
1.59320E 02	1.06815E 02	-9.01501E-01
1.68708E 02	1.13098E 02	-9.39045E-01
1.78097E 02	1.19381E 02	-9.74741E-01
1.87488E 02	1.25664E 02	-1.00863E 00
1.96880E 02	1.31947E 02	-1.04078E 00

Figure A-90-Part of result of program.

of $d\phi/df$ is $-.03998$ which is slightly different from the value of $-.03997$ in the Mimic program. Both these values gave an oscillatory response. Liu's result was obtained from a Fortran program using double precision arithmetic.

A TORSIONAL VIBRATION SYSTEM (EXAMPLE 9) Kenneth W. Stark

Problem Description

Figure A-91 shows a three-degree-of-freedom torsional vibration system which is quite common in a mechanical system where rotational motion must be transmitted from a power source to the driven mechanism. Both speed reduction and torque multiplication are achieved. Normally, in systems where a very accurate speed is required, belts are used between the pulleys. In very delicate apparatus such as satellite tape recorders, the belts are made of mylar.

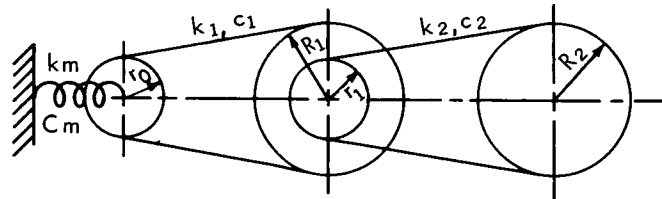


Figure A-91—Diagram of system.

When the pulley-belt system is excited into resonance which perturbs the ideal velocity transmission, problems arise. The problem is to analyze and compute the system shown in Figure A-91.

Mathematical Equations

The pulley-belt system can be described by the following set of differential equations,

$$\ddot{\theta}_0 + M_1 \dot{\theta}_0 + M_2 \dot{\theta}_1 + M_3 \theta_0 + M_4 \theta_1 = 0 \quad (50)$$

$$\ddot{\theta}_1 + M_6 \dot{\theta}_1 + M_7 \dot{\theta}_2 + M_8 \dot{\theta}_0 + M_9 \theta_1 + M_{10} \theta_0 + M_{11} \theta_2 = 0 \quad (51)$$

$$\ddot{\theta}_2 + M_{12} \dot{\theta}_2 + M_{13} \dot{\theta}_1 + M_{14} \theta_2 + M_{15} \theta_1 = 0 \quad (52)$$

where

$$M_1 = (C_m + 2C_1 r_0^2)/I_0$$

$$M_2 = -2 C_1 R_1 r_0/I_0$$

$$M_3 = (k_m + 2k_1 r_0^2)/I_0$$

$$M_4 = -2k_1 R_1 r_0/I_0$$

$$M_6 = (2C_1 R_1^2 + 2C_2 r_1^2)/I_1$$

$$M_7 = -2C_2 R_2 r_1/I_1$$

$$M_8 = -2C_1 R_1 r_0/I_1$$

$$M_9 = (2k_1 R_1^2 + 2k_2 r_1^2)/I_1$$

$$M_{10} = -2k_1 R_1 r_0/I_1$$

$$M_{11} = -2k_2 R_2 r_1/I_1$$

$$M_{12} = 2 C_2 R_2^2/I_2$$

$$M_{13} = -2 C_2 R_2 r_1/I_2$$

$$M_{14} = 2 k_2 R_2^2/I_2$$

$$M_{15} = -2 k_2 R_2 r_1/I_2$$

For the above, k_1 and k_2 are the belt spring constants, k_m is the torsional spring constant, C_1 and C_2 are the belt damping constants, C_m is the torsional damping constant, I_0 , I_1 and I_2 are the pulley inertias and r_0 , r_1 , R_1 and R_2 are the pulley radii.

Constants and Initial Conditions

The following values of the constants and initial conditions are chosen,

$$M_1 = 1$$

$$M_2 = -2$$

$$M_3 = 10$$

$$M_4 = -20$$

$$M_6 = 2.25$$

$$M_7 = -1$$

$$M_8 = -.5$$

$$M_9 = 22.5$$

$$M_{10} = -5$$

$$M_{11} = -10$$

$$M_{12} = 5.3$$

$$M_{13} = -1.3$$

$$M_{14} = 53.3$$

$$M_{15} = -13.3$$

$$\theta_0(0) = .0146 \text{ radians}$$

$$\theta_1(0) = .0112 \text{ radians}$$

$$\theta_2(0) = .0174 \text{ radians}$$

$$\dot{\theta}_0(0) = \dot{\theta}_1(0) = \dot{\theta}_2(0) = 0$$

The Mimic Program

The Mimic program is to simulate the torsional vibration system described by the equations (50) through (52) together with the above values of constants and initial conditions. For convenience, symbol θ 's are replaced by X's. The Mimic program is shown in Figure A-92, and the printout in Figure A-93. A plot of the result showing the oscillations is shown in Figure A-94.

```
***MIMIC SOURCE-LANGUAGE PROGRAM***  
  
TORSIONAL VIBRATION SYSTEM W/DAMPING ' 3 DEGREE SYSTEM KENNETH W. STARK  
CON(M1,M2,M3,M4,M6)  
CON(M7,M8,M9,M10,M11,M12)  
CON(M13,M14,M15)  
CON(X10,1DX10,X20,1DX20,X30,1DX30)  
DT      = .01  
2DX1    = -M1*1DX1-M2*1DX2-M3*X1-M4*X2  
1DX1    = INT(2DX1,1DX10)  
X1      = INT(1DX1,X10)  
2DX2    = -M6*1DX2-M7*1DX3-M8*1DX1-M9*X2-M10*X1-M11*X3  
1DX2    = INT(2DX2,1DX20)  
X2      = INT(1DX2,X20)  
2DX3    = -M12*1DX3-M13*1DX2-M14*X3-M15*X2  
1DX3    = INT(2DX3,1DX30)  
X3      = INT(1DX3,X30)  
FIN(T,5.)  
HDR(TIME,X1,X1DOT,X2,X2DOT,X3)  
OUT(T,X1,1DX1,X2,1DX2,X3)  
END  
  
***SORT DIAGNOSTICS FOLLOW***
```

Figure A-92-Mimic program.

TIME	X1	X1DOT	X2	X2DOT	X3
0.	1.46000E-02	0.	1.12000E-02	0.	1.74000E-02
10.00000E-03	1.46039E-02	7.75219E-04	1.11996E-02	-8.66395E-05	1.73618E-02
2.00000E-02	1.46155E-02	1.53931E-03	1.11980E-02	-2.47220E-04	1.72499E-02
3.00000E-02	1.46346E-02	2.28982E-03	1.11944E-02	-4.82178E-04	1.70688E-02
4.00000E-02	1.46612E-02	3.02421E-03	1.11881E-02	-7.91234E-04	1.68229E-02
5.00000E-02	1.46950E-02	3.73980E-03	1.11784E-02	-1.17343E-03	1.65168E-02
6.00000E-02	1.47359E-02	4.43389E-03	1.11644E-02	-1.62718E-03	1.61551E-02
7.00000E-02	1.47836E-02	5.10358E-03	1.11456E-02	-2.15030E-03	1.57424E-02
8.00000E-02	1.48379E-02	5.74637E-03	1.11212E-02	-2.74005E-03	1.52836E-02
9.00000E-02	1.48985E-02	6.35910E-03	1.10906E-02	-3.39320E-03	1.47832E-02
10.00000E-02	1.49650E-02	6.93905E-03	1.10531E-02	-4.10604E-03	1.42458E-02
1.10000E-01	1.50371E-02	7.48340E-03	1.10083E-02	-4.87446E-03	1.36761E-02
1.20000E-01	1.51145E-02	7.98937E-03	1.09555E-02	-5.69399E-03	1.30784E-02
1.30000E-01	1.51968E-02	8.45424E-03	1.08942E-02	-6.55984E-03	1.24572E-02
1.40000E-01	1.52835E-02	8.87536E-03	1.08241E-02	-7.46694E-03	1.18167E-02
1.50000E-01	1.53741E-02	9.25018E-03	1.07448E-02	-8.41002E-03	1.11610E-02
1.60000E-01	1.54683E-02	9.57625E-03	1.06558E-02	-9.38360E-03	1.04941E-02
1.70000E-01	1.55655E-02	9.85123E-03	1.05570E-02	-1.03821E-02	9.81972E-03
1.80000E-01	1.56652E-02	1.00729E-02	1.04481E-02	-1.13998E-02	9.14159E-03
1.90000E-01	1.57668E-02	1.02393E-02	1.03290E-02	-1.24310E-02	8.46311E-03
2.00000E-01	1.58697E-02	1.03486E-02	1.01995E-02	-1.34699E-02	7.78754E-03
2.10000E-01	1.59735E-02	1.03989E-02	1.00596E-02	-1.45109E-02	7.11793E-03
2.20000E-01	1.60775E-02	1.03888E-02	9.90927E-03	-1.55483E-02	6.45714E-03
2.30000E-01	1.61811E-02	1.03170E-02	9.74864E-03	-1.65765E-02	5.80781E-03
2.40000E-01	1.62837E-02	1.01823E-02	9.57779E-03	-1.75901E-02	5.17239E-03
2.50000E-01	1.63845E-02	9.98383E-03	9.39690E-03	-1.85840E-02	4.55310E-03
2.60000E-01	1.64831E-02	9.72091E-03	9.20620E-03	-1.95530E-02	3.95197E-03
2.70000E-01	1.65787E-02	9.39303E-03	9.00594E-03	-2.04923E-02	3.37080E-03
2.80000E-01	1.66708E-02	8.99994E-03	8.79646E-03	-2.13973E-02	2.81121E-03
2.90000E-01	1.67585E-02	8.54160E-03	8.57812E-03	-2.22637E-02	2.27459E-03
3.00000E-01	1.68414E-02	8.01820E-03	8.35133E-03	-2.30875E-02	1.76216E-03
3.10000E-01	1.69187E-02	7.43017E-03	8.11653E-03	-2.38649E-02	1.27493E-03
3.20000E-01	1.69898E-02	6.77813E-03	7.87420E-03	-2.45925E-02	8.13720E-04
3.30000E-01	1.70540E-02	6.06295E-03	7.62485E-03	-2.52671E-02	3.79176E-04
3.40000E-01	1.71108E-02	5.28572E-03	7.36904E-03	-2.58860E-02	-2.82316E-05
3.50000E-01	1.71595E-02	4.44772E-03	7.10733E-03	-2.64467E-02	-4.08199E-04
3.60000E-01	1.71996E-02	3.55046E-03	6.84031E-03	-2.69471E-02	-7.60580E-04
3.70000E-01	1.72303E-02	2.59564E-03	6.56859E-03	-2.73855E-02	-1.08538E-03
3.80000E-01	1.72513E-02	1.58516E-03	6.29281E-03	-2.77604E-02	-1.38274E-03
3.90000E-01	1.72619E-02	5.21109E-04	6.01360E-03	-2.80708E-02	-1.65295E-03
4.00000E-01	1.72615E-02	-5.94244E-04	5.73161E-03	-2.83158E-02	-1.89640E-03
4.10000E-01	1.72498E-02	-1.75846E-03	5.44750E-03	-2.84952E-02	-2.11361E-03
4.20000E-01	1.72262E-02	-2.96896E-03	5.16193E-03	-2.86089E-02	

Figure A-93-Printout of Mimic program.

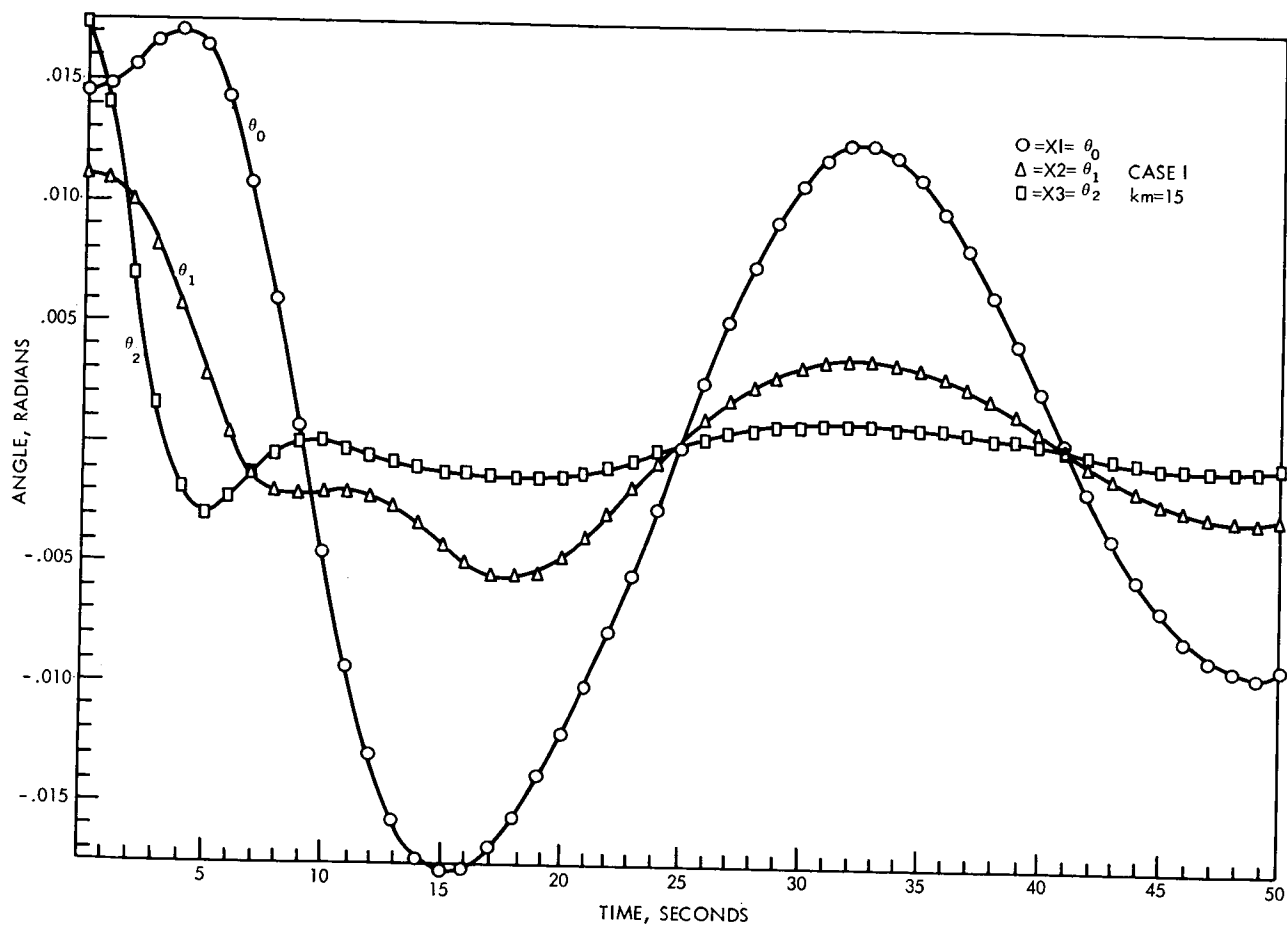


Figure A-94—Graph of result.

NON-LINEAR FREE VIBRATION (EXAMPLE 10)

William F. Bangs

Problem Description

In the course of vibration testing of spacecraft structures, nonlinear characteristics are often observed. A particular type of structural nonlinearity shown in Figure A-95 was assumed and the free vibration characteristics were computed in this problem.

If a linear structure is excited by a sinusoidal force, the response of the structure at every point will also be sinusoidal. When a structure is nonlinear, a sinusoidal force produces responses which are not sinusoidal. Highly distorted waveforms are common occurrences in spacecraft vibration testing.

It was desired to estimate the nonlinear response of a system having a nonsymmetrical stiffness with little or no damping. The first phase of the problem, discussed here, was to define the system and compute its free vibration behavior.

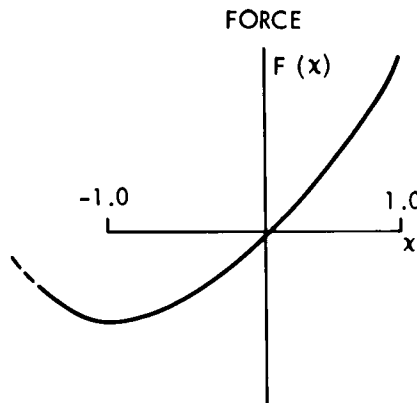


Figure A-95

Let us use the simple dynamic system as shown in Figure A-96. The parabolic force-deflection relation of the nonlinear spring of Figure A-95 can be expressed as,

$$F(x) = 1970 [(x + 1)^2 - 1] \quad (53)$$

and the equation of motion is,

$$M \frac{d^2 x}{dt^2} + F(x) = 0 \quad (54)$$

The Mimic Program

It is required to find the time history of the deflection $x(t)$ and the acceleration $\ddot{x}(t)$. The initial condition is established by giving an initial deflection in the $-x$ direction and then releasing. The following values of initial displacement are chosen:

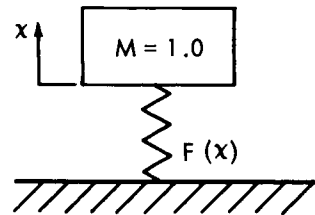
$$\dot{x}(0) = 0$$

$$x(0) = -.3, -.6, -.9$$

and the value of M is chosen as unity.

The program is shown in Figure A-97 and the result for the case of $x(0)$ equal to $-.9$ is shown in Figure A-98. In this program, a fairly small DT and $DTMAX$ were required, because the problem was designed to have a natural period of about $1/10$ second. It was decided to compute 25 points per full cycle so as to adequately describe the response waveform. The result is plotted into a curve shown in Figure A-99.

Figure A-96—Diagram of system.



```

***MIMIC SOURCE-LANGUAGE PROGRAM***

*
NONLINEAR VIBRATION PROB      W F BANGS
      CON(DT,DTMAX)
      PAR(B)
      2DX      -1970.*A
      A      (X+1.)*(X+1.)-1.
      1DX      INT(2DX,0.)
      X      INT(1DX,8)
      FIN(T,.25)
      HDR(TIME,DISPL,ACCL,DIS)
      HDR
      OUT(T,X,2DX,B)
      END

.004      .004      ***SORT DIAGNOSTICS FOLLOW***
-.3
-.6
-.9

```

Figure A-97—Mimic program.

B
-9.00000E-01

TIME	DISPL	ACCL	IDIS
0.	-9.00000E-01	1.95030E 03	-9.00000E-01
4.00000E-03	-8.84406E-01	1.94368E 03	-9.00000E-01
8.00000E-03	-8.37738E-01	1.91813E 03	-9.00000E-01
1.20000E-02	-7.60426E-01	1.85693E 03	-9.00000E-01
1.60000E-02	-6.53486E-01	1.73346E 03	-9.00000E-01
2.00000E-02	-5.18939E-01	1.51410E 03	-9.00000E-01
2.40000E-02	-3.60341E-01	1.16395E 03	-9.00000E-01
2.80000E-02	-1.83331E-01	6.56111E 02	-9.00000E-01
3.20000E-02	3.95591E-03	-1.56171E 01	-9.00000E-01
3.60000E-02	1.90808E-01	-8.23508E 02	-9.00000E-01
4.00000E-02	3.64394E-01	-1.69729E 03	-9.00000E-01
4.40000E-02	5.10880E-01	-2.52703E 03	-9.00000E-01
4.80000E-02	6.17168E-01	-3.18201E 03	-9.00000E-01
5.20000E-02	6.72938E-01	-3.54348E 03	-9.00000E-01
5.60000E-02	6.72503E-01	-3.54061E 03	-9.00000E-01
6.00000E-02	6.15908E-01	-3.17398E 03	-9.00000E-01
6.40000E-02	5.08922E-01	-2.51539E 03	-9.00000E-01
6.80000E-02	3.61921E-01	-1.68401E 03	-9.00000E-01
7.20000E-02	1.88031E-01	-8.10492E 02	-9.00000E-01
7.60000E-02	1.07974E-03	-4.25646E 00	-9.00000E-01
8.00000E-02	-1.86125E-01	6.65086E 02	-9.00000E-01
8.40000E-02	-3.62909E-01	1.17041E 03	-9.00000E-01
8.80000E-02	-5.21178E-01	1.51834E 03	-9.00000E-01
9.20000E-02	-6.55328E-01	1.73597E 03	-9.00000E-01
9.60000E-02	-7.61829E-01	1.85825E 03	-9.00000E-01
10.00000E-02	-8.38680E-01	1.91873E 03	-9.00000E-01
1.04000E-01	-8.84878E-01	1.94389E 03	-9.00000E-01
1.08000E-01	-8.99998E-01	1.95030E 03	-9.00000E-01
1.12000E-01	-8.83930E-01	1.94346E 03	-9.00000E-01
1.16000E-01	-8.36792E-01	1.91753E 03	-9.00000E-01
1.20000E-01	-7.59020E-01	1.85560E 03	-9.00000E-01
1.24000E-01	-6.51642E-01	1.73093E 03	-9.00000E-01
1.28000E-01	-5.16697E-01	1.50984E 03	-9.00000E-01
1.32000E-01	-3.57771E-01	1.15746E 03	-9.00000E-01
1.36000E-01	-1.80537E-01	6.47106E 02	-9.00000E-01
1.40000E-01	6.83001E-03	-2.70021E 01	-9.00000E-01
1.44000E-01	1.93581E-01	-8.36534E 02	-9.00000E-01
1.48000E-01	3.66859E-01	-1.71056E 03	-9.00000E-01
1.52000E-01	5.12828E-01	-2.53864E 03	-9.00000E-01
1.56000E-01	6.18416E-01	-3.18996E 03	-9.00000E-01
1.60000E-01	6.73360E-01	-3.54626E 03	-9.00000E-01
1.64000E-01	6.72056E-01	-3.53767E 03	-9.00000E-01
1.68000E-01	6.14638E-01	-3.16590E 03	-9.00000E-01
1.72000E-01	5.06957E-01	-2.50371E 03	-9.00000E-01
1.76000E-01	3.59444E-01	-1.67073E 03	-9.00000E-01
1.80000E-01	1.85252E-01	-7.97498E 02	-9.00000E-01
1.84000E-01	-1.79508E-03	7.06629E 00	-9.00000E-01
1.88000E-01	-1.88915E-01	6.74019E 02	-9.00000E-01
1.92000E-01	-3.65472E-01	1.17683E 03	-9.00000E-01
1.96000E-01	-5.23411E-01	1.52254E 03	-9.00000E-01
2.00000E-01	-6.57162E-01	1.73845E 03	-9.00000E-01
2.04000E-01	-7.63225E-01	1.85956E 03	-9.00000E-01
2.08000E-01	-8.39615E-01	1.91933E 03	-9.00000E-01
2.12000E-01	-8.85343E-01	1.94410E 03	-9.00000E-01
2.16000E-01	-8.99989E-01	1.95030E 03	-9.00000E-01
2.20000E-01	-8.83447E-01	1.94324E 03	-9.00000E-01
2.24000E-01	-8.35839E-01	1.91691E 03	-9.00000E-01
2.28000E-01	-7.57607E-01	1.85425E 03	-9.00000E-01
2.32000E-01	-6.49791E-01	1.72839E 03	-9.00000E-01

Figure A-98—Result of Mimic program ($x(0) = -.9$).

INITIAL DISPLAC. = -0.9

ACCELERATION VS TIME

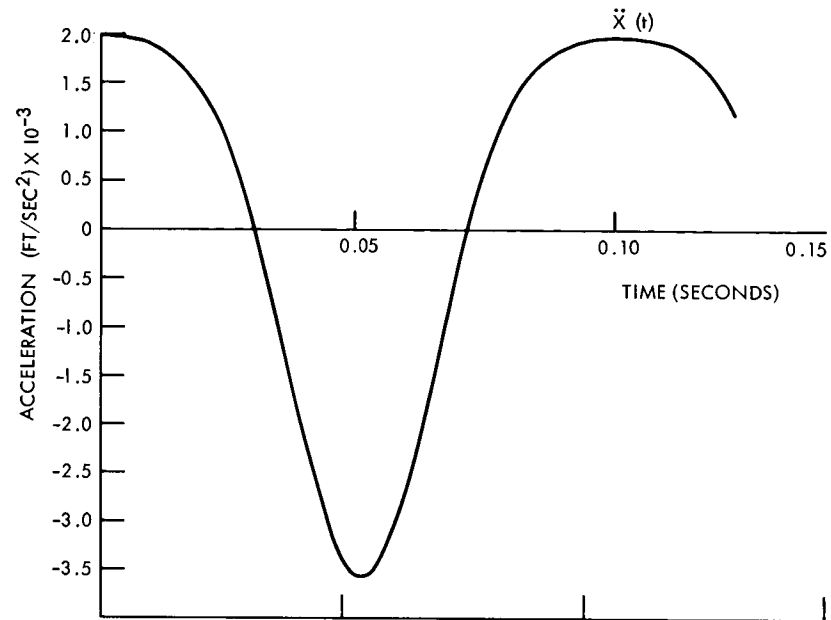


Figure A-99-Plot of result of one cycle.

SPIRAL ANTENNA FIELD PROBLEM (EXAMPLE 11)

Leonard F. Deerkoski

Problem Description

Spiral antennas are beneficial for many applications, especially those that require a circularly polarized axial beam that maintains its pattern and impedance characteristics over a relatively large bandwidth. When the arms of a spiral antenna are fed in the proper phase relationship, a different radiation mode is established which results in a conical beam with a null along the axis. Information from these two beams may be processed to give instantaneous target position.

In the calculation of the theoretical near field radiation patterns of a logarithmic spiral antenna by Dr. Bernard Ru-Shao Cheo,* discrepancies exist between these results and experimental observations as to the magnitude of the radiated field. A plot of the theoretical radiated field included in Dr. Cheo's report is given in Figure A-100, where the curves are designated by the parameter "n" in the equation

$$|F(\theta)| = \frac{1}{2} \frac{\cos \theta \tan^n (\theta/2) e^{N/A \tan^{-1}(A \cos \theta)}}{\sin(\theta) (1 + A^2 \cos^2 \theta)^{1/2}} \quad (55)$$

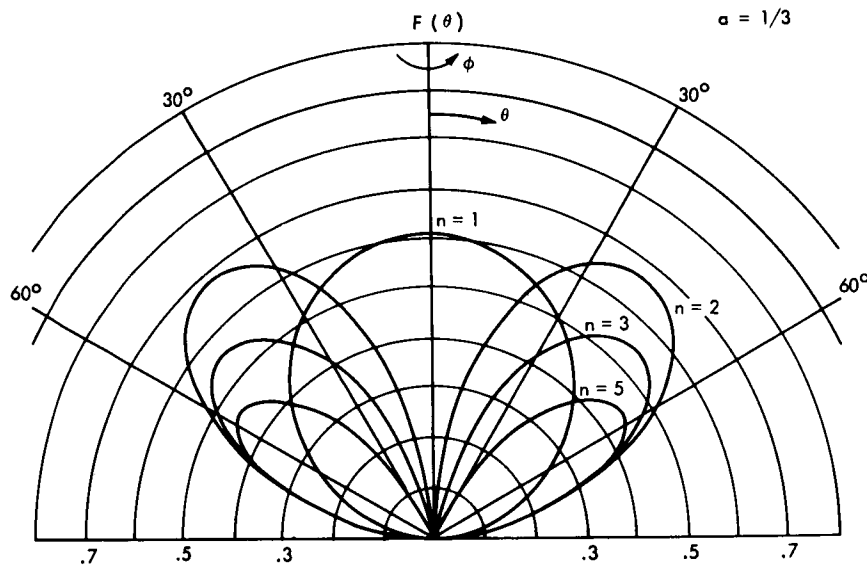


Figure A-100—Plot of radiation pattern.

The derivation of $|F(\theta)|$ has been verified, and a check of the graphical representation of this equation is desirable. The symmetry of the radiation pattern only requires a variation in θ from 0° to 90° to yield the entire result.

*Bernard Ru-Shao Cheo, "A Solution to the Equiangular Spiral Antenna Problem," University of California, Berkeley California, November 1, 1960.

In addition, the relative phase of $F(\theta)$ for $n = 1$ and $n = 2$ is assumed small as θ covers a 180° region. As a verification of this relationship, a calculation of the phase of $F(\theta)$ is included in the analysis using the equation

$$P(\theta) = \frac{N}{2A} \ln(1 + A^2 \cos^2 \theta) + \tan^{-1}(A \cos \theta) \quad (56)$$

The Mimic Program

The Mimic program for the computation of $|F(\theta)|$ and $P(\theta)$ is shown in Figure A-101, and the result is given in Figure A-102 from which the plot in Figure A-103 is obtained. A list of equivalent symbols is shown in Table A-14.

Table A-14
Equivalent Symbols

Program Symbols	Equation Symbols
A	$= A = 1/3$
N	$= N = 1, 2, 3, 5$
Theta	$= \theta$
M4	$= \tan^N(\theta/2)$
P2	$= \tan^{-1}(a \cos \theta)$
P4	$= (N/a) \tan^{-1}(a \cos \theta)$
S4	$= \text{Denominator of Equation (55)}$
S5	$= \text{Numerator of Equation (55)}$
U2	$= (n/2a) \ln(1 + a^2 \cos^2 \theta)$
S2	$= (1 + a^2 \cos^2 \theta)$
V2	$= F(\theta) $
U3	$= P(\theta)$

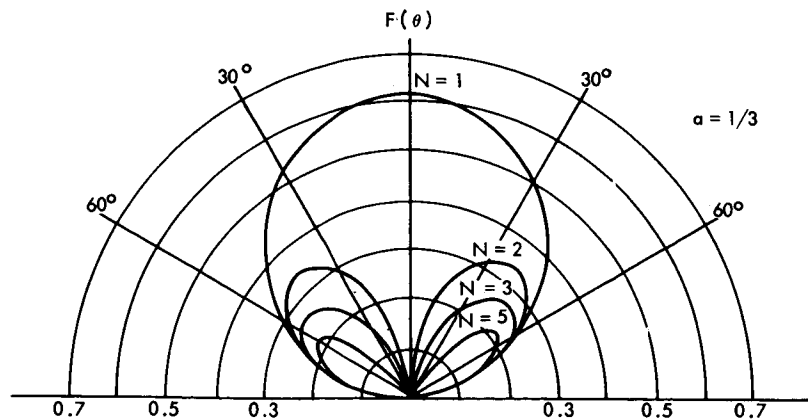


Figure A-101—Mimic program.

MIMIC SOURCE-LANGUAGE PROGRAM

CHEU SPIRAL ANTENNA FIELD PATTERN AMPLITUDE AND PHASE L.DEERKOSKI

```

*
      CON(DT)
      PAR(N,A)
*
      DTMIN = DTMAX
      DTMAX = 1.0
      DT     = 1.0
*
      THETA  = T*3.1416/180.
      L      = COS(THETA)
      M1     = SIN(THETA/2.)
      M2     = COS(THETA/2.)
      M3     = M1/M2
*
      CC      M4 = EXP(N,M3)
      DD      M4 = 0.0
      CC      FSW(1,FALSE,FALSE,TRUE)
      DD      NOT(CC)
*
      P1      = A*L
      P2      = ATN(P1)
      P3      = P2*(N/A)
      P4      = EXP(P3)
      Q       = L*M4*P4
      R       = SIN(THETA)
      S1      = 1.+(A*COS(THETA))*(A*COS(THETA))
*
      EE      S2 = EXP(.5,S1)
      FF      S2 = 0.0
      EE      FSW(T,FALSE,FALSE,TRUE)
      FF      NOT(EE)
*
      AA      S3 = Q/(S2*R)
      BB      S3 = 1.24
      BB      FSW(T,FALSE,TRUE,FALSE)
      AA      NOT(BB)
*
      *DENOMENATOR OF EQUATION (1)
      S4      = S2*R
*
      *NUMERATOR OF EQUATION (1)
      S5      = .5*Q
*
      V1      = .5*S3
      V2      = ABS(V1)
      U1      = LOG(S1)
      U2      = U1*(N/(2.*A))
      U3      = U2+P2
*
      FIN(T,89.)
      HDR(THETA,MAGNI,PHASE,NUMER,DENOM)
      HDR
      OUT(T,V2,U3,S5,S4)
      END

```

SORT DIAGNOSTICS FOLLOW

Figure A-102-Result of Mimic program.

N	A	THETA	MAGNI	PHASE	NUMER	DENOM
1.00000E 00	3.33330E-01					
0.					0.	0.
1.00000E 00	6.20000E-01			4.79787E-01	1.14527E-02	1.83962E-02
2.00000E 00	6.22557E-01			4.79696E-01	2.28872E-02	3.67851E-02
3.00000E 00	6.22188E-01			4.79421E-01	3.42856E-02	5.51595E-02
4.00000E 00	6.21572E-01			4.78965E-01	4.56296E-02	7.35120E-02
5.00000E 00	6.20710E-01			4.78326E-01	5.69016E-02	9.18354E-02
6.00000E 00	6.19603E-01			4.77505E-01	6.80836E-02	1.10123E-01
7.00000E 00	6.18253E-01			4.76503E-01	7.91582E-02	1.28366E-01
8.00000E 00	6.16659E-01			4.75320E-01	9.01081E-02	1.46559E-01
9.00000E 00	6.14823E-01			4.73956E-01	1.00916E-01	1.64695E-01
1.00000E 01	6.12747E-01			4.72414E-01	1.11566E-01	1.82765E-01
1.10000E 01	6.10432E-01			4.70692E-01	1.22040E-01	2.00764E-01
1.20000E 01	6.07880E-01			4.68794E-01	1.32324E-01	2.18684E-01
1.30000E 01	6.05093E-01			4.66719E-01	1.42402E-01	2.36519E-01
1.40000E 01	6.02073E-01			4.64469E-01	1.52257E-01	2.54261E-01
1.50000E 01	5.98822E-01			4.62045E-01	1.61877E-01	2.71904E-01
1.60000E 01	5.95344E-01			4.59448E-01	1.71245E-01	2.89442E-01
1.70000E 01	5.91640E-01			4.56681E-01	1.80350E-01	3.06867E-01
1.80000E 01	5.87714E-01			4.53744E-01	1.89178E-01	3.24174E-01
1.90000E 01	5.83569E-01			4.50640E-01	1.97716E-01	3.41356E-01
2.00000E 01	5.79208E-01			4.47370E-01	2.05952E-01	3.58406E-01
2.10000E 01	5.74633E-01			4.43937E-01	2.13876E-01	3.75320E-01
2.20000E 01	5.69850E-01			4.40342E-01	2.21476E-01	3.92090E-01
2.30000E 01	5.64861E-01			4.36587E-01	2.28743E-01	4.08711E-01
2.40000E 01	5.59670E-01			4.32675E-01	2.35668E-01	4.25177E-01
2.50000E 01	5.54281E-01			4.28608E-01	2.42241E-01	4.41483E-01
2.60000E 01	5.48698E-01			4.24388E-01	2.48456E-01	4.57623E-01
2.70000E 01	5.42926E-01			4.20019E-01	2.54304E-01	4.73591E-01
2.80000E 01	5.36970E-01			4.15502E-01	2.59780E-01	4.89383E-01
2.90000E 01	5.30832E-01			4.10840E-01	2.64878E-01	5.04993E-01
3.00000E 01	5.24518E-01			4.06037E-01	2.69594E-01	5.20417E-01
3.10000E 01	5.18034E-01			4.01095E-01	2.73922E-01	5.35650E-01
3.20000E 01	5.11382E-01			3.96017E-01	2.77859E-01	5.50686E-01
3.30000E 01	5.04569E-01			3.90806E-01	2.81404E-01	5.65522E-01
3.40000E 01	4.97600E-01			3.85456E-01	2.84553E-01	5.80153E-01
3.50000E 01	4.90480E-01			3.80000E-01	2.87306E-01	5.94575E-01
3.60000E 01	4.83213E-01			3.74411E-01	2.89662E-01	6.08784E-01
3.70000E 01	4.75805E-01			3.68703E-01	2.91622E-01	6.22776E-01
3.80000E 01	4.68261E-01			3.62379E-01	2.93186E-01	6.36547E-01
3.90000E 01	4.60588E-01			3.56943E-01	2.94356E-01	6.50094E-01
4.00000E 01	4.52789E-01			3.50899E-01	2.95133E-01	6.63413E-01
4.10000E 01	4.44871E-01			3.44750E-01	2.95523E-01	6.76502E-01
4.20000E 01	4.36839E-01			3.38500E-01		

Figure A-103—Graph of result.

The program requires the use of three FSW statements to guard against any possible discontinuities. The first FSW statement employed the logical control variables CC and DD to prevent the raising of zero to a power when $M3 = 0$. The second FSW statement performs the same operation as the first in preventing $S1 = 0$. Division by zero in the calculation of $S3$ is avoided by using the third FSW statement and the logical control variables AA and BB.

Discussion

Comparing Figures A-100 and A-101, the amplitudes of the curves representing $n = 2, 3, 5$ indicate that the $1/2$ coefficient used in finding $|F(\theta)|$ had not been included in Dr. Cheo's plot; and, consequently, his radiation patterns indicate twice their true magnitude for all values of "n" except $n = 1$.

The printout of the phase of $F(\theta)$ indicated that the maximum phase difference between outputs for $n = 1$ and $n = 2$ did not exceed 11 degrees. This difference is within the expected variation of phase of $F(\theta)$, thus verifying our original assumption.

SIMULATION OF PULSE FREQUENCY MODULATION ANALOG PROCESSOR (EXAMPLE 12) R. L. Martin

Problem Description

The system simulated here is not a type of control system but rather a telemetry signal processor which could be described by differential equations and a nonlinearity (which existed in the MIMIC language). The input signal, a pulse frequency modulated (PFM) wave, is a series of constant amplitude tone bursts each of which is 40 ms long and has a frequency of 1.1, 1.6, 1.7, 1.8, or 3.1 kc. At the instant the input signal changes from one frequency to another, the effect of the processor is to produce a short pulse which could be used for synchronization of the signal with a bank of matched filters.

Figure A-104 shows the block diagram of the processor consisting of four major elements each describable as typical analog elements. The first block, an FM to AM converter and noise filter, is simply three second order filters each having an "s" in the numerator. By setting the corner frequencies such that the input frequencies occur on the leading slope of the filter, the resulting signal then has amplitude proportional to frequency. The subsequent slope is used to attenuate noise which is assumed already in the signal and which would be amplified otherwise.

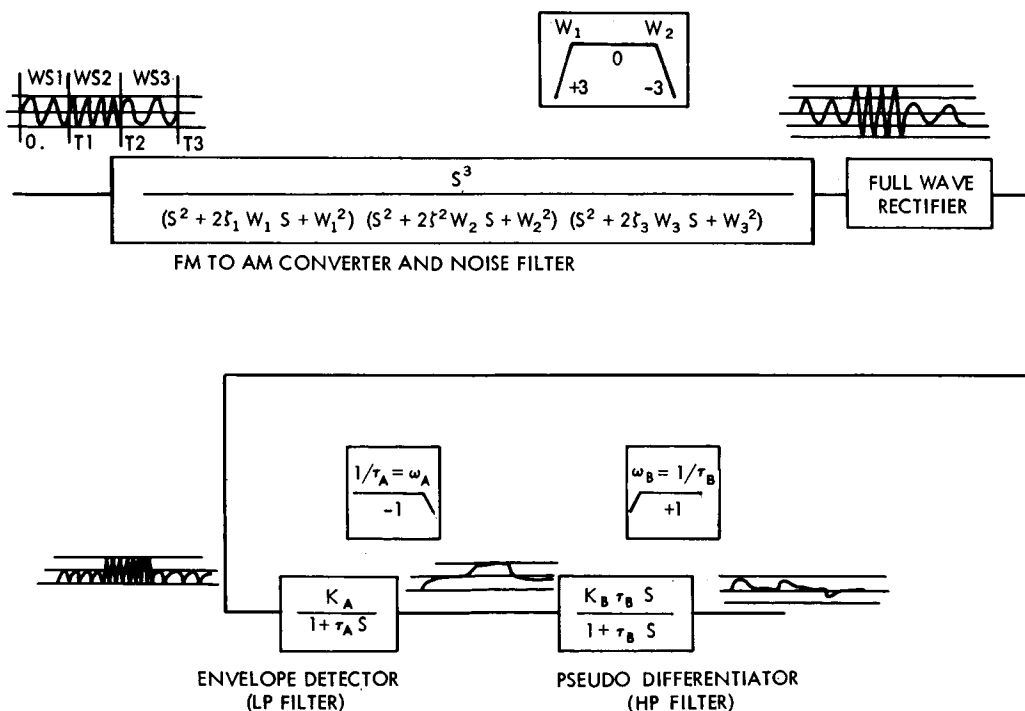


Figure A-104—Block diagram of processor.

A dc level, proportional to frequency, is obtained through the full wave rectifier. A low pass filter with its corner much below the signal frequencies acts as an envelope detector such that only the envelop of the rectified signal is produced. Then the high pass filter (or pseudo-differentiator), in its steady state response, takes out the dc level of the signal. What is left is a relatively short pulse at the instant the input frequency changes.

In the actual processor many pulses (on the order of 100) would be delayed in time and added together to obtain a single, large, less noisy pulse which would be used to synchronize a much longer PFM signal.

Model to be Simulated

Figure A-105 shows the block diagram redrawn from that in Figure A-104 to show the individual integrators. The input signal was synthesized using the function switches and signal generators shown in Figure A-106. An alternative using Mimic Statements is shown in Figure A-106, though these statements have not been tested.

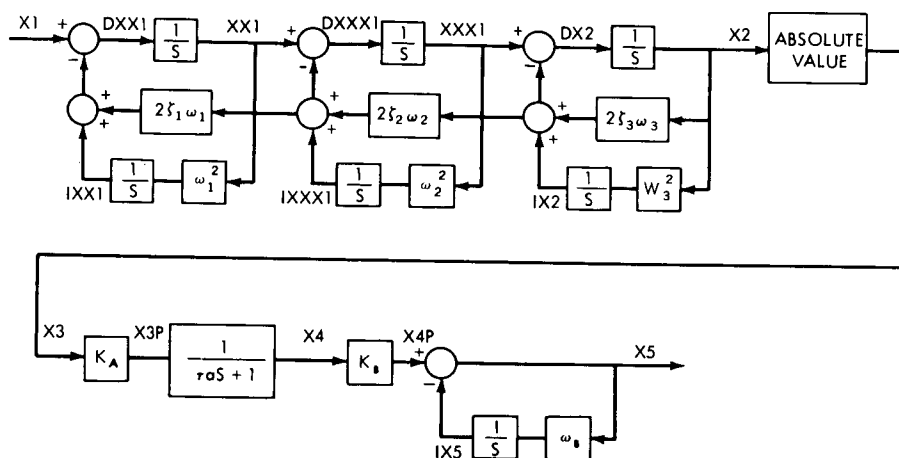


Figure A-105—Block diagram (showing integrators).

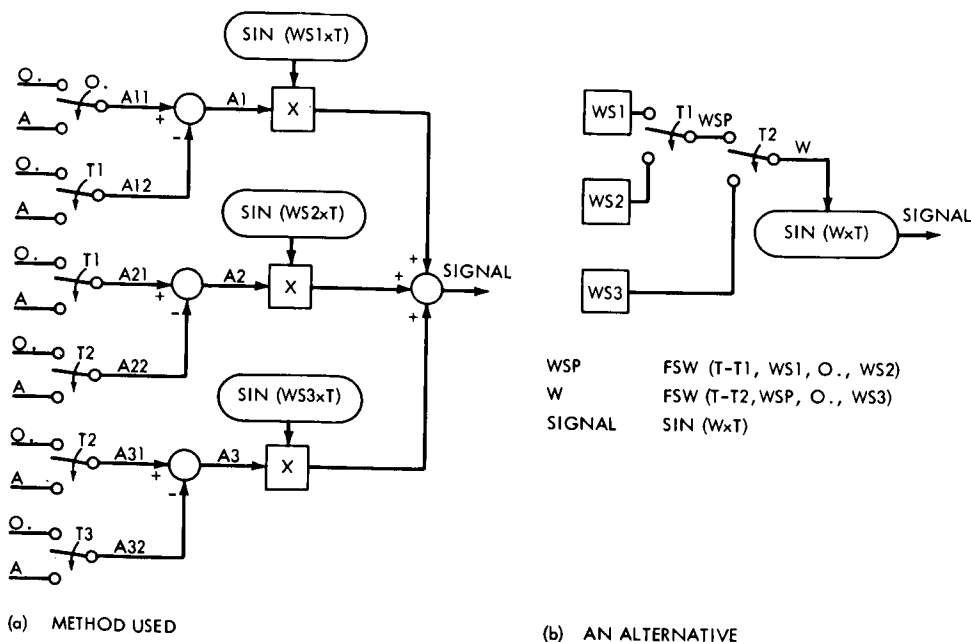


Figure A-106

Constants and Parameters

The values of the constants are:

A = 10
T1 = 20
T2 = 40
T3 = 60
ZETA1 = ζ_1 = .4
ZETA2 = ζ_2 = .4
ZETA3 = ζ_3 = 1
OMEGA1 = ω_1 = 18.85
OMEGA2 = ω_2 = 25.133
OMEGA3 = ω_3 = 21.75
KA = K_A = 1
KB = K_B = 1
TAUB = τ_B = .9175
OMEGAB = $1/\tau_A$ = 0.7320

The values of the parameters are,

WS1 = 10.0531
WS2 = 14.4513
WS3 = 18.8496

The Mimic Program

The Mimic program simulates the block diagram in Figure A-105 and the function switch logic in Figure A-106(a) together with the above values of constants and parameters. The Mimic program is shown in Figure A-107 and a portion of the printout is shown in Figure A-108. Some of the equivalent symbols are shown above. After some trials, DTMIN was set at 0.01, while both DTMAX and DT were set at .05. Card outputs were also obtained by using PLO statement (see Figure A-107) for offline plotting.

The system input was chosen to be three tone bursts long. Particular values as used in this example for the three input frequencies are 1.6, 2.3, and 3.0 kc. In terms of kiloradians these are approximately 10.05, 14.45, and 18.85. All of the system parameters were chosen to match an existing hardware model and are shown on the computer printout. The radian frequency OMEGA3 which appears in the FM to AM converter is set such that the overdamped second order has real roots OMEGA1 and OMEGA2.

MIMIC SOURCE-LANGUAGE PROGRAM

SIGNAL BURST PROCESSOR

3 BURSTS - FREQUENCIES WS1, WS2, WS3
 PROCESSING BLOCKS - $S / (S^2 + 2 * ZETA1 * OMEGA1 * S + OMEGA1^2)$
 PROCESSING BLOCKS - FULL WAVE RECTIFIER = ABS VALUE
 PROCESSING BLOCKS - $KA / (1. + TAU * S)$
 PROCESSING BLOCKS - $KB * (S / OMEGA1) / (1. + S / OMEGA1)$
 UNITS ARE MS, KC, KILOBYTES

CON(A, T1, T2, T3)
 CON(ZETA1, OMEGA1, ZETA2, OMEGA2, ZETA3, OMEGA3)
 CON(KA, TAU, KB, OMEGA1)
 PAR(WS1, WS2, WS3)
 PAR(DT, DTMAX, DTMIN)

SOLVE EQUATIONS

A11 FSW(T, C., C., A)
 A12 FSW(T-T1, C., C., A)
 A1 SUB(A11, A12)
 A21 FSW(T-T1, C., C., A)
 A22 FSW(T-T2, C., C., A)
 A2 SUB(A21, A22)
 A31 FSW(T-T2, C., C., A)
 A32 FSW(T-T3, C., C., A)
 A3 SUB(A31, A32)
 SIGNAL A1 * SIN(WS1 * T) + A2 * SIN(WS2 * T) + A3 * SIN(WS3 * T)
 X1 SIGNAL
 IXX1 INT(OMEGA1 * OMEGA1 * X1)
 DXX1 X1 - 2. * ZETA1 * OMEGA1 * X1 - IXX1
 XX1 INT(DXX1)
 IXXX1 INT(OMEGA2 * OMEGA2 * XXX1)
 DXXX1 XXX1 - 2. * ZETA2 * OMEGA2 * XXX1 - IXXX1
 XXX1 INT(DXXX1)
 IX2 INT(OMEGA3 * OMEGA3 * X2)
 DX2 XXX1 - 2. * ZETA3 * OMEGA3 * X2 - IX2
 X2 INT(DX2)
 X3 ABS(X2)
 X3P MPY(X3, KA)
 X4 FTR(X3P, TAU)
 IX5 INT(OMEGA1 * X5)
 X4P MPY(X4, KB)
 X5 SUB(X4P, IX5)

FINISH STATEMENTS

FIN(T, 60.)
 FIN(X2, 50.)
 FIN(X5, 50.)

PUNCH CARDS FOR OUTPUT

PLO(T, X1, X2, X3, X4, X5)
 END

SORT DIAGNOSTICS FOLLOW

Figure A-107-Mimic program.

WS1	WS2	WS3	DT	DTMAX	DTMIN	X1 VOLTS	X2 VOLTS	X3 VOLTS	X4 VOLTS
1.00531E 01	1.44513E 01	1.88496E 01							
DT	DTMAX	DTMIN							
5.00000E-02	5.00000E-02	10.00000E-03							
TIME									
MS									
0.									
5.00000E-02	4.81754E 00	1.13023E-05							
1.00000E-01	8.44328E 00	5.66836E-05							
1.50000E-01	9.98027E 00	5.12115E-05							
2.00000E-01	9.04827E 00	-4.42119E-05							
2.50000E-01	5.87785E 00	-1.37504E-04							
3.00000E-01	1.25333E 00	-1.34984E-04							
3.50000E-01	-3.68125E 00	-4.24749E-05							
4.00000E-01	-7.70513E 00	6.58928E-05							
4.50000E-01	-9.82287E 00	1.27834E-04							
5.00000E-01	-9.51057E 00	1.29953E-04							
5.50000E-01	-6.84547E 00	9.22986E-05							
6.00000E-01	-2.48690E 00	3.93811E-05							
6.50000E-01	2.48690E 00	-1.36696E-05							
7.00000E-01	6.84547E 00	-5.91144E-05							
7.50000E-01	9.51057E 00	-9.08177E-05							
8.00000E-01	9.82287E 00	-1.02607E-04							
8.50000E-01	7.70513E 00	-9.07211E-05							
9.00000E-01	3.68125E 00	-5.67175E-05							
9.50000E-01	-1.25333E 00	-8.22850E-06							
10.00000E-01	-5.87785E 00	4.28268E-05							
1.05000E 00	-9.04827E 00	8.35557E-05							
1.10000E 00	-9.98027E 00	1.03616E-04							
1.15000E 00	-8.44328E 00	9.79239E-05							
1.20000E 00	-4.81754E 00	6.78952E-05							
1.25000E 00	-6.03497E-06	2.10243E-05							
1.30000E 00	4.81753E 00	-3.10359E-05							
1.35000E 00	8.44328E 00	-7.53863E-05							
1.40000E 00	9.98027E 00	-1.01063E-04							
1.45000E 00	9.04827E 00	-1.01731E-04							
1.50000E 00	5.87786E 00	-7.72390E-05							
1.55000E 00	1.25334E 00	-3.36469E-05							
1.60000E 00	-3.68124E 00	1.82635E-05							
1.65000E 00	-7.70513E 00	6.56563E-05							
1.70000E 00	-9.82287E 00	9.68088E-05							
1.75000E 00	-9.51057E 00	1.04014E-04							
1.80000E 00	-6.84548E 00	8.54878E-05							
1.85000E 00	-2.48691E 00	4.58131E-05							
1.90000E 00	2.48689E 00	-5.19567E-06							

Figure A-108--Part of printout.

Results and Remarks

The simulation showed the result as expected, giving a rather noisy pulse on the output. The noise is not just a single frequency reflection of the input frequency, but is a combination of higher harmonics due to the full wave rectification. It was intended to add random noise to the input signal, and a Monte Carlo study might be performed to optimize some of the system parameters. However, this problem resulted in longer execution times than hoped for. Also since Monte Carlo methods are considered dubious, that type of study was not recommended although a study of selected parameter changes with noise would probably be worthwhile.

A typical run of 3 bursts, each 40 ms long, took approximately 4 minutes of execution time. Since the effects of the frequency changes settled out after about 15 ms, the bursts were shortened to 20 ms duration, thus halving the execution time. The cause of the long run times was simply that many cycles of the input signal were processed, and execution time is directly proportional to the highest system natural frequency, the highest forcing function frequency, and the number of cycles to be processed. In this case, for a 3.1 kc signal, 40 ms represents 124 cycles.

To adequately display the signal waveforms, points had to be plotted (or printed) every 0.05 ms which resulted in rather long printouts. Here again however the difficulties are inherent in this type of problem and are not due to Mimic.

DEFECTS STUDY IN SEMICONDUCTORS BY ENERGETIC RADIATION (EXAMPLE 13)

Martin M. Sokoloski

Problem Description

When energetically charged particles such as electrons and protons bombard a solid, they knock out atoms that are located systematically on so-called lattice sites. The resultant damage then consists of an empty lattice site, called a vacancy position, and an atom now located in a "non-lattice site", or an interstitial position. Being possibly the most basic defects in solids, these vacancies and interstitials, created in pairs, are capable of migrating throughout the lattice, and upon meeting annihilate each other (the vacancy and interstitial position disappear leaving an atom at a regular lattice site). However, in elemental semiconductors, such as silicon and germanium, these basic defects can form more complicated defects at a later time. For instance, two vacancies can meet and form a divancy, or a vacancy in wandering can meet an immobile impurity, i.e. an oxygen atom in silicon, and become trapped by it. The divancy and resultant vacancy-impurity defect are all second generation defects in that a basic defect (vacancy) is needed for their formation. Different combinations of defects can form higher order defects, escalating the hierarchy of defect structures ad infinitum.

The following chemical kinetic model describes a prevalent type of radiation damage usually encountered in semiconductors, particularly Silicon:



Reaction (57) represents the creation of the basic vacancy-interstitial pairs by some source term, i.e., outer space radiation or an accelerator on earth. Reaction (58) is the annihilation vacancies and interstitials that change to meet, while (59) and (60) represent the trapping of vacancies by two different impurities, I_1 and I_2 . The arrows running from the right to the left represent reversible reactions in which the defect is capable of breaking into its reactants. The K_i 's are just constants which tell how fast the reaction proceeds.

Mathematical Model

The differential equations for the time rate of change of the defects can be written by using the chemical laws of mass action:

$$\frac{dV}{dt} = -K_1 V^2 - (K_2 I_{10} + K_4 I_{20}) V + (K_2 - K_1) VC_1 + (K_4 - K_1) VC_2 + K_3 C_1 + K_5 C_2 + K_0 \varphi \quad (61)$$

$$\frac{dC_1}{dt} = K_2 I_{10} V - K_2 VC_1 - K_3 C_1 \quad (62)$$

$$\frac{dC_2}{dt} = K_4 I_{20} V - K_4 VC_2 - K_5 C_2 \quad (63)$$

The differential equation for i has been eliminated by the relationship, $i = V + (C_1 - C_2)$, also $I_1 = I_{10} + C_1$ and $I_2 = I_{20} - C_2$, where I_{10} and I_{20} are the initial impurity concentrations at $t = 0$. The K_i 's are given by the following equation whose constants are all known:

$$K_i = \gamma_i \nu_i \exp(-E_i/kT) \quad (64)$$

Constants, Parameters, and Initial Conditions

The values of the constants used in the program are,

$$\gamma_1 = G1 = 26$$

$$\gamma_2 = G2 = 26$$

$$\gamma_3 = G3 = 7$$

$$\gamma_4 = G4 = 26$$

$$\gamma_5 = G5 = 7$$

$$\nu_i = N_i = 7.63 \times 10^{12} \text{ per sec for } i = 1, 2, \dots, 5$$

$$k = KS = 8.6165 \times 10^{-5}$$

$$K_{0\phi} = KOP = 7.5358 \times 10^{-10}$$

$$I_{10} = I_{20} = 2.0 \times 10^{-5}$$

$$E_1 = 0.06$$

$$E_2 = 0.20$$

$$E_3 = 1.30$$

$$E_4 = 0.30$$

$$E_5 = 0.93$$

The values of the parameter are,

$$T = 225^\circ, 250^\circ, 275^\circ, 300^\circ, 325^\circ \text{ K}$$

The values of the initial conditions are (at $t = 0$),

$$X(0) = .01 \times KOP$$

$$Y(0) = Z(0) = .001 \times KOP$$

The Mimic Program

The Mimic program specifies the equations (61) through (64) together with the above values of constants, parameters, and initial conditions. The program is shown in Figure A-109 and a portion of the printout is shown in Figure A-110. A log-log plot of the result is shown in Figure A-111.

MIMIC SOURCE-LANGUAGE PROGRAM

DEFECTS STUDY IN SEMICONDUCTORS BY ENERGETIC RADIATION

```

CON(G1,G2,G3,G4,G5)
CON(N1,N2,N3,N4,N5)
CON(KS,KOP)
CON(E1,E2,E3,E4,E5)
CON(I10,I20)
PAR(TEMP)

C1      DT      = .0001
C2      DT      = .001
C3      DT      = .01
C4      DT      = .1
C1      C1      = C1
D2      = AND(C2,NOT(C1))
C3      = AND(C3,NOT(C1),NOT(C2))
D4      = AND(C4,NOT(C1),NOT(C2),NOT(C3))
C1      = FSW(T-.001,TRUE,FALSE,FALSE)
C2      = FSW(T-.01,TRUE,FALSE,FALSE)
C3      = FSW(T-.1,TRUE,FALSE,FALSE)
C4      = FSW(T-1.,TRUE,FALSE,FALSE)
X0      = .01*KOP
Y0      = .001*KOP
Z0      = Y0
1DX     = A11*X+A12*X+A13*X*Y+A14*X*Z+KOP-B13*Y-C13*Z
1DY     = B11*X+B12*X*Y+B13*Y
1DZ     = C11*X+C12*X*Z+C13*Z
X       = INT(1DX,X0)
Y       = INT(1DY,Y0)
Z       = INT(1DZ,Z0)
A11     = -K1
A12     = -B11-C11
A13     = K2-K1
A14     = K4-K1
B11     = K2*I10
B12     = -K2
B13     = -K3
C11     = K4*I20
C12     = -K4
C13     = -K5
C       = KS*TEMP
K1      = +G1*N1*EXP(-E1/D)
K2      = +G2*N2*EXP(-E2/D)
K3      = +G3*N3*EXP(-E3/D)
K4      = +G4*N4*EXP(-E4/D)
K5      = +G5*N5*EXP(-E5/D)
RATE1   = 1DY/KOP
RATE2   = 1DZ/KOP
PRINT   = FSW(T,TRUE,TRUE,FALSE)
        FIN(T,1.)
        HDR(K1,K2,K3,K4,K5)
        OUT(K1,K2,K3,K4,K5)
        HDR
        HDR(T,X,Y,Z,RATE1,RATE2)
        OUT(T,X,Y,Z,RATE1,RATE2)
        END

```

PRINT

SORT DIAGNOSTICS FOLLOW

Figure A-109-Mimic program.

TEMP	K1	K2	K3	K4	K5
2.25C00E 02	8.98312E 12	6.56541E 09	4.03728E-16	3.77697E 07	7.84377E-08
	T	X	Y	Z	RATE1
0.	0.	7.53580E-10	7.53580E-11	7.53580E-11	1.313C8E 03
10.00C00E-05	5.39413E-13	7.88729E-10	7.88729E-10	7.94619E-11	9.39867E-01
2.00C00E-04	5.38595E-13	7.95802E-10	7.95802E-10	7.95026E-11	9.38442E-01
3.00C00E-04	6.25179E-13	8.02791E-10	8.02791E-10	7.95428E-11	1.08931E 00
4.00C00E-04	5.38080E-13	8.09939E-10	8.09939E-10	7.95840E-11	9.37544E-01
5.00C00E-04	5.37800E-13	8.17003E-10	8.17003E-10	7.96246E-11	9.37057E-01
6.00C00E-04	5.37023E-13	8.24063E-10	8.24063E-10	7.96652E-11	9.35702E-01
7.00C00E-04	5.37326E-13	8.31120E-10	8.31120E-10	7.97058E-11	9.36229E-01
8.00C00E-04	5.37104E-13	8.38174E-10	8.38174E-10	7.97464E-11	9.35842E-01
9.00C00E-04	5.33198E-13	8.45228E-10	8.45228E-10	7.97870E-11	9.29036E-01
10.00C00E-04	5.36467E-13	8.52272E-10	8.52272E-10	7.98275E-11	9.34731E-01
2.00C00E-03	5.34163E-13	9.22572E-10	9.22572E-10	8.02319E-11	9.30714E-01
3.00C00E-03	5.31827E-13	9.92557E-10	9.92557E-10	8.06345E-11	9.26640E-01
4.00C00E-03	5.29487E-13	1.06223E-09	1.06223E-09	8.10353E-11	9.22561E-01
5.00C00E-03	5.27132E-13	1.13160E-09	1.13160E-09	8.14344E-11	9.18453E-01
6.00C00E-03	5.24280E-13	1.20066E-09	1.20066E-09	8.18317E-11	9.13482E-01
7.00C00E-03	5.97632E-13	1.26936E-09	1.26936E-09	8.22269E-11	1.04128E 00
8.00C00E-03	5.20342E-13	1.33790E-09	1.33790E-09	8.26211E-11	9.06614E-01
9.00C00E-03	5.18108E-13	1.40608E-09	1.40608E-09	8.30134E-11	9.02719E-01
1.00C00E-02	5.15633E-13	1.47397E-09	1.47397E-09	8.34039E-11	8.98403E-01
2.00C00E-02	4.95153E-13	2.13782E-09	2.13782E-09	8.72230E-11	8.62691E-01
3.00C00E-02	4.77448E-13	2.77645E-09	2.77645E-09	9.08970E-11	8.31819E-01
4.00C00E-02	4.60645E-13	3.39253E-09	3.39253E-09	9.44415E-11	8.02519E-01
5.00C00E-02	4.43806E-13	3.98830E-09	3.98830E-09	9.78691E-11	7.73160E-01
6.00C00E-02	4.33224E-13	4.56562E-09	4.56562E-09	1.01191E-10	7.54702E-01
7.00C00E-02	4.20250E-13	5.12613E-09	5.12613E-09	1.04416E-10	7.32081E-01
8.00C00E-02	4.07320E-13	5.67121E-09	5.67121E-09	1.07552E-10	7.09536E-01
9.00C00E-02	4.01135E-13	6.20206E-09	6.20206E-09	1.10607E-10	6.98744E-01
1C.00C00E-02	3.89652E-13	6.71975E-09	6.71975E-09	1.13586E-10	6.78725E-01
1.10000E-01	3.80965E-13	7.2521E-09	7.2521E-09	1.16494E-10	6.63576E-01
2.10C00E-01	3.23864E-13	1.17529E-08	1.17529E-08	1.42547E-10	5.63988E-01
3.10C00E-01	2.70083E-13	1.56107E-08	1.56107E-08	1.64748E-10	4.70241E-01

Figure A-110-Portion of printout.

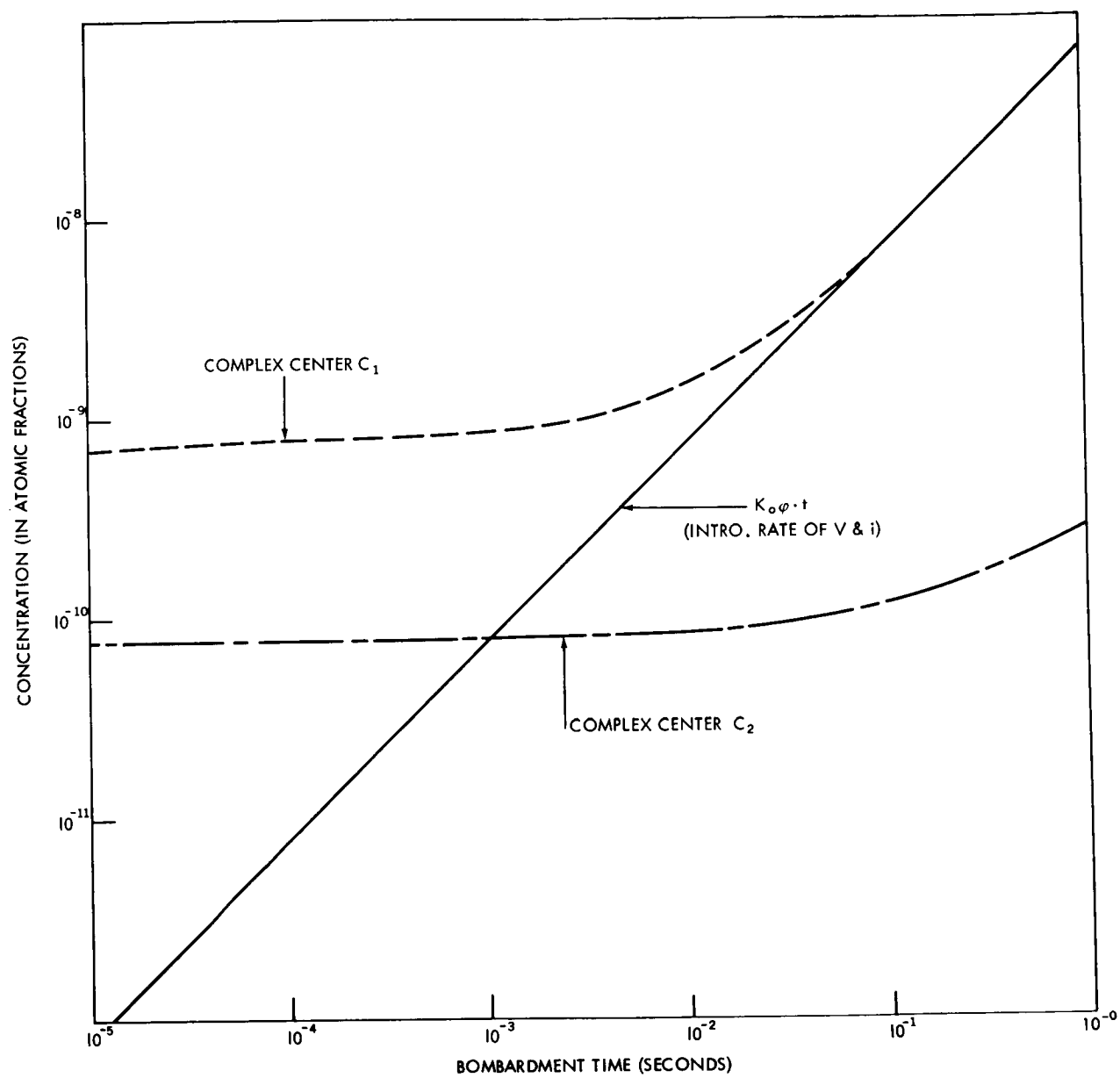


Figure A-111—Graph of result.

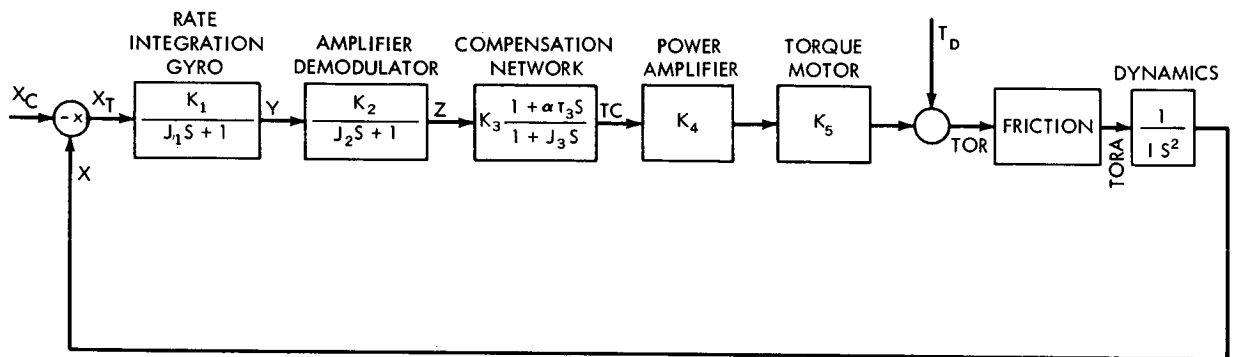
SATELLITE ROLL AXIS CONTROL SYSTEM (EXAMPLE 14)

R. V. Welch

Problem Description

A control system is needed to drive a satellite to any commanded position up to 1° and to hold within 60 arc-sec of that position with jitter rates of 1 arc-sec/sec or less. The roll axis is to be controlled.

The roll axis is controlled through a position servo loop. A high grade rate integrating gyro coupled with a dc direct drive torque motor are used for the attitude position reference and control actuator. The gyro output is ac amplified, demodulated and fed to the compensation network. This output is amplified and supplied to the torque motor. The block diagram is shown in Figure A-112.



NOTE: $K = K_1 \cdot K_2 \cdot K_3 \cdot K_4 \cdot K_5 = 1510 \text{ ft.} \cdot \text{lb/rad.} = .0073 \text{ ft.} \cdot \text{lb/arc-sec}$
 $I = 200 \text{ Slug} \cdot \text{ft}^2$
 $\tau_1 = .006 \text{ SEC}$
 $\tau_2 = .01 \text{ SEC}$
 $\tau_3 = .0555 \text{ SEC}$
 $\alpha = 10.$

Figure A-112—Block diagram of control system.

The transfer function for the integrating rate gyro to be used is:

$$\frac{V}{\theta} = \frac{14.6}{1 + .006 S} \quad (65)$$

The transfer function for the AC amplifier and demodulator is:

$$\frac{V}{V} = \frac{1000}{1 + .01 S} \quad (66)$$

The compensation network

$$\frac{V}{V} = .1 \frac{1 + .555 S}{1 + .0555 S} \quad (67)$$

is used since it gives a phase margin of 50° at the 4.5 rad/sec crossover frequency. The torque motor selected is a 1.0 ft-lb direct drive torque motor requiring 15 volts and 5.55 amps max. With a dc resistance of 2.1 ohms the motor transfer function is:

$$T = .067V - .24 \ddot{\theta} \quad (68)$$

Since the maximum rate, $\dot{\theta}$, is to be less than 3 arc-min/sec or 3.6×10^{-4} rad/sec, this term can be ignored; hence

$$T = .067V \quad (69)$$

The satellite dynamics are assumed to be

$$\frac{\theta}{T} = \frac{1}{200S^2} \quad (70)$$

To determine the overall gain of the system, a static friction torque of 0.22 ft-lbs is assumed and for 1 arc-min excursions a torque sensitivity of $K_T = 1510$ ft-lb/rad is required. Therefore the system gain is

$$G = \frac{1510}{200} = 7.5; \quad (71)$$

and the system open loop equation is;

$$G = \frac{7.5 (1 + .555S)}{S^2 (1 + .006S) (1 + .01S) (1 + .0555S)} \quad (72)$$

Static and coulomb friction are to be included. Table A-15 is used to determine which value of torque (TORA in Figure A-112) is required and when. In this table ω is the velocity of the satellite.

Table A-15
Torque Values

TOR	ω	TORA
< fs	0	0
> fs	0	fs + TOR
< fc	$\neq 0$	fc + TOR
> fc	$\neq 0$	fc + TOR

The coulomb friction torque f_c and static friction torque f_s are defined below,

$$f_c = - |f_c| (\omega / |\omega|) \quad (73)$$

$$f_s = - |f_s| (TOR / |TOR|) \quad (74)$$

Other equations to be used are:

$$\ddot{X} = -(A) \text{ TOR}/I \quad (75)$$

$$X_T = X - X_C \quad (76)$$

$$X = \ddot{X} \quad (77)$$

$$\dot{Y} = (X_T - Y)/\tau_1 \quad (78)$$

$$Z = (Y - Z)/\tau_2 \quad (79)$$

$$T_C = (Z - T_C)/\tau_3 + \alpha \dot{Z} \quad (80)$$

$$\text{TOX} = K_1 * K_2 * K_3 * K_4 * K_5 * T_C + T_D = K T_C + T_D \quad (81)$$

$$\text{TOR} = \begin{cases} +1 & \text{TOX} > 1.0 \\ \text{TOX} & 1.07 \text{ TOX} > -1.0 \\ -1 & \text{TOX} < -1.0 \end{cases}$$

Constants

The numerical constants to be used for computation are,

$$K = K_1 * K_2 * K_3 * K_4 * K_5 = .0073 \text{ ft-lb/arc-sec}$$

$$I = 200 \text{ slug-ft}^2$$

$$\tau_1 = .006 \text{ sec}$$

$$\tau_2 = 0.01 \text{ sec}$$

$$\tau_3 = 0.0555 \text{ sec}$$

$$\alpha = 10$$

$$f_c = 0.1 \text{ ft-lb}$$

$$f_s = 0.2 \text{ ft-lb}$$

$$T_D = 0$$

The Mimic Program

The Mimic program, Figure A-113, can be separated into 4 parts. Part I is a logic part used to eliminate a zero/zero situation. Part II is the program of equations (67) through (76). In Part III the friction is taken into account. This part was written by the following logic.

Let

$$C = f_s + \text{TOR}$$

$$D = f_c + \text{TOR}$$

$$B = 1DX = \omega$$

$$A = TOR = \begin{cases} 0 & TOR < fs, \quad TOR < fc \\ 1 & TOR > fs, \quad TOR > fc \end{cases}$$

MIMIC SOURCE-LANGUAGE PROGRAM

			COM(EPS,A,D,C,EPS2)
			COM(T1,T2,T3,ALPHA,K,I)
			PAR(AFS,AFC,XC,TD)
		DD	ABS(1DX)
I		L1	FSH(1DX,FALSE,TRUE,FALSE)
		L2	NOT(L1)
		L3	FSH(TOR,FALSE,TRUE,FALSE)
		L4	NOT(L3)
	L1	FC	B
	L2	FC	-AFC*(1DX/DD)
	L3	FS	B
	L4	FS	-AFS*(TOR/ABS(TOR))
<hr/>			
		2DX	-A*TORA/I
		1DX	INT(2DX,0.)
		XT	X-XC
		X	INT(1DX,0.)
		1DY	(XT-Y)/T1
II		Y	INT(1DY,0.)
		1DZ	(Y-Z)/T2
		Z	INT(1DZ,0.)
		TC	INT(1DTC,0.)
		1DTC	(Z-TC)/T3+ALPHA*1DZ
		TOX	K*TC+TD
		TOR	LIE(TOX,-1.,+1.)
<hr/>			
		A1	FSH(TOR+FS,FALSE,FALSE,TRUE)
		A2	NOT(A1)
		B1	FSH(1DX,TRUE,FALSE,TRUE)
		B2	NOT(B1)
III		C1	AND(A1,B2)
		E1	AND(A2,B2)
	B1	TORA	TOR+FC
	C1	TORA	TOR+FS
	E1	TORA	B
		TRA	TORA-TOR
<hr/>			
		F1	FSH(DD-EPS2,TRUE,TRUE,FALSE)
		DELX	ABS(X-XC)
		G1	FSH(DELX-EPS,TRUE,FALSE,FALSE)
		H1	AND(F1,G1)
		H2	NOT(H1)
IV	H1	ED	C
	H2	ED	B
			FIN(ED,1.)
			FIN(T,24.)
			HDR(TIME,FRICTION,X,XDOT,TORQUE,LEAD)
			HDR
			OUT(T,TRA,X,1DX,TORA,TC)
			END

SORT DIAGNOSTICS FOLLOW

Figure A-113-Mimic program.

AFS	AFS	AFS	XC	TD	TORQUE
TIME	ICION	X	XDOT		
2.00000E-01	1.00000E-01	6.00000E 01	0.	0.	0.
0.	0.	0.	0.	0.	-1.10000E 00
1.00000E-01	-10.00000E-02	5.22268E 00	1.08760E 02	1.65554E 02	-8.99697E-02
2.00000E-01	-10.00000E-02	1.98793E 01	1.65554E 02	1.53297E 02	2.54881E-01
3.00000E-01	-1.00000E-01	3.61112E 01	1.22148E 02	8.95097E 01	3.24748E-01
4.00000E-01	-1.00000E-01	4.99411E 01	6.11669E 01	3.86369E 01	3.00647E-01
5.00000E-01	-1.00000E-01	6.05024E 01	7.29312E 01	2.17983E 01	2.47599E-01
6.00000E-01	-1.00000E-01	7.79904E 01	7.59081E 01	9.90466E 00	1.90195E-01
7.00000E-01	-1.00000E-01	7.29312E 01	7.74559E 01	2.01755E 00	1.38025E-01
8.00000E-01	-1.00000E-01	7.59081E 01	7.80226E 01	-1.57901E 01	9.44670E-02
9.00000E-01	-1.00000E-01	7.74559E 01	7.75381E 01	-3.41892E 01	6.02012E-02
1.00000E 00	1.00000E-01	7.80226E 01	7.49643E 01	-4.36221E 01	2.20275E-01
1.10000E 00	1.00000E-01	7.75381E 01	7.10032E 01	-4.57550E 01	1.34105E-01
1.20000E 00	1.00000E-01	7.49643E 01	6.64837E 01	-4.30281E 01	5.22424E-02
1.30000E 00	1.00000E-01	7.10032E 01	6.20138E 01	-3.75742E 01	-6.73921E-03
1.40000E 00	1.00000E-01	6.64837E 01	5.45364E 01	-3.09771E 01	-4.27336E-02
1.50000E 00	1.00000E-01	6.20138E 01	5.17753E 01	-2.42962E 01	-6.06118E-02
1.60000E 00	1.00000E-01	5.45364E 01	4.96584E 01	-1.81701E 01	-6.58246E-02
1.70000E 00	1.00000E-01	5.17753E 01	4.81117E 01	-1.29253E 01	-6.29153E-02
1.80000E 00	1.00000E-01	4.96584E 01	4.70400E 01	-5.39203E 00	-5.55253E-02
1.90000E 00	1.00000E-01	4.81117E 01	4.59327E 01	-2.97698E 00	-4.61472E-02
2.00000E 00	1.00000E-01	4.70400E 01	4.57248E 01	-1.29207E-03	-3.64519E-02
2.10000E 00	1.00000E-01	4.59327E 01	4.56534E 01	-1.83461E-01	-2.74508E-02
2.20000E 00	1.00000E-01	4.57248E 01	4.62833E 01	1.59343E 01	-1.96764E-02
2.30000E 00	1.00000E-01	4.56534E 01	4.87025E 01	3.11749E 01	-1.33285E-02
2.40000E 00	1.00000E-01	4.62833E 01	5.22606E 01	3.87899E 01	-8.39536E-03
2.50000E 00	1.00000E-01	4.87025E 01	5.62538E 01	4.02184E 01	-1.83400E-01
2.60000E 00	-10.00000E-02	5.22606E 01	6.01653E 01	3.75567E 01	-1.10071E-01
2.70000E 00	-10.00000E-02	5.62538E 01	6.36902E 01	2.67902E 01	-4.05414E-02
2.80000E 00	-1.00000E-01	6.01653E 01	6.66845E 01	2.67902E 01	9.29207E-03
2.90000E 00	-1.00000E-01	6.36902E 01	6.90481E 01	2.09332E 01	3.94133E-02
3.00000E 00	-1.00000E-01	6.66845E 01	7.08687E 01	1.55959E 01	5.40588E-02
3.10000E 00	-1.00000E-01	6.90481E 01	7.21937E 01	1.10477E 01	5.79118E-02
3.20000E 00	-1.00000E-01	7.08687E 01	7.31076E 01	4.55163E 00	5.49596E-02
3.30000E 00	-1.00000E-01	7.21937E 01	7.36972E 01	2.48155E 00	4.82458E-02
3.40000E 00	-1.00000E-01	7.31076E 01	7.40431E 01	1.04194E 00	3.99184E-02
3.50000E 00	-1.00000E-01	7.36972E 01	7.42145E 01	1.02889E-01	3.14010E-02
3.60000E 00	-1.00000E-01	7.40431E 01	7.42681E 01	-1.73367E 01	2.35737E-02
3.70000E 00	10.00000E-02	7.42681E 01	7.35108E 01	-3.19400E 01	1.68364E-02
3.80000E 00		7.35108E 01	7.09826E 01		1.13558E-02
3.90000E 00		7.09826E 01			7.09044E-03
4.00000E 00					1.77955E-01
4.10000E 00					1.03844E-01
4.20000E 00					

Figure A-114-Portion of printout.

A	B	C	D
0	0	0	0
1	0	1	0
0	1	0	1
1	1	0	1

$$C = A \cap \bar{B}$$

$$D = B$$

$$\therefore \text{TORA} = 0 \text{ when } \bar{A} \cap \bar{B} \text{ is true}$$

$$\text{TORA} = C \text{ when } \bar{A} \cap \bar{B} \text{ is true}$$

$$\text{TORA} = D \text{ when } B \text{ is true}$$

In Part IV, more logic is required to test for the end of a run and to print the outputs. The run is to be considered over when $\dot{x} < 0.1$ arc-sec/sec and $x_T < 16$ arc-sec. The outputs wanted are time, friction, x , \dot{x} , torque (TORA), and the compensation network output (TC).

Other constants used in the Mimic program are,

$$B = 0$$

$$C = 1$$

$$A = 2.06 \times 10^5 \text{ (used so that all calculations were in arc-sec)}$$

$$\text{Eps} = 16$$

$$\text{Eps2} = 0.1$$

Table A-16
Equivalent Symbols

Program Symbols	Equation Symbols
AFC, AFS	$= f_c, f_s$
1DX	$= \omega$
2DX	$= \ddot{x}$
XT, XC	$= x_T, x_C$
T1, T2, T3	$= \tau_1, \tau_2, \tau_3$
ALPHA	$= \alpha$
1DZ, 1DY	$= \dot{z}, \dot{y}$
TC, TD	$= T_c, T_d$

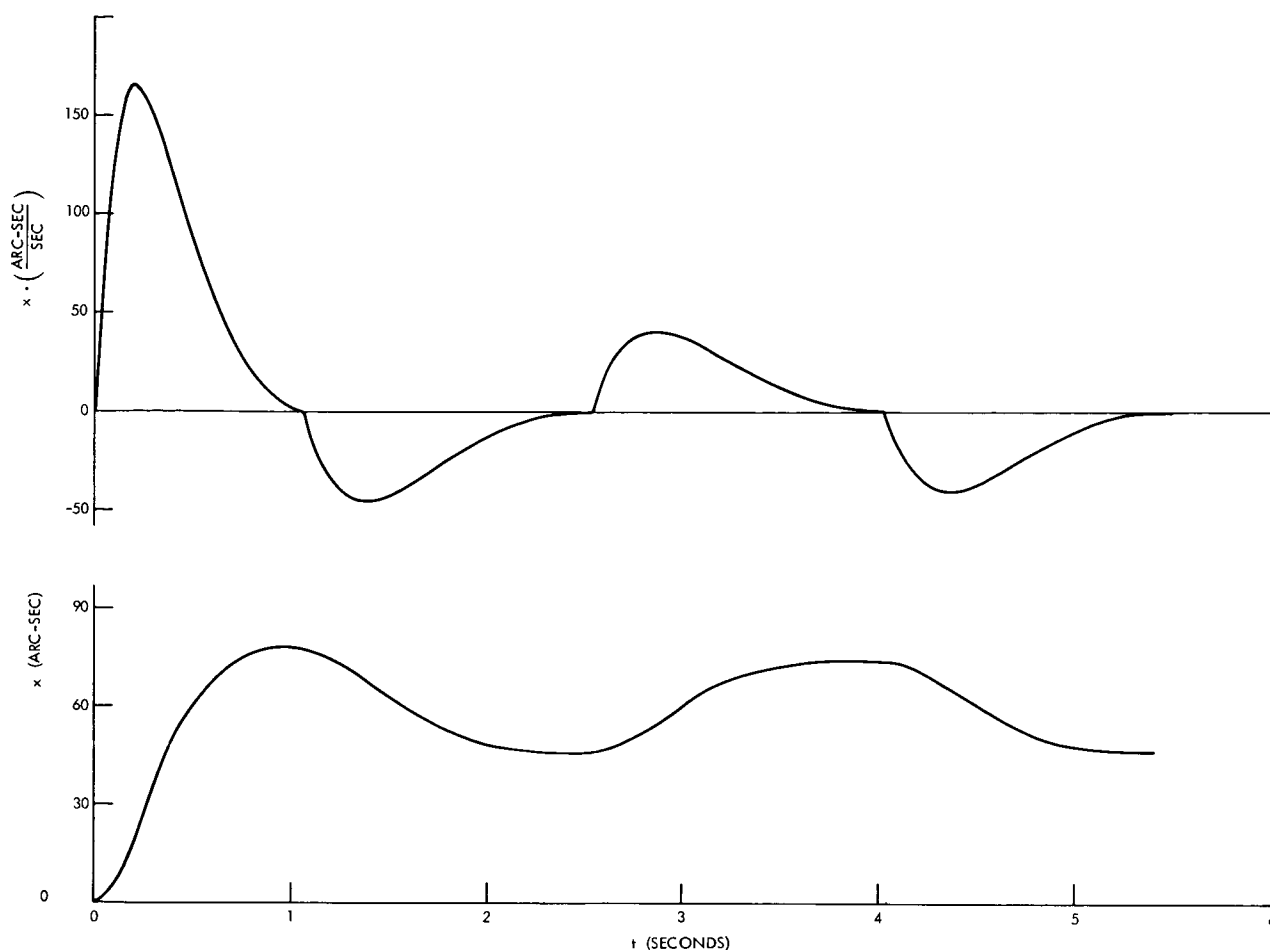


Figure A-115—Plot of response.

For convenience in reading the names of the Mimic program, equivalent symbols are provided in Table A-16.

RESULT

A portion of the printout from the Mimic program is shown in Figure A-114. Figure A-115 shows the plot of the response for the output x and \dot{x} when the input is a 60 seconds in angular position.

The results of the Mimic program were compared with those from an analog computer. The two programs gave identical outputs with comparable running times — assuming the analog computer to run at a real time speed. The integration time needed on the analog computer was 60 seconds as compared to 84 seconds for the digital computer.

The overall time for programming and running the problem was in favor of the analog computer. On the analog computer it took approximately two days to get results as compared with 4-5 days on the digital computer. This was mainly due to turn around time on the digital machine.

DYNAMIC ANALYSIS OF APPENDAGE DEPLOYMENT OF A SPINNING SPACECRAFT **(EXAMPLE 15) George Honeycutt**

Problem Description

Many of the smaller spacecraft being launched today have folded appendages to enable them to fit inside the limited shroud space during launch. They also frequently use spin stabilization during the final stage prior to injection into orbit. Thus, after launch, the appendages are released and the centrifugal force pulls them out away from the spacecraft until they are locked into place. During this short period of deployment, the appendages experience forces and accelerations while at the same time the complete assembly despins. If the appendages consist of a relatively heavy mass attached to the end of a very light, folded boom, then the mass will remain in a plane and the problem can be reduced to the one shown in Figure A-116.

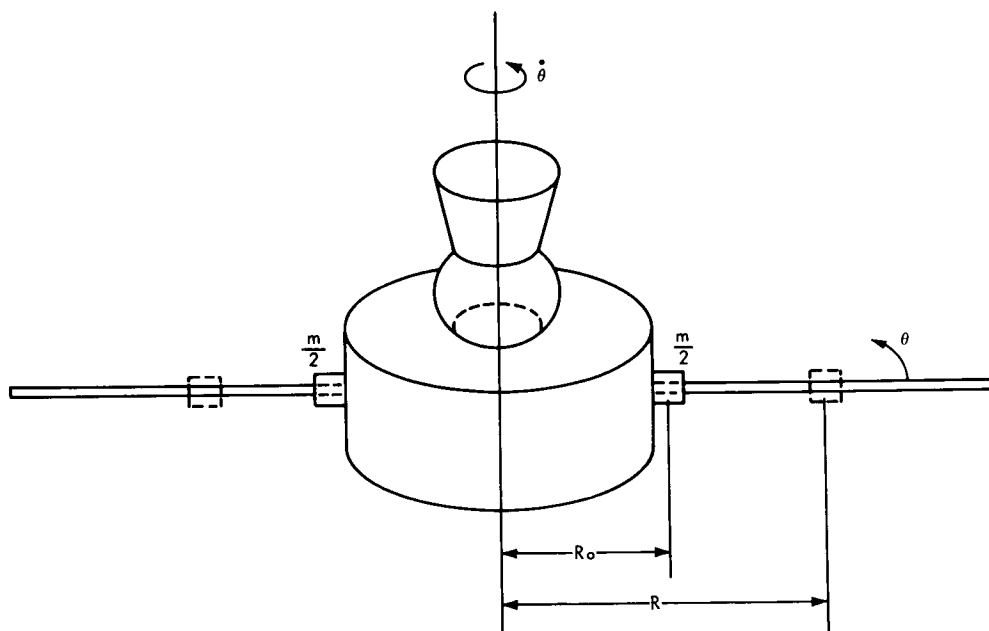


Figure A-116—Spacecraft geometry.

In Figure A-116, the spacecraft is shown with two diametrically opposed booms with two sliding weights initially secured at $R(0)$. The weights are assumed to slide frictionlessly on the booms. The spacecraft has constant moment of inertia I and an initial spin rate $\dot{\theta}(0)$.

Equations of Motions

The equations of the motion of the masses are:

$$\ddot{R} = R(\dot{\theta})^2 \quad (82)$$

$$\ddot{\theta} = -\frac{2MR\dot{\theta}}{I + MR^2} \quad (83)$$

where

R = Radial distance to weights

\dot{R} = Radial velocity of weights

\ddot{R} = Radial acceleration of weights

$\dot{\theta}$ = Angular velocity

$\ddot{\theta}$ = Angular acceleration

M = Combined mass of both weights

I = Moment of inertia of spacecraft.

The Mimic Program

The program is to compute the radial distance, radial velocity, radial acceleration, angular velocity, and angular acceleration by using equations (82) and (83). The following values of the constants and initial values are chosen:

$M = 0.25$ slugs

$I = 10.5$ slug-ft²

$R(0) = 1$ foot

$\dot{\theta}(0) = 4.85$ radians/second

$\theta(0) = 0$ radians

$\dot{R}(0) = 0$ feet/second

It is required to compute until the time is 2 seconds.

The program is shown in Figure A-117. Since the symbols in the program and those in the equations are easily recognizable, no table of equivalent symbols is provided. The results for radial distance, velocity, acceleration and angular velocity are shown in Figure A-118.

```
***MIMIC SOURCE-LANGUAGE PROGRAM***  
  
*  
SPINNING BODY WITH SLIDING WEIGHTS - G. MCNEYCUTT  
      CON(M,I,DT)  
      ZDR  = R*10TH*10TH  
      1DR  = INT(2DR,0.)  
      R    = INT(1DR,1.)  
      A    = -2.*M*R/(I+M*R*R)  
      ZDTH = A*10TH*1DR  
      1DTH = INT(2DTH,4.85)  
      TH   = INT(1DTH,0.)  
      FIN(T,2.)  
      HDR(TIME,R,RDOT,RDDOT,THDOT,THDDOT)  
      HDR  
      OUT(T,R,1DR,ZDR,1DTH,2DTH)  
      END  
  
***SORT DIAGNOSTICS FOLLOW***
```

Figure A-117-Mimic program.

TIME	R	RDOT	RDDOT	THDOT
0.00000E-02	1.00000E 00	0.	2.35225E 01	4.85000E 00
0.00000E-01	1.02953E 00	1.18653E 00	2.41498E 01	4.84325E 00
1.00000E-01	1.11970E 00	2.43587E 00	2.60301E 01	4.82155E 00
1.50000E-01	1.27521E 00	3.61014E 00	2.91411E 01	4.78039E 00
2.00000E-01	1.50380E 00	5.36897E 00	3.33856E 01	4.711178E 00
2.50000E-01	1.81624E 00	7.16326E 00	3.84935E 01	4.60396E 00
3.00000E-01	2.22458E 00	9.22345E 00	4.38955E 01	4.44208E 00
3.50000E-01	2.74272E 00	1.15420E 01	4.86403E 01	4.21122E 00
4.00000E-01	3.38207E 00	1.40562E 01	5.15105E 01	3.90262E 00
4.50000E-01	4.14959E 00	1.66440E 01	5.14638E 01	3.52167E 00
5.00000E-01	5.04508E 00	1.91488E 01	4.82267E 01	3.09179E 00
5.50000E-01	6.06062E 00	2.14255E 01	4.25250E 01	2.64889E 00
6.00000E-01	7.18224E 00	2.33821E 01	3.56674E 01	2.22846E 00
6.50000E-01	8.39304E 00	2.49933E 01	2.88718E 01	1.85471E 00
7.00000E-01	9.67625E 00	2.62829E 01	2.28782E 01	1.53765E 00
7.50000E-01	1.10168E 01	2.72991E 01	1.79529E 01	1.27656E 00
8.00000E-01	1.24024E 01	2.80956E 01	1.40673E 01	1.06500E 00
8.50000E-01	1.38235E 01	2.87206E 01	1.10561E 01	8.94724E-01
9.00000E-01	1.52723E 01	2.92139E 01	8.76779E 00	7.57692E-01
9.50000E-01	1.67432E 01	2.96063E 01	7.00882E 00	6.46999E-01
10.00000E-01	1.82317E 01	2.99215E 01	5.65704E 00	5.57034E-01
1.00000E 00	1.97343E 01	3.01771E 01	4.61097E 00	4.83376E-01
1.10000E 00	2.12486E 01	3.03864E 01	3.79464E 00	4.22591E-01
1.15000E 00	2.27724E 01	3.05595E 01	3.15174E 00	3.72024E-01
1.20000E 00	2.43041E 01	3.07038E 01	2.64070E 00	3.29625E-01
1.25000E 00	2.58424E 01	3.08252E 01	2.23072E 00	2.93803E-01
1.30000E 00	2.73853E 01	3.09282E 01	1.89886E 00	2.63318E-01
1.35000E 00	2.89349E 01	3.10161E 01	1.62793E 00	2.37196E-01
1.40000E 00	3.04877E 01	3.10918E 01	1.40494E 00	2.14668E-01
1.45000E 00	3.20440E 01	3.11572E 01	1.22000E 00	1.95122E-01
1.50000E 00	3.36033E 01	3.12143E 01	1.06550E 00	1.78068E-01
1.55000E 00	3.51653E 01	3.12642E 01	9.35549E-01	1.63108E-01
1.60000E 00	3.67296E 01	3.13082E 01	8.25547E-01	1.49921E-01
1.65000E 00	3.82960E 01	3.13470E 01	7.31870E-01	1.38242E-01
1.70000E 00	3.98642E 01	3.13816E 01	6.51645E-01	1.27854E-01
1.75000E 00	4.14341E 01	3.14124E 01	5.82575E-01	1.18576E-01
1.80000E 00	4.30054E 01	3.14400E 01	5.22812E-01	1.10258E-01
1.85000E 00	4.45753E 01	3.14648E 01	4.70858E-01	1.02774E-01
1.90000E 00	4.61518E 01	3.14872E 01	4.25492E-01	9.60177E-02
1.95000E 00	4.77267E 01	3.15074E 01	3.85713E-01	8.98983E-02
2.00000E 00	4.93025E 01	3.15258E 01	3.50696E-01	8.43394E-02
2.05000E 00	5.08793E 01	3.15426E 01	3.19755E-01	7.92753E-02

Figure A-118—Results of Mimic program.

RADIATION FROM A DIPOLE ANTENNA IMMERSED IN A HALF SPACE OF UNIAXIAL ANISOTROPIC PLASMA

M. Javid

INTRODUCTION

The geometry of the problem under study is shown in Figure A-119. In this figure the plane $y = 0$ divides the space into two regions. In the region $y > 0$ the space is free of matter and charge (free space with permittivity ϵ_0 and permeability μ_0), and the region $y < 0$ contains a plasma, subjected to a strong static magnetic field $\hat{a}_z H_0$, where \hat{a}_z is the unit vector along the z direction and the symbol \sim under \hat{a} indicates a vector quantity. At the point $(0, -b, 0)$ a dipole of (infinitesimal) length h carrying a current $I_0 \cos \omega t$ is oriented along the z axis, constituting a current density

$$\vec{J} = \hat{a}_z I_0 h \delta(x) \delta(y + b) \delta(z) \cos \omega t \quad (1)$$

where

$$\delta(x) = \frac{1}{2\pi} \int_{-\infty}^{\infty} e^{jux} du$$

is the Dirac delta function.

It is required to find the field of this dipole antenna in the region $y > 0$.

The permittivity and permeability of a plasma subjected to a strong static magnetic field in the z direction is given in (Reference 1), to a good degree of accuracy by the tensor

$$\tilde{\epsilon} = \epsilon_0 \begin{vmatrix} 1 & 0 & 0 \\ 0 & 1 & 0 \\ 0 & 0 & \kappa \end{vmatrix} \quad (2)$$

and

$$\mu = \mu_0 \quad (3)$$

$$\kappa = 1 - \left(\frac{\omega_p}{\omega} \right)^2 \left(1 + j \frac{\nu}{\omega} \right) \quad (4)$$

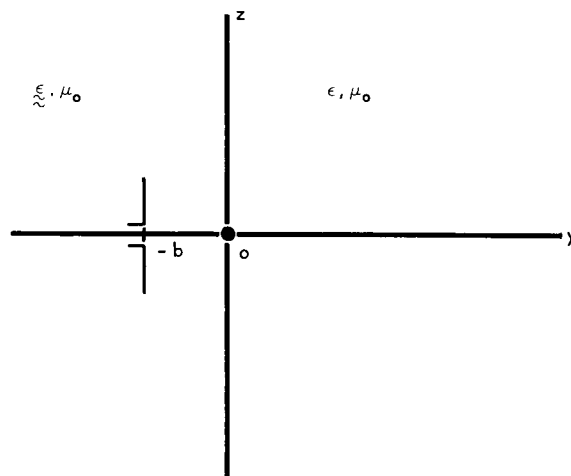


Figure A-119

where ω_p is the plasma frequency (Reference 1) and symbol \approx under $\underline{\epsilon}$ indicates a tensor quantity, and ν is the effective collision frequency for electrons.

A medium described by the permeability and permittivity of Equation (2) and Equation (3) is referred to as a uniaxial anisotropic medium with the optical axis oriented along the z axis. The assumption that the dipole is oriented along the optical axis simplifies formulation of the problem, but the technique described below is applicable to arbitrary orientations.

A search of literature shows that the following problems which are related to the problem under study have been solved.

1. Given the field of a source distribution in free space, the field of that source immersed in unbounded uniaxial anisotropic medium may be found by a specified scaling of the source free field (Reference 2). The field of a dipole in free space is known, thus its field, when immersed in an unbounded uniaxial medium, may be found (Reference 3).

2. If the plane boundary at $y = 0$ in Figure A-119 is a perfect conductor and region $y < 0$ contains a uniaxial plasma, then the field in region $y < 0$ may be calculated by classical image techniques (Reference 4).

3. A two dimensional version of the problem under study has been solved (Reference 5). Where the source and medium are independent of one cartesian coordinate. In this problem the dipole is assumed to be infinitely long with no spatial variation in current distribution along its length. This is not, of course, a physical problem.

The technique of solution of the problem under study is as follows:

- a. Express the field of a dipole immersed in free space as the sum (integral) of uniform plane waves propagating in all possible directions.
- b. From the above expression, using the scaling theorem of (Reference 2), find the field of the dipole immersed in unbounded uniaxial medium as the sum (integral) of uniform plane waves.
- c. Calculate the amplitude of transmitted plane wave corresponding to each of the above plane waves when incident on the boundary at $y = 0$, and sum up (integrate) these to obtain the transmitted wave.

The details of the implementation of this procedure are shown below. The results are given in Equation (20) which is an integral expression for the components of the magnetic field in the region $y > 0$, and Equation (22) where, using the method of stationary phase (Reference 7), the integral representation is evaluated for the far field at the antenna's horizon. Equation (24) gives the attenuation due to electron collisions as the wave propagates in plasma.

THE PLANE WAVE REPRESENTATION OF THE FIELD OF THE DIPOLE IN FREE SPACE

For the sake of simplicity in the following analysis the phasor notation will be used. Thus Equation (1) will be written as

$$\underline{J} = \underline{a}_z I_0 h \delta(x) \delta(y + b) \delta(z)$$

the symbols Re (Real Part) and $e^{j\omega t}$ being implicit. If a dipole with current density

$$\underline{J} = \underline{a}_z I_0 h \delta(x) \delta(y) \delta(z) \quad (5)$$

is located at origin in free space its magnetic field is given by (Reference 6)

$$H_x^0 = -j \frac{I_0 h k^2}{4\pi} \sin \varphi \sin \theta \left(1 - \frac{j}{kr}\right) \frac{e^{-jkr}}{kr} \quad (6)$$

$$H_y^0 = j \frac{I_0 h k^2}{4\pi} \cos \varphi \sin \theta \left(1 - \frac{j}{kr}\right) \frac{e^{-jkr}}{kr}$$

where

$$H_z^0 = 0$$

$$k^2 = \omega^2 \mu_0 \epsilon_0$$

$$\varphi = \tan^{-1} \frac{y}{x}$$

$$\theta = \cos^{-1} \frac{z}{r}$$

$$r^2 = x^2 + y^2 + z^2$$

that is, k is the wave number in free space, x , y , z are the Cartesian coordinates and r , θ , φ the corresponding spherical coordinates. However the plane wave expansion of the Cartesian components of the field may be achieved directly as follows:

If we use the notation

$$\underline{H}^0 = (H_x^0, H_y^0, H_z^0) = (H_x^0, H_y^0, 0)$$

to indicate the components of, \underline{H}^0 the magnetic field of the dipole immersed in free space, then its plane wave representation may be written in the form

$$\underline{H}^0 = \int_{-\infty}^{\infty} \int_{-\infty}^{\infty} (P, Q, 0) e^{-jk(ux+vy+wz)} du dw \quad (7)$$

where u , v and w are the direction cosines of the plane-wave-normals with

$$u^2 + v^2 + w^2 = 1 \quad (8)$$

and the quantities P and Q are functions of u and w . At all points

$$\nabla \cdot \underline{H}^0 = 0$$

and for the plane waves the operator ∇ is replaced by

$$\nabla \rightarrow -jk(\underline{a}_x u + \underline{a}_y v + \underline{a}_z w)$$

This requires that

$$uP + vQ = 0, \quad Q = -\frac{u}{v} P.$$

Since H^0 must have a discontinuity at origin, where there exists a singularity in current density J , as given in Equation (5), the expression (7) is valid only for region $y > 0$. We indicate the magnetic field in this region by

$$\tilde{H}^{0+} = \int_{-\infty}^{\infty} \int_{-\infty}^{\infty} (P, -\frac{u}{v} P, 0) e^{-jk(ux+vy+wz)} du dw.$$

If we express the magnetic field \tilde{H}^{0-} in the region $y < 0$ as

$$\tilde{H}^{0-} = \int_{-\infty}^{\infty} \int_{-\infty}^{\infty} (-P, -\frac{u}{v} P, 0) e^{-jk(ux-vy+wz)} du dw,$$

we find that

$$\nabla \cdot \tilde{H}^{0-} = 0$$

is satisfied.

By choosing

$$\tilde{E}^0 = \frac{1}{j\omega\epsilon_0} \nabla \times \tilde{H}^0$$

with

$$\nabla \rightarrow -jk(\hat{a}_x u \pm \hat{a}_y v + \hat{a}_z w)$$

for the plane wave we find

$$\tilde{E}^0 = \frac{1}{\eta} \int_{-\infty}^{\infty} \int_{-\infty}^{\infty} \left(-\frac{uw}{v} P, \pm wP, \frac{1-w^2}{u} P \right) e^{-jk(ux\pm vy+wz)} du dw$$

where

$$\eta = \sqrt{\mu_0/\epsilon_0}$$

and the signs refer to the cases $y > 0$ and $y < 0$ respectively. This insures that the current density \mathbf{J} is zero everywhere except at the plane $y = 0$ where due to the discontinuity in \mathbf{H}^0 , there exists a surface current density given by

$$\mathbf{K}|_{y=0} = \mathbf{a}_y \times (\mathbf{H}^{0+} - \mathbf{H}^{0-})|_{y=0} = \mathbf{a}_y \times \int_{-\infty}^{\infty} \int_{-\infty}^{\infty} 2\mathbf{a}_x P e^{-jk(ux+wz)} du dw. \quad (9)$$

From Equation (5) we have

$$\mathbf{K}|_{y=0} = \mathbf{a}_z I_0 h \delta(x) \delta(z).$$

From definition of two dimensional delta functions

$$\delta(x) \delta(z) = \frac{k^2}{4\pi^2} \int_{-\infty}^{\infty} \int_{-\infty}^{\infty} e^{-jk(ux+wz)} du dw$$

and

$$\mathbf{K}|_{y=0} = \mathbf{a}_z \frac{I_0 h k^2}{4\pi^2} \int_{-\infty}^{\infty} \int_{-\infty}^{\infty} e^{-jk(ux+wz)} du dw. \quad (10)$$

A comparison of Equation (9) and (10) shows that

$$P = - \frac{I_0 h k^2}{8\pi^2}. \quad (11)$$

For the sake of simplicity we may choose the strength of the dipole

$$I_0 h = \frac{8\pi^2}{k^2}, \quad \mathbf{J} = \mathbf{a}_z \frac{8\pi^2}{k^2} \delta(x) \delta(y) \delta(z) \quad (12)$$

resulting in

$$P = -1.$$

For the antenna with strength given in Equation (12) the plane wave representation is

$$\mathbf{H}^0 = \int_{-\infty}^{\infty} \int_{-\infty}^{\infty} \left(\pm 1, \frac{u}{v}, 0 \right) e^{-jk(ux \pm vy + wz)} du dw.$$

If the antenna is located at $y = -b$ with current density

$$\mathbf{J} = \hat{\mathbf{a}}_z \frac{8\pi^2}{k^2} \delta(x) \delta(y+b) \delta(z) \quad (13)$$

the plane wave representation of its magnetic field is

$$\mathbf{H}^0 = \int_{-\infty}^{\infty} \int_{-\infty}^{\infty} \left(\pm 1, \frac{u}{v}, 0 \right) e^{-jk[ux \pm v(y+b) + wz]} du dw$$

where the signs are now for $y > -b$ and $y < -b$ respectively.

The corresponding electric field is

$$\mathbf{E}^0 = \eta \int_{-\infty}^{\infty} \int_{-\infty}^{\infty} \left(\frac{uw}{v}, \pm w, \frac{1-w^2}{v} \right) e^{-jk[ux \pm v(y+b) + wz]} du dw.$$

FIELD OF DIPOLE IN UNBOUNDED UNIAXIAL MEDIUM

In accordance with the scaling theorem (Reference 2) the components H_x and H_y of the field of an antenna with current density given by Equation (13) located in unbounded uniaxial plasma is obtained from the free space components H_x^0 and H_y^0 by the following scaling:

$$H_x(x, y, z) = \sqrt{\kappa} H_x^0(\sqrt{\kappa} x, \sqrt{\kappa} y, z)$$

$$H_y(x, y, z) = \sqrt{\kappa} H_y^0(\sqrt{\kappa} x, \sqrt{\kappa} y, z)$$

$$H_z(x, y, z) = 0 = H_z^0(x, y, z).$$

Hence the magnetic field of the dipole in unbounded plasma is

$$\mathbf{H}_{\text{TM}i} = \sqrt{\kappa} \int_{-\infty}^{\infty} \int_{-\infty}^{\infty} \left(-1, \frac{u}{v}, 0 \right) e^{-jk[u\sqrt{\kappa} x + v\sqrt{\kappa}(y+b) + wz]} du dw \quad (14)$$

where the subscript TM refers to the fact that the \mathbf{H} field is transverse to the z -axis, and i indicates that this field will be considered to be incident on the boundary at $y = 0$. Since the boundary on which the wave is incident is at $y = 0$, the incident wave is in the region $y > -b$ and the corresponding sign is used in Equation (14).

TRANSMISSION COEFFICIENTS

In the problem under discussion, the optical axis of the medium is along z -axis and the incident TM-waves have the propagation factors

$$\psi_{\text{TMi}} = e^{-jk[u\sqrt{\kappa}x + v\sqrt{\kappa}(y+b) + wz]} = e^{-jkv\sqrt{\kappa}b} e^{-jk(u\sqrt{\kappa}x + v\sqrt{\kappa}y + wz)} \quad (15)$$

with

$$u^2 + v^2 + w^2 = 1$$

The TM waves, referred to as the extraordinary waves (Reference 1) are solutions of

$$\left(\frac{1}{\kappa} \frac{\partial^2}{\partial x^2} + \frac{1}{\kappa} \frac{\partial^2}{\partial y^2} + \frac{\partial^2}{\partial z^2} + k^2 \right) \psi = 0$$

whereas the TE waves satisfy

$$\left(\frac{\partial^2}{\partial x^2} + \frac{\partial^2}{\partial y^2} + \frac{\partial^2}{\partial z^2} + k^2 \right) \psi = 0.$$

In the plane wave expansion of the magnetic field given in (14) the individual plane waves are of the form

$$h_{\text{TMi}} = \sqrt{\kappa} \left(-1, \frac{u}{v}, 0 \right) \psi_{\text{TMi}}. \quad (16)$$

If the corresponding electric field is denoted as e_{TMi} its components are found from

$$j\omega\epsilon_0 (e_x, e_y, \kappa e_z) = \nabla \times h_{\text{TMi}}. \quad (17)$$

But for propagation factor ψ_{TMi} given in (15) we have

$$\nabla \rightarrow -jk (\hat{a}_x u \sqrt{\kappa} + \hat{a}_y v \sqrt{\kappa} + \hat{a}_z w)$$

Using this operator in (17) we find

$$e_{\text{TMi}} = \eta \sqrt{\kappa} \left(\frac{uw}{v}, w, -\frac{1}{\sqrt{\kappa}} \frac{u^2 + v^2}{v} \right) \psi_{\text{TMi}}.$$

This incident wave gives rise to reflected waves. Since the medium can support two types of waves we must consider the possibility of both TE and TM reflected waves. The propagation factors of the TM and TE reflected waves are

$$\psi_{\text{TMi}} = e^{-jk(u\sqrt{\kappa}x - v\sqrt{\kappa}y + wz)}$$

and

$$\psi_{TEr} = e^{-jk(u\sqrt{\kappa}x - ry + wz)}$$

where

$$u^2\kappa + r^2 + w^2 = 1. \quad (18)$$

The transmitted wave has a propagation factor

$$\psi_t = e^{-jk(u\sqrt{\kappa}x + ry + wz)}$$

These propagation factors are "matched" at $y = 0$ and except for a phase factor of $e^{-jkv\sqrt{\kappa}b}$, they also match with the incident propagation factor ψ_{TMi} given in Equation (15). Since

$$\nabla \cdot \mathbf{h}_{TMr} = 0 = \nabla \cdot \mathbf{h}_{TEr} = \nabla \cdot \mathbf{h}_t$$

using the relationship

$$jw\mathbf{D} = \nabla \times \mathbf{H}$$

the components of the various \mathbf{H} and \mathbf{E} fields, corresponding to the incident \mathbf{h}_{TMi} given in (16) are shown in Table A-17. In this table the quantities F , G , M , and N are unknown reflection and transmission coefficients, being functions of u and w , and their value is to be found by matching the tangential components of the fields at $y = 0$.

The continuity of the tangential components of the magnetic and electric field at $y = 0$ requires that

$$-e^{-jkv\sqrt{\kappa}b} - F = M$$

$$\frac{u^2\kappa + r^2}{r} G = N$$

$$\frac{uw}{v} e^{-jkv\sqrt{\kappa}b} - \frac{uw}{v} F + G = -\frac{N(r^2 + w^2) + uw\sqrt{\kappa}M}{r}$$

$$-\frac{u^2 + v^2}{\sqrt{\kappa}v} e^{-jkv\sqrt{\kappa}b} + \frac{u^2 + v^2}{\sqrt{\kappa}v} = \frac{M(r^2 + \kappa u^2) + uw\sqrt{\kappa}N}{r}.$$

Comparing the equations (18) and (8) it is seen that

$$r^2 + \kappa u^2 = u^2 + v^2.$$

Table A-17
Components of Various \vec{H} and \vec{E} Fields

$\vec{h}_{TMi} = \sqrt{\kappa} (-1$	$, \frac{u}{v}$	$, 0) e^{-jk[u\sqrt{\kappa}x + v\sqrt{\kappa}(y+b) + wz]}$
$\vec{h}_{TMr} = \sqrt{\kappa} (-F$	$, -\frac{u}{v} F$	$, 0) e^{-jk[u\sqrt{\kappa}x - v\sqrt{\kappa}y + wz]}$
$\vec{h}_{TEr} = \sqrt{\kappa} \left(-\frac{uw\sqrt{\kappa}}{r} G$	$, wG$	$, \frac{u^2\kappa + r^2}{r} G) e^{-jk[u\sqrt{\kappa}x - ry + wz]}$
$\vec{h}_t = \sqrt{\kappa} (M$	$, -\frac{u\sqrt{\kappa}M + wN}{r}$	$, N) e^{-jk[u\sqrt{\kappa}x + ry + wz]}$
$\vec{e}_{TMi} = \eta \sqrt{\kappa} \frac{uw}{v}$	$, w$	$, -\frac{u^2 + v^2}{\sqrt{\kappa}v} e^{-jk[u\sqrt{\kappa}x + v\sqrt{\kappa}(y+b) + wz]}$
$\vec{e}_{TMr} = \eta \sqrt{\kappa} \left(-\frac{uw}{v} F$	$, wF$	$, +\frac{u^2 + v^2}{\sqrt{\kappa}v} F) e^{-jk[u\sqrt{\kappa}x - v\sqrt{\kappa}y + wz]}$
$\vec{e}_{TEr} = \eta \sqrt{\kappa} (G$	$, \frac{u\sqrt{\kappa}G}{r}$	$, 0) e^{-jk[u\sqrt{\kappa}x - ry + wz]}$
$\vec{e}_t = \eta \sqrt{\kappa} \left(-\frac{N(r^2 + w^2) + uw\sqrt{\kappa}M}{r} \right.$	$, -wM + u\sqrt{\kappa}N,$	$, \frac{M(r^2 + \kappa u^2) + uw\sqrt{\kappa}N}{r}) e^{-jk[u\sqrt{\kappa}x + ry + wz]}$

(19)

Using this identity in previous equations we find

$$G = 0, \quad N = 0, \quad M = -\frac{2re^{-jkv\sqrt{\kappa}b}}{r + \sqrt{\kappa}v}$$

From the above and Equation (19), (see Table A-17) we find that the components of the transmitted magnetic fields are:

$$h_{tx} = -\frac{2\sqrt{\kappa}re^{-jkv\sqrt{\kappa}b}}{r + \sqrt{\kappa}v}$$

$$h_{ty} = \frac{2\sqrt{\kappa}ue^{-jkv\sqrt{\kappa}b}}{r + \sqrt{\kappa}u}$$

$$h_{tz} = 0$$

and the transmitted magnetic field is

$$H_t = \int_{-\infty}^{\infty} \int_{-\infty}^{\infty} (-r, u, 0) \frac{2\sqrt{\kappa} e^{-jkv\sqrt{\kappa}b}}{r + \sqrt{\kappa}v} e^{-jk(u\sqrt{\kappa}x + ry + wz)} du dw \quad (20)$$

where

$$u^2\kappa + r^2 + w^2 = 1 = u^2 + v^2 + w^2.$$

In particular the x-component of the transmitted magnetic field is

$$H_{tx} = - \int_{-\infty}^{\infty} \int_{-\infty}^{\infty} \frac{2\sqrt{\kappa} r e^{-jkv\sqrt{\kappa}b}}{r + \sqrt{\kappa}v} e^{-jk(u\sqrt{\kappa}x + ry + wz)} du dw \quad (21)$$

Recalling the normalization used in Equation (11), in terms of the actual dipole strength the x-component of the transmitted magnetic field is given by (21) multiplied by $T_0 h k^2 / 8\pi^2$.

ASYMPTOTIC VALUE OF THE FIELD AT (0, y, 0) AS $y \rightarrow \infty$

An idea of the nature of the transmitted field is obtained if we consider the field at $x = 0$, $z = 0$ as $y \rightarrow \infty$. From (21) we have

$$H_{tx}(0, y, 0) = - \int_{-\infty}^{\infty} \int_{-\infty}^{\infty} \frac{2\sqrt{\kappa} r e^{-jkv\sqrt{\kappa}b}}{r + \sqrt{\kappa}v} e^{-jkry} du dw.$$

We shall first consider the integration with respect to w and write

$$r(w) = (1 - \kappa u^2 - w^2)^{1/2}$$

$$A(w) = \frac{2\sqrt{\kappa} r e^{-jkv\sqrt{\kappa}b}}{r + \sqrt{\kappa}v}.$$

The asymptotic value of the integral

$$I(u, y, b) = \int_{-\infty}^{\infty} A(w) e^{-jkyr(w)} dw$$

as $y \rightarrow \infty$ is given by (Reference 7).

$$I(u, y, b) \simeq A(w_0) \sqrt{\frac{2\pi}{-\kappa y r''(w_0)}} e^{-j[ky r(w_0) - \pi/4]}$$

where w_0 is the root of the derivative of $r(w)$ and $r''(w)$ is the second derivative of r with respect to w . From

$$\frac{dr}{dw} = \frac{d}{dw} (1 - \kappa u^2 - w^2)^{1/2} = -w(1 - \kappa u^2 - w^2)^{-1/2}$$

we have

$$w_0 = 0$$

$$r''(w_0) = -(1 - \kappa u^2)^{-1/2}$$

$$I(u, y, b) \simeq \frac{2\sqrt{\kappa}\sqrt{1-\kappa u^2} e^{-jk\sqrt{1-u^2}}\sqrt{\kappa}b}{\sqrt{1-\kappa u^2} + \sqrt{\kappa}\sqrt{1-u^2}} \sqrt{\frac{2\pi}{ky}} (1 - \kappa u^2)^{1/4} e^{-j[ky(1-\kappa u^2)^{1/2} - \pi/4]}$$

We now define

$$B(u) = \frac{2\sqrt{\kappa}\sqrt{1-\kappa u^2} e^{-jk\sqrt{1-u^2}}\sqrt{\kappa}b}{\sqrt{1-\kappa u^2} + \sqrt{\kappa}\sqrt{1-u^2}} \sqrt{\frac{2\pi}{ky}} (1 - \kappa u^2)^{1/4}$$

and

$$\rho(u) = (1 - \kappa u^2)^{1/2}$$

The asymptotic value of $H_{tx}(0, y, 0)$ as $y \rightarrow \infty$ is (Reference 7).

$$H_{tx}(0, y, 0) \simeq - \int_{-\infty}^{\infty} B(u) e^{j\pi/4} e^{-jky\rho(u)} du$$

$$\simeq -e^{j\pi/2} B(u_0) \sqrt{\frac{2\pi}{-ky\rho''(u_0)}} e^{-jky\rho(u_0)}$$

where u_0 is the root of the derivative of $\rho(u)$, and $\rho''(u)$ is the second derivative of

$$\frac{d\rho}{du} = -ku(1 - ku^2)^{-1/2}$$

$$u_0 = 0$$

$$\rho''(u_0) = -k$$

$$H_{tx} = (0, y, 0) = -j \frac{2}{1 + \sqrt{\kappa}} e^{-jk\sqrt{\kappa}b} \frac{2\pi}{ky} e^{-jky} \text{ as } y \rightarrow \infty. \quad (22)$$

Taking the normalization factor of Equation (11) into account, we have

$$H_{tx}(0, y, 0) = -j \frac{2}{1 + \sqrt{\kappa}} e^{j\sqrt{\kappa}b} \frac{I_0 h k^2}{4\pi} \frac{1}{ky} e^{-jky}, \quad y \rightarrow \infty \quad (23)$$

A comparison of Equation (23) with Equation (6) shows that at the antenna's horizon ($x = 0, y \rightarrow \infty, z = 0$) the effect of the interface is given by the "transmission coefficient" $2/(1 + \sqrt{\kappa})$ and, the effect of propagation in the ionized medium is given by the factor $e^{-j\sqrt{\kappa}b}$. From Equation (4) we have

$$\begin{aligned} \sqrt{\kappa} &= \left[1 - \left(\frac{\omega_p}{\omega} \right)^2 \left(1 + j \frac{\nu}{\omega} \right) \right] = \alpha + j\beta \\ \alpha &= \frac{1}{\sqrt{2}} \left\{ 1 - \frac{\omega_p^2}{\omega^2} + \left[\left(1 - \frac{\omega_p^2}{\omega^2} \right)^2 + \frac{\nu^2 \omega_p^4}{\omega^6} \right]^{1/2} \right\}^{1/2} \\ \beta &= -\frac{1}{2} \frac{\nu \omega_p^2}{\omega^2 \alpha} \end{aligned} \quad (24)$$

The field is attenuated by the factor $e^{-\alpha b}$. This attenuation is of course due to energy dissipation when each electron collides with a particle at an effective frequency of ν times per second.

The procedure described above may be applied when the antenna is in an arbitrary direction described by

$$\tilde{J} = I_0 h [\hat{a}_x u_0 + \hat{a}_y v_0 + \hat{a}_z w_0] \delta(x) \delta(y + b) \delta(z)$$

where u_0, v_0 , and w_0 are direction cosines of the antenna relative to the x, y, z axis. The field due to the z -component is found as above. The fields due to the x - and y -components of the source are no longer TM (to the optical axis z) and must be resolved into TE and TM components as described in Reference 3. The above procedure must then be applied to each of these components.

REFERENCES

1. Budden. K.G., Lectures on Magnetoionic Theory, New York: Gordon and Breach, 1964.
2. Clemmow, P.C., "Theory of electromagnetic waves in a simple anisotropic medium," Proc. I.E.E., 110(1): January, 1963.
3. Clemmow, P.C., "The resolution of a dipole field into transverse electric and transverse magnetic waves," Proc. of I.E.E., 110(1): January, 1963.
4. Rao, B. Rama and Wu, T.T., "On the applicability of image theory in anisotropic media," IEEE Trans. on Antennas and Propagation, AP-13(5): September, 1965.
5. Felsen, L.B., "Radiation from a uniaxially anisotropic plasma half space," IEEE Trans. on Antennas and Propagation, AP-11(4): July, 1963.
6. Javid, M. and Brown, P.M., Field Analysis and Electromagnetic Theory, New York: McGraw Hill Book Co. Inc., 1962.
7. Erdelyi, A., Asymptotic Expansions, New York: Dover Publications, Inc., 1956.

SUMMER WORKSHOP 1966

Program Outline and Team Participants

PROJECT B: Structural Dynamics

Problem Topics

- B-1 Finite-element modelling of thin plate
- B-2 Study of plate associated with reflector dynamics of the Rosman I antenna
- B-3 Frequency response of the Rosman I antenna
- B-4 Calculation of the radiation pattern of the Rosman I antenna
- B-5 Dynamic responses of the Rosman I antenna

TEAM B

Academic Personnel

Dr. Yu Chen
Principle Investigator
Dr. J. M. Dalrymple
Dr. T. G. Toridis
Mr. George Eichmann

Goddard Personnel

Dr. R. J. Coates
Division Chief
Mr. George C. Winston
Staff Advisor
Mr. Thomas G. Butler
Mr. Stewart Chaney
Mr. Richard D. McConnell
Mr. Nicholas A. Raumann

NSF Summer Science Students

Mr. William Irwin
Mr. Richard Strauss

PRECEDING PAGE BLANK NOT FILMED.

PROJECT B: STRUCTURAL DYNAMICS

CONTENTS

	<u>Page</u>	
SOME RESULTS IN THE FINITE ELEMENT MODELLING OF THIN PLATE	239	✓
Yu Chen and T. G. Toridis		
A STUDY OF PLATE ASSOCIATED WITH REFLECTOR DYNAMICS OF THE		
ROSMAN I ANTENNA	243	✓
Yu Chen and T. G. Toridis		
FREQUENCY RESPONSE OF THE ROSMAN I 85-FOOT DISH ANTENNA	247	✓
J. Dalrymple		
CALCULATION OF RADIATION PATTERN OF ROSMAN 85-FOOT PARABOLOIDAL		
DISH	253	✓
G. Eichman		
ANALYSIS OF THE DYNAMIC RESPONSES OF THE ROSMAN I ANTENNA	271	✓
W. Irwin		

PRECEDING PAGE BLANK NOT FILLED.

INTRODUCTORY REMARKS ON PROJECT B STRUCTURAL DYNAMICS

George C. Winston

The purpose of this note is to present a brief chronology of the effort on the dynamic analysis of large steerable antenna structures. This is done to assist the reader of the following reports to place them in their proper context. The work undertaken by the Summer Workshop group originated from a need for a more exact transfer function description of an X-Y mounted, amplitude sensing, monopulse antenna structure. The function relating the far-field pattern, particularly the angle of the difference pattern null to the angle of the driving pinion gear, was of primary concern. Additional transfer functions relating the axis of the optical boresighting system and the shaft angle encoders to the pinion were also of interest. A number of closely related requirements exist in addition, such as:

1. Improved methods of analyzing antenna structural designs prior to erection, leading, hopefully, to improved design methods.
2. Improved acceptance testing methods for qualifying erected structures without subjecting them to potentially destructive forces such as those occurring in sinusoidal excitation tests.
3. A better understanding of the R. F. performance of distorted parabolic reflector antennas.

During the 1965 Summer Workshop session, two complementary approaches to the problem were initiated. These were a computer analysis of a mathematical model of an existing antenna structure and a set of measurements of structural responses of the same antenna. The antenna selected was the NASA-GSFC Rosman I 85-foot antenna located near Rosman, North Carolina. The measurement results are to be used to verify and, if need be, correct the computer model. The model, in turn, would then be used in a detailed study of the structure.

In the measurement program, accelerometers were mounted at strategic points and the structure excited through its drive system by a variety of test signals consisting of sine waves, square waves, impulses, and white noise. The structure's response, as measured by the accelerometers, was recorded under many conditions on a magnetic tape recorder for later analysis. A start was made on the development of procedures for analyzing this data for modal frequencies and damping factors.

For the computer analysis, the model development was begun based upon data derived from the original construction drawings. Because of the size and complexity of the structure it was necessary to produce the model in six segments. Static analyses of each of these segments and then of the entire structure will be made. Information drawn from these analyses will be used in deriving a simplified model for dynamic analysis.

Because of the size of this task and its pioneering nature it was decided to continue the effort at GSFC through the winter. This would permit the accomplishment of time consuming chores and allow the 1966 Workshop session to resume at a higher level of analysis. The winter work consisted of a basic reduction of the experimental data and a continuation of the modeling and programming effort under contract to the Martin Company, Baltimore, Maryland.

In the 1966 session a third line of work was undertaken to extend the analysis into the far-field radiation pattern. This is a necessary step to translate the structural response, with the resulting

reflector distortion and feed point displacement, into an R.F. boresight response. The work is based upon a considerable background of analysis performed previously by Mr. Richard F. Schmidt of GSFC. Mr. Schmidt joined the Workshop group this year to assist in this area.

Significant progress, as illustrated by the following reports, was made in all aspects of the effort during the 1966 Summer Workshop session. At the close of the session the basic structural modeling and its programming are nearing completion. A detailed examination of the reflector surface preparatory to the far-field analysis is well underway. The current distribution method has been selected for the radiation pattern analysis and programming requirements examined. Computation of the patterns will be based upon numerical integration at this time. The analysis procedures for the experimental data are well established and much of the analysis has been performed.

Supporting work in each area will continue during the 1966-67 winter season. It is anticipated that the 1967 Workshop session will begin with a comparison of the experimental and computer results followed by adjustments to the model and a detailed structural analysis. The computer program for determining the radiation patterns is expected to be completed and ready for the insertion of structural response data.

SOME RESULTS IN THE FINITE-ELEMENT MODELLING OF THIN PLATES

Y. Chen, T. G. Toridis* 7

N 67-22753

INTRODUCTION

With the usual assumptions made in the theory of thin plates, the governing differential equation of the free vibration of the plate is given by

$$\nabla^4 w = w_{xxxx} + 2w_{xxyy} + w_{yyyy} = -\frac{m}{D} w_{tt} \quad (1)$$

where w denotes the deflection of the plate in the transverse direction, D is the flexural rigidity, t is the time variable, m is the mass of the plate per unit area. Many possible types of boundary conditions are associated with Equation (1), which correspond to various ways of supporting the plate as a stable structure. For example, a square plate simply supported at all edges requires that the deflection and the moments vanish along all edges, namely $w = \nabla^2 w = 0$ for all edges. Among all the boundary conditions, only in a limited few cases can Equation (1) be solved in closed form. In other cases it can only be solved by approximate methods such as Rayleigh-Ritz, finite-differences, etc.

The finite-element method of structural analysis is a recent development which solves structural problems by first constructing a model containing finite elements to replace the actual physical structure being analyzed. Each type of element has predetermined properties of elastic behavior. These elements are assembled into a system of grid points which are chosen to define the physical domain of the structure. The finite element model thus constructed is a discrete representation of the actual structure. This modelling concept applies quite naturally to an ordinary framed structure. The structural elements employed in such a case are simple beams, columns, and girders. An extension of the concept is to represent an elastic continuum by one or two dimensional elements in a similar manner. This application differs from the first one (framed structure) in that a physical approximation to the actual structure is made. However, once the modelling has been done, the subsequent mathematical steps in solving the structural model do not necessarily involve approximations. This is not the case in the finite difference method. The latter method solves a structural problem by solving the equation governing the behavior of the continuum by an approximate mathematical procedure, while the governing differential equation itself may be an exact description of the continuum within the assumptions made. Consequently, it can be seen that in the former method no matter how accurate the mathematical analysis used in solving the model may be, the result can be valid only to the extent that the behavior of the model simulates the behavior of the structure subject to the boundary conditions of the particular solution. In order to improve the results, the model itself must be improved. This improvement could be made in some instances by using elements which would give a closer description of the behavior of the actual structure.

Many different types of finite elements have been worked out by investigators in this field. The behavior of the model is derived from the properties of the elements which constitute the model

*Dr. Toridis is a NASA Summer Faculty Fellow who participated in the Summer Workshop.

as well as the way in which the elements are arranged. Since the elements are assumed to be interconnected only at a limited number of grid points, the essential elastic characteristics of an element are represented by the relationship between the forces applied to the grid points and the deflections resulting therefrom. This force-deflection relationship is expressed by the compliance matrix of the element.

When the element properties have been defined, the static and the dynamic analyses of the model become a standard structural problem. Essentially the problem is to enforce equilibrium and compatibility conditions throughout the structure. Equilibrium conditions require that the internal element forces acting at each grid point must balance the externally applied load at that point, and compatibility conditions demand that the element deformations must be such that continuity is maintained at grid points. There are two general approaches in structural analysis based on the choice of the governing variables of analysis popularly known as the force and the displacement methods.

A structure of some degree of complexity in its geometrical configuration and physical make-up can best be described in mathematical terms through the use of the matrix formulation. Matrix formulation has the essential advantage of being adapted with ease to calculations by means of digital computers.

The present study is carried out with the aid of "A Digital Program for Static and Dynamic Analysis of Complex Structures" (SB038) developed by the Martin Company (Reference 1). It is a program based on the Matrix-Force method.

THE STRUCTURAL MODEL

In modelling a thin plate by finite elements, the plate is replaced by a discrete system of grid points and elements. On the boundary grid points, reaction elements in the form of forces or moments are introduced to simulate the conditions of support. For example, a built in edge is simulated by applying at each grid point of the boundary a reaction element in the transverse direction and a moment whose vector is in the direction of the edge. At all inner grid points bending elements are placed between every two adjacent grid points to simulate the bending stiffness in the x- and the y- directions. The twisting resistance is provided by quadrilateral panels with their corners coinciding with four neighboring grid points. Thus, a total of 16 twist panels are used in a 4×4 model. If in such a model each grid point is given a degree of freedom in each linear direction, there would be 75 equations of equilibrium in total. Since the number of primary elements which constitute a base structure or primary structure must be equal to the number of equations of equilibrium, we shall have 75 primary elements. In the case shown in Figure B-1, 144 elements were used to simulate the whole structure; therefore, 69 elements are redundant. The detailed arrangement of the element is shown in Figure B-1.

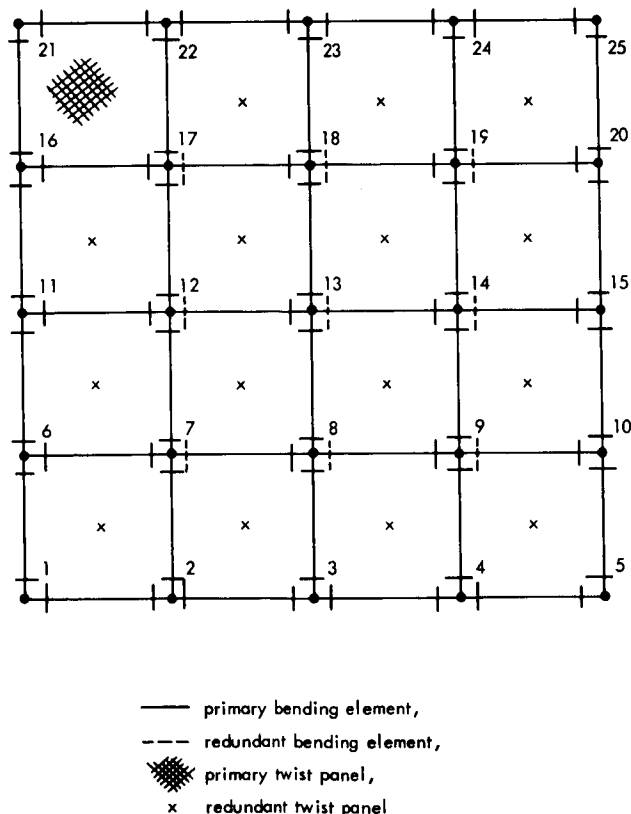


Figure B-1—Bending twisting model.

Some experimentation was performed before a primary structure with good matrix conditioning was obtained. A well composed primary structure should attain a behavior close to the actual behavior of the structure under load, thus resulting in only weak coupling between the primary and the redundant structure.

The elements of the compliance matrix for the bending elements are calculated according to $L/3EI$ for the diagonal terms and $L/6EI$ for the off diagonal or coupled terms. The compliance for the twist panel is given by $12A(1+\nu)/Eh^3$. In the above formulae L is the distance between the grid points, E is Young's modulus, I is the moment of inertia, h is the thickness of the plate, A is the area of the twist panel, ν is Poisson's ratio. In calculating the compliances of the bending elements at the inner grid points the full cross-sectional area of the panel is used for I , whereas in calculating the same quantity for the boundary points only half of this area is used, resulting in a value of compliances for the boundary bending elements twice as large as that for the elements at the inner grid points.

Within the availability of elements supplied by the SB038 program, a second model was constructed by replacing the twist panels with two diagonal bending elements. This model, known as the Hrennikoff model (Reference 2), is obtained by a consideration of the equilibrium of a plate panel, and the deflection of the panel when subjected to pure bending in both directions and to pure twist. The compliances of the parallel elements are calculated as $ah^3/16$, while those of the diagonal elements are given by $ah^3/16\sqrt{2}$, where a is the element length. Figure B-2 shows the Hrennikoff model in finite element representation.

Satisfactory models by finite element techniques are still being sought. Results were obtained which indicate further improvements are needed in the analysis. Additional work is required before acceptable models of the thin plates, and subsequently thick plates, can be obtained. Attention should be given to the use of consistent mass matrices for improving dynamic analysis. It is recommended that this study be extended until finite element models compare within a prescribed tolerance of known classical solutions. Only after obtaining reasonable agreement on the thin plate model should work proceed on the thick plate problem.

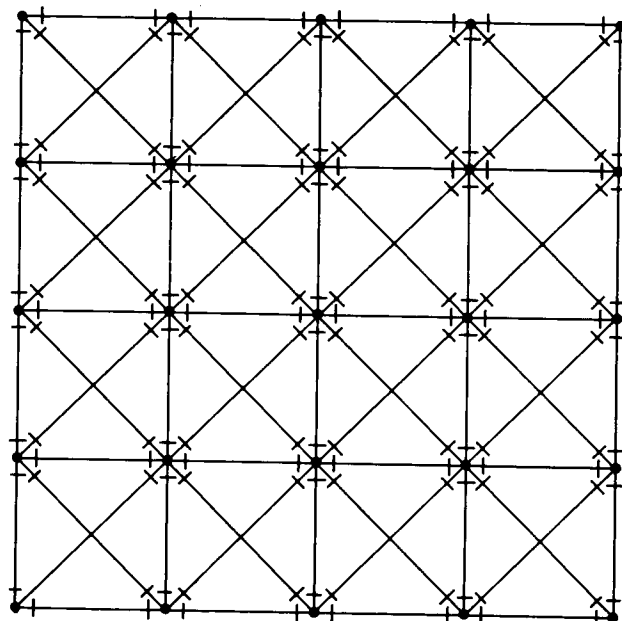


Figure B-2—Hrennikoff model in finite element representation.

ACKNOWLEDGEMENTS

The authors are indebted to E. S. Chaney and R. F. Strauss for their valuable assistance throughout the whole effort of this study. Thanks are due to Mr. George C. Winston, and Mr. Nicholas E. Raumann of the Antenna Systems Branch, Mr. Thomas G. Butler of the Structural Analysis Computer Group, and other Goddard Staff members for their cooperation.

REFERENCES

1. Clark, T. L., A Digital Program for Static and Dynamic Analysis of Complete Structure, Martin Company, Baltimore, Maryland.

2. Hrennikoff, A., "Solution of problems of elasticity by the framework method," Journal of Applied Mechanics, Trans. ASME Vol. 63, Dec. 1941.

A PLATE STUDY ASSOCIATED WITH REFLECTOR DYNAMICS OF THE ROSMAN-I ANTENNA

Y. Chen, T. G. Toridis*

N 67-22754

INTRODUCTION

The Rosman-I antenna essentially consists of an 85-foot diameter paraboloidal reflector mounted on X and Y gears that are supported by a tower structure. The radio signal receiving system is located at the focal point of the paraboloidal reflector. Dynamic forces are induced in the structure due to mechanical disturbances incurred during the process of tracking of a satellite as well as natural phenomena, such as wind forces.

The effect of dynamic forces is to produce deformations of the antenna structure as a whole. Such deformations of the antenna result in deviations of the reflecting surface from a true paraboloid and displacement of the receiving elements from the focus of the paraboloid. This, in turn, distorts the received signals and limits the tracking accuracy of the antenna. Therefore, the investigations of the dynamic response of the antenna is of interest from the viewpoint of increasing its tracking accuracy and the possibility of incorporating the findings of such studies into the design of future antennas.

The task for the structural Dynamics Group of the Summer Workshop was to conduct a detailed study of the dynamics of the paraboloidal reflector. A study revealed that the structural arrangement of the reflector surface essentially consists of a series of quadrilateral plates mounted on a truss structure, which displace independently of each other. Consequently each panel can be analyzed as a quadrilateral plate with proper conditions of support. The preliminary study on thin plates discussed on pages 239 through 242 preceded the analysis of the reflector panels.

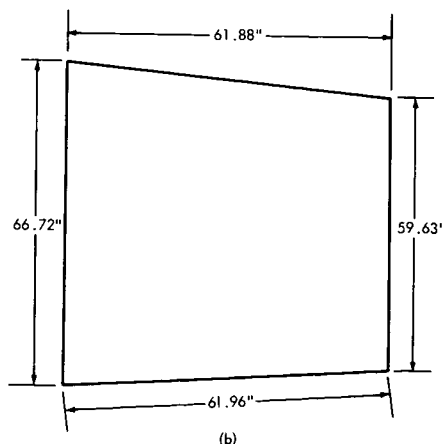
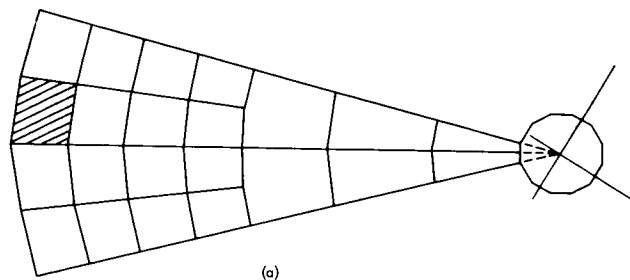


Figure B-3—Typical sector of the reflector surface.

THE MODELS

The reflector surface can be divided into many sectors, typical of which is shown in Figure B-3(a). Each sector can be analyzed as a single panel of sandwich construction. Figure B-4 illustrates a cut through one of the panels. An aluminum z-section connects the top and the bottom skin (0.032 in thick) which are kept apart by a 0.0016 inch thick aluminum honeycomb. The z-section totally encloses the honeycomb

*Dr. Toridis, Assistant Professor of Engineering Mech., George Washington University, is a NASA Summer Faculty Fellow who participated in the Summer Workshop.

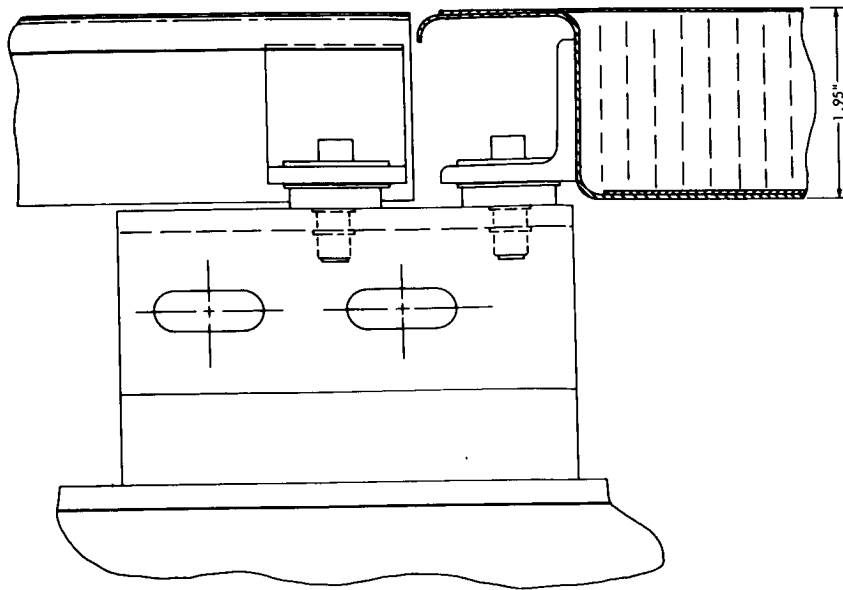


Figure B-4—Cross-section of a typical panel.

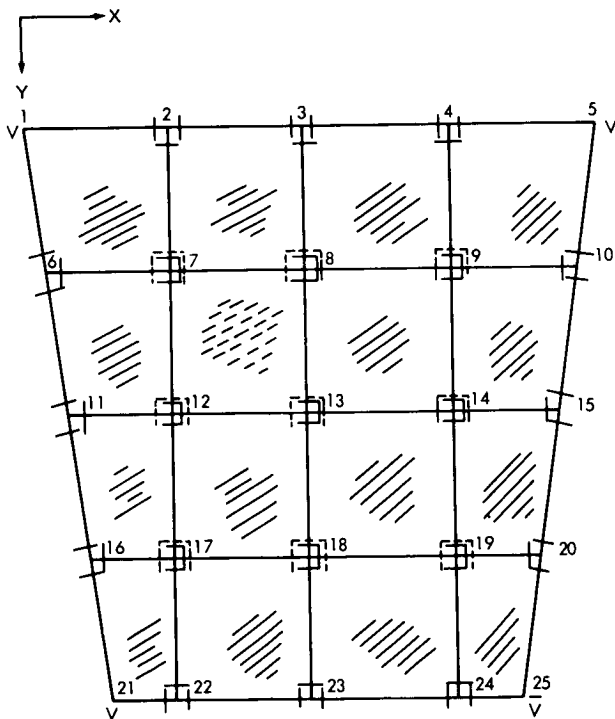


Figure B-5—Model representation of a typical panel.

to form a box-type construction. Supports are provided at four corners of each panel which are connected to the back-up structure by aluminum bolts with a rubber washer between the angle support and the connecting plate as shown in Figure B-4. Uplift is resisted by aluminum bolts while downward movement is opposed by rubber washers, resulting in nonlinear spring supports.

The typical panel can be reduced to model representation by two different approaches. The first approach is to consider the panel as a thin plate which has an area moment of inertia equal to that of the z-section (1.693 in^4) for the boundary, and equal to the sum of the moments of inertia of the skin and the honeycomb for the interior (0.0634 in^4). These values are used in computing the compliances of the two-digit bending elements on the boundary and the three-digit bending elements in the interior of the plate, a finite-element model of which is shown in Figure B-5.

A second model is constructed as a three-dimensional tension-shear representation. The compliances are calculated by physical lumping. The details of modelling can be traced by referring to Figure B-6.

In obtaining the numerical results for the reflector panel, two types of supports have been used. Both are elastic spring supports. The spring constant is that of the aluminum bolt for the

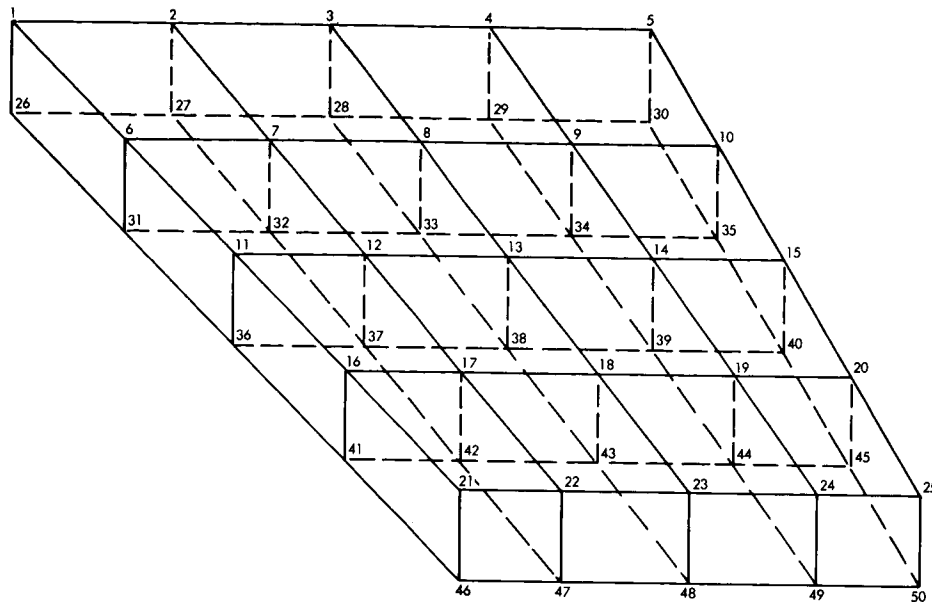


Figure B-6—Three-dimensional tension-shear representation.

first type, and that of the rubber washer for the second type. Obviously, the actual static deflections of the plate should be equal to that found using the second type of support. As for the natural frequencies and the model shapes, it is believed that they should lie between the values computed for the two types of supports. At the present state of art, the strict nonlinear analysis is not yet possible.

RESULTS

According to the approaches discussed above, four different computer runs were made, two runs for each model to accommodate the two different types of support springs. The first five natural frequencies are tabulated below. For the two different approaches used, the results are quite comparable. This comment holds true also for the mode shapes calculated. Since there are no theoretical solutions available for comparison purposes, the above results give some support of the correctness of either approach. Intuitively, the three-dimensional model gives a closer description of the physical structure. These results can be further improved if a technique is developed to use a consistent mass matrix.

Table B-1
Natural Frequencies of a Typical Panel

Model Type \ Frequencies cycles/sec	1st	2nd	3rd	4th	5th
3-D (bolt support)	50.5	109.2	110.6	140.4	240.0
3-D (rubber support)	36.8	68.8	68.8	138.6	154.2
Plate (bolt support)	43.6	115.4	155.2	159.3	309.4
Plate (rubber support)	34.1	75.6	75.8	116.6	158.6

FREQUENCY RESPONSE OF THE ROSMAN I 85-FOOT DISH ANTENNA

Jean M. Dalrymple

N 67-22755

SUMMARY

A technique was developed for producing spectrum analyzer charts from which frequency, amplitude, and damping factor could be obtained. A table is given listing results from several sensors due to impulse excitation at the antenna. Details of the antenna frequency response which need cross-checking are discussed.

INTRODUCTION

During the summer of 1965, data from accelerometers and other sensors were recorded on magnetic tape in response to various types of excitation of the Rosman I 85-foot dish antenna (Reference 1). Of the types of excitations given (square wave, impulse, white noise, side wave), the impulse appears to be most useful thus far. It was found that the white noise generator did not produce true white noise, which makes the response to the noise excitation more difficult to analyze. Analysis of the impulse response is somewhat easier to perform than that of the square wave response; but the square wave response can provide verification of results obtained from the impulse response, as well as supplementary information.

PROCEDURE

Original intentions were to obtain natural frequencies and associated amplitudes from the output of a spectrum analyzer, and to obtain damping factors from the waveform obtained by passing the response signal through a band-pass filter. However, the band-pass filter originally used was not selective enough; and when a more selective filter was used, the filter ringing obscured the desired waveform. Although it is possible to set up a computer program using the transfer function of the band-pass filter to ultimately come up with the damping factors of the antenna response signal, it was decided to measure damping factor directly off the charts obtained from the spectrum analyzer. Thus frequencies, amplitudes, and damping factors were all obtained from the spectrum analyzer charts. The procedure was as follows:

1. Record an 80 to 90-foot magnetic tape loop from the original data tape for the test to be analyzed.
2. Run the tape loop signal through an analog computer to obtain
 - a. blanking of tape splice and any other undesired signal appearing on the tape loop.
 - b. removal of any D.C. bias voltage on the signal, and
 - c. desired amplification of small signals.
3. Feed the signal output of the analog computer into the spectrum analyzer.

4. Obtain frequencies, amplitudes, and damping factors from the spectrum analyzer chart.

The original data were recorded at 1-7/8 ips, whereas the tape loop was run at 30 ips, giving an apparent 16:1 frequency magnification on the spectrum analyzer. This spreads the spectrum from the analyzer, making it easier to distinguish the frequencies present, and reduces analyzer scan time. For each sensor scan response, up to five spectrum analyzer charts were made over the apparent frequency range from 0-400 cps. The apparent frequency range of each chart was 100 cps, with enough overlap between charts to check consistency. Actual frequency response was obtained by dividing the apparent frequencies obtained from the spectrum analyzer charts by sixteen.

Amplitudes were read directly from the spectrum analyzer charts in decibels down from a reference. Damping factors were obtained by means of the approximate formula (Reference 2)

$$\zeta = \frac{\Delta f}{2f_0}$$

where

ζ = damping factor

f_0 = frequency at amplitude peak

Δf = width of frequency spectrum at a point 3db down from the peak.

A typical spectrum analyzer chart is shown in Figure B-7.

RESULTS

A listing of frequencies, amplitudes levels, and damping factors for various sensor responses due to different excitations and a given sensor, the relative amplitudes are repeatable for a specific impulse. It was found that there was some variation of relative amplitudes from impulse to impulse. This may be due to random noise, but needs to be investigated further. To

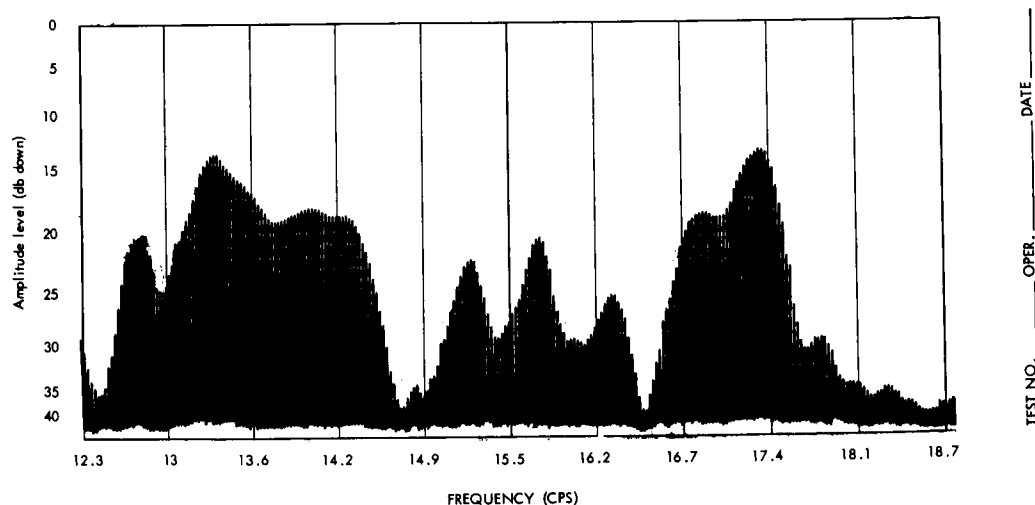


Figure B-7—Spectrum analyzer chart.

Table B-2
Relative Amplitude and Damping Factor for Various Sensors Due to Impulse Excitation

[illegible]

Table B-2 (continued)
Relative Amplitude and Damping Factor for Various Sensors Due to Impulse Excitation

Y Angle													X Angle Zenith	Excitation Antenna Attitude
Zenith											Horizon (East)			
Frequency (cps)	Feed box (X direction)	Dish North	Rim SSE	Vertex		Y Axis Bull gear	Y Axis Brg. (Z Direction)	Tachometer		Seismometer			Vertex (Y Direction)	Dish Rim SSE
				(X direc- tion	(Y direc- tion			No. 1	No. 2					
12.6					25					29		32		
12.8	20	17.5	18.5	32	.008	35	26			.02	32	32	19	
13.1	.007	.02	.008	.01		.009	.008				.007	.005	.01	
13.3	14	12.5	16.5	28	.01	26					31			
13.5	.007	.009	.01	.003	.01	32	29			30	.009	33	23	
13.7	16	13		26		.008	.007			.02		.01	.01	
13.8	.01	.009		.01		.01	.01							
14.1	18		18	34	22		27				34		22	
14.3	.02		.009	.008	.008		.01				.01	30	.006	
14.6	.01						.007			31	.02	.02	.008	
14.8	35	17	14.5	27	23						31	.009	25	
15.0		.01	.01	.009	.005		25			.01			.003	
15.2	22	22	19	31	.008		.009				25	34	35	
15.4	.005	.01	.007	24	.007		.003				.006		.003	
15.7	21	21.5	22.5	27	.009	32	33				27	35	33	
16.0	.005	.01	.004	.007	.009	32	.007				.005	.006	.003	
16.2	26	20	30			35	30				31	39	31	
16.4	.005	.007	.005			.004	.007				.006		.006	
16.6		20		32	35		40							
16.8	19	15		.008	.006	32	.01						25	
17.0	.01	.008		28	.005	30	.009						.006	
17.3	14			.01										
17.5	.007													
17.8	30	17		33	35	32	.004							
18.0	.005	.006		.005	.004	39								
18.2	36	27.5					34				33			
18.4	.005	.001					.004				.004			
18.7	39										31			
18.8		26			36		39				8.5			
18.9		.002			.005						.006			
19.2	31	.003												
19.4	34	.002												
19.8	33.5	.002									35			
20.0	34	.002									.003			
20.3	27	.003									39			
	31	.003									.003			
											34			
											.005			

compare amplitudes among different sensors and different excitations, a measure of absolute amplitude is necessary. This was to be accomplished by calibration checks made at the time the original data were recorded. Preliminary checks of the amplitude calibration data indicated some discrepancies, however; and this too needs to be reconciled.

It will be noticed in Table B-2 that for a given frequency there is some variation in damping factor at different sensor locations. This variation may be due to instrumentation error in the response analysis or it may indicate system nonlinearities. This will need to be checked out after a more complete listing (extension of Table B-2) is obtained and after other nonlinearity checks have been made.

DISCUSSION

The results given in this report represent but one step in the analysis of the dynamic response of the Rosman I 85-foot dish antenna. A digital computer simulation of the antenna system (without damping) is being prepared. The results given in this report will be used to check the validity of the computer simulation with respect to frequency and to provide damping information to supplement computer outputs. In addition, a simpler analog simulation is contemplated for use in antenna control system analysis. This too will rely on the results given here. Supplementary information for the extension to these results should include:

1. Investigation of relative amplitude differences between the responses of two apparently identical exciting impulses.
2. Spectrum analysis of background noise data in conjunction with 1.
3. Normalization of relative amplitudes with respect to damping.
4. Formulation of absolute amplitude calibration procedure.
5. Extension of Table B-2 to include all sensors for all impulse excitations.
6. Computer analysis to give amplitude vs. frequency and phase vs. frequency diagrams directly from recorded data. In addition to checking the spectrum analyzer results, this would give phase information and information about the transfer function zeros not obtainable from the spectrum analyzer.
7. Investigation of system nonlinearities by means of the square wave excitations and the side wave excitations.
8. Investigation of differences in response between positive and negative half-cycles of the square wave excitation.
9. Cross-checking between impulse response data and square wave response data in order to clear up any inconsistencies.
10. Cataloging of impulse response data by sensor location to indicate which antenna sub-systems are responsible for various resonant frequencies.
11. Analog simulation of antenna responses.

ACKNOWLEDGEMENTS

The author is deeply indebted to Mr. N. A. Raumann of the Antenna Systems Branch for assistance in setting up various portions of the equipment and for discussions of data analysis. In

addition, the author received significant encouragement and advice from Mr. G. C. Winston of the Antenna Systems Branch and considerable technical assistance from Mr. J. E. Lewis of Lockheed Electronics.

Additional information on procedure as well as original data information is available through either Mr. Winston or Mr. Raumann.

REFERENCES

1. Dalrymple, J.M., "Measurements of the dynamic response of the Rosman I 85-foot dish antenna", Final Report of the Goddard Summer Workshop Program, 1965.
2. Vibration Theory and Application, W. T. Thomson, Prentice-Hall, 1965, p. 74.

CALCULATION OF RADIATION PATTERN OF ROSMAN 85-FOOT PARABOLOIDAL DISH

George Eichmann

N 67-22756

INTRODUCTION

The aim of this report is two-fold;

1. To summarize existing results in the area of finite paraboloidal reflectors and to evaluate their applicability to the problem of radiation from a distorted paraboloidal dish with off-set feed.
2. To suggest and help to implement ways to calculate radiation patterns of such paraboloidal dish.

EXISTING RESULTS

All antenna problems are boundary value problems, namely, if source distributions are given (feed) and boundaries are specified (paraboloid) the object is then to calculate the electromagnetic fields due to the given source distribution.

The following "exact" results are often quoted in the literature:

1. Stratton's formula (Reference 1). It states that if the sinusoidal steady-state tangential electric or magnetic fields are specified on a closed surface and if all the sources inside the closed surface are zero, then the fields inside the closed region are uniquely specified. For example, the electric field is given by the following expression;

$$\bar{E}(\underline{r}') = \frac{-1}{4\pi} \int_A \left\{ j\omega\phi \bar{K}_e + \nabla\phi \times \bar{K}_m - \frac{\nabla_1 \bar{K}_e}{j\omega t} \nabla\phi \right\} dS \quad (1)$$

A detailed derivation and interpretation of this formula is given in Appendix A.

2. Huygens'-Fresnel-Kirchhoff (HFK) formula (Reference 2). It states that if a scalar field is specified at an opening of an "opaque" screen then the field behind the screen is given by the following expression:

$$u(\underline{r}) = \int_A u(\underline{r}') F(\theta) \frac{e^{j\beta r''}}{r''} dS \quad (2)$$

For a detailed derivation and interpretation of this formula see Appendix B.

3. Kottler's formula (Reference 3). This formula is the vector analogue of HFK formula. It states that if the tangential electromagnetic fields are specified at an opening of an "opaque" screen, then the fields behind the screen are specified. For example, the electric field is given by the following expression:

$$\bar{E}(r') = -\frac{1}{j\omega\epsilon} \frac{1}{4\pi} \oint_C \nabla\phi\bar{H} \cdot ds + \bar{E}(r')^{\text{STRATTON}} \quad (3)$$

As is apparent, the difference between Equation (2) and Equation (3) is in the ad hoc addition of a fictitious line source to compensate for edge effects. As is also apparent, none of so-called "exact" formulas are directly applicable to paraboloidal antennas and, therefore, approximations must be utilized to render the problem manageable.

In almost all of the approximating models, the problem of radiation from a paraboloidal dish is decomposed into three parts;

1. A mathematical idealization of the physical source, called feed or primary pattern.
2. A description of the scattering process.
3. A method of calculation of the field components at the point of observation.

In almost all cases, the physical source is idealized for mathematical manipulation as a directive dipole, i.e., a dipole with complex, direction dependent dipole moment.

The scattering surface, i.e., paraboloidal dish, is usually taken to be in the far-field of the directive dipole. It is always assumed that the scattered radiation does not interact back to the source. Now, there are two common methods of calculating the field components at the point of observation; geometrical optics approximate and current distribution approximate.

GEOMETRICAL OPTICS APPROXIMATION

The "dipole," as seen at point P on the surface of the paraboloid appears as an incident plane wave impinging on an infinite tangent plane at the point P on the surface and is reflected according to the law of geometrical optics, i.e., Snell's law.

PRIMARY CURRENT DISTRIBUTION APPROXIMATION

At each point P on the surface of the paraboloid, we draw an infinite tangent plane. The direction-dependent "dipole" as viewed at each point P on the surface of the paraboloid is imaged about the infinite tangent plane drawn at point P. The resulting surface current distribution is then taken as the primary induced current on the paraboloid. The current thus obtained neglects both edge effects as well as mutual interactions between current elements.

SECONDARY CURRENT APPROXIMATION

Maxwell's equations are approximated at the surface of the paraboloid. By requiring that charge should be conserved on the surface of the dish, a scalar equation is derived with the incident

field as a driving force. The solution of this scalar equation, the confluent hypergeometric equation, is the current that takes into account mutual interactions among current elements. Edge effects are, however, taken care of by means of Kottler's formula.

After reflection about point P on the surface, there are two ways to correct for diffraction phenomena if we use geometrical optics approximation. One is Keller's theory of quasi-optical diffraction, however, so far it has found only limited use. The other is the introduction of the so-called physical optics approximation. In this approximation, the primary pattern is reflected, with appropriate phase tag, to a plane called plane-aperture (p.a.) or exit pupil. Then the HFK principle is invoked and the field is then computable as an integral (Reference 2). The validity of this assumption stems from the following reasoning, i.e., if the feed was linearly polarized, then at p.a. it is still linearly polarized approximately, hence the scalar theory is justified. In most cases, however, the HFK integral is not amenable to analytical evaluation and further approximations are necessary. Two of these approximations are of importance since they lend themselves to physical interpretation.

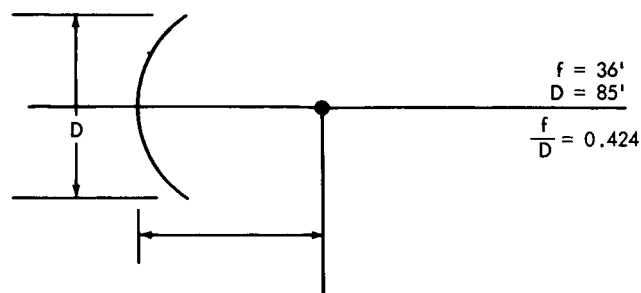
1. Transform solution. If in the HFK formula we only wish to evaluate the far-field contribution, then the amplitude of the integrand of (2) is $O(1/r)$ and the phase is linear. Neglecting the angle factor, we obtain the result that the far-field is the spatial Fourier transform of the aperture distribution. Therefore we can interpret the paraboloidal dish as a spatial filter in the far field domain.
2. Stationary Phase approximation. In this approximation the phase of HFK formula is expanded in a Taylor series about the point (u_0, v_0, w_0) where $\nabla\phi = 0$. If the phase is rapidly varying, i.e., $\lambda \rightarrow 0$ or $r \rightarrow \infty$ and the amplitude of the integrand is slowly varying, then the integral can be replaced by a ray emanating from the aperture in the direction of stationary phase to the point of observation. There are further approximations possible to take care of edges in the aperture; these are discussed in the literature (References 4 and 5). However, if the current distribution approximation is used, then the induced current on the surface of the dish is treated as a new vector source, i.e., as a given field distribution on a curved aperture. Since the source is now known, the known is substituted into Stratton's vector formula (Reference 1) and the fields are given in terms of integrals. Again, for simple cases, this expression is directly integrable. However, in general, it is further assumed that only radiation fields are of interest and therefore fields that vary as $O(1/r)$ as $r \rightarrow \infty$ are retained and the remaining terms are neglected.

There is another approximation that assumes that the "dipole" is embedded deep in the paraboloid and therefore an infinite paraboloidal surface is a reasonable approximation. This problem then can be solved exactly as a boundary value problem and the solution is given in terms of a infinite sum of Laguerre polynomials. A summary of approximation appears in Figure B-9.

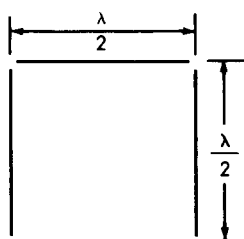
ROSMAN 85-FOOT PARABOLOIDAL DISH

Physical Characteristics

The structure of the antenna, as far as radiation is concerned, consists of the following configuration:

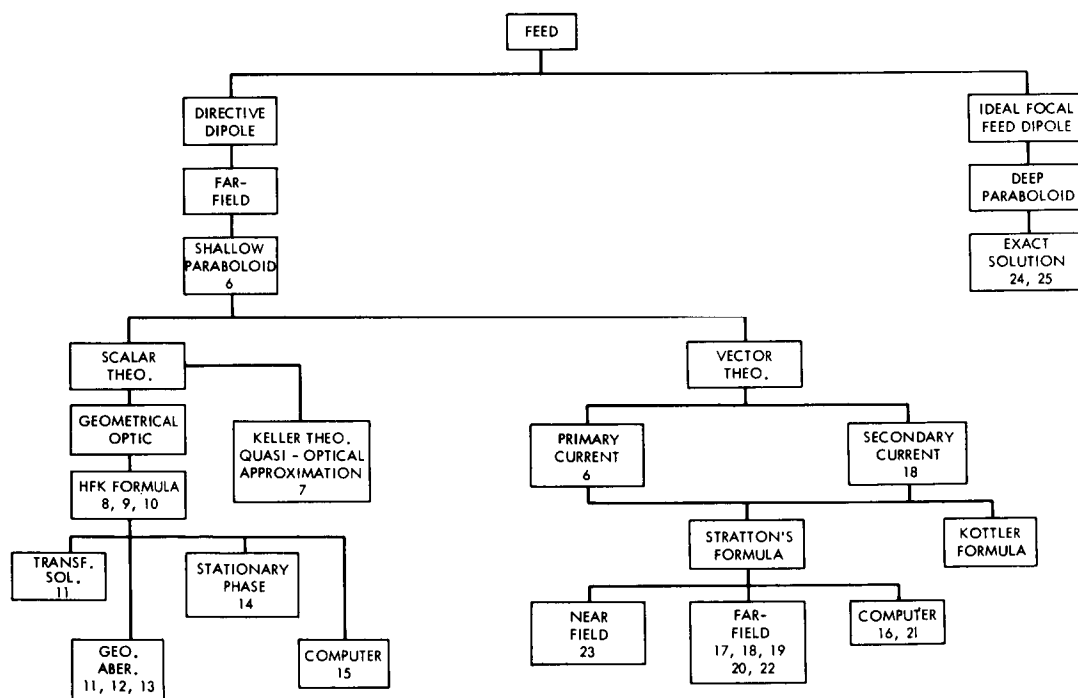


(a) DIMENSIONS OF THE DISH



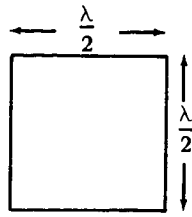
(b) FEED IN THE FOCAL PLANE
WHERE λ IS THE OPERATING FREQUENCY.

Figure B-8—Configuration of the Rosman I antenna.



(The number refers to bibliography)

Figure B-9—Paraboloidal approximations.



Dimensions of the Dish

Feed in the focal plane where λ is the operating frequency. In the case of Rosman antenna the operating frequencies are the following:

$$f_1 = 136 \text{ Mc}$$

$$f_2 = 400 \text{ Mc}$$

$$f_3 = 1705 \text{ Mc}$$

$$f_4 = 2300 \text{ Mc (contemplated)}$$

The feed consists of four dipoles mounted at the edge of a square shown in Figure B-8(b). Each dipole emits direction-dependent (amplitude-tapered) nearly circularly polarized radiation. Since both the dish and the feed are subject to mechanical as well as wind loads, the position of the feed-box relative to the scattering surface, i.e., distorted dish, is a variable quantity.

Taking all this information into account, an acceptable theory should be:

1. Frequency-dependent—Ruling out geometrical optics, to show differences between responses under various frequencies. Quasi-optical approximations, aberration theory, or stationary phase approximation would be acceptable for order of magnitude effects only.
2. Polarization-dependent—To take into consideration the elliptically polarized nature of source in conjunction with the depolarizing effect of the dish.
3. "Far" and "near" field-dependent—There should be ways to obtain corrections for near fields.
4. Geometry-dependent—The model should take into account the distortions from the ideal geometry.

All these restrictions on the model preclude an analytical study and, therefore, it necessitates a numerical analysis.

Computer Study

For a computer study the following formula has been selected (Reference 6)

$$\bar{I} = N \iint_{s_0} \frac{1}{\rho} [G_f(\theta, \Phi)]^{1/2} [\bar{n} \times \bar{\rho}_1 \times \bar{e}_i] e^{-j \mathbf{k} \cdot (\rho - \bar{\rho}_1 + \bar{R}_1)} dS \quad (4)$$

where

N is a normalization constant

G_f is the measured feed pattern

ρ is the distance between feed and a point on the scattering surface

$\bar{\rho}_1$ is a unit vector pointing from the feed to a point on the scattering surface

\bar{n} is the vector surface normal

\bar{e}_i is the complex polarization vector of the feed

S_0 is the area of the scatterer

\bar{R}_1 is a unit vector pointing from a point on the scatterer to the point of observation

k is the wave number of free space

Equation (4) has the following restrictions:

1. The scatterer is in the far-field of the feed.
2. Currents on the scatterer are the ones given by the current distribution method, i.e., all edge effects and mutual current interactions are neglected.
3. The point of observation is in the far-field of the scatterer.

This implies linear phase as well as transversality of fields in the far-field region. These restrictions can be weakened to some extent (Reference 6).

The variables in Equation (4) can be categorized in the following manner:

1. Input Variables - G_f , \bar{e}_i and \bar{n} to be specified numerically
2. Internal Variables - ρ , $\bar{\rho}_1$, \bar{R}_1 and dS . These variables presume a coordinate system. However, for a distorted off-focal fed dish there are no symmetries involved, and any system will do.
3. Output Variable - \bar{I} to be computed in the principal planes.

SUMMARY

This paper has given the background and the analysis necessary for a computer study of Rosman 85-foot distorted paraboloidal dish. The model for the study is based on the current distribution method. This model is reasonable as a first-order approximation; however, higher order model should use Fock's potentials for the analysis (Reference 7).

REFERENCES

1. Stratton, J. A., Electromagnetic Theory, McGraw-Hill, 1941, pp. 464-66.
2. Born, M., and Wolf, E., Principles of Optics, Pergamon Press, Oxford.
3. Stratton, J. A., op. cit., pp. 469-70.
4. Bremmer, H., Propagation of Electromagnetic Waves, Handbuch der Physik, Springer-Verlag (1958) Berlin, p. 445.

5. Braun, G., Zur methode der stationaren phasen, Acta Phys. Astriaca, Vol. 10, No. 8 (1956).
6. Hansen, R. C., and Bailin, L. B., "A new method of near field analysis," IRE Trans. Ant. Prop., Dec. 1959, p. S458.
7. Fock, V. A., Electromagnetic Diffraction, Pergamon Press, Oxford, Ch. 3 (1965).

APPENDIX A STRATTON'S FORMULA

Vector Green's Identity

From Gauss' theorem we have

$$\int_v \nabla \cdot \bar{A} \, dv = \int_s \bar{A} \cdot \bar{n} \, da \quad (A1)$$

where \bar{A} is any vector, S is a closed surface, v is the volume enclosed by S , and \bar{n} is a positive surface normal. Let

$$\bar{A} = \bar{P} \times \nabla \times \bar{Q} \quad (A2)$$

then, by (A1)

$$\int_v \nabla \cdot \bar{A} \, dv = \int_v \nabla \cdot \bar{P} \times \nabla \times \bar{Q} \, dv = \int_s \bar{P} \times \nabla \times \bar{Q} \cdot \bar{n} \, da \quad (A3)$$

but

$$\nabla \cdot (\bar{P} \times \nabla \times \bar{Q}) = \nabla \times \bar{P} \cdot \nabla \times \bar{Q} - \bar{P} \cdot \nabla \times \nabla \times \bar{Q} \quad (A4)$$

therefore

$$\int_v \nabla \cdot (\bar{P} \times \nabla \times \bar{Q}) \, dv = \int_v [\nabla \times \bar{P} \cdot \nabla \times \bar{Q} - \bar{P} \cdot \nabla \times \nabla \times \bar{Q}] \, dv \quad (A5)$$

Interchange \bar{P} and \bar{Q}

$$\int_v \nabla \cdot (\bar{Q} \times \nabla \times \bar{P}) \, dv = \int_v [\nabla \times \bar{Q} \cdot \nabla \times \bar{P} - \bar{Q} \cdot \nabla \times \nabla \times \bar{P}] \, dv \quad (A6)$$

Subtract (A6) from (A5)

$$\int_v \nabla \cdot [\bar{P} \times \nabla \times \bar{Q} - \bar{Q} \times \nabla \times \bar{P}] dv = \int_v [\bar{Q} \cdot \nabla \times \nabla \times \bar{P} - \bar{P} \cdot \nabla \times \nabla \times \bar{Q}] dv \quad (A7)$$

by the use of Equation A-1 we have the following Green identity.

$$\int_v [\bar{Q} \cdot \nabla \times \nabla \times \bar{P} - \bar{P} \cdot \nabla \times \nabla \times \bar{Q}] dv = \int_s [\bar{P} \times \nabla \times \bar{Q} - \bar{Q} \times \nabla \times \bar{P}] \cdot \bar{n} da \quad (A8)$$

Derivation of Vector Wave Equation

From Maxwell's equations with $e^{-j\omega t}$ time dependence, we have

$$\nabla \times \bar{E} = j\omega\mu\bar{H} \quad (A9)$$

$$\nabla \times \bar{H} = \bar{J} - j\omega\epsilon\bar{E} \quad (A10)$$

where \bar{E} and \bar{H} are the electric and the magnetic vectors respectively, ϵ and μ are the electric and magnetic permittivities, \bar{J} is free current density vector, ω is the radian frequency and $j = \sqrt{-1}$. Taking the curl of (A9) and substitute into (A10) we have

$$\nabla \times \nabla \times \bar{E} = j\omega\mu [\bar{J} - j\omega\epsilon\bar{E}] \quad (A11)$$

let

$$k^2 = \omega^2 \epsilon \mu \quad (A12)$$

then

$$\nabla \times \nabla \times \bar{E} - k^2 \bar{E} = j\omega\mu \bar{J} \quad (A13)$$

Solution of Wave Equation

Following Stratton, we take the Green function of Equation (A13) as

$$\bar{G} = \phi \underline{a} = \frac{e^{jk_r r''}}{r''} \underline{a} \quad (A14)$$

where \underline{a} is a constant vector, and ϕ is the Green function of the scalar Helmholtz equation, i.e.,

$$\nabla^2 \phi + k^2 \phi = -4\pi \delta(\underline{r} - \underline{r}') \quad (\text{A15})$$

where

$$r'' = [(x - x')^2 + (y - y')^2 + (z - z')^2]^{1/2} \quad (\text{A16})$$

Now let $\bar{P} = \bar{E}$ and $\bar{Q} = \bar{G}$ in (A8). We need the following expressions:

$$\nabla \times \bar{Q} = \nabla \times \phi \underline{a} = \nabla \phi \times \underline{a} \quad (\text{A17})$$

$$\nabla \times \nabla \times \bar{Q} = \nabla \phi \nabla \cdot \underline{a} - \underline{a} \nabla^2 \phi + (\underline{a} \cdot \nabla) \nabla \phi - (\nabla \phi \cdot \nabla) \underline{a} \quad (\text{A18})$$

but

$$\nabla \cdot \underline{a} = (\nabla \phi \cdot \nabla) \underline{a} \equiv 0$$

since $\underline{a} \equiv$ constant vector

$$\nabla \times \nabla \times \bar{Q} = -\underline{a} \nabla^2 \phi + (\underline{a} \cdot \nabla) \nabla \phi \quad (\text{A19})$$

From (A15)

$$\nabla^2 \phi = -k^2 \phi - 4\pi \delta(\underline{r} - \underline{r}')$$

and

$$\nabla(\underline{a} \cdot \nabla \phi) = (\underline{a} \cdot \nabla) \nabla \phi + (\nabla \phi \cdot \nabla) \underline{a} + \underline{a} \times \nabla \times \nabla \phi + \nabla \phi \times \nabla \times \underline{a} \quad (\text{A20})$$

but

$$\nabla \phi \cdot \nabla \underline{a} \equiv \nabla \times \nabla \phi \equiv \nabla \times \underline{a} \equiv 0$$

rewriting Equation (A19) we have

$$\nabla \times \nabla \times \bar{Q} = \underline{a} [k^2 \phi + 4\pi \delta(\underline{r} - \underline{r}')] + \nabla(\underline{a} \cdot \nabla \phi) \quad (\text{A21})$$

Now substitute into Equation (A8) and work on LHS first.

$$\int_{\mathbf{v}} \{ \underline{\mathbf{a}} \phi \cdot \nabla \times \nabla \times \bar{\mathbf{E}} - \bar{\mathbf{E}} \cdot \underline{\mathbf{a}} [k^2 \phi + 4\pi \delta(\underline{\mathbf{r}} - \underline{\mathbf{r}}')] - \bar{\mathbf{E}} \cdot \nabla (\underline{\mathbf{a}} \cdot \nabla \phi) \} d\mathbf{v} \quad (\text{A22})$$

but

$$\nabla \times \nabla \times \bar{\mathbf{E}} = k^2 \bar{\mathbf{E}} + j\omega\mu \bar{\mathbf{J}} \quad \text{from Equation (A13).}$$

$$\int_{\mathbf{v}} \{ \phi \underline{\mathbf{a}} \cdot j\omega\mu \bar{\mathbf{J}} - \bar{\mathbf{E}} \cdot [\underline{\mathbf{a}} 4\pi \delta(\underline{\mathbf{r}} - \underline{\mathbf{r}}') + \nabla (\underline{\mathbf{a}} \cdot \nabla \phi)] \} d\mathbf{v} \quad (\text{A23})$$

but

$$\nabla \cdot [\bar{\mathbf{E}} (\underline{\mathbf{a}} \cdot \nabla \phi)] = \bar{\mathbf{E}} \cdot \nabla (\underline{\mathbf{a}} \cdot \nabla \phi) + (\underline{\mathbf{a}} \cdot \nabla \phi) \nabla \cdot \bar{\mathbf{E}} \quad (\text{A24})$$

$$\int_{\mathbf{v}} \{ \phi \underline{\mathbf{a}} \cdot j\omega\mu \bar{\mathbf{J}} - \bar{\mathbf{E}} \cdot \underline{\mathbf{a}} 4\pi \delta(\underline{\mathbf{r}} - \underline{\mathbf{r}}') - \nabla \cdot [\bar{\mathbf{E}} \underline{\mathbf{a}} \cdot \nabla \phi] + (\underline{\mathbf{a}} \cdot \nabla \phi) \nabla \cdot \bar{\mathbf{E}} \} d\mathbf{v} \quad (\text{A25})$$

but

$$\nabla \cdot \bar{\mathbf{E}} = \rho/\epsilon \quad (\text{A26})$$

and

$$\int_{\mathbf{v}} \nabla \cdot (\bar{\mathbf{E}} \underline{\mathbf{a}} \cdot \nabla \phi) d\mathbf{v} = \int_{\mathbf{A}} (\bar{\mathbf{E}} \cdot \bar{\mathbf{n}}) \underline{\mathbf{a}} \cdot \nabla \phi dS \quad (\text{A27})$$

Substitute Equations (A26) and (A27) into (A25) and note

$$\bar{\mathbf{E}}(\mathbf{r}') = \int_{\mathbf{v}} \bar{\mathbf{E}}(\underline{\mathbf{r}}) \delta(\underline{\mathbf{r}} - \underline{\mathbf{r}}') d\mathbf{v} \quad (\text{A28})$$

we have

$$-4\pi \bar{\mathbf{E}}(\mathbf{r}') \cdot \underline{\mathbf{a}} + \int_{\mathbf{v}} \left\{ j\omega\mu \phi \underline{\mathbf{a}} \cdot \bar{\mathbf{J}} + \underline{\mathbf{a}} \cdot \nabla \phi \frac{\rho}{\epsilon} \right\} d\mathbf{v} - \int_{\mathbf{A}} (\bar{\mathbf{E}} \cdot \bar{\mathbf{n}}) \underline{\mathbf{a}} \cdot \nabla \phi dS \quad (\text{A29})$$

Now work on RHS of (A8)

$$\int_A \{\bar{\mathbf{P}} \times \nabla \times \bar{\mathbf{Q}} - \bar{\mathbf{Q}} \times \nabla \times \bar{\mathbf{P}}\} \cdot \bar{\mathbf{n}} \, d\mathbf{S} = \int_A \{\bar{\mathbf{E}} \times \nabla \times \phi \underline{\mathbf{a}} - \phi \underline{\mathbf{a}} \times \nabla \times \bar{\mathbf{E}}\} \cdot \bar{\mathbf{n}} \, d\mathbf{S} \quad (\text{A30})$$

but $\nabla \times \bar{\mathbf{E}} = j\omega\mu \bar{\mathbf{H}}$ from Equation (9)

and $\nabla \times \bar{\mathbf{Q}} = \nabla \phi \times \underline{\mathbf{a}}$ from Equation (A17)

$$\int_A \{\bar{\mathbf{E}} \times \nabla \phi \times \underline{\mathbf{a}} \cdot \bar{\mathbf{n}} - j\omega\mu \phi \underline{\mathbf{a}} \times \bar{\mathbf{H}} \cdot \bar{\mathbf{n}}\} \, d\mathbf{S} \quad (\text{A31})$$

but

$$\underline{\mathbf{a}} \times \bar{\mathbf{H}} \cdot \bar{\mathbf{n}} = \underline{\mathbf{a}} \cdot \bar{\mathbf{H}} \times \bar{\mathbf{n}} = -\underline{\mathbf{a}} \cdot \bar{\mathbf{n}} \times \bar{\mathbf{H}} \quad (\text{A32})$$

and

$$\bar{\mathbf{E}} \times (\nabla \phi \times \underline{\mathbf{a}}) \cdot \bar{\mathbf{n}} = (\bar{\mathbf{n}} \times \bar{\mathbf{E}}) \cdot (\nabla \phi \times \underline{\mathbf{a}}) = (\bar{\mathbf{n}} \times \bar{\mathbf{E}}) \times \nabla \phi \cdot \underline{\mathbf{a}} \quad (\text{A33})$$

Substituting Equations (A32) and (A33) into (A31) we have

$$\underline{\mathbf{a}} \left[\int_A \{(\bar{\mathbf{n}} \times \bar{\mathbf{E}}) \times \nabla \phi + j\omega\mu \phi (\bar{\mathbf{n}} \times \bar{\mathbf{H}})\} \, d\mathbf{S} \right] \quad (\text{A34})$$

Equating LHS (Equation A29) with RHS (Equation A34)

$$\begin{aligned} \bar{\mathbf{E}}(\mathbf{r}') &= \frac{1}{4\pi} \int_V \left\{ j\omega\mu \phi \bar{\mathbf{J}} + \nabla \phi \frac{\rho}{\epsilon} \right\} \, d\mathbf{v} \\ &\quad - \frac{1}{4\pi} \int_A \{(\bar{\mathbf{n}} \times \bar{\mathbf{E}}) \times \nabla \phi + j\omega\mu \phi (\bar{\mathbf{n}} \times \bar{\mathbf{H}}) + (\bar{\mathbf{E}} \cdot \bar{\mathbf{n}}) \nabla \phi\} \, d\mathbf{S} \end{aligned} \quad (\text{A35})$$

Let

$$\bar{\mathbf{E}} \cdot \bar{\mathbf{n}} = \frac{\sigma_e}{\epsilon} \quad (\text{A36})$$

where σ_e = electric surface charge

$$\bar{n} \times \bar{E} = -\bar{K}_m \quad (A37)$$

where \bar{K}_m = magnetic surface current

$$\bar{n} \times \bar{H} = \bar{K}_e \quad (A38)$$

where \bar{K}_e = electric surface current. Substituting Equations (A36), (A37), and (A38) into Equation (A35) we have

$$\bar{E}(\underline{r}') = \frac{1}{4\pi} \int_V \left\{ j\omega\mu\phi \bar{J} + \nabla\phi \frac{\rho}{\epsilon} \right\} dv - \frac{1}{4\pi} \int_A \left\{ \nabla\phi \times \bar{K}_m + j\omega\mu\phi \bar{K}_e + \frac{\sigma_e}{\epsilon} \nabla\phi \right\} dS \quad (A39)$$

However, since charge must be conserved on the surface

$$\nabla \cdot \bar{K}_e + j\omega\sigma_e = 0 \quad (A40)$$

Substituting Equations (A40) and (A39) we have

$$\bar{E}(\underline{r}') = \frac{1}{4\pi} \int_V \left\{ j\omega\mu\phi \bar{J} + \nabla\phi \frac{\rho}{\epsilon} \right\} dv - \frac{1}{4\pi} \int_A \left\{ \nabla\phi \times \bar{K}_m + j\omega\mu\phi \bar{K}_e - \frac{\nabla \cdot \bar{K}_e}{j\omega\epsilon} \nabla\phi \right\} dS \quad (A41)$$

If all sources inside S are zero, then

$$\bar{E}(\underline{r}') = \frac{-1}{4\pi} \int_A \left\{ \nabla\phi \times \bar{K}_m + j\omega\mu\phi \bar{K}_e - \frac{\nabla \cdot \bar{K}_e}{j\omega\epsilon} \nabla\phi \right\} dS \quad (A42)$$

on a copper surface $\bar{K}_m \equiv 0$

$$\bar{E}(\underline{r}') = \frac{1}{4\pi} \int_A \left\{ \nabla\phi \frac{\nabla \cdot \bar{K}_e}{j\omega\epsilon} - j\omega\mu\phi \bar{K}_e \right\} dS \quad (A43)$$

APPENDIX B

HUYGENS'-FRESNEL-KIRCHOFF FORMULA (HFK)

There are basically two methods to obtain the Green function of an infinite conducting plane; one is by the method of images and the other by a method introduced by Sommerfeld. Since the latter method is less known, HFK formula will be developed along the Sommerfeld approach. The problem Sommerfeld solves is the following: given the tangential electric field at an infinite plane, taken for convenience to be $Z = 0$, i.e., $\bar{E}_T(x, y, 0)$. The problem is then to find $\bar{E}(x, y, z)$ for $Z > 0$.

Solution:

From Appendix A, Equation (A13)

$$\nabla \times \nabla \times \bar{E} - k^2 \bar{E} = j \omega \mu \bar{J} \quad (B1)$$

but

$$\nabla \times \nabla \times \bar{E} = \nabla(\nabla \cdot \bar{E}) - \nabla^2 \bar{E} \quad (B2)$$

and

$$\nabla \cdot \bar{E} = \frac{\rho}{\epsilon} \equiv 0 \quad (B3)$$

also there are no free currents

present

$$\bar{J} \equiv 0 \quad (B4)$$

Using Equations (B2), (B3), and (B4) in Equation (B1)

$$\nabla^2 \bar{E} + k^2 \bar{E} = 0 \quad (B5)$$

Let the solution of Equation (B5) be an infinite plane wave spectrum with unknown amplitude $\bar{F}(u, v)$, i.e.,

$$\bar{E}(x, y, z) = \iint_{-\infty}^{\infty} \bar{F}(u, v) e^{j k (xu + yv + zw)} du dv \quad (B6)$$

Substituting Equation (B6) into (B5) we get the eigen-value equation

$$u^2 + v^2 + w^2 = 1 \quad (B7)$$

at $Z = 0$

$$\bar{E}(x, y, z) = \bar{E}_T(x, y, 0).$$

From (B6)

$$\bar{E}_T(x, y) = \iint_{-\infty}^{\infty} \bar{F}(u, v) e^{jk(xu + vy)} du dv \quad (B8)$$

Invert

$$\bar{F}(u, v) = \left(\frac{k}{2\pi} \right)^2 \iint_{-\infty}^{\infty} \bar{E}_T(x, y) e^{-jk(xy + vy)} dx dy. \quad (B9)$$

Substituting Equation (B9) into Equation (B6)

$$\bar{E}(r) = \iint_{-\infty}^{\infty} \left[\left(\frac{k}{2\pi} \right)^2 \iint_{-\infty}^{\infty} \bar{E}_T(x_0, y_0) e^{-jk(x_0 u + y_0 v)} \right] e^{jk[xu + vy + wz]} du dv. \quad (B10)$$

Invert order of integration, and note

$$\frac{e^{jkr}}{r} = \iint_{-\infty}^{\infty} \frac{1}{W} e^{jk[ux + vy + \sqrt{1-u^2-v^2}z]} du dv. \quad (B11)$$

where

$$r = [x^2 + y^2 + z^2]^{1/2}$$

and

$$\frac{d}{dz} \left(\frac{e^{jkr}}{r} \right) = \iint_{-\infty}^{\infty} e^{jk[ux + vy + \sqrt{1-u^2-v^2}z]} du dv \quad (B12)$$

we get

$$\bar{E}(x, y, z) = \iint_{-\infty}^{\infty} \bar{E}_T(x_0, y_0) \frac{z}{r} \left(1 - \frac{1}{jkr}\right) \frac{e^{jkr}}{r} dx_0 dy_0 \quad (B13)$$

where

$$r = [(x - x_0)^2 + (y - y_0)^2 + z^2]^{1/2} \quad (B14)$$

Let

$$\frac{z}{r} = \cos \theta \approx 1 \quad (B15)$$

$$\begin{aligned} \frac{1}{jkr} \ll 1 \mid \bar{E}_T(x_0, y_0) &= u(x_0, y_0) a_x \text{ on } A \\ &= 0 \text{ on } \bar{A} \end{aligned}$$

Where A is the aperture, we have

$$u(\underline{r}') = \iint_A u(\underline{r}_0) \frac{e^{jkr}}{r} dx_0 dy_0. \quad (B16)$$

This equation can be interpreted as a Huygens' principle in the following sense: $u(\underline{r}')$ is a linear superposition of spherical wavelets emanating from the aperture with amplitude $u(\underline{r}_0)$. If

$$\underline{r} \gg \underline{r}_0 \quad (B17)$$

then

$$u(\underline{r}') = \frac{e^{jkr'}}{r'} \iint_A u(\underline{r}_0) e^{-jkr_0} dx_0 dy_0 \quad (B18)$$

where

$$r' = [x^2 + y^2 + z^2]^{1/2}, \quad r_0 = [x_0^2 + y_0^2]^{1/2} \quad u(\underline{r}') = \left(\frac{2\pi}{k} \right)^2 \frac{e^{ikr'}}{r'} F\{u(r_0)\} \quad (\text{B19})$$

Equation (B19) can be interpreted then in the usual fashion; namely, the far-field is the spatial Fourier transform of the aperture distribution.

Equation (B13) is an exact solution of the Sommerfeld problem. However, starting from a scalar formulation of Huygen's principle, we are led to the notation of "black screen," i.e., a screen where u and $\partial u / \partial n$ equals to zero. These boundary conditions are incompatible, and, therefore, the Huygens' solution is said to be inconsistent with the assumed boundary conditions.

ANALYSIS OF THE DYNAMIC RESPONSES OF THE ROSMAN-I ANTENNA

William J. Irwin

N 67-22757

This project was commenced by the Summer Workshop of 1965 and is expected to be continued by the Goddard staff during the months following the summer of 1966. Because of the progressive nature of this project some knowledge of the first summer's activities and a general description of the project will be useful.

The Rosman I Antenna is an 85 foot paraboloid, possessing an x-y mounting arrangement which permits motion about two axes. The feed box (signal acquisition apparatus) is mounted at the focus of the dish and is supported by a quadrapod structure. During tracking operations the mechanical responses of the structure are excited by the effects of wind, servo driving torque, and servo starting transients. These effects produce deviation of the dish from a true parabola and displacement of the receiving elements from its focus, thus distorting the received signal and limiting the resolution of the antenna. It is therefore necessary to find a transfer function relating signal distortion (as created by these effects) to servo output.

The mechanical characteristics (resonances) of the antenna can be excited by modulating the servo output torque with sine wave, square wave, or impulse functions.

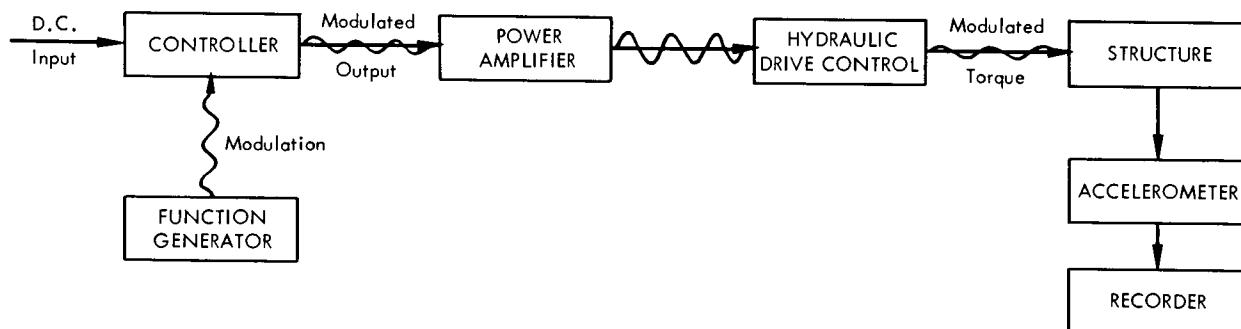


Figure B-10—Dynamic response test set-up.

Accelerometers, which indicate relative motion in a plane, were mounted at critical areas on the structure.

Two series of tests were run, the first with X axis servo modulation, the second with Y axis modulation. Orientation of the dish varied from the horizontal lock-on tests to zenith position. Placement of the accelerometers varied with the test series.

The axis gears were tested successively, as well as the dish and feedbox structures. A seismograph mounted on the concrete base recorded the effects of structural motion on the surrounding earth. Servo output torque was

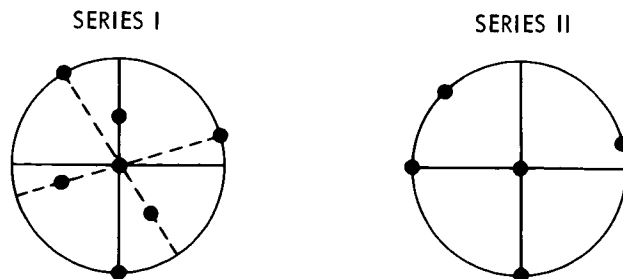


Figure B-11—Accelerometer mounting positions (dish).

also monitored to check the output of the drive assembly. Data were recorded on F.M. magnetic tape and brought to GSFC for analysis.

The reduction of data, which has been the primary concern of 1966 efforts, was proposed to cover 4 steps:

1. Transferral of data from magnetic tape to oscillograph charts for preliminary visual examination.
2. Re-recording of data from tape reel to "endless" loop for spectrum analysis to determine component frequencies.
3. Frequency discrimination by the use of bandpass filter to recover a single frequency from original accelerometer output and determine amplitude damping characteristics.
4. Use of an analog computer to determine transfer characteristics from response to an impulse function. (This last stage remains to be started and thus will not be discussed.)

The data output of the accelerometer is a complex waveform consisting of many damped sine waves of varying frequency. (See Figure B-12.)

The object of data investigation is to determine the frequency, amplitude, and damping factor of each component waveform.

The frequency-modulated* tapes were replayed on an instrumentation tape recorder. Data was recorded at 1-7/8 inches per second, and replayed at 30 inches per second to comply with the frequency range of the spectrum analyzer. This necessitated dividing all frequencies by 16 to obtain the true frequency. Tape recorder output was fed directly to a recording oscillograph provided the gain was sufficient, D.C. amplifiers remedied the situation if not. Chart speed was variable but was usually run at 20 mm/sec to evaluate data for loop recording and subsequent spectral analysis.

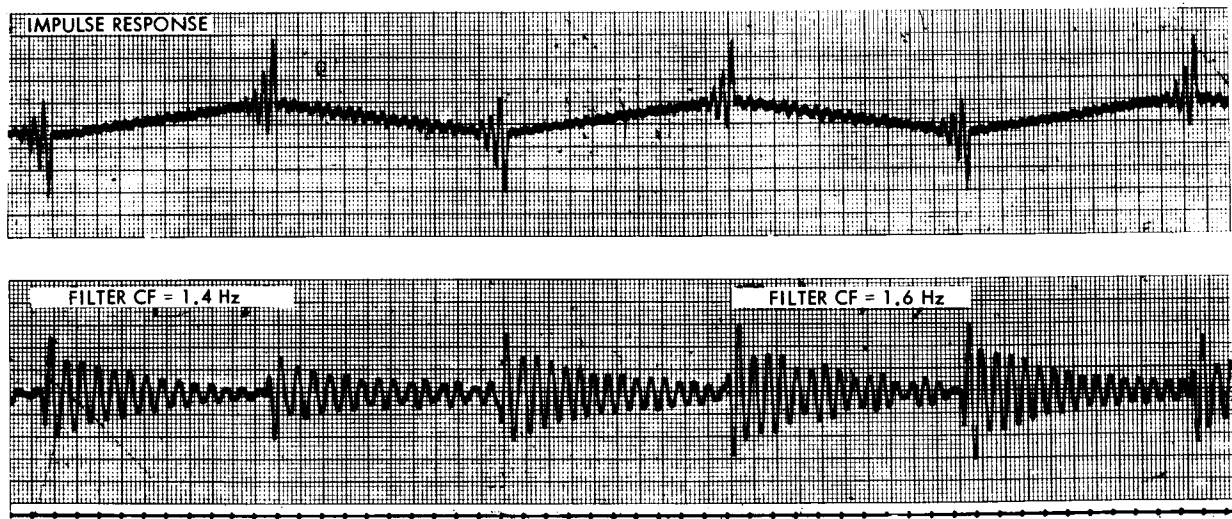


Figure B-12—Filtered impulse responses—vertex. The upper channel on the graph indicates the complete output of an accelerometer mounted on the vertex of the parabolic dish, while a square wave is applied to the antennastructure via the hydraulic servo motors. The lower channel is a filtered response between 1.4 and 1.6 Hz. This method proved unfeasible due to excessive filter ringing and subsequent distortion of the original damped oscillation.

*Frequency-modulation was used because the extremely low frequency, < 20 cps, would undergo considerable distortion using ordinary recording means.

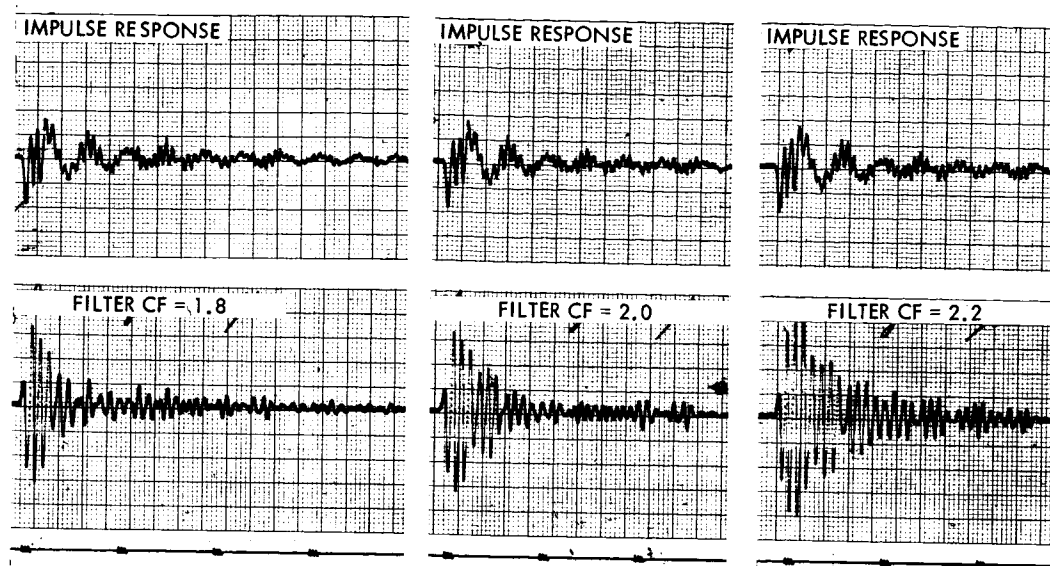


Figure B-13—Filtered impulse response-feebox. The upper channel indicates complete output (repeated three times) of the accelerometer mounted on the feebox while subjected to an impulse on the Y-axis. The lower channel shows the filtered response with the filter center frequency set at three values.

Data to be analysed was selected from the original tape and re-recorded on a loop which was also run at 30 ips. Data from the loop was displayed again on a strip chart and a single response was selected for frequency analysis. With some modifications the splice blanking circuit of the tape recorder was adapted to blank the entire loop except the selected response. The signal from the recorder was then fed to the spectrum analyzer which scanned a preselected frequency range

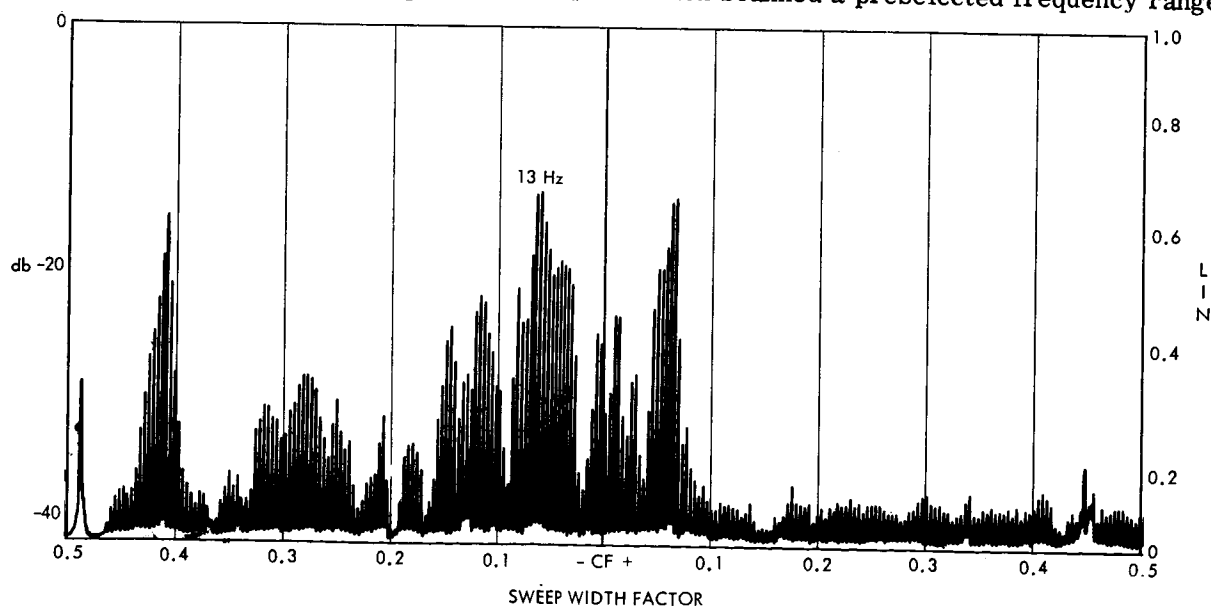


Figure B-14—Impulse Response Frequency Spectrum. Spectrum analysis of response in Figure B-13 to determine component frequencies. Sweep range is 500 Hz with a center frequency of 250 Hz. Characteristics of the analyzer made it necessary to multiply all true frequencies by 16 during analysis, hence the center frequency of 250 Hz is actually 15.6 Hz.

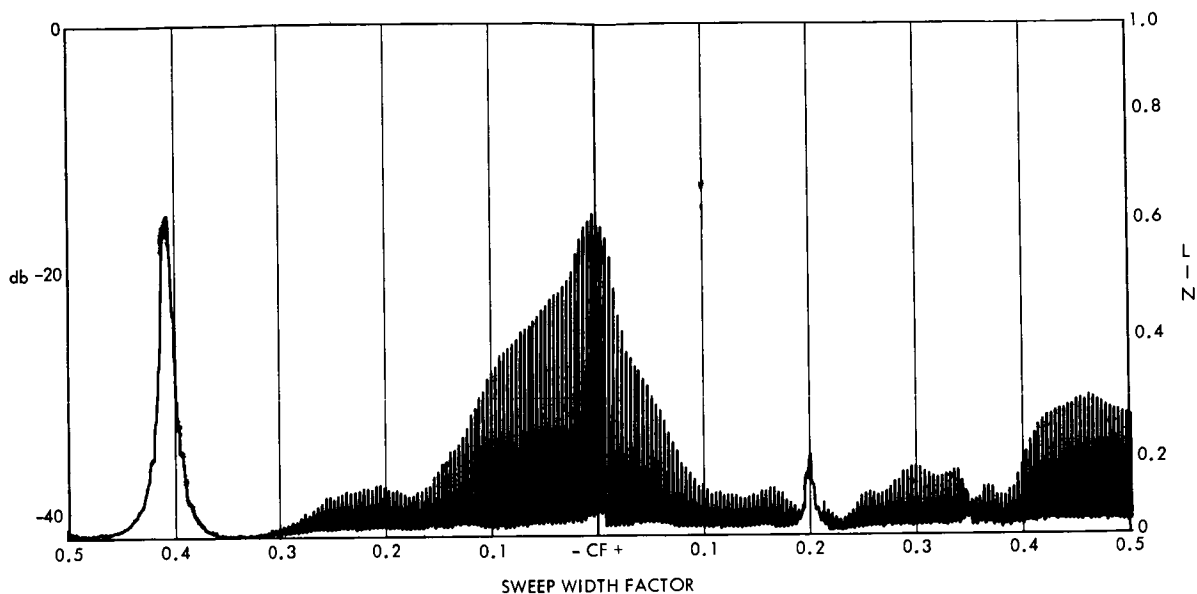


Figure B-15—Expanded scale frequency spectrum. An expanded portion of Figure B-14 scanning from 0-5 Hz which corresponds to responses between -0.5 and -0.3 on an arbitrary sweep width scale. The zero frequency pipe is visible on both scans.

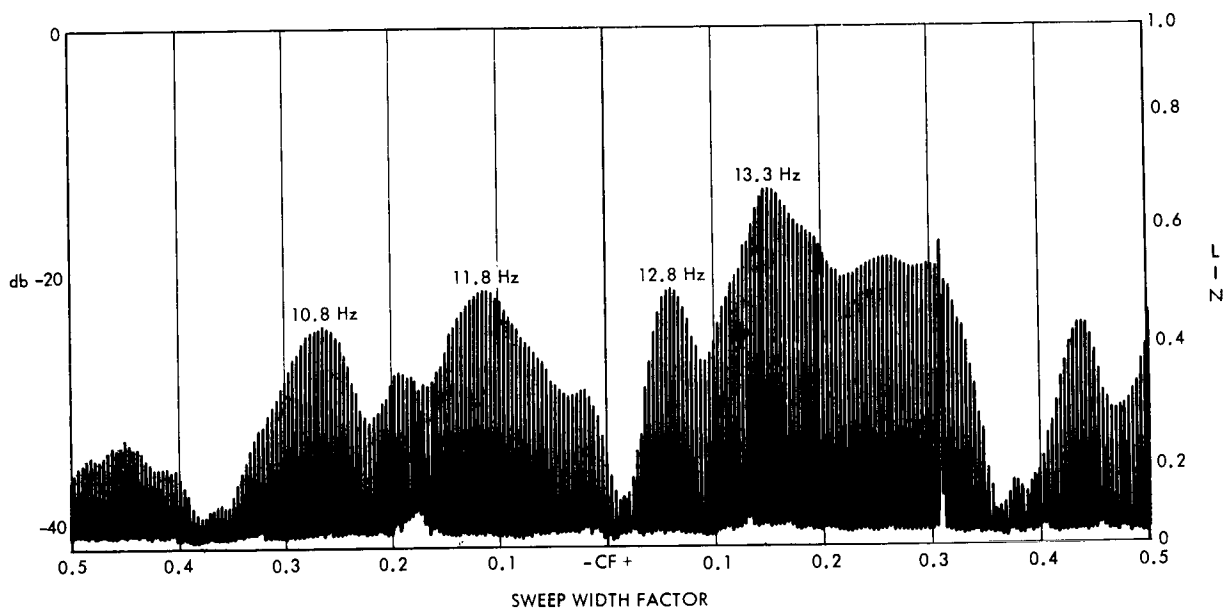


Figure B-16—Expanded scale frequency spectrum. Expanded analysis of responses between -0.2 and CF on Figure B-15. Damping is readily computed from responses such as these. In general, the more peaked responses indicate a lesser damping factor than the broad band responses.

and indicated the presence of various components. An attempt was made to separate the frequency components by means of a narrow band filter. However, due to resonance effects of the selective bandpass filter, separation of frequencies by this method for damping computation was not feasible, as the original damped wave and the "ringing" of the filter combined to produce a distorted output. By generating damped sine waves on an analog computer, and observing the resultant spectral analysis, a method was derived for determining damping from the spectrum analyzer strip charts. (Provided the response was relatively noise-free.)

Damping was readily obtained from the equation:

$$2\zeta = \frac{\Delta F}{F_0}$$

where

ζ = damping factor

ΔF = change in frequency at 3 db down

F_0 = center frequency

Results are not available in great quantity at the time of this writing as the project has not yet advanced to that stage. The methods of data analysis and instrumentation techniques are being standardized however and it is expected that progress will be made in the coming year.

MAGNETIC SHIELDING

D. L. Waidelich

N 67-22758

One method of reducing the effect of the earth's magnetic field for the testing of components and spacecraft in very low magnetic fields is to use some form of magnetic shielding. The present study was confined almost entirely to the consideration of shielding against static magnetic fields although some of the references are also concerned with shielding against low frequency fields as well.

The shielding effects of iron appear to have been known in the early part of the Nineteenth Century [D1] although the first solution for the special case of one spherical shield seems to have been given by Maxwell [M6] in 1873. In 1882 Stefan [S3] treated the case of infinitely long hollow iron cylinders with the applied magnetic field perpendicular to the axis. In 1894 Rucker [R1] considered the shielding properties of concentric spherical shells while three years later duBois [D1], [D2], [D7], [D8] studies spherical and cylindrical double shields. In 1899 Wills [W1], [D3] presented an analysis of three concentric spherical or cylindrical shields.

In the third year of the twentieth century Russell [R3] reported on the shielding factors measured experimentally of hollow iron cylinders. The results indicated that the shielding ratio is affected also by the retentivity of the iron and also by the presence or absence of other magnetic fields. In 1907 Wills [W4] showed that the best shielding occurs when the radii of the multiple shells are approximately in a geometrical progression, while in 1908 Nichols and Williams [N3] described the cylindrical shields for a galvanometer and gave the experimentally determined shielding ratios for a number of different shields. Esmarch [E1], [E2] in 1912 measured the shielding factor as the distance along the axis of a solenoid was varied. The solenoid was wound with one or more layers of high permeability iron wire. A theoretical investigation was also given in which determinants were used to solve a shield of N layers of material. The shielding factor was found to be a function of N and the permeability and thickness of the shell. In 1916 Coblenz [C4] described and tested various cylindrical shields for galvanometers while Wilson and Nicholson [N3] gave a theory of shielding using a number of shells. An example using four shells and some experimental results were presented.

During the 1920's, iron sheets with paper in between were wound on a form to make a shield [B2], and later ring stampings of high permeability material were used as a shield [D4]. About this same time mumetal and permalloy were being used for shielding purposes [D5], [D6], [H1]. In the 1930's the shielding of transformers was discussed [C6], [C7], [G1], [G2] and [M3] and it was suggested that high permeability material such as mumetal and permalloy [R2], [R4] be used with welded joints. These materials were also employed as shields for cathode ray tubes [S6]. A theoretical solution for N shells using difference equations was presented [S1], [W5]. During the 1940's the shield for a beta-ray spectrometer [A1] was described and a number of review articles appeared [T2], [S5], [M7], [M3], [K2]. The idea of shielding using a superconductor also appeared [L2]. In the 1950's the use of high permeability material to shield color television tubes was presented [T1], [T3] and very high shielding factors were obtained theoretically [W2], although errors in the values of the permeabilities used seemed to invalidate the results [C1]. A shield surrounding a Helmholtz coil pair was used to produce a very uniform magnetic field at the center of the coil system [S7].

In the first half of the 1960's the interest in shielding seemed to increase considerably. One topic of much importance was the shielding of magnetic fields by the use of superconductors [V1], [B1], [B3], [B4], [H3], [F1]. Another topic was the use of shields in the testing of components for spacecrafts [E3], [N1], [N2], [C3], while a third was the development of room-size shields [P2], [C2]. Shields were also used for the screening of solenoids [H4] and Helmholtz coil pairs [S4], [G3]. They were also found useful in a mass spectrometer [M5] and in the watch industry [P1]. Theoretical studies appeared solving the n-shell problem by the use of matrices [S2] and obtaining the shielding factor of a static dipole at the center of n concentric shells [E5].

REFERENCES

- A1 Alburger, D.E., "Beta-Ray Spectrometer Magnetic Shielding," Review of Scientific Instruments, V. 19, p. 474, 1948.

Iron rings separated but with the same axis help in shielding object from undesirable magnetic fields.

- A2 Albach, W. and Voss, G.A., "Ein durch vorerregte Dynamobleche magnetisch abgeschirmter Messraum," Zeitschrift für angewandte Physik, V. 9, p. 111 to 115, March 1957.

Magnetic material in the form of three concentric cylinders is used as a shield to produce a screening factor of about 100.

- B1 Brown, R.E., "Stable Field Environment for Magnetometer Testing," NASA STAR N66-11289.

Suggests the use of superconductors to shield from magnetic noise. The shield was a cylinder of lead cooled by liquid helium. Curves of the variation of transverse and axial fields along the axis of the cylinder are presented. Also discusses the use of a flux pump to provide shielding.

- B2 Benedicks, C., "Magnetischer Schutzpanzer aus spiralgewickeltem Eisen blech," Annalen der Physik, V. 72, p. 236 to 240, 1923.

Iron sheets are wound with paper in between to make a shield. The shielding factor is obtained experimentally.

- B3 Brown, R.E. and Hubbard, W.M., "Magnetic Field Reduction in an Expandable Superconducting Enclosure," Review of Scientific Instruments, V. 36, p. 1378 to 1379, September 1965.

The cross-sectional area of a hollow superconducting lead cylinder is increased and the resulting flux density inside the cylinder is reduced by a factor of about 0.03. For further reduction it is suggested that two cylinders, one within the other, could be used.

- B4 Benaroya, R. and Mogensen, H.P., "Magnetic Shielding by Superconducting Niobium Tin Plates," Journal of Applied Physics, V. 37, p. 2162 to 2166, April 1966.

An experimental investigation and theoretical analysis is made of the shielding effect of superconducting plates. It was found that the field was reduced by a factor of eleven. Flux jumps lower the shielding effect and may make it asymmetrical. The flux jumps may be eliminated by decreasing sufficiently the time rate of change of the flux density.

- C1 Cravath, A.M., "Magnetic Shielding with Multiple Cylindrical Shells," Review of Scientific Instruments, V. 28, p. 659, August 1957.

Points out that errors in the values of the permeabilities in Wadey's [W2] paper invalidate his results.

- C2 Connor, A.V., "Room-Size Magnetic Shield Facility," NASA STAR N66-11285.

The shield facility was designed for a field intensity of less than 100 gammas and used the design method of Patton and Fitch [P2]. Constructional details are given including the method of constructing the access door. The field intensity measured in the room is eighteen gammas.

- C3 Christy, J.R., "Magnetic Shielding of Spacecraft Hardware," NASA STAR N66-11292.

Use of mumetal and molypermalloy shields to shield magnetic components on the Mariner Mars spacecraft. Components shielded were latching relays, a power switch, and R.F. circulator switches.

- C4 Coblenz, W.W., "Sensitivity and Magnetic Shielding Tests of a Thomson Galvanometer for Use in Radiometry," Bureau of Standards Bulletin, V. 13, p. 423 to 446, 1916.

Various cylindrical shields are described and measured. The maximum shielding factor obtained was about 2000.

- C5 Curtis, H.L., "Shielding and Guarding Electrical Apparatus Used in Measurements - General Principles," Journal of the American Institute of Electrical Engineers, V. 48, p. 453 to 457, 1929.

This is a review article reporting previous investigations.

- C6 Constable, J.E.R. and Aston, G.H., "The Screening of Transformers Against Electromagnetic 'Pick-Up' Effects," Journal of Scientific Instruments, V. 13, p. 295 to 297, 1936.

An experimental comparison was made of various metals as shields over a range of frequencies. At low frequencies the only effective shield was the high permeability alloy.

- C7 Constable, J.E.R., "Electromagnetic Screening," Wireless World, V. 40, p. 198 to 199, 1937.

Shielding measurements indicate that high permeability alloys are the best particularly at low frequencies.

- D1 duBois, H., "Ueber magnetische Schirmwirkung," Annalender Physik, V. 63, p. 348 to 353, 1897.

Formulas are developed for spherical and cylindrical double shields.

- D2 duBois, H., "Ueber magnetische Schirmwirkung," Annalender Physik, V. 65, p. 1 to 37, 1898.

This article is a continuation of [D1]. The shielding factors for two spherical and two cylindrical shields are obtained and a number of special cases is considered. The effects of thin and thick layers of shielding material are shown and a comparison of theoretical and observed shielding factors for two layers is presented with good agreement. The effects of shielding magnets and currents are shown by the use of iron filings.

- D3 duBois, H. and Wills, A.P., "Ueber Magnetische Schirmwirkung," Annalen der Physik, V. 2, p. 78 to 83, 1900.

The shielding factors for three spherical and three cylindrical shells are presented. The comparison of calculated and observed factors are given.

- D4 Dye, D.W., "Note on the Use of Stalloy Ring Stampings for Magnetic Shielding Purposes," Journal of Scientific Instruments, V. 3, p. 65 to 69, 1925-1926.

Formulas and curves are presented giving the shielding factors for various ratios of the radii and for one to four shields. Ring stampings are suggested as the shields and the results of experimental tests are presented.

- D5 "Magnetic Screening," Journal of Scientific Instruments, V. 3, p. 89, 1925-1926.

A short note suggests the use of permalloy or mumetal for the stampings mentioned in [D4].

- D6 Dye, D.W., "Further Note on Magnetic Screening of Galvanometers," Journal of Scientific Instruments, V. 3, p. 141 to 143, 1925-1926.

The use of permalloy and mumetal as shielding material is discussed along with the advantages and disadvantages.

- D7 duBois, H., Electrotechnische Zeitschrift, V. 18, p. 502, 1897.

- D8 duBois, H., Electrician, V. 39, p. 579, 1897.

- D9 duBois, H., Electrician, V. 40, p. 218, 316, 511, 624 and 814 to 817, 1898.

- E1 Esmarch, W., "Experimentelle Untersuchung der magnetischen Schirmwirkung multilamellarer Zylinderpanzer," Annalen der Physik, V. 39, p. 1540 to 1552, 1912.

Measurements are made of the shielding factor versus distance along the axis of a number of multilayer solenoids wound with high permeability iron wire.

- E2 Esmarch, W., "Theorie der magnetischen Schirmwirkung, multilamellarer Zylinder-und Kugelpanzer," Annalen der Physik, V. 39, p. 1553 to 1566, 1912.

Determinants are used in the solution of a shield employing n layers of material. Curves are given of the calculated shielding factor as a function of the number of layers, the permeability of the magnetic material, and the thickness of the material.

- E3 Edgar, R.B. and Morrison, J.M., "Magnetic Moment Control for Spacecraft Electronics," Space Aeronautics, V. 44, p. 94 to 95, September 1965.

A double-shielded mumetal chamber is used to reduce the ambient field to about 50 gammas. Pictures of the chamber are shown.

- E4 Ellwood, W.B., "Magnetic Shields," Bell Laboratories Record, V. 17, p. 93 to 96, November 1938.

The theoretical results for single spherical and cylindrical shields are given. For greater shielding factors, multiple shields are suggested.

- E5 Epstein, D.J., "Magnetic Shielding," Proceedings of the Institute of Electrical and Electronics Engineers, V. 53, p. 655 to 656, June 1965.

The theory for both spherical and cylindrical concentric magnetic shields is examined for the shielding of a static dipole at the center. It is shown that the shielding factor of N shells for a uniform external field is the same as the shielding factor for a dipole at the center of the shells.

- F1 Freedman, N.S., Schindler, H.C., Nyman, F.R., and Strater, K., "High Magnetic Field Superconducting Properties of Nb_3Sn Films," NASA STAR N66-10448.

The magnetic shielding properties of superconducting films of niobium-stannide are investigated. Rings plated with Nb_3Sn were tried as a shielding device and were found to be successful.

- G1 Gustafson, W.G., "Magnetic Shielding of Transformers at Audio Frequencies," Bell System Technical Journal, V. 17, p. 416 to 437, 1938.

Some of the earlier work on shielding is reviewed. The viewpoint of this paper is concerned with shielding against low frequency magnetic fields rather than static fields. Curves of the shielding efficiency are presented. Measured curves of shielding efficiency versus frequency are given along with results using two and three cylinders with covers.

- G2 Gustafson, W.G., "Magnetic Shields for Transformers," Bell Laboratories Record, V. 17, p. 97 to 99, November 1938.

Measured shielding efficiencies are given for various materials and for multiple shields.

- G3 Grivet, P., Sauzade, M., and Lory, H., "A Secondary Standard of Current Based on a Nuclear Resonance Spin Oscillator," IEEE Transactions on Instrumentations and Measurement, V. IM-13, p. 231 to 238, December 1964.

The theory of the effect of a shield on a Helmholtz coil pair is given. The shield constructed had two layers of mumetal.

- G4 Gokhale, S.L., "Magnetic Shielding," Transactions of the American Institute of Electrical Engineers, V. 48, p. 1307, 1929.

- H1 Hill, A.V., "A 'Mumetal' Magnetic Shield for Sensitive Galvanometer," Journal of Scientific Instruments, V. 3, p. 335 to 336, 1925-1926.

The construction and testing of a shield is given. The shielding factor was found to be about 1000.

- H2 Herrmannsfeldt, W.B. and Salsburg, B.L., "Demagnetization of Magnetic Shield in the Presence of the Earth's Field," Review of Scientific Instruments, V. 35, p. 906, July 1964.

A method is given to demagnetize a long cylindrical shield in the earth's field.

- H3 Hildebrandt, A.F., "Superconductor Shields Test Chamber from Ambient Magnetic Fields," NASA TECH BRIEF B65-10297.

A chamber made from lead foil in the superconducting state shields the interior volume from the ambient magnetic field.

- H4 Hanson, R.J. and Pipkin, F.M., "Magnetically Shielded Solenoid with Field of High Homogeneity," Review of Scientific Instruments, 36, p. 179 to 188, February 1965.

An analysis is made for the field of a solenoid inside a cylindrical shield. Computations show that the presence of the shield improves the homogeneity of the field of the solenoid. In the construction of the shield, three layers of material were used, the inner made of iron and the two outer of Mumetal. Coils were wound on the shields for demagnetization purposes. The shielding factor was about 100.

- J1 Jorgensen, C.M., "Electromagnetic Interference Shielding Techniques," Electro-Technology, V. 77, p. 95, May 1966.

A brief description of the use of magnetic foils to shield components from an outside magnetic field. The medium-permeability material should form the outer layer while the high-permeability material should form the inner layer for maximum shielding.

- K1 King, L.V., "Electromagnetic Shielding at Radio Frequencies," Philosophical Magazine, V. 15, p. 201 to 223, 1933.

The shielding factors for high frequency work are derived theoretically. As special cases, the shielding factor for one thin spherical and one thin cylindrical shield is obtained.

- K2 Kaden, H., "Die elektromagnetische Schirmung in der Fernmelde-und Hochfrequenz Technik," Springer Verlag Berlin, 1950.

- L1 Lepping, R.P., "An Introductory Theoretical Study of Constant Permeability Magnetic Shielding," NASA STAR N66-18634.

The shielding factor for a single spherical shell is derived. The results for double and triple spherical shells are given.

- L2 Love, W.F., Blunt, R.F., and Alers, P.B., "Magnetic Effects of a Rotating Superconductor," Physical Review, 76, 305, 1949.

A cylinder of tin rotated at 5000 RPM and cooled so that it became superconducting was found to have no magnetic flux inside.

- M1 Morecroft, J.H. and Turner, A., "The Shielding of Electric and Magnetic Fields," Proceedings Institute of Radio Engineers, V. 13, p. 477 to 505, 1925.

The shielding effects of plane and curved iron shields are measured experimentally.

- M2 Meerovich, E.A. and Arakelyan, A.M., "Screening Action of Ferromagnetic Plates on the Magnetic Field Produced by Direct Current," Elektrichestvo, No. 9, p. 51 to 57, Sept. 1959. A brief abstract appeared in Electric Technology USSR, p. 496, 1960.

The shielding of a static magnetic field is studied using the method of images. Flat and cylindrical shields are considered.

- M3 Maschke, A., "Abschirmung magnetischer Felder," Archiv für Technisches Messen, p. T90 to T91, July 1939.

Shielding at low frequencies is discussed. Much of the paper is a review of the work of Gustafson (G1), (G2).

- M4 Meissner, W. and Doll, R., "Höchstempfindliches Panzergalvanometer," Zeitschrift für angewandte Physik, V. 7, p. 461 to 468, October 1955.

A three-layer shield is computed for the galvanometer and magnetic material with a relative permeability of 37000 is used.

- M5 Marmet, P., Morrison, J.D., and Swingler, D.L., "Neutralization of Fringing Magnetic Fields in the Ion Source of a Mass Spectrometer," Review of Scientific Instruments, V. 33, p. 239 to 240, February 1962.

A shield of mumetal is used to help reduce the effect of the earth's magnetic field.

- M6 Maxwell, J.C., A Treatise on Electricity and Magnetism, Dover Publications, Third Edition 1954, V. 2, p. 59 to 62.

The case of one spherical shield is treated theoretically. In addition he mentions that Sir W. Thomson used a tube of soft iron to shield his marine galvanometer.

M7 Maschke, A., "The Screening of Magnetic Fields; Survey of Literature," Zeitschrift für Instrument Kunde, V. 60, p. 378, December 1940.

N1 Norris, D.D., "Magnetic Shielding Experiences," NASA STAR N66-11293.

The construction of shields used to test a magnetometer in a vacuum environment and in calibration work is discussed.

N2 Norris, D.D., "Component Shielding," NASA STAR N66-11294.

A description of a shield for reed switch relays is given along with some environmental tests that were made.

N3 Nichols, E.F. and Williams, S.R., "A Convenient Form of Galvanometer with Magnetic Shielding," Physical Review, V. 27, p. 250 to 257, 1908.

Cylindrical shields for a galvanometer are described and the shielding ratios for a number of different shields are determined experimentally.

P1 Perucchi, N., "Calculs et Experiences sur des Ecrans Magnetiques Multiples," NASA STAR N65-26749.

The screening factor is given for one and for two cylindrical screens and an approximate factor is given for n screens. Curves are given showing the screening factor variation with permeability and also some experimental results.

P2 Patton, B.J. and Fitch, J.L., "Design of a Room-Size Magnetic Shield," Journal of Geophysical Research, V. 67, p. 1117-1121, March 1962.

A short resume of shielding formulas and the properties of magnetic materials is given. The design of a doubly shielded cubical room approximately eight feet on a side is presented. The shielding factor is about 700. The field is less than five gammas with gradients two gammas per foot.

R1 Rucker, A.W., "On the Magnetic Shielding of Concentric Spherical Shells," Philosophical Magazine, V. 37, p. 95, 1894.

R2 Randall, W.F. and Sowter, G.A.V., "Mumetal Magnetic Shields," Journal of Scientific Instruments, V. 15, p. 342 to 344, 1938.

Shields using mumetal are discussed and the suggestion is made that all joints be welded using mumetal weld. For a layer shielding effect multiple shields are required.

R3 Russell, J., "Magnetic Shielding in Hollow Iron Cylinders," Royal Society of Edinburgh Transactions, V. 40, p. 631 to 681, 1903.

An experimental investigation of magnetic shielding using hollow iron cylinders was reported. It was shown that in addition to the usual factors considered such as the thickness of the cylinders and their permeabilities, the shielding ratio depends also on the retentivity of the cylinders and the presence or absence of other magnetic fields.

R4 Randall, W.F., "Nickel-Iron Alloys for Magnetic Screening," The Nickel Bulletin, V. 9, p. 73, April 1936.

- S1 Sterne, T.E., "Multi-Lamellar Cylindrical Magnetic Shields," Review of Scientific Instruments, V. 6, p. 324 to 326, October 1935.

A solution of the shielding by n coaxial cylinders is made using recurrence formulas. A numerical example is also given.

- S2 Schweizer, F., "Magnetic Shielding Factors of a System of Concentric Spherical Shells," Journal of Applied Physics, V. 33, p. 1001 to 1003, March 1962.

The shielding factor of a system of concentric spherical shells is found by the use of matrices. The shielding factors for one, two and three shells are obtained. Special cases of thin shells and high permeability are given.

- S3 Stefan, J., "Ueber die magnetische Schirmwirkung des Eisens," Annalen der Physik, V. 17, p. 928 to 955, 1882.

Shielding using iron cylinders is discussed.

- S4 Sauzade, M. and Sallé, F., "Influence d'un blindage magnétique sur l'homogenie d'un champ magnétique créé par une paire de Helmholtz, Application à un spectrographe à résonance nucléaire à champ faible," Comptes Rendus de l'Académie des Sciences, V. 259, p. 73 to 76, July 6, 1964.

A spherical mumetal shield is assumed and an analysis is given. The experimental shield is made of two concentric cubes.

- S5 Schmid, H., Berechnungs grundlagen und Eigen schaften geschichteter Magnetikas, G. Leemann & Co., Zürich, 1944 (Library of Congress QC753.535).

The shielding factors for a cylinder and a sphere are derived and curves for various permeabilities are presented. Some experimental results for cylinders at low frequencies are also given.

- S6 Sowter, G.A.V., "Screening Cathode Ray Tubes," Wireless World, V. 39, p. 138 to 140, August 14, 1936.

The application of mumetal shields to cathode ray tubes is discussed. Multiple layer shields for higher shielding ratios are suggested.

- S7 Schlosser, E.G., "Ein abgeschirmtes homogenes Magnetfeld," Zeitschrift für angewandte Physik, V. 7, p. 59 to 61, 1955.

A mumetal cylindrical shield with both ends closed was used to shield a Helmholtz coil pair and to produce a very uniform field at the center of the coil pair.

- S8 Smythe, W.R., Static and Dynamic Electricity, McGraw-Hill Book Co., Inc., 1950, Second Edition, p. 288 to 291.

The shielding effect of a cylindrical and a spherical shield are derived.

- T1 Teasdale, R.D., "Magnetic Alloy Shields for Color Television Tubes," Proceedings of the National Electronics Conference, V. 9, p. 580 to 590, 1953.

Equations and curves are presented for spherical and cylindrical shields using four different magnetic alloys. Experimental results are presented for cylindrical and conical shields and the effect of varying the applied field strength is considered. The cost of the various alloys is discussed.

- T2 Tuckerman, B., "Graphs of the Induced Magnetic Moment and Shielding Effect of a Spherical Shell in a Uniform Magnetic Field," Journal of Geophysical Research, V. 52, p. 369 to 373, September 1947.

Formulas and curves for the shielding factor of a single spherical shell are given.

- T3 Teasdale, R.D., "Magnetic Alloy Shields for Color TV Tubes," Electronic Industries, V. 12, p. 74 to 76 and 138 to 146, December 1953.

This contains essentially the same information as [T1].

- V1 Vant-Hull, L.L. and Mercereau, J.E., "Magnetic Shielding by a Superconducting Cylinder," Review of Scientific Instruments, V. 34, p. 1238 to 1242, November 1963.

An experiment is described in which a rotating conducting cylinder in a magnetic field has eddy currents generated in it. The cylinder is cooled at the same time to the superconducting state and the result is that the internal magnetic field becomes quite small.

- W1 Wills, A.P., "On the Magnetic Shielding Effect of Trilamellar Spherical and Cylindrical Shells," Physical Review, V. 9, p. 193 to 213, October 1899.

Three concentric spherical or cylindrical shields are analyzed with the cylinders assumed infinitely long and with their axes perpendicular to the applied magnetic field. The results are expressions for the shielding factors for the spherical and cylindrical cases. Various special cases are discussed and curves are presented for single, double and triple shields.

- W2 Wadey, W.G., "Magnetic Shielding with Multiple Cylindrical Shells," Review of Scientific Instruments, V. 27, p. 910 to 916, November 1956.

Uses the work of Wills [W1], Stern [S1], and Esmarch [E1] along with the newer materials such as Mumetal and Permendur to produce multiple shields having a shielding factor greater than 1.5×10^5 . See Cravath [C1] for remarks on errors in this paper.

- W3 Wilson, E. and Nicholson, J.W., "Magnetic Shielding of Large Spaces," Proceedings of the Royal Society, Series A, V. 92, p. 529 to 549, 1916.

A theory of shielding is presented using a series of shells. An example using four shells is worked out and some experimental results are given.

- W4 Wills, A.P., "On Magnetic Shielding," Physical Review, V. 24, p. 243, 1907.

The abstract of a paper which shows that the best shielding occurs when the radii of the shells are approximately in geometrical progression for the cases of both spheres and cylinders.

- W5 Walker, L.R., "Multi-Lamellar Cylindrical Magnetic Shields," Review of Scientific Instruments, V. 6, p. 416, Dec. 1935.

The difference equations given by Sterne [S1] are solved in such a way that the number of shells needed to produce a specified shielding factor can be calculated.

- Z1 Zickner, G., "Schirmung und Schützung," Zeitschrift für Instrumentenkunde, V. 66, p. 195 to 199, October 1958.

A short description of the methods of shielding magnetically are given.

THE PRODUCTION OF UNIFORM MAGNETIC FIELDS BY COMPENSATED SOLENOIDS

D. L. Waideleicher

N 67-22759

A magnetic solenoid has been employed for the production of uniform fields for more than a century. As the need for larger volumes of more uniform fields became apparent, longer and larger solenoids became necessary. About sixty five years ago the idea of a compensated solenoid appeared. This used one or more auxiliary coils to produce a more uniform magnetic field than was possible using the same size solenoid without the compensation. The compensated solenoid would be of advantage particularly in the magnetic testing of cylindrical objects such as a sounding rocket or a long thin spacecraft.

Probably the earliest reference to a compensated solenoid is that of Houllevigue [H5] in 1898 who placed two truncated conical coils inside the ends of a solenoid to produce a more uniform magnetic field along the axis of the solenoid. In 1911 Bestelmeyer [B6] used two smaller solenoids placed near the ends of a larger solenoid to make a more uniform field. Cioffi [C1] in 1924 used two end coils on a solenoid for compensation. Buhl and Coeterier in 1932 [B1] suggested the possibility of either a single compensating coil at the center of the solenoid or the two coils at the ends of the solenoid. In addition they presented an analysis which indicated that a sixth-order field was possible. Hak in 1936 [H1], [H7] suggested that the winding thickness along the solenoid could be varied in such a manner as to produce a more uniform field at the center of the solenoid. In 1939 Bitter [B5] suggested the use of short-circuited turns at the center of a solenoid to improve the uniformity while McKeehan [M1] analyzed the case of a solenoid with a correcting coil carrying reversed current wound over the center of the solenoid. Two cases were calculated, one of which was a fourth-order solenoid and the other made the sum of the second and fourth-order terms zero at one point on the axis of the solenoid.

During the 1940's an integral equation used to find the required winding variation for a uniform field was developed [G10] and solved using Fourier transforms. A lengthy review article and bibliography appeared [N2], and a solenoid with two end compensating coils was used in a beta-ray spectrometer [W1], [H3]. In the 1950's methods of producing sixth- and eighth-order solenoids were discussed [G5] and a numerical design [H2] and a graphical design [L1] of a compensated solenoid were presented. The application of compensated solenoids in nuclear spectrometry [S1] and naval ordnance [W4] were given.

During the 1960's a large amount of work was done on the methods of producing sixth-order solenoids [B4], [B9], [B10], [G2], [G3], [M2], [M3], [S2], [Y3]. Also a great deal of attention was paid to the possibilities of superconducting solenoids with compensation [B2], [H6], [M5], [N1], [W2], [W3]. Various end corrected solenoids are described [G4], [G9], [K1], including some with rectangular turns [Y1], [Y2], instead of the more usual circular turns. Shielding was used to improve the uniformity of the solenoid [H4], [T1]. An approximation method using matrices [G1], a numerical method [Z1] and the use of Chebyshev polynomials [O1] were some of the means employed to design the compensated solenoids. Applications in travelling wave tubes [Z2] and in nuclear resonance [G6] were presented.

REFERENCES

- B1 Buhl, A. and Coeterier, F., "Zur Herstellung homogener Magnetfelder," Physikalisches Zeitschrift, V. 33, p. 773 to 774, 1932.

A coil with reversed current is wound about the center of the solenoid. The number of turns is calculated to make a sixth-order solenoid.

- B2 Boom, R.W. and Livingston, R.S., "Superconducting Solenoids," Proceedings of the Institute of Radio Engineers, V. 50, p. 274 to 285, 1962.

The uniformity of the field in various rectangular solenoids can be estimated by the use of the curves given.

- B3 Barker, J.R., "The Magnetic Field Inside a Solenoid," British Journal of Applied Physics, V. 1, p. 65 to 67, March 1950.

Formulas are given that allow the extent of the uniform field inside a solenoid to be calculated.

- B4 Bitter, F., "Water Cooled Magnets," Review of Scientific Instruments, V. 33, p. 342 to 349, March 1962.

The uniformity of a sixth-order solenoidal coil using compensating coils is discussed.

- B5 Bitter, F., "The Design of Powerful Electromagnets, Part IV, The New Magnet Laboratory at M.I.T.," Review of Scientific Instruments, V. 10, p. 373 to 381, December 1939.

Short-circuited turns at the center of the coil are used to increase the homogeneity of the field at the expense of a small decrease in the maximum field in intensity.

- B6 Bestelmeyer, A., "Berechnung, Herstellung und Messung eines homogenen Magnetfeldes," Physikalische Zeitschrift, V. 12, p. 1107 to 1111, 1911.

One large solenoid and two smaller solenoids placed at the ends of the large solenoid were used to produce a very uniform field. Calculated and measured curves are given of the axially directed field measured both on and off the axis of the solenoids. The results for two different spacings of the small solenoids from the large solenoid are presented.

- B9 Bitter, F., "Water-Cooled Magnets," in High Magnetic Fields, p. 85 to 100, 1962, J. Wiley and Sons, Inc.

Attempts at producing a very uniform field using a solenoid are presented. A description is given of a solenoid with compensating windings inside the main coil such that a sixth-order field is obtained. In addition, a superconducting shield in the center is expected to hold the field constant with time.

- B10 Bitter, F., "New Developments in High-Magnetic Field Research," Physics Today, V. 14, p. 22 to 28, September 1961.

A brief discussion is given of attempts to produce a very uniform field in a solenoid, See [B4] and [B9].

- C1 Cioffi, P.P., "Magnetic Measurements on Materials of High Initial Permeability," Journal of the Optical Society of America and the Review of Scientific Instruments, V. 9, p. 53 to 60, 1924.

End coils are used to increase the uniformity of a solenoid.

- G1 Gygi, E. and Schneider, F., "A High Precision Air Core Magnet," NASA STAR N66-10175.

An approximation method using matrices is set up as a computer program to determine the number of turns on each part of a solenoid for a uniform field along the axis of the solenoid. The solenoid was constructed of oxidized aluminum strip and measured field intensities along the axis are shown.

- G2 Grivet, P. and Sauzade, M., "A High Homogeneity-High Field Superconducting Magnet for Nuclear Resonance," NASA STAR N66-16876.

A notch is made in the solenoid winding of rectangular cross-section so that a sixth-order field results. Also the chosen solenoid has a minimum winding volume, and the design and construction is presented. The measured homogeneity is 5×10^{-7} over an axial length of 3 centimeters.

- G3 Girard, B. and Sauzade, M., "Calcul des Solenoides Compenses du 6^{ème} Ordre à Volume de Bobinage Minimum," Nuclear Instruments and Methods, V. 25, p. 269 to 284, 1964.

It was decided to study the solenoid with two end compensating coils as a means to produce a sixth-order solenoid by the use of successive approximations. Curves are given for the dimensions of the compensated solenoid, the zero- and sixth-order terms in the series for the field along the axis and the volume of the coil windings. The results are selected for the minimum of the volume of the coil windings and are plotted as a series of curves and a table useful in design. A numerical example is also given.

- G4 Gardner, M.E., Jungerman, J.A., Lichtenstein, P.G., and Patten, C.G., "Production of a Uniform Magnetic Field by Means of an End-Corrected Solenoid," Review of Scientific Instruments, V. 31, p. 929 to 934, September 1960.

The conditions used are that at a point away from the center, the field is made equal to the field at the center and also the derivative of the field is made zero. The analysis is used in designing and constructing a thick solenoid with 0.01 per cent homogeneity in the axial region comprising 63 percent of the solenoid. Curves of the theoretical and experimental field both on and off axis are given.

- G5 Garrett, M.W., "Axially Symmetric Systems for Generating and Measuring Magnetic Fields. Part I," Journal of Applied Physics, V. 22, p. 109 to 1107, September 1951.

Sixth-order solenoids with end coils are discussed and the constants for one example are given. Also two eighth-order systems composed of a solenoid and two coil-pairs are presented.

- G6 Grivet, P., Sauzade, M., and Lory, H., "A Secondary Standard of Current Based on a Nuclear Resonance Spin Oscillator," IEEE Transactions on Instrumentation and Measurement, V. IM-13, p. 231 to 238, December 1964.

A description of a solenoid is given with a compensating winding at both ends to increase the field homogeneity. At the center the field is constant to one part in 10^5 over a volume of 50 cubic centimeters.

- G7 Garrett, M.W., "The Method of Zonal Harmonics, High Magnetic Fields, p. 14 to 26, 1962, J. Wiley and Sons, Inc.

A method of calculating solenoids is given which would be useful in determining the homogeneity of the field of solenoid.

- G8 Gaume, F., "New Solenoid Magnets" in High Magnetic Fields, p. 27 to 38, 1962, J. Wiley and Sons, Inc.

The axial field distribution of two solenoids are compared.

- G9 Grivet, P., "High Field Magnetometry, High Magnetic Fields, p. 54 to 84, 1962, J. Wiley and Sons, Inc.

The use of compensating coils to increase the homogeneity of a solenoid is mentioned.

- G10 Glaser, W., "Über die zu einem vorgegebenen Magnetfeld gehörende Windungsdichte einer Kreisspule," Zeitschrift für Physik, V. 118, p. 264 to 268, 1941.

It is proposed to determine the winding variation on a solenoid to produce a given axial variation of magnetic field. The result is an integral equation which can be solved using Fourier transforms.

- H1 Hak, J., "Eisenlose Zylinderspulen mit ungleichmässiger Windungsdichte zur Erzeugung von homogenen Feldern," Archiv für Electrotechnik, V. 30, p. 736 to 745, 1936.

The windings of various cross-sectional shapes on a solenoidal are used to produce as uniform a field as possible.

- H2 Heddle, T.A., "A Method of Designing a Compensated Solenoid Giving Approximate Uniform Fields," British Journal of Applied Physics, V. 3, p. 95 to 97, March 1952.

A method of designing a solenoid with two or more pairs of end coils is given. A numerical design showing two pairs of end coils and the experimental measurements on the solenoid are presented.

- H3 Haggstrom, E., "The B-ray Spectra of Rubidium⁸⁶, Strontium⁸⁹, Ekatantalum and Protactinium," Physical Review, V. 62, p. 144 to 150, 1942.

A solenoid with end correction coils [W1] is shown.

- H4 Hanson, R.J. and Pipkin, F.M., "Magnetically Shielded Solenoid with Field of High Homogeneity," Review of Scientific Instruments, V. 36, p. 179 to 188, February 1965.

The design of a sixth-order solenoid using compensating coils is given along with the constructional details. Computations showed that a magnetic shield placed around the coil would improve the homogeneity considerably. A three layer shield was constructed and experimental results indicated a considerably better homogeneity for the shielded solenoid.

- H5 Houllevigue, L., "Champ Axial d'une Bobine Tronc-Conique," Journal de Physique, V. 7, p. 466 to 468, 1898.

A solenoid is compensated by the use of two truncated conical coils placed inside the ends of the solenoid. The calculated field variation is less than 1 in 1000 over 2/5 of the length of the solenoid compared to 11 in 1000 without compensation.

- H6 Hildebrandt, A.F., Wahlquist, H., and Elleman, D.D., "Configurations of Superconducting Shells Required for Near Critical Uniform Magnetic Fields," Journal of Applied Physics, V. 33, p. 1798 to 1800, 1962.

Formed toroidal superconductors are used to produce very uniform magnetic fields. In a cylinder of lead a field homogeneity of about three percent is obtained.

- H7 Hak, J., "Eisenlose Drosselspulen," K.F. Koehler, Leipzig, 1938.

The variation of winding turns along the axis of the solenoidal is used to produce a uniform magnetic field H1 .

- I1 Ingarden, R.S., "On the Wroclaw Magnet and Related Investigations" High Magnetic Fields, p. 427 to 434, 1962, J. Wiley and Sons, Inc.

An analysis is presented to show that the conditions for maximum field and maximum homogeneity are not consistent and so a compromise must be made.

- K1 Kifer, I.I., "Testing of Ferromagnetic Materials," NASA STAR N64-31801.

Discusses solenoids with end windings to improve the uniformity of the field.

- L1 Lewis, B., "A Note on the Improvement of the Field of a Solenoid by End Coils," British Journal of Applied Physics, V. 1, p. 238 to 239, September 1950.

The field plot along the axis of the solenoid is obtained. A similar plot for the two compensating coils is made and adjusted so that its negative is approximately the same as the field plot of the solenoid itself. Then the compensation should be quite good. Experimental results are shown.

- M1 McKeehan, L.W., "A Method for Improving the Uniformity of the Central Magnetic Field in a Thick Solenoid," Review of Scientific Instruments, V. 10, p. 371 to 373, December 1939.

A correcting coil with reversed current is wound over the center of a solenoid of rectangular cross-section. Two cases are calculated, the first involves making the second order term zero and the second makes the sum of the second and fourth order terms zero at one particular point on the axis of the solenoid.

- M2 Montgomery, D.B. and Terrell, J., "Some Useful Information for the Design of Air-Core Solenoids," Report AFOSR-1525, National Magnet Laboratory, Massachusetts Institute of Technology, 1961.

Sixth-order solenoid tables are given for an outside notch in a solenoid and for other winding configurations.

- M3 Montgomery, D.B., "Superconducting Magnets," IEEE Spectrum, V. 1, p. 103 to 113, February 1964.

A table for a sixth-order solenoid is given.

- M4 Montgomery, D.B., "The Generation of High Magnetic Fields," in Reports on Progress in Physics, V. 26, p. 69 to 104, 1963 and published by the Institute of Physics and the Physical Society, London.

A short discussion of compensated solenoids is given.

- M5 Marshall, H.L. and Weaver, H.E., "Application of the Garrett Method to Calculation of Coil Geometries for Generalizing Homogeneous Magnetic Fields in Superconducting Solenoids," Journal of Applied Physics, V. 34, p. 3175 to 3178, November 1963.

A sixth-order solenoid with two end coils [M2] is used, and a field uniform to one part of 10^5 was obtained over a distance of one inch.

- N1 Nelson, F.A. and Weaver, H.E., "Nuclear Magnetic Resonance Spectroscopy in Superconducting Magnetic Fields," Science, V. 146, p. 223 to 232, 9 October 1964.

Discusses the practicality of altering the cross section of a right circular solenoid for homogeneity of the sixth-order. Three suggested methods of compensation involve the use of an outside notch, an inside notch and a central notch.

- N2 Neumann, H., "Herstellung räumlich und zeitlich konstanter Magnetfelder für Messzweck," Archiv für Technisches Messen.

Part 1, p. T128 and T129, November 1940
Part 2, p. T138 and T138, December 1940
Part 3, p. T14 and T15, January 1941
Part 4, p. T28 and T29, February 1941

Review and bibliography of methods of producing uniform magnetic fields using solenoids.

- O1 Overshott, K.J. and Smith, I.R., "A Solenoid with a Nearly Uniform Axial Magnetic Field," Journal of Scientific Instruments, V. 41, p. 507 to 508, 1964.

A solenoid is wound in eight longitudinal sections with the number of turns on the end sections increased to produce a more uniform field over a greater axial length. Eight points were chosen along the axis in various ways and the resulting turns per section and the axial field distribution are found through the use of Chebyshev polynomials. The final choice has the axial field within $\pm 0.5\%$ over 70% of the solenoid length.

- P1 Papoular, M., "Uniformisation du Vecteur Champ Magnétique sur l'Axe d'une Hélice," Journal de Physique et le Radium, V. 22, p. 775 to 776, November 1961.

Suggests that two identical helices be wound in the same sense and with the same current but the second is moved one half turn parallel to the axis with respect to the first.

For such a solenoid it is shown that the transverse components on the axis are very small.

- R1 Ramsay, B.P. and Yost, F.L., "Facilities Provided by the Kensington Magnetic Laboratory," Journal of Geophysical Research, V. 52, p. 357 to 367, 1947.

Several large solenoids used in ordnance work and with end correction coils are described.

- S1 Schmidt, F.H., "A Uniform Solenoidal Magnetic Field Nuclear Spectrometer," Review of Scientific Instruments, V. 23, p. 361 to 366, July 1952.

The solenoid has two end correcting coils. The axial field is uniform to 0.3 percent over 17 inches, and the radial field to 0.04 percent out to 4 inches.

- S2 Snow, C. and Driscoll, R.L., "A Compensated Solenoid Giving a Uniform Magnetic Field Over a Large Volume," Journal of Research of the National Bureau of Standards, V. 69c, p. 49 to 54, January-March 1965.

An analysis is made of a solenoid with two compensating coils near the ends of the solenoid. The axial and radial field components are obtained at any point near the center of the solenoid. Two terms in the series were made zero to produce a sixth-order field. Two tables are given listing various compensating coils for a given solenoid as an example.

- S3 Stekly, Z.J.J., deWinder, T.A., and El Bindari, A., "Field Coils for Magnetohydrodynamics Generators," High Magnetic Fields, p. 139 to 155, 1962, J. Wiley and Sons, Inc.

Circular [R1] and rectangular cross section coils are used to produce very uniform fields. Analyses of the various coils are presented in the Appendices.

- T1 Troxel, L.M., "Superconducting Magnet for Variable-Bandwidth Traveling-Wave Masers," IEEE Transactions on Magnetics, v. MAG-1, p. 378 to 381, December 1965.

A short solenoid in a low reluctance shield has the effect of having two infinitely long image solenoids. The resulting 3300 gauss field is uniform to 0.1 percent.

- W1 Witcher, C.M., "An Electron Lens Type of Beta-Ray Spectrometer," Physical Review, V. 60, p. 32 to 42, 1941.

Two correcting coils are connected in series with a rheostat across the main winding of the solenoid to provide a one percent field over a length of 90 centimeters.

- W2 Williams, W.L., Stephen, M.J., and Lane, C.T., "Homogenization of a Magnetic Field with a Superconducting Cylinder," Physics Letters, V. 9, p. 102 to 103, April 1, 1964.

The homogeneity of the magnetic field within a superconducting tin cylinder is measured and calculated. The field was homogeneous to at least 400 ppm over an axial distance of 5 centimeters.

- W3 Wood, M., "Some Aspects of the Design of Superconducting Solenoids," Cryogenics, V. 2, p. 297 to 300, September 1962.

Homogeneity of the solenoids are discussed and reference is made to the works of Garrett [G5] and Montgomery [M2].

- W4 Warburton, F.W., "Design of Coil Systems for Magnetic Field Control at the Naval Ordnance Laboratory," AD-105974.

A number of solenoidal systems are described along with compensating methods.

- Y1 Yavor, S. Ya., Shpak, E.V., and Minina, R.M., "Cylindrical Magnetic Lenses with a Plane of Symmetry," Soviet Physics - Technical Physics, V. 5, p. 369 to 377, 1960.

Two rectangular solenoids are used with their axes at right angles to compensate for the vertical and horizontal components of the earth's magnetic field. Some extra turns are placed on the end of one of the solenoids to decrease the inhomogeneity of the field. An expression is given for the field along the axis of a rectangular solenoid.

- Y2 Yavor, S. Ya. and Silad'i, M., "Creation of a Homogeneous Magnetic Field with a Rectangular Solenoid of Finite Length," Instruments and Experimental Techniques, No. 5, p. 151 to 153, January, 1961.

The expressions for the field components of a rectangular solenoid are presented, and the variation of the field intensity along the axis is given as a curve and in a table. The effect of putting end turns on the solenoid to decrease the inhomogeneity is shown also.

- Y3 Yamada, A., "Uniform Magnetic Field," University of Missouri Engineering Library Report, 1966.

Compensation of solenoids was discussed and the possibilities of producing fourth, sixth and eighth-order solenoids was presented.

- Z1 Zacharov, B., "A Method for the Design of Axially Symmetric Magnetic Fields for Image Tube Systems," Nuclear Instruments and Methods, V. 17, p. 132 to 136, 1962.

The outline is given for a method of obtaining the currents in a solenoid composed of a series of equal coils with a common axis to produce any axial field variation desired such as a homogeneous field. An example is given in which the current densities in 19 coils were calculated to produce a field uniform to better than 0.1 percent over a axial distance of 44 centimeters. The measured value was about one percent and was caused by differences in the individual coils and misalignments.

- Z2 Zack, A., "Solenoids for Travelling-Wave Tubes and Klystrons," Electronics V. 34, p. 66 to 70, December 8, 1961.

In the discussion he indicates that the uniformity can be increased by varying the turns in the axial direction.

OK

TWO PLASMA PROBE TECHNIQUES

D. L. Waidelich

N 67-22760

PLASMA RESONANCE PROBE

A brief survey was made of the work done on two plasma probe techniques, one of which was the plasma resonance probe. The first mentions [1], [2] of this probe technique were probably those published in 1960. Radio frequency voltages near the plasma frequency are applied to the probe and the resulting direct current flow, because of the sheath nonlinearity, is measured. The current rises considerably near the plasma frequency and the electron density may be obtained from the resonant frequency. A theoretical analysis [3] of the probe appeared in 1962 and indicated that resonance occurs at the plasma frequency and that the half width of the resonance peak is equal to the collision frequency. This analysis was extended [4] for frequencies higher than the resonant frequency. Experiments [5] were made to test the theory [3] and showed that to the first order the experiment and theory agreed. Another analysis [6], [7] of the probe was made, and the response [8] of the probe in a magnetic field was determined. Surveys [9], [11], [13] of the early work on the resonance probe appeared, and further experimental results [10], [12], [16], [27] were reported. An attempt [14] to improve the earlier theory appeared but was criticized [15], [17] for neglecting the variation of the number density in the sheath and assuming a penetration depth of the sheath. Further work has been done on the resonance probe in a magnetic field [18], [20] and a new theoretical treatment [19] was advanced, which indicated that the resonant frequency is always smaller than the plasma frequency and it depends not only on the electron density but also on the probe geometry, the dc potential on the probe and the Debye length.

In 1965 and 1966 further work [21], [25], [26] on the above theories appeared along with a comparison of the theory with various experimental measurements. Also an explanation of a method of using the resonance probe to measure electron density and collision frequency [22], [24], [29] and some considerations of the reflection of electrons in the sheath and the transit time of the electrons across the sheath [23], [28] were given. Several review articles [47], [48] also were found.

SECOND-DERIVATIVE METHOD

The idea of using the second derivative of the current-voltage characteristic of the Langmuir probe as a means of finding the electron energy distribution function of a plasma seems to have originated with Druyvesteyn [30] in 1930 and this is the second probe technique to be discussed here. A graphical differentiation [31] was tried in 1933 but was quite inaccurate. A method [32] was tried in 1934 using a small alternating voltage applied to the probe which produced a small increase in the direct current to the probe and which in turn was proportional to the second derivative. The increase in the direct current could then be used to plot the energy distribution curve of the electrons in the plasma. In 1936 a method [33] of obtaining the first derivative curve was given using a bridge circuit with an alternating voltage applied. The second derivative was then found from the slope of the first derivative curve.

Resistance-capacitance circuits were used as differentiators and the distribution curve was displayed on the screen of a cathode-ray tube [34]. Two years later in 1953 amplitude modulation was used [35] giving an output signal proportional to the second derivative at the modulating frequency. A modulated carrier frequency of voltage was used [36] and oscilloscope pictures of the

electron energy distribution functions were obtained. Another graphical method [37] was presented in 1956, while a method [38] using a square wave modulating the probe voltage appeared in 1959. The fundamental current to the probe was measured to determine the second derivative. A pulsed probe technique [39] was used to obtain the usual probe characteristic and the electron energy distribution curve was obtained graphically.

In the 1960's the second derivative method was used to obtain the energy distribution function in a number of different studies [40], [41], [42], [51]. Automatic electronic devices [43] - [45] for plotting the second derivative of probe curves were developed using both harmonic and inter-modulation methods. Several reviews [9], [46], [47] of these methods have appeared, and one of these methods has been used to measure the electron energy distribution and the space potential in the ionospheric plasma [49]. The space potential is taken as the point at which the second derivative curves is zero. The theoretical error in the second derivative has been discussed [50] as has been the effects [52] of finite signal amplitude, finite size resistors, noise, and system hysteresis.

REFERENCES

1. Takayama, K., Idegami, H., and Miyasaki, S., "Plasma Resonance in a Radio-Frequency Probe," Physical Review Letters, V. 5, p. 238 to 240, 1960.
2. Miyasaki, S., Hirao, K., Aono, Y., Takayama, K., Idegami, H., and Ichiyama, T., "Resonance Probe-A New Probe Method for Measuring Electron Density and Electron Temperature in the Ionosphere," Report of Ionospheric and Space Research in Japan, V. 14, p. 148 to 159, 1960.
3. Ichikawa, Y.H. and Idegami, H., "Theory of Resonance Probe," Progress of Theoretical Physics, V. 28, p. 315 to 322, August 1962.
4. Ichikawa, Y.H., "Effets du Temps de Transit des electrons dans une sonde haute frequence," Comptes Rendue de l'Academic de Sciences, V. 256, p. 3434 to 3437, 1963.
5. Cairns, R.B., "Measurements of Resonance Rectification Using a Plasma Probe," Proceedings of the Physical Society, V. 82, p. 243 to 251, 1963.
6. Harp, R.S., "A Theory of the Resonance Probe," Stanford University Microwave Laboratory Report No. 1117, December 1963.
7. Harp, R.S., "The Behavior of the Resonance Probe in a Plasma," Applied Physics Letters, V. 4, p. 186 to 188, June 1, 1964.
8. Uramoto, J., Ikegami, H. and Takayama, K., "Resonance Probe in a Magnetic Field," Nagoya University Institute of Plasma Physics Report No. 15, Japan, October 1963.
9. Crawford, F.W. and Mlodnosky, R.F., "Langmuir Probe Response to Periodic Waveforms," Journal of Geophysical Research, V. 69, p. 2765 to 2773, July 1, 1964.
10. Peter, G., Muller, G., and Rabben, H.H., "Measurements with the High-Frequency Resonance Probe in a Cesium Plasma," Proceedings of the Sixth International Conference on Ionization Phenomena in Gases, S.E.R.M.A. Publishing Co., Paris, V. 4, p. 147 to 155, 1964.
11. Harp, R.S. and Crawford, F.W., "Characteristics of the Plasma Resonance Probe," Journal of Applied Physics, V. 35, p.3436 to 3446, December 1964.
12. Ikegami, H., Takayama, K., Hagiware, S., and Kojima, S., "Resonance Probe," Proceedings of the Sixth International Conference on Ionization Phenomena in Gases, S.E.R.M.A. Publishing Co., Paris, V. 4, p. 135 to 145, 1964.
13. Crawford, F.W. and Harp, R.S., "The Resonance Probe - A Tool for Ionospheric and Space Research," DDC AD-608440 also Journal of Geophysical Research, V. 70, p. 587 to 596, February 1, 1965.
14. Ichikawa, Y.H., "Finite Transit Time Effect in the Radio-Frequency Probe," Proceedings of the Sixth International Conference on Ionization Phenomena in Gases, S.E.R.M.A. Publishing Co., Paris, V. 4, 1. 125 to 128, 1964.
15. Wimmel, H.W., "Theory of the Plasma Resonance Probe," Zeitschrift fur Naturforschung, V. 19a, p. 1099 to 1106, September 1964.
16. Uramoto, J., Fujita, J., Ikegami, H., and Takayama, K., Nagoya University Institute of Plasma Physics Research Report No. 19, Japan, December 1963.

17. Fejer, J.A., Proceedings of the Conference on Nonlinear Processes in the Ionosphere, Boulder Colorado, December 1963. National Bureau of Standards Technical Note No. 211, V. 3, p. 101, 1963.
18. Crawford, F.W., and Harp, R.S., "The Plasma Resonance Probe in a Magnetic Field," Physics Letters, V. 11, p. 126 to 127, July 15, 1964.
19. Messiaen, A., "Théorie de la Sonde à Résonance," Comptes Rendus de l'Académie des Sciences, V. 259, p. 1710 to 1713, September 7, 1964.
20. Crawford, F.W., "Plasma Resonance Probe Characteristics in a Magnetic Field," Journal of Applied Physics, V. 36, p. 3142 to 3145, October 1965.
21. Lepechinsky, D., "La Sonde à Résonance," L'Onde Électrique, V. 45, p. 1480 to 1485, December 1965.
22. Lepechinsky, D., Rolland, P., and Taillet, J., "Méthode Simple de Mesure de la Densité Électronique et de la Fréquence de Collisions d'un Plasma par la Sonde Sphérique à Résonance Haute Fréquence," Comptes Rendus de l'Académie des Sciences, V. 261, p. 663 to 664, July 19, 1965.
23. Rolland, P., "Les Amortissements Non Collisionnels dans la Résonance d'une Sonde Haute Fréquence," Comptes Rendus de l'Académie des Sciences, V. 261, p. 5366 to 5369, December 20, 1965.
24. Lepechinsky, D., Messiaen, A., and Rolland, P., "On the Resonance Probe," Journal of Nuclear Energy Part C, Plasma Physics, Accelerators, Thermonuclear Research, V. 8, p. 165 to 167, March-April 1966.
25. Buckley, R., "A Theory of Resonance Rectification - The Response of a Spherical Plasma Probe to Alternating Potentials," Proceedings of the Royal Society, Series A, V. 290, p. 186 to 219, February 22, 1966.
26. Dote, T. and Ichimiya, T., "Characteristics of Resonance Probes," Journal of Applied Physics, V. 36, p. 1866 to 1872, June 1965.
27. Gierke, G.V., Muller, G., Peter, G. and Rabben, H., "On the Influence of Ion Sheaths Upon the Resonance Behavior of a R.F. Plasma Probe," Zeitschrift für Naturforschung, V. 19a, p. 1107 to 1111, September 1964.
28. Lepechinsky, D. and Rolland, P., "La Sonde à Résonance. Etude Experimentale des Amortissements Non Collisionnels," Comptes Rendus de l'Académie des Sciences, V. 262, p. 926 to 928, April 4, 1966.
29. Messiaen, A.M. and Vandenplas, P.E., "High-Frequency Dielectric Resonance Probe for the Measurement of Plasma Densities," Journal of Applied Physics, V. 37, p. 1718 to 1724, March 15, 1966.
30. Druyvesteyn, M.J., "Der Niedervoltbogen," Zeitschrift für Physik, V. 64, p. 781 to 798, 1930.
31. Sloane, R.H. and Emeléus, K.G., "An Effect of Positive Space Charge in Collector Analysis of Discharges," Physical Review, V. 44, p. 333 to 337, 1933.
32. Sloane, R.H. and MacGregor, E.I.R., "An Alternating Current Method for Collector Analysis of Discharge-Tubes," Philosophical Magazine, V. 18, p. 193 to 207, 1934.

33. Van Gorcum, A.H., "Determination of the Velocity Distribution of Electrons in a Low Pressure Discharge Tube," Physica, V. 3, p. 207 to 218, 1936.
34. Kagan, Y.M., Fedorov, V.L., Malyshev, G.M., and Gavallas, L.A., "On a Technique for Measuring the Electronic Velocity-Distribution Function in a Gas Discharge," Doklady Akademiia Nauk SSSR, V. 76, p. 215 to 217, 1951.
35. Malyshev, G.M. and Fedorov, V.L., "Use of a Narrow-Band Amplifier in Oscillographic Investigation of the Electron Velocity Distribution Functions in an Electrical Discharge," Doklady Akademiia Nauk SSSR, V. 92, p. 269 to 271, 1953.
36. Boyd, R.L.F. and Twiddy, N.D., "Electron Energy Distribution in the Striated Hydrogen Discharge," Nature, V. 173, p. 633, April 3, 1954.
37. Medicus, G., "Simple Way to Obtain the Velocity Distribution of the Electrons in Gas Discharge Plasmas from Probe Curves," Journal of Applied Physics, V. 27, p. 1242 to 1248, October 1956.
38. Boyd, R.L.F., and Twiddy, N.D., "Electron Energy Distribution in Plasmas," Proceedings of the Royal Society, Series A, V. 250, p. 53 to 69, 1959.
39. Waymouth, J.F., "Pulse Technique for Probe Measurements in Gas Discharges," Journal of Applied Physics, V. 30, p. 1404 to 1412, September 1959.
40. Medicus, G., "Theory of Electron Collection of Spherical Probes," Journal of Applied Physics, V. 32, p. 2512 to 2520, December 1961.
41. Medicus, G., "Spherical Langmuir Probe in 'Drifting' and 'Accelerated' Maxwellian Distribution," Journal of Applied Physics, V. 33, p. 3094 to 3100, 1962.
42. Smith, L.G., "Langmuir Probes for Measurements in the Ionosphere," N65-33113 and N66-12867.
43. Branner, G.R., Friar, E.M., and Medicus, G., "Automatic Plotting Device for the Second Derivative of Langmuir Probe Curves," Review of Scientific Instruments, V. 34, p. 231 to 237, March 1963.
44. Friar, E.M., Jr., "Determination of the Second Derivative of Langmuir Probe Characteristics by an Intermodulation Method," N63-23625.
45. Friar, E.M., Jr., "Plasma Diagnostics by Second Derivative Methods," AD-476719. Also Proceedings of the National Electronics Conference, V. 19, p. 696 to 699, 1963.
46. Aisenberg, S., "Modern Probe Techniques for Plasma Diagnosis," in Engineering Aspects of Magnetohydrodynamics, Gordon and Breach, p. 89 to 126, 1964.
47. Medicus, G., "Probe Techniques for the Study of Plasma Phenomena," AD-474007.
48. Sagalyn, R.C., "Space Electricity, Physical Problems and Experimental Techniques," in "Problems of Atmospheric and Space Electricity," Proceedings of the Third International Conference on Atmospheric and Space Electricity. Elsevier Publishing Co., 1965.
49. Hiroa, K. and Miyazaki, S., "Measurement of Electron Energy Distribution in the Ionosphere," A65-25359.

50. Call, S.M., "Theoretical Error of the Automatic Second Derivative Device," Review of Scientific Instruments, V. 36, p. 850 to 852, June 1965.
51. Peterson, C.C., Dienst, J.F., and d'Agostini, D., "Simultaneous Plasma Analysis Techniques," AD-480106.
52. Medicus, G., "Accuracy of an Automatic Second Derivative Plotter," N64-13995.

SUMMER WORKSHOP 1966

Program Outline and Team Participants

PROJECT C: Magnetic Fields and Plasma Studies

Problem Topics

- C-1 Magnetic shielding
- C-2 The production of uniform magnetic fields by compensated solenoids
- C-3 Two plasma probe techniques
- C-4 Positive ion collection by spherical langmuir probes
- C-5 Four-coil-systems with a prolate volume of uniformity
- C-6 The design of a system of equally spaced coaxial coils to produce a uniform magnetic field
- C-7 The plasma-resonance probe
- C-8 A nitrogen plasma
- C-9 A probe to measure plasma conductivity
- C-10 The production of uniform gradient magnetic fields

TEAM C

Academic Personnel

Dr. D. L. Waidelich
Principal Investigator
Dr. G. R. Joyce
Professor John Kinnier
Mr. J. C. Morrison
Mr. J. D. Murphy
Mr. M. P. Smith

Goddard Personnel

Mr. J. C. New
Staff Advisor
Mr. J. E. Stern
Mr. D. R. Burrowbridge
Mr. R. E. Gebhardt
Mr. Don Frericks

NSF Summer Science Student
Jeff L. Zurkow

PRECEDING PAGE BLANK NOT FILMED.

PROJECT C: MAGNETIC FIELDS AND PLASMA STUDIES

CONTENTS

	<u>Page</u>
POSITIVE ION COLLECTION BY SPHERICAL LANGMUIR PROBES G. R. Joyce and J. D. Murphy	301 ✓
FOUR COIL SYSTEMS WITH A PROLATE VOLUME OF UNIFORMITY J. C. Morrison	311 ✓
THE DESIGN OF A SYSTEM OF EQUALLY SPACED, COAXIAL COILS TO PRODUCE A UNIFORM MAGNETIC FIELD. J. C. Morrison	321 ✓
THE PLASMA-RESONANCE PROBE M. P. Smith	333 ✓
A NITROGEN PLASMA J. H. Kinnier	359 ✓
A PROBE TO MEASURE PLASMA CONDUCTIVITY..... D. L. Waidelich, G. R. Joyce and J. Zurkow	373 ✓
THE PRODUCTION OF UNIFORM GRADIENT MAGNETIC FIELDS D. L. Waidelich	389 ✓

PRECEDING PAGE BLANK NOT FILMED.

INTRODUCTORY REMARKS ON PROJECT C MAGNETIC FIELDS AND PLASMA STUDIES

D. C. Kennard, Jr.

The magnetic fields studies of this group are an outgrowth of work started in the 1962 Summer Workshop and continued in successive sessions. In the early years these studies produced data that helped in developing the designs of the 20-foot diameter coils in Goddard's Magnetic Fields Component Test Facility and the 40-foot diameter coils in the Attitude Control Test Facility. The subsequent successful construction and performance of these unique facilities attest to the effectiveness and importance of these studies.

The 1965 and 1966 Workshop sessions developed data for a handbook on coil systems for uniform magnetic fields and weakly magnetic materials. A preliminary publication was made of this material in a supplement to the Final Report of the Summer Workshop for 1965 (X-100-65-407 (s)). The completed handbook is being published as a NASA Technical Note which is expected to be available in July 1967.

Also during the workshop sessions of 1965 and 1966, experimental and analytical studies were initiated to investigate various approaches to the problem of simulating and measuring space plasmas in ground testing facilities. This effort contributed to Goddard's successful testing of such spacecraft hardware as the Princeton Experimental Package in an environment that simulates space plasma conditions in orbit. Such testing constitutes a new state-of-the-art in environmental technology for space systems.

POSITIVE ION COLLECTION BY SPHERICAL LANGMUIR PROBES

Glenn R. Joyce*
and
James D. Murphy** 7

SECTION I

N 67-22761

In the first comprehensive theory of electrostatic probes immersed in a collisionless plasma, Mott-Smith and Langmuir (Reference 1) assumed that the electric field around the probe terminated at the edge of a sharply defined sheath. Bohm, Burhop, and Massey (Reference 2) showed that there was field penetration into the plasma, but they calculated neither potential profiles nor positive ion-voltage characteristics. They assumed an a priori separation into sheath and plasma regions.

Allen, Boyd, and Reynolds (Reference 3) analyzed particle orbits around the probe using the general conservation laws of energy and angular momentum. They discussed the case of zero ion temperature and negligible electron collection to a negative probe. Solving Poisson's equation reduced to integrating numerically an ordinary differential equation under the particular conditions λ_{Dt} (The ion Debye length) much greater than R_p , (the probe radius), and T_e (the electron temperature) much greater than T_i (the ion temperature).

Bernstein and Rabinowitz (Reference 4) were also able to reduce the problem to an ordinary differential equation. They assumed a monoenergetic ion distribution and negligible electron collection. Assuming that the ions move in a central force field, they made a detailed study of possible orbits. Using a solution of the collisionless Boltzmann equation, they integrated Poisson's equation numerically for values of the probe potential, V_p , much greater than kT_e , and $\lambda_{Dt} \gg R_p$. S. H. Lam (Reference 5) performed asymptotic analyses of the Bernstein and Rabinowitz differential equation for regions of very small and very large potentials.

Gurevich (Reference 6) derived expressions for the density and flux of particles in a rarified gas in a centrally symmetric field. He calculated characteristics for situations where the dimensions of the charged spherical body were much smaller and much greater than the Debye radius. The effects of interparticle collisions and reflection of particles from the probe surface were discussed.

In a series of papers Hall (Reference 7) treated systems where the undisturbed distributions of attracted and repelled particles at infinity were arbitrary. By combining Vlasov's equation with an integral form of Poisson's equation, he developed a technique for computing the self-consistent potential distribution around a probe. Limiting himself to the case of λ_{Dt} and R_p much less than all other pertinent dimensions (i.e., mean free paths, system dimensions, cyclotron radii), he computed characteristics for a cylindrical probe with a Maxwellian ion distribution.

A useful table was presented by Chen (Reference 8) who summarized numerical results from theories developed before 1964.

* University of Iowa

** Catholic University

For the case of monoenergetic ions, Kagan and Perel (Reference 9) calculated characteristics for spherical and cylindrical probes. Analyzing ion trajectories through the use of the general conservation laws and neglecting electron collection, they numerically integrated an ordinary differential equation.

Walker (Reference 10) following the work of Opik (Reference 11) calculated probe characteristics for a Maxwellian ion distribution using an integral form of Poisson's equation. He made a careful examination of particle orbits, and solved the resulting integral equation. Details of the computational scheme, said to involve no iteration procedure, are unclear.

Laframboise (Reference 12) took the theory of Bernstein and Rabinowitz (Reference 4) in its most general form. He assumed a fully poly-energetic Maxwellian distribution for the attracted and repelled species, and developed an iterative procedure for solving the resulting system of non-linear integral equations. The infinite plasma was replaced by an outer boundary of finite radius, beyond which a power-law potential was specified. Numerical computations involved a sequence of successive approximations to potential and charge distributions. The calculation procedure became progressively more ill-behaved as the ion temperature decreased because the form of the potential at large radii became relatively more important.

Both Walker and Laframboise accounted for the reflection of attracted particles at the probe surface.

Laframboise succeeded in calculating characteristics for a much wider range of physical parameters (probe potentials, probe radii, and plasma temperatures) than was previously achieved. He concluded that the monoenergetic model was a good approximation for plasmas where $R_p/\lambda_{De} > 5$, but gave marked deviations from the Maxwellian model for smaller values of R_p/λ_{De} .

SECTION II

In the papers discussed in Section I, the use of a Maxwellian distribution for particles in the ambient plasma leads to a non-linear integral equation for the electrostatic potential. Because of the difficulty in solving this equation, the assumption of monoenergetic velocity distribution has often been made. With this assumption, the integral equation becomes a differential equation. Reduction of the integral equation by other physically reasonable approximations would seem useful. The authors have attempted to reduce the integral equation to a differential equation by a low temperature assumption. That is, for low ion temperatures there is so small a spread of velocities in the ambient plasma that with the insertion of an electrostatic probe into the plasma, the velocity spread of ions reaching the probe is small. It has been shown that for particles which are attracted by a spherical probe, there is a sphere centered on the probe, but with a larger radius than the probe radius, which acts as the effective gathering body. The gathering sphere radius is a function of the initial velocity of the attracted particle. It was hoped that an "average" gathering sphere radius could be defined if the spread of initial velocities were small. It seems, however, that for all but the lowest ion temperatures, this approximation is not valid.

The treatment of probe characteristics has become almost standard. The problem treated is that of a spherical electrostatic probe, of radius R_p , immersed in a tenuous plasma. The plasma is considered to be collisionless and it is assumed that for large distances from the probe the plasma is electrically neutral on a macroscopic scale and in thermodynamic equilibrium. This is called the quasi-neutral region. For a collisionless plasma, according to the Liouville theorem, the phase space distribution function along particle trajectories is constant

$$f(\vec{r}, \vec{v}) = f(\vec{r}_0, \vec{v}_0).$$

The electron and ion densities are calculated using

$$n_e = n_0 \int f_e(\vec{r}, \vec{v}) d\vec{v}$$

where n_0 is the electron and ion density in the undisturbed plasma. The densities are used in Poisson's equation to determine the spatial dependence of the potential which is then used to calculate the probe characteristic.

The derivation of the integral equation will follow that of Kagan and Perel (Reference 9) which is outlined below. The derivation will be restricted to large negative probe potentials for which the ion is the attracted particle. Kagan and Perel have shown that in this potential region, the electron density can be approximated by the Boltzmann barometric formula,

$$n_e(r) = n_0 e^{\frac{eV(r)}{kT_e}}$$

Ion densities are somewhat more involved since one must determine the gathering sphere radius. An ion impinging on the probe with a velocity v_0 and impact parameter p in the undisturbed plasma is governed by

$$\frac{1}{2} m v_0^2 = \frac{1}{2} m v^2 + e V(r)$$

where $V(r)$ is the potential due to the probe, v_0 is the velocity of the ion in the quasi-neutral region, v is the velocity of the ion at the point r , m is the ion mass, and

$$v_0 p = v r \sin \theta$$

where θ is the angle between the vectors \vec{r} and \vec{v} . Unless the ion strikes the probe, it will attain some minimum distance from the probe before receding to the undisturbed plasma. At this minimum distance there will be no component of velocity along the radius vector and $\sin \theta = 1$. If r_{\min} is the minimum distance,

$$p^2 = r_{\min}^2 \left[1 - \frac{2eV(r_{\min})}{m v_0^2} \right] \equiv G(r_{\min})$$

For an attractive potential $G(r_{\min})$ is the product of two terms. One is a monotonically increasing function of r_{\min} , r_{\min}^2 , and the other is a monotonically decreasing function of r_{\min} . If one determines the curve $G(V_{\min})$ vs. V_{\min} , a minimum may occur. Let this value of r_{\min} be denoted by r_ℓ . If there is a minimum, which seems to occur in practice, for impact parameters $p^2 \leq G(r_\ell)$ there is no corresponding minimum distance and the particle must hit the probe. If r_ℓ is greater than the probe radius it becomes the effective probe radius. The ion density can be computed by calculating

$$n_i(\vec{r}) = n_0 \int f_i(\vec{r}, \vec{v}) d\vec{v}.$$

A point of phase space (\vec{r}, \vec{v}) , which is accessible to particles starting at infinity without their striking the probe, is said to be in the unscreened region. The distribution function for the unscreened region is

$$f_i(\vec{r}, \vec{v}) = f_0(v_0),$$

where $f_0(v_0)$ is the Maxwellian distribution function. The distribution function for phase space points not in the unscreened region is

$$f_i(\vec{r}, \vec{v}) = 0$$

since no particles can reach those points. The ion density becomes

$$n_i(r) = n_0 \int f_0(v_0) d\vec{v}$$

The unscreened region is determined by the impact parameter and conservation of energy. The first requirement is

$$\frac{m v_0^2}{2} = \frac{m v^2}{2} - e V(r) > 0.$$

If $r > r_\ell$ the point (\vec{r}, \vec{v}) belongs to the unscreened region if $\theta > \pi/2$ or if $\theta < \pi/2$ but $p^2 > G(r_\ell)$. This can be written $\theta > \theta_1$, where

$$\sin^2 \theta_1 = \frac{v_0^2 G(r_\ell)}{v^2 r^2}.$$

$$n_i(r) = 2\pi \int_{\frac{\sqrt{-eV(r)}}{m}}^{\infty} n_0 f_0 \left(\frac{m v^2}{2} + e V(r) \right) v^2 dv \int_{\theta_1}^{\pi} \sin \theta d\theta.$$

$$= 2\pi n_0 \int_{\frac{\sqrt{-2eV(r)}}{m}}^{\infty} dv v^2 f_0 \left(\frac{m v^2}{2} + e V(r) \right) \left[1 + \sqrt{1 - \frac{v_0^2 G(r_\ell)}{v^2 r^2}} \right]$$

Using the form of the Maxwellian

$$n_i(r) = e^{-\frac{eV(r)}{kT_i}} \left\{ \frac{n_0}{2} \int_{-eV(r)}^{\infty} \epsilon^{1/2} \left(\frac{4}{\pi (kT_i)^3} \right)^{1/2} e^{-\frac{\epsilon}{kT_i}} d\epsilon \right. \\ \left. + \frac{n_0}{2} \left(\frac{4}{\pi (kT_i)^3} \right)^{1/2} \int_{-eV(r)}^{\infty} \epsilon^{1/2} e^{-\frac{\epsilon}{kT_i}} \sqrt{1 - \frac{\epsilon_0}{\epsilon r^2} G(r_e)} d\epsilon \right\}.$$

If one assumes that r_ℓ is not a function of velocity, these integrals can be evaluated.

The result is

$$n_i(r) = n_0 e^{-\frac{eV(r)}{kT_i}} \left\{ \frac{1}{\sqrt{\pi}} \sqrt{\frac{-eV(r)}{kT_i}} e^{\frac{eV(r)}{kT_i}} + \frac{1}{2} \left[1 - \Phi \left(\sqrt{\frac{-eV(r)}{kT_i}} \right) \right] \right. \\ \left. + \left(1 - \frac{r_\ell^2}{r^2} \right)^{1/2} e^{-\left(\frac{r_\ell^2}{r^2} \frac{e(V(r) - V(r_\ell))}{1 - r_\ell^2/r^2} \right)} \left[\frac{1}{\sqrt{\pi}} \sqrt{y_0} e^{-y_0} + \frac{1}{2} (1 - \Phi(\sqrt{y_0})) \right] \right\}$$

where

$$y_0 = \frac{-eV(r) + r_\ell^2/r^2 V(r_\ell)}{kT_i (1 - r_\ell^2/r^2)}$$

and $\Phi(x)$ is the error function.

When $r < r_\ell$ one can determine the ion density because the ion flux across any sphere of radius less than r_ℓ is a constant. The flux at r_ℓ is

$$4\pi r_\ell^2 \int v \cos \theta n(r_\ell) f_0 \left[\frac{1}{2} m v^2 + eV(r_\ell) \right] dv,$$

and for $r < r_\ell$ the flux is

$$4\pi r^2 \int v \cos \theta n(r) f_0 \left[\frac{1}{2} m v^2 + eV(r) \right] dv.$$

Equating the two expressions

$$n(r) = \frac{r_\ell^2}{r^2} n(r_\ell) e^{-\frac{e}{kT_i} (r(r_\ell) - V(r))}$$

The expressions for n_i and n_e can be placed in Poisson's equation

$$\nabla^2 V(r) = -\frac{e}{\epsilon_0} (n_i - n_e).$$

Defining dimensionless variables makes the formalism simpler. Let

$$\eta(r) = -\frac{eV(r)}{kT_i}$$

$$x = \sqrt{\frac{n_0 e^2}{kT_i \epsilon_0}} r$$

$$\beta = \frac{T_e}{T_i}$$

Poisson's equation with spherical symmetry becomes

$$\frac{d^2 \eta}{dx^2} + \frac{2}{x} \frac{d\eta}{dx} = f_i(x) - e^{-\eta/\beta}, \quad (1)$$

where

$$\begin{aligned} f_i(x) &= \frac{1}{\sqrt{\pi}} \sqrt{\eta} + \frac{1}{2} [1 - \Phi(\sqrt{\eta})] e^\eta \\ &+ \left(1 - \frac{x_\ell^2}{x^2}\right)^{1/2} \left\{ \frac{1}{\sqrt{\pi}} \sqrt{\eta_0} + \frac{1}{2} [1 - \Phi(\sqrt{\eta_0})] e^{\eta_0} \right\} x > x_\ell, \\ f_i(x) &= \frac{x_\ell^2}{x^2} e^{(\eta_\ell - \eta)} \left\{ \frac{1}{\sqrt{\pi}} \sqrt{\eta_\ell} + \frac{1}{2} [1 - \Phi(\sqrt{\eta_\ell})] e^{\eta_\ell} \right\} x < x_\ell \end{aligned}$$

and

$$y_0 = \frac{\eta - x_\ell^2/x^2 \eta_\ell}{(1 - x_\ell^2/x^2)}$$

$$x_{\ell} = r_{\ell} \sqrt{\frac{n_0 e^2}{k T_i t_0}}$$

$$\eta_{\ell} = - \frac{e V(r_{\ell})}{k T_i}.$$

If x_{ℓ} is equal to the probe radius, this relation is identical to one derived by A. V. Gurevich (Reference 6).

These equations should allow one to calculate the potential and the probe characteristics. In practice, however, a serious problem arises because the value of y_0 is negative at $x = x_{\ell}$. This can be demonstrated by finding the minimum of the $G(r_{\min})$ curve and calculating y_0 at $r = r_{\ell}$. The problem apparently arises because in the integration of the expression for $\sin \theta_1$, for initial velocities greater than the thermal velocity, the sine expression becomes greater than one.

This problem would not occur if r_{ℓ} were treated as a function of velocity. An integral equation is the result of letting r_{ℓ} vary with v_0 . The conclusion is that if one wants to treat Maxwellian distributions, one must solve the integral equation. If it is not possible to use an average gathering radius to calculate probe characteristics, it may be that calculating characteristics using mono-energetic ion distributions which, in effect, is analogous to defining an "average" gathering radius, is not meaningful.

REFERENCES

1. Mott-Smith, H.M., and Langmuir, I., Physical Review V. 28, p. 727 (1926).
2. Bohm, D., Burhop, E.H.S., and Massey, H.S.W., "The characteristics of electrical discharges in magnetic fields," A. Guthrie and R. K. Wakerling, eds McGraw-Hill Book Company, Inc., New York, 1949.
3. Allen, J.E., Boyd, R.L.F., and Reynolds, P., Proceedings of the Physical Society V. 70B, p. 297, 1957.
4. Bernstein, I.B., and Rabinowitz, I., Physics of Fluids V. 2, p. 112, 1959.
5. Lam, S.H., Physics of Fluids V. 7 (1964), V. 8, p.73, 1965.
6. Gurevich, A.V., Geomagnetism and Aeronomy, V. 3, p. 151, 1963.
7. Hall, L.S., University of California Lawrence Radiation Laboratory (Livermore), Reports UCRL-6535, 1961, UCRL-7660, 1964, UCRL-12480, 1965.
8. Chen, F.F., Princeton University Plasma Physics Laboratory, Report Matt 252, 1964, (N64-23211).
9. Kagan and Perel, Soviet Physics Uspekhi, p. 767, 1964.
10. Walker, E.H., "Interactions of space vehicles with an ionized atmosphere" ed. by S.F. Singer Pergamon Press, New York, 1965, p. 61-162.
11. Opik, E.J., "Interactions of space vehicles with an ionized atmosphere," ed. by S. F. Singer Pergamon Press, New York, 1965, p. 3-60.
12. Laframboise, J.G., University of Toronto Institute for Aerospace Studies, Report UTIAS - 100, 1966.

APPENDIX

NOTE ON NUMERICAL SOLUTION

As noted in Section II, the differential equation derived from the "average" gathering radius is inconsistent with the gathering radius determined from the minimum of the $G(r_{\min})$ curve. One may find a solution to the equation if a somewhat unjustified assumption is made about the system. The assumption is that $y_0 = 0$ at r_ℓ . This corresponds to calling $\sin \theta_1 = 1$. The effect of the assumption is to change the value of r_ℓ from what would be calculated from the minimum condition.

Equation (1) is defined as a boundary-value problem. At $r = R_p$, $v(r) = v_p$ and in the limit of large r , $v(r) \rightarrow 0$. Numerical solutions of this type are not easy to solve as they must step through successive points from an initial determination of the function and its slope. An additional complication is that r_ℓ must be determined simultaneously with the solution of Equation (1). In this particular case it is easier to solve an "eigenvalue" problem as suggested by Bernstein and Rabinowitz (Reference 4). This is implemented by changing variables.

Let

$$y = \frac{x_\ell}{x}$$

Equation (1) becomes

$$\frac{1}{x_\ell^2} y^4 \frac{d^2 \eta}{dy^2} = f_i(y) - e^{-\eta(y)/\beta}$$

where

$$f_i(y) = \frac{1}{\sqrt{\pi}} \sqrt{\eta} + \frac{1}{2} (1 - \Phi \sqrt{\eta}) e^\eta$$

$$+ (1 - y^2)^{1/2} \left\{ \frac{1}{\sqrt{\pi}} \sqrt{y_0} + \frac{1}{2} [1 - \Phi(\sqrt{y_0})] e^{y_0} \right\} \quad y \leq 1$$

$$f_i(y) = y^2 e^{(\eta_e - \eta)} \left[\frac{1}{\sqrt{\pi}} \sqrt{\eta_\ell} + \frac{1}{2} (1 - \Phi \sqrt{\eta_\ell}) e^{\eta_\ell} \right] \quad y \geq 1$$

and

$$y_0 = \frac{\eta - y^2 \eta_\ell}{1 - y^2}$$

Letting $\lambda = x_\ell^2$, the form of the equation becomes

$$\frac{d^2 \eta}{dy^2} = \lambda F(\eta, \eta_\ell, y) \quad (\text{A-1})$$

Where η_ℓ is the value of η at $y = 1$. Each value of η_ℓ corresponds to some value of the probe potential which can be determined through the solution of Equation (A-1) as a function of η_ℓ . The procedure for determining λ is to start the solution at $y = 1$ with a given η_ℓ . The derivative is determined from the condition on y_0 at $y = 1$. The "eigenvalue", λ , is varied until the solution goes through $\eta = 0$ at $y = 0$. In practice this is never accomplished because of the $1/y^4$ term on the right hand side of Equation (A-1). However, λ can be determined to the limit of the computer since the solution will pass either above or below $\eta = 0$ as y approaches zero. Once λ has been determined, the solution can be integrated outward from $y = 1$ to the value of y corresponding to the probe radius.

FOUR COIL SYSTEMS WITH A PROLATE VOLUME OF UNIFORMITY

John C. Morrison

ABSTRACT

N 67-22762

The power series method for a system of four circular coils is modified in order to extend the region of uniformity along the axis of the coils. Using this method a particular solution is found having a length of 1 percent uniformity along the axis equal to 1.74 times the radius of the inner coils. This represents an improvement along the axis of 47 percent over the Braunbek solution presently used at the Goddard Magnetic Test Facility, with a corresponding loss in uniformity off axis.

INTRODUCTION

During the three past Summer Workshop programs the problem of producing a weak magnetic field with a large volume of uniformity has been considered. The work has been primarily concerned with systems of coaxial coils, and in particular, a four coil Braunbek system was found having a volume of 1 percent uniformity which is approximately spherical in shape and extends 0.57 of the distance from the origin to the first coil pair ($0.57 r_1$ in Figure C-1).

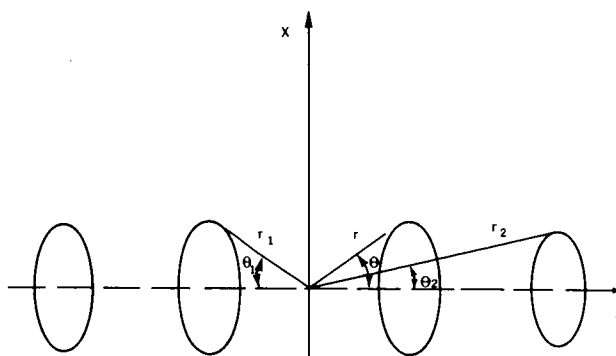


Figure C-1—Four coil system.

In testing the magnetic properties of some objects, however, a prolate volume of uniformity is desirable. Garrett has pointed out (see Reference 1) that the usual power series solution, in which the leading coefficients in the series expansion of the magnetic field are made to vanish, leads to an approximately spherical volume of uniformity. In order to produce a prolate volume it is necessary to modify the series method.

METHOD OF SOLUTION

For a symmetric system of four circular coils the components of the magnetic field may be expressed as a series:

$$H_z = \sum_{n=0,2,4,\dots}^{\infty} a_n r^n p_n(\cos \theta)$$

$$H_x = - \sum_{n=2,4,\dots}^{\infty} \frac{1}{(n+1)} a_n r^n \sin \theta p'_n(\cos \theta)$$

for $r > r_1$

where

$$a_n = \sum_{p=1}^z \frac{4\pi}{c} i_p (1 - \mu_p^2) \frac{1}{r_p^{n+1}} p'_{n+1}(\mu_p)$$

i_p = current in pth loop

$\mu_p = \cos \theta_p$

Along the axis of the coils this becomes

$$H_z = a_0 + a_2 Z^2 + a_4 Z^4 + \dots$$

$$H_x = 0$$

The Braunbek solution mentioned above was obtained by selecting μ_p , r_p , and i_p so that $a_2 = a_4 = a_6 = 0$ and a_8 is a minimum. The expression for the field along the axis then becomes

$$H_z = a_0 + a_8 Z^8 + \dots$$

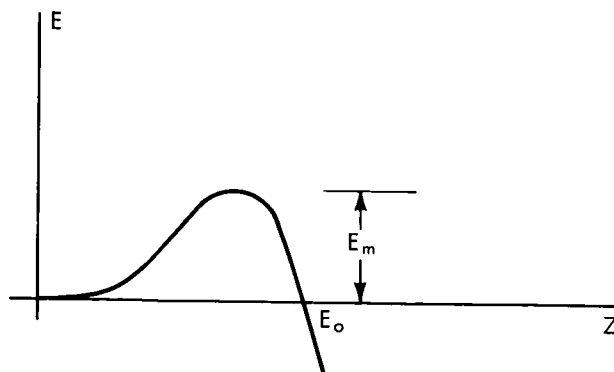
the principal error being given by the term of eighth order, $a_8 Z^8$.

In the method which is used in this report the condition upon the coefficient, a_6 , is relaxed. Then the error in the field along the axis, $(H_z - H_z(0))/H_z(0)$, is given approximately by

$$E = \frac{a_6}{a_0} Z^6 + \frac{a_8}{a_0} Z^8.$$

It is required, then, that a_6 and a_8 have opposite sign. If this is true, the error along the axis has the appearance shown in Figure C-2.

Figure C-2



Near the origin E has the sign of a_6 and for large values the sign of a_8 , at some intermediate point, Z_0 say, it vanishes. Finally it is required that $|E_m| \leq .01$ and that Z_0 be a maximum.

In this way it has been possible to extend the region of uniformity along the axis from $0.57 r_1$ to $0.78 r_1$ with a corresponding loss off axis, since a_6 is no longer zero. The Fortran program which was used to obtain this solution is given and described in the appendix.

The error function along the axis for the Braunbek solution and for the new solution are shown in Figure C-3. The exact expression for the magnetic field along the axis was used to obtain these plots.

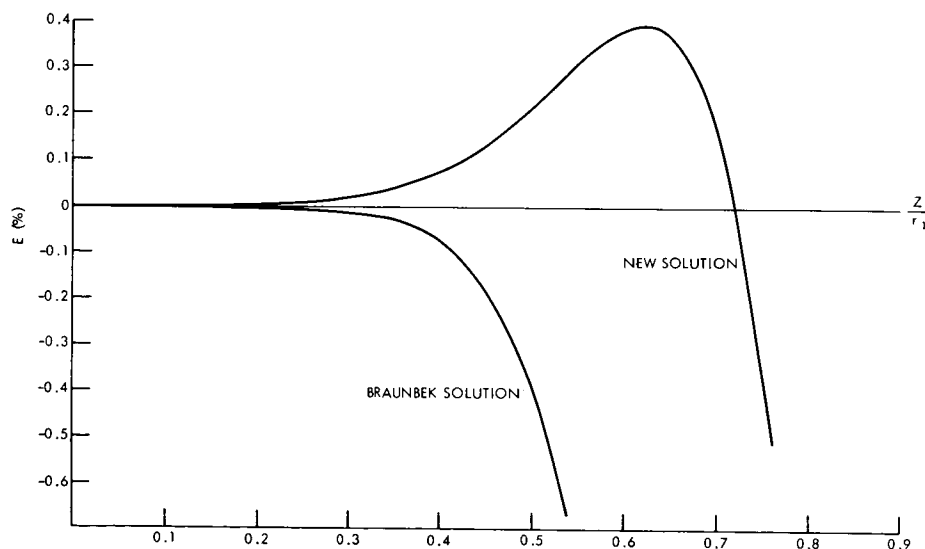


Figure C-3—Error function along the axis for the Braunbek solution ($\mu_1 = .742$, $\mu_2 = .268$, $r_2/r_1 = .914 + i_2/i_1 = 1$) and for a new solution ($\mu_1 = 1$, $\mu_2 = .38$, $r_2/r_1 = 1.4868$, $i_2/i_1 = 8.9958$).

It can be seen in a qualitative way how the Braunbek solution and the new solution are related. If one is added to the two error functions, the form of the magnetic field along the axis for these solutions is obtained (Figure C-4). The new coil dimensions are obtained from the old by stretching the two coil pairs away from the origin along the axis. Apparently, as a result, the value of the field at the origin drops creating a kind of trough with a double maximum. The length of the region is in this way extended.

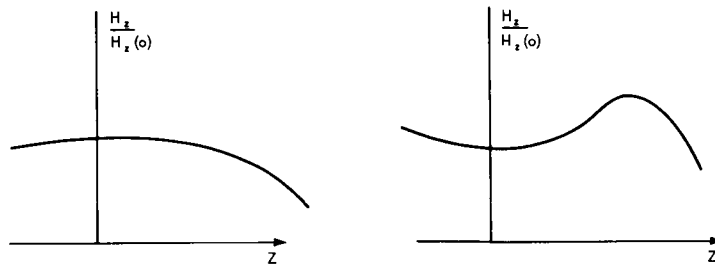


Figure C-4—Form of the magnetic field along the axis for the Braunkbek solution (left) and the new solution (right).

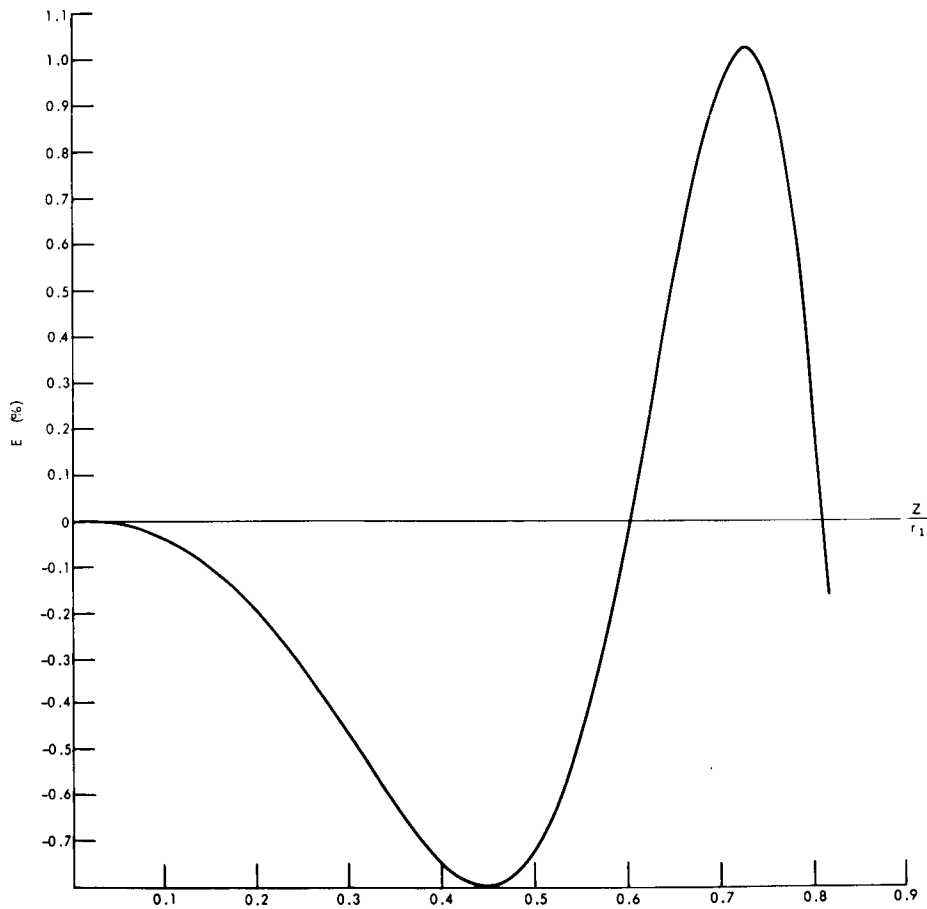


Figure C-5—Error function along the axis for another solution.

The new solution was improved by scanning the region in which it lies using a brute force computer method. The error function along the axis, E , may be written as a function of μ_1 , μ_2 , $U = Z/r_1$, $\zeta = r_2/r_1$, and $i = i_2/i_1$. The method consists in scanning separately through the variables μ_1 , μ_2 , ζ , and i , and for each set of values of these variables finding that value of U , say U_1 , for which E becomes equal to 0.01. μ_1 , μ_2 , ζ , and i are chosen so that U is maximized.

In this way the region of uniformity along the axis was extended from $0.78 r_1$ to $0.84 r_1$. The values of μ_1 , μ_2 , ζ , and i corresponding to this solution are

$$\mu_1 = 0.89, \quad \mu_2 = 0.37$$

$$\zeta = 1.041, \quad i = 2.818$$

An exact error plot of this solution is given in Figure C-5.

REFERENCE

Garrett, M., "Axially symmetric systems for generating and measuring magnetic fields," Journal of Applied Physics, V. 22, p. 1091 to 1107, September 1951.

APPENDIX

FORTTRAN PROGRAM FOR FOUR-COIL SOLUTION USING A MODIFICATION OF THE POWER SERIES METHOD

This program scans through the variables $\cos \theta_1 + \cos \theta_2$ separately. For each set of values of $\cos \theta_1 + \cos \theta_2$ it uses the conditions $a_2 = 0$ and $a_4 = 0$ to solve for $\zeta = r_2 / r_1$ and $i = i_2 / i_1$. It then checks to see whether a_6 and a_8 have opposite signs, and if they do, whether $|E_m| \leq 0.01$. If both of these conditions are satisfied it calculates Z_0 and prints out Z_0 together with the values of $\cos \theta_1$, $\cos \theta_2$, ζ , and i .

The program shown in Figure C-8 generates a plot of the percent error of the field along the axis on magnetic tape. The tape serves as input for the next program to be plotted on an incremental plotter.

The program shown in Figure C-9 plots the tape generated by the previous program on an incremental plotter.

```

C      PROGRAM FIELD
C      **CS1= U1
C      **CS11= INITIAL VALUE OF U1
C      **CS1N=INCREMENT IN U1
C      **N1= NUMBER OF INCREMENTS IN U1
C      ** CS2,CS21,CS2N,N2 ARE SIMILARLY DEFINED FOR THE SECOND COIL
16  READ(10,CS11,CS1N,N1,CS21,CS2N,N2
    IF(CS11-10.) 17,18,18
17  PRINT(10,1
    ZERO=0.
    II=0
    CS1=CS11-CS1N
    CS2=CS21-CS2N
    DO 11 I=1,N1
    CS1=CS1+CS1N
    DO 6 J=1,N2
    CS2=CS2+CS2N
    C21=CS1*CS1
    C22=CS2*CS2
    Y1=5.*C21-1.
    Y2=5.*C22-1.
    X1=1.-C21
    X2=1.-C22
    IF(X1*X2*Y1*Y2)1,6,1
    1 R1=1.-C21*(14.-C21*21.)
    IF(R1)9,6,9
    9 R2=1.-C22*(14.-C22*21.)
C      ** TRHO= R2/R1
    TRHO=(Y1*R2)/(Y2*R1)
    IF (TRHO)6,6,10
10  TRHO=SUM(1,TRHO)
    IF((TRHO-.66)*(1.5-TRHO))6,12,12
12  T1=-(TRHO*.3)*(X1*Y1)/(X2*Y2)
C      ** T1 =12/11
    P9P1=45.*(7.-C21*(308.-C21*(2002.-C21*(4004.-C21*2431.)))/128.
    P9P2=45.*(7.-C22*(308.-C22*(2002.-C22*(4004.-C22*2431.)))/128.
    P7P1=7.*(-5.+C21*(135.-C21*(495.-C21*429.)))/16
    P7P2=7.*(-5.+C22*(135.-C22*(495.-C22*429.)))/16
    Q1=((TRHO*.07)*X1*P7P1)+T1*X2*P7P2
    Q2=((TRHO*.09)*X1*P9P1)+T1*X2*P9P2
    Q4=TRHO*X1+T1*X2
    IF(Q2*Q4)2,6,2
    2 IF(Q1*Q2)3,6,6
    3 Q3=-Q1/Q2
    TLIMIT=ABS(27.*Q1*(Q3*.3)/(Q4*256.))*100.
    IF(TLIMIT-1.)4,4,6
    4 TZERO=SUM(1,TRHO*TRHO*Q3)
C      ** TZERO =Z0
    IF(TZERO-0.5)6,13,13
13  II=II+1
    PRINT 102,II,CS1,CS2,TRHO,T1,TLIMIT,TZERO
    IF(TZERO-ZERO)6,6,5
    5 ZERO=TZERO
    ALIMIT=TLIMIT
    IJ=II
    RHO=TRHO
    CUR=T1
    CTH1=CS1
    CTH2=CS2
    6 CONTINUE
11  CS2=CS21-CS2N
    IF(II)7,8,7
    7 PRINT 103,IJ,CTH1,CTH2,RHO,CUR,ALIMIT,ZERO
    GOTO16
    8 PRINT 104
    GOTO16
18  STOP
100 FORMAT(2F10.0,5X,15,2F10.0,5X,15)
101 FORMAT(1H1,1H0,4X,4HCASE,5X,5HMU(1),6X,5HMU(2),9X,3HHRHO,13X,
    11H1,10X,7HMAX DEV ,5X,11HLOCATION OF ,67X,7HPERCENT ,5X,
    112HZERO IN R1-S,1H0)
102 FORMAT(5X,13,2(F8.5,5X),2(F10.4,5X),F6.3,5X,E12.5)
103 FORMAT(1H0,1H0,10X,24HMAXIMUM OF ZERO FOR CASE,15,5X,8HMU(1) = ,
    1F8.5,5X,8HMU(2) = ,F8.5,5X,8HHRHO = ,F10.5,6X,7H1 = ,F10.5,
    17H0,1H0,20HMAXIMUM DEVIATION = ,F6.3,9H PER CENT,16HZERO LOCATE
    10 AT ,E12.5,16H RADII FROM ORIGIN,1H1)
104 FORMAT (17X,25HNO SOLUTION IN THIS RANGE,1H1)
    END

```

Figure C-6-Brute force program.

DEFINED FOR THE SECOND COUNCIL

Figure C-7—Error plot programs.

```

PROGRAM ER PLOT
J1=1
J2=2
J3=3
J4=4
XS=1.0
YS=0.1
WRITE(33,300)J1,XS,YS
X0=-5.
Y0=0.
WRITE (33,300) J2,X0,Y0
XI=0.
YI=0.
WRITE(33,300)J3,XI,YI
READ100,UI,UN,N
READ101,U1 ,U2 ,RHO,TI
X1=1.-U1**2
X2=1.-U2**2
Q4=X1*RHO +TI*X2
U=UI-UN
DO 2 K=1,N
  U= U+ UN
  DMU1 =((U+U1)**2+X1) **1.5
  DPU1 =((U+U1)**2 +X1 )**1.5
  DU1 =(1.0)/DMU1 +(1.0)/DPU1
  DMU2=((U/RHO -U2 )**2+X2)**1.5
  DPU2=((U/RHO +U2 )**2+ X2) **1.5
  DU2 =(1.0)/DMU2 +(1.0)/DPU2
  E =((X1*RHO+DU1+TI* X2 * DU2 )/ Q4)* 50.-100.
PRINT200,U,E
2 WRITE (33,300) J4,E,U
END FILE 33
STOP
100 FORMAT(2F10.5,5X,15)
101 FORMAT(4F10.5)
200 FORMAT(2F10.5)
300 FORMAT(13,2F20.8)
END

```

Figure C-8

```

1160 FORMAT(I3,2F20.8)
1 READ INPUT TAPE 3, 1160,J,E,U
IF(XEOF(D))3,2,3
2 Q=PLOT(F(E,U,J)
GO TO 1
3 STOP
END

```

Figure C-9

THE DESIGN OF A SYSTEM OF EQUALLY SPACED, COAXIAL COILS TO PRODUCE A UNIFORM MAGNETIC FIELD

John C. Morrison

ABSTRACT

N 67-22763

An infinite system of circular coaxial coils is treated using Fourier analysis. A general method is described for selecting the spacing and radius of the coils to produce a given radius of uniformity of the magnetic field. The infinite system is then terminated, and a Fortran program is described which adjusts the current in the last three coils to minimize fringing effects. Finally a particular numerical example is worked.

INTRODUCTION

For the design of magnetic fields with a prolate volume of uniformity, a system having a large number of equally-spaced, coaxial coils has several advantages. It provides a test area which is more accessible than that of a solenoid which may be entered only through the ends; and, it is generally easier to construct than a four coil system which may require massive supporting members to produce a long region of uniformity.

An infinite system of coaxial coils provides a useful mathematical idealization of this system. Since the infinite system is periodic, it may be treated using Fourier analysis.

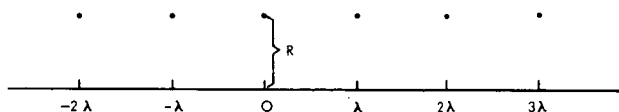


Figure C-10—Calculation of B_z .

North has shown (Reference 1) that the axial component of the magnetic field of an infinite set of circular loops is given by

$$B_z = \frac{\mu i}{\lambda} \left[1 + \sum_{n=1}^{\infty} A_n(X) \cos \left(n 2\pi \frac{Z}{\lambda} \right) \right] \quad (1)$$

where

$$A_n(X) = 4\pi \frac{R}{\lambda} n K_1 \left(n 2\pi \frac{R}{\lambda} \right) I_0 \left(n 2\pi \frac{X}{\lambda} \right) \quad (2)$$

λ = Spacing of coils

R = radius of coils

i = current in coils

x = distance from axis

z = distance along axis

K_1, I_0 are modified Bessel functions.

Along the axis of the system Equation (2) reduces to

$$A_n = 4\pi \frac{R}{\lambda} n K_1 \left(n 2\pi \frac{R}{\lambda} \right)$$

the Fourier amplitudes in the expansion of the field along the axis depend only upon R/λ . The first three Fourier amplitudes together with the maximum percent deviation of the field along the axis, E_m , are given in Table C-1. E_m is approximately equal to $(A_1 + A_2 + A_3) 100$. The Fortran program which produced Table C-1 is given in the appendix.

From this table the value of R/λ which is necessary for a given percent uniformity may be selected. For example, if a volume of 1 percent uniformity is desired $R/\lambda = 1.2$ would be a good choice.

Once the value of R/λ is selected, the second program in the appendix uses Equation (2) to tabulate $A_n(x)$. A sample output of this program, for the case $R/\lambda = 1.2$, is given in Table C-2. From this output the value of x/λ , say x_u/λ , which corresponds to the radius of desired uniformity may be selected. For example, if 1 percent uniformity is desired and if R/λ is chosen to be 1.2, x_u/λ is approximately equal to 0.3 (Table C-2).

The radius of the coils and the coil spacing is then given by the equations

$$R = \frac{R/\lambda}{x_u/\lambda} x_u$$

$$\lambda = \frac{R}{R/\lambda} \quad (3)$$

where x_u is the desired radius of uniformity and R/λ and x_u/λ have been found above.

The design of an infinite system having a given radius and percent uniformity is thus complete. It remains to terminate the coil system and to minimize fringing effects. First the number of coils in the system must be selected. Here there are no good general rules. If 1 percent uniformity is desired, however, about 7/10 of the length of the coil system will be available, with correspondingly shorter lengths for a system of higher uniformity. For the 1 percent case the number of coils is approximately given by

$$N = \frac{z_u/\lambda}{0.7} + 1 \quad (4)$$

where z_u is the desired length of uniformity.

Table C-1

R/ λ	A1	A2	A3	MAX DEV PERCENT
.70	6.9836E-02	1.1710E-03	1.7411E-05	7.1024E-06
.80	3.9478E-02	3.5456E-04	2.8167E-06	3.9835E-06
.90	2.2182E-02	1.0663E-04	4.5244E-07	2.2289E-06
1.00	1.2403E-02	3.1891E-05	7.2261E-08	1.2435E-06
1.10	6.9070E-03	9.4925E-06	1.1488E-08	6.9165E-07
1.20	3.8333E-03	2.8167E-06	1.8191E-09	3.8362E-07
1.30	2.1213E-03	8.3289E-07	2.8714E-10	2.1221E-07
1.40	1.1710E-03	2.4562E-07	4.5196E-11	1.1712E-07
1.50	6.4496E-04	7.2201E-08	7.0968E-12	6.4504E-07
1.60	3.5456E-04	2.1215E-08	1.1120E-12	3.5458E-07
1.70	1.9459E-04	6.2174E-09	1.7391E-13	1.9459E-07
1.80	1.0663E-04	1.8191E-09	2.7155E-14	1.0663E-07
1.90	5.8349E-05	5.3149E-10	4.2336E-15	5.8350E-07
2.00	3.1891E-05	1.5508E-10	6.5918E-16	3.1891E-07
2.10	1.7411E-05	4.5196E-11	1.0251E-16	1.7411E-07
2.20	9.4955E-06	1.3128E-11	1.5924E-17	9.4955E-07
2.30	5.1739E-06	3.8268E-12	2.4713E-18	5.1739E-07
2.40	2.8167E-06	1.1120E-12	3.8317E-19	2.8167E-07
2.50	1.5322E-06	3.2285E-13	5.9359E-20	1.5322E-07
2.60	8.3289E-07	9.3605E-14	9.1885E-21	8.3289E-07
2.70	4.5244E-07	2.7155E-14	1.4213E-21	4.5244E-07
2.80	2.4562E-07	7.8673E-15	2.1971E-22	2.4562E-07
2.90	1.3326E-07	2.2779E-15	3.3942E-23	1.3326E-07
3.00	7.2261E-08	6.5918E-16	5.2404E-24	7.2261E-07
3.10	3.9164E-08	1.9065E-16	8.0869E-25	3.9164E-07
3.20	2.1215E-08	5.5113E-17	1.2473E-25	2.1215E-07
3.30	1.1488E-08	1.5924E-17	1.9228E-26	1.1488E-07
3.40	6.2174E-09	4.5992E-18	2.9629E-27	6.2174E-07
3.50	3.3637E-09	1.3278E-18	4.5637E-28	3.3637E-07
3.60	1.8191E-09	3.8317E-19	7.0266E-29	1.8191E-07
3.70	9.8346E-10	1.1023E-19	1.0814E-29	9.8346E-07
3.80	5.3149E-10	3.1874E-20	1.6638E-30	5.3149E-07
3.90	2.8714E-10	9.1885E-21	2.5590E-31	2.8714E-07
4.00	1.5508E-10	2.6480E-21	3.9344E-32	1.5508E-07

Once the desired percent uniformity, R/λ , and number of coils are selected, the third program in the appendix adjusts the current in the last three coils to minimize fringing effects.

Finally, once the radius, spacing, and current of the coils is selected, the fourth and fifth program in the appendix use the exact expression for the field along the axis,

$$B_z = \frac{\mu i R^2}{\lambda} \sum_{k=-M}^M \frac{1}{[(Z - K\lambda)^2 + R^2]^{3/2}}$$

to plot the error function along the axis. The fourth program generates the information on magnetic tape. This tape serves as input for the fifth program to be plotted on an incremental plotter.

The last program in the appendix uses the expression for the magnetic field in terms of elliptic integrals to produce a two dimensional error plot in tabular form. This program has been checked in a number of ways. For a nine coil system the error along the axis has been compared

Table C-2

X/λ	A(1)	A(2)	A(3)
0	3.8333E-03	2.8167E-06	1.8191E-09
.01	3.8371E-03	2.8278E-06	1.8353E-09
.02	3.8485E-03	2.8614E-06	1.8844E-09
.03	3.8675E-03	2.9177E-06	1.9675E-09
.04	3.8941E-03	2.9974E-06	2.0870E-09
.05	3.9285E-03	3.1016E-06	2.2461E-09
.06	3.9708E-03	3.2315E-06	2.4491E-09
.07	4.0210E-03	3.3885E-06	2.7014E-09
.08	4.0793E-03	3.5746E-06	3.0099E-09
.09	4.1460E-03	3.7920E-06	3.3831E-09
.10	4.2211E-03	4.0434E-06	3.8313E-09
.11	4.3050E-03	4.3317E-06	4.3669E-09
.12	4.3978E-03	4.6604E-06	5.0047E-09
.13	4.4999E-03	5.0336E-06	5.7628E-09
.14	4.6115E-03	5.4559E-06	6.6626E-09
.15	4.7330E-03	5.9323E-06	7.7295E-09
.16	4.8648E-03	6.4687E-06	8.9943E-09
.17	5.0072E-03	7.0718E-06	1.0493E-08
.18	5.1607E-03	7.7492E-06	1.2270E-08
.19	5.3257E-03	8.5091E-06	1.4376E-08
.20	5.5028E-03	9.3611E-06	1.6873E-08
.21	5.6924E-03	1.0316E-05	1.9835E-08
.22	5.8951E-03	1.1386E-05	2.3350E-08
.23	6.1116E-03	1.2584E-05	2.7522E-08
.24	6.3425E-03	1.3926E-05	3.2477E-08
.25	6.5886E-03	1.5429E-05	3.8363E-08
.26	6.8505E-03	1.7113E-05	4.5359E-08
.27	7.1290E-03	1.8998E-05	5.3677E-08
.28	7.4251E-03	2.1110E-05	6.3571E-08
.29	7.7396E-03	2.3475E-05	7.5344E-08
.30	8.0734E-03	2.6126E-05	8.9356E-08
.31	8.4277E-03	2.9095E-05	1.0604E-07
.32	8.8035E-03	3.2424E-05	1.2592E-07
.33	9.2020E-03	3.6154E-05	1.4960E-07
.34	9.6243E-03	4.0337E-05	1.7783E-07
.35	1.0072E-02	4.5027E-05	2.1148E-07
.36	1.0546E-02	5.0286E-05	2.5162E-07
.37	1.1048E-02	5.6186E-05	2.9950E-07
.38	1.1580E-02	6.2805E-05	3.5663E-07
.39	1.2144E-02	7.0233E-05	4.2483E-07
.40	1.2740E-02	7.8569E-05	5.0625E-07
.41	1.3371E-02	8.7926E-05	6.0347E-07
.42	1.4040E-02	9.8431E-05	7.1961E-07
.43	1.4747E-02	1.1023E-04	8.5835E-07
.44	1.5495E-02	1.2348E-04	1.0241E-06
.45	1.6288E-02	1.3836E-04	1.2223E-06
.46	1.7126E-02	1.5507E-04	1.4592E-06
.47	1.8014E-02	1.7386E-04	1.7424E-06

with the plot obtained from the fourth and fifth programs; also, the error off axis has been confirmed within 10 percent by using Fourier analysis. For a 101 coil system where Fourier analysis should yield very good results, the error program has been confirmed to three significant figures for points selected at random.

A NUMERICAL EXAMPLE

A volume of 1 percent uniformity is desired with

$$Z_u = 15'$$

$$X_u = 1'$$

From Equations (3) and (4) it follows that

$$R = 4', \lambda = 3-1/3'$$

and that

$$N = 7.4$$

A nine coil system should then suffice.

The program to minimize fringing was thus run with $RHO = 1.2$, $PERERR = 0.5$, $M = 4$, and the optimum values for the current in the last three coils found to be 1.02 i, 0.8 i, and 2.15 i for the third from the end, second from the end, and the end coils respectively. Here i is the current in the inner three coils.

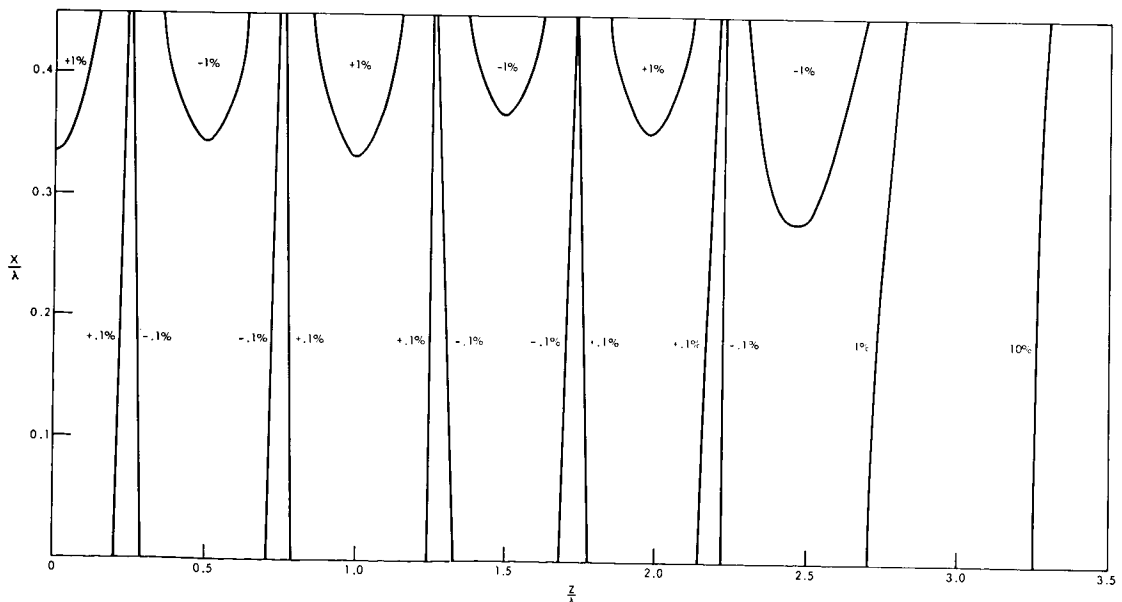


Figure C-11—Contour curves for the axial magnetic field of a nine coil system.

The last program in the appendix produced the error plot shown in Figure C-11. The fourth and fifth programs in the appendix plotted the error function along the axis as shown in Figure C-12.

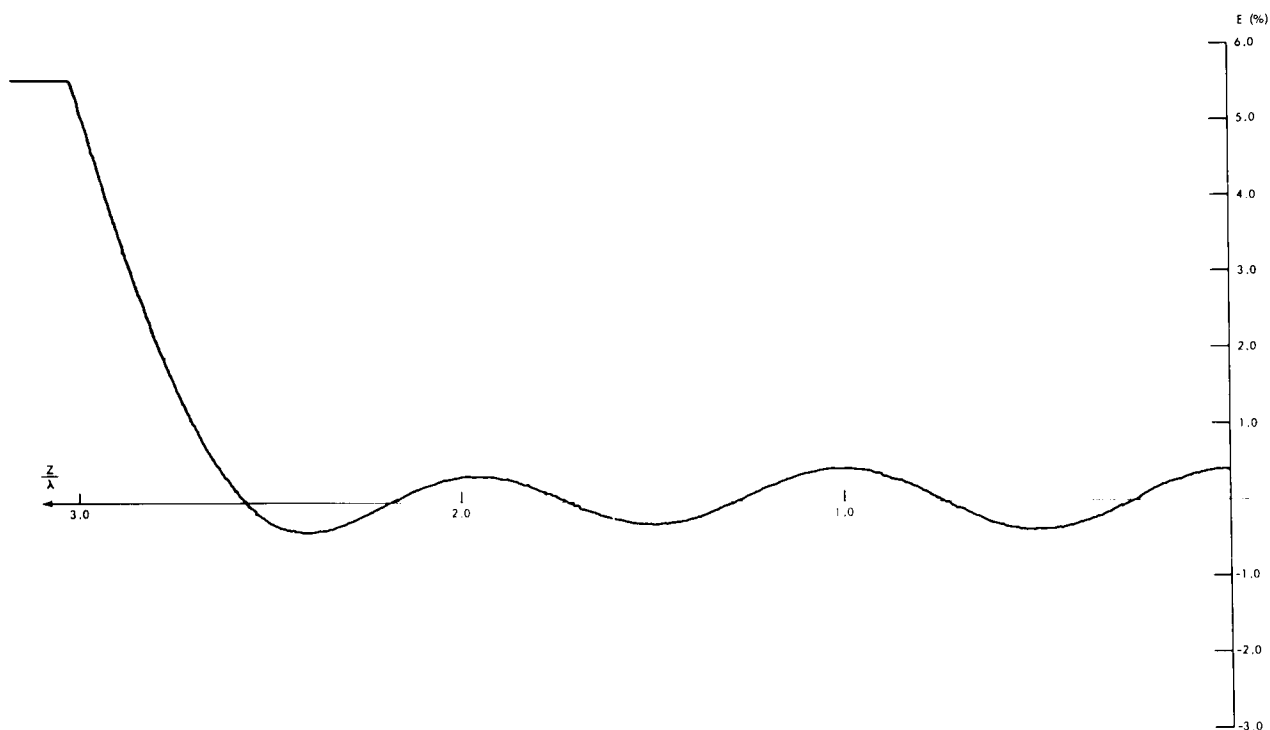


Figure C-12—Error plot of the magnetic field along the axis of a nine coil system.

REFERENCE

1. North, G.R., "Some properties of infinite lumped solenoids," Report ORNL-2975, Oak Ridge National Laboratory, Oak Ridge, Tennessee, September, 1961.

APPENDIX

```

C      PROGRAM FOU AMP
C      ***R=RADIUS OF COIL IN UNITS OF THE COIL SPACING
C      ***RI=INITIAL VALUE OF R
C      ***RN=INCREMENT IN R
C      *** N=NUMBER OF INCREMENTS IN R
C      *** A(I)=I-TH FOURIER AMPLITUDE IN EXPASION OF MAGNETIC FIELD ALONG AXIS
      DIMENSION A(10)
      READ100,RI,RN,N
      PRINT 102
      R=RI-RN
      DO1 I=1,N
      R=R +RN
      DO2 J=1,3
      AJ =J
      S=AJ*R*6.2831853072
      SM1= 2./S
      TK1S= SQRTF(.5*SM1)* EXPF( -S)* (1.25331414 +SM1*(.23498619 -SM1
1*(.00055020 -SM1*(.0100-200 - SM1 *(.00700000 -SM1*(.0002001*
1-SM1*.00068245 )))))
2 A(J) =S* 2.* TK1S
      E=0.
      DO3 K=1,3
3 E=E+A(K)*100.
1 PRINT101,R,(A(J),J=1,3),E
      STOP
100 FORMAT(2F10.5,5X,I5)
101 FORMAT(5X,F12.2,4(5X,E12.4)
102 FORMAT(/1H1,/1H0,12X,1HR,14X,2HA1,15X,2HA2,15X,2HA3,13X,7HMAX DEV,
1/76X,7HPERCENT,/1H0 )
      END

```

Figure C-13—Program for Fourier amplitudes along axis.

```

C      PROGRAM FOU AMP
C      *** U= DISTANCE FROM AXIS IN UNITS OF THE COIL SPACING
C      *** UI= INITIAL VALUE OF U
C      *** UN= INCREMENT IN U
C      *** N = NUMBER OF INCREMENTS IN U
C      *** A(I) =I-TH FOURIER AMPLITUDE IN EXPANSION OF MAGNETIC FIELD
C      ALONG A LINE A DISTANCE U FROM THE AXIS OF THE COIL SYSTEM
      DIMENSION B(10),TIO(10),A(10)
      READ100,RHO
      PRINT 110
      DO1 I=1,10
      AI=I
      S= AI*RHO *6.2831853072
      SM1=2./ S
      TK1S= SQRTF(.5*SM1)* EXPF( -S)* (1.25331414 +SM1*(.23498619 -SM1
1*(.03655620 -SM1*(.01504268 - SM1      *(.00780353 -SM1*(.00325614
1-SM1*.00068245 )))))
1 B(I) = S* 2.*TK1S
      UI=0.
      UN=.01
      N= RHO *60. +1.0001
      U=UI-UN
      DO2 I=1,N
      U=U+UN
      DO3 J =1,10
      AJ=J
      UP= AJ*U*1.675516081
      UP2=UP*UP
      IF(UP -1.0) 4,4,5
4 TIO(J) =1. +UP2*(3.5156229 +UP2*(3.0899424 + UP2*(1.2067492 +UP2*(
1.2659732 +UP2*(.0360768 + UP2*.0045813))))))
      GO TO 3
5 UPM1 =1./ UP
      TIO(J) = EXPF(3.75 * UP)*SQRTF(UPM1/3.75)*( .39894228 +UPM1*(.01328
1592 +UPM1*(.00225319 -UPM1*(.00157565 -UPM1*(.00916281- UPM1*(.020
157706 -UPM1*(.02635537-UPM1*(.01647633 -UPM1*.00392377))))))
3 CONTINUE
      E= 0.
      DO6 K=1,10
      A(K) =B(K) * TIO(K)
6 E=E+ A(K)
      E =100.* E
      PRINT111,U,(A(L) ,L=1,5 ),E
      STOP
100 FORMAT(F10.5)
110 FORMAT(1H1,/1H0,6X,1HU,13X,4HA(1),15X,4HA(2),15X,4HA(3),15X,4HA(4)
1,15X,4HA(5),13X,7HPERCENT,/116X,3HDEV,/1H0)
111 FORMAT(2X,F6.2,6(7X,E12.4))
      END

```

Figure C-14—Program for Fourier amplitudes off axis.

Figure C-15—Program to minimize fringing effects.

Error Plot Programs (Along Axis)

This program generates a plot of the percent error of the field along the axis on magnetic tape. The tape serves as input for the next program to be plotted on an incremental plotter.

```

PROGRAM ER PLOT
J1=1
J2=2
J3=3
J4=4
READ101,RHO,TI1,TI2,TI3,M
AM=M
AMM1=M-1
AMM2=M-2
XS=1.0
YS= 0.05 *AM
PRINT 300,J1,XS,YS
WRITE(33,300)J1,XS,YS
X0=-5.
Y0=0.
PRINT 300, J2,X0,Y0
WRITE (33,300) J2,X0,Y0
MM3=M-3
RH02=RHO*RHO
U1=0.
UN=.01
N=M*100 +1
SUMD0 = RHO**(-3)
DO5U1=1,MM3
A1=1
50 SUMD0=SUMD0 +2.*(A1*U1 +RH02 )**(-1.5)
BU= SUMD0 +TI1*2.*(AMM2**2+RH02)**(-1.5) +TI2*2.*(AMM1**2+RH02)**(
1-1.5) + TI3*2.*(AM**2+RH02)**(-1.5)
R1=B0
U=0.
DO5 K1= 1,61
U= U+.01
SUMDU= (U*U +RH02 )**(-1.5)
DO 6 L= 1,MM3
AL=L
6 SUMDU =SUMDU+((AL+U)**2 +RH02 )**(-1.5) +((AL-U)**2+RH02)**(-1.5)
R2= SUMDU +TI1*(((AM+2+U)**2+RH02)**(-1.5)+((AMM2-U)**2+RH02)**(
1-1.5))+ TI2* (((AMM1+U)**2+RH02)**(-1.5) +((AMM1-U)**2+RH02)**(-
11.5)) +TI3*(((AM+U)**2+RH02)**(-1.5) +((AM-U)**2+RH02)**(-1.5))
IF(B2-R1)5,7,7
5 R1=B2
7 BU =(B1+B0)*.5
U=U1-UN
DO 4 J =1,N
U=U+UN
SUMDU= (U*U +RH02 )**(-1.5)
DO41K= 1,MM3
AK=K
41 SUMDU =SUMDU+((AK+U)**2 +RH02 )**(-1.5) +((AK-U)**2+RH02)**(-1.5)
BU= SUMDU +TI1*(((AM+2+U)**2+RH02)**(-1.5)+((AMM2-U)**2+RH02)**(
1-1.5))+ TI2* (((AMM1+U)**2+RH02)**(-1.5) +((AMM1-U)**2+RH02)**(-
11.5)) +TI3*(((AM+U)**2+RH02)**(-1.5) +((AM-U)**2+RH02)**(-1.5))
E =(BU/B0)*100. -100.
IF( J-1) 3,3,2
3 WRITE(33,300) J3,E,U
PRINT 300, J3,E,U
GO TO 4
2 WRITE (33,300) J4,E,U
PRINT 300, J4,E,U
4 CONTINUE
END FILE 33
STOP
101 FORMAT (4F10.5,5X,I5)
300 FORMAT(2X,I1,2F20.8)
END

```

Figure C-16

This program plots the tape generated by the previous program on an incremental plotter.

Figure C-17

```

1160 FORMAT(I3,2F20.8)
1 READ INPUT TAPE 3, 1160,J,E,U
  IF(XEOF(D))3,2,3
2 Q=PLOT(F,E,U,J)
  GO TO 1
3 STOP
  END

```

Error Plot Program (In Two Dimensions)

```

PROGRAM EN PLOT
DIMENSION A(4),B(4),C(4),U(4),T(3),Z(50,2),F( 50,2),ALF( 50,2)
DIMENSION AK( 50,2),E( 50,2),BXZ(20),LN(20)
C *** R= RADIUS OF COIL IN UNITS OF THE COIL SPACING
C *** T(1)= CURRENT IN THIRD COIL FROM END / CURRENT IN INNER COILS
C *** T(2)AND T(3) ARE SIMILARLY DEFINED FOR SECOND FROM END AND END COILS
C *** ZM= NUMBER OF COILS
C READ(5,*)T(1),T(2),T(3),M
C *** Z= DISTANCE ALONG AXIS
C *** Z1= INITIAL VALUE OF Z
C *** ZN= INCREMENT IN Z
C *** N1= NUMBER OF INCREMENTS IN Z
C READ(10,1,Z1,ZN,N1)
C *** X= DISTANCE FROM AXIS
C *** X1= INITIAL VALUE OF X
C *** XN= INCREMENT IN X
C *** N2= NUMBER OF INCREMENTS IN X
C X1=0.
C XN=.04
C --- --
C AM=M
C AMM1=M-1
C AMM2=M-2
C P=INT(110)
C AD=1.3462943011
C A(1)= .09666344259
C A(2)= .03590092363
C A(3)= .03742563713
C A(4)= .01451196212
C B(1)= .12496593597
C B(2)= .06680246576
C B(3)= .03328355346
C B(4)= .00441787012
C C(1)= .44325141463
C C(2)= .06260601220
C C(3)= .04757363546
C C(4)= .01736506451
C U(1)= .24498368310
C U(2)= .09200160037
C U(3)= .04069697526
C U(4)= .03526449639
C MM3=M-3
C MM2=M-2
C MM1=M-1
C SUMD0 =R**(-3)
C DO1 I=1,MM3
C A1=1
1 SUMD0 =SUMD0 +2.*(A1+A1+K2)**(-1.5)
  BXZG=SUMD0 +T(1)**2.*(AMM2+K2)**(-1.5)+T(2)**2.*(AMM1+K2+K2)**
  1-1.5)+T(3)**2.*(AMM+K2)**(-1.5)
  D1=BXZG
  Z=0.
  GU2 I=1,N1
  Z=Z+U1
  SUMDU =(Z+K2)**(-1.5)
  U(3 J=1,MM3
  AJ=J
3 SUMDU=SUMDU+((AJ+Z)**2+K2)**(-1.5) +((AJ-Z)**2+K2)**(-1.5)
  O2=SUMDU +T(1)**2.*((AMM2+Z)**2+K2)**(-1.5) +((AMM2-Z)**2+K2)**2
  1-1.5)+T(2)**2.*((AMM1+Z)**2+K2)**(-1.5) +((AMM1-Z)**2+K2)**2+
  11.5)+T(3)**2.*((AM+Z)**2+K2)**(-1.5) +((AM-Z)**2+K2)**2+(-1.5))
  IF(O2-O1)/2,4,4
2 B1=O2
4 BXZ0 =(B1+BXZ0)*.5
  BXZ0=BXZ0+RZ*3.1415926536
  Z=Z1-ZN
  X=X1-XN
  U(51)=1,N1
  Z=Z+ZN
  Z20 = Z*Z
  DU6 J=1,M
  AJ=J
  Z2(J,1)=(Z+AJ)**2
  Z2(J,2)=(Z-AJ)**2
  --- --
  X=X+XN
  XPR2= (X+R)**2
  XMR2= (X-R)**2
  R2X2= R*R-X*X
  R4X = 4.*R *X
  F0= 1. -R4X/(XPR2 +Z20)
  ALF0 =ALOG(1./F0)
  AK0 =A0 +B0*ALF0
  E0 =1.
  DO8 K=1,4
  AK0 =AK0 +(A(K)+B(K)*ALF0)*F0**K
  E0 =E0 +(C(K)+D(K)*ALF0)*F0**K
  DU9 K1=1,2
  DU9 K=1,M
  F(K,K1)=1.-R4X/(XPR2+ Z2(K,K1))
  ALF(K,K1) =ALOG(1./F(K,K1))
  AK(K,K1)=A0 +B0*ALF(K,K1)
  E(K,K1) =1.
  DU9 L=1,4
  AK(K,K1) =AK(K,K1) +(A(L)+B(L)*ALF(K,K1))*F(K,K1)**L
  E(K,K1) =E(K,K1) +(C(L)+D(L)*ALF(K,K1))*F(K,K1)**L
  BXZ(J) =SUMTF(1./(XPR2+Z20))*(AK0 +E0*(R2X2-Z20)/(XMM2 +Z20))
  DU10 K=1,2
  DU10 L=1,MM3
10 BXZ(J) =BXZ(J) +SUMTF(1./(XPR2+ Z2(L,K)))*(AK(L,K) +E(L,K)*(M2K2-
  1Z2(L,K))/(XMM2 + Z2(L,K)))
  DU11 K=1,2
  DU11 L=MM2,M
  L1=L-M+3
11 BXZ(J) =BXZ(J)+ T(1)**2*SUMTF(1./(XPR2+Z2(L,K)))*(AK(L,K)+ E(L,K)*
  1H2K2 -Z2(L,K))/(XMR2 +Z2(L,K)))
  7 LN(J)= (BXZ(J)/BXZ0)*100. -100.
  PRINT(11,2,( LN(K),K=1,N2)
  5 X=X1-XN
  STOP
100 FORMAT(4F10.5,5X,15)
101 FORMAT(2F10.5,5X,15)
110 FORMAT(1M1,/1M0,3X,1HZ,7X,4H+0 L,6X,4H,04L,6X,4H,08L,6X,4H,12L,6X,
  14H,10L,6X,4H,2 L,6X,4H,24L,6X,4H,28L,6X,4H,32L,6X,4H,36L,6X,4H,4 L
  16X,4H,44L,/1M0)
111 FORMAT(2X,F5.2,2X,12E10.2)
  END

```

Figure C-18—Error plot program (in two dimensions).

THE PLASMA-RESONANCE PROBE

Michael P. Smith

N 67-22764

INTRODUCTION

The plasma-resonance probe is a diagnostic device used in determining some of the properties of a plasma environment. It consists of an electrode to which a radio-frequency voltage is applied. The probe is operated by recording the direct current drawn from the plasma by the probe as a function of the radio-frequency applied to the probe, obtaining a typical resonance peak such as shown in Figure C-19. From the frequency at which the current (i_p) is a maximum (ω_m), one can obtain a value for the electron density (n) from the relation

$$\omega_m^2 = \omega_p^2 = \frac{4\pi n e^2}{m} \quad (\text{CGS units})$$

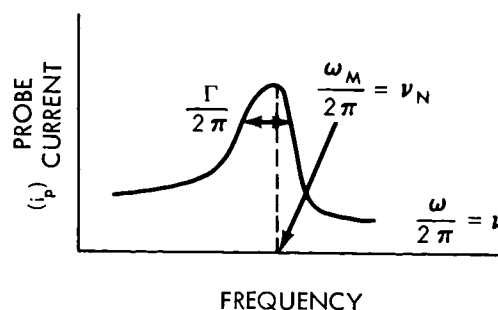
Here m is the electron mass and e the electron charge. From the full width at half-maximum (Γ), one can obtain the electron neutral particle collision frequency (ω_c) by using the expression

$$\omega_c = \frac{\Gamma}{2}$$

This report consists of six parts:

1. The theory of the resonance probe
2. Experimental apparatus and technique
3. Data; Experiments
4. Conclusions; Discussion of Experiments
5. Recommendations for space research work
6. Bibliography

Figure C-19—Typical resonance probe data.



THEORY OF THE RESONANCE PROBE

Here we develop a simple-minded theory of the resonance probe. The treatment leans heavily upon the work of S. Chandrasekhar (Reference 1), especially Chapters VI and VII. This theory embodies the essential results of a more rigorous treatment by Ichikawa et. al., (Reference 2) in which they carry out an integration of the linearized Boltzmann-Vlasov equation.

The environments with which we concern ourselves are typically low-density ($10^4 - 10^8$ electrons/cm³), partially-ionized gases (< 2%) consisting of electrons (m, - e), ions (M, + e), and neutrals ($\sim M$). We take the much heavier ions and neutrals to be essentially at rest, while the electrons are vibrating within the ion-neutral host with an equilibrium characteristic frequency ω_p , called the plasma frequency. The model* works because the dominant behavior of such a field-free plasma is charge neutrality: the charges distribute themselves so as to maintain macroscopic charge neutrality within several Debye-lengths.

To this situation we add a sinusoidally varying electric field typically in the megacycle range. We might expect a resonance to occur when the external electric field frequency ω matches the electron plasma frequency ω_p . We shall assume that the sole mechanism of damping is due to electron-neutral particle collisions; we are neglecting effects such as

1. Thermal electron energies
2. Landau damping
3. Electron-ion collisions; electron-electron collisions
4. Radiation reaction effects

the more sophisticated treatment of (Reference 2) shows that this is a valid assumption for our model.

This resonance phenomenon is really a collective behavior effect in which many electrons in a volume λ^3 ($\approx C/\omega_p$) participate. Presumably this is why ion resonances have not been observed, in view of their much smaller mobility; i.e., not all the ions in such a volume can respond in phase to the external signal.

We first develop longitudinal plasma oscillations; these waves do not propagate in the plasma, but represent local density and charge fluctuations. When a charge separation occurs in the plasma due to a displacement of the electrons, an electric field appears, and we write

$$m \ddot{\vec{r}} = e \vec{E}(\vec{r}, t) \quad (1)$$

(\vec{E} does not refer to an external field.) Assuming a solution of the form

$$\vec{E}(\vec{r}, t) = \vec{E} \cdot (\vec{r}) e^{i\omega t}, \quad (2)$$

and assuming appropriate boundary conditions, Equation (1) gives

$$\vec{r} = \frac{-e}{m \omega^2} \vec{E} \quad (3)$$

*This has been called the Lorentz Gas Model or the Cold Plasma Model.

On the other hand, in CGS units, the following relations are valid:

$$\vec{p} = ne\vec{r} \quad \vec{p} = \alpha \vec{E} \quad \epsilon = 1 + 4\pi\alpha \quad (4)$$

(Here \vec{P} is the polarization, n the electron density, e the electric charge, \vec{r} the displacement from equilibrium, α the polarizability, and ϵ the dielectric constant). Then Equations (3) and (4) imply

$$\alpha = \frac{-ne^2}{m\omega^2} \quad (5)$$

and

$$\epsilon = 1 - \frac{4\pi ne^2}{m\omega^2} \quad (6)$$

In CGS units, Maxwells' equations are

$$\nabla \cdot \vec{E} = 4\pi\rho \quad \nabla \cdot \vec{B} = 0$$

$$\nabla \times \vec{E} = -\frac{1}{c} \frac{\partial \vec{B}}{\partial t} \quad \nabla \times \vec{B} = \frac{4\pi}{c} \vec{J} + \frac{1}{c} \frac{\partial \vec{E}}{\partial t} \quad (7)$$

The total charge and current densities ρ and \vec{J} can be broken up into two parts:

1. Plasma contribution $-\nabla \cdot \vec{p}$ and $\partial \vec{p} / \partial t$

2. External sources ρ_r and \vec{J}_r

so that

$$\rho = \rho_r - \nabla \cdot \vec{P} \quad \text{and} \quad \vec{J} = \vec{J}_r + \frac{\partial \vec{P}}{\partial t} \quad (8)$$

Putting

$$\vec{D} \equiv \vec{E} + 4\pi\vec{P} = \epsilon \vec{E}, \quad (9)$$

We can rewrite the Equation (7) in the usual manner as

$$\nabla \cdot \vec{D} = 4\pi\rho_r \quad \nabla \cdot \vec{B} = 0$$

$$\nabla \times \vec{E} = -\frac{1}{c} \frac{\partial \vec{B}}{\partial t} \quad \nabla \times \vec{B} = \frac{4\pi}{c} \vec{J}_r + \frac{1}{c} \frac{\partial \vec{D}}{\partial t} \quad (10)$$

Now in an electrically neutral plasma, and neglecting thermal effects

$$\rho_r = 0 \quad \text{and} \quad \vec{J}_r = 0$$

thus Equation (10) becomes finally

$$\begin{aligned} \epsilon \nabla \cdot \vec{E} &= 0 & \nabla \cdot \vec{B} &= 0 \\ \nabla \times \vec{E} &= -\frac{1}{c} \frac{\partial \vec{B}}{\partial t} & \nabla \times \vec{B} &= \frac{\epsilon}{c} \frac{\partial \vec{E}}{\partial t} \end{aligned} \quad (11)$$

for the Maxwell equations. As is well known, these sourceless equations can be uncoupled, yielding wave equations which admit of plane-wave solutions of the form

$$\begin{aligned} \vec{E}(\vec{r}, t) &= \vec{E}_0 e^{i(\vec{K} \cdot \vec{r} - \omega t)} \\ \vec{B}(\vec{r}, t) &= \vec{B}_0 e^{i(\vec{K} \cdot \vec{r} - \omega t)} \end{aligned} \quad (12)$$

Running these back through Equation (11) shows that this is indeed the case if only

$$\begin{aligned} \epsilon \vec{E}_0 \cdot \vec{K} &= 0 & \vec{B}_0 \cdot \vec{K} &= 0 \\ \vec{K} \times \vec{E}_0 &= \frac{\omega}{c} \vec{B}_0 & \vec{K} \times \vec{B}_0 &= -\epsilon \frac{\omega}{c} \vec{E}_0 \end{aligned} \quad (13)$$

These represent conditions on \vec{K} and ω that Equation (12) be solutions of the uncoupled Maxwell equations.

In general, Equation (13) admits of two solutions:

1. Transverse Oscillations ($\epsilon \neq 0$) These are the electromagnetic oscillations of a field-free plasma; they undergo a definite dispersion because $\epsilon = \epsilon(\omega)$. They are of no interest to us here.
2. Longitudinal Oscillations ($\epsilon = 0$) There is the choice of putting

$$\epsilon \equiv 0 \quad (14)$$

in (13); this leaves us with the conditions

$$\vec{B}_0 \cdot \vec{K} = 0 \quad \text{and} \quad \vec{K} \times \vec{B}_0 = 0 \quad (15)$$

It is clear that Equation (15) requires $\vec{B}_0 = 0$ if we want $\vec{K} = 0$; then we see that $\vec{K} \times \vec{E}_0 = 0$ implies a longitudinal type wave ($\vec{E}_0 \cdot \vec{K}$ is not necessarily vanishing). This represents a local disturbance moving in the plasma and is not to be confused with a true transverse electromagnetic wave. From Equations (14) and (6), we obtain the frequency:

$$\omega_p^2 = \frac{4 \pi n e^2}{m} \quad (16)$$

This of course is just the frequency with which the electrons of our model are vibrating about equilibrium amid the ion-neutral background; i.e., their motion is the local density fluctuation or charge fluctuation.

We now consider what happens when an external electric field and electron-neutral collisions are added to the above picture. For convenience, we shall work in one-dimension. Three forces act on the electrons:

1. The internal field: $F_{int} = e E = e E_0$
2. The external field: $F_{ex} = e E_{ex} = e E_1 e^{i\omega t}$

(Here ω now represents the frequency of the externally applied radio-frequency field).

3. The electron-neutral collisions: Really the origin of this force is electrical, but we can statistically gloss over this if we assume a "collision dominated plasma" in which an electron undergoes many collisions per second. In a linear approximation, we write

$$F_{collision} = R v$$

Suppose $\tau_c = 1/\omega_c$ is the average time between these collisions; then the light electrons undergo a momentum transfer of $2mv$, and so a force of $2mv/\tau_c$. Thus it is clear that

$$F_{collision} = 2 m \omega_c v$$

Thus Newton's equation for a single electron is

$$m \ddot{x} + 2 m \omega_c \dot{x} + e E_0 = e E_1 e^{i\omega t} \quad (17)$$

In view of Equation (14), Equation (17) can be written as

$$m \ddot{x} + 2 m \omega_c \dot{x} + 4 \pi n e^2 x = e E_1 e^{i\omega t}, \quad (18)$$

which is just the equation of motion of a damped, driven harmonic oscillator. The solution of Equation (18) consists of 2 parts, the complimentary function and the partial integral.

The Complementary Function

This is the solution of Equation (18) with the R.H.S. set equal to zero; it embodies two Arbitrary constants which are eliminated by choosing particular initial conditions. This solution describes the transient behavior of the electrons. Thus in

$$m \ddot{x}_c + 2 m \nu_c \dot{x}_c + 4 \pi n e^2 x_c = 0$$

putting $x_c = A e^{\mu t}$ shows that this is indeed a solution provided only

$$m \mu^2 + 2 m \nu_c \mu + 4 \pi n e^2 = 0$$

thus

$$\mu = -\nu_c \pm \sqrt{\nu_c^2 - \frac{4 \pi n e^2}{m}} \quad (19)$$

It is clear that transients die out in a time of the order of the collision frequency $\nu_c \approx 10^{-6}$ sec, so they are of no consequence to us.

The Particular Integral

The particular integral describes the steady-state behavior of the electron; we can coax it from Equation (18) by assuming that the electron follows the external electric field: i.e., suppose

$$x_p = B e^{i\omega t}, \quad (20)$$

then the differential equation shows that it is a solution if

$$B(-m\omega^2 + 2 i m \nu_c \omega + 4 \pi n e^2) = e E_1$$

or

$$B = \frac{\left(\frac{e}{m}\right) E_1}{\omega_p^2 - \omega^2 + 2 i \nu_c \omega} \quad (21)$$

that is, the steady-state solution is just

$$X_p = \frac{\left(\frac{e}{m}\right) E_1 e^{i\omega t}}{\omega_p^2 - \omega^2 + 2 i \nu_c \omega}$$

and

$$v_p = \frac{\left(\frac{e}{m}\right) i \omega E_1 e^{i\omega t}}{\omega_p^2 - \omega^2 + i 2 v_c \omega} \quad (22)$$

Now the meaningful quantity here is the electron kinetic energy; this comes about in the following way: the probe is operated with a D.C. voltage in such a way that, without the R.F. voltage, the net current to the probe is zero; it turns out that a negative D.C. voltage is required to do this for reasons of high electron mobility, i.e., the electrons are largely biased out. When the R.F. voltage is superimposed, the electrons absorb this energy as kinetic energy and are then able to surmount the D.C. potential barrier; this shows up as an increase in the direct current to the probe. At any rate, the electron kinetic energy is

$$\frac{1}{2} m v^2 = \frac{1}{2} m v^* v = \frac{\frac{m}{2} \left(\frac{e}{m}\right)^2 \omega^2 E_1^2}{(\omega_p^2 - \omega^2)^2 + 4 v_c^2 \omega^2}$$

or

$$\frac{1}{2} m v^2 = \frac{\frac{e^2}{2m} E_1^2 \omega^2}{(\omega_p^2 - \omega^2)^2 + 4 v_c^2 \omega^2} \equiv f(\omega) \quad (23)$$

This is a typical resonance curve; according to the discussion just above, we would expect the direct current to the probe to have the same general features.

1. $f(\omega)$ has a maximum at $\omega = \omega_p$. This follows as a sufficient condition for the vanishing of $df(\omega)/d\omega$:

$$\omega_M = \omega_p \quad (24)$$

2. $f(\omega)$ has a full-width at half-maximum of $2 v_c$:

$$\Gamma = 2 v_c \quad (25)$$

First of all, we have

$$f_{\max} = f(\omega = \omega_p) = \frac{e^2 E_1^2}{8 v_c^2} \quad (26)$$

This predicts that the maximum probe current should be proportional to the square of the impressed R.F. field. Then with (26) we can find ω such that $f = t_{\max}/2$; this gives the condition

$$4 v_c^2 \omega^2 = (\omega_p^2 - \omega^2)^2$$

or

$$\pm 2 v_c \omega = \omega_p^2 - \omega^2$$

These two equations, together with the physical requirement that $\omega \geq 0$, give the solutions

$$\omega_1 = -v_c + \sqrt{v_c^2 + \omega_p^2} \quad \text{and} \quad \omega_2 = v_c + \sqrt{v_c^2 + \omega_p^2}$$

Hence we have justified

$$\Gamma \equiv \omega_2 - \omega_1 = 2 v_c$$

Equations (24) and (25) demonstrate the most useful properties of the resonance probe.

A computer plot of $f(\omega)$ is enclosed for the ratios $Q \equiv \omega_p/v_c = 10$. It turns out that the theoretical curve is skewed just the wrong way to fit the experimental curves; this occurs at low electron kinetic energies and is probably due to neglecting the distribution of electron energies at equilibrium. We notice how the curve is not quite symmetric about $\omega = \omega_p$ even near the maximum point - this is very important in determining ω_p by graphic interpolation.

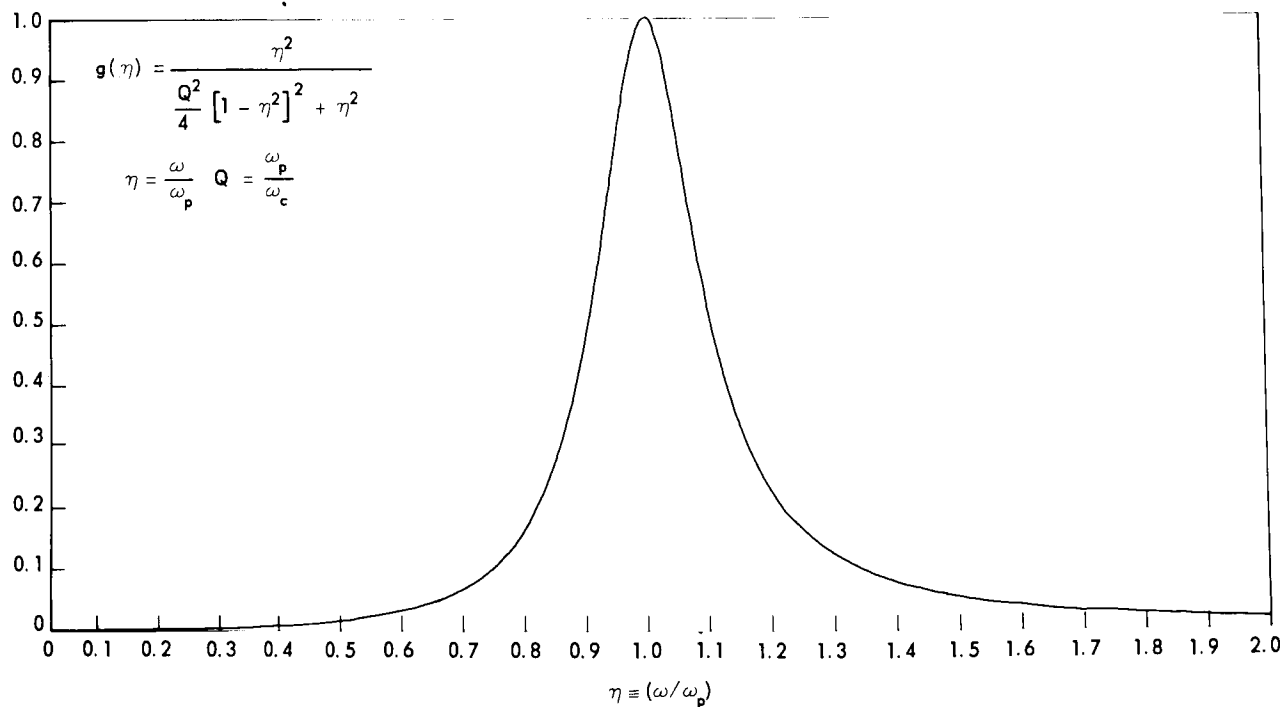


Figure C-20—Computer plot of $P(\omega)$ for the ratio $Q \equiv \omega_p/v_c$.

EXPERIMENTAL APPARATUS AND TECHNIQUE

The Apparatus

Following the lead of Takayama et. al. (Reference 3) we set up the following circuit (see Figure C-20): The only modification was to reverse the biasing power supply ϵ . The R.F. supply was an H.P. 606 signal generator, with a frequency range including 1 to 50 megacycles and a peak to peak voltage from 0 to 3 volts. The ammeter was an H.P. 425A micro-microammeter, capable of being floated above ground without leakage problems in the nanoampere range. Coax cable was used from the probe to point 2 and from the signal generator to point 1, with the shields floating at both 1 and 2. The components L_1 , L_2 , and C were chosen so that loop B had a much higher impedance at 10 megacycles than loop A; thus we took

$$L_1 = L_2 = 10^4 \mu h \text{ and } c = .001 \mu f$$

In this way, we are assured that $L\omega \gg 1/\omega c$, since

$$L\omega = 2 \times 10^5$$

and

$$\frac{1}{\omega c} = 10^2$$

Incidentally, the resonant frequency is

$$\omega^2 = \frac{1}{LC} = 5 \times 10^{10}$$

or

$$\nu = \frac{\omega}{2\pi} \approx 35.7 \text{ Kc}$$

Experimental Technique

Looking again at Figure C-20, it becomes evident that the resonance probe is just a negatively biased Langmuir probe with an R.F. voltage superimpressed. The following technique was developed: with the R.F. voltage supply on, but turned down to zero, a null current was obtained at the ammeter A by adjusting ϵ to the floating potential; then the R.F. voltage was set at the desired value and i_p versus ω plots recorded. This is quite convenient because the floating potential is easy to find. The main precaution is to use R.F. voltage in the range 0-2 volts only. A picture of the operation is as follows: Looking at the operating region of Figure C-22, one can see that if $V_{R.F.}$ gets too large, one can slide up the Langmuir curve quite a distance: this results in non-linear contributions to a resonance, so that extra broad peaks appear, especially to the right of a genuine resonance peak. These broad, spurious humps can always be distinguished from the central peak and biased out by operating ϵ at the floating potential and keeping the R.F. voltage in the range 0-2 volts.

Data, Experiments. Two very distinct plasma environments were analysed with the resonance probe.

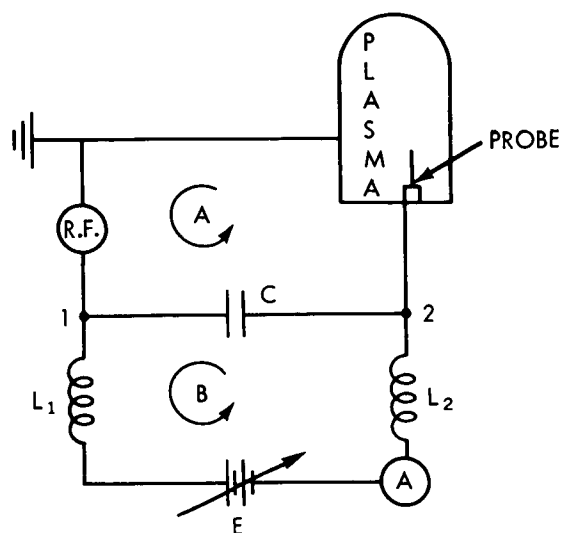
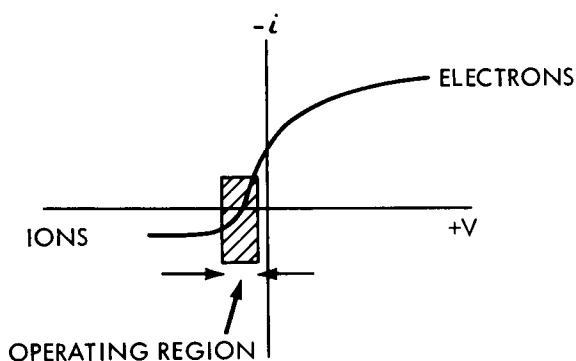


Figure C-21—Typical circuitry for resonance probe.

Figure C-22—Resonance probe operating curve.



Bell Jar

A bell jar (volume: $\sim 8000 \text{ cm}^3$) system was available to generate conventional plasmas in nitrogen, helium, and argon. The following electrode geometry was found satisfactory: This configuration in combination with helium provided a uniform, stable plasma. A variety of experiments was performed. These of course included various checks to make sure circuit resonances were not being observed: for example, a duplicate external circuit with a capacitor of $.005 \mu\text{f}$ was constructed, with no noticeable changes. With the circuit of Figure C-21 and the parameters indicated, a prominent circuit resonance occurred at about 75 kilocycles, but this did not affect our work at all.

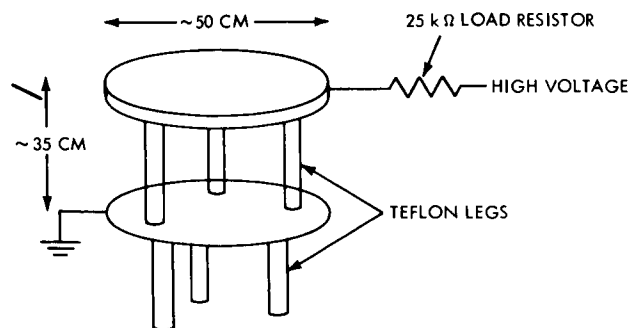
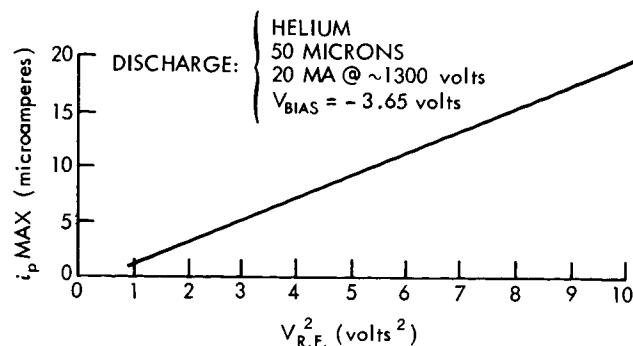


Figure C-23—Electrode configuration used.

1. One of the simplest experiments was to record the maximum direct current at resonance as a function of the R.F. voltage:

Figure C-24—Maximum probe current at resonance vs. square of R.F. voltage in anticipation of Equation (26).



2. Following Takayama and Ikegami, one can record the probe current i_p as a function of the R.F. frequency for several R.F. voltages in various fixed environments; at the same time, one can obtain Langmuir curves for comparison of the two techniques. (See 1965 Summer Workshop Report for Langmuir Probe Techniques).

a. Helium. In helium, the following data was observed:

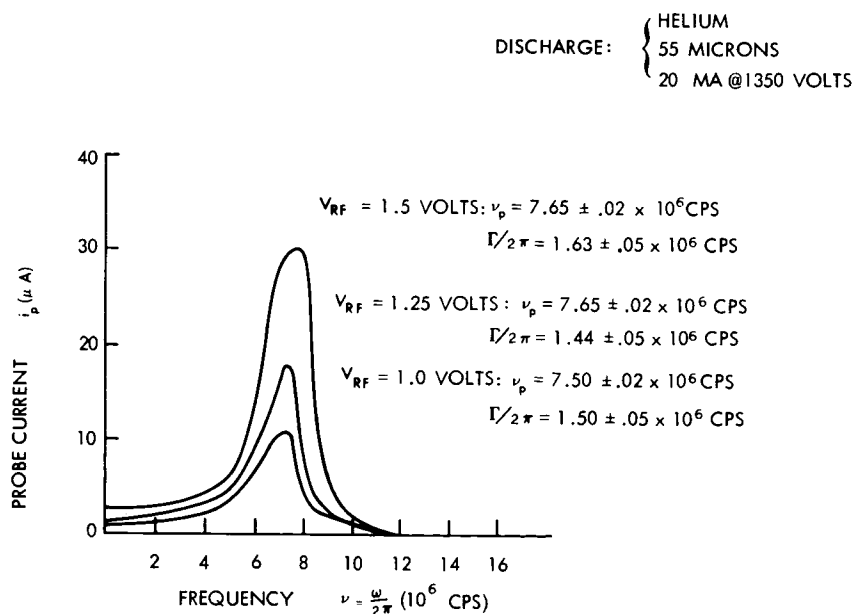


Figure C-25—Typical resonance probe data in helium. ν_p is the Frequency at Which i_p is a maximum; $\Gamma/2\pi$ is the full width of the peak When i_p is half its maximum value.

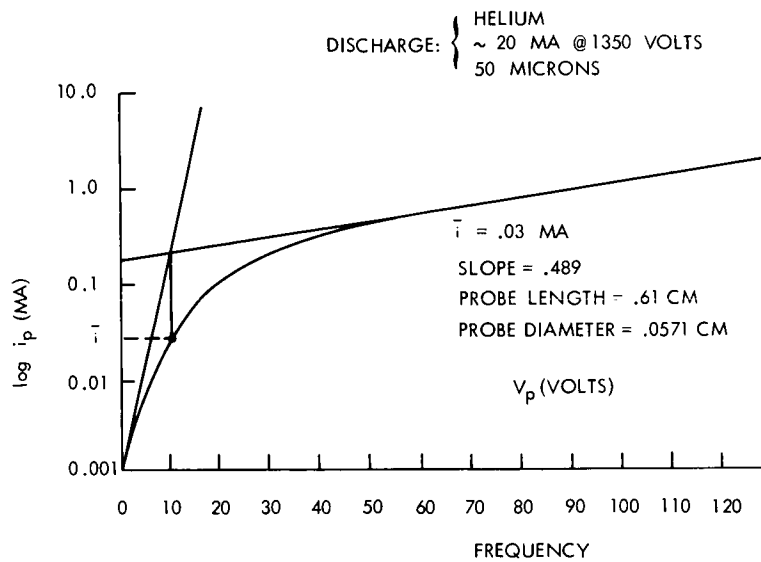


Figure C-26—Typical Langmuir probe data in helium at approximately the same operating parameters as Figure C-25.

b. Nitrogen:

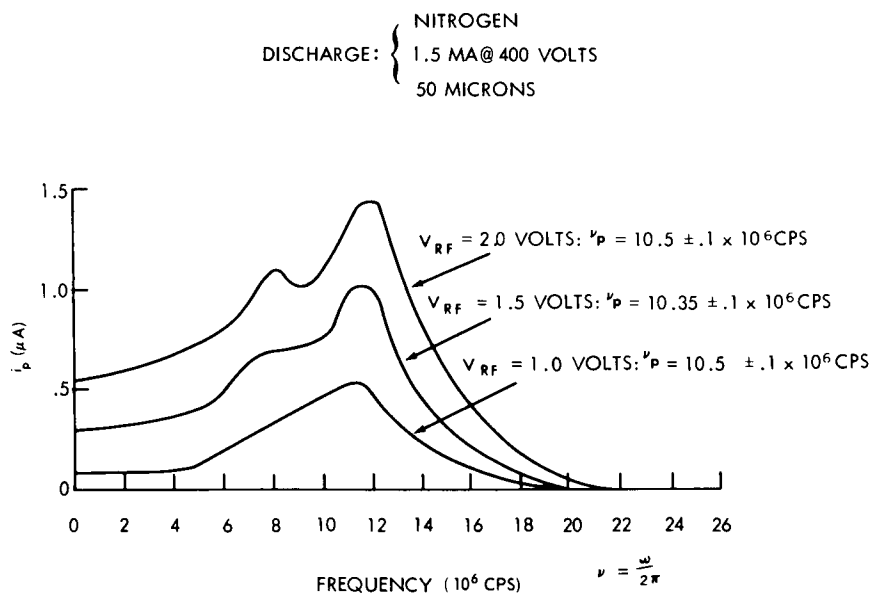


Figure C-27—Nitrogen resonance probe data. The secondary peaks to the left of the main peaks are presumably due to helium contamination caused by not allowing the bell jar sufficient time to clear. No half widths were measured here.

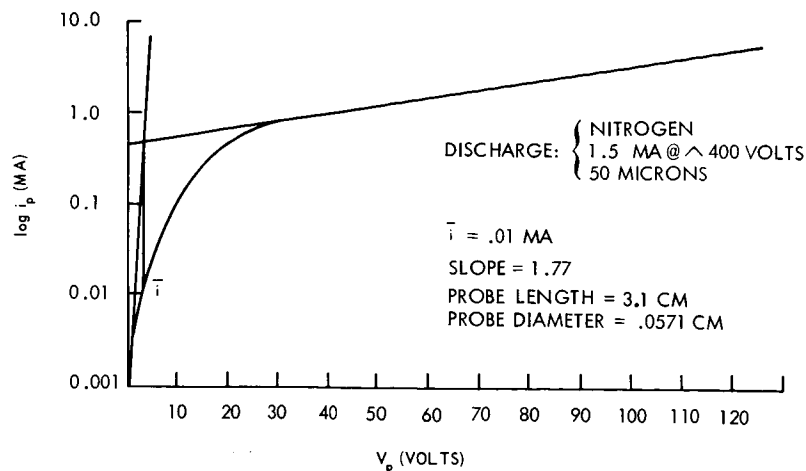


Figure C-28—Langmuir probe data in nitrogen.

c. Argon. Finally, the following peaks were observed in Argon:

DISCHARGE: { ARGON
~ 40 MA @ 1500 VOLTS
~ 50 MICRONS

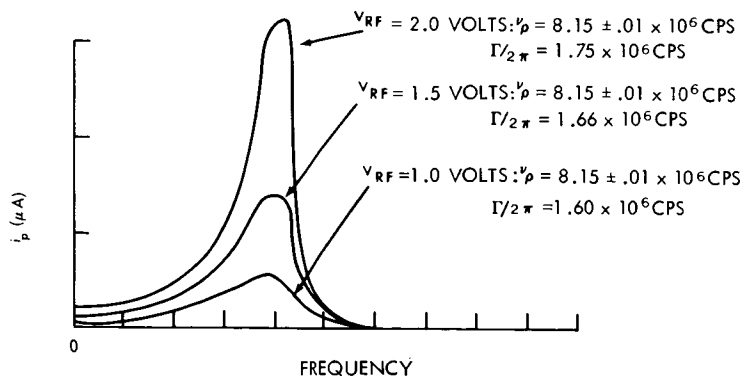


Figure C-29—Typical resonance probe data in argon; there was insufficient data to calculate $\Gamma/2\pi$ for the peaks to real precision.

3. Another set of experiments which were performed in helium was to record resonance peaks at a fixed discharge voltage at several different pressures:

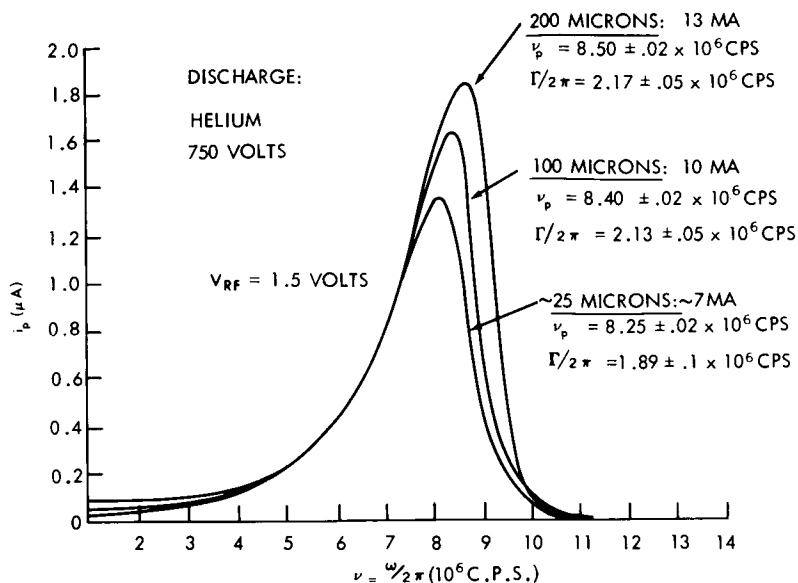


Figure C-30—Resonance probe data in helium showing the effect of varying the pressure of the discharge while holding the discharge voltage fixed.

- One can obtain resonance peaks at constant pressure, but varying the discharge current and voltage; this gives the following results in helium:

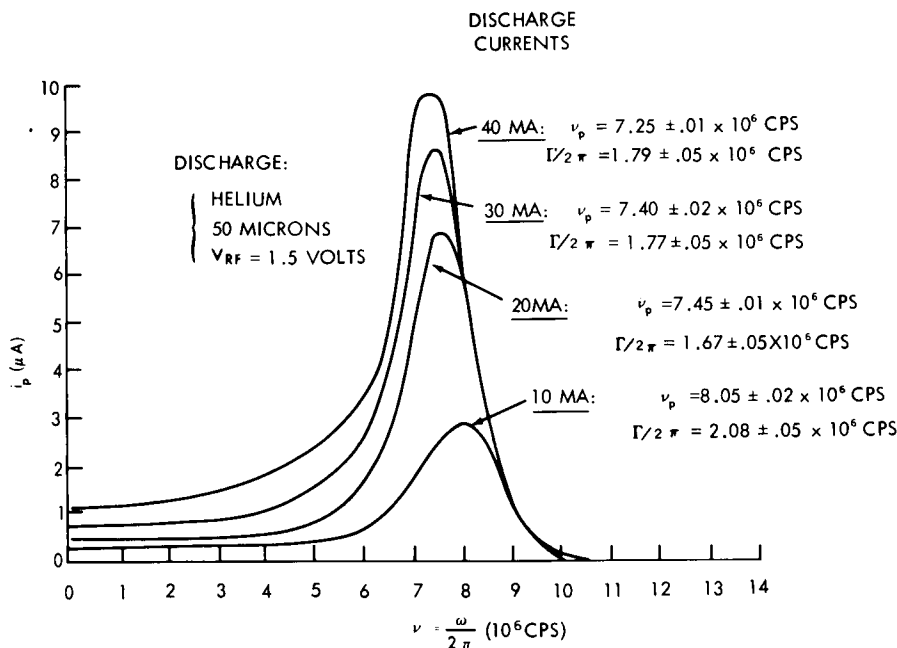


Figure C-31—Resonance probe data showing the effect of varying the discharge current and voltage at constant pressure.

5. Finally, one can vary the pressure and voltage keeping the discharge current fixed:

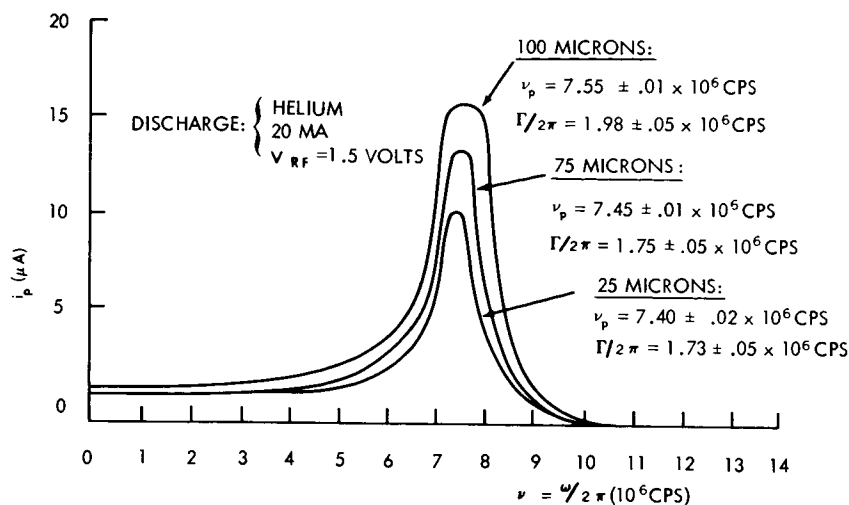
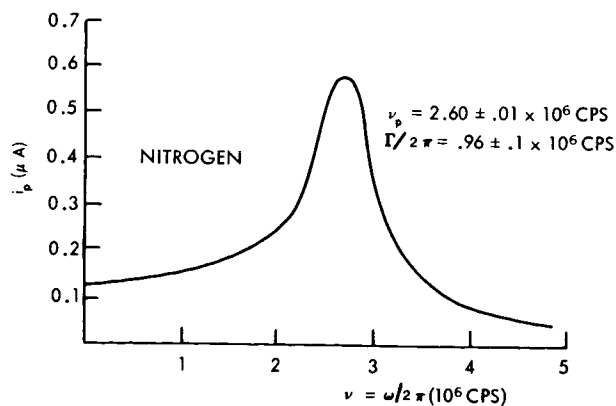


Figure C-32—Resonance probe data showing the effect of varying the pressure and holding the discharge current constant.

Larger Volume Plasmas

The resonance probe was used in a much larger volume plasma ($\sim 300 \text{ ft}^3$) generated with an ion engine; the gas used was nitrogen (at $\sim 10^{-5}$ torr). Three separate peaks were observed:

Figure C-33—The electron plasma resonances in the summer workshop ion-engine plasma, peak No. 1 (J. Kinnier).



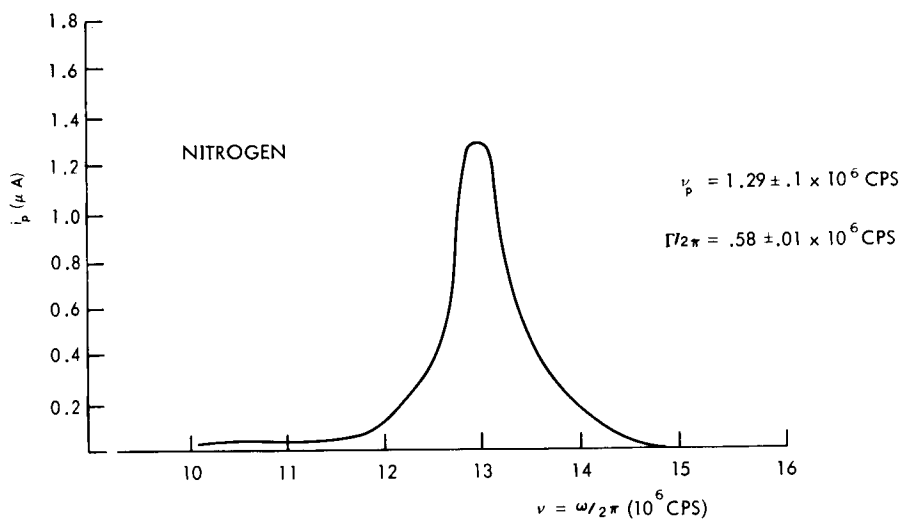


Figure C-34—The electron plasma resonances in the summer workshop ion-engine plasma, Peak No.2 (J. Kinnier).

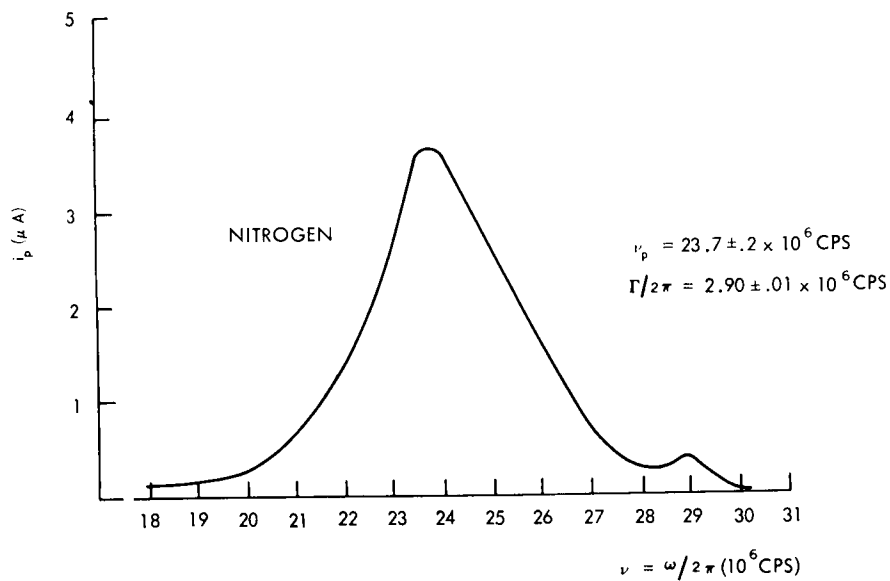


Figure C-35—The electron plasma resonance in the summer workshop ion-engine plasma, Peak No. 3 (J. Kinnier).

CONCLUSIONS; DISCUSSION OF EXPERIMENTS

Bell Jar

1. It is very satisfying to compare Figure C-24 with Equation (26), since $E \sim v/L$. This is direct experimental evidence that our somewhat simplified assumptions centered about energy considerations in the experimental operation of the probe are quite good. It shows that the resonance probe is essentially a temporal device which doesn't depend strongly on spatial effects such as sheath formation. It also demonstrates that neglecting temperature effects is probably quite valid, in complete agreement with Reference 3.

2. Looking at Figures C-25, C-26, and C-27, we can see that the plasma frequency is quite independent of the applied R.F. voltage as predicted in the theory leading to Equation (16) and (24). This means that current collection by the probe is really a frequency effect, not a voltage effect as in a Langmuir probe. (The errors quoted here and elsewhere are merely an estimate of the experimental error and the error in graphic interpolation; by far the larger of the two is due to the interpolation). Using Equation (16) and the experimental values of ω_p , we can calculate the electron density for each of the gases. We do average the values for ω_p , because the meaning is not yet clear; instead we pick a representative value for each gas:

Table C-3
Electron Densities Obtained From Figures C-25, C-27 and
C-29 and Using Equation (16)

Gas	ν_p (10^6 cps)	(electrons/cm ² $\times 10^5$)
Helium	$7.65 \pm .02$	$7.26 \pm .04$
Argon	$8.15 \pm .01$	$8.25 \pm .02$
Nitrogen	$10.5 \pm .1$	$13.7 \pm .01$

These results are quite reasonable and in agreement with the literature on discharge plasmas at low pressures.

From Figures C-26 and C-28, we can obtain an independent value for the electron density using standard Langmuir techniques.

1. For helium, we have:

$$\text{probe area} = 11.3 \times 10^{-2} \text{ cm}^2$$

$$\text{electron temperature} = 23,700^\circ\text{K}$$

$$\text{electron density } \eta = 6.94 \times 10^7 \text{ electrons/cm}^3$$

2. For nitrogen, we have:

$$\text{probe area} = 55.9 \times 10^{-2} \text{ cm}^2$$

$$\text{electron temperature} = 6550^\circ\text{K}$$

$$\text{electron density } \eta = 8.89 \times 10^6 \text{ electrons/cm}^3$$

The agreement between these results and those of Table C-3 is not very satisfactory.

Beyond any doubt the resonance probe method is far more precise than that of the Langmuir probe method. This is not hard to see. Looking at Figures C-26 and C-28, we notice how steeply the $\log i_p$ versus V_p curve climbs near the origin; this causes serious inaccuracies in attempting to determine $\bar{\Gamma}$ for use in the formula

$$\eta = \frac{\bar{\Gamma}}{Ae} \left[\frac{2\pi m e}{KT e} \right]^{1/2}$$

This difficulty has been reported by several groups of observers (Reference 4); also, the Japanese group which first reported the plasma resonances mentioned this at the 1963 International Conference on Ionized Gases.

On the other hand, one can question the accuracy of the resonance probe method; the most serious of these is whether the resonance occurs at the plasma frequency. We can see no theoretical reason whatever for obtaining such a result, i.e., some mechanism which would change the resonant frequency itself, or change the coupling of the plasma to an external field at $\omega = \omega_p$. The approximations made in obtaining our simplified theory in no way affect the position of the maximum at $\omega = \omega_p$, but would only change the shape and half width of $f(\omega)$.

Again looking at Figures C-25 and C-29, we see that Γ changes with $V_{R.F.}$. Since $V_{R.F.}$ is related to the electron displacement from equilibrium, in view of Equation (25) this says we have departures from the linear approximation of collision = Rv . In the helium data at $V_{R.F.} = 1.0$ volts, $\Gamma/2\pi$ is seen to increase after having decreased from $V_{R.F.} = 1.5$ volts to $V_{R.F.} = 1.25$ volts; it may be that electron-ion collisions contribute to the damping; also, one might expect temperature effects to be more important here, since the electron kinetic energy is approaching the equilibrium thermal energy.

Much more work is needed to determine whether the resonance probe can yield accurate data on collision frequencies and of even precise half-widths.

Using the data from Figures C-25 and C-29, we can obtain a typical value for the electron-neutral collision frequency in helium and argon by using Equation (25):

$$\Gamma/2\pi \approx 1.6 \times 10^6$$

$$\nu_e = \Gamma/2 \approx 5 \times 10^6 \text{ collisions/sec.}$$

This is quite in accord with cross-sections obtained from atomic theory. The fact that helium and argon have nearly the same collision frequencies means the two plasmas are physically very similar.

For completeness, we can list values of Q ($\equiv \omega_p/\nu_e$) which was used earlier as a plotting parameter for $g(\eta)$ versus η ($\equiv \omega/\omega_p$). We used that data at $V_{R.F.} = 1.5$ volts:

$$\text{Helium: } Q = 2\nu_p/\Gamma/2\pi = 9.39$$

$$\text{Argon: } Q = 2\nu_p/\Gamma/2\pi = 9.81$$

This again shows that the two plasmas have a similar structure; and also, it points out why $Q = 10$ was used in the computer plot.

Looking at Figure C-27, we (presumably) see the effects of the presence of two ions: two distinct electron resonant frequencies appear. Notice how the resolution of the peaks increases with increasing $V_{R.F.}$. For a given R.F. voltage, we can also see that the resonant frequencies are different and the peak heights are different. Hopefully one can theoretically relate the peak height to the percentage ionization. This whole effect needs confirmation and much further study, particularly in various nitrogen-oxygen mixtures.

3. In the experiments at constant discharge voltage and variable discharge current and pressure, it is evident that the plasma frequency decreases as the pressure and current decrease, as well as the halfwidths. We have the following table:

Table C-4
Reduction of The Data of Figure C-30

Pressure (μm)	ν_p (10^6 cps)	η (electrons/ $\text{cm}^3 \times 10^5$)	$\Gamma/2\pi$ (10^6 cps)	ν_c (10^6 cps)
200	$8.50 \pm .02$	$8.95 \pm .04$	$2.17 \pm .05$	$6.81 \pm .05$
100	$8.40 \pm .02$	$8.75 \pm .04$	$2.13 \pm .05$	$6.69 \pm .05$
25	$8.75 \pm .02$	$6.51 \pm .04$	$1.89 \pm .05$	$5.99 \pm .05$

It is clear that the plasma environment doesn't change much over the pressure range examined; it is felt that more significant changes would occur at somewhat lower pressures, as evidenced in the trend in the data of Table C-4. A much more carefully controlled plasma would be desirable, i.e., one that would allow us to separate our changes in electron density from changes in the neutral particle density.

4. The data on Figure C-31 indicates the effects of varying the discharge current and voltage at a constant pressure of 50 microns: the plasma frequency is seen to increase as the current and voltage decrease. We have a table:

Table C-5
Reduction of the Data of Figure C-31

Discharge Current (MA)	ν_p (10^6 cps)	η ($\frac{\text{electrons}}{\text{cm}^3} \times 10^5$)	$\Gamma/2\pi$ (10^6 cps)	ν_c (10^6 cps)
40	$7.25 \pm .01$	$6.51 \times .02$	$1.79 \pm .05$	$5.62 \pm .05$
30	$7.40 \pm .02$	$6.79 \pm .04$	$1.77 \pm .05$	$5.55 \pm .05$
20	$7.45 \pm .01$	$6.89 \pm .02$	$1.67 \pm .05$	$5.25 \pm .05$
10	$8.05 \pm .02$	$8.04 \pm .04$	$2.08 \pm .05$	$6.54 \pm .05$

One might expect higher currents and voltages to produce more electrons per unit volume, but this is not the case at 50 microns – apparently for reasons of high mobility and long mean free path, the electrons are collected at the cathode before suffering a significant number of collisions with neutrals to form ions, at the higher voltages. On the other hand, we notice that the low density plasmas produce a greater signal; it is hoped that theoretical investigation into the relation between peak height and percentage ionization will elucidate matters here. What is even worse, the full-width at half maximum decreases as ω_p increases, and then increases again. In view of Equation (25), this may indicate other sources of damping besides electron-neutral collisions. However, it is entirely possible that the technique used in obtaining $\Gamma/2\pi$ is inaccurate as mentioned before; of course, it also can indicate temperature effects.

5. Finally, consider what happens when we vary the pressure and voltage, keeping the discharge current fixed (Figure C-32). Again we have a table:

Table C-6
Reduction of the Data of Figure C-32

Pressure (μm)	ν_p (10^6 cps)	η (electrons/ $\text{cm}^3 \times 10^5$)	$\Gamma/2\pi$ (10^6 cps)	ν_c (10^6 cps)
100	$7.55 \pm .01$	$7.06 \pm .02$	$1.98 \pm .05$	$6.21 \pm .05$
750	$7.45 \pm .01$	$6.88 \pm .02$	$1.75 \pm .05$	$5.50 \pm .05$
25	$7.40 \pm .01$	$6.79 \pm .02$	$1.73 \pm .05$	$5.44 \pm .05$

This behavior is much more in line with what is to be expected. When we compare these results with those of Table C-5, it is clear that varying the discharge at constant current but variable voltage and pressure is inherently a simpler physical process than varying the current and voltage at constant pressure.

We can summarize the results of the resonance work in the bell-jar-environment:

1. We have been able to confirm that simpler aspects of our theory. The plasmas in helium, argon, and nitrogen each exhibit a single resonant frequency in the range

$$\nu_p \approx 7.5 \times 10^6 \text{ CPS}$$

From this we are able to obtain electron densities of

$$\eta \approx 7 \times 10^5 \text{ electrons/cm}^3$$

Moreover, our results indicate electron-neutral particle collision frequencies of

$$\nu_c \approx 5.5 \times 10^6 \text{ collisions/sec}$$

2. The resonance probe method is quite sensitive to variation of such discharge parameters as
- pressure, current, voltage
 - type of gas
 - percentage composition

Ion-Engine Plasma in a Larger Volume

Now consider the plasma of the ion-engine in a larger volume. We have the following results from the data of Figures C-33, C-34, and C-35.

Table C-7
Data Reduction of the Three Resonant Frequencies Observed in the
Ion-Engine Plasma. Equations (24) and (25) Have Been
Assumed to Obtain These Numbers

ν_p (10^6 cps)	η (electrons/cm ³ $\times 10^5$)	$\Gamma/2\pi$ (10^6 cps)	ν_c (10^6 cps)	$Q (\equiv \omega_p/\nu_0)$
$2.60 \pm .01$	$.838 \pm .002$	$.96 \pm .1$	$3.01 \pm .1$	5.42
$12.9 \pm .1$	$20.6 \pm .2$	$.58 \pm .01$	$1.82 \pm .01$	44.4
$23.7 \pm .2$	$69.6 \pm .4$	$2.90 \pm .01$	$9.11 \pm .01$	16.4

The most important question here is why three resonances appeared. In addition to a lower pressure than the bell jar (50 microns versus 10^{-2} microns), this plasma has a magnetic field in it (~ 1 gauss); moreover, it is a streaming plasma. A temporary hypothesis for the three peaks is: two of the peaks (which?) could be due to two populations of ions present in the chamber; these could be N_{\perp} and N_{\parallel} or perhaps due to the two distinct energy populations reported by J. Kinder. Then one of the peaks could be a cyclotron resonance, whose nature will be described in the appendix; this cyclotron resonance would be due to the presence of the magnetic field in the chamber which was used to operate the ion engine. The maximum of the cyclotron resonance peak would be expected to occur at the cyclotron or Larmor frequency ω_L given by

$$\omega_L = \frac{e B}{m c}$$

For example, for $B = 1.3$ gauss, we have a Larmor frequency of

$$\nu_L \approx 3.6 \times 10^6 \text{ CPS}$$

Without further study, the resonance method cannot yield any definite results on the ion-engine plasma.

RECOMMENDATIONS FOR SPACE RESEARCH WORK

Without any doubt, the plasma-resonance probe is a welcome tool for analyzing the very low density plasma environments of the ionosphere and solar wind or their earth-bound simulants. We list here the main findings and recommendations of this report:

A. The Langmuir probe method is probably not a very good way to determine electron densities, though it can give useful information about electron temperatures. On the other hand, the resonance probe can very easily give precise and accurate values for the electron density. In this regard, we urge a study of the following questions:

1. What is the best method of obtaining the resonant frequency? i.e., how valuable is the graphic procedure used in this report as compared with, say, displaying the resonance peak on an oscilloscope? (In this regard, check the Japanese report in the 1963 Conference on Ionization Phenomena in Gases). Also, other external circuits might give better results.

2. Are there any theoretical grounds for saying that the resonant frequency occurs at other than the plasma frequency?

B. The resonance probe can probably yield valuable information about collision frequencies. What is needed is a more carefully controlled plasma environment which would allow us to study discharge pressure, voltage, and current effects.

C. The resonance probe is sensitive to the type of gas used and the percentage ionization. A particularly useful set of experiments would be: What is the behavior of oxygen and nitrogen separately? Then one could carefully examine various mixtures of these gases. Of particular theoretical interest would be the exact relation between the peak height and the percentage ionization.

D. We also urge the study of the effects of magnetic fields on resonances probes. (See Appendix).

ACKNOWLEDGMENTS

The author wishes to give special thanks to J. Kinnier, S. J., who guided his work through the summer; and to Dr. G. Joyce for many valuable suggestions.

REFERENCES

1. Chandrasekhar, S., Plasma Physics; The University of Chicago Press, 1960.
2. Ichikawa, Yoshi H.; et. al., Progress of Theoretical Physics, 28 (1962) p. 315-322.
3. Takayama, K., et. al., Physical Review Letters 1960, 238-240.
4. Cairns, R.B., Proceedings of the Physical Society, V. 82, p. 243-251, 1963.

APPENDIX

As is well-known, the earth's magnetic field plays an important role in the physics of the upper atmosphere. We give the beginnings of an investigation of the effects of an external magnetic field $B = B_0 \hat{k}$ on the operation of a resonance probe. The results here are that a cyclotron resonance may appear in the megacycle range, which could interfere with plasma-resonance methods.

The treatment is quite similar to that for the plasma resonance. Assume for the sake of argument that we can neglect the effects of plasma oscillations at $\omega = \omega_p$. Then Newton's law becomes, for an electron,

$$m \ddot{x} + R \dot{x} + \frac{e B_0}{c} \dot{y} = e E_{x0} e^{i\omega t} \quad (1)$$

$$m \ddot{y} + R \dot{y} - \frac{e B_0}{c} \dot{x} = e E_{y0} e^{i\omega t} \quad (2)$$

$$m \ddot{z} + R \dot{z} = e E_{z0} e^{i\omega t}$$

Here R is a viscous damping factor due to electron-neutral collisions and ω is the angular frequency of the externally applied electric field. We immediately neglect the Z -direction motion. Multiplying Equation (2) by i and adding it to Equation (1) gives

$$m \ddot{x} + i m \ddot{y} + R \dot{x} + i R \dot{y} + \frac{e B_0}{c} \dot{y} - i \frac{e B_0}{c} \dot{x} = e E_{x0} e^{i\omega t} + i e E_{y0} e^{i\omega t}$$

or

$$\frac{d^2}{dt^2} (x + i y) + \left(\frac{R}{M} - i \frac{e B_0}{mc} \right) \frac{d}{dt} (x + i y) = \frac{e}{m} E e^{i\omega t} \quad (3)$$

We use the complex vectors $\eta = x + i y$ and $E = E_{x0} + i E_{y0}$, then Equation (3) becomes

$$\ddot{\eta} + \left(\frac{R}{M} - i \omega_L \right) \dot{\eta} = \frac{e}{M} E e^{i\omega t} \quad (4)$$

where $\omega_L \equiv e B_0 / mc$ is the Larmor or cyclotron frequency. The complementary function which describes the transient behavior of the electron is a solution of Equation (4) with the R.H.S. set equal to zero; it involves 2 arbitrary constants and yields a circular motion in the (x, y) plane whose radius is damped by a time factor R/M .

We are chiefly interested in the particular integral of Equation (4), which will describe the steady-state behavior of the electron. Putting the trial solution

$$\eta = A e^{i\omega t} \quad (5)$$

into (4) gives the condition

$$A \left(-\omega^2 + i\omega \frac{R}{M} - i\omega_L \right) = \frac{e}{m} E,$$

or

$$A = \frac{-\frac{e}{m} E}{\omega (\omega - \omega_L - i R/M)} \quad (6)$$

Then the steady-state position and velocity are

$$\eta = \frac{-\frac{e}{m} E e^{i\omega t}}{\omega (\omega - \omega_L - i R/M)} \quad (7)$$

and

$$\dot{\eta} = \frac{-i \frac{e}{M} E e^{i\omega t}}{(\omega - \omega_L - i R/M)} \quad (8)$$

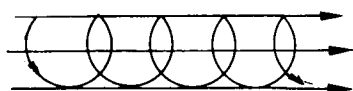
Again, suppose we obtain the electron kinetic energy:

$$\frac{1}{2} m v^2 = \frac{\frac{e^2}{2m} E^2}{\left[(\omega - \omega_L)^2 + \frac{R^2}{M^2} \right]} \quad (9)$$

The electron kinetic energy has a maximum at

$$\omega = \omega_L \quad (10)$$

This is the so-called cyclotron-resonance. We can give a simple physical picture:



$$\vec{B} = B_0 \hat{k}$$

The electrons move about the lines of \vec{B} in a helix; if the field is uniform, the radius of curvature is fixed and the rotational angular frequency is ω_L . If an external electric field of the correct frequency ($\omega = \omega_L$)

is applied, we get a resonance - i.e., a maximum transfer of energy between E and the electron motion.

A typical field in the path of a satellite is $B = 0.3$ gauss; this gives a Larmor frequency of

$$\omega_L \simeq 5 \times 10^6$$

or

$$\nu_L \approx .84 \times 10^6 \text{ CPS}$$

Thus it is conceivable that plasma and cyclotron resonances can interfere with one another.

Since ω_p is a pressure dependent effect, while ω_L depends on the magnetic field strength, one could study such interference effects experimentally by varying the pressure until $\omega_p \approx \omega_L$.

A comparison of Equation (9) with that of Equation (23) in the report may help in differentiating between the two types of resonances. More theoretical work is needed in this regard.

A NITROGEN PLASMA

John H. Kinnier

N 67-22765

INTRODUCTION

The simulation of the space environment encountered by a satellite in terms of temperature, vacuum, and solar flux has proved to be of great assistance in the design and perfection of space vehicles and their experiments. The results of sounding rocket and orbiting satellite data have confirmed and extended our previous earth-based knowledge of high altitude charged particle regions. Table C-7 derived from the ARCD Model Atmosphere lists parameters pertinent to those regions. The ionic composition by mass number and its variation with solar flux is shown in Figure C-36 and C-37. Figure C-37 indicates the steady decrease in ion density with increasing altitude. The predominant species in the topside ionosphere, above 500 km, are He^+ , H^+ , and O^+ . The complex atomic and molecular ions of the ionosphere and its variations in density render exact duplication within the finite boundaries of a vacuum test chamber exceedingly difficult. While exact ionosphere duplication may not be possible, the production of a uniform plasma of the proper density and energy can be a very useful medium for the pre launch diagnosis of the response of spacecraft systems and sensors to an ionized environment.

Table C-7
Ionosphere Data*

Altitude km	Temperature °K	Particle Speed m/sec	Free Path m	Collision Frequency sec^{-1}	Concentration n/m^3	Pressure mm Hg.	Ionosphere Region
50	283	454	7.5 (-5)	6.06 (6)	2.25 (22)	0.66	D 50-85 km
80	166	348	3.80 (-3)	9.10 (4)	4.42 (20)	7.56 (-3)	
90	166	348	2.90 (-2)	1.22 (4)	5.90 (19)	1.02 (-3)	E 85-140 km
140	850	795	26.3	30.0	6.40 (16)	5.63 (-6)	
200	1404	1062	201	5.30	8.40 (15)	1.22 (-6)	
400	1480	1266	6,098	0.21	2.77 (14)	4.25 (-8)	
600	1691	1429	74,270	0.019	2.28 (13)	3.98 (-9)	

*ARDC Model atmosphere

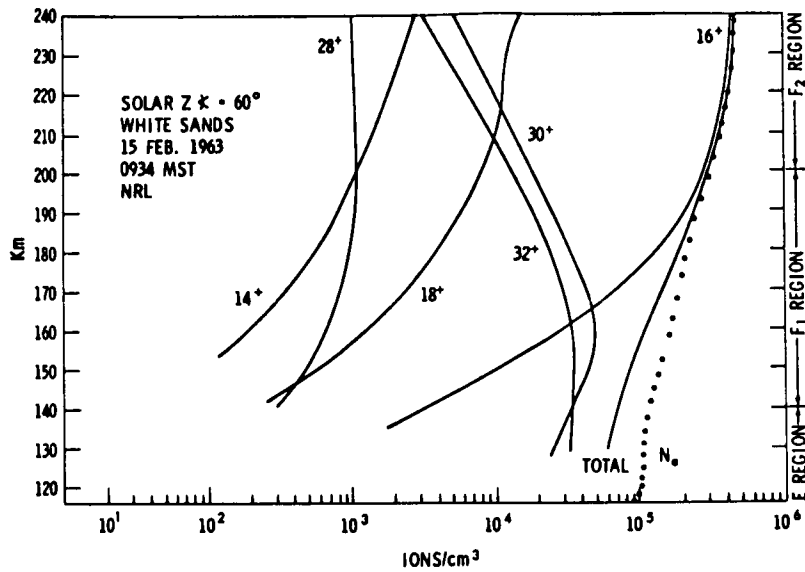


Figure C-36—Ion composition of the daytime ionosphere.

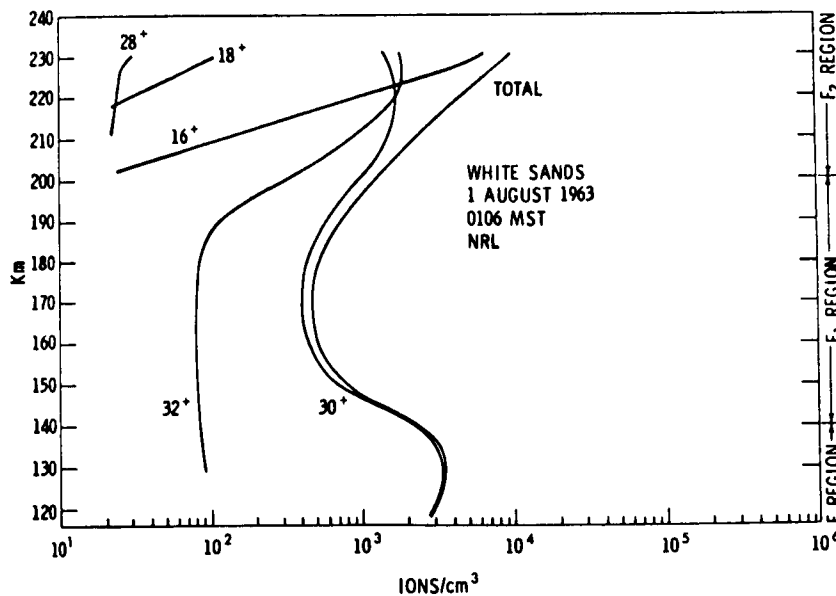


Figure C-37—Ion composition of the nighttime ionosphere.

A satellite in circular orbit about the earth will have orbital velocities ranging from 8 to 7 km/sec., depending upon its altitude. In comparison, the average ion velocities at the same altitude range from 0.4 to 1.0 km/sec with the result that the vehicle is subject to a directed ion velocity due to its own motion. Electron velocities are approximately 100 km/sec and appear as a random isotropic flux incident upon the relatively slowly moving spacecraft. Generally, the laboratory production problem is to generate an ion and electron flux of sufficiently low velocity. The relative

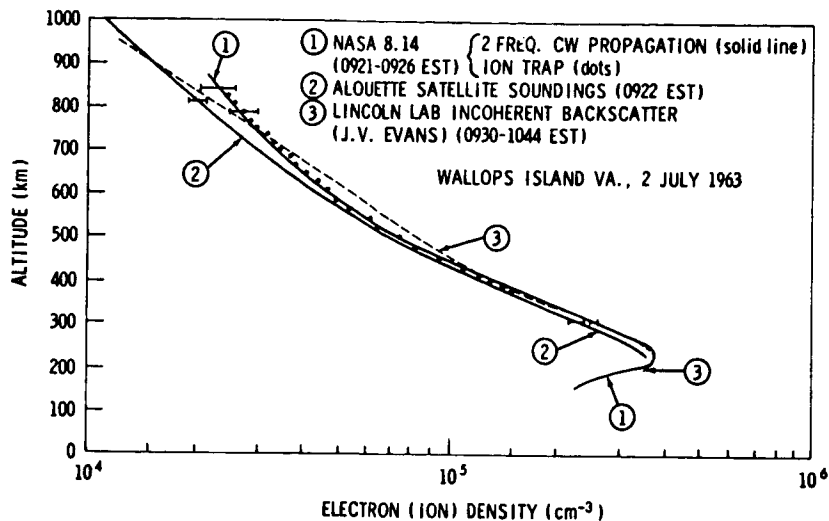


Figure C-38—Charge particle density of the upper ionosphere.

motion of a satellite moving through the ionosphere can be simulated by directing an ion stream having a velocity of approximately 8 km/sec and a density of not more than 10^6 ions/cm³ against a stationary test object. Ideally, the test object might be the spacecraft itself or one of its major components which introduces the additional requirement that the test plasma be uniform over a large region. Table C-7 makes it immediately apparent that under thermal-vacuum test conditions, the mean free path of ions and electrons becomes equal to or even larger than the chamber dimensions and collision frequencies become correspondingly small. These are not favorable conditions for the production of the type of plasma required for ionosphere simulation. More efficient ion production and more precise energy control can be exercised if a separate ion source is used to generate the plasma under favorable conditions. This plasma is then projected into the test volume.

PLASMA SOURCE

The ion source employed for plasma generation was a model 7J Thrustor supplied by the Lewis Research Center.* It is a 20 cm electron-bombardment engine developed for electrostatic propulsion applications. The general structure of the source and its associated power supplies are shown schematically in Figure C-39. As a propulsion device, the source is normally used with mercury or cesium as the propellant or element to be ionized. As a plasma source it has been adapted to utilize many gases such as krypton, argon, nitrogen, helium and hydrogen.

The source was mounted on a stand at the center of one end of a 4' × 5' vacuum chamber. A small copper tube brought nitrogen gas from a needle type vacuum leak valve through the vacuum wall into the rear of the engine. The gas then passed through a distributor and into the ionization chamber. This chamber is circular in cross-section and consists of an axially mounted tantalum filament, the cathode, surrounded by a cylindrical anode. Electrons emitted by the cathode are accelerated through a variable potential difference of 50 - 100 volts towards the anode. The anode accelerating voltage must impart an energy to the electrons greater than the ionization potential of the gas used; the ionization potential of nitrogen is 14.48 volts. To further enhance the probability than an electron will make an ionizing collision, an axial magnetic field of approximately 20 gauss, derived from a coil wound about the engine's outer structure, causes the electrons to travel in a spiral path on their way to anode. Neutrals and ions formed within the chamber will diffuse towards

*Courtesy of Harold Kaufman, Lewis Research Center.

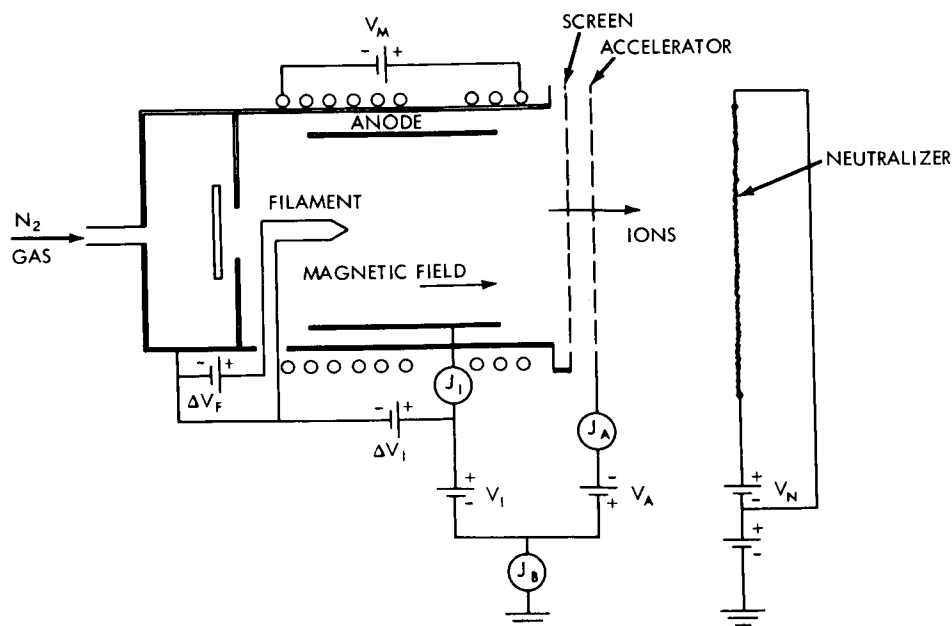


Figure C-39—20-cm ion bombardment source and power supplies.

the grid system which covers one end of the chamber. The grid system extracts, focuses, and accelerates the ion stream. With respect to the anode, the cathode and the ends of the chamber are at a negative potential to prevent the escape of electrons. With respect to ground, the chamber is at a high positive potential V_I , and the accelerating grid at a negative potential V_A . The negative potential on the accelerating grid prevents electron backstreaming. The ions after leaving the grid system are close to ground potential and have been accelerated through a net potential difference V_I , Figure C-40. The total ion beam current J_B is strongly dependent upon filament emission, discharge potential, and the magnetic field strength for fixed values of V_I and V_A . For set values of all electrical parameters, it is a sensitive function of the nitrogen gas flow rate. The vacuum chamber was pumped to a base pressure of 2×10^{-6} mm Hg by a 3200 liter/sec oil diffusion pump with a liquid nitrogen cold trap. Under normal operating conditions, the pressure rose to approximately 4×10^{-5} mm Hg with the source operating.

BEAM NEUTRALIZATION

The exhaust beam of the electron bombardment source contains only the positive ion component of the desired neutral plasma. Operation of the source in space, for purposes of ionic propulsion, results in an electrically isolated beam and charge neutralization must be provided. A suitable electron source for charge neutralization is the emission provided by a hot filament or an auxiliary gaseous discharge. The number of electrons entering the ion stream is dependent upon the physical location of the electron source with respect to the ion source. It may be in the form of a heated tungsten wire stretched across the beam diameter or a smaller filament located off the beam axis. Assuming that the hot wire electron source is not temperature limited, electrons leaving it at a temperature of 2500°K

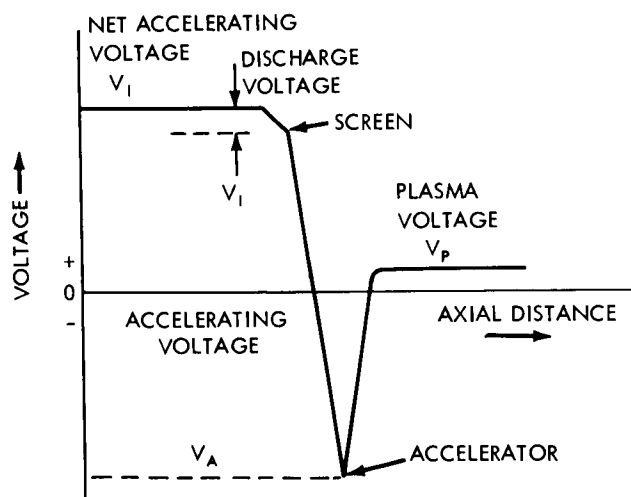


Figure C-40—Potential distribution.

will have an energy of 0.3 eV and a velocity of 3×10^7 cm/sec. The existing plasma potential V_p , which will be positive for the streaming ions, accelerates the emitted electrons through a potential difference $V_p - V_N$ where V_N is the neutralizer potential. The value of this potential difference may be altered by superimposing a positive bias on the neutralizer heating voltage. The effect of neutralization is seen as a decrease in plasma potential and the fact that $V_p - V_N$ be small is a measure of its adequacy.

When the electron bombardment source is operated in a vacuum tank facility the ion beam usually makes contact with the chamber walls which provide an electrical ground return path. In this case, current neutralization is not required except to produce more stable operation at very low pressures. Charge neutralization results from the conducting boundaries which can modify the electric field structure, absorb particles from the stream, and to some extent emit secondary particles. The residual gas may interact with the ions and electrons of the beam through ion-neutral charge exchange and electron-neutral elastic and inelastic scattering. The time required for an electron of thermal energy or higher to traverse a $4' \times 5'$ vacuum chamber is a few microseconds. Excitation and ionization processes induced by thermal electrons are quite improbable, although electrons of increased energy may be expected to produce some excitation and ionization of the residual gas. Electrons of low to moderate energies (~ 1 eV) interacting with the common atoms or molecules are scattered approximately isotropically and the total and momentum transfer cross-sections do not differ appreciably. While the electron-neutral interaction has a rapidly decreasing cross-section at low electron energies, electron-ion interaction and electron scattering processes are of considerable magnitude at these energies. The trajectories of electrons scattered within the plasma column will be modified by its electrical field structure and its boundaries. Since the mean free path of the scattered electron is proportional to the number density which is in turn dependent upon the column cross-sectional area, it is to be expected that scattering processes will be of less relative importance as one recedes from the plasma source.

PRACTICAL SOURCE OPERATION

The operation of the source and its required power supply capacity can be conveniently stated in terms of the beam current, J_B , desired. Because low energy ions were required, the voltages V_I and V_A were set in the range 150-200 volts. The positive supply should have a current capacity of $2J_B$ and the negative $J_B/2$. For proper operation of the particular set of power supplies used, V_I was always set greater than ΔV_I . The discharge supply, ΔV_I , was variable up to 150 volts and had a current capacity of $30 J_B$. The normal operating point for the filament was 26 amperes at 8-10 volts. Some excess capacity in this supply proved to be very valuable. The magnetic field supply was variable and normally supplied 10 amperes at 10 volts. Adjustment of this supply has a significant effect on the ion current recorded in the chamber. Variation of the filament temperature afforded a practical method of exercising control over the beam density. The temperature attained by the filament as a function of the heating current was measured by an optical pyrometer and the results appear in Figure C-41.

GENERAL PLASMA DIAGNOSIS

The characteristics of the plasma and its distribution throughout the test volume were determined by a variety of probes. The probe array, Figure C-42, consisted of a set of insulated wires whose ends were exposed and presented an area of 0.5 cm^2 to the beam. The probes, set 6" apart, were mounted along the axis of the source. A second set, transverse to the beam, measured its lateral distribution. From these probes the floating potential throughout the chamber could be determined in a reasonable period of time. The results of a typical set of data are presented in Figure C-43. The net accelerating voltage applied to the source was less than 1/10 of its capacity and in this mode of operation it is space-charge limited or more ions are produced within the source than are drawn into the chamber.

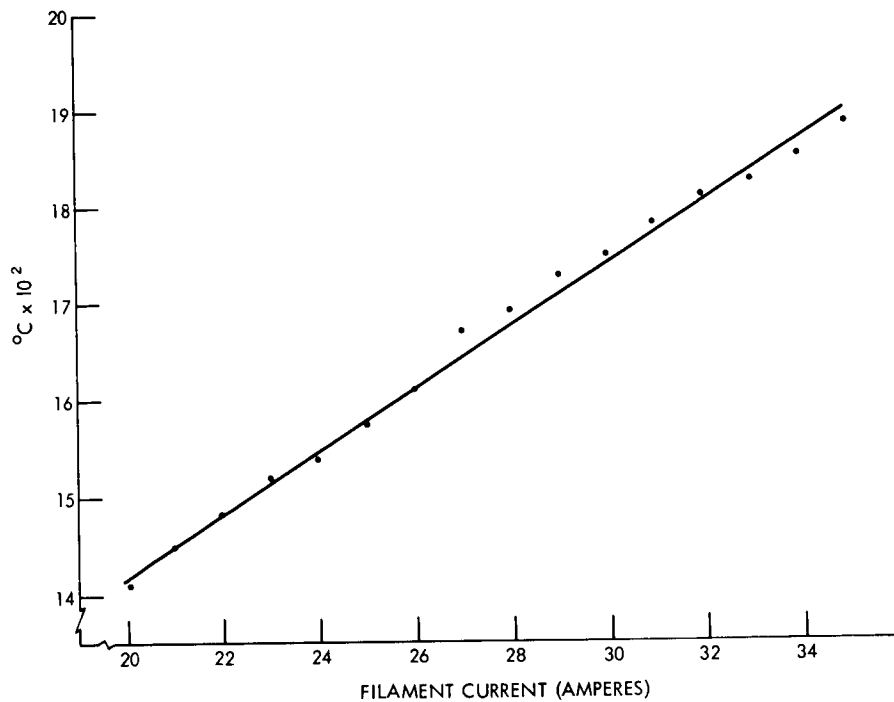


Figure C-41—The variation of the tantalum filament temperature with heating current.

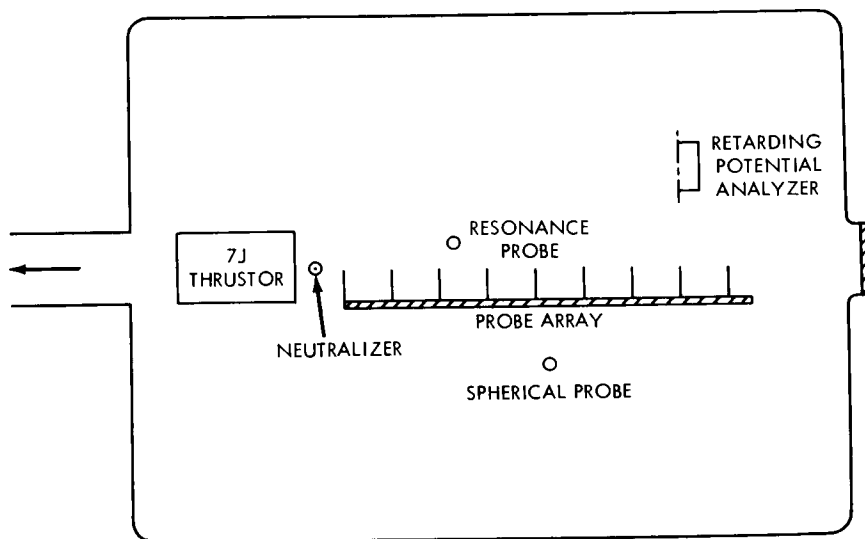


Figure C-42—Schematic diagram of the ion source and detectors in the 4' x 5' vacuum chamber.

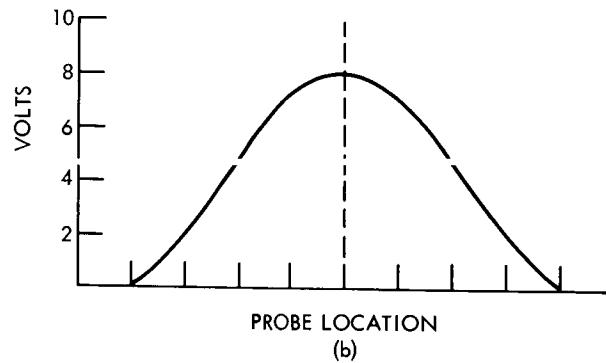
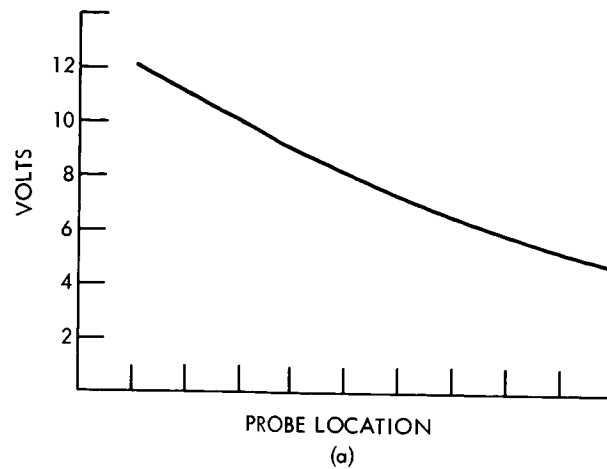


Figure C-43—(a) floating potential along the axis of the chamber; (b) floating potential perpendicular to the beam axis 25" from the source.

Operation under these conditions is specified by Child's Law. The beam current density, J_B , is a measure of the rate at which ions pass through a unit area of the grid structure per unit time and the current density in amperes per square meter is defined as,

$$J = nev \quad (1)$$

where n is the particle density per cubic meter, e its charge in coulombs and v the drift velocity in meters per second. The drift velocity, or the initial ion velocity within the ionization region, is a small quantity compared to the velocity given to the ion by the accelerating field. The beam current density can be calculated from Child's Law,

$$J = \frac{\Sigma_0}{225} \sqrt{\frac{2e}{m}} \frac{v^{3/2}}{d^2} \quad (2)$$

V = the accelerating potential

d = grid spacing

Σ_0 = the permittivity of space

e/m = the charge to mass ratio for the ion.

To facilitate initial operation of the source, its effective diameter was decreased from 20 to 15 centimeters. With this modification, calculated total beam currents of singly charged nitrogen atoms in the low milliampere range were obtained.

One of the probes in the center of the chamber was used to measure the change in floating potential as the discharge current was increased. Figure C-44 shows that the relation between these quantities is essentially linear.

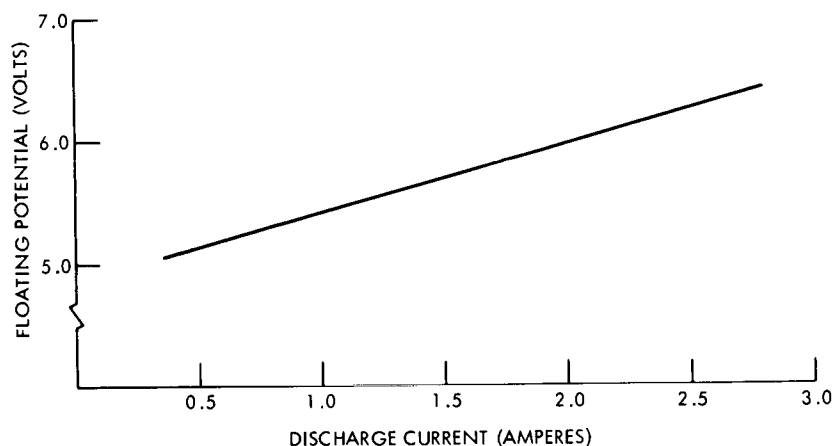


Figure C-44—Variation of the floating potential with a change in discharge current, other voltages being held constant.

Ion trajectories from the source are governed by the potentials applied to the screen and accelerator grids. The potential difference between the accelerator and the plasma column appears as an ion sheath whose gradient contributes to the electrostatic focusing properties of the source. In the region adjacent to the source the column is sharply defined; further downstream the column expands and potential profile taken at a distance of 25 inches, (Figure 43b), reveals that it has reached its maximum diameter consistent with the location of the chamber walls. Along the axis of the column, the floating potential decreases steadily, falling abruptly at the end of the chamber. The slope of the curves of Figure C-43 yields an indication of the electric field structure. The axial field decreases smoothly along the column and a strong radial field exists near the chamber walls.

An evaluation of the plasma potential from Langmuir data did not seem to be justified, however, an approximate value of the potential was determined from a series of emissive probe measurements. The probe was a 2 centimeter diameter loop of 0.002" tungsten wire heated to emission temperature by a step down transformer. The potential drop across the wire of about 0.5 volts limited the precision of measurement. The probe current to the wire as a function of bias voltage was measured in two temperature states, one when heated to 2500°K and the other in a hot but non-emissive condition. The difference between these two values was the net electron current taken up

by the plasma. As the direct current bias of the probe approached the plasma potential, the emitted current decreased rapidly to zero. It was assumed that the ion current intercepted by the small cross-sectional area of the probe wire was unaffected by the direct current bias. From these measurements it appears that the plasma potential is within one volt of the floating potential.

RETARDING POTENTIAL ANALYSER

Two of the more important characteristics of the plasma were the energy and density of its ions. An indication of the ion energy is always available when the net accelerating voltage applied to the beam is known. This value was generally 200 volts. For more precise measurement a retarding field analyser was used and a cross-section of its structure and power supplies is shown in Figure C-45. The analyser operates on the principle that the kinetic energy of ions may be deduced from the height of the potential barrier that they just surmount. More exactly stated the height of the potential barrier is not a measure of kinetic energy but rather of the component of momentum perpendicular to the equipotential lines. In the case of an ion stream where velocity components transverse to the stream are small compared to the longitudinal component, this distinction is of lesser importance. The first grid and case of the analyser were grounded to provide a fixed potential with respect to the plasma. A negative bias was applied to the second grid to exclude electrons from the analyzing region. The fourth grid was also biased negatively to force low energy secondary electrons to return to the collector. The third grid was used to produce the variable ion retarding field. The applied positive voltage was varied in small steps starting from zero and the current to the collector observed. Eventually this current reduces to zero if no secondary processes interfere. A record of the current versus voltage provides an integral spectrum of the ion distribution. Graphical differentiation of this curve produces a plot of the number of ions received per unit voltage interval or per unit energy.

An energy spectrum of the ions in the chamber is displayed in Figure C-46.

The plot shows that the ions occur in two well defined energy groups. Since the applied accelerating voltage was 200, the high energy group having a maximum at 165 volts was as expected. The low energy group was not expected and the exact processes which produced it were not fully investigated. It was found, however, that when the analyser aperture was perpendicular to the beam axis, only the low energy group was observed. This suggests production by a scattering mechanism.

The aperture grid of the analyser had an area of 4.9 cm² and a calculated transmission of over 90 percent. When directed toward the source, particles enter the analyser in a nearly parallel beam and their velocity can be calculated from the simple relation

$$\text{Energy} = \frac{1}{2} m V^2$$

The high energy ion group has a velocity of 47.7 km/sec and the low energy group 18.5 km/sec. These values are in excess of the desired value of 7-8 km/sec. The ion density may be determined from the average ion collector current and entrance area of the aperture grid. The current density and particle density can be obtained from the relations,

$$j = \frac{i}{A} \quad (4)$$

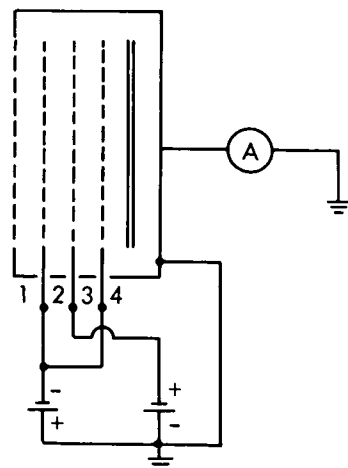


Figure C-45—Retarding potential analyzer.

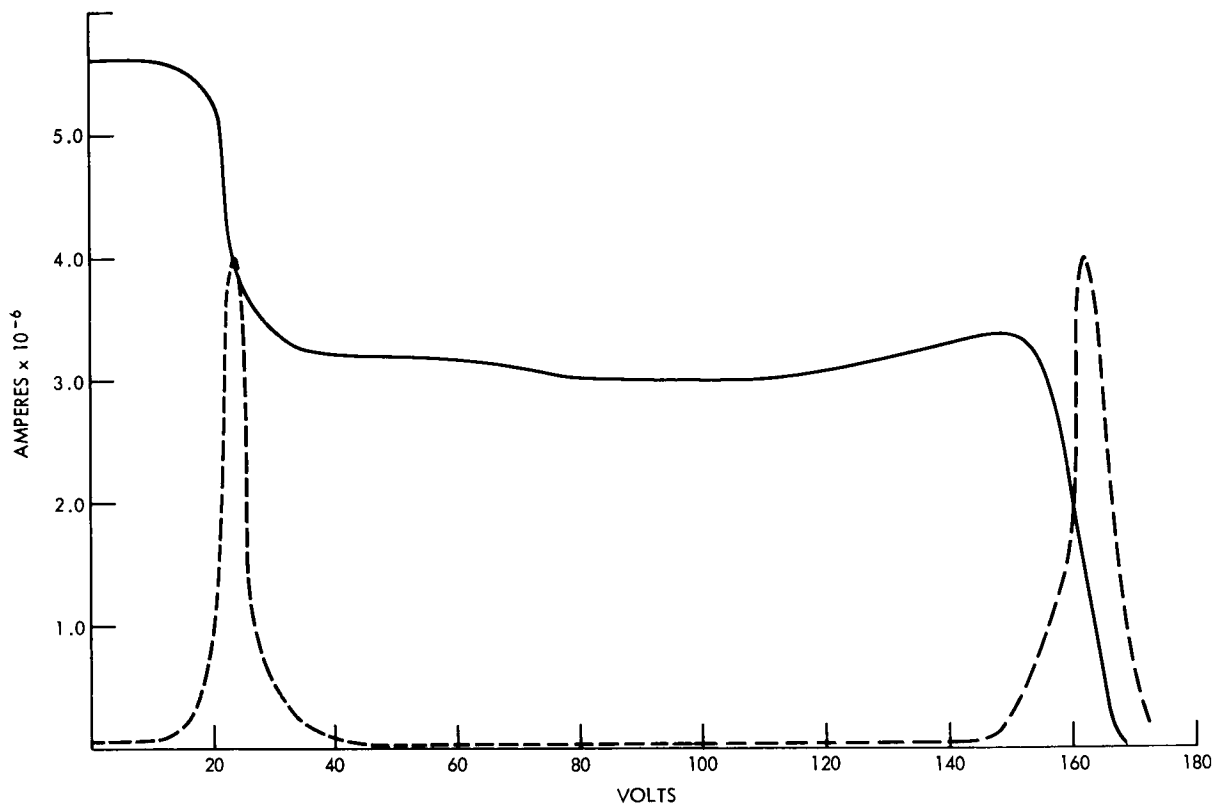


Figure C-46—Ion energy spectrum.

$$\eta_+ = \frac{j}{e v_+} \quad (5)$$

The ion density reached well into the range of 10^7 ions/cm³ and could be easily reduced by decreasing the cathode emission.

RESONANCE PROBE

Langmuir probe techniques have frequently been used to measure the electron temperature and density of a plasma. In many instances the method is difficult to apply especially where the electron saturation region of the curve is not clearly defined. A resonance probe is a Langmuir probe held at a fixed dc potential in the electron repelling region modulated by an R.F. signal of the form $V \sin \omega t$.

As the frequency of the R.F. voltage is changed, the incremental dc component to the probe passes through a maximum. An example of such a resonance curve taken in the test plasma appears in Figure C-47. The plasma frequency ω_p is directly related to the electron density, N_e , by,

$$\omega_p = \left(\frac{N_e e^2}{m \Sigma_0} \right)^{1/2} \quad (6)$$

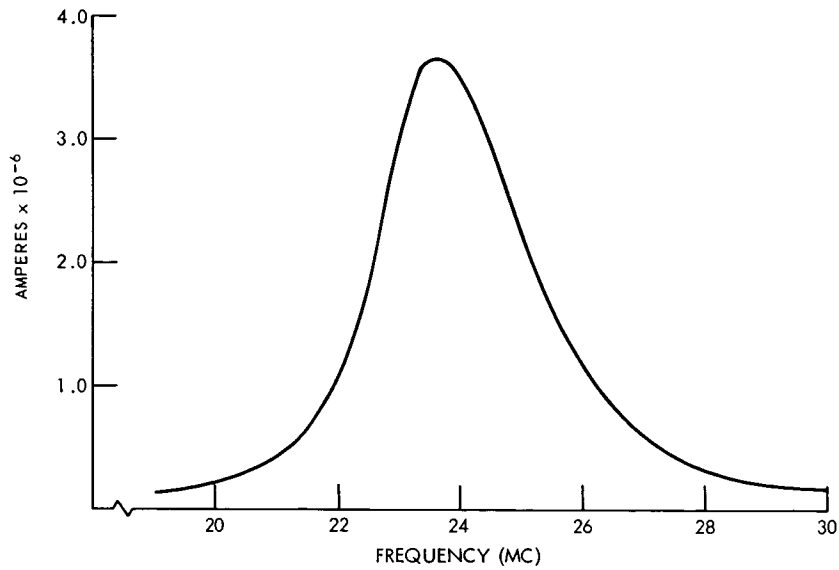


Figure C-47—Resonant probe response curve.

If we assume that the resonance maximum occurs at ω_p then the electron density becomes 4×10^6 electrons/cm³.

THE SPHERICAL PROBE

An evaluation of the electron density having been achieved through the use of a resonant probe, a copper sphere one inch in diameter was employed in a simple Langmuir probe circuit and its current-voltage characteristic measured. Druyvesteyn has shown that the electron distribution in a plasma may be derived from the second derivative of its current-voltage characteristic, i.e.,

$$N\phi(V) = \frac{2}{Ae} \left(\frac{2mV}{e} \right)^{1/2} \frac{d^2 i}{dV^2} \quad (7)$$

where N is the electron concentration, A the probe area, e the electron charge and m its mass.

The current-voltage curve for the sphere is sketched in Figure C-48 and its first and second derivatives in Figure C-49. The derivatives were obtained through graphical analysis of the original curve.

This method is subject to serious inaccuracies because the least error in the initial data is amplified with each increasing order of the derivative and the precision with which a slope can be obtained graphically varies with the slope itself. Despite the shortcomings, this method does at least give a qualitative idea of the electron distribution in the plasma.

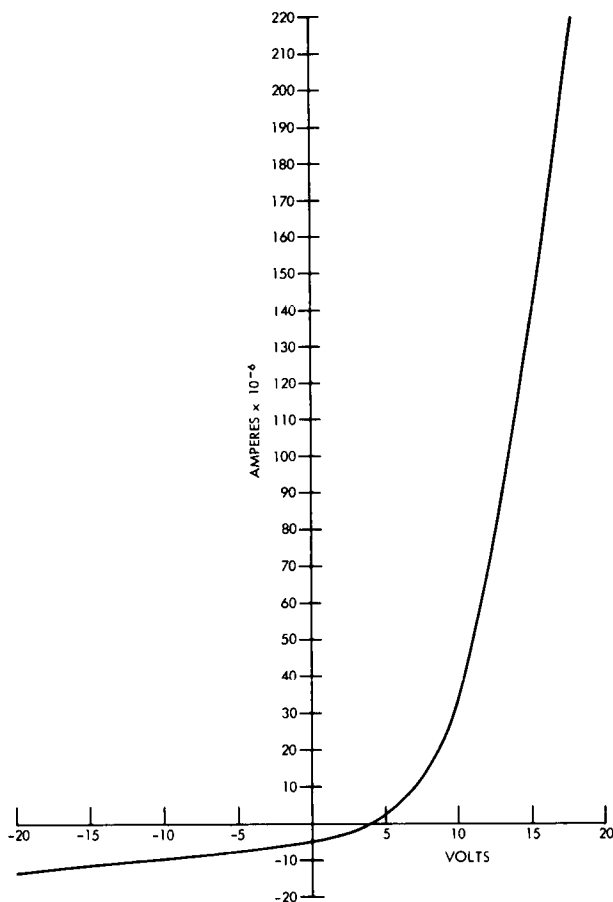


Figure C-48—Spherical probe characteristics.

THE MAGNETIC FIELD

A study was made to determine the penetration of the magnetic field of the electron-bombardment source into the vacuum chamber. The source was not operating at this time and a field current of 10 amperes was used. The field strength was measured by a Rawson-Lush rotating coil gaussmeter. A uniform magnetic field due to the earth and other causes existed throughout the chamber and had a value of 0.4 gauss. A survey was made across the axis of the source. The field peaked rapidly opposite the ends of the coil and decreases more slowly as the wall of the chamber is approached (Figure C-50). It decreased receding from the source and at a distance of 15 inches could not be distinguished from the background field.

The cyclotron radius of a particle moving perpendicular to a magnetic field B at a velocity v is

$$r = \frac{mv}{eB} \quad (8)$$

Thus the ions of the plasma in a field of one gauss have a radius of curvature of nearly 7 meters. The electrons, being much lighter, and of lesser energy, have a radius of curvature of 10 centimeters.

CONCLUSIONS

The electron-bombardment source is capable of producing a steady nitrogen plasma of varying density over a considerable volume. As the plasma spreads out from the source it becomes more uniform and the plasma potential approaches ground potential. In those circumstances wherein an ion energy somewhat greater than those of the ionosphere is acceptable, a medium is produced which is suitable for the study of the behavior of many objects and devices in a streaming plasma.

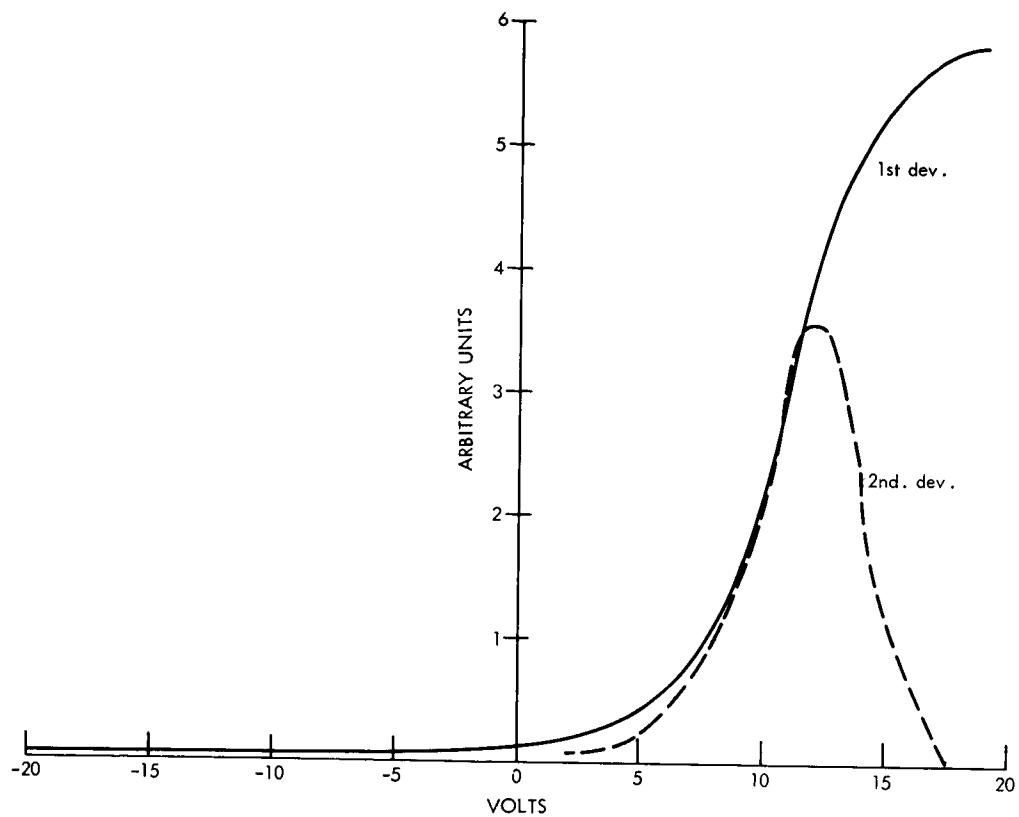


Figure C-49—Derivatives

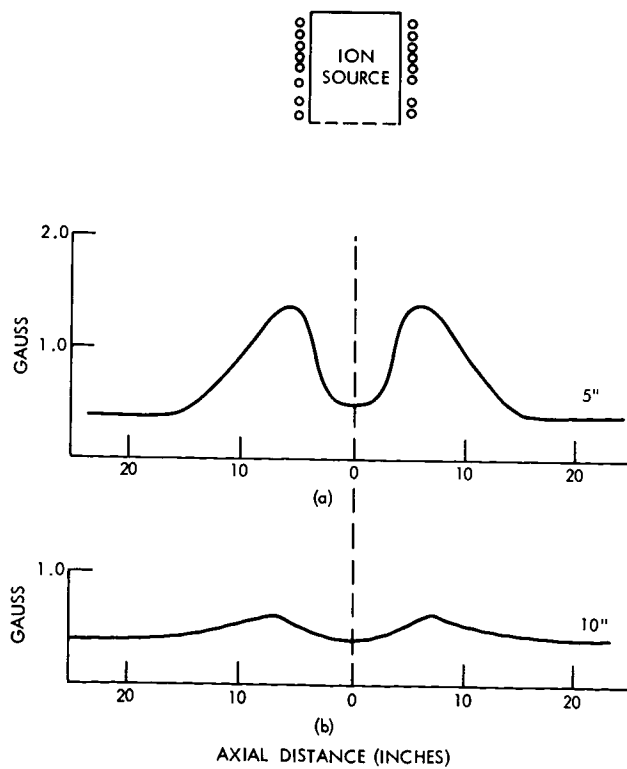


Figure C-50—The magnetic field of the source in the vacuum chamber, (a) 5" from the accelerator grid; (b) 10" from the accelerator grid.

REFERENCES

1. Bauer, S. J., et al., "Simultaneous rocket and satellite measurement of the topside ionosphere," Journal of Geophysical Research, V. 69, p. 196, 1964.
2. Bonetti, A., et al., "Explorer 10 plasma measurements" Space Research I, p. 304 North Holland Pub. Co., 1960.
3. Boyd, R.L.F., and Twiddy, N.D., "Electron energy distribution in plasmas I," Proceedings of the Royal Society A, V. 250, p. 53, 1959.
4. Halmes, J.C., Johnson, C.Y., and Young, J.M., "Ionospheric chemistry in Space Research V," (R. Muller ed.) p. 756, John Wiley, New York 1965.
5. Harp, R.S. and Crawford, F.W., "Characteristics of the plasma resonance probe," Journal of Applied Physics, v. 35, p. 3436, 1964.
6. Kaufman, Harold R., "An ion rocket with an electron-bombardment ion source," NASA TN D-585, 1961.
7. Kaufman, Harold R., "The neutralization of ion rocket beams," NASA TN D-1055, 1961.
8. Medicus, G., "Simple way to obtain the velocity distribution of the electrons in gas discharge plasmas from probe curves," Journal of Applied Physics, v. 27, p.(10), p. 1242, 1956.
9. Reader, Paul D., "Investigation of a 10-centimeter diameter electron-bombardment ion rocket," NASA TN D-1163, 1962.
10. Reader, Paul D., "The operation of an electron-bombardment ion source with various gases," NASA TM X-52006, 1964.
11. Simpson, J. A., "Design of retarding field energy analysers," Review of Scientific Instruments V. 32, p. (12), p. 1283, 1961.
12. Spitzer, L., "Physics of fully ionized gases," Interscience Publishers, V. 5, p. 328, 1962.

A PROBE TO MEASURE PLASMA CONDUCTIVITY

D. L. Waidelich, G. R. Joyce and J. Zurkow

N 67-22766

INTRODUCTION

The particular plasma conductivity probe considered here appears to be about ten years old at the present time and has been used primarily for measurements in very dense plasmas and at relatively high radio frequencies. The purpose of this study was to investigate the possibilities of making measurements with this probe in a low density plasma and at a relative low frequency and to make a theoretical analysis of the change of impedance of the probe when it is measured in a plasma.

Possibly the first mention of the use of a conductivity probe was that used in a study [1], [2], [4], [10] of the electrical conductivity of shock-ionized argon. The coils surrounded the glass tube in which the ionized argon traveled, and calibration was accomplished by passing a piece of metal through the glass tube in place of the ionized gas. The output voltage of the search coil was viewed on the screen of an oscilloscope.

A coil probe was used in magnetohydrodynamic flow experiments [3] to measure the conductivity as indicated by the reduction of inductance in the coil surrounding a plasma at a frequency of 50 MHz. This meant that measurements could be made without requiring motion of the plasma and this property was employed in an instrument [5] in which the frequency was about 10 MHz. Another application [6] used a coil surrounding the plasma in which 300 KHz radio frequency energy was dissipated and detected externally. Still other methods used the ideas of measuring the Q of the coil surrounding the plasma and of pulsing [17] a coil in a bridge circuit.

The next work [8], [9], [16] used a coil inserted into the plasma and measurements were made with the help of a grid-dip meter at frequencies from 10 to 50 MHz. The electrical conductivity of the wake of a projectile was measured [11] using methods [1] given previously, while that of seeded gases was measured [12], [13] using a conductivity probe [5]. The effect [14] of the radial variation of conductivity using numerical methods of solution has been studied. A non-linear network [15] has been suggested for the comparison of conducting materials.

The purpose of the present work is to present an analysis of the probe and also some preliminary experimental results.

ANALYSIS

Actually two configurations of the probe were considered. The first was that of a flat plate much longer and wider than its thickness. The turns of wire carrying the current would be wound paralleled to the long side of the plate. The coordinate system used is shown in Figure C-51 with the z axis perpendicular to the plane of the paper and directed downwards. It is also assumed that all field components, currents and voltages are sinusoidal of frequency $f = (\omega/2\pi)$. The analysis is given in detail in Appendix A and uses the method of obtaining expressions for the electric and magnetic field intensities both within and without the probe coil. The values of the field intensities are matched at the boundary of the coil. The admittance of the coil is obtained from the current flowing in the coil divided by the voltage developed in the coil. The result for the admittance may be interpreted as the equivalent circuit for the probe coil as shown in Figure C-52.

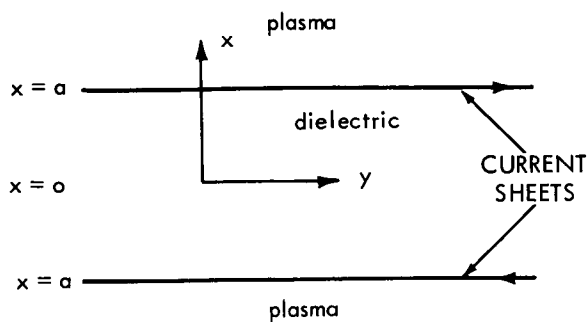


Figure C-51—Coordinate system used.

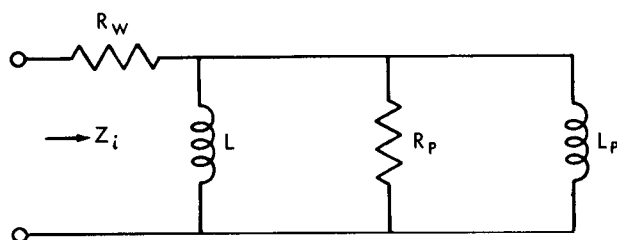


Figure C-52—Probe coil, equivalent circuit.

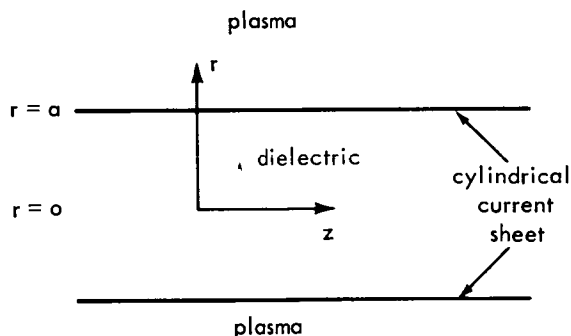


Figure C-53—Alternate configuration of probe.

The winding resistance R_w was added to account for the ohmic resistance of the coil when no plasma was present. When the surrounding plasma is removed, the conductivity σ_2 of the plasma approaches zero, the skin depth δ_2 of the plasma increases without limit and both R_p and L_p approach open circuits. The probe coil then appears to be the winding resistance R_w in series with the coil inductance L . The presence of the plasma is indicated by both R_p and L_p being finite and thus the input impedance Z_i is changed from its value with no plasma present.

The second configuration considered was that of a solenoid wound on a long circular cylinder as shown in Figure C-53. The z axis is directed along the axis of the solenoid and the properties are assumed to be independent of the azimuth angle ϕ . Also all field components, voltages, and currents are sinusoidal of frequency $f = (\omega/2\pi)$. The analysis is given in detail in Appendix B and the method employed is that used in Appendix A on the parallel plane probe. As a result, an equivalent circuit is obtained that is exactly the same as that of Figure C-52 for the parallel plane probe except for the values of the circuit components.

Various values were assumed for the number of turns N , the conductivity σ , the radius of the coil and the frequency $f = (\omega/2\pi)$, and the values of R_p and L_p were computed and plotted as curves. A typical curve for R_p is shown in Figure C-54 and indicates that the resistance increases with frequency and with the diameter of the coil. Figure C-55 shows that the inductance decreases with the increase of frequency.

The conductivity of the plasma is considered in more detail in Appendix C. This analysis assumes that the cold plasma equa-

tions may be used and that the charged particles react with the neutral particles through a drag force. Also there is to be no streaming; the fields are small and sinusoidal and the equations may be linearized about the first order quantities. The result is a plasma conductivity which is the sum of the conductivities of each of the i^{th} species of charged particles and which depends both on the frequency and the drag force or collision frequency coefficient. At low frequencies the dependence on frequency becomes unimportant and the collision frequency coefficient becomes very important.

If instead of the equivalent circuit of Figure C-52, the coil probe is assumed to have a simple series circuit, then the effect of placing the coil in a plasma is to increase its apparent resistance by an amount ΔR . At low frequencies, by the use of the results of Appendix B, it is possible to show that ΔR varies as the square of the frequency. A coil was wound on a toroidal core of ferrite and

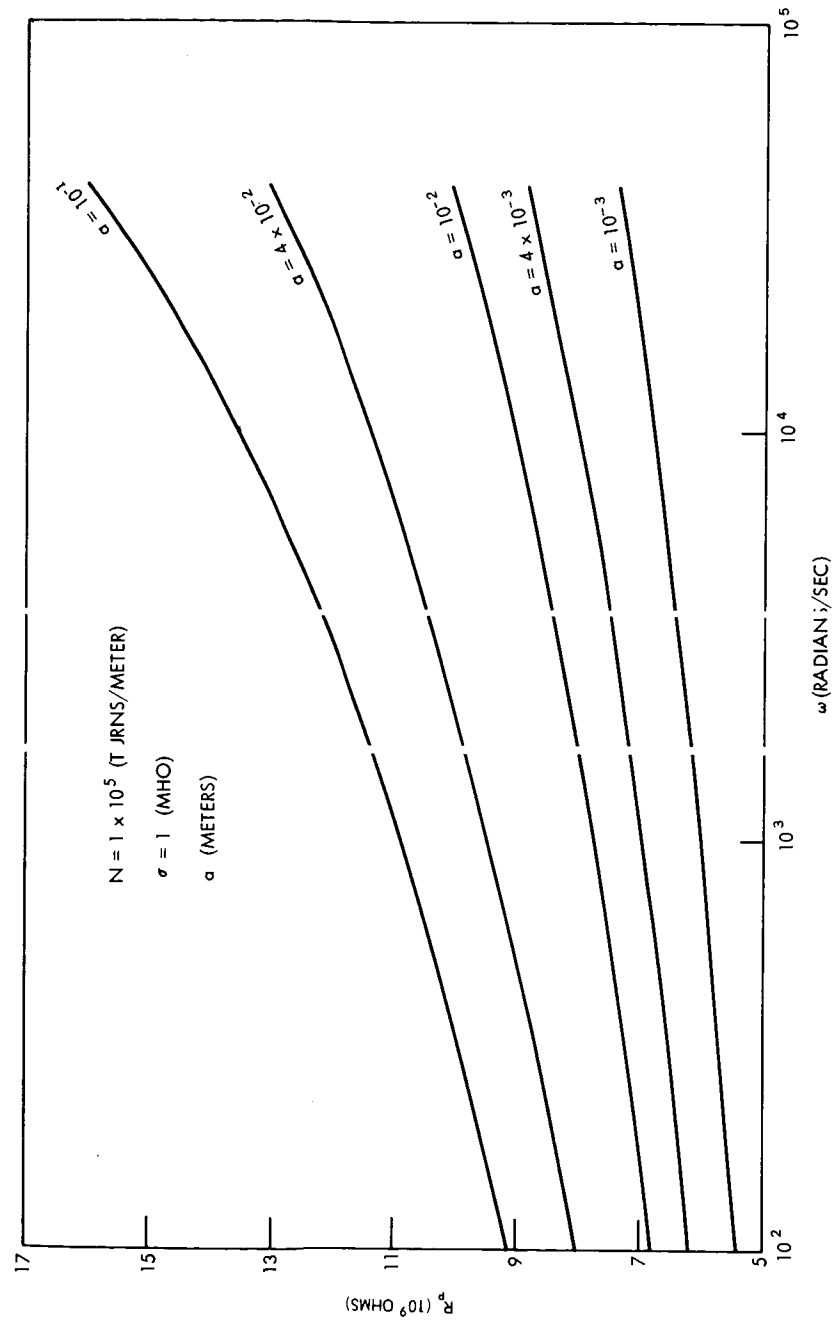


Figure C-5.—Typical curve for R_p .

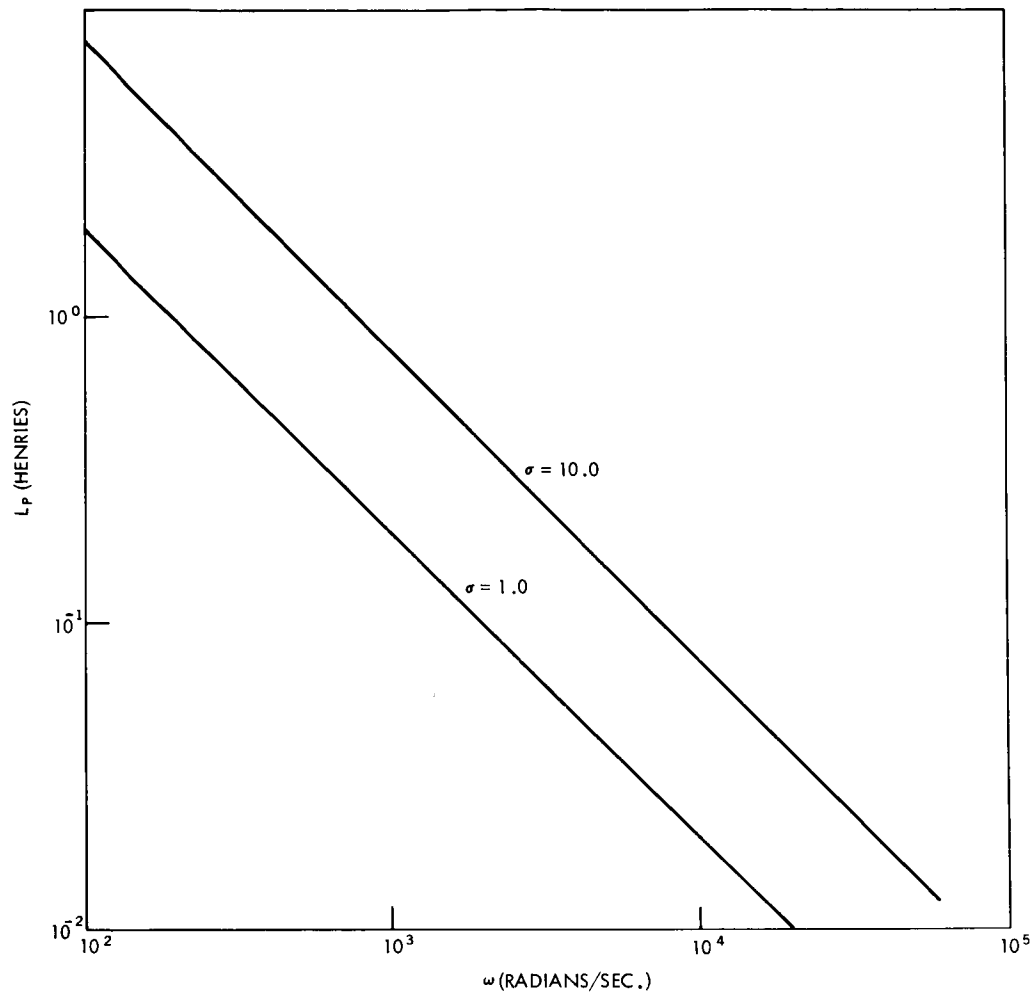


Figure C-55

was placed in a low pressure plasma in air. The impedance was measured by the use of a bridge circuit and then was measured again with no plasma. This was repeated at a number of frequencies and the ΔR is shown as points in Figure C-56. A straight line representing the square of the frequency is also shown. Fair agreement resulted but it was felt that further work should be done to improve the accuracy.

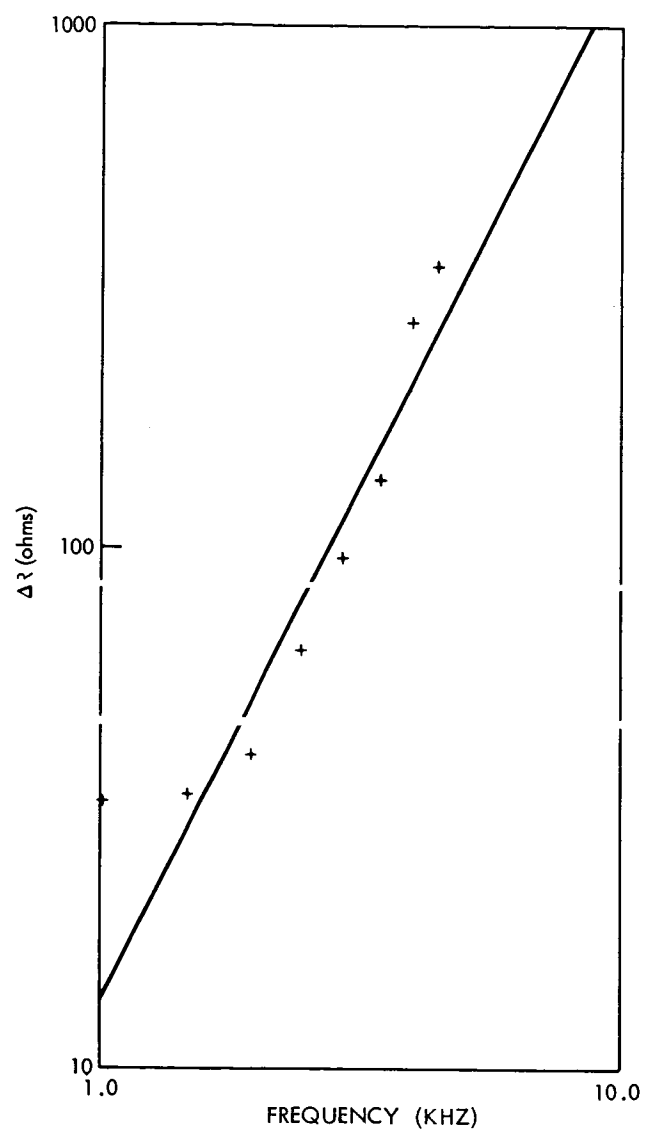


Figure C-56

REFERENCES

1. Lin, S.C., Resler, E.L., and Kantrowitz, A., "Electrical Conductivity of Highly Ionized Argon Produced by Shock Waves," Journal of Applied Physics, V. 26, p. 95 to 109, January 1955.
2. Lamb, L. and Lin, S.C., "Electrical Conductivity of Thermally Ionized Air Produced in a Shock Tube", Journal of Applied Physics, V. 28, p. 754 to 759, July 1957.
3. Blackman, V.H., "Magnetohydrodynamic Flow Experiments of a Steady State Nature," American Rocket Society Preprint No. 1007-59. Presented at the 14th Annual Meeting of the ARS, Washington, D.C., November 1959.
4. Pain, H.J. and Smy, P.R., "The Electrical Conductivity of Shock-Ionized Argon," Journal of Fluid Mechanics, V. 9, p. 390 to 400, 1960.
5. Savic, P. and Boulton, G.T., "A Frequency Modulation Circuit for the Measurement of Gas Conductivity and Boundary Layer Thickness in a Shock Tube," Journal of Scientific Instruments, V. 39, p. 258 to 266, 1962.
6. Rosa, J.R., "Physical Principles of Magnetohydrodynamic Power Generation," Physics of Fluids, V. 4, p. 182 to 194, February 1961.
7. Donskoi, K.V., Dunnaev, Ye. A., and Prokofev, I.A., "Measurement of Electrical Conductivity in Gas Streams," Soviet Physics - Technical Physics, V. 7, p. 805 to 807, March 1963.
8. Olson, R.A. and Lary, E.C., "Electrodeless Plasma Conductivity Probe Apparatus," Review of Scientific Instruments, V. 33, p. 1350 to 1353, December 1962.
9. Lary, E.C. and Olson, R.A., "A Plasma Conductivity Probe," in Engineering Aspects of Magnetohydrodynamics, Gordon and Breach, p. 127 to 140, 1964.
10. Brogan, T.R., "Electrical Properties of Seeded Combustion Gas" in "Ionization in High-Temperature Gas," Progress in Astronautics and Aeronautics, V. 12, Academic Press, p. 319 to 345, 1963.
11. Koritz, H.E. and Keck, J.C., "Techniques for Measuring the Electrical Conductivity of Wake of Projectiles at Hypersonic Speeds," Review of Scientific Instruments, V. 35, p. 201 to 208, February 1964.
12. Lan, J., "Electrical Conductivity of Inert Gases-Seed Combination in Shock Tubes, Part I," Canadian Journal of Physics, V. 42, p. 1548, August 1964.
13. Lau, J., and Mills, E., "Electrical Conductivity of Inert Gases-Seed Combination in Shock Tubes Part II," Canadian Journal of Physics, V. 43, p. 1334 to 1341, July 1965.
14. Stokes, A.D., "Induction-Field Calculations and Their Application to Measurements of Conductivity Distribution in Cylindrical Plasmas," Proceedings of the Institution of Electrical Engineers, V. 112, p. 1583 to 1588, August 1965.
15. Lubin, B.T., Foldvari, T.L., and Jackson, W.D., "Nonlinear Networks for the Measurement of the Relative Electrical Conductivity Between High Conducting Materials," Review of Scientific Instruments, V. 36, p. 1663 to 1664, November 1965.
16. Stubbe, E.J., "A Measurement of the Electrical Conductivity of Plasmas," American Institute of Aeronautics and Astronautics, Plasmadynamics Conference, Monterey, Calif. March 2-4, 1966, Paper 66-181.

17. Persson, K.B., "A Method for Measuring the Conductivity in a High Electron Density Plasma," Journal of Applied Physics, V. 32, p. 2631 to 2640, 1961.
18. Abramowitz, M. and Stegun, I.A., Editors, "Handbooks of Mathematical Functions," National Bureau of Standards Applied Mathematics Series No. 55, Government Printing Office, Washington, D.C.

APPENDIX A

ANALYSIS OF PLANE PROBE

In the dielectric, $|x| < a$, the permeability is μ , and the permittivity is ϵ_1 . Then the vector potential is

$$A_y = A_1 \sin (2\pi x/\lambda_1) \quad (\text{A-1})$$

where $\omega \sqrt{\mu_1 \epsilon_1} = 2\pi/\lambda_1$. The field components are

$$H_z = (2\pi A_1/\lambda_1) \cos (2\pi x/\lambda_1) \quad (\text{A-2})$$

$$E_y = -j\omega\mu_1 A_1 \sin (2\pi x/\lambda_1) \quad (\text{A-3})$$

In the plasma, $x > a$, the permeability is μ_2 and the conductivity is assumed constant and equal to σ_2 . The vector potential is

$$A_y = -B_1 e^{-(1+j)(x-a)/\delta_2} \quad (\text{A-4})$$

where the skin depth $\delta_2 = 1/\sqrt{\pi f \mu_2 \sigma_2}$. The field components are

$$H_z = [(1+j)/\delta_2] B_1 e^{-(1+j)(x-a)/\delta_2} \quad (\text{A-5})$$

$$E_y = j\omega\mu_2 B_1 e^{-(1+j)(x-a)/\delta_2} \quad (\text{A-6})$$

Assume now that there are N turns of wire per meter length in the Z direction and that each wire carries a current I . The magnetic boundary condition is then obtained from (A-2) and (A-5):

$$(2\pi A_1/\lambda_1) \cos (2\pi a/\lambda_1) - (1+j) (B_1/\delta_2) = NI \quad (\text{A-7})$$

Similarly the electric boundary condition from (A-3) and (A-6) is

$$j\omega\mu_1 A_1 \sin (2\pi a/\lambda_1) - j\omega\mu_2 B_1 = 0 \quad (\text{A-8})$$

The constants A_1 and B_1 are obtained from Equation (A-7) and (A-8):

$$A_1 = \frac{NI}{(2\pi/\lambda_1) \cos(2\pi a/\lambda_1) + [(1+j)/\delta_2] (\mu_1/\mu_2) \sin(2\pi a/\lambda_1)} \quad (A-9)$$

$$B_1 = - \frac{NI (\mu_1/\mu_2) \sin(2\pi a/\lambda_1)}{(2\pi/\lambda_1) \cos(2\pi a/\lambda_1) + [(1+j)/\delta_2] (\mu_1/\mu_2) \sin(2\pi a/\lambda_1)} \quad (A-10)$$

The admittance of the probe is

$$Y = - \frac{I}{2NE_y|_{x=a}} = - \frac{I}{2j\omega\mu_2 B_1 N} \quad (A-11)$$

If Equation (A-10) is substituted in Equation (A-11),

$$Y = \frac{1}{2j\omega\mu_1 N^2} \left[\left(\frac{2\pi}{\lambda_1} \right) \cos \left(\frac{2\pi a}{\lambda_1} \right) + \left(\frac{1+j}{\delta_2} \right) \frac{\mu_1}{\mu_2} \right] \quad (A-12)$$

Now assume that the frequency is low enough so that $\lambda_1 \gg a$, then

$$Y = \frac{1}{j\omega 2N^2 \mu_1 a} + \frac{1}{2N^2 \delta_2 \omega \mu_2} + \frac{1}{j\omega 2N^2 \delta_2 \mu_2}.$$

This may be interpreted as a circuit as shown in Figure C-52 where $R_p = 2N^2 \delta_2 \omega \mu_2$ is the resistance caused by the conduction of the plasma, $L_p = 2N^2 \delta_2 \mu_2$ is the inductance caused by the conduction of the plasma, $L = 2N^2 \mu_1 a$ is the inductance of the coil with no plasma present, and R_w is the ohmic resistance of the coil with no plasma present.

APPENDIX B

ANALYSIS OF CYLINDRICAL PROBE

In the dielectric $r < a$, the permeability is μ and the permittivity ϵ_1 . The coil is assumed very long so that the magnetic field intensity is in the axial direction. Then

$$\frac{1}{r} \frac{d}{dr} \left(r \frac{dH_z}{dr} \right) + \left(\frac{2\pi}{\lambda_1} \right)^2 H_z = 0 \quad (\text{B-1})$$

and

$$H_z = A_1 J_0 (2\pi r / \lambda_1) \quad (\text{B-2})$$

$$E_\phi = -j \sqrt{\mu_1 / \epsilon_1} A_1 J_1 (2\pi r / \lambda_1) \quad (\text{B-3})$$

where

$$\omega \sqrt{\mu_1 \epsilon_1} = (2\pi / \lambda_1) \text{ and } J_0(x)$$

and $J_1(x)$ are Bessel functions of the first kind of zero and first order respectively.

In the plasma, $r > a$, μ_2 is the permeability and σ_2 is the conductivity assumed constant. Then

$$\frac{1}{r} \frac{d}{dr} \left(r \frac{dH_z}{dr} \right) = \left(\frac{1+j}{\delta_2} \right)^2 H_z \quad (\text{B-4})$$

where the skin depth, $\delta_2 = (1 / \sqrt{\pi f \mu_2 \sigma_2})$.

Then

$$H_z = B_1 K_0 [(1+j) r / \delta_2] \quad (\text{B-5})$$

and

$$E_\phi = \frac{B_1 (1+j)}{\delta_2 \sigma_2} K_1 [(1+j) r / \delta_2] \quad (\text{B-6})$$

where $K_0(x)$ and $K_1(x)$ are modified Bessel functions of the second kind of zero and first orders respectively.

Assume that there are N turns of wire per meter length in the axial direction and that each wire carries a current I . The magnetic boundary condition is then obtained from Equation (B-2) and Equation (B-5)

$$A_1 J_0 (2\pi a/\lambda_1) - B_1 K_0 [(1+j)a/\delta_2] = NI \quad (B-7)$$

Similarly the electric boundary condition from Equation (B-3) and (B-6) is

$$-j\sqrt{\mu_1/\epsilon_1} A_1 J_1 (2\pi a/\lambda_1) - \frac{B_1 (1+j)}{\delta_2 \sigma_2} K_1 [(1+j)a/\delta_2] = 0 \quad (B-8)$$

The two equations (B-7) and (B-8) are solved for A and B . The admittance for a meter length is

$$Y = \frac{I}{NE_\phi|_{r=a}} = -\frac{I\delta_2\sigma_2}{NB_1(1+j)K_1[(1+j)a/\delta_2]} \\ = \frac{1}{j\eta_1 N^2 2\pi a} \left\{ \frac{J_0(2\pi a/\lambda_1)}{J_1(2\pi a/\lambda_1)} + \frac{\eta_1(1+j)\mu_0[(1+j)a/\delta_2]}{2R_s K_1[(1+j)a/\delta_2]} \right\} \quad (B-9)$$

where

$$\eta_1 = \sqrt{\mu_1/\epsilon_1} \quad \text{and} \quad R_s = (1/\sigma_2 \delta_2). \quad (B-10)$$

Now assume that the frequency is low enough so that $\lambda_1 \gg a$, then

$$Y = \frac{1}{j\omega(\mu_1 N^2 \pi a^2)} + \frac{1}{R_p} + \frac{1}{j\omega L_p} \quad (B-11)$$

and

$$\frac{1}{R_p} + \frac{1}{j\omega L_p} = \frac{(1-j)}{N^2 4\pi a R_s} \frac{K_0[(1+j)a/\delta_2]}{K_1[(1+j)a/\delta_2]} \quad (B-12)$$

This may be interpreted as the circuit of Figure C-52 where $L = \mu_1 N^2 \pi a^2$ is the inductance of the coil with no plasma. It is possible to show also that with no plasma ($\sigma_2 = 0$), $R_p \rightarrow \infty$ and $L_p \rightarrow \infty$. The ohmic resistance of the coil per meter of length is taken as R_w .

$$K_\nu(x e^{j\pi/4}) = (\ker_\nu x + j \operatorname{kei}_\nu x) e^{(j\pi\nu/2)} \quad (\text{B-13})$$

Then:

$$R_p = -4\pi a N^2 R_s [(\ker_1 x)^2 + (\operatorname{kei}_1 x)^2] / D \quad (\text{B-14})$$

$$L_p = 4\pi a N^2 R_s [(\ker_1 x)^2 + (\operatorname{kei}_1 x)^2] / \omega D \quad (\text{B-15})$$

where

$$D = (\ker x)(\ker_1 x) + (\operatorname{kei} x)(\operatorname{kei}_1 x) + (\operatorname{kei} x)(\ker_1 x) - (\ker x)(\operatorname{kei}_1 x)$$

and $x = \sqrt{2} a / \delta_2$. For small values of the following approximate values may be used:

$$K_0(x e^{j\pi/4}) = -\ln x - (j\pi/4)$$

$$K_1(x e^{j\pi/4}) = (1 - j) / \sqrt{2} x \quad (\text{B-16})$$

When Equation (B-16) is used in Equation (B-12):

$$R_p = - \frac{4\pi N^2}{\sigma_2 \ln(\omega \mu_2 \sigma_2 a^2)}$$

$$L_p = (8N^2 / \sigma_2 \omega) \quad (\text{B-17})$$

APPENDIX C

CONDUCTIVITY MODEL

Assume that the plasma can be described by the cold plasma equations and that the electrons and ions interact with the neutral particles through a drag force. Then

$$\frac{\partial n_i}{\partial t} + \nabla \cdot (n_i \bar{v}_i) = 0 \quad (C-1)$$

$$\frac{\partial \bar{v}_i}{\partial t} + (\bar{v}_i \cdot \nabla) \bar{v}_i = \frac{e_i}{m_i} (\bar{E} + \bar{v}_i \times \bar{B}) - \nu_i \bar{v}_i \quad (C-2)$$

where i represents the species type e_i is the charge of the i th species, m_i is the mass of the i th species, \bar{v}_i is the velocity of the i th species, $\nu_i \bar{v}_i$ is the drag on the i th species caused by momentum transfer to neutral particles.

The field equations are

$$\nabla \cdot \bar{E} = \frac{\partial \bar{B}}{\partial t} \quad (C-3)$$

$$\nabla \times \bar{H} = J + \epsilon_0 \frac{\partial \bar{E}}{\partial t} \quad (C-4)$$

$$\nabla \cdot \bar{B} = 0 \quad (C-5)$$

where

$$J = \sum_i e_i n_i \bar{v}_i$$

Now assume that there is no streaming and that the fields are small, then the equations may be linearized about the first order quantities represented by the superscript (1). Thus,

$$\bar{V}_i = \bar{V}_i^{(1)}$$

$$\bar{E} = \bar{E}^{(1)}$$

$$\bar{B} = \bar{B}^{(1)}$$

$$n_i = N_i + n_i^{(1)} \quad (C-6)$$

where N_i is the unperturbed density of the i^{th} species. Also sinusoidal solutions will be assumed. Then

$$j \omega \bar{V}_i^{(1)} = \frac{e_i}{m_i} \bar{E}^{(1)} - \nu_i \bar{V}_i^{(1)} \quad (C-7)$$

$$\nabla \times \bar{B}^{(1)} = \mu_0 \bar{J}^{(1)} + \mu_0 \epsilon_0 j \omega \bar{E}^{(1)} \quad (C-8)$$

$$\nabla \times \bar{E}^{(1)} = -j \omega \bar{B}^{(1)} \quad (C-9)$$

$$\bar{J}^{(1)} = \sum_i e_i N_i \bar{V}_i^{(1)} \quad (C-10)$$

$$\nabla \cdot \bar{B}^{(1)} = 0 \quad (C-11)$$

substitute Equation (C-7) in (C-10) and Equation (C-10) in (C-8):

$$\nabla \times \bar{B}^{(1)} = \left[\mu_0 \sum_i \frac{e_i^2 N_i}{m_i} \left(\frac{1}{j \omega + \nu_i} \right) + \mu_0 \epsilon_0 j \omega \right] \bar{E}^{(1)} \quad (C-12)$$

Now take the curl of Equation (C-12):

$$\nabla^2 \bar{B}^{(1)} = \left[\mu_0 \sum_i \frac{e_i^2 N_i}{m_i} \left(\frac{1}{j \omega + \nu_i} \right) + \mu_0 \epsilon_0 j \omega \right] j \omega \bar{B}^{(1)} \quad (C-13)$$

If now the plasma conductivity

$$\sigma = \sum_i \frac{e_i^2 N_i}{m_i} \left(\frac{1}{j\omega + \nu_i} \right)$$

Then Equation (C-13) becomes

$$\nabla^2 \bar{B}^{(1)} - (j\omega\mu_0\sigma - \mu_0\epsilon_0\omega^2) \bar{B}^{(1)} = 0 \quad (C-15)$$

which is the usual form of the wave equation. For low frequencies ω would be small compared to ν_i and the conductivity would become

$$\sigma = \sum_i \frac{e_i^2 N_i}{m_i \nu_i} \quad (C-16)$$

THE PRODUCTION OF UNIFORM GRADIENT MAGNETIC FIELDS

D. L. Waidehch

N 67-22767

A magnetic field with a constant gradient over a large volume is useful in helping to cancel the gradients present in the magnetic field produced by a coil system. The purpose here is to present some information on many of the papers that have discussed various phases of the subject of gradients in coil systems.

The first works on coil systems designed to produce very uniform gradient fields appear to be those of McKeehan [M1], [M2], who was interested in measuring the properties of ferromagnetic materials. He presented the theory for both the two-coil, fifth-order gradient coil system and a four-coil, ninth-order system with the same number of ampere - turns in each of the four coils. The conditions for a rectangular coil cross sections were also discussed. The next work was that of Shortley and May [S2] who were concerned with the use of magnetic gradients in naval ordnance work. They presented various cylindrical and spherical coil systems to produce very uniform gradients. Bertein [B2], [B4] advanced the idea that five coils could be used to cancel the constant field and linear gradient field components of the total magnetic field. His work was concerned primarily with electron optics.

In the last fifteen years the number of papers on gradient fields has increased considerably. Very large gradients [L1] have been produced, and current shims [A1] have been used to reduce the field gradients in magnetic resonance experiments. The conditions for a two-coil gradient system of the fifth-order [Bp] as well as the results for rectangular coil cross section have been given. A seventh-order gradient system [P1] was designed and constructed, and experimental results were presented. Gradient coils were constructed [G1] in such a way that each pair produced a field described by one of a set of the spherical harmonics. Thirteen coil pairs were used and thirteen current adjustments could be made without interfering with each other. Two types of coils were used, one was plane and the other was on the surface of a sphere. Various gradient coils were constructed for reducing transverse and longitudinal gradients in nuclear magnetic resonance work [V1].

In the 1960's, printed circuits coils [E1] were employed in reducing the axial field gradients in NMR work, while rectangular coils were used to produce gradients [D1] to compensate for existing gradients present in the magnetic field being measured by a nuclear magnetometer. Rectangular and circular shim coils were designed and constructed to counteract the more important gradients [A2] in NMR work. Current shims in the form of parallel wires [Z1] were also used in nuclear resonance experiments. The gradient in the axial field for a four-coil system used in space research [W1] was determined. McKeehan's work [M1] was continued on four-coil systems to produce gradients uniform to the ninth order over the whole possible range of parameters [S1]. Many of the various possible gradients that can be produced in a large octagonal coil system for use in space research have been computed [B3]. The work of Golay [G1] was extended to cylindrical coils [F1] for use in NMR work. Two coils to produce a gradient field were placed between two iron pole faces [T1]. The effect of the magnetic images in the pole faces on the optimum spacing of the coils was calculated.

REFERENCES

- A1 Arnold, J.T., "Magnetic Resonances of Protons in Ethyl Alcohol," Physical Review, V. 102, p. 136 to 150, 1956.

Current shims in the form of nine concentric flat spiral coils attached to each iron pole face were used to reduce the field gradients. The currents in the coils were adjusted by trial and error.

- A2 Anderson, W.A., "Electrical Current Shims for Correcting Magnetic Fields," Review of Scientific Instruments, V. 32, p. 241 to 250, March 1961.

An analysis is presented giving the various gradients that would be important in a particular field direction. Rectangular shim coils in parallel planes are then designed to counteract these various gradients. A similar design is given for circular shim coils. Experimental shim curves were made and appeared to work satisfactorily although some of the higher order gradient coils were not completely independent of the lower order coils.

- B1 Berger, W., and Butterweck, H.J., "Die Berechnung von Spulen zur Erzeugung homogener, Magnetfelder und konstanter Feldgradienten," Archiv für Elektrotechnik, V. 42, p. 216 to 222, 1956.

The conditions for a two coil system of the fifth order and for coils of finite rectangular cross section M2 are given.

- B2 Bertein, F., "Sur la réalisation de champs statiques uniformes," Comptes Rendus Académie des Sciences Paris, V. 234, p. 308 to 309, January 14, 1952.

The magnetic potential may be expanded in a series which has five constants if powers above the second are neglected. Theoretically then five magnets or five coils could be placed to eliminate the linear and second order terms in the potential thus making a more uniform field.

- B3 Bloom, A.A., Innes, D.J., Rempel, R.C. and Ruddock, K.A., "Octagonal Coil Systems for Cancelling the Earth's Magnetic Field," Journal of Applied Physics, V. 36, p. 2560 to 2565, August 1965.

Tables are given for the gradients created in an octagonal coil system of four coils. The reasons for the gradients would be an increase in the diameter of a coil, the movement of the coil parallel or perpendicular to the axis of the system, and displacement of one side of a coil parallel or perpendicular to the axis.

- B4 Bertein, F., "Relation entre les Defauts de Realisation de Lentilles et la Nettete des Images," Annales de Radioelectricite, V. 11, p. 379 to 408, October 1947.

It is shown that there are five first-order gradients and that these might be corrected by the use of five coils carrying current.

- D1 Denisov, Y.N., "Nuclear Magnetometers for Measuring Field Strength and Gradient in Highly Inhomogeneous Fields," Instruments and Experimental Techniques, p. 89 to 90, 1961.

Rectangular coils are used to produce gradients for compensation of the existing gradients in a magnetic field. The equations for the gradients produced are given for two different cases of rectangular coils.

- E1 Evans, B.A. and Richards, R.E., "Temperature-controlled Permanent Magnet for High-Resolution Nuclear Magnetic Resonance," Journal of Scientific Instruments, V. 37, p. 353 to 355, 1960.

The construction and use of two printed-circuit coils are described for the reduction of axial field gradients.

- F1 Frolov, V.V. and Kolikhov, I.A., "Orthogonal Compensators of Inhomogeneity of Magnetic Field for a Nuclear Magnetic Resonance Spectrometer," NASA N65-17569.

The idea of Golay [G1] was applied to the calculation of compensating coils for a solenoid. The coils were located on the surface of a cylinder and resulted in a homogeneity an order of magnitude better than the solenoid without compensation.

- G1 Golay, M.J.E., "Field Homogenizing Coils for Nuclear Spin Resonance Instrumentation," Review of Scientific Instruments, V. 29, p. 313 to 315, April 1958.

Gradient coils are designed in the form of two thin flat stacks which contain 13 coil pairs, each pair of which produced at the center a magnetic field describable by one of a set of spherical harmonics. The 13 current adjustments can be made without interfering with each other. The coils were also placed on the surfaces of a sphere.

- L1 Lin, S.T. and Kaufmann, A.R., "Helmholtz Coils for Production of Powerful and Uniform Fields and Gradients," Review of Modern Physics, V. 25, p. 182 to 190, January 1953.

A gradient coil 5.2 centimeters in mean radius is used. The gradient produced is 100 oersteds per centimeter at a power of 2.5 kilowatts, and the uniformity of the gradient is 140 parts per million.

- M1 McKeehan, L.W., "Combinations of Circular Currents for Producing Uniform Magnetic Field Gradients," Review of Scientific Instruments, V. 7, p. 178 to 179, April 1936.

Using one pair of coils for a fifth-order gradient, the spacing is $\sqrt{3}$ times the radius of the coils. With two pairs of coils and the same current and turns in each coil, a ninth-order gradient system is calculated. The conditions for a finite rectangular coil cross section is also given.

- M2 McKeehan, L.W., "Pendulum Magnetometer for Crystal Ferromagnetism," Review of Scientific Instruments, V. 5, p. 265 to 268, 1934.

The parameters for a fifth-order gradient system using two coils are given with the spacing as $\sqrt{3}$ times the radius of one coil. If the cross section of the coils are rectangular, the ratio of the axial length to the radial depth of the coil should be $\sqrt{37/44}$.

- P1 Primas, H. and Günthard, H.H., "Herstellung sehr homogener axialsymmetrischer Magnetfelder," Helvetica Physica Acta, V. 30, p. 331 to 346, 1957.

An analysis is made for the gradient coils in the gap between two iron pole faces assumed infinite in extent and of infinite permeability. A seventh order gradient system is then designed and constructed and an experimental curve of the results is presented.

- S1 Shiao, S.F., "Production of a Uniform Magnetic Field Gradient," University of Missouri Report, Engineering Library, January 1964.

Four-coil systems with gradients uniform to the ninth order are calculated over the whole possible range of parameters. The results are tabulated and also shown as curves.

- S2 Shortley, G.H. and May, A., "Coil Systems for Producing Transverse and Longitudinal Magnetic Gradients," Journal of Applied Physics, V. 16, p. 841 to 843, December 1945.

Cylindrical and spherical coil systems are given for producing very uniform gradients. Deviation of the gradients from their values in the center are presented in the forms of equations, curves, and tables.

- T1 Tanner, J.E., "Pulsed Field Gradients for NMR Spin-Echo Diffusion Measurements," Review of Scientific Measurements, V. 36, p. 1086 to 1087, August 1965.

It is assumed that two coils are between two infinite parallel slabs of infinite permeability. The optimum spacing of the coils for a uniform field gradient is given as a curve. Some constructional details of the coils and a field gradient plot are also presented.

- V1 Vincent, C.H., King, W.G., and Rowles, J.B., "A Modification of the Nuclear Resonance Method for Measurements of Non-Uniform Magnetic Fields," Nuclear Instruments and Methods, V. 5, p. 254 to 258, 1959.

The construction of coils used to compensate for transverse and longitudinal magnetic field gradients is presented.

- W1 Waidelich, D.L. and Pittman, M.E., "Magnetic Field Simulation," NASA STAR N65-35427.

The gradient in the axial field is determined for the case that one of the inner coils of a four coil system is moved a small distance parallel to the axis of the system.

- Z1 Zupanviv, I., "Current Shims for High-Resolution Nuclear Magnetic Resonance on the Problem of Correcting Magnetic Field Inhomogeneities," Journal of Scientific Instruments, V. 39, p. 621 to 624, 1962.

Straight parallel wires are placed on the iron pole faces and the axial flux density is obtained using the method of images.

SUMMER WORKSHOP 1966

Program Outline and Team Participants

PROJECT D: Atmospheric Studies

Problem Topics

- D-1 Thermopile calibration
- D-2 Calibration of the six-foot spherical integrator
- D-3 Absorption coefficients of various gases from 1000A to 2000A

PRECEDING PAGE BLANK NOT FILMED.

PROJECT D: ATMOSPHERIC STUDIES

CONTENTS

	<u>Page</u>	
CONTINUING INVESTIGATION OF THERMOPILE CALIBRATION	393	✓
E. I. Mohr		
CALIBRATION OF THE SIX-FOOT SPHERICAL INTEGRATOR	399	✓
E. I. Mohr		
A HIGH RESOLUTION SPECTROMETER FOR MEASURING ABSORPTION CROSS- SECTIONS BETWEEN 1000A AND 2000A	409	✓
J. H. McElaney		

CONTINUING INVESTIGATION OF THERMOPILE CALIBRATION

E. I. Mohr* /

N 67-22768

INTRODUCTION

In connection with the 1965 Summer Workshop, a report was made on the testing and calibration of thermopiles (Reference 1). The report included the results of measurements of the field of view of the thermopile, the reflectance of Parson's black, and the calibration of the thermopile by means of quartz-iodine lamps and by means of a blackbody operating at several temperatures.

One would expect that the calibration curves would be the same regardless of the respective standard sources used. However, different calibration curves were obtained for the quartz-iodine lamp and for each blackbody temperature. In the case of each calibration curve, it was found that the responsivity of the thermopile decreased as the intensity of the source decreased (i.e., as the distance between source and detector increased). Moreover the responsivity was greater as the temperature of the source decreased. When the intensity was varied by means of a rotating sector, the responsivity remained constant.

It was suggested that the difference between the curves might be due to inaccuracy in determining the temperature of the blackbody and/or the effect of the absorption by water vapor and carbon dioxide. Thus it was proposed that the blackbody temperature be re-examined and that an attempt be made to vary the intensity of the source by use of neutral density filters instead of varying the distance between the detector and the source.

THE TEMPERATURE OF THE BLACKBODY

In the investigation of 1965, a Barnes' blackbody was used. In the present investigation an Infrared Industries blackbody model 406 was used. The latter has the advantage of having a face plate which does not get as hot as in the case of the former. It also has a larger aperture, thus giving a greater amount of flux. In addition, there is a built-in thermocouple of platinum-platinum plus 10 percent rhodium to measure the operating temperature of the blackbody. The temperatures given by this thermocouple were checked by inserting a platinum-platinum plus 13 percent rhodium thermocouple into the blackbody cavity. The two measurements agreed within two to three degrees Kelvin.

The responsivity of the Eppley thermopile 4928A was determined by using apertures of 0.6" and 0.4" at each of the following temperatures: 897°K, 1102°K and 1217°K. This was repeated for the standard 200w quartz-iodine lamp QL-46. Each aperture as well as each blackbody temperature gave a different calibration curve. Moreover each one of these curves differs from that for the quartz-iodine lamp. These results are shown in Figure D-1.

Although the blackbody temperatures used seemed to be correct as determined by the two thermocouples, it seemed best to check this further. Thus it was assumed that the temperature used might be in error and calculations were made to determine what the blackbody temperature ought to be in order to obtain a responsivity of the thermopile which agreed with that for the quartz-iodine lamp. The calculations were made assuming the source to be placed 25 cm. from the detector

*Chairman, Physics Department, Columbia Union College

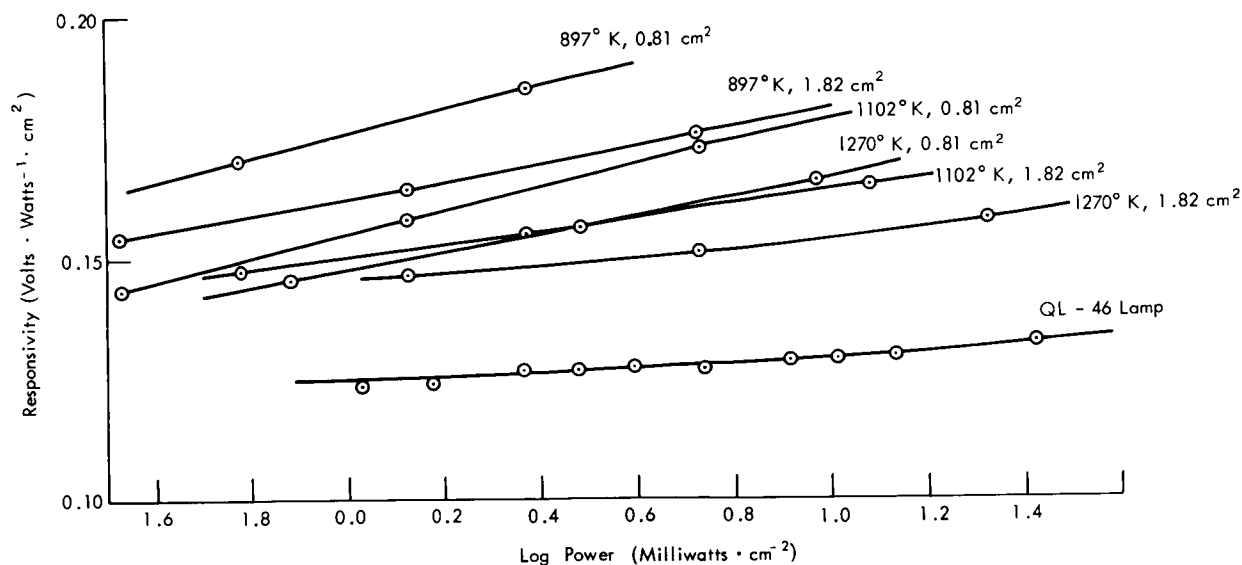


Figure D-1—Responsivity of thermopile 4928A to Infrared Industries blackbody and to quartz iodine lamp QL-46.

in each case. Using these hypothetical temperatures, new calibration curves were determined for each temperature. The resulting data for a blackbody aperture of 0.6" are shown in Figure D-2. It will be noted that the resulting curves do not coincide nor do they have the same slope as that for the quartz-iodine lamp. Hence it would seem that the accuracy of the blackbody temperature may not be the explanation for the difference in the curves in Figure D-1.

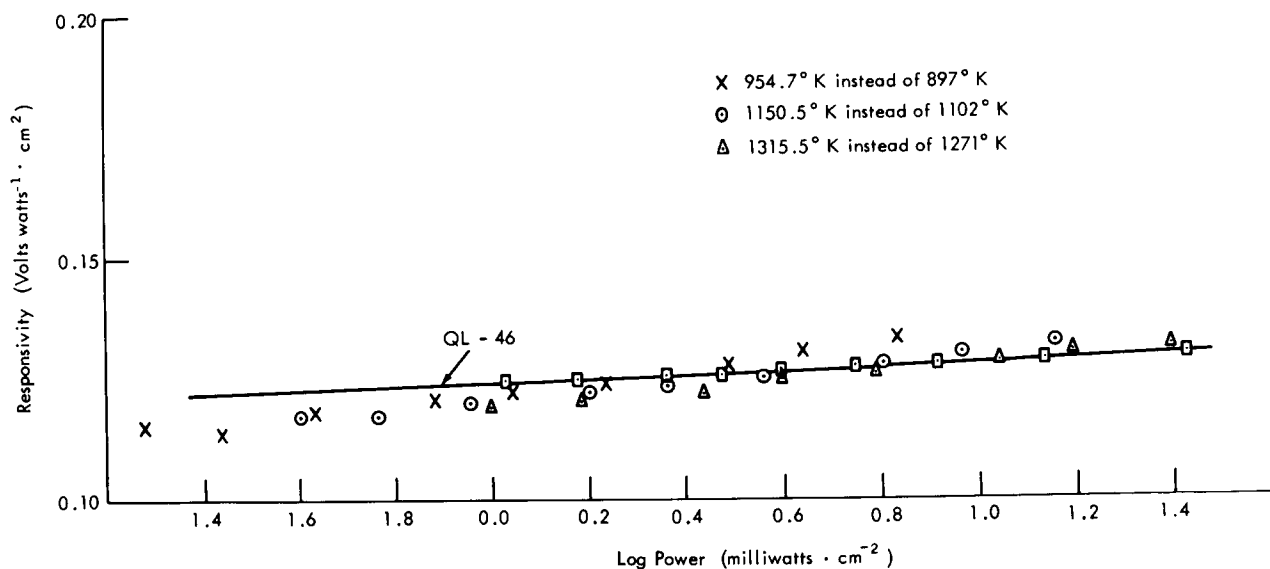


Figure D-2—Responsivity of thermopile 4928A to Infrared Industries blackbody normalized to responsivity to quartz iodine lamp QL-46 at 25 cm.

EFFECT OF ABSORPTION BY WATER VAPOR AND CARBON DIOXIDE

Theoretical calculations on the effect of absorption of infrared radiation by water vapor and carbon dioxide have been reported by Wyatt, Stull, and Plass (References 2 and 3). These calculations

agree quite well with experimental results reported by Burch et al. (Reference 4). Most of this work was done for rather long air paths and is not applicable for paths varying between 25 cm. and 125 cm. The most useful data are the experimental values by Burch et al., which give the total absorption by H_2O and CO_2 in the various absorption bands. This data was plotted on semilogarithmic paper. The absorption for the various path lengths used in calibrating the thermopile was read from these curves. This is illustrated by the curve for the CO_2 band at 4.25 microns (Figure D-3).

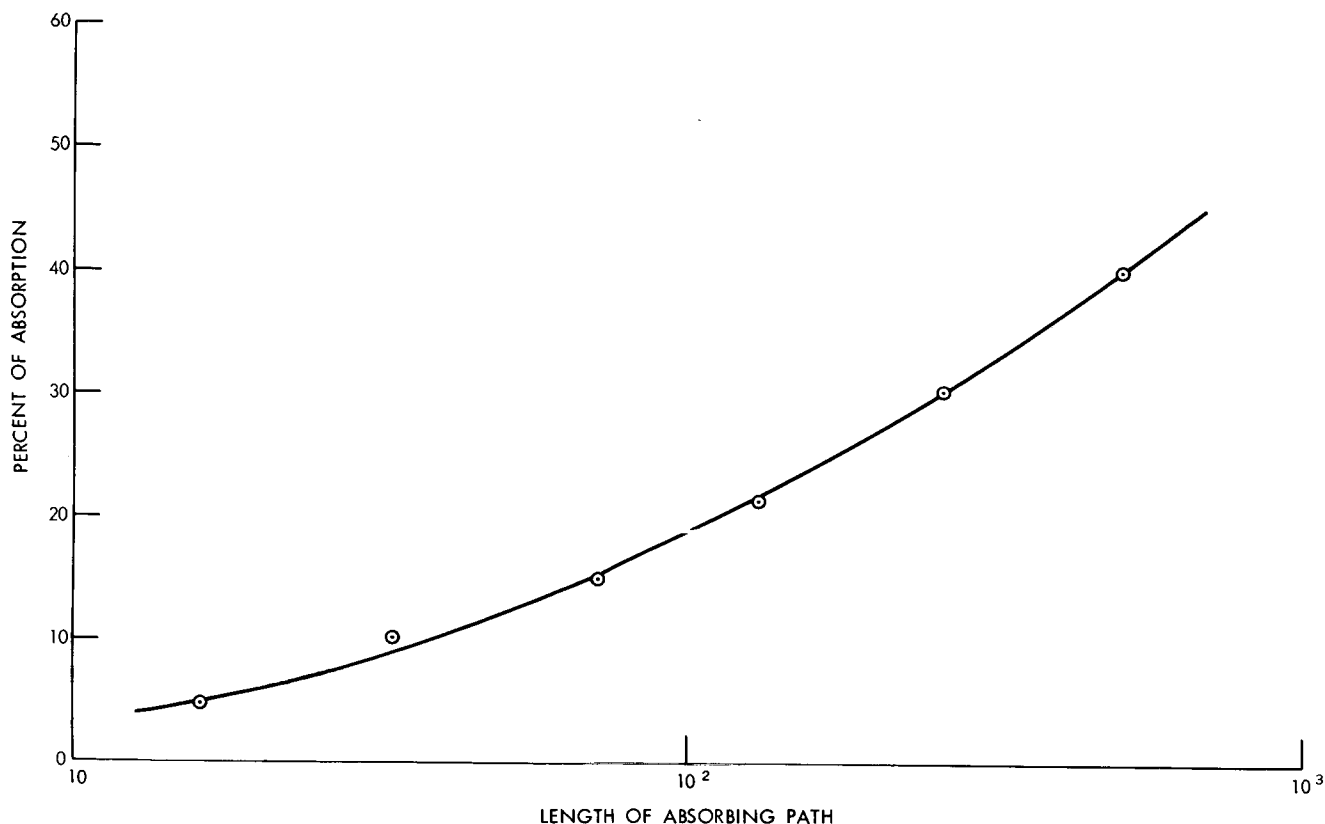


Figure D-3—Total IR absorption by carbon dioxide in the 4.25M band

The intensity of the flux corresponding to each position of the thermopile was determined by the inverse square law, corrected for the finite size of the source. The resulting intensity was corrected for the effect of the absorption by the H_2O and CO_2 bands. The resulting net flux was used to calculate the responsivity of the thermopile. This is shown in Figure D-4 for two black-body temperatures and the quartz-iodine lamp. A comparison of Figures D-1 and D-4 shows the responsivity is slightly higher and the slope slightly less after the correction has been made for absorption. Nevertheless, the responsivities at the different temperatures are still quite different.

Calculations were also made to determine the responsivity of the thermopile when the flux was corrected both for the effect of absorption by H_2O and CO_2 , and for possible error in black-body temperature by normalizing it to the quartz-iodine lamp output at 25 cm. The combined effect of correction for absorption and possible temperature error gave calibration curves differing one from the other in slope, similar to the results shown in Figure D-2.

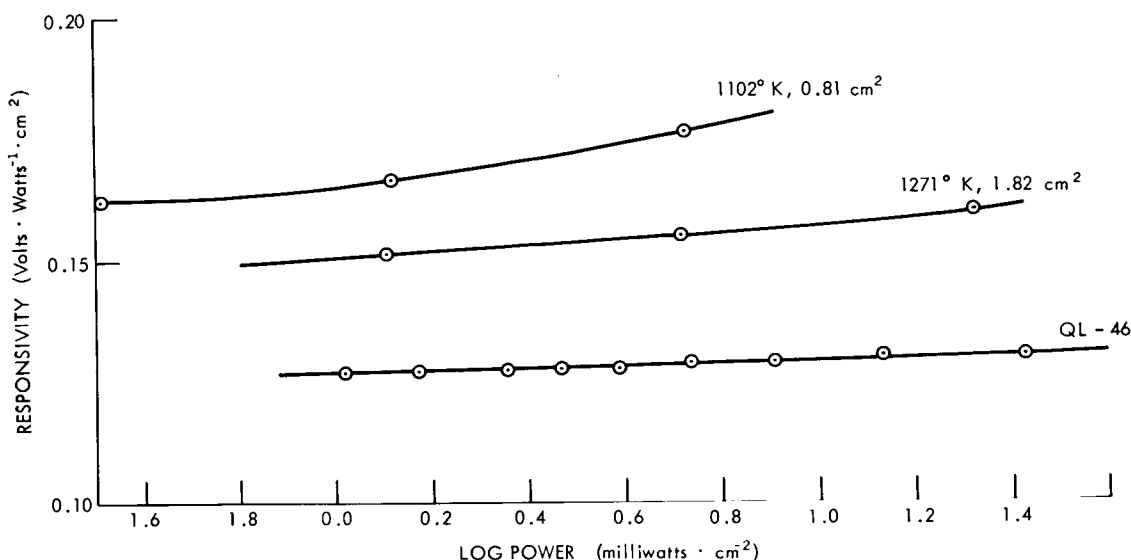


Figure D-4—Responsivity of thermopile 4928A to Infrared Industries Blackbody and to quartz iodine lamp QL-46 after correction for H_2O and CO_2 absorption.

THE USE OF NEUTRAL DENSITY FILTERS

In order to determine the responsivity of a detector as a function of flux intensity, one must be able to vary the amount of flux which the detector receives from a standard source. This may be done by varying the distance between source and detector and applying the inverse-square law. As noted above, the responsivity in this case is not constant but decreases as distance increases. As reported previously in Reference 1, when the intensity was varied by means of a rotary sector, the responsivity remained relatively constant.

It was suggested that the use of neutral density filters might be investigated as a means of varying the intensity. Thus a number of neutral density filters were made by mounting etched metallic screens. These screens were of two kinds; a coarse screen etched on a thin sheet of copper and a fine screen etched on a thin sheet of nickel. The resulting perforations are in the shape of small squares uniformly distributed on the screens. Two filters were made by using a single layer of each kind of screen and two more were made using two layers of a given screen.

The transmittance of these screens in the infrared (2.5 to 20 microns) was measured by means of a Cary 90 double beam spectrophotometer. A Cary 14 double beam spectrophotometer was used to measure the transmittance in the UV, visible, and near IR (0.25 to 2.5 microns). The transmittance of two filters is shown in Table D-1. It will be observed that these screens are not completely neutral in the infrared since the transmittance decreases slightly with increasing wavelength.

The responsivity of the thermopile was determined by using these neutral density filters to vary the flux received by the thermopile, while detector and source were held at a fixed separation of 25 cm. The results for the quartz-iodine lamp and for two blackbody temperatures is shown in Figure D-5. It will be observed that there is a small increase in responsivity as the intensity of the flux decreases.

Some preliminary measurements of the transmittance in the IR (2.5 to 40 microns) were made with a Perkin-Elmer double beam spectrophotometer model 621. Since the instrument was taken

Table D-1
Transmissions of Neutral Density Filters

λ	τ 90		λ	τ 90		λ	τ 90	
Microns	Screen 7	Screen 8	Microns	Screen 7	Screen 8	Microns	Screen 7	Screen 8
.25	53.9	29.2	1.5	53.0	29.0	4.6	52.6	28.4
.26	53.9	29.2	1.6	52.9	29.0	4.8	52.5	28.4
.27	53.9	29.2	1.7	52.9	29.0	5.0	52.5	28.4
.28	53.9	29.2	1.8	52.9	29.0	5.5	52.4	28.3
.29	53.9	29.2	1.9	52.9	29.0	6.0	52.3	28.1
.30	53.9	29.2	2.0	52.9	29.0	6.5	52.3	28.0
.32	53.9	29.2	2.1	52.8	29.0	7.0	52.3	27.9
.35	53.9	29.2	2.2	52.8	29.0	7.5	52.3	27.9
.37	53.9	29.2	2.3	52.8	29.0	8.0	52.3	27.7
.40	53.9	29.2	2.4	52.8	29.0	8.5	52.1	27.6
.45	53.8	29.2	2.5	52.8	29.0	9.0	52.0	27.5
.50	53.8	29.2	2.6	52.8	29.0	9.5	52.0	27.2
.55	53.8	29.2	2.7	52.8	29.0	10.0	51.9	27.2
.60	53.7	29.2	2.8	52.8	29.0	11.0	51.7	27.1
.65	53.7	29.2	2.9	52.8	28.9	12.0	51.6	27.0
.70	53.7	29.2	3.0	52.8	28.9	13.0	51.6	27.0
.75	53.7	29.2	3.2	52.7	28.8	14.0	51.6	27.0
.80	53.6	29.2	3.4	52.7	28.8	15.0	51.6	27.0
.90	53.6	29.2	3.6	52.7	28.7	16.0	51.6	27.0
1.00	53.5	29.1	3.8	52.7	28.7	17.0	51.6	26.8
1.1	53.5	29.0	4.0	52.7	28.6	18.0	51.3	26.4
1.2	53.2	29.0	4.2	52.6	28.5	19.0	51.0	26.3
1.3	53.2	29.0	4.4	52.6	28.5	20.0	51.0	26.3
1.4	53.1	29.0						

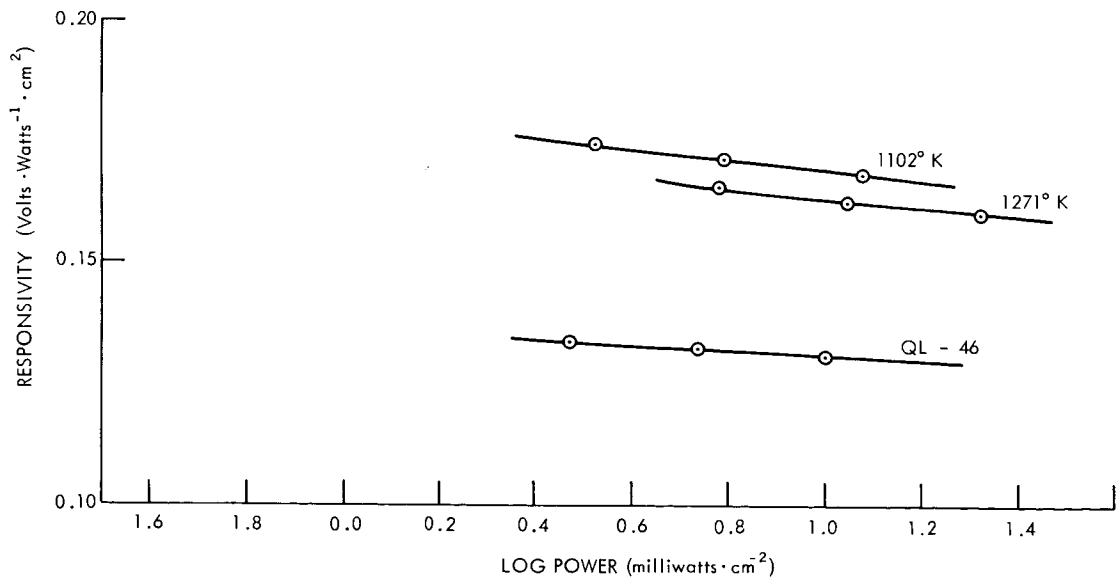


Figure D-5—Responsivity of thermopile 4928A to Infrared Industries blackbody and to quartz iodine lamp QL-46 by use of neutral density filters.

to the factory for adjustment, it was not possible to get final measurements on the transmittance with the Perkin-Elmer. It is interesting, however, to note that the preliminary measurement gave a transmittance of the screens in the IR which was slightly higher than the values obtained with the Cary 90. If the data with the Perkin-Elmer is taken at face value, the responsivity of the thermopile would be approximately constant as one would expect, since distance and hence any decrease in intensity which might be produced by absorption should remain constant.

CONCLUSIONS

In view of the results reported here in 1965 (reference 1), it is not possible to explain the different calibration curves of the thermopile in terms of the absorption by H_2O and CO_2 nor by errors in the determination of the blackbody temperature.

It is possible, however, that the difference in responsivity might be due in part to a variation in the absorption of the radiation at different wavelengths by Parson's black which is used in the thermopile. Another factor might be a difference in the reflectivity of the Parson's black at different wavelengths. Such a wavelength dependence could make a considerable difference between the theoretical and actual energy received by the thermopile from the blackbody at different temperatures, and thus in the responsivity of the thermopile.

REFERENCES

1. GSFC Final Report of the Summer Workshop Program, p. B-23.
2. Wyatt, P. J., Stull, V. R. and Plass, G. N., "The infrared absorption of water vapor." Infrared Transmission Studies, Final Report, SSD-TDR-62-127 - Volume II, 1962.
3. Stull, V. R., Wyatt, P. J. and Plass, G. N., "The infrared absorption of carbon dioxide," Infrared Transmission Studies, Final Report, Vol. III, SSD-TDR-62-127, Volume III, 1963.
4. Burch, D. E., Gryvnak, D., Singleton, E. B., France, Wilbur L. and Williams, D., "Infrared absorption by carbon dioxide, water vapor, and minor atmospheric constituents," Ohio State University, 1962. Contract AF 19(604)-2633. AFCRL-62-698.

OK

CALIBRATION OF THE SIX-FOOT SPHERICAL INTEGRATOR

E. I. Mohr*

N 67-22769

INTRODUCTION

Several years ago the Planetary Radiation Branch of the Laboratory for Atmospheric and Biological Sciences purchased a six-foot spherical integrator for possible use as a wide angle source for the calibration of radiometers in the visible and near infrared regions.

Some members of team A of the 1964 Summer Workshop calibrated this spherical integrator (Reference 1). The calibration was based on the use of the Eppley water-cooled thermopile 4928A. Subsequent investigations have shown decided differences in the response of the thermopile to a standard quartz-iodine lamp and to a blackbody operated at various temperatures (References 2 and 3). These differences in the response of the thermopile to various sources indicate that the calibration of the spherical integrator by means of the thermopile is in doubt. For this reason a new approach was proposed. The present report is based on the initial work done to implement this proposal.

THEORY OF THE SPHERICAL INTEGRATOR

The principle of spherical integration was proposed by Sumpner (Reference 4) in 1892. He showed that if a source of light is placed inside a hollow sphere which is coated internally with a perfectly diffusing coat, the luminance of any position of the surface due to light reflected from the rest of the sphere is everywhere the same and is directly proportional to the total flux emitted by the source.

It is easy to show that the theoretical expression for this relation in terms of the reflectance ρ , of the perfectly diffusing coat of the sphere wall due to an infinite number of reflections is given by

$$\Phi = \frac{F}{4\pi r^2} \frac{\rho}{1 - \rho} \quad (1)$$

where Φ is the total radiant flux reaching unit area of the spherical surface by reflection, F the total flux emitted by the source and r the radius of the sphere (see Reference 5). In the derivation of Equation (1) it is assumed that ρ is constant, that the surface is a perfect diffuser, that the sphere is empty and that it has no ports. As a matter of fact, the reflectance, ρ , of the coating varies with wavelength. Moreover there is no perfect diffuser so that Lambert's cosine law does not hold accurately. In addition, the sphere has sources, shields, and ports, all of which affect the total radiant flux. Because of these uncertainties one cannot expect to make absolute measurements of flux. This does not prevent one, however, from using it to find relative values of flux from two sources if proper precautions are taken.

It has been shown that the error introduced by the finite size of holes and sample may be as much as 25 percent (Reference 6). Moreover, the spectral dependence of the reflectance can modify considerably the spectral distribution of the flux streaming from the port of the sphere (Reference 1).

Thus the intensity is increased for those wavelengths for which the reflectance is high and decreased for wavelengths for which the reflectance is low.

THE SPHERICAL INTEGRATOR

The spherical integrator of the Planetary Radiation Branch is a six-foot diameter fiberglass shell mounted on a movable frame. The inner surface is painted with Burch sphere paint. The source consists of twelve 200-watt quartz-iodine lamps to provide for twelve levels of output intensity. There are two 1.5 inch viewing ports. A fan is mounted on top of the sphere over a 1.5 inch hole, which together with a three inch port, provides ventilation. (A more complete description has been given in Reference 1.)

THE RELATIVE SPECTRAL DISTRIBUTION

Since the integrating effect of the sphere is influenced by the spectral dependence of the reflectance, it is necessary to compare the spectral distribution of the output with that from a standard of spectral irradiance. Tests have shown that the number of lamps has little effect upon the spectral distribution of the output (Reference 1), hence twelve lamps were used in order to get satisfactory intensity for the calibration.

The measurements of the spectral distribution of the sphere were made with a Perkin-Elmer model 99 double-pass monochromator. The slit of the monochromator was positioned as close to a port of the spherical integrator as possible. The spectral distribution of the output flux from the sphere was recorded by a Leeds and Northrup recorder. For the wavelength range from 0.45 to 2.6 microns, a Reeder thermocouple detector with quartz-window was used, while a photomultiplier detector 1P28 served as detector for the range from 0.35 to 0.7 microns. Whenever it was necessary to change the slit width of the monochromator or the gain of the amplifier, a portion of the previously recorded spectral range was scanned in order to normalize all parts of the recorded range.

In order to get the spectral distribution of the standard of irradiance, the NBS calibrated 1000-watt quartz-iodine lamp QM-95 was positioned about 3 meters in front of the slit of the monochromator and on a line with its axis. The spectral distribution of the standard lamp was obtained under the same conditions of slit width and gain as were used to obtain the spectral distribution of the output of the sphere. The results were normalized as before.

The normalized recorder deflections obtained for the output of the sphere were divided by the corresponding normalized recorder deflections obtained for the standard lamp. This was accomplished wavelength by wavelength over the entire spectral range which was scanned. These ratios were then multiplied wavelength by wavelength by the known spectral radiance of the standard lamp in order to obtain the relative spectral distribution of the output of the spherical integrator.

ABSOLUTE SPECTRAL DISTRIBUTION

The spherical integrator as a source of radiant flux has a different spectral configuration from that of an approximate point source such as the standard quartz-iodine lamp. In order to obtain an absolute calibration it is necessary to eliminate the effects of this difference. For this reason, a 16-inch spherical integrator was mounted on the front of the Perkin-Elmer monochromator. This small sphere consists of two plastic hemispherical shells painted with Burch sphere paint. The two shells are held together by clamps. One of the hemispheres was rigidly fastened to the monochromator so that a 3/4 inch diameter exit port was centered in front of the monochromator slit. The second hemisphere has a 1-7/16 inch diameter entrance port designed to be

rotated alternately into a position (a) such that it is flush against the exit port of the six-foot integrator to receive its output flux, or (b) so as to be in line with the quartz-iodine lamp situated at 22 cm. from it and thus receive flux from this lamp. In this way the monochromator alternately saw the flux from the port of the six-foot integrator or from the standard lamp at 22 cm., as integrated by the small spherical integrator.

Using a given slit width of the monochromator and gain of the recorder, a direct comparison was made between the energy the small sphere received from the six-foot integrator and from the standard lamp at four wavelengths using the photomultiplier 1P28 as the detector. A similar comparison was made at ten wavelengths by means of the Reeder thermocouple, several of which duplicated those obtained with the photomultiplier. Since the relative distribution of the sphere was determined as discussed above, it was only necessary to establish the absolute value of a few points on the relative distribution in order to obtain a complete calibration.

CALIBRATION OF THE SPHERICAL INTEGRATOR

Let P_{λ}^{ℓ} watts \cdot micron $^{-1}$ cm $^{-2}$ be the spectral radiant power per unit area entering the port of the small sphere from the standard lamp QM-95 placed 22 cm from the port. Then

$$P_{\lambda}^{\ell} = \frac{cN_{\lambda}}{r^2} \text{ watts} \cdot \text{micron}^{-1} \text{ cm}^{-2} \quad (2)$$

where N_{λ} is the spectral radiance in watts per steradian per micron of the standard lamp, r the distance from the lamp to the port, and c the correction factor for inverse square failure. This flux which entered the small sphere was integrated by it and then viewed by the monochromator at several wavelengths and recorded. The resulting recorder deflection D_{λ}^{ℓ} was proportional to the integrated flux and thus proportional to the spectral radiant power P_{λ}^{ℓ} entering the port from the standard lamp.

When the small sphere receives the flux from the six-foot integrator, the spectral radiant power entering it must be given in terms of the spectral radiant power coming from the diffusing surface of the six-foot sphere. Let W_{λ}^S watts cm $^{-2}$ μ^{-1} be diffusely reflected into the solid angle 2π . Then the diffuse spectral radiation in the normal direction is W_{λ}^S/π . The spectral radiant power incident at the effective area of the port, dA' , from the curved diffusely reflecting surface of the spherical segment of area dA is equal to

$$dP_{\lambda}^S = \frac{W_{\lambda}^S}{\pi} \frac{dA \cos \theta/2 \cdot dA' \cos \theta/2}{d^2}$$

where d is the distance between the element of area dA and the port, and $\theta/2$ is the angle between the line of propagation and the normal to the surface of the sphere, as shown in Figure D-6.

Since

$$d = 2 r \cos \theta/2$$

and

$$dA = 2\pi r^2 \sin \theta d\theta$$

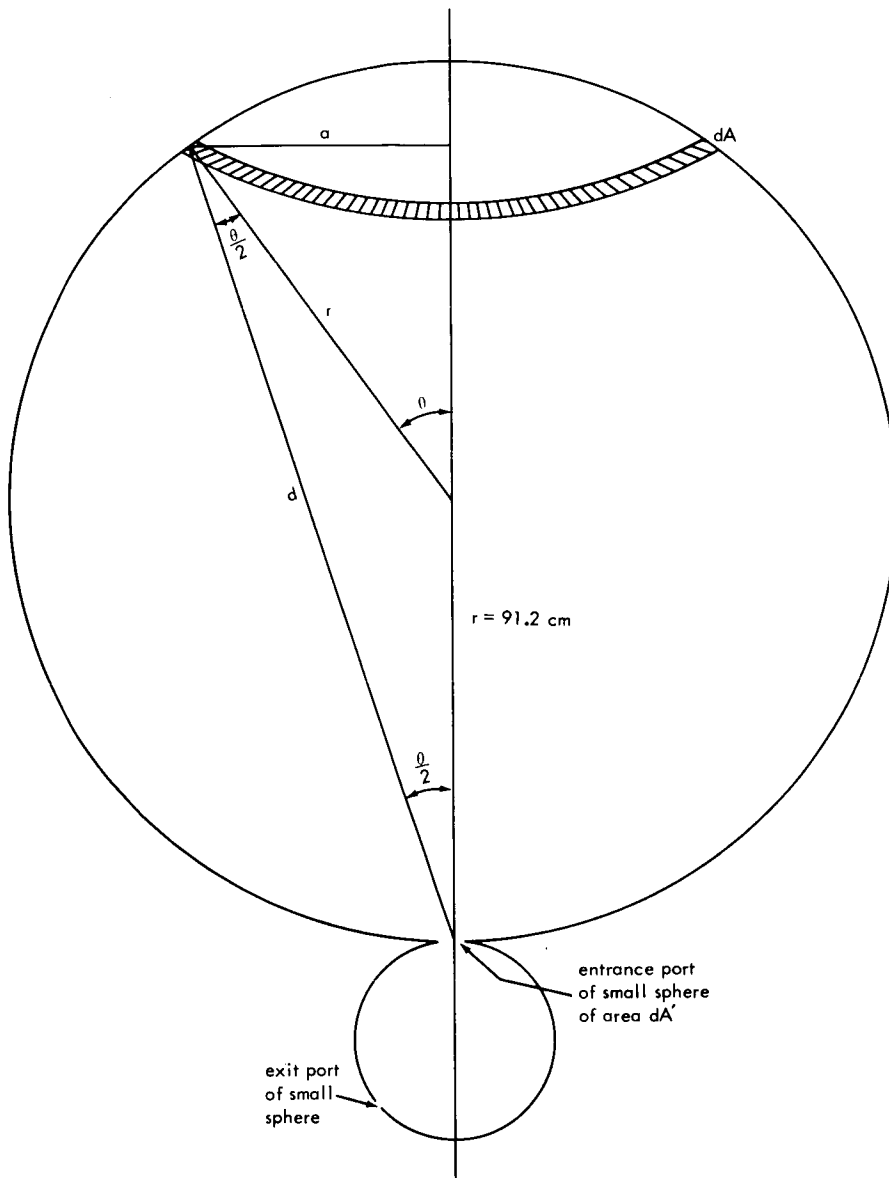


Figure D-6—Cross section of large and small spheres showing data used to derive equation.

the spectral radiant power is given by

$$dP_{\lambda}^s = \frac{W_{\lambda}^s}{\pi} \frac{2\pi r^2 \sin \theta d\theta \cdot \cos^2 \theta/2 dA'}{4r^2 \cos^2 \theta/2}$$

or

$$dP_{\lambda}^s = \frac{1}{2} W_{\lambda}^s dA' \sin \theta d\theta$$

This gives

$$P_{\lambda}^S = \frac{1}{2} W_{\lambda}^S dA' \int_0^{\theta} \sin \theta d\theta$$

or

$$P_{\lambda}^S = \frac{1}{2} W_{\lambda}^S dA' (1 - \cos \theta) \quad (3)$$

If one assumes that θ varies from 0° to 180°

$$P_{\lambda}^S = W_{\lambda}^S dA' \text{ watts} \cdot \mu^{-1} \quad (4)$$

Due to the six millimeter wall of the large sphere, the limits of integration may be shown to be 0° to 162.4° and thus we get

$$P_{\lambda}^S = 0.977 W_{\lambda}^S dA' \text{ watts} \cdot \mu^{-1} \quad (5)$$

or

$$P_{\lambda}^S = 0.977 W_{\lambda}^S \text{ watts} \cdot \mu^{-1} \text{ cm}^{-2} \quad (6)$$

The value of W_{λ}^S diffusely reflected by unit surface of the sphere into the solid angle 2π is

$$W_{\lambda}^S = 1.023 P_{\lambda}^S \text{ watts} \cdot \text{cm}^{-2} \mu^{-1} \quad (7)$$

This flux from the large sphere, entering the small sphere, was integrated by the latter and then viewed by the monochromator. The resulting recorder deflection D_{λ}^S was proportional to the integrated flux and hence proportional to the spectral radiant power P_{λ}^S entering the small sphere from the large sphere.

Thus one may compare the spectral radiant power which the small sphere received respectively from the large sphere and from the standard lamp in terms of the corresponding deflections of the monochromator recorder. Thus

$$P_{\lambda}^S / P_{\lambda}^L = D_{\lambda}^S / D_{\lambda}^L$$

or

$$P_{\lambda}^S = (D_{\lambda}^S / D_{\lambda}^L) P_{\lambda}^L$$

Since the value of $D_{\lambda}^S / D_{\lambda}^L$ was found to be 1.0468, one obtains

$$P_{\lambda}^S = 1.0468 P_{\lambda}^L \quad (8)$$

Table D-2
Spectral Distribution of the Spherical Integrator and Lamp QM-95

λ	H_λ	P_λ	W_λ	λ	H_λ	P_λ	W_λ
.30	.956	.100	.102	1.3	94.61	74.50	76.21
.32	1.826	.175	.179	1.4	84.38	39.12	40.02
.35	4.194	.580	.593	1.5	74.67	35.74	36.56
.37	6.495	1.326	1.356	1.6	65.46	31.12	31.84
.40	11.30	3.922	4.012	1.7	57.28	20.30	20.77
.45	22.54	11.71	11.98	1.8	49.75	14.25	14.58
.50	37.58	31.89	32.62	1.9	43.06	11.83	12.10
.55	54.72	57.28	58.60	2.0	37.13	6.43	6.58
.60	72.62	91.81	93.92	2.1	32.53	5.68	5.81
.65	89.50	117.56	120.26	2.2	28.74	4.50	4.60
.70	103.31	142.87	146.15	2.3	25.61	2.63	2.69
.75	113.54	158.73	162.38	2.4	23.12	1.75	1.79
.80	119.67	168.57	172.45	2.5	21.17	1.16	1.19
.90	124.27	156.90	160.51	2.6	18.45	.554	.567
1.10	121.17	135.42	138.53	2.7	16.52	.330	.338
1.1	114.56	115.09	117.74	2.8	14.89	.175	.179
1.2	104.84	90.69	92.78	2.9	13.39	.100	.102

Substituting this into Equation (7) one obtains

$$W_\lambda^S = 1.071 P_\lambda^L \text{ watts} \cdot \text{cm}^{-2} \quad (9)$$

for the diffuse spectral radiation of the six-foot spherical integrator in terms of the spectral radiant power per unit surface entering the small sphere from the standard lamp at 22 cm. Using Equation (9) the diffuse spectral radiation of the sphere was calculated wavelength by wavelength. The resulting data is given in Table D-2. The second column gives the spectral irradiance H_λ (in milliwatts $\text{cm}^{-2}\mu^{-1}$) of the standard lamp at 22 cm. The third column gives the spectral distribution of the flux from the sphere P_λ (in milliwatts $\text{cm}^{-2}\mu^{-1}$) and the fourth column gives the diffuse spectral radiation of the walls of the six-foot integrator, W_λ (in watts $\cdot \text{m}^2$). Figure D-7 shows the spectral distribution of the six-foot integrator compared with the spectral distribution of the standard lamp.

CALIBRATION OF A TIROS RADIOMETER

The foregoing calibration of the spherical integrator was used to check the calibration of channel 3 of the five-channel Tiros radiometer number 306 which had been calibrated in 1964. As discussed in the 1964 report (Reference 1), the total energy originating at the diffuse surface of the sphere which produces the actual radiometer response was found by the use of the relation

$$W \simeq R_n \sum_{\lambda_1}^{\lambda_2} W_\lambda^S \rho_\lambda \Delta\lambda \text{ watts} \cdot \text{m}^2 \quad (10)$$

where R_n is the ratio of the intensity of the flux from the sphere for n lamps to the flux for all twelve lamps, and ρ_λ is the spectral responsivity of the radiometer. The resulting data is given in Table D-3 where V is the output of the radiometer as measured in 1964, W (1966) is the total

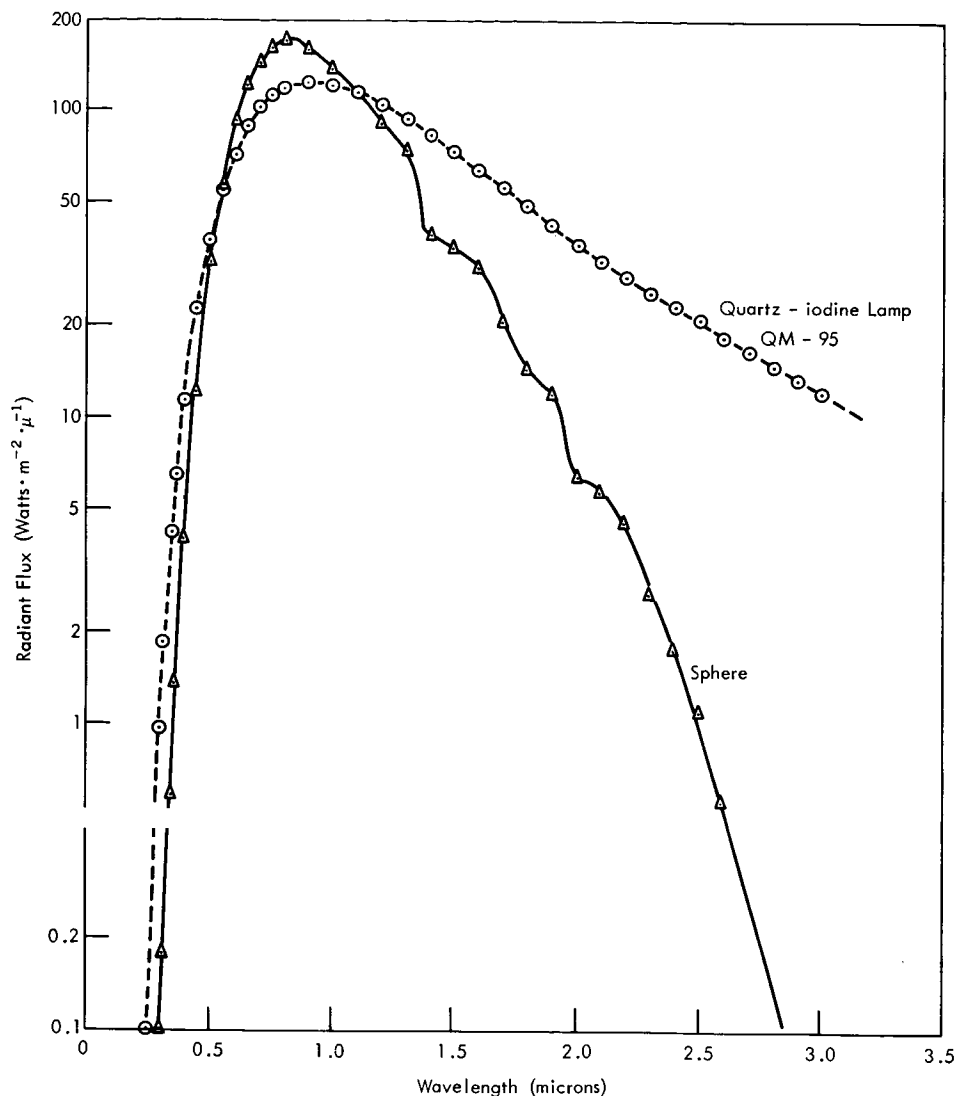


Figure D-7—Spectral curve of sphere.

energy originating at the diffuse surface as determined above, W (1964) is the corresponding value obtained in 1964 as determined by a calibrated thermopile, and W_p is the value obtained by reflection from diffusing white kodak paper, see Reference 1. The data for 1966 is plotted in Figure D-8.

CONCLUSIONS

It will be observed that the present values for the diffuse radiation from the integrator are somewhat lower than those obtained in 1964. This amounts to about 7 percent at the higher energy levels. This difference may not be too significant. A comparison of the present spectral distribution of the integrator with that obtained in 1964 shows a significant difference. This may be due in part to the method used in 1964 to get the spectral distribution, and to a much greater extent to a change in the Burch sphere paint. The paint is two years old and is soiled and slightly yellowish so that its reflectivity may have changed considerably. The radiometer output was measured in 1964 when the paint was relatively new. For this reason one might expect that the

Table D-3
Calibration of Channel 3 (Radiometer 306)
(V in volts; W in watts m^2)

V	W_s (1966)	W_s (1964)	W_p
5.25	356	380	
5.00	337	360	282
4.75	318	340	264
4.50	300	321	249
4.25	282	302	234
4.00	265	283	219
3.75	249	265	206
3.50	234	248	193
3.25	220	231	179
3.00	206	214	166
2.75	192	198	153
2.50	177	182	139
2.25	162	166	126
2.00	148	150	113
1.75	132	134	100
1.50	116	118	86
1.25	101	101	73
1.00	84	85	59
0.75	66	65	45
0.50	47	45	

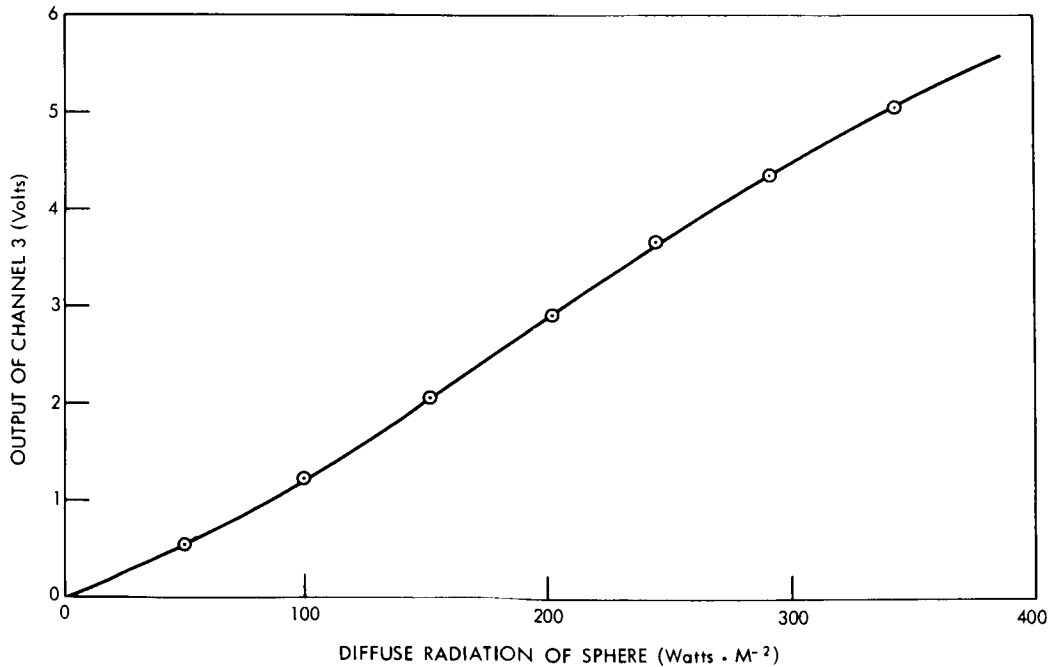


Figure D-8—Calibration of radiometer.

radiometer output would be less now than it was in 1964. Hence the use of the 1964 output of the radiometer with the recently determined diffuse radiation of the sphere may account for the apparent change in the calibration.

The six-foot sphere will be repainted shortly and the measurement reported above will be repeated in order to get a reasonably satisfactory calibration of the sphere.

The author wishes to express appreciation to Nathan J. Miller, formerly of the Planetary Radiations Branch for the initial work in providing the 16 inch integrating sphere, and to James McClean (Planetary Radiations Branch) for some of the initial measurements.

REFERENCES

1. GSFC Final Report of the Workshop Program 1964 p. A-17.
2. GSFC Final Report of the Workshop Program 1965 p. B-23.
3. GSFC Final Report of the Workshop Program 1966 p.
4. W. E. Sumpner, Physics Society Proceedings, Vol. 12, p. 10, 1892.
5. J. W. T. Walsh, Photometry, London, Constable and Co. 1958, p. 258.
6. A. C. Hardy and O. W. Pineo, Journal of the Optical Society of America, Vol. 21, p. 502, 1931.

A HIGH RESOLUTION SPECTROMETER FOR MEASURING ABSORPTION CROSS-SECTIONS BETWEEN 1000A AND 2000A

J. H. McElaney* 7

N 67-22770

During the past dozen years, the photoionization cross sections of various gases have been measured in the region 200-2000A. The cross-sections for the absorption of vacuum ultraviolet radiation by various gases are of interest for atmospheric physics. Quantitative measurements of cross-sections were first made by Ladenburg and Van Voorhis (Reference 1) using a hydrogen-discharge source and photographic photometer. These measurements were repeated at selected wavelengths by Schneider (Reference 2). Ditchburn and Heddle (Reference 3) remeasured the Schumann-Runge continuum absorption coefficients, again photographically. Later, measurements were made photoelectrically by Watanabe, Zelikoff, and Inn (Reference 4), by Metzger and Cook (Reference 5), and by Huffmann, Tanaka, and Larrabee (Reference 6). Samson and Cairns (Reference 7) measured photo-ionization and total absorption cross-sections for wavelengths corresponding to some intense solar emission lines. Recently, Bethke (Reference 8) and Blake, Carver, and Haddad (Reference 9) have conducted further investigations of molecular oxygen in the vacuum ultraviolet region. A compilation of these results up to 1962 has been prepared by Schultz et al. (Reference 10).

There is a considerable spread in the reported data of these investigations. This may be due in part to differences in the wavelength resolution used by the different investigators. Some gases, such as O₂ and N₂, exhibit band structure so narrow that the absorption cross-section may vary appreciably within a small fraction of an angstrom. Thus, high resolution and precise wavelength identification is required in making absorption measurements. The purpose of the work which has been undertaken is to prepare equipment to determine more accurate values for the absorption cross-sections of various gases in the region 1000-2000A using a high resolution vacuum scanning spectrometer.

The spectrometer which is being used in the Jarrell-Ash 1.83 meter vacuum scanning spectrometer. The Ebert mounting, using a 7620 grooves per inch grating, yields a spectrum from 1200 A to 62,000A, and has a resolution of 0.005A at 3000A, in the XX order. The instrument is based on a design by W. G. Fastie, H. M. Crosswhite, and P. Gloersen (Reference 1), Figure D-9. The instrument is equipped with a precision screw and 12 speed drive for rotating the grating. An 8" plane grating with 7620 grooves per inch is used with the spectrometer and is blazed for approximately 59° (57,000A). The effective aperture ratio of the spectrometer is F/11.6. A premonochromator, with a 30 × 50 mm grating is mounted before the entrance slit. The spectrometer, premonochromator, and sample chamber may be conveniently evacuated to 10⁻⁶ torr.

The light sources providing the background continuum for the absorption studies in the vacuum ultraviolet were developed by Wilkinson and Tanaka (Reference 12 and 13). They are mounted before the grating of the premonochromator. These light sources are high intensity, microwave excited, continuous discharge tubes for the vacuum ultraviolet. They are air cooled and excited by a Jarrell-Ash microwave generator operating at 2450 MHz. The argon, krypton, and xenon lamps provide nearly continuous wavelength coverage from the lithium fluoride cutoff at 1090A to nearly 2000A, well within the useful range of the hydrogen continuum, Figure D-10. The hydrogen continuum is provided by a water-cooled, quartz window Nester lamp.

*Fairfield University

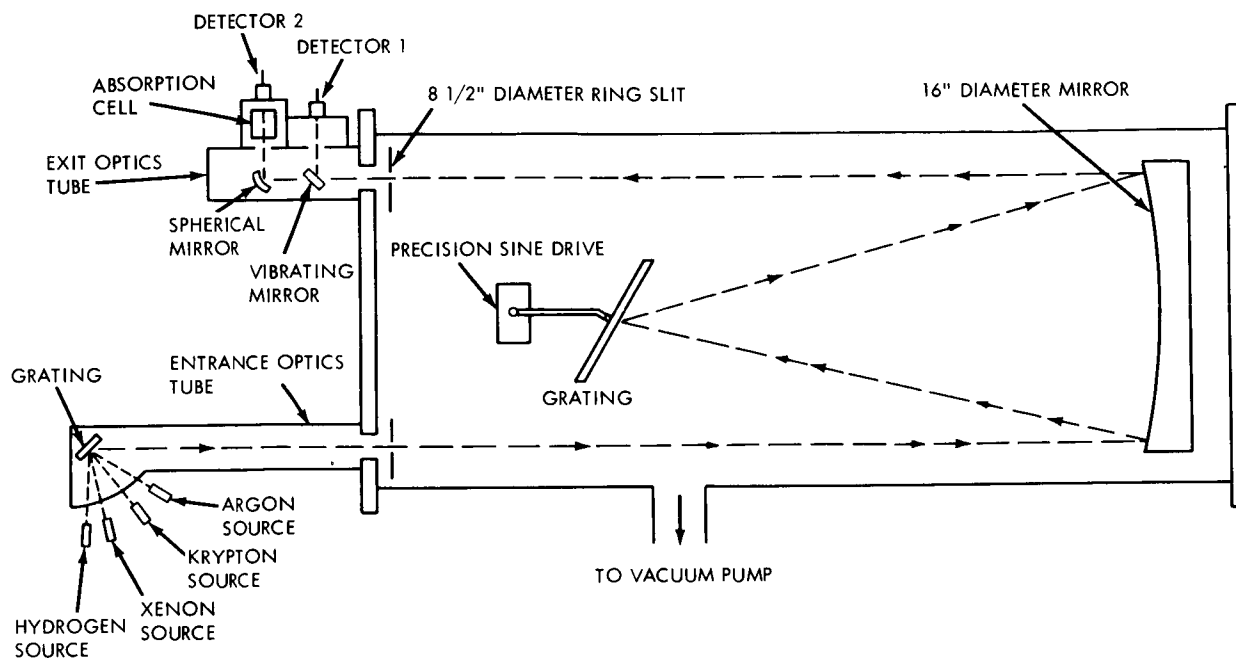


Figure D-9—Optical schematic of the vacuum scanning spectrometer, 1.8 meter Ebert,

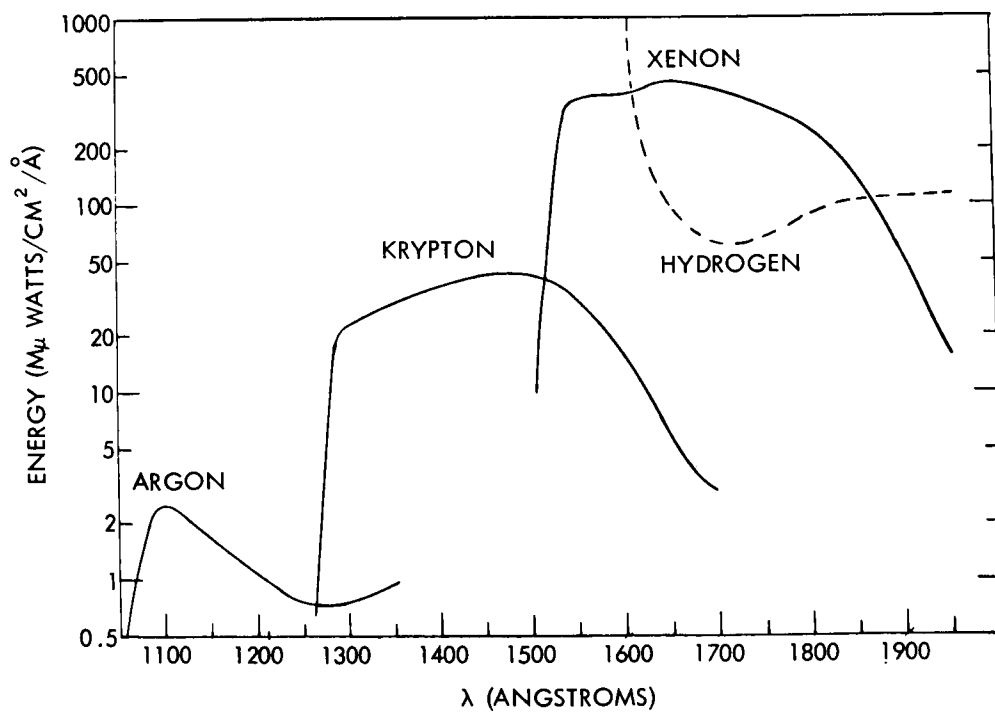


Figure D-10—Energy distribution of ultraviolet sources.

The wavelength intervals are: for xenon, 1500-1825A, Figure D-11; for krypton, 1250-1500A, Figure D-12; for argon, 1150-1250A, Figure D-13 and hydrogen, 1825-3600A (Reference 14).

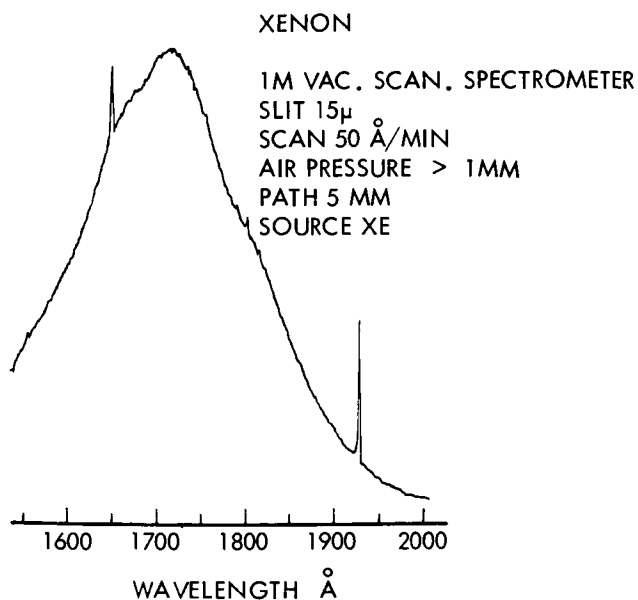


Figure D-11—Xenon: useful range 1600-1950A with little line emission.

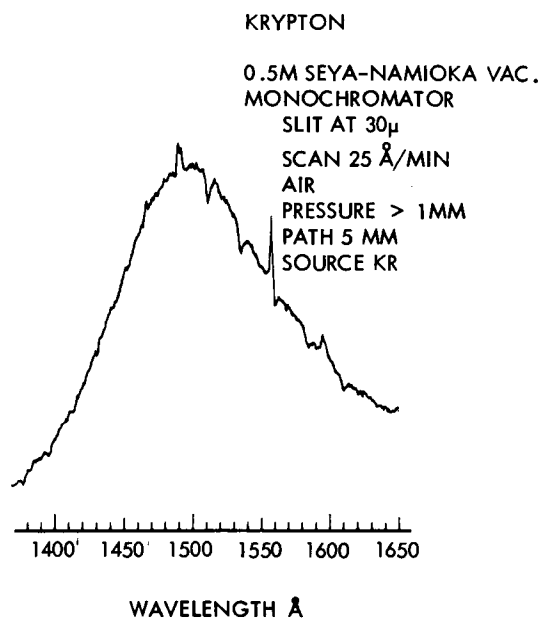


Figure D-12—Krypton.

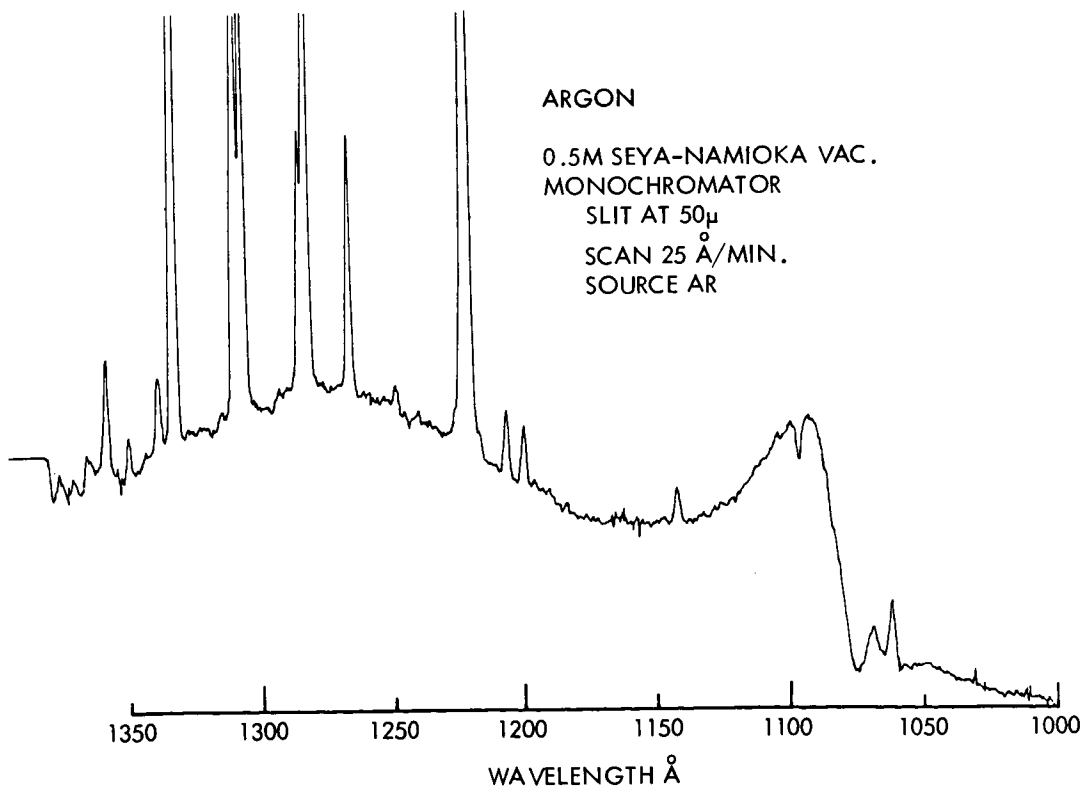


Figure D-13—Argon: Useful range 1090-1300A, rather severe line emission but still useful.

The MgF_2 -coated rotatable grating deflects the energy from each source to the entrance slit. The spectral regions will be calibrated with a copper hollow cathode source. A series of 10 potentiometers in the double beam electronics permits a flattening of the baseline as it varies as a function of wavelength.

The double beam section of the spectrometer is mounted before the exit slit as indicated in Figure D-9. A Brower ratio recording synchronous amplifier is used with a light beam chopper to measure the relative radiation intensities at two detectors. Basically, the instrument comprises two complete detection and recording channels and an electronic servo comparison system. This arrangement enables accurate measurement of intensity ratios to be made independently of variations in signal source amplitude. The amplifier may be used in either of two ways. In the independent mode, the instrument may be used as two independent amplifier recorders operating from different detectors and indicating outputs on separate meters and charts. In the comparison mode, the output of the selected reference channel is held constant and the signal ratio is indicated directly on the meter and chart of the other channel. Light which passes through the exit slit of the spectrometer strikes an oscillating mirror and produces the reference beam. When the oscillating mirror is out of the beam the light from the exit slit passes to a second fixed mirror. The light reflected by the second mirror forms an image in the sample compartment where the gas to be studied may be contained. Passing through the sample chamber, the absorbed beam will strike a sodium salicylate phosphor in front of the photomultiplier detector.

The absorbing gas is introduced into the sample cell from a Granville-Phillips gas fill system. This consists of a capacitance manometer which is a sensitive differential pressure measuring instrument. It permits the accurate comparison of the pressure in a clean vacuum system with the pressure in another system without exposing the clean system to impurities. The instrument will measure differential pressures from 0 to 10 torr, with a minimum detectable pressure differential of less than 5×10^{-3} torr. An automatic pressure controller is designed to regulate the gas pressure in the system from one atmosphere to 10^{-11} torr. Pressure control is accomplished by automatically admitting the correct gas flow to the system to compensate for gas being removed from the system by some means. An NRC alphasatron gauge is used to provide the standard for pressure measurements.

The coefficients of absorption (STP) may be calculated using the expression

$$k = \frac{1}{x_0} \cdot \left(\frac{P_0}{P} \right) \cdot \frac{T}{T_0} \cdot \ln \left(\frac{I_0}{I} \right) \text{ cm}^{-1}$$

where x_0 is the path length of the absorbing gas, P is the measured gas pressure (torr), T is the gas temperature, and I_0/I is the intensity ratio of the unabsorbed to absorbed beam of light. The absorption cross-sections may be determined by dividing the coefficient of absorption by the Loschmidt number.

From the measured coefficients of absorption, the continuum oscillator strength f may be calculated from

$$f = \frac{mc^2}{\pi e^2} \cdot N_0 \int_{\bar{\nu}_1}^{\bar{\nu}_2} k(\bar{\nu}) \cdot d\bar{\nu}$$

where $\bar{\nu}$ is the wavenumber, N_0 is the Loschmidt number, c is the speed of light, and m and e are electronic mass and charge respectively.

The performance of the spectrometer at the present time is indicated by a number of recorder traces. Figure D-14 shows the mercury line at 5461A. The mercury line at 4358A is shown in Figure D-15; while Figure D-16 illustrates the separation of the components of the 2537A line. These lines are from the high orders indicated in the figures. The resolution of these lines is estimated to be over 500,000. It is expected that further work will improve the resolution of lines appreciably. The S-R bands in Figure D-17 were made using the single beam electronics already described.

As yet no measurements of absorption cross-sections have been made. A number of normal experimental difficulties have been encountered. While most of the difficulties have been eliminated it is clear that some redesigning of the premonochromator is necessary to obtain adequate intensity through the system from the argon and krypton sources. Also, the 8" grating furnished

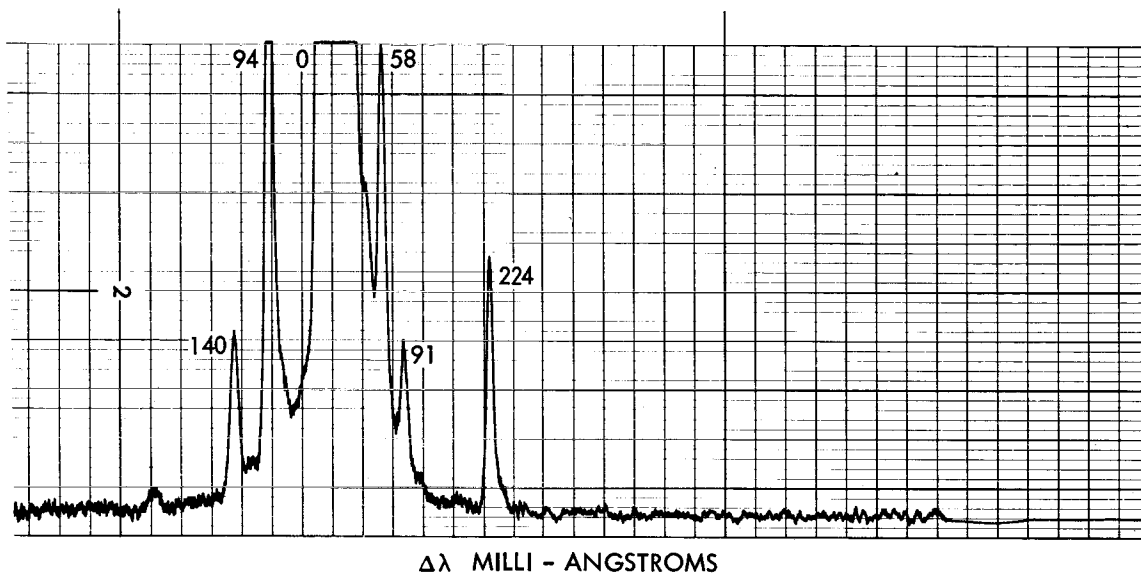


Figure D-14—Hg 5461A, XI, scan - 5A/min.

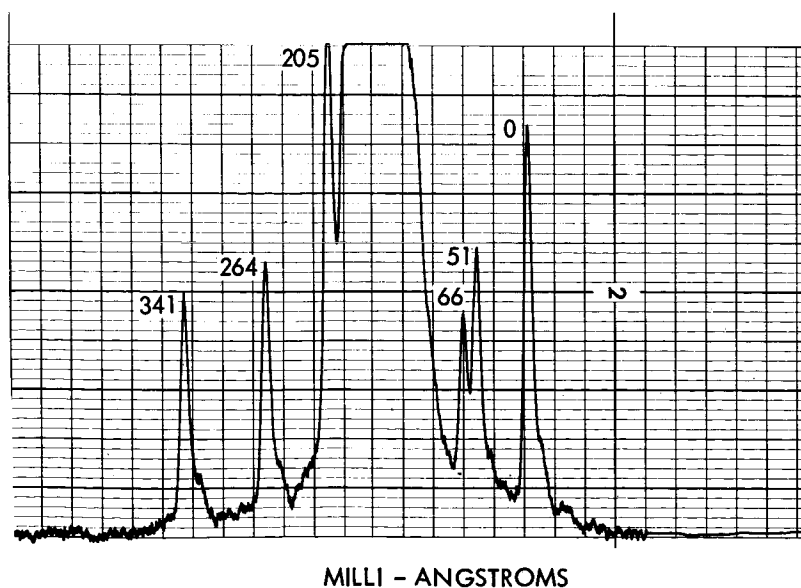


Figure D-15—Hg 4358A, XIV, scan 5A/min.

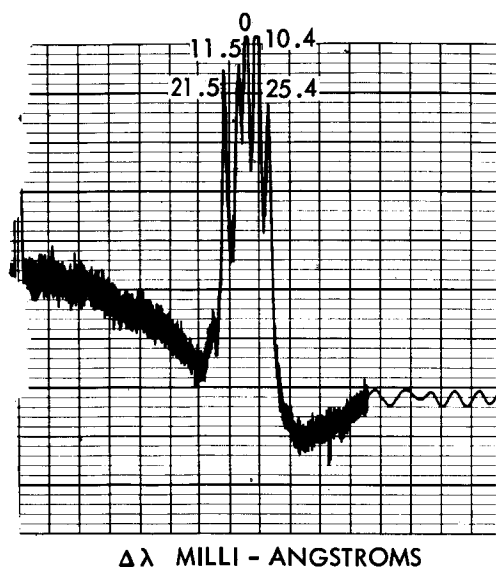


Figure D-16-Hg 2537A, XXIV, scan 10A/min.

for this work has such a poor figure that it is impossible to maintain good resolution over an extended wavelength region. This grating will have to be replaced by another. Thereafter the absorption cross-sections will be determined at high resolution for various gases. The spectrometer will be of great value for numerous research and analytical applications in the vacuum ultraviolet.

REFERENCES

1. Ladenburg, R. and Van Voorhis, C. C., Physical Review, Vol. 43, p. 315, 1933.
2. Schneider, E. C., Journal of Chemical Physics, Vol. 5, p. 106, 1937.
3. Ditchburn, R. W. and Heddle, D. W. O., Proceedings of the Royal Society (London) Vol. 61, p. A220, 1953.
4. Watanobe, K., Zelikoff, M., and Inn, E. C. Y., Journal of Chemical Physics, Vol. 21, p. 102, 1953 and Vol. 25, p. 965, 1956.
5. Metzger, P. H., and Cook, G. R., Journal of Quantitative and Spectroscopic Radiation Transfer, Vol. 4, p. 107, 1964.
6. Huffman, R. E., Tanaka, Y., and Larrabee, J. E., Discussions Faraday Society, Vol. 37, p. 159, 1964.
7. Samson, James A. R., Cairns, R. B., Journal of Geophysical Research, Vol. 69, p. 21, 1964.
8. Bethke, G. W., Journal Chemical Physics, Vol. 31, p. 3, 1959.
9. Blake, A. J., Carver, J. H., and Haddad, G. N., J. Quant. Spectry. Radiat. Transfer, Vol. 5, 1966.
10. Schultz, E. D., Holland, A. C., Marmo, F. F., G. C. A. Technical Report 62-15-N, 1962.
11. Fastie, W. G., Journal of the Optical Society of America, Vol. 42, 1952.
12. Wilkinson, P. G., Journal of the Optical Society of America, Vol. 45, 1953.

13. Wilkinson, P. G. and Tanaka, Y., Journal of the Optical Society of America, Vol. 45, p. 344, 1955.
14. High Intensity Continuous Vacuum Ultraviolet Sources, Jarrell-Ash Company, Jarrell-Ash Literature.

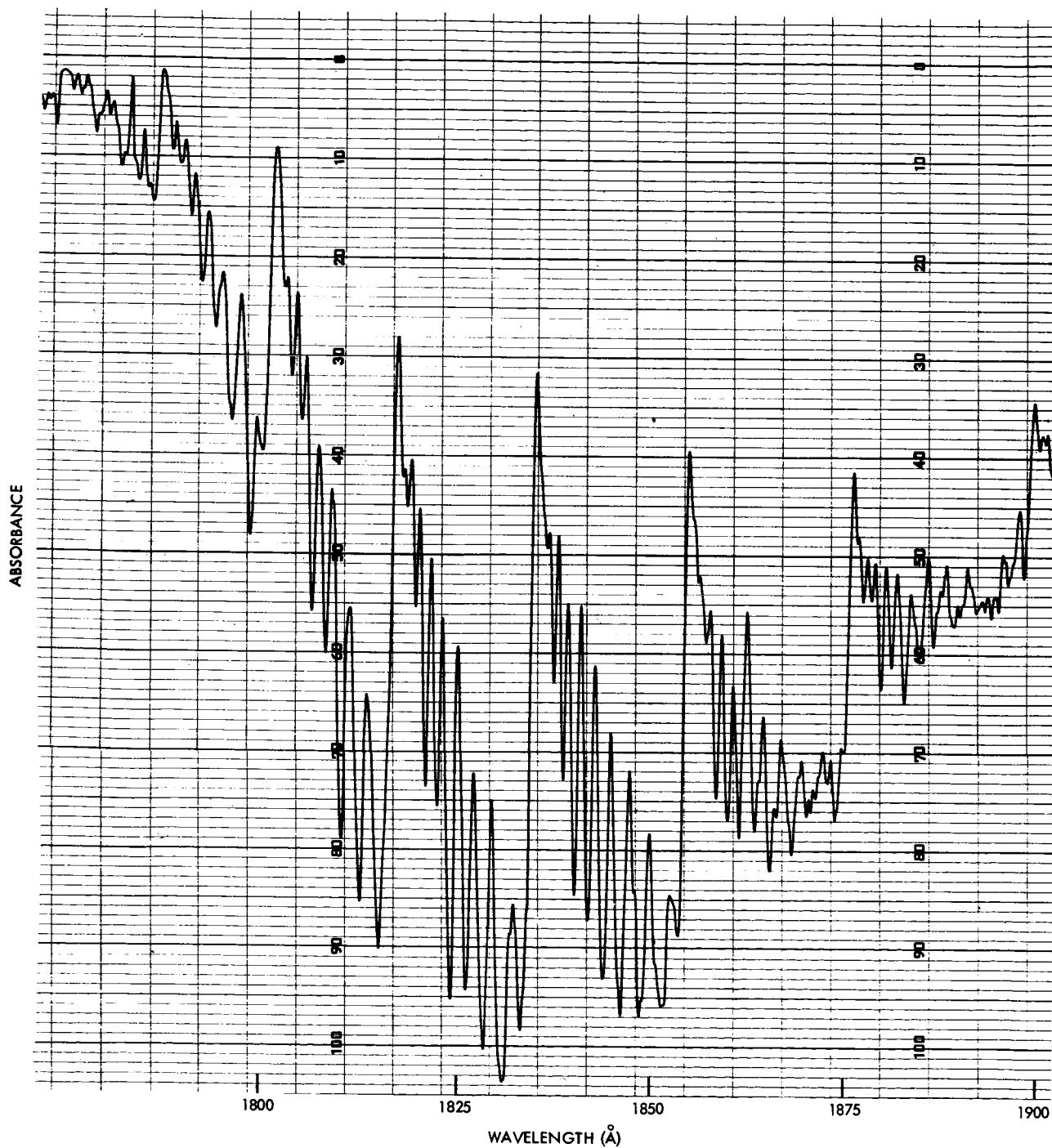


Figure D-17—The oxygen Schumann-Runge bands in absorption

SUMMER WORKSHOP 1966

Program Outline and Team Participants

PROJECT E: Radiation Simulation Problems

Problem Topics

- E-1 Data reduction techniques for spectral radiance analysis
- E-2 Evaluation of the cone radiometer
- E-3 Calibration of working standards of spectral irradiance for laboratory use
- E-4 Spectral irradiance measurements on solar simulation sources
- E-5 Photon flux of substandard quartz-iodine lamp in the range 2500A to 8000A

TEAM E

Academic Personnel

Dr. M. P. Thekaekara
Acting Principal Investigator
Mr. J. M. Crowell
Mr. D. L. Henry
Mr. E. D. Reed
Mr. Paul Schoen

Goddard Personnel

Mr. J. C. New
Staff Advisor
Miss Jesselle Mays
Miss Sandra Read
Mr. Arthur McNutt
Mr. Ray Kruger
Mr. H. H. Hoehn
Mr. A. R. Winker

NSF Summer Science Student
Jan M. Slavin

PRECEDING PAGE BLANK NOT FILMED.

PROJECT E: RADIATION SIMULATION PROBLEMS

CONTENTS

	<u>Page</u>	
DATA REDUCTION TECHNIQUES FOR SPECTRAL RADIANCE ANALYSIS	417	✓
J. M. Crowell		
EVALUATION OF THE CONE RADIOMETER	429	✓
J. M. Crowell, D. L. Henry and E. D. Reed		
CALIBRATION OF WORKING STANDARDS OF SPECTRAL IRRADIANCE FOR LABORATORY USE	439	✓
A. McNutt, J. Slavin, and M. P. Thekaekara		
SPECTRAL IRRADIANCE MEASUREMENTS ON SOLAR SIMULATOR SOURCES	447	✓
S. Read and M. P. Thekaekara		
PHOTON FLUX OF SUBSTANDARD QUARTZ-IODINE LAMPS IN THE RANGE 2500A TO 8000A	463	✓
P. Schoen and J. Mayes		

PRECEDING PAGE BLANK NOT FILMED.

INTRODUCTORY REMARKS ON PROJECT E
RADIATION SIMULATION PROBLEMS

D. C. Kennard, Jr.

The studies conducted in previous Summer Workshops were continued in 1966 in an effort to come nearer to solving the problem of accurately measuring the total energy and spectral content of solar simulators used for ground testing of space systems. Techniques were developed enabling us to make measurements in the ultraviolet region down to 2500\AA which previously had been unattainable in the Thermodynamics Branch of the Test and Evaluation Division.

Some interesting new techniques were explored in the use of a cone radiometer developed by GSFC. This radiometer shows promise of providing good absolute measurements of total irradiation and plans are underway to evaluate its performance in measuring solar radiation from a high-altitude airplane.

Notable advancements also were made in calibrating working standards of spectral irradiance and developing data reduction techniques for spectral irradiance analysis.

OK

DATA REDUCTION TECHNIQUES FOR SPECTRAL RADIANCE ANALYSIS

John Crowell

N 67-22771

The conventional method for measuring the spectral radiant flux of an unknown source involves making some record of the spectrum of the unknown source and that of some standard source. If the measurements of both sources are made with the same monochromator, recording system, and optical geometry, the signals from the monochromator at a particular wavelength should be in the same ratio as the spectral radiant flux.

The studies of solar simulation in the summer workshop utilize the Perkin-Elmer Model 112-U monochromator. The data obtained from the monochromator consist of a drum count corresponding to the wavelength of the energy observed, the gain factor of the recording amplifier, and the amplitude of the output of the amplifier.

If

- F = radiant flux of a source at a given wavelength
- A = amplitude of the amplifier signal at that wavelength
- G = gain factor of the amplifier

then

$$F_x = \frac{A_x G_x}{A_s G_s} F_s, \quad (1)$$

where subscripts x and s refer to the unknown and the standard respectively.

There are two programs for the CDC-3100 computer in use which perform the above operation. These programs, called the "Fixed Point Program" and the "Manual Program" also normalize the curve of F_x vs wavelength so that the area under the curve is the same as that of the solar spectral curve within the limits of the wavelengths investigated. In this way the effect of different geometries can be neglected, and the structure of the spectrum can be examined. Magnetic tapes are printed for use with the digital plotter on line with a CDC-160A computer so that the normalized flux of the unknown can be plotted as a function of wavelength. A solar spectral curve can be superimposed upon that of the unknown, so the two can be compared directly.

THE FIXED POINT PROGRAM

The data for the Fixed Point Program consist of a list of the wavelengths examined, and the standard lamp flux, amplitudes and gain settings of the standard lamp run, and the amplitudes and gain settings of the unknown run corresponding to those wavelengths. A table is provided for conversion of gain settings to gain factors. The program first finds the area under the solar curve between the limits of the wavelengths to be considered. The method for computing the area under the curve is discussed in the following paragraphs.

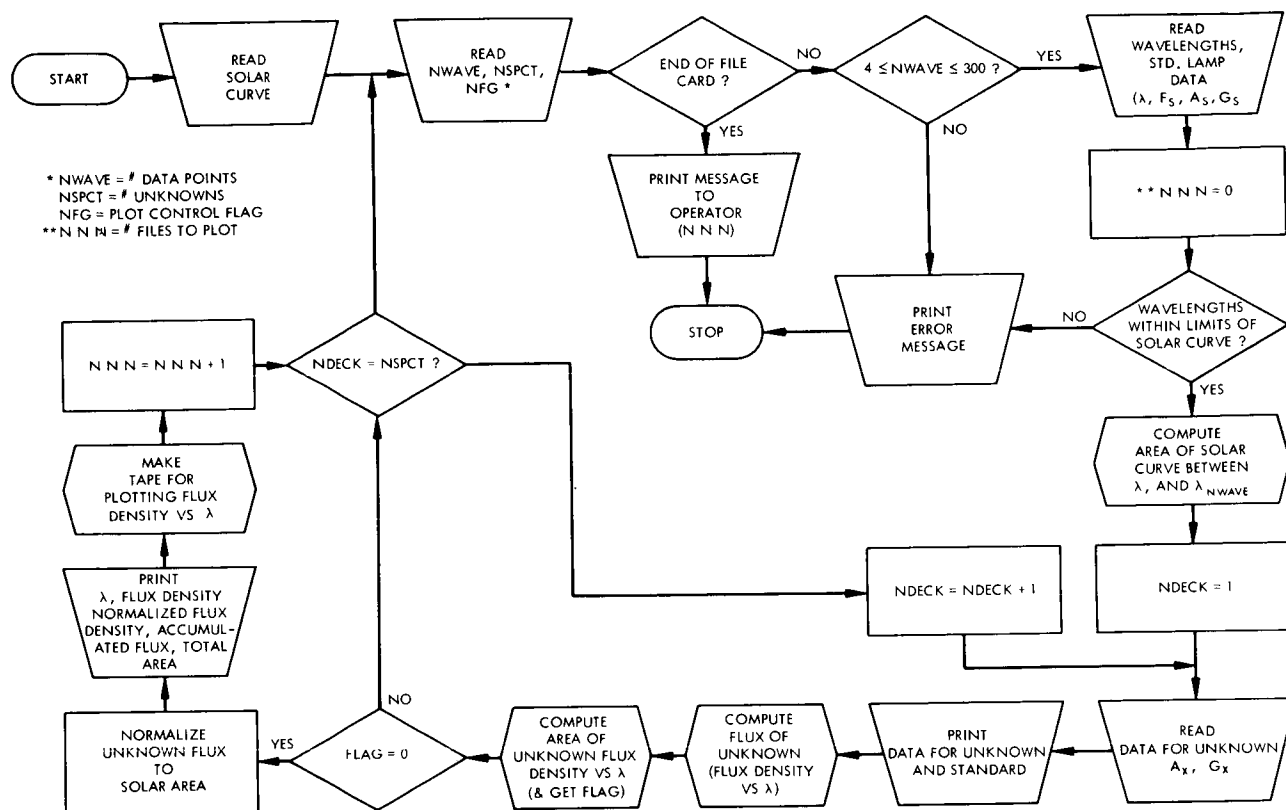


Figure E-1—Fixed point program.

The flux for the unknown source at each wavelength is computed according to Equation (1). The area under the curve of flux vs wavelength is computed, and the curve is normalized so that it has the same area as the solar curve. The flux and normalized flux for each wavelength are printed in a table along with the accumulated normalized flux up to that wavelength. A magnetic tape is printed for use with the digital plotter so that a polygonal graph of the normalized flux can be plotted as a function of wavelength. If desired, a graph of the solar curve may be superimposed on that of the unknown.

THE MANUAL PROGRAM

The Manual Program has somewhat greater facility in that preparation of the data is easier. The data points for the standard lamp amplitudes and unknown amplitudes need not all be for the same wavelengths. In addition, the actual wavelengths and the amplifier gain factors are not necessary. The drum count, amplitude, and gain control setting are all that is needed for each data point. Computation of the variables to be used in Equation (1) is accomplished by a sub-routine which interpolates linearly between points of a curve, e.g., the wavelength for a particular data point may be found by interpolating between two of a set of points of drum count vs wavelength, and the standard lamp flux at that wavelength can be interpolated from a table of such points. The flux of the unknown is computed as a function of wavelength by Equation (1); and, as before, that curve and the solar curve are integrated so that the flux can be normalized.

The program then scans the unknown flux curve between some desired wavelengths λ_{\min} and λ_{\max} in intervals of width $\Delta\lambda$. In each interval the area of the unknown curve and that of the solar curve are computed.

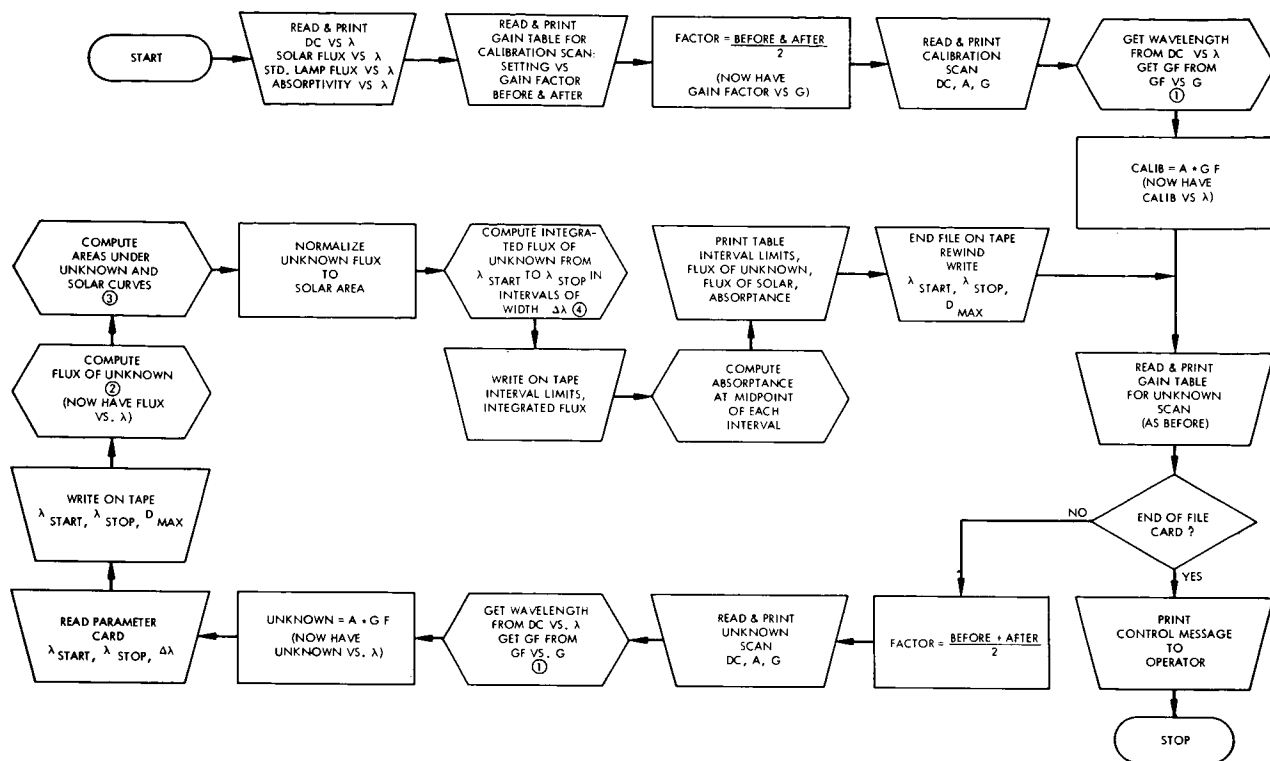


Figure E-2—Manual program.

A table is printed containing the extent of each interval, the two computed areas, and the accumulated unknown flux up to that interval. As in the Fixed Point Program, a magnetic tape is printed. This tape contains the area of each interval and the wavelengths of the end points of the intervals. A histogram of the unknown spectrum can then be plotted. In addition, the Manual Program can examine the absorptivity curves of various surface coatings, and compute the amount of energy in each wavelength interval which will be absorbed by that surface coating. This information is also printed in the output table.

METHODS OF INTEGRATION

Numerical integration of functions for which discrete points are known is usually accomplished by approximating the function with an interpolating function, usually a polynomial, which passes through the known points, and the integral of which is exactly known (Reference 1). If the area of a particular interval is to be computed, a low order polynomial is fitted to points surrounding that interval. As the density of known points increases, so does the accuracy of the computed area. The density of known points should be large in regions where the slope of the function changes rapidly (Reference 2). Three such integration methods are described below, two of which are used in the Manual and Fixed Points Programs, and the third, proposed for use in the Fixed Point Program.

Linear Interpolation (Manual Program)

The Manual Program computes the area of a function $y(x)$ in some interval x_A to x_B which may or may not contain the known data points. The values of y at A and B are approximated by interpolating along a straight line between points surrounding x_A and x_B . If the interval contains no

known points, the area is taken to be that of the trapezoid formed by the points $(x_A, 0)$ (x_A, y_A) , (x_B, y_B) , $(x_B, 0)$, i.e., the integrating polynomial is of 1st degree. (See Figure E-3.)

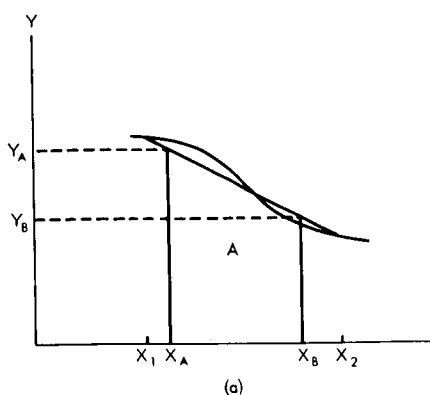
$$A = \frac{(y_B + y_A)(x_B - x_A)}{2}.$$

If known points corresponding to x_j , x_{j+1} - - - x_{j+n} lie between x_A and x_B , then the area is approximated by the sum of trapezoidal areas formed by these points. (See Figure E-3b.)

$$A = \frac{1}{2} \left[(y_j + y_A)(x_j - x_A) + (y_B + y_{j+n})(x_B - x_{j+n}) + \sum_{k=1}^n (y_{j+k} + y_{j+k-1})(x_{j+k} - x_{j+k-1}) \right]$$

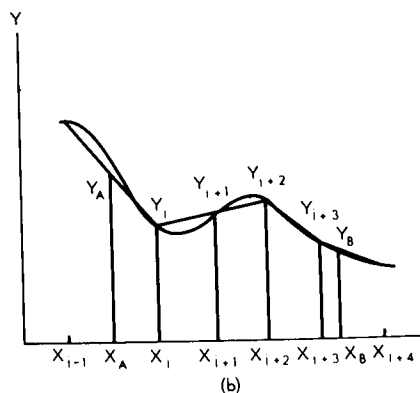
When finding the total area under a curve, however, this program uses only the N known points. The area has several equivalent geometric representations. It can be interpreted as the sum of areas of triangles formed by the points (x_j, y_j) , $(x_{j-1}, 0)$ and $(x_{j+1}, 0)$ or as the sum of rectangles of height y_j and width $1/2(x_{j+1} - x_{j-1})$. The formulae used in the program represent these figures, but the method is equivalent to the trapezoid method above; i.e., the area is the sum of areas of trapezoids between x_j and x_{j+1} . (See Figure E-4)

$$A = \sum_{i=1}^N \frac{y_i(x_{i+1} - x_{i-1})}{2} = \sum_{i=1}^N \frac{(y_{i+1} + y_i)(x_{i+1} - x_i)}{2}$$



KNOWN POINTS x_1 AND x_2

$$A = \frac{(y_B + y_A)(x_B - x_A)}{2}$$



$$A = \frac{(y_1 + y_A)(x_1 - x_A)}{2} + \frac{(y_B + y_{1+3})(x_B - x_{1+3})}{2} + \sum_{k=1}^3 \frac{(y_{1+k} + y_{1+k-1})(x_{1+k} - x_{1+k-1})}{2}$$

Figure E-3—Trapezoidal integration in the Manual Program.

Quadratic Interpolation (Fixed Point Program)

The Fixed Point Program utilizes parabolic approximation to integrate a function $y(x)$. To compute the area in an interval between two known points x_j and x_{j+1} , the program considers two sets of three points each (x_{j-1}, y_{j-1}) , (x_j, y_j) , (x_{j+1}, y_{j+1}) and (x_j, y_j) , (x_{j+1}, y_{j+1}) , (x_{j+2}, y_{j+2}) . If either of these sets of points lies along a straight line, the area in the interval is taken to be that of a trapezoid between points j and $j+1$. If neither set of points forms a straight line, parabolas are constructed through each set, and the area in the interval is approximated by the average of the areas of the two parabolas in the interval. If $x_j = x_{j+1}$, i.e., there is a step jump, the area is set to zero, and the areas between x_{j-1} and x_j and between x_{j+1} and x_{j+2} are determined by the trapezoid method.

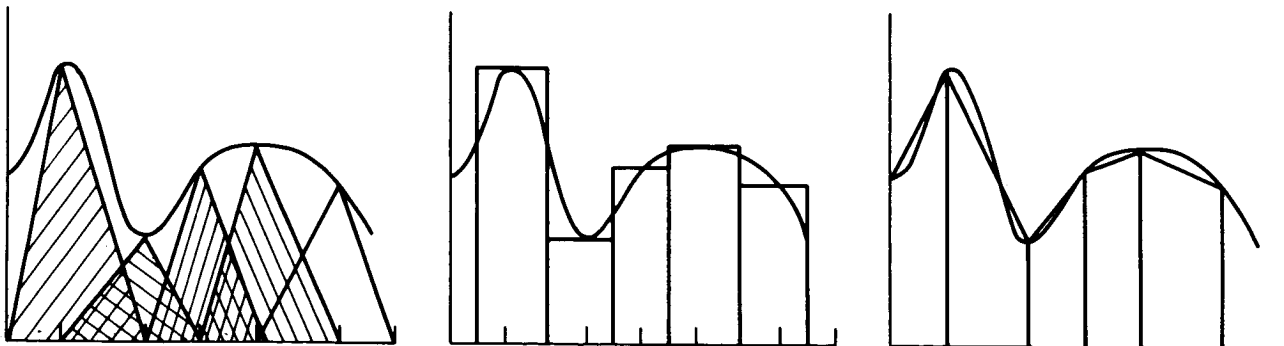
The method proposed for the Fixed Point Program also uses parabolic interpolation. This routine does not, however, look for straight lines; but instead it treats straight lines as degenerate parabolas. Except at step jumps, the area in an interval is taken to be the average of the parabolic areas. At step jumps, the parabolic rather than the trapezoidal approximation is used. For continuous curves, the two methods treat the data in an identical manner except in two special cases.

If a curve suddenly becomes a straight line, and a known point occurs at the place where the line starts, the proposed method will be incurred in the interval following that point because it will average the exact area under the line with that under a parabola. For example, consider the function.

$$f(x) = \begin{cases} x^3 + 1 & \text{for } 0 \leq x \leq 1 \\ 3x - 1 & \text{for } 1 \leq x \end{cases}$$

with known points

x	y
0.0	1.0
0.5	1.125
1.0	2.0
1.5	3.5
2.0	5.0



$$A = \sum_{k=1}^N \frac{Y_k (X_{k+1} - X_{k-1})}{2}$$

Figure E-4—Equivalent representations of area formula.



Then the methods yield results as shown below:

Interval	Actual Area	Area Computed By Existing Method	% Error	Area Computed By Proposed Method	% Error
0.0 - 0.5	0.515625	0.50	-3.0%	0.50	-3.0%
0.5 - 1.0	0.734375	0.7508	+2.2%	0.7508	+2.2%
1.0 - 1.5	1.375	1.375	0 %	1.3620	-0.94%
1.5 - 2.0	2.125	2.125	0 %	2.125	0 %

In the third interval, where the straight line starts, the proposed method is less accurate than the existing method.

If there is an inflection point in the curve, and three known points happen to fall in a straight line, then the existing routine considers only the straight line approximation, while the proposed method compensates with adjacent parabolas. For example the function

$$f(x) = x^3 - 3x^2 + 3x$$

has an inflection point at $x = 1$. If known points are

X	Y
0.0	0.0
0.5	0.875
1.0	1.000
1.5	1.125
1.75	1.421875

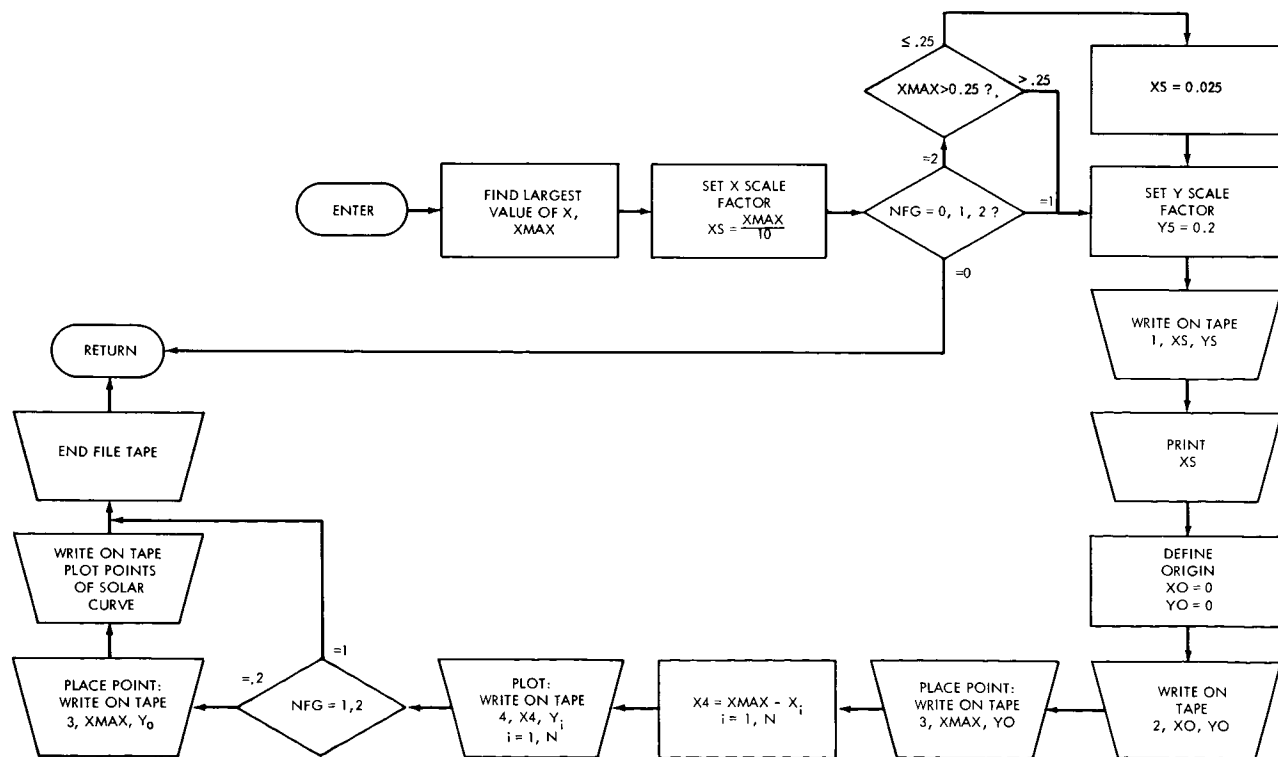
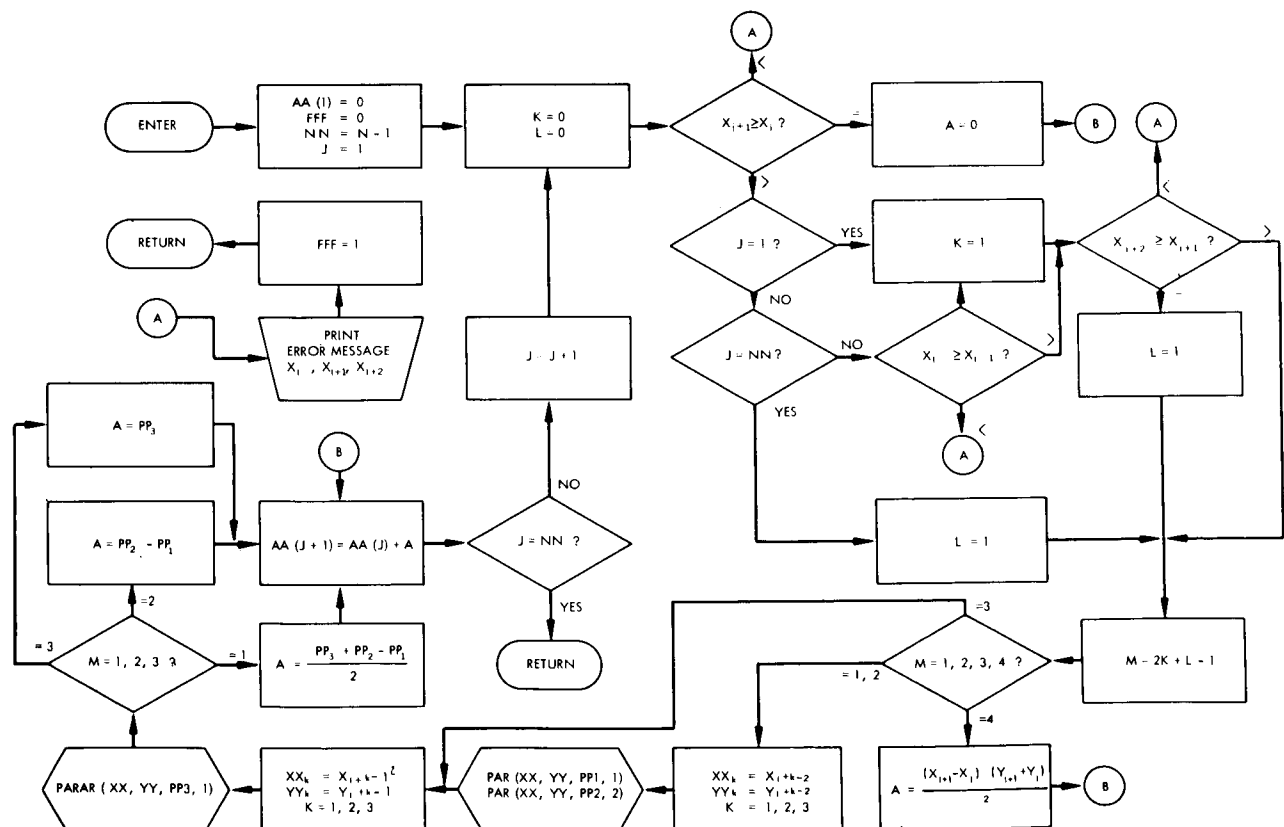


Figure E-6—Plot sub-routine for fixed point program.

Interval	Actual Area	Area Computed By Existing Method	% Error	Area Computed By Proposed Method	% Error
0.0 - 0.5	0.265625	0.25	-5.9%	0.25	-5.9%
0.5 - 1.0	0.484375	0.46875	-3.2%	0.484375	0 %
1.0 - 1.5	0.515625	0.53125	+3.0%	0.51823	+0.51%
1.5 - 1.75	0.3134765625	0.3151	+0.52%	0.3151	+0.52%

ACCURACY OF INTEGRATION METHODS

The Manual and Fixed Point Programs have to integrate functions which are not well behaved. The line spectrum of most sources displays sharp peaks and deep valleys. The spacing of data points is very critical. To test the relative accuracies of the linear and quadratic methods, test curves which display the same effect as a spectral curve were integrated using both methods. Analysis of one of these has been completed. This is a curve of the function



424

$$y = 1 + \cos \pi x e^{-.2x} \text{ in the interval } 0 \leq x \leq 10.$$

The errors incurred by the two methods are shown in the Tables E-1 and E-2.

Table E-1
Errors Incurred Using Linear Method

Point Spacing	Interval Width	Average Absolute Error per Interval	Error in Total Area
1.0	1.0	3.0%	} 0.26%
1.0	0.5	5.4%	
1.0	0.2	8.1%	
0.5	1.0	0.5%	} 0.04%
0.5	0.5	0.5%	
0.5	0.2	4.2%	
0.2	1.0	0.4%	} 0.02%
0.2	0.5	0.4%	
0.2	0.2	0.4%	

Table E-2
Errors Incurred Using Quadratic Method

Point Spacing	Average Absolute Error per Interval	Error in Total Area
1.0	6.0%	3.2%
0.5	0.31%	0.07%
0.2	0.01%	0.004%

Although further tests may be needed, a few rules for selecting data points can be formulated.

1. For large and/or sharp peaks and valleys, points should be taken at relative maximum and minimum and, if possible, at least one point between.
2. If the shape of lines is critical, several points should be taken on either side of the maximum.
3. In the Manual Program, the width of intervals investigated should be about as large as the spacing between local maximum and minimum (about 0.01 micron wavelength interval is sufficient). A larger interval loses the shape of the spectrum. A smaller interval increases the error in each interval.

REFERENCES

1. Milne, William E., Numerical Calculus, Ch. 4
2. Richardson, C. H., Calculus of Finite Differences, Ch. 2, 4

APPENDIX

PREDEFINED PROCESSES FOR MANUAL PROGRAM

1. For each data point, find the wavelength for the drum count by interpolating linearly between points of the drum count to the wavelength conversion tables; select the gain factor for each point from the table of FACTOR vs. G.
2. For each wavelength of data points for the unknown, find the flux from the standard, FS by linear interpolation from the standard curve; find the signal from the standard by interpolating from CALIB vs. λ (SIGS), then the flux of unknown, FX is given by

$$FX = \frac{UNKNOWN \times FS}{SIGS} .$$

3. The area under the curve Y vs. X with N known points is

$$A = \sum_{k=1}^N \frac{Y_k (X_{k-1} - X_{k+1})}{2}$$

where $X_0 = X_1$ and $X_{N+1} = X_N$

4. In interval λ to $\lambda + \Delta\lambda$, if there are no known points in the interval then find f_λ and $f_{\lambda+\Delta\lambda}$ from FX vs. λ .

$$A = \frac{\Delta\lambda}{2} (f_\lambda + f_{\lambda+\Delta\lambda})$$

If known points $\lambda_j, \lambda_{j+1}, \dots, \lambda_{j+n}$, lie within the interval, then

$$A = \frac{(\lambda_j - \lambda)}{2} (FX_j + f_\lambda) + \frac{(\lambda + \Delta\lambda - \lambda_{j+n})}{2} (f_{\lambda+\Delta\lambda} + FX_{j+n}) + \sum_{k=1}^n \frac{(\lambda_{j+k} - \lambda_{j+k-1})}{2} (FX_{j+k} - fX_{j+k-1})$$

5. At midpoint of each interval, $\lambda + \Delta\lambda/2$, find absorptivity, ABS, from absorptivity vs. λ curve. Absorptance is given by

$$A = ABS \times f_{\lambda + \frac{\Delta\lambda}{2}}$$

PREDEFINED PROCESS FOR PROPOSED AREA SUBROUTINE

PARAR (XX, YY, PP, K)

$$\begin{aligned} P_1 &= XX_2 - XX_1 & P_2 &= XX_3 - XX_1 \\ Q_1 &= YY_1 - YY_1 & Q_2 &= YY_3 - YY_1 \end{aligned}$$

$$A = \frac{Q_1 P_2^2 - Q_2 P_1^2}{2P_1 P_2 (P_2 - P_1)}$$

$$B = \frac{Q_2 P_1 - Q_1 P_2}{3P_1 P_2 (P_2 - P_1)}$$

$$PP = P_K (YY_1 + P_K (A + P_K B))$$

EVALUATION OF THE CONE RADIOMETER

John M. Crowell, Donald L. Henry, and Edward D. Reed

INTRODUCTION

N 67-22772

Experiments with two wire-wound cone radiometers were carried out using two different types of enclosures for the cones. The resistance of a cone is temperature dependent. This phenomenon allows the cone to be used for absolute measurements of incident light flux by calibrating the cone with respect to resistance with I^2R heating, provided the temperature of the cone enclosure remains constant. The two enclosures tested were a heated copper jacket and an evacuated copper jacket cooled with circulating ice water. Measurements of the flux from standardized quartz-iodine tungsten lamps were taken.

THEORY

The cone radiometer consists of two parts: a wire-wound cone and a constant temperature enclosure. The cone is a coil of 2 mil nickel wire wound on a conical-shaped mandril having an apex angle of approximately 30 degrees. See Figure E-8. The outside and, after the mandril has been removed, the inside of the coil are covered with a thin layer of heat-conducting epoxy for mechanical stability. The inside and outside are then painted with flat-black paint.

Two cones were tested, each with a different enclosure. The cones are referred to as cone 3 and cone 4.

The conical shape of the coil increases the absorptivity of the device above the absorptivity of the black paint alone, so that virtually all incident radiation is absorbed. Under conditions of equilibrium the following heat balance equation holds:

$$PA\alpha = A\sigma\epsilon_1 T_1^4 + A_{s_1}\sigma\epsilon_1 T_1^4 - A_{s_2}\sigma\epsilon_2 T_2^4 - G\sigma\epsilon_s T_3^4 + Q \quad (1)$$

where

- σ = Stefan-Boltzmann Constant
- P = Incident power per unit area
- A = Area of circular cone aperture
- α = Fraction of incident power absorbed
- A_{s_1}, A_{s_2} = Geometrical factors which depend on the slant areas of the cone and the jacket cavity, respectively
- ϵ_1, T_1 = Emissivity and temperature, respectively, of cone
- ϵ_2, T_2 = Emissivity and temperature, respectively, of inside of jacket
- ϵ_s, T_3 = Emissivity and temperature, respectively, of secondary sources (e.g., walls of lab)
- G = Geometrical factor for secondary sources
- Q = Heat transfer due to convection.

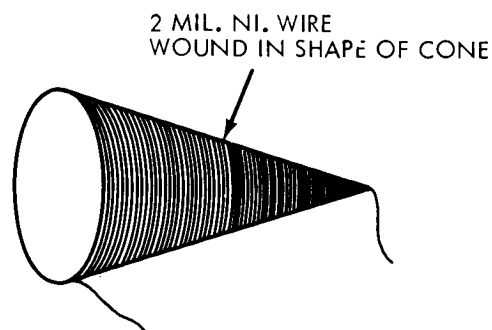


Figure E-8—The wire-wound cone.

The incident power can thus be calculated if T_1 , T_2 and T_3 can be determined. In practice the electrical resistance of the cone is measured since it is uniquely determined by the temperature. The calibration procedure involves determining the cone resistance as a function of I^2R heating, and then the incident power merely equals the I^2R power that produces the same resistance:

$$PA\alpha = I^2R$$

or

$$P = \left(\frac{1}{A\alpha} \right) I^2R \quad (2)$$

This procedure assumes that the right hand side of Equation (1) is the same during both I^2R heating and flux measurement. Hence, the uncontrollable terms $G\sigma\epsilon_3 T_3^4$ and Q need not be considered if the surroundings remain at the same temperature during the calibration and testing.

HEATED JACKET DESIGN

Cone 3 was mounted on a copper ring faceplate with a small quantity of non-heat-conducting epoxy. The faceplate was then mounted on a cylindrical copper block with the cone projecting into a cavity in the copper jacket. The jacket is 5.4 cm long and 2.6 cm in diameter. See Figure E-9.

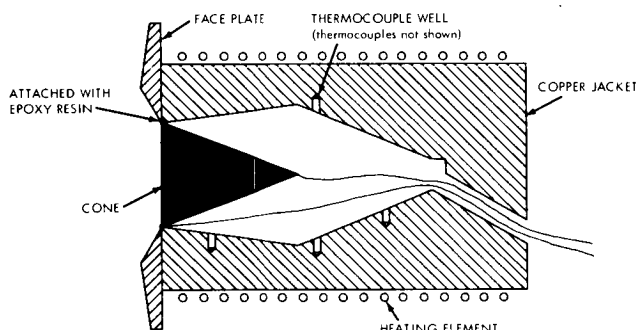


Figure E-9—Cone 3 mounted in a heated jacket.

Four copper-constantan thermocouples were mounted in the jacket, one on the cavity wall at the front of the jacket, two in the middle, and one at the rear. Flat black paint covered the inside of the cavity. For heating purposes a copper wire was wound around the outside of the jacket.

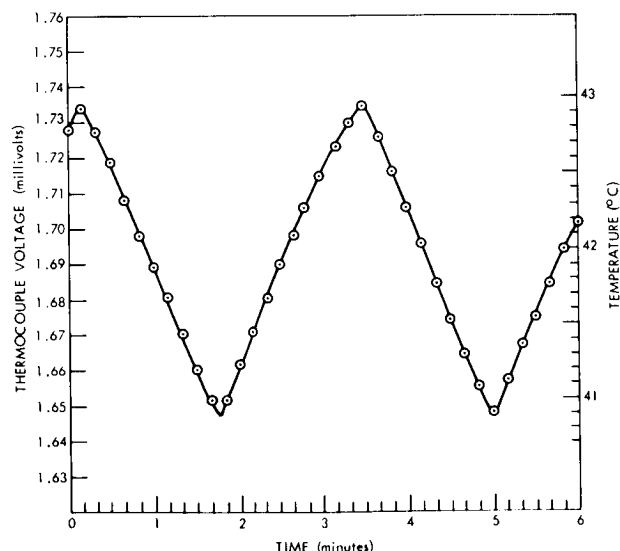


Figure E-10—Time vs thermocouple monitor voltage and corresponding temperature for cone 3 using zero Q circuit.

Current through the heating coil was controlled by balancing the emf output of one of the thermocouples mounted inside the copper jacket against a preset external emf using a "zero-Q" bridge. The jacket temperature as monitored by a second thermocouple remained within one degree of the mean value, but even this small variation caused very noticeable fluctuations in the calibration curve of the cone. Hence, readings were made only when the heater current turned off during a heating cycle. The heater turned off at the same temperature within 0.1 degree centigrade, and as a result the calibration curve smoothed out considerably. The variation in jacket temperature as a function of time is shown in Figure E-10.

The aperture area of cone 3 was measured with a Nikon Shadow-Graph. Several measurements led to an average diameter giving an area of 0.688 cm².

Calibration of the cone radiometer consisted of supplying $I^2 R_c$ power to the cone and measuring the corresponding cone resistance R_c . This was achieved by connecting a 500Ω resistance, R_0 , in series with the cone and then measuring the voltage across the cone, V_c , and across the resistor, V_0 , while varying the power supplied to R_0 and R_c . Then $I = V_0/R_0$, $R_c = (V_c/V_0)R_0$, and $P = I^2 R_0$. As mentioned previously, it is important to insure that the right hand side of Equation (1) be the same during calibration as during testing. A screen containing a rectangular aperture used to shield the light source from the observers was maintained at the same temperature for calibration as for testing by operating the source with the screen aperture blocked off during calibration. The results of the calibration are shown in Figure E-11.

In a later experiment a 3.3mm thick Suprasil quartz plate was positioned in front of the cone. With the plate in place, six values of $I^2 R_c$ vs. R_c were checked and each point fell on the curve of Figure E-11. It was therefore assumed that the cone calibration was still valid with the quartz in place.

Using a standard quartz-iodine lamp (QM 20) as a source, the equilibrium resistance of the cone was noted at three distances from the lamp; 20 cm, 28 cm, and 37 cm. The data are shown in Table E-3. The source of computed flux values will be explained shortly.

The cone resistance was measured with a Dana digital voltmeter with circuitry for measuring resistance. Measurements had to be made quickly to reduce the heating of the cone by the voltmeter, since the meter can supply as much as 10 ma. to the object whose resistance is being measured.

Listed in Table E-4 are the results of a test using another quartz-iodine lamp (QM 18) at the same distances as for the QM 20.

As a third test of the cone radiometer, measurements were made using the quartz plate mentioned above in conjunction with the QM 18 lamp. This test was of interest because the cone will eventually be operated in a vacuum with a quartz window. Table E-5 shows the results of this test. The large error at 37 cm was probably due to the difficulty of accurately measuring the cones resistance; the heating effects of the Dana caused large fluctuations in R_c .

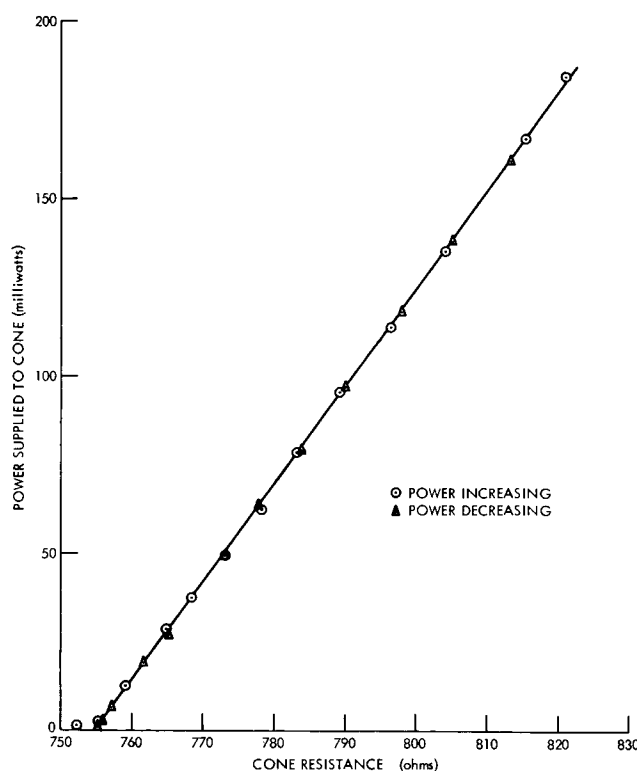


Figure E-11—Calibration curve for cone 3 in heated jacket.

Table E-3
Results of Cone Radiometer Test with QM20 Standard Lamp

Distance (cm)	Measured Flux (Solar constant)	Computed Flux (Solar constant)	Percent Difference
20.0	1.475	1.565	-5.9
28.0	0.761	0.799	-4.9
37.0	0.431	0.457	-5.8

Table E-4
Results of Cone Radiometer Test With QM 18 Standard Lamp

Distance (cm)	Measured Flux (Solar constant)	Computed Flux (Solar constant)	Percent Difference
20.0	1.560	1.590	-1.9
28.0	0.789	0.812	-2.9
37.0	0.458	0.465	-1.5

Table E-5
Results of Cone Radiometer Test with QM 18 Lamp and Quartz Window

Distance (cm)	Measured Flux (Solar constant)	Computed Flux (Solar constant)	Percent Difference
20.0	1.354	1.311	3.2
28.0	0.687	0.669	2.7
37.0	0.417	0.384	8.3

The computed flux values in Tables E-3 and E-4 were obtained in the following manner. The total integrated flux seen by the cone is given by $\int_0^{\infty} N_{\lambda} \alpha_{\lambda} d\lambda$ watts/steradian, where N_{λ} is the spectral radiance of the lamp and α_{λ} is the water vapor absorption coefficient. N_{λ} was obtained from NBS tables for the lamps and from the results of the 1965 Summer Workshop (ref. 1) and is assumed to be nonzero only between 0.25μ and 20μ .

Atmospheric water vapor absorption was considered only for the 2.7μ water vapor band. Values for α_{λ} were computed from experimental absorption data taken under conditions which were unfortunately not the same as those in the radiometer experiments, but the data were used only to provide a rough estimate of the absorption effects. The calculations indicated that about 2 percent of the total flux emitted by the lamp was absorbed by the 2.7μ water vapor band, and this value was used for both lamps and for all distances. It is very probable that this figure is much too large for the conditions of these experiments.

The computed flux values listed in Table E-5 are corrected for the transmittance of the quartz window. The integrated flux in this case is $\int_{0.25\mu}^{20\mu} N_{\lambda} T_{\lambda} \alpha_{\lambda} d\lambda$, where T_{λ} is the quartz transmittance. T_{λ} was obtained by direct measurements using Beckman IR-9 and DK-2A spectrophotometers and includes reflection losses. About 18 percent of the flux incident on the window was absorbed and reflected. The spectral transmittance of the quartz plate is shown in Figure E-12.

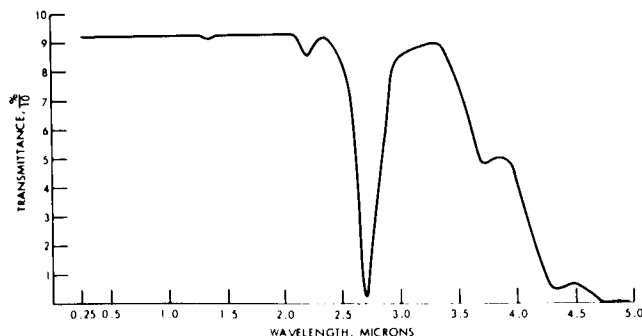


Figure E-12—Transmission of quartz window, 3.3 mm thickness.

COOLED JACKET DESIGN

A different jacket was designed to provide a low temperature environment for the cone and was tested using cone 4. Cooling was provided by copper coils through which a liquid circulated.

These coils surrounded a copper block containing a conical cavity. The cavity was covered with a quartz plate and evacuated. (See Figure E-13.)

The evacuation of the cavity eliminated condensation of water vapor inside the cavity while maintaining the jacket at a low temperature. A mechanical pump reduced the cavity pressure to roughly 50μ of Hg.

To determine the effect of convection currents in the cavity both at 760 mm and 50μ of Hg, a calculation was made using the crude analogy of two concentric cylinders having radii of the bases of the cone and cavity (References 2 and 3). This calculation indicated that the heat transfer due to convection at both pressures was very negligible.

Heat transfer due to conduction through air at atmospheric pressure is on the order of 20 mW/cm². Hence, evacuation of the enclosure cavity will also eliminate any variations in heat conduction through air surrounding the cone.

Eight wires, four fastened with epoxy near the top of the cone and four at the bottom, secured the cone to a teflon ring. A silver-coated Mylar film with an aperture about the same size as the cone aperture was fastened to the teflon ring. A second teflon ring insulated the mounting wires from the jacket. See Figure E-14.

The area A in Equation (1) was measured with the aid of the Nikon shadow-graph, which projected a magnified (20x) image of the aperture onto a screen. A tracing of the image was made on graph paper and the area determined by counting squares printed on the paper. The smallest printed square was 1/400 in.² in area.

The interior of the cone absorbed about 99.6% (i.e., $\alpha = 0.996$ in Equation (1)) of the incident power (ref. 4) and the absorptivity of the front edge of the cone wall was that of the black point, viz. 0.95. If A_1 is the aperture area bounded by the wide edge of the wall and A_2 is the area bounded by the outside edge, then the effective product $A\alpha$ in Equation (2) is

$$A\alpha = A_1 (0.996) + (A_2 - A_1) (0.95).$$

A_1 was measured to be 0.684 cm² and A_2 was 0.772 cm²; hence,

$$A\alpha = 0.717 \text{ cm}^2$$

This figure should be accurate to within 0.5%.

The cone was not securely fastened to the teflon mounting ring, and the aperture very likely

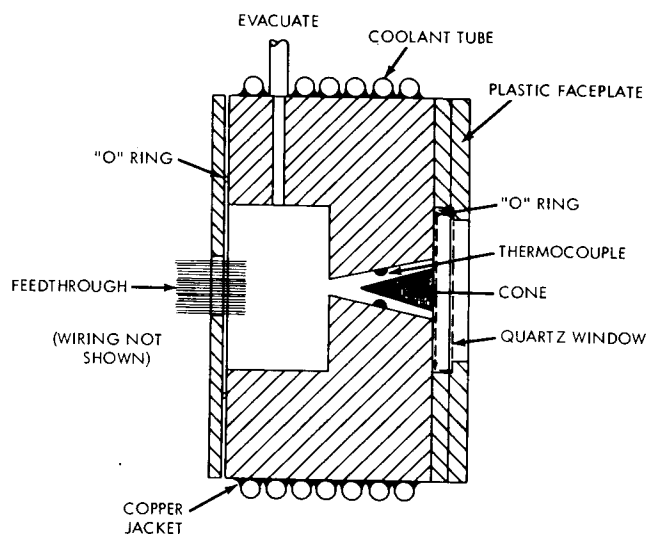


Figure E-13—Cone 4 mounted in ice water cooled, evacuated jacket.

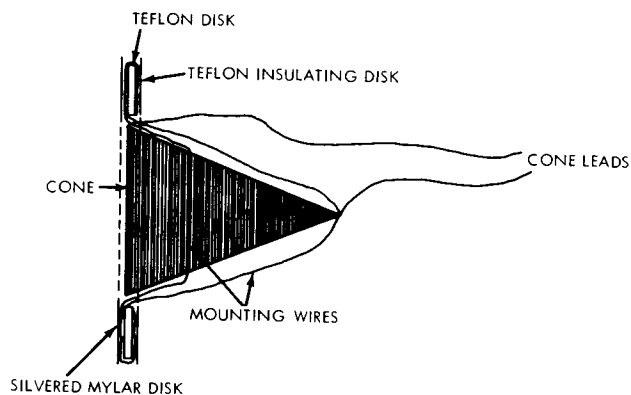


Figure E-14—The mounting for cone 4.

changed slightly during handling of the cone, but there was only 0.4% difference between area measurements before and after testing of the cone.

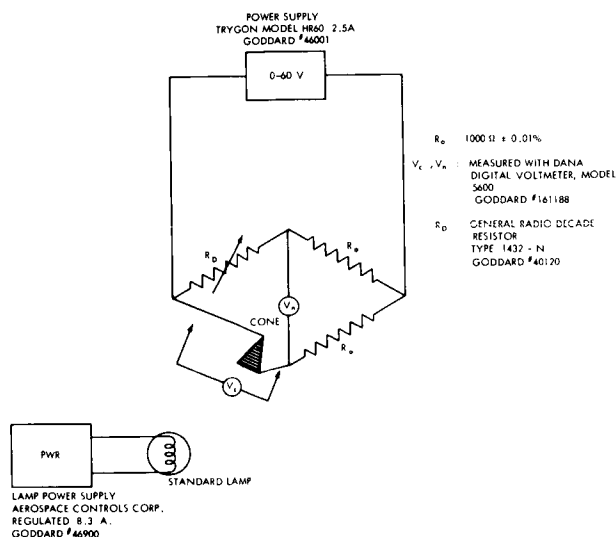


Figure E-15—Wheatstone bridge for measuring cone resistance.

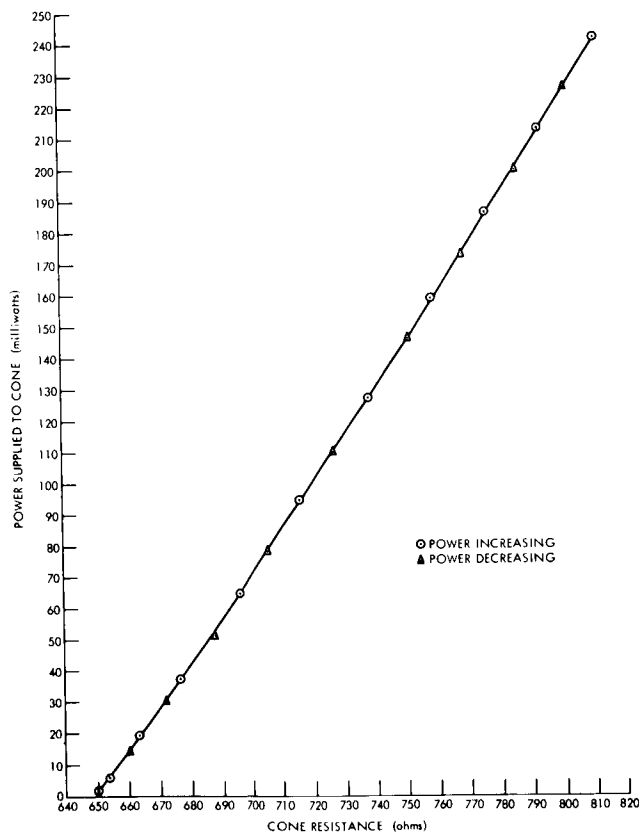


Figure E-16—Calibration curve for cone 4 in ice water cooled, evacuated jacket, R_C measured using the bridge method.

A nylon ring, held in place the quartz window covering the jacket cavity and a rubber "O" ring provided the vacuum seal.

Four copper-constantan thermocouples were mounted with epoxy inside the cavity, one at the front, two in the middle on opposite sides of the cavity, and one at the rear.

Liquid nitrogen was first circulated through the coils, but two problems developed. First, moisture began to freeze on the quartz window, and second, the vacuum could not be maintained when the rubber "O" rings hardened at LN_2 temperature. The decision was then made to pump ice water around the jacket in place of the LN_2 . The high heat capacity of water and the relative ease in holding the bath at a constant $0^\circ C$ makes ice water thermally very stable.

The temperature gradient in the cavity, as monitored by the four thermocouples, changed with cone temperature (T_1), but the gradient was fairly well repeatable for a given T_1 . Hence, the gradient for a given T_1 should be the same during both calibration and testing and should not affect the results. Temperature gradients along the cone itself could not be measured with the design used. Such a gradient, if it exists to a significant degree, could very well induce an error in calibration.

The largest temperature observed was $2.3^\circ C$, and this was monitored by a middle thermocouple which may have been located very near one of the cone leads. It was observed during both calibration and testing. The other thermocouples registered temperatures around 1.2 to $1.6^\circ C$. The largest temperature difference between the front and rear thermocouples was $0.3^\circ C$.

One method for measuring the power absorbed by the cone required $I^2 R_C$ calibration, and two calibration procedures were followed. The first setup consisted of a 500Ω resistor in series with the cone and a dc power supply across the two, as was done for cone 3 in the heated jacket. The second calibration procedure made use of the bridge circuit of Figure E-15. The power supplied to the bridge was varied and the bridge balanced so that $R_D = R_C \cdot V_C$ was then measured, and $P = V_C^2 / R_C$. A straight line

best represents the calibration data obtained with the series method. A least-squares calculation yielded the curve:

$$P(\text{in mW}) = 1.474 R_c - 958.2$$

The maximum deviation is 3.6 mW at 170.5 mW and the mean deviation is 1.11 mW. For R_c greater than 680Ω , the maximum error is 2.8 percent at 62.5 mW. A polynomial of order 2 also seems to fit these data fairly well, and because of some lack of confidence in the least-squares computer program used in the calculation, it cannot be definitely stated which curve is better.

The bridge calibration data, plotted in Figure E-16 are best fitted to a parabola:

$$P(\text{in mW}) = -590.2 + 0.442 R_c + 0.000717 R_c^2$$

In this case the maximum deviation is 0.787 mW at 1.43 mW and the maximum percent deviation is 90% at 0.54 mW. The mean deviation is 0.351 mW and the mean percent deviation 5.5%. For R_c greater than 680Ω the maximum percent deviation is 1.0%. It seems clear that the cone is not reliable for low power inputs, i.e., inputs less than about 50 mW.

Two quartz-iodine lamps (SW 101 and SW 102), calibrated with respect to standard lamps obtained from the National Bureau of Standards, were used as sources for the testing of the radiometer.

Two procedures were followed in determining the flux received by the cone, one of which involved measuring the resistance of the cone and then obtaining the power from the cone calibration curve. Resistance was measured in two ways. A direct measurement was made using the Dana digital voltmeter, but the device caused excessive extraneous heating. This heating was reduced considerably by connecting the cone in series with a 9000Ω resistor and using the voltmeter to measure the combined resistance. The measurements were accurate to within 0.1Ω . For an R_c of about 700Ω , the voltmeter supplied roughly 0.7 mW to the cone.

The unwanted heating was further reduced by placing the cone in the bridge circuit as shown in Figure E-15. The bridge was nulled by varying R_D so that $R_c = R_D$ at null. With a power supply voltage of 0.5V, 0.07 mW heated the cone for $R_c = 700\Omega$. Unfortunately this method was not used for the majority of the readings.

For the second method of testing the cone, the bridge circuit was again used. The cone was maintained at a constant resistance, by $I^2 R_c$ heating, corresponding to a temperature higher than the maximum temperature which the cone would reach at any time when exposed to radiant flux alone. When lamp measurements were taken, the decade box was set at 800Ω and the power supply adjusted until null was obtained. The power absorbed by the cone from the lamp was then $P_c = P_{\max} - P$, where P_{\max} is the electrical power heating the cone with no light and P is the electrical power supplied with the lamp on.

The latter method was abandoned for two reasons. While, ideally, it offered a very fast response time for the cone since the total power dissipated in the cone need not change, practically, it was a slow process when used as in this experiment, i.e., manually operating the power supply voltage while noting the bridge null voltage. Secondly, the possibility of greater error than with the previous method was introduced, since two power readings were necessary to obtain the incident flux.

Table E-6
Results of Cone Radiometer Test With Lamp SW 102, With Screen

Distance (cm)	Measured Flux (Solar constant)	Computed Flux (Solar constant)	Percent Difference
20.9	1.202	1.172	2.5
23.8	0.921	0.902	2.1
26.6	0.743	0.724	2.6
53.2	0.210	0.192	4.5

Table E-7
Results of Cone Radiometer Test With Lamp SW 101, With Screen

Distance (cm)	Measured Flux (Solar constant)	Computed Flux (Solar constant)	Percent Difference
20.9	1.226	1.193	2.7
23.8	0.977	0.921	5.9
26.6	0.798	0.738	7.8
53.2	0.224	0.197	13.5

Table E-8
Results of Cone Radiometer Test With Lamp SW 102, Without Screen

Distance (cm)	Measured Flux (Solar constant)	Computed Flux (Solar constant)	Percent Difference
53.2	0.191	0.192	-0.5
30.7	0.556	0.541	2.7
26.6	0.749	0.724	3.4
25.1	0.836	0.812	2.9
23.8	0.934	0.902	3.5
22.7	1.024	0.995	2.9
20.9	1.204	1.172	2.7
18.3	1.569	1.530	2.5
20.9	1.213	1.172	3.4
22.7	1.022	0.995	2.7
23.8	0.927	0.902	2.7

The radiated power data measured by the radiometer and their comparison with computed values are shown in Tables E-6, E-7, E-8 and E-9. Values are in units of one solar constant, where one solar constant is 139.5 mW/cm². The data from tables E-8 and E-9 are plotted in Figures E-17 and E-18 respectively.

Table E-9
Results of Cone Radiometer Test With Lamp SW 101, Without Screen

Distance (cm)	Measured Flux (Solar constant)	Computed Flux (Solar constant)	Percent Difference
53.2	0.183	0.197	-7.4
30.7	0.567	0.554	2.3
26.6	0.759	0.738	2.8
25.1	0.868	0.827	4.8
23.8	0.968	0.921	5.0
22.7	1.062	1.012	4.8
20.9	1.259	1.193	5.2
18.3	1.626	1.554	4.5
18.3	1.667	1.554	7.0
20.9	1.263	1.193	5.7
22.7	0.928	1.012	-8.7
23.8	0.974	0.921	5.6
25.1	0.862	0.827	4.1
26.6	0.760	0.738	2.9
30.7	0.579	0.554	4.4
53.2	0.182	0.197	-7.9

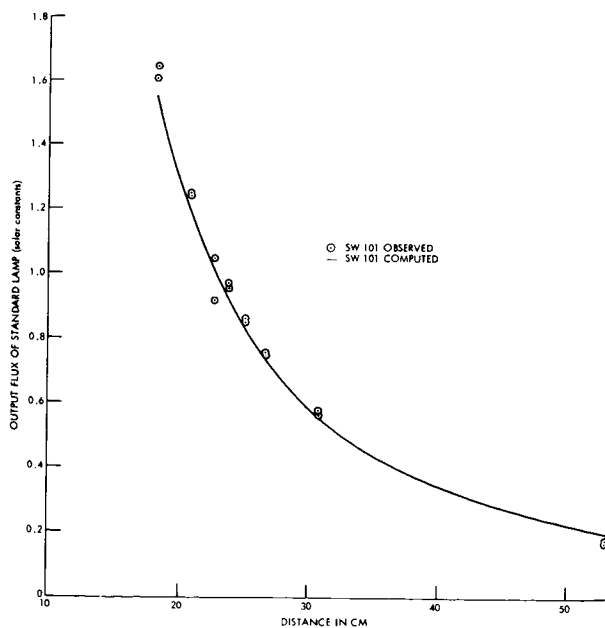


Figure E-17—Comparison of output measured with the cone radiometer and calculated output for lamp SW 101.

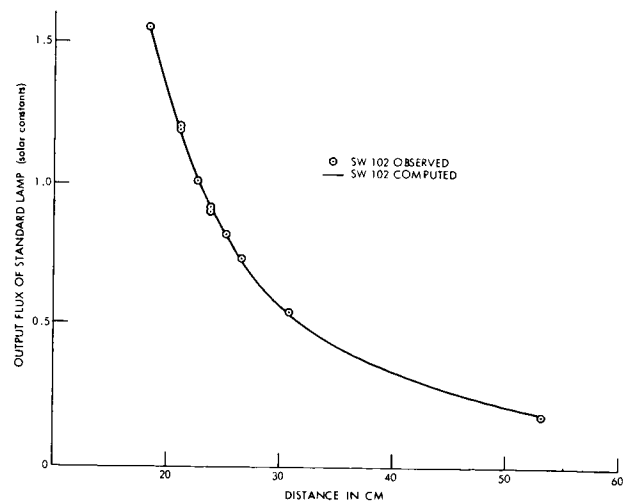


Figure E-18—Comparison of output measured with the cone radiometer and calculated output for lamp SW 102.

The computed power values were obtained from tables for the SW101 and SW102 lamps, and a correction was made for the effect of the quartz window of the radiometer. As mentioned above, 82 percent of the incident radiation from the QM 18 lamp was transmitted by the window. While the outputs of SW101 and SW102 are not exactly the same as that of the QM 18 lamp, the spectral distribution of the outputs are very nearly identical and hence 82 percent should be the percent transmitted for the SW lamps also. Thus the tabulated outputs of these two lamps were multiplied by 0.82 before a comparison with experimental results was attempted.

Two sources of experimental error are the uncertainties in resistance measurements and the uncertainties in the calibration curve. Assuming an error of $\pm 0.1\Omega$ with either the series or the bridge method of resistance measurement, an error of ± 0.16 mW at 800Ω and ± 0.14 mW at 664Ω results. Combining this with the 0.001% and 1.6% errors in the parabolic least squares fit for 800Ω and 664Ω respectively gives errors in the power of ± 0.14 mW, or 0.06%, at 800Ω and 0.45 mW or 2.3% at 664Ω . However, as mentioned previously, the least squares fit is not good for R_c less than 680Ω .

The absorptivity (α) of the cone has been assumed to be unity. The error in this assumption is less than 0.5%.

Tests for the repeatability of measurements established that the data are reliable to within only 2 percent.

With improvement in the repeatability of the cone radiometer, accurate results should be obtainable. Assuming repeatable measurements, very accurate measurements of flux above about 0.7 solar constant can be realized.

ACKNOWLEDGMENTS

We wish to express our thanks to Dr. M. P. Thekaekara for his guidance and helpful suggestions and to Mr. A. R. Winker and Mr. T. A. Riley for their indispensable help in the laboratory.

REFERENCES

1. Thekaekara, M. P., and Mohr, E. I., "The tungsten lamps as a secondary standard for total radiant flux." Final Report of the Goddard Summer Workshop Program in Analysis of Space Data and Measurements of Space Environments. GSFC X-100-65-407 pp. B-39-B-46, 1965.
2. Jakob, Max, Heat Transfer, Vol. 1, John Wiley & Sons, Inc., 1949
3. Jakob, Max and Hawkins, George, Elements of Heat Transfer, John Wiley & Sons, Inc., 1957
4. Korb, C. L., Rancourt, J. D., and Thekaekara, M. P., "Conical radiation detectors." Final Report of the Goddard Summer Workshop Program in the Analysis of Space Data and Measurements of Space Environments. GSFC X-100-65-407, pp. B-22, 1965.

OK

CALIBRATION OF WORKING STANDARDS OF SPECTRAL IRRADIANCE FOR LABORATORY USE

Arthur McNutt, Jan Slavin and Matthew P. Thekaekara

INTRODUCTION

N 67-22773

Standards of spectral irradiance are an important laboratory tool for measuring the spectral irradiance of other unknown sources. Many different types of standards for spectral irradiance have been issued in the past by the National Bureau of Standards (NBS). The most recent type is the quartz iodine lamp described by Stair, Schneider and Jackson (ref. 1). The QM type lamp of 1000 watts rated power was previously supplied by the NBS. More recently this type of lamp is being supplied by the Eppley Laboratory, Newport, Rhode Island, for about \$400.

The spectral irradiance of the QM type lamp is in the range of 0.25 to 2.5 microns and can be extended to 20 microns by methods described in "The Tungsten Lamp as a Secondary Standard for Total Radiant Flux" by M. P. Thekaekara and E. I. Mohr (ref. 2). Similar lamps are commercially available for about \$12, but are uncalibrated. If calibrated, such lamps would be more economical for routine use in the laboratory, since both types have a limited life (about 800 hours), during which their calibration is valid. The objective of this project was to calibrate four commercial 1000 watt quartz iodine lamps using two NBS standard lamps.

EXPERIMENTAL PROCEDURE

The general procedure was to measure the flux output of one of the lamps at a given wavelength using a monochromator and associated electronics. The result was a signal, recorded on a chart recorder, proportional to the flux from the lamp. If a series of measurements is made on the NBS standard, and then the same series of measurements is made on the commercial lamps, the following equation should be valid.

S_{sw} - signal of commercial lamp calibrated by the Summer Workshop

$$\frac{S_{sw}}{F_{sw}} = \frac{S_{qm}}{F_{qm}}$$

F_{sw} - Flux of commercial lamp calibrated by the Summer Workshop

S_{qm} - signal of standard QM lamp (quartz iodine, 1000W)

F_{qm} - flux of standard lamp

From this equation, using the experimental data S_{sw} , S_{qm} and the NBS values for F_{qm} , the flux F_{sw} of the commercial lamp can be calculated. The validity of the equation, however, rests on the assumption that the optical arrangement and response of the instruments were exactly the same in each case. The degree to which the arrangements were the same and the factors involved are discussed later in this report.

The experimental setup is shown in Figure E-19. The lamps were inserted in the holder supplied by NBS. The holder was fastened to a ringstand which was then fastened to the table top. The lamps were positioned using two telescopes mounted on the table. There were two NBS lamps, the QM 18 and QM 20. They were positioned as shown in Figure E-20a. There were four commercial lamps; SW-101, SW-102, SW-103, and SW-104. They were positioned as shown in Figure

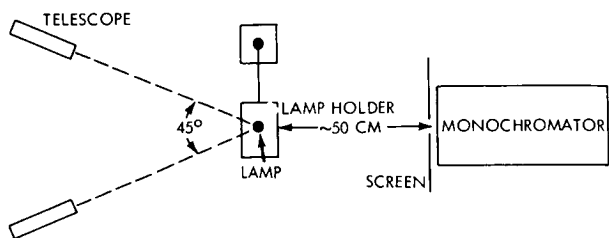


Figure E-19—Experimental arrangement for comparison of spectral irradiance of quartz iodine lamps.

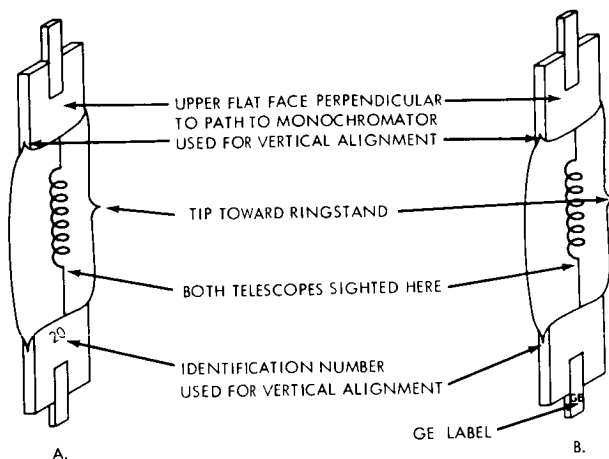


Figure E-20—Identifying marks used to position lamps.

E-20b. The monochromator was set on the same table and not moved until measurements were completed on all six lamps. The monochromator was a Perkin-Elmer 112-U with a photomultiplier and thermocouple detector. The upper half of the entrance and exit slits was blocked off to reduce scattered light in the instrument. An aluminum foil covered cardboard screen was placed just in front to the entrance to the monochromator to help keep out stray light and to prevent heating of the monochromator case. A fan blew on the back of the screen to cool it. The amplifier, chart recorder, and other control equipment were on a rack on the floor. The gain range of the amplifier was from zero to twenty. The measurements were made in three different ranges of wavelength using the detector and slit as indicated in Table E-10. This particular order for the ranges was chosen for several reasons. A 200μ slit was used for the 0.24 to 0.31μ range in order to get a large enough signal. A narrow 10μ slit was used for 0.28 to 0.71μ range because the signal was strong enough to allow it, giving better resolution. Another reason for the use of the narrow slit in this range is that the wide slit would cause saturation of the PM tube. The thermocouple was used for the 0.49 to 2.5μ range because the photomultiplier sensitivity drops off sharply above 0.5μ . It was necessary to use the 500μ slit to achieve a large enough signal. The particular

order was necessary since the 10μ slit had to be set by matching the signal with signal value from the previous 10μ slit run at a particular wavelength. The 10μ slit was also set in this manner before changing lamps, so the first measurements using the new lamp had to be made with the 10μ slit. The overlap region can be used as a check as will be discussed later. Two runs were made on each lamp in order to check the reproducibility of the measurements.

The factors which should be the same from one set of measurements to the next are:

1. Power input to the lamp.
2. Amplifier and chart recorder gain, response, and stability.
3. Wavelength calibration of the monochromator.
4. Position of the lamps.
5. Slit width.

Table E-10
Regions Where Measurements Were Made, Slit Width, and Detector

Drum Number	λ (microns)	Slit Width	Detector
1035-525	.28- .71	10μ	Photomultiplier
625-200	.49-2.5	500μ	Thermocouple
1265-900	.24- .31	200μ	Photomultiplier

The data were taken from the charts. Signal values were read every ten drum numbers to an accuracy of $\pm 0.2\mu$; full scale was 100. The signal values for two runs on the same lamp differed by as much as $\pm 3.5\mu$ in some cases. This was due to one set of signals being consistently above the other. The difference in signal values for the two runs was examined at fourteen arbitrary points for the four SW lamps. After an adjustment for any consistent difference in the signals, the root mean square of the differences in the signals was found to be 0.80 or less in all four cases. The values of the signals on the two runs were averaged so the error in the average value can be assumed to be ± 0.4 , an error of 0.8% for a midscale value of 50. This agreement between runs supports the assumptions that the power input to the lamps was regulated accurately enough and that the amplifier and chart recorder gain and response were sufficiently stable. The drum number marks on the charts were observed to be uncertain by $\pm 1/2$ drum count or 3A at drum number 800, 3,538A. This is an error of less than 0.1%, so the assumption of a constant wavelength calibration is valid.

Once positioned, a lamp was not moved until all measurements had been made on it. There is an uncertainty, however, that different lamps were in exactly the same position. Being nearer or further from the monochromator than the standard lamp would cause the calculated flux for the commercial lamps to be too large or too small respectively. A slight left or right displacement could also result in an error due to nonuniform sensitivity across the surface of the detector. Either positioning error will cause all the calculated flux values of the particular lamp to be in error by a constant factor. If this constant factor can be determined, the error can be corrected. The area under the flux vs. wavelength curve gives the total energy output of the lamp. Thus the ratio curves should be in the same ratio as the energy output of the lamps. If the ratios are not in agreement, the multiplication factor should be used to correct the calculated flux.

TOTAL IRRADIANCE MEASUREMENTS

The energy output of the lamp can be measured using a thermopile radiometer. The thermopile measures the output up to about 3.2 microns where its quartz window starts to absorb. The output of the six lamps was measured using the Epply radiometer #6590, a Dana digital voltmeter, and an optical bench. The lamps were positioned by a telescope placed perpendicular to the optical bench so as to accurately measure the lamp-to-detector distance. Measurements were made at several distances.

These measurements showed that the ratio of the thermopile signals due to the two lamps QM 18 and QM 20 did not agree with the ratio of their total irradiances at a given distance. The total irradiance was found by integrating the area under the spectral irradiance curve by the method explained in Reference 2. This disagreement seemed to show that one or the other lamp or perhaps both had deteriorated due to prolonged use. Measurements were also made with a Corning glass filter 2-64 in front of the lamp. This is a red filter which transmits about 90 percent of the energy in the IR beyond 6.7μ but is opaque to all shorter wavelength radiation. The difference between the thermopile readings with and without the filter afforded a means of checking the normalization factor for the range covered by the photomultiplier tube.

The discrepancy between the thermopile readings for the QM 18 and QM 20 lamps showed the desirability of more extensive measurements to compare these two lamps, the four SW lamps, and any other NBS certified standard lamps which may be readily available. Three such lamps with relatively few burning hours were secured from other laboratories at the Center, QM 21, QM 23 and QM 95. The measurements were made with the water-cooled Eppley thermopile 6590. The lamp was mounted at the zero mark of an optical bench and the thermopile on a stand at a known distance away from the lamp. The output was measured at four positions; in each position the zero reading was taken prior to exposing the thermopile to the radiation. The exposure was for 30 seconds. Four sets of readings were taken for each experiment; two sets for increasing distance and the other two for decreasing distance. The experiments were repeated on five different days and by different persons.

Table E-11
Weighted Averages of Measurements for Comparing NBS Standard Lamps and SW Lamps

	Distance	QM 18	QM 20	QM 21	QM 23	QM 95	SW 101	SW 102	SW 103	SW 104
Experiment I	60	1.0155	1.0047				1.0031	.9592	.9663	.9750
	41	1.0164	1.0041				.9983	.9561	.9653	.9720
	31	1.0180	1.0025				.9975	.9544	.9657	.9697
	25	1.0194	1.0016				.9954	.9505	.9657	.9660
	Average	1.017	1.003				.999	.955	.966	.971
Experiment II	60	1.0256	.9996	.9880	1.0120	.9763				
	41	1.0330	1.0003	.9898	1.0103	.9730				
	31	1.0416	1.0065	.9906	1.0100	.9752				
	25	1.0679	1.0148	.9906	1.0092	.9767				
	Average	1.042	1.005	.990	1.010	.975				
Experiment III	60	1.0237	.9957							
	41	1.0272	.9940							
	31	1.0274	.9949							
	25	1.0308	1.0164							
	Average	1.027	1.000							
Experiment IV	70	1.0116	.9984	.9815	1.0185		.9889			
	60	1.0137	1.0035	.9831	1.0208		.9945			
	41	1.0156	1.0034	.9840	1.0160		.9940			
	31	1.0132	1.0012	.9854	1.0146		.9912			
	Average	1.014	1.002	.984	1.017		.992			
Experiment V	70	1.0137		.9462			.9689		.9615	.9747
	60	1.0192		.9557			.9726		.9659	.9784
	41	1.0178		.9558			.9755		.9676	.9800
	31	1.0155		.9569			.9744		.9653	.9784
	Average	1.017		.954			.973		.965	.978
Irradiance at 50 cm.		1.0190	.9801	.9892	1.0108	.9731				

The results are presented in Table E-11. The value given for each lamp and distance is on a relative scale with reference to the standard which for all experiments is the average of the emf due to QM 21 and 23. In experiments which did not include a measurement of QM 21, and QM 23, one of the other QM lamps was used as a transfer standard. It is assumed that the irradiances of the different lamps are so close to each other that the thermopile has the same sensitivity for all lamps at a given distance and hence that the ratio of the emf is also the ratio of the irradiance of the lamps. The readings for a given lamp in different experiments and at a different distances are within one or two percent of each other. The differences are greater than might be expected and are presumably due to air currents in the laboratory or small changes in the temperature of the water which cools the casing. All serious discrepancies could be explained as being due to some experimental precaution being overlooked, and these values were discounted in the final average. A clear example of such a discrepancy are the values for QM 21 in Experiment V which are four percent lower than in Experiments II and IV. During this particular set of measurements a small air blower was turned towards the lamp instead of being turned towards the screen, which apparently lowered the temperature of the lamp. Great care was taken to ensure that the current input to the lamp remained constant at 8.3 amperes. The current was regulated by a power supply, the Aerospace Control Corporation Model 4809. During the experiments, the null indicator needle remained within ± 50 on the scale. A deviation of 75 from zero corresponds to a change in current of 0.03%, that is, ± 2.5 milliamp, and to a change in irradiance of 0.1%. Thus it is seen that changes in emf due to line fluctuations are one order of magnitude less than those due to other causes.

The last line in Table E-11 gives the irradiance of each of the standard lamps as determined by integrating the area under the spectral irradiance curve. These values also are on a relative scale with reference to the average of the lamps QM 21 and 23.

Comparison of the irradiance with the thermopile emf shows that all four lamps, QM 18, 21, 23, and 95, are in fairly close agreement, but that the emf of QM 20 is 2.2% higher than the irradiance. This explains the lack of agreement observed in our computer results on the spectral irradiance of the SW lamps with reference to QM 18 and QM 20. The conclusion from the thermopile measurements is that QM 20 has changed to some extent due to extended use. An increase in the resistance of the tungsten coil due to partial crystal formation in the metal would cause the lamp to run at a higher temperature and hence increase its irradiance.

Comparing the emf values of the SW lamps with the QM lamps we may now assign values of total irradiance at 50 cm and or radiance (per steradian) for the SW lamps. The values of radiance are given in Table E-12. The procedure for these computations is given in Reference 2. The value of QM 20 is 2.2% higher than the one computed from the NBS spectral irradiance table and given in Reference 2.

COMPUTATION OF SPECTRAL IRRADIANCE

The data from spectral measurements of the SW lamps was reduced using the "Fixed Points Program" described elsewhere in this publication (paper by J. Crowell). The computations were made with both QM 18 and QM 20 as reference standards for calibration, but the results with reference to QM 20 were later discarded.

The equation for the computation is: $f_{sw} = (S_{sw}/S_{qm}) F_{qm}$. The output consisted of:

1. F_{sw} for the various input wavelengths.
2. The area under the flux vs. wavelength curve for a given wavelength interval.
3. The total cumulative area of that wavelength, and thus eventually the total area under the curve.
4. A graph of flux vs. wavelength.

Comparing the ratios given by the radiometer with those calculated from the total area given by the computer, a correction factor can be arrived at. This method should account for any error in lamp position.

Table E-12
Radiance of Standard Lamps and SW Lamps Based on Thermopile Measurements

N = radiance from the whole lamp and in the entire wavelength range
in watts per steradian in a horizontal direction

N_w = radiance from the tungsten coil (watts ster⁻¹)

N_q = radiance from the quartz envelope of the lamp (watts ster⁻¹)

Lamp	N_w^{1} .245 to 2.55 μ	N_w^{2} 2.55 to 4.65 μ	N_w .245 to 4.65 μ	N_q 2.95 to 20 μ	N .245 to 20 μ
QM 18	74.108	7.404	81.512	8.768	90.280
QM 20	72.850	7.321	80.171	8.768	88.939
QM 21	71.938	7.266	79.204	8.768	87.972
QM 23	73.505	7.351	80.856	8.768	89.624
QM 95	70.773	7.714	78.487	8.768	87.255
SW 101	72.625	7.299	79.924	8.768	88.692
SW 102	70.100	8.237	78.337	8.768	87.105
SW 103	70.213	8.074	78.287	8.768	87.055
SW 104	70.870	7.619	78.489	8.768	87.257

Using the scale on the slit adjustment dial it was estimated that the slit could be set to an accuracy of ± 0.5 microns. For the 500μ and 200μ slits this is an error of 0.1% and 0.25% respectively, but for the 10μ slits the error is 5%. An attempt to be more accurate was made by setting the 10μ slit by matching signals as described earlier. The graphs of the calculated flux, however, showed that the slit was not consistently 10μ . The overlap region of measurements taken with the 200μ and 10μ slit was examined near its end points at 915μ and 1015μ . The ratio of the signals for the 200μ and the 10μ slit was taken for each lamp at both of these points. For a given lamp the ratio was the same at both points within 2%. The ratio differed greatly, however, from lamp to lamp. The magnitude of this ratio should reflect the difference in the slit widths since this was the only factor that was not the same for both measurements. This leads to the conclusion that the 10μ slit was not really 10μ in each case.

Two methods were used to arrive at a correction factor which could be used to adjust the data taken in the region with the 10μ slit. The first method consisted of finding the factor which would adjust the last point in the 10μ slit region, to match properly with the first point in the 500μ region. The second method was to find the ratio of the areas under the curve in the 10μ slit region and the 500μ slit region. This ratio was compared with the ratio of the areas for the same two regions calculated from the radiometer measurements with and without the Corning 2.64 filter. The ratios were not the same. The factor necessary to make them the same was the correction factor. These two separate methods gave correction factors which agreed with 1%, 3%, 10%, and 12% for the four lamps. The factors from the two methods were averaged resulting in a correction factor for the 10μ slit data for each lamp.

The input data to the computer were the signals thus corrected so as to make the signals to 10μ , agree with those of 200μ , and 500μ , thermocouple. The final table of the computer output, as

Table E-13
Spectral Irradiance of Lamps Calibrated by the Summer Workshop SW 101, 102, 103, 104
in Milliwatts per (cm^2 -Micron) at a Distance of 50 cm Where Operated at 8.3 Amperes

	SW 101	SW 102	SW 103	SW 104		SW 101	SW 102	SW 103	SW 104
.25	.0222	.0184	.0217	.0190	1.1	22.9	22.1	22.6	22.5
.26	.0316	.0246	.0331	.0256	1.2	21.3	20.3	20.7	20.8
.27	.0516	.0445	.0506	.0463	1.3	18.9	18.1	18.7	18.8
.28	.0820	.0704	.0798	.0730	1.4	16.8	16.3	16.7	16.9
.29	.125	.107	.122	.112	1.5	15.1	14.9	14.8	16.3
.30	.187	.162	.181	.169	1.6	13.4	13.3	13.1	13.3
.32	.355	.309	.344	.327	1.7	12.1	11.8	11.5	12.0
.35	.826	.739	.792	.782	1.8	10.6	10.4	10.2	10.7
.37	1.32	1.19	1.26	1.26	1.9	9.27	9.18	8.73	9.23
.40	2.32	2.11	2.19	2.20	2.0	7.96	7.89	7.58	7.97
.45	4.50	4.18	4.38	4.40	2.1	6.97	6.65	6.24	6.89
.50	7.57	7.10	7.17	7.51	2.2	5.91	5.60	5.33	5.09
.55	10.7	10.2	10.2	10.5	2.3	5.10	4.82	4.67	4.68
.60	14.5	14.1	13.7	13.9	2.4	4.42	3.98	4.06	3.92
.65	17.9	17.3	16.8	17.2	2.5	3.80	3.13	3.46	3.16
.70	19.9	19.0	19.0	18.9					
.75	21.7	21.1	21.5	20.8					
.80	23.2	22.2	22.8	22.9					
.90	24.6	23.6	23.8	25.2					
1.00	24.1	23.6	23.8	24.3					

Table E-14
Total Absorptance of Typical Spectrally Sensitive Surfaces When Exposed to High Pressure Xenon Arc, Compared to Absorptance When Exposed to Solar Radiation

	70A CB (1)	70A CB (2)	70A EB	95A EB	95A IB	95A CB	95 CB No Filter	Solar
Solar Cell	.418	.409	.394	.405	.422	.408	.494	.416
Evap. gold	.192	.187	.206	.213	.195	.193	.151	.199
Cat-o-lac White	.187	.193	.216	.200	.185	.182	.165	.180
Evap. silver	.041	.040	.043	.045	.041	.043	.042	.050
RAE Silver	.119	.116	.125	.130	.120	.121	.101	.126
Seidenberg White	.187	.189	.197	.195	.187	.190	.167	.188
Alzak	.148	.146	.147	.149	.148	.147	.148	.148
Evap. Aluminum	.081	.080	.080	.081	.082	.081	.086	.082
Ti O White	.171	.177	.190	.180	.170	.174	.162	.170
Methyl White	.274	.276	.303	.296	.276	.275	.236	.274

stated earlier, gives the normalized flux at each wavelength for which signals were measured, the cumulative normalized flux up to that wavelength, and a graph of normalized flux versus wavelength. The normalization procedure is one that makes the total area under the curve over the whole range of measurement, viz. 0.24 to 2.61μ , equal to the area under the solar (Johnson) curve over the same range. Thus the final value of the cumulative radiant flux on all four tables of SW lamps is .13701 (watts per cm^2). From this table we can determine A, the area normalized to the solar curve in the range 0.24μ to 2.61μ which is covered by the NBS table. If the ordinates were in the same spectral irradiance units as the NBS table for QM lamps, the total area under the curve would be P, the total irradiance. P is related to J, the radiance given in Table E-12, second column, by the equation $P = Jr^2$, where r is 50 cm. Hence to obtain the spectral irradiance from the computer tables, the normalized flux should be multiplied by P/A. In practice it was found convenient to read the values of normalized flux from the computer generated graph for the range of wavelengths longer than 0.55μ , and from the output table by interpolation for the shorter wavelength range below 0.55μ where the values are too small to be read accurately from the graph. The final results are presented in Table E-13.

These results should be accepted only on a provisional basis since several correction factors had to be applied to the input data and to the computer results. The measurements will be repeated later with improved experimental techniques. More reliable standard lamps will have to be used and the lamps should be made to illumine the slit either through an integrating sphere or through a quartz diffusing plate.

ACKNOWLEDGMENTS

The authors wish to acknowledge the help of J. Crowell for the computer program, A. R. Winker and T. A. Riley for the experimental setup, and S. Read for measurement of the charts.

REFERENCES

1. Stair, R., Schneider, W. E., and Jackson, J. K., Journal of Applied Optics v. 2, p. 1151, 1963.
2. Klein, Elias (Editor) Final Report of the Goddard Summer Workshop Program X-320-65-407, pp. B-39 to B-46.

OK

SPECTRAL IRRADIANCE MEASUREMENTS ON SOLAR SIMULATOR SOURCES

Sandra Read and Matthew P. Thekaekara

N 67-22774

INTRODUCTION

Measurements of the spectral radiant flux of high-pressure mercury-xenon arc lamps had been discussed in earlier summer workshop reports. These measurements had been made on the lamps then in use in the Space Environment Simulator; they were all of 2.5 kilowatt rating. More recently it was observed that the 2.5 kw lamp array did not yield in the test volume an irradiance averaging one solar constant. Hence they were replaced by stronger lamps of 3.5 kw rating. No detailed spectral radiance measurements have been reported on these lamps. The major questions which occur during routine tests with solar simulation lamps are: do different lamps of the same manufacturer have the same spectral radiance; do lamps by different manufacturers differ spectrally; is there any appreciable spectral degradation due to aging of the lamps; are the absorptances of typical satellite coatings significantly different when exposed to different lamps?

To find an answer to the above questions, spectral radiance measurements were made. Four different lamps were measured: a Hanovia lamp (Hg-Xe 646356) and three Westinghouse lamps T58, T97, and T367. Lamp T367 is relatively new and the other three have over 800 hours running time. At least two runs were made on each lamp, and in the case of Hg - Xe 646356, as a rigorous check on the repeatability of the measurements, four runs were made at intervals separated by several days.

The results of the measurements made on the mercury-xenon lamps are compared with results of similar measurements made on the high pressure xenon arcs. The xenon arc filtered by a suitable interference filter affords a close spectral match to the solar spectrum existing outside the earth's atmosphere.

MERCURY-XENON LAMPS - EXPERIMENTAL PROCEDURE

The mercury-xenon lamps were placed in an aluminum enclosure 20 inches deep, 20 inches tall, and 19 inches wide with a 6 inch diameter aperture. The inside of this enclosure was painted black. The opening of the enclosure was covered with a quartz plate approximately one centimeter thick. The Perkin Elmer Monochromator 112U with a quartz prism was used. The detectors used were the 1P28 photomultiplier for the wavelength range 0.24 to 0.58 microns and a thermocouple for the wavelength range 0.58 to 2.6 microns. Focussing optics were not used in positioning the lamps. Instead the lamp was allowed to shine on the slit at a given drum count number or wavelength with a specific gain setting. The lamp was then adjusted to provide the maximum signal. The power input of these lamps was kept at approximately 3500 ± 50 watts. The voltage was approximately 59.5 volts and the current 58.8 amperes throughout all of the lamp runs. This gave a constant input power of about 3480 watts.

In the original plans it had been decided to see if the positioning of the lamp had any effect on the signal as read by the monochromator. The lamp was moved about one inch within its enclosure to either side, forward, and backward, but the intensity was too low for any meaningful measurements. Instead, the lamp and box enclosure were completely removed and again set up as before. The same positioning was used. As a result there was no appreciable difference in runs of a lamp after resetting the lamp and enclosure.

There were several minor problems encountered in taking the data by the Perkin Elmer monochromator. First a 10 micron slit width was used when viewing the wavelength range 0.24 to 0.58 microns with the 1P28. This slit width was extremely hard to reproduce since the same setting of the micrometer screw of the slit did not guarantee the same 10 micron width of the slit. An attempt was made to reproduce the slit width by adjusting it till a given signal for a given drum count could be reproduced. In this manner the slit was brought more closely to its previous width.

Another problem was that the monochromator became extremely warm during a run. Since large temperature gradients might affect the calibration of the instrument, the monochromator was moved approximately 30 centimeters away from the lamp enclosure instead of the original 10 centimeters. A cardboard lamp shield was placed between the monochromator and lamp enclosure and a fan was directed at the face of the monochromator. This caused a noticeable decrease in temperature. The shield also cut down scattered light reflected from the walls of the room.

Another error occurred in the reading of the charts. It was noticed that the drum count marks at every 10 counts did not always occur at the same place. With any one peak the count would vary by as much as one drum count. This made it necessary to identify the wavelengths of the peaks on the charts. A wavelength calibration could then be drawn on the chart and the signals read off as identified by this wavelength instead of the less reliable drum count.

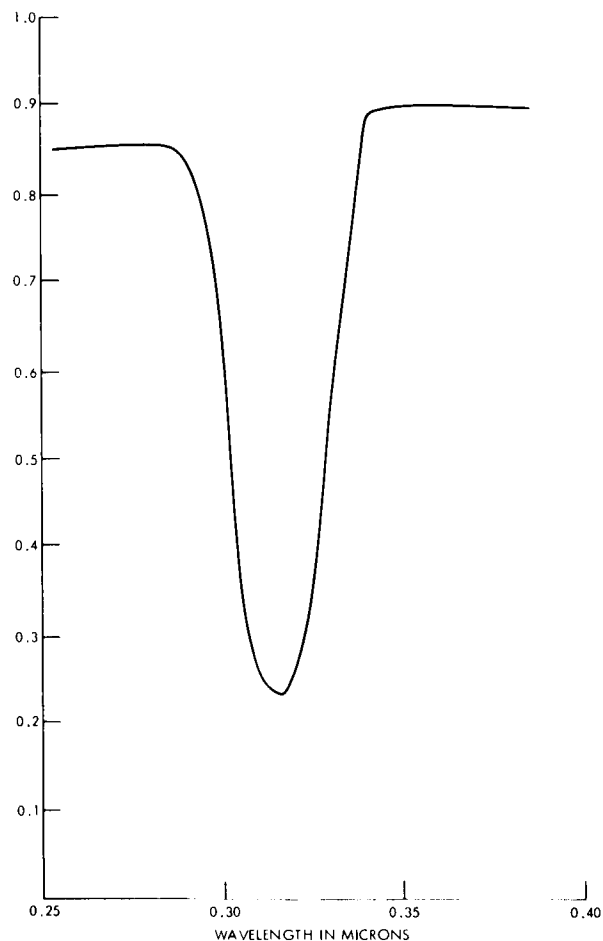


Figure E-21—Spectral transmittance of the filter of X-25 in the UV range.

An effort was also made to recalibrate the gain factors of the system. It was found that they differed slightly from the last time they had been determined which was a year ago. The differences were well within the experimental errors of these measurements. The gain factors used for the present computation are an average of the determination of this year and last year.

Two computer programs were available for determining the spectral radiant flux of an unknown source; the manual program and the fixed points program. They are discussed more fully by J. Crowell elsewhere in this report. A check on the accuracy of the manual program seemed desirable. The data on two runs made previously were suitable for this purpose. One of these runs was made on the Spectrolab Xenon Arc Solar Simulator at maximum power (XECB95) and the other run was on the same source with the filter of solar simulator (XENF95). The filter cuts out some of the strong Xenon radiation in the range 0.28 to 0.36 microns and 0.70 to 1.25 microns and thus makes the Xenon arc a closer match to solar radiation. As a check on the accuracy of the computer program we examined the ratio of the input signals, reduced to the same gain-setting, at different drum counts, of the two runs. The ratio gives the transmittance of the filter. The data on the lamps had been reduced by two different versions of the manual program, one by the IBM 7040/7094, and the other by the CDC 3100. The output of the computer gave the irradiance integrated over 100A ranges. These values also permitted the calculation of the spectral transmittance of the filters. Thus three curves were

obtained for the transmittance of the filters, one from the input signals and the other two from the computer output. These three curves were in close agreement. The average of the transmittance values graphed as a function of the wavelength are shown in Figures E-21 and E-22.

Measurements were made during the Summer Workshop Program on four different lamps. In taking the signals from the charts it was necessary to decide which points were to be taken. Points were taken on peaks and dips with the necessary points within the continuum. Several extra points in the exceptionally strong lines were also taken on the rise and descend of those peaks so that the computer would have more complete information on the line profile.

Since there were a number of runs for each lamp, and there was some slight disagreement between them, it had to be determined if a straight average of the different runs would be meaningful. Figure E-23 shows the differences between the four runs of the Hanovia lamp 646356 for the 10 micron slit width using the 1P28. The points are as given by the spectrum charts, without correction for the sensitivity of the monochromator, but with all signals reduced to the same gain-setting. The continuum is relatively the same while there are some slight differences for the signals at the peaks. It was decided that the differences within runs are small and are due to random variations in lamp output and other experimental factors rather than any change in relative spectral radiant flux. Hence in averaging the sets of values for the runs, the extra work involved in taking a geometric mean was not worth the time or effort, and an arithmetic average was found to be sufficient.

In the runs made with the Hanovia lamp and two Westinghouse lamps T58 and T97, the region observed did not extend beyond 2.2 microns or below 0.25 microns. This created a serious lack in the data points needed for the computer program. Therefore, points had to be extrapolated for this region. There was one run available on T367 with data in the entire region 0.24 to 2.5 microns. It was decided to use this run as a basis for extending the points. This was done by taking the ratio of the runs without data points to the run with points in the range right after 0.25 micron and before 2.2 microns. Thus by multiplying the given data by the ratio, points could be added to extend the signals of the others. This was acceptable even though in a region where small variations occur from one lamp to the other, because of the fact that it was also the region with the least amount of energy involved. Therefore, any errors introduced would be of little consequence.

There were also two regions where sharp dips in the spectrum occurred in the region 1.2 to 1.5 microns and 2.0 to 2.3 microns. The first region due to the 1.4μ H_2O band did not raise any major problem since it was easy to interpolate the values from the curve on the chart. The second region due to the 2.24μ band of quartz was more difficult since the curve shows a strong downward and upward slope involving several changes in the gain-settings as can be seen in Figure E-24. It was necessary for a graph to be drawn, converting all signals to gain 20, from which interpolation could be made to determine what the values of the signals should have been in the absence of the absorption.

Another problem occurred in changing from the 1P28 photomultiplier detector to the thermocouple detector. Only one lamp, the T367, had an overlap region from which a conversion factor

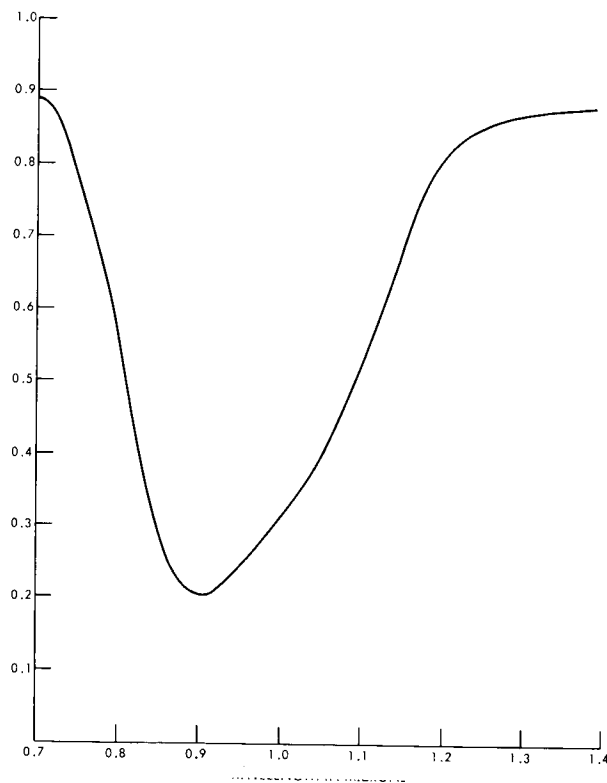


Figure E-22—Spectral transmittance of the filter of X-25 in the IR range.

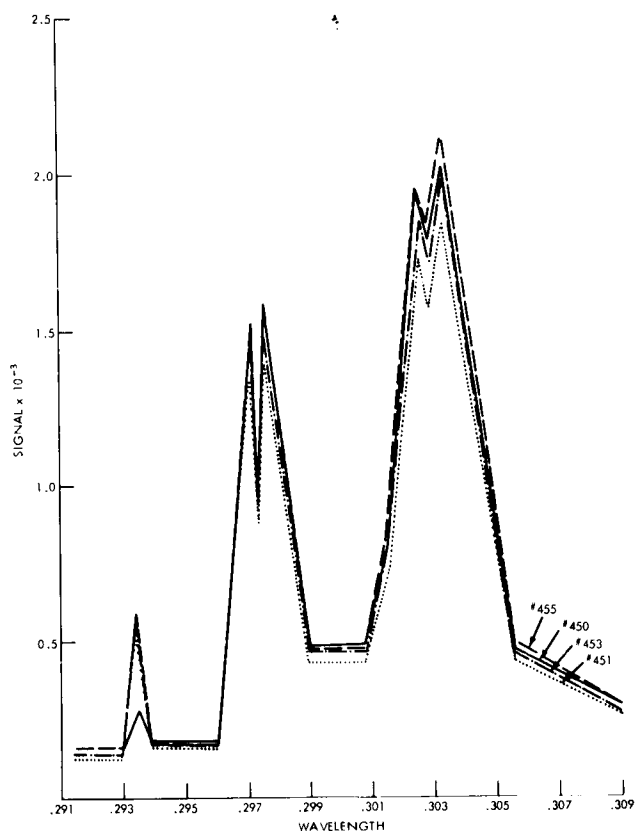


Figure E-23—Signal output of the Hanovia lamp #646356 as read from each of four charts.

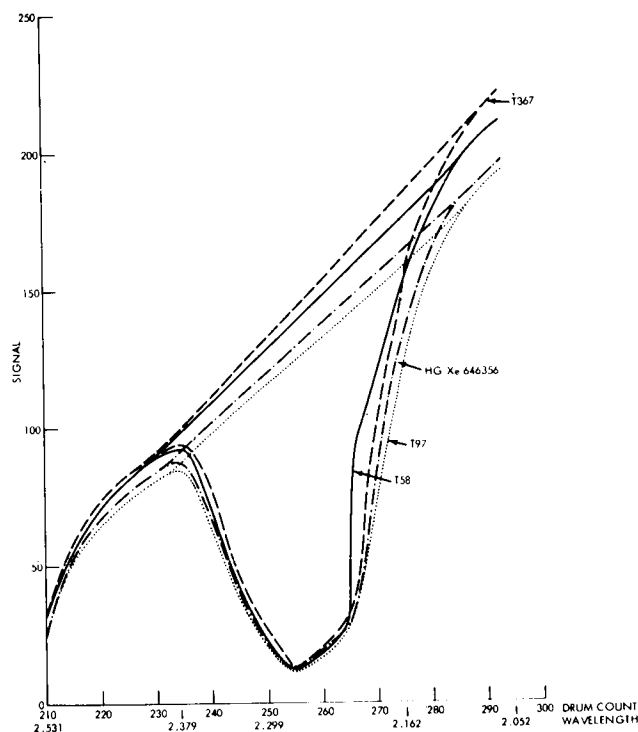


Figure E-24—Correction for the signals of Hg-Xe lamps in the 2.23μ region.

could be determined which would bring the signals of the thermocouple down to those signals which would have been seen if the photomultiplier had been used. This conversion factor was found by first obtaining the sensitivity of the two detectors. Signals were read from two charts of Hg-Xe lamp in the overlap range of .4785 to .7460 microns and all the signals were converted to gain 20 for both thermocouple and photomultiplier 1P28. The sensitivity of the instruments was then obtained by dividing the signals by the flux of the QM18 lamp. The sensitivities of the 1P28 and the thermocouple runs are shown in Figures E-25 and E-26. Since flux = signal/sensitivity, and sensitivity was known, the flux of the Hg-Xe lamp could be determined. From the runs on Westinghouse lamp T367, the flux of that lamp in the overlap region of the two detectors for both 1P28 and thermocouple was determined. The ratio of the two gave the factor by which the thermocouple signal was divided in order to bring it to the same scale as that of the photomultiplier. This factor was found to be 2.86. The points in the continuum alone were used to determine this conversion factor. For comparing the peaks, a more detailed study of the area under the line profile was required since the slit width of the 1P28 runs was 10 microns and the slit width of the thermocouple run was 500 microns. The areas were determined in a few cases and the corresponding radiant flux was determined. Because of the errors involved in computing the area, the ratio was not as constant as in the continuum; however, it was close to 2.86. This ratio could be determined directly only for the Hg-Xe lamp T367.

In order to determine the conversion factor for the other three lamps it was necessary to run a program without the conversion factor, except for the one lamp whose factor was already known. Then ratios of the areas were found from which conversion factors were determined. The area of one region of the photomultiplier to another region of the thermocouple for one lamp should be the

same for the corresponding regions of another lamp. From this fact the conversion factor for the lamps without overlap regions was found using the lamp with the known conversion factor as a standard. The error introduced by this approximation was small.

A further adjustment of input data was required for the signals of the standard lamp. The standard lamp, QM18, with which the Hg-Xe lamps were to be compared was run at a slit width of 200 microns in the range 0.24 to 0.30 microns, whereas the 10 micron slit width was used in this range 0.24 to 0.30 μ microns for the Hg-Xe lamps and for both Hg-Xe lamps and the QM18 in the range longer than 0.3 microns. Therefore, a conversion factor had to be found which would bring the signals down to what they would have been at the 10 micron slit width. In the range 0.27 to 0.3 microns we had readings with 200 micron and 10 micron slit widths. The ratio of the two signals at any given count was found to be very nearly a constant, 184, with an average deviation of 1.37. This low average deviation shows that the signals were read with an accuracy better than 1 percent. The signals obtained with 200 micron slits are divided by 184 to give what they would have been had the 10 micron slit been used.

Before the program could be run, more cards had to be punched to extend the region viewed by the computer. Since the monochromator can now detect meaningful signals in the 0.24 to 0.26 micron range, it will be necessary to extend the Johnson Cruve, absorptivity curves, wavelength calibration tables, and flux of the standard lamp before this region can be analyzed.

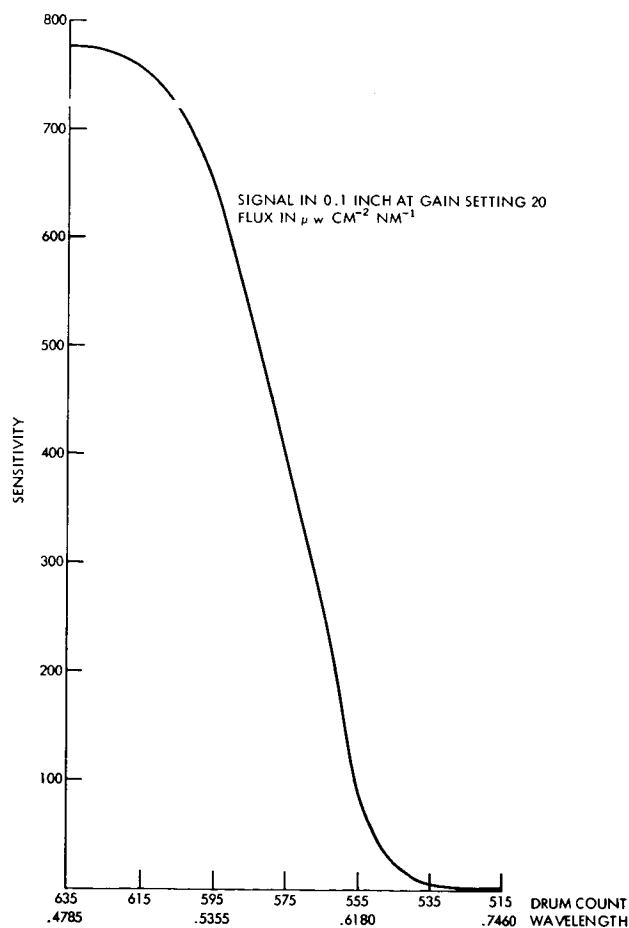


Figure E-25—Spectral sensitivity of 1P28.

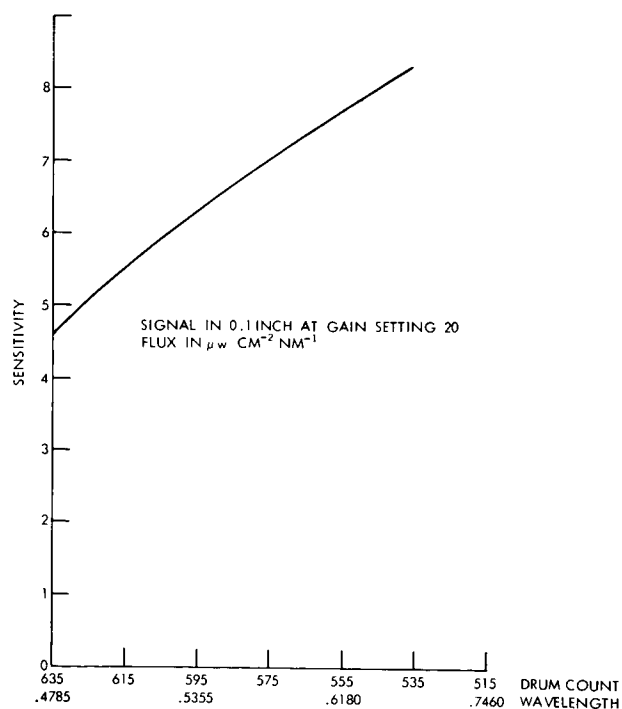


Figure E-26—Spectral sensitivity of the thermocouple.

Values for the Johnson Curve were obtained from Johnson's original paper (Reference 1).

Values needed for the absorptivity curves used in the computer program which were below 0.24 microns were extrapolated. This was done by studying the general trend of each curve and determining the next point.

The flux for the standard lamp QM18 is known down to 0.25 microns. A value for flux below 0.24 microns was needed. Therefore, through extrapolation, a point was added. The known values of the flux in the range down to 0.25 were plotted on a logarithmic scale, which permitted a rather plausible extrapolation.

The drum count to wavelength conversion table also needed to be extended since the earlier table ended at 0.25 microns (Reference 2). This was done by plotting the known curve to find its general shape and then extending the curve out into the unknown region. In this way, wavelength values could be assigned to drum counts in this range.

ANALYSIS OF THE Hg-Xe ARC SPECTRUM

The results of the analysis of the data by the manual program using the CDC 3100 computer are presented in Figures E-27, E-28, E-29, E-30 and in Tables E-15, E-16, and E-17. As is well known, most of the energy of the Hg-Xe arc is in a relatively few strong emission lines. A cursory glance at the four figures shows that the spectral distribution of the lamps varies very little from one lamp to another. All the curves look very much alike, with strong peaks occurring at the same wavelengths. It is also seen that the spectral match to the sun is rather poor unless the energy is integrated over fairly wide wavelength ranges. This is no serious drawback since most absorbing surfaces effectively perform this integration.

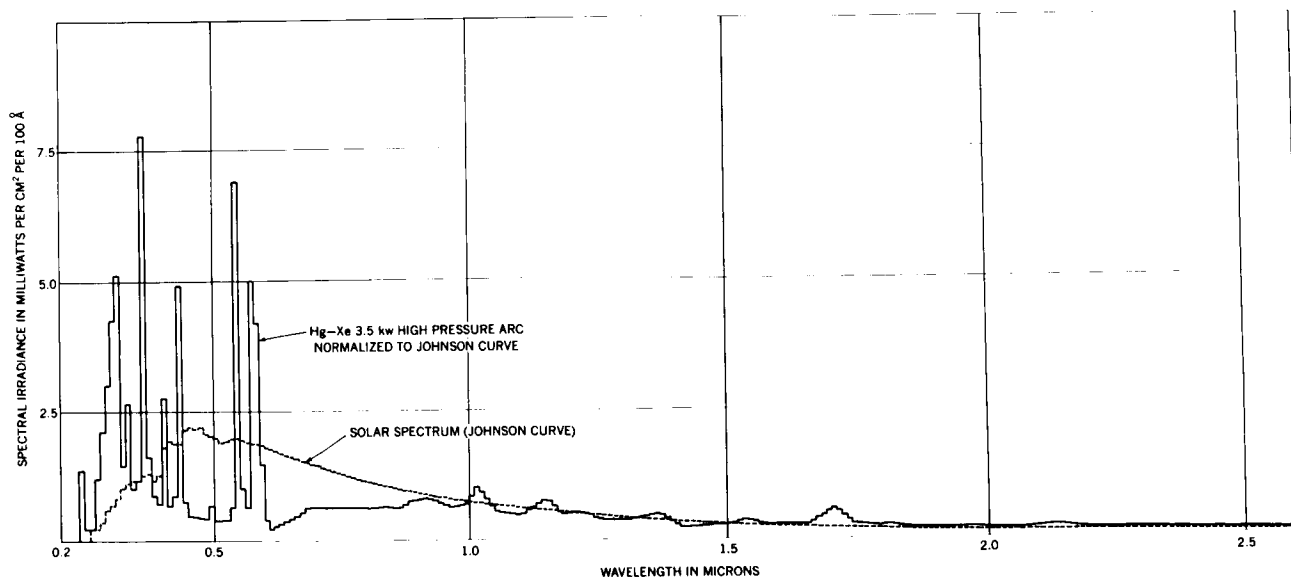


Figure E-27—Westinghouse lamp T367 when relatively new.

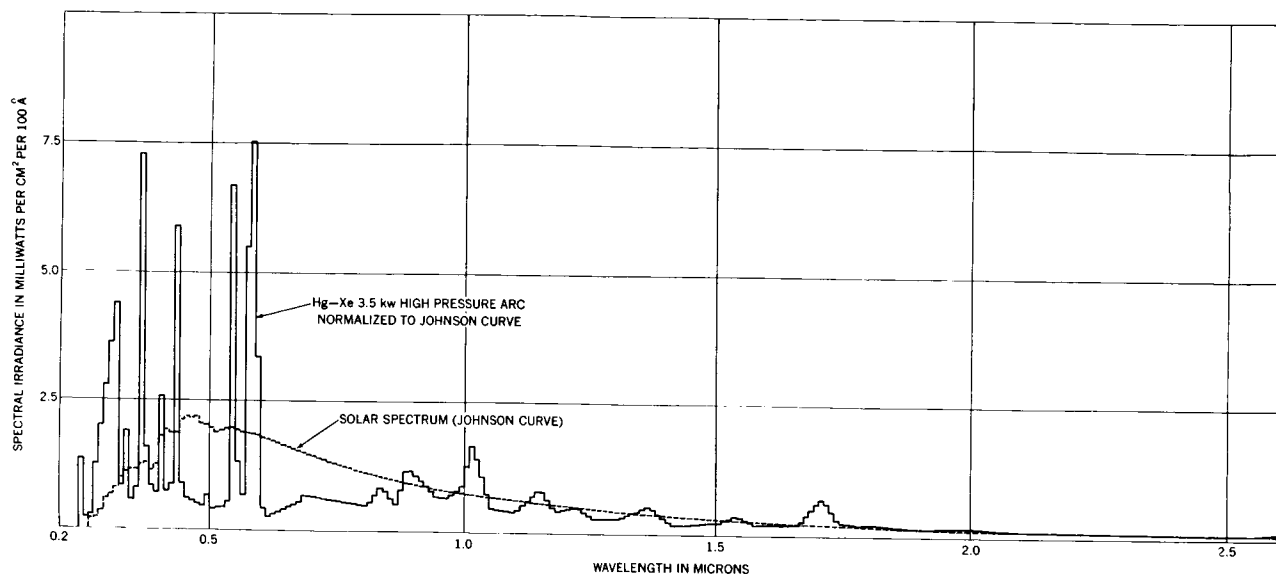


Figure E-28—Westinghouse lamp T97 with 800 hours running time.

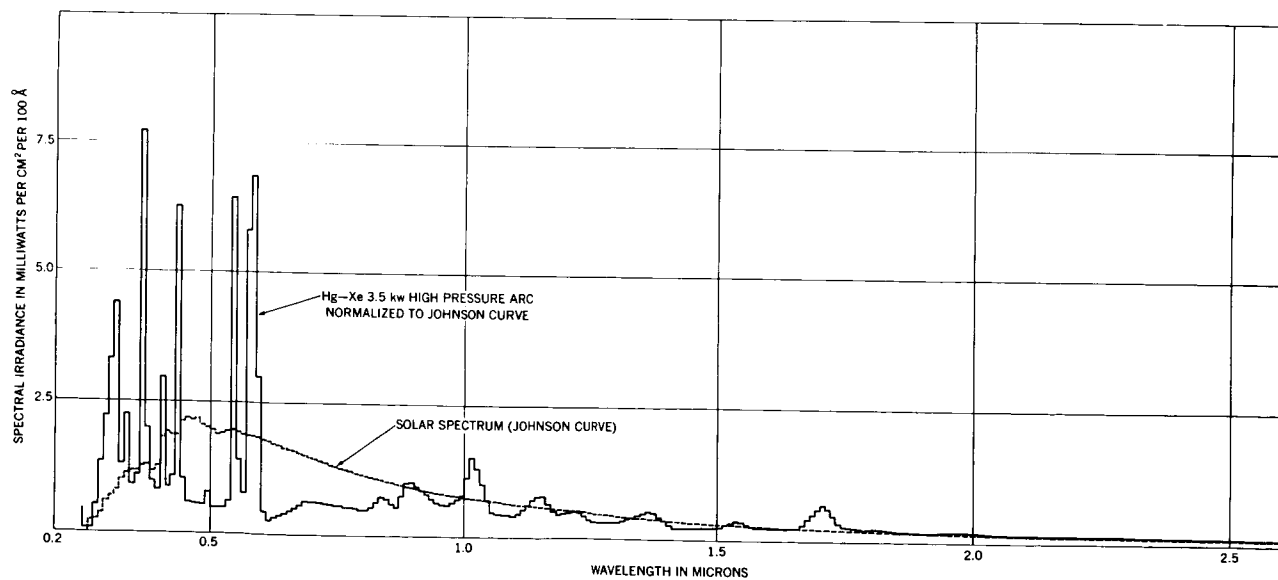


Figure E-29—Westinghouse lamp T58 with 800 hours running time.

Tables E-15, E-16 and E-17 present selected information from the computer printout sheets. They help to study the minor points of difference in the spectral output of the four lamps and the solar spectrum. As stated earlier the T367 was a relatively new lamp while the others had been burnt for nearly 800 hours. The lamps T367, T97 and T58 are Westinghouse lamps and the fourth, 646356, is a Hanovia lamp. Table E-15 gives the energy (normalized to one solar constant) in wide wavelength ranges, UV, visible, near IR, IR and distant IR. The mismatch between the solar spectrum and the Hg-Xe lamps is noticeable in the UV, 0.20 to 0.40 μ where the Hg-Xe lamps are stronger, and in the near IR, 0.60 to 1.20 μ where the solar energy is stronger. The mismatch was greater in the new lamp than in the older ones. The spectral distribution of the range below 0.3 μ is of some significance. Great care was taken to ensure that no scattered light occurred in the spectrograph. It seems certain that there was no measurable radiation from the Hg-Xe lamp below 0.24 μ . As the spectrum is scanned from 0.24 μ to longer wavelengths the signal rises gradually, and beyond 0.25 μ drops suddenly to near zero. This is due to the strong self-reversal of the pressure broadened resonance line at 0.2537 μ . At 0.26 μ the signal again begins to increase. There are several very broad emission lines in this range from 0.26 to 0.3 μ , which are not listed in literature. The total energy is small, but the behavior of these lines seems to be highly dependent on excitation parameters of the lamp.

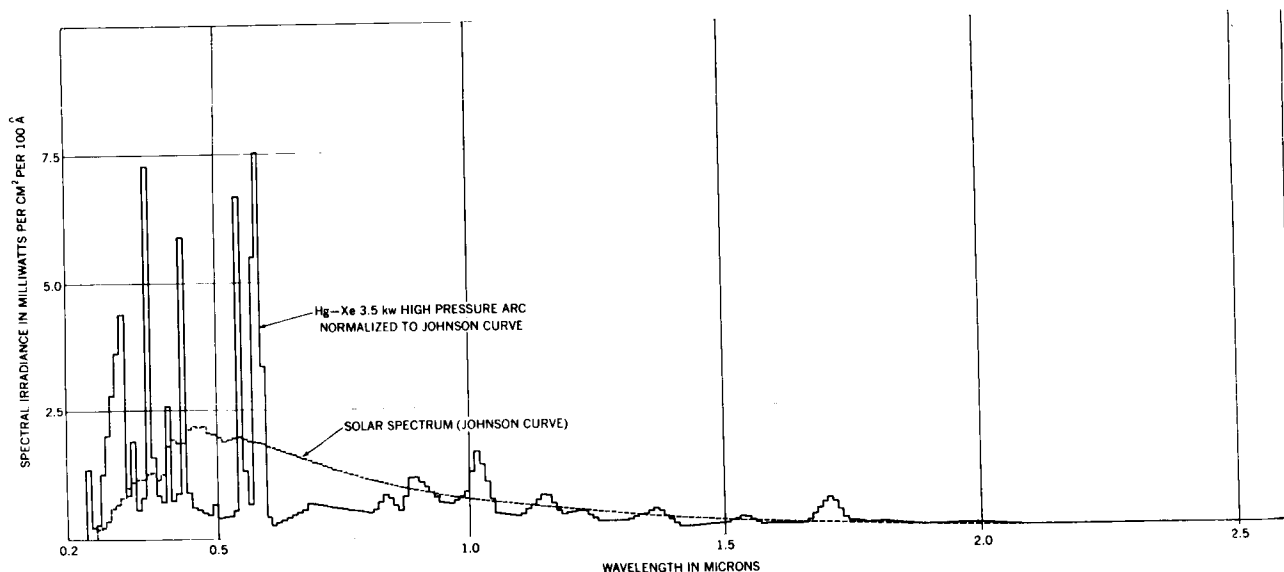


Figure E-30—Hanovia lamp 646356 with 800 hours running time.

Since a major part of the energy in the UV and visible is due to the emission of mercury, a more detailed study was made of the energy in 100Å bandwidths in the vicinity of these lines. The results are presented in Table E-16. It should be noted that the energy as given here includes both the emission lines and the continuum. The lines have on an average a half-width of 20Å and hence, the energy at the peaks as seen by a highly dispersive monochromator is considerably greater. The values of the solar energy in these bands are the spectral radiant flux as given in the Johnson Curve for the center of the respective 100Å ranges. The difference in spectrum between the old lamps and the new lamp which was observed in Table E-15 is seen in Table E-16 also. The emission lines of short wavelength are relatively stronger in the new lamp.

Table E-15
Comparison of Energy in Wide Wavelength Ranges Between Four Hg-Xe Lamps
and the Sun. (Energy in Milliwatts per cm²)

Range μ	T367*	T97	T58	646356	Solar
0.20 to 0.40	34.72	28.20	29.52	30.50	12.6
0.40 to 0.60	33.42	43.31	41.56	40.56	39.3
0.60 to 1.20	36.61	38.39	37.39	39.18	59.1
1.20 to 2.00	23.43	20.37	21.18	19.83	19.9
2.00 to 2.60	6.99	5.01	5.60	5.03	4.2

*NOTE: T367 is new; the others have about 800 hours running time. T367, T97, and T58 are Westinghouse lamps; 646356 is a Hanovia lamp.

Table E-16
Comparison of the Energy in Discrete Wavelength Bands of 100Å Width in the Vicinity of the Strong
Emission Lines of Hg-Xe Between Four Hg-Xe 3.5 kw Lamps. (Energy in Milliwatts per cm² per
100Å)

Range	T367	T97	T58	646356	Solar
0.28 to 0.29	2.11	1.18	1.36	2.02	.34
0.29 to 0.30	3.01	2.14	2.23	2.80	.63
0.30 to 0.31	4.25	3.28	3.33	2.62	.67
0.31 to 0.32	5.12	4.22	4.42	4.38	.82
0.36 to 0.37	7.78	7.06	7.73	7.26	1.29
0.40 to 0.41	2.76	3.20	2.99	2.58	1.88
0.43 to 0.44	4.91	5.62	6.28	5.86	1.82
0.54 to 0.55	6.90	7.26	6.44	6.65	1.98
0.57 to 0.58	4.99	5.94	5.81	5.46	1.87
0.58 to 0.59	4.19	7.54	6.86	7.50	1.85
0.59 to 0.60	1.47	3.36	2.99	3.34	1.83

Table E-17
Total Absorptance of Typical Spectrally Sensitive Surfaces When Exposed to Four High Pressure
Hg-Xe Arcs Compared to Absorptance When Exposed to Solar Radiation (Johnson Curve)

Surfaces	T367	T97	T58	646356	Solar
Solar cell	.270	.312	.301	.312	.415
Evap. gold	.257	.244	.249	.247	.200
Cat-a-lac White	.339	.286	.297	.300	.181
Evap. silver	.149	.115	.119	.133	.051
RAE silver	.222	.194	.198	.207	.127
Seidenberg White	.306	.261	.269	.278	.188
Alzak	.144	.144	.144	.145	.148
Evapo. Aluminum	.074	.076	.075	.076	.082
Ti O White	.318	.266	.276	.284	.171
Methyl White	.396	.361	.370	.372	.275

From the point of view of solar simulation the spectral match over very small wavelength ranges is of less significance than the total absorptance of typical satellite surfaces when exposed to a given solar simulator irradiance. Computed values for ten typical surfaces are given in Table E-17. The reliability of these values depends partly on the method used by the computer. Let P_{λ_i} be the spectral irradiance of the given source, the Hg-Xe lamp in our case, at a given wavelength λ_i ; let α_{λ_i} be the absorptance of the surface at the same wavelength. The λ_i values are those for which signals were read from the spectrum charts. The linear approximation method used by the computer assumes that P_{λ_i} is constant over the wavelength range $1/2 (\lambda_{i+1} + \lambda_i)$ to $1/2 (\lambda_i + \lambda_{i+1})$. Let $\Delta\lambda_i$ be the width of this range.

$$\Delta\lambda_i = \frac{1}{2} (\lambda_{i+1} - \lambda_{i-1}).$$

The values of spectral absorptance of paint samples and surfaces are taken from tables published in literature or from curves obtained in our laboratory. The input data to the computer are absorptance at a small number of wavelengths which are not necessarily the same as λ_i of the spectrum charts. A linear interpolation is used to compute the α_{λ_i} for each λ_i . The total absorptance α is given by the equation,

$$\alpha = \frac{\sum P_{\lambda_i} \alpha_{\lambda_i} \Delta\lambda_i}{\sum P_{\lambda_i} \Delta\lambda_i}.$$

The summation is over all the wavelengths at which spectrum chart signals were measured. The denominator in the above equation is equal to one solar constant. For the computation of solar absorptance the values of λ_i and P_{λ_i} are those of the Johnson Curve.

Table E-17 shows that for most of the surfaces the absorptances are nearly the same for all four lamps. A difference exceeding 10 percent is seen between the new lamp and the old lamps for solar cell and cat-a-lac white. This difference is consistent with the small variations in spectral distribution between the lamps. There are larger differences between Hg-Xe absorptance and solar absorptance. In many cases the solar absorptance is less, as is seen for the white paints and for evaporated silver and gold. Alzac and evaporated aluminum have practically the same absorptance for solar radiation as for Hg-Xe radiation. The absorptance of the solar cell for solar radiation is about 30 percent higher than for Hg-Xe radiation. These results are of considerable significance in testing integrated systems in the space environment simulator.

The so-called manual program which was used for the analysis of the data is a rather complex one. There are many steps involving linear interpolation and numerical integration; and small errors involved at each of these steps may well have a cumulative effect. The input tables are (1) drum count to wavelength conversion, (2) solar spectral irradiance (3) spectral irradiance of the standard lamp, (4) to (13) spectral absorptance tables for the 10 surfaces, (15) standard lamp calibration scan giving drum counts, amplitudes of the spectrum charts and gain settings, (16) conversion table for gain setting to amplification factor. These are followed by tables similar to (15) and (16) for each measurements scan of unknown sources. Difference values of wavelength and drum count are involved in each of the tables, hence the need for extensive linear interpolation. The errors would be small if the tables represented smooth curves, but this is hardly the case especially for the measurement scans of the unknown source.

An alternate program, referred to as the fixed points program has been developed for computing normalized values of spectral irradiance. All input data for the standard lamp and the unknown source have to be supplied at the same wavelengths, and hence the errors in computation

should be small. The data on all four lamps have been reduced by the fixed points program. Point by point comparison of the output data confirms the results of the manual program. The plot for one of the lamps, the relatively new Westinghouse lamp T367, is given in Figure E-31. The wavelength axis is on a scale half that of Figure E-27 to E-30 and the irradiance axis is also on a reduced scale. Figures E-27 and E-31 refer to the same lamp and same computer input data. The difference in scales of the two ordinates accounts partially for the apparent difference in the spectrum charts. The main difference, however, is that the fixed points program evaluates the normalized irradiance at each point where the spectrum charts were measured and hence presents a more accurate picture of the line profiles.

THE XENON HIGH PRESSURE ARC

A high pressure arc that had long been considered as an alternate source for solar simulation uses xenon instead of a mixture of mercury and xenon as the carrier gas. For long term stability, trouble-free operation, and other similar features, the xenon high pressure lamp has all the advantages of the Hg-Xe arc, but the spectrum is too rich in the near IR to give a satisfactory spectral match to solar irradiance. More recently, interference filters have been developed to filter out selectively certain ranges of the spectrum so as to improve the spectral match. A solar simulator which is used in many laboratories is the Model X-25 which consists of a xenon 2500 watt lamp and an interference filter, developed by Spectrolab, a Division of Textron Electronics, Inc. The transmittance of the filter is shown in Figures E-21 and E-22.

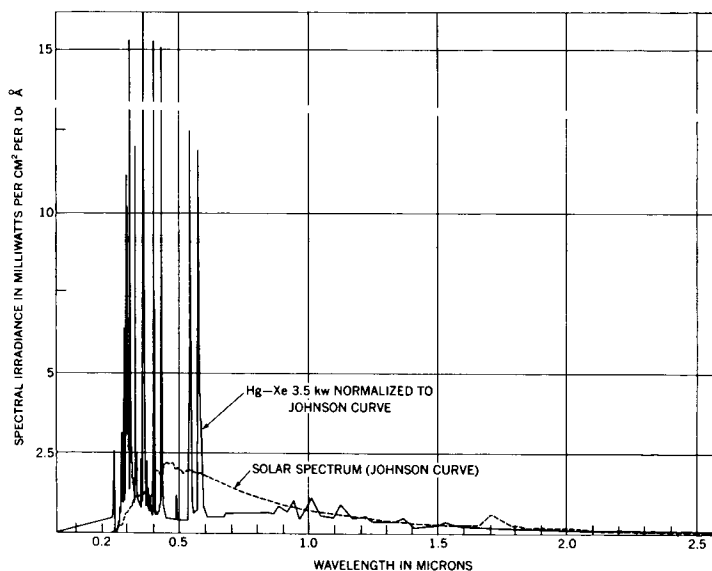


Figure E-31-Spectral irradiance of Westinghouse lamp T367 (hg-Xe 3.5 kw) as computed by the fixed point program.

Extensive measurements were made to determine the spectral irradiance of an X-25 solar simulator. These measurements included the variation of spectral energy distribution with both the input power to the lamp and with the position in the illuminated plane. The Perkin-Elmer, Model 112U monochromator with quartz prism was used. The slit was 0.083 mm. The detectors were the 1P28 in the wavelength range 2670 to 3770Å and the thermocouple in the range 3300 to 25600Å. During the photomultiplier runs, a wire mesh filter was placed at some distance from the slit to safeguard against saturation of the detector. A small plane mirror inclined at 45° to the direction of the beam was mounted in front of the exit slit of the solar simulator and the reflected light was focused on the slit of the monochromator by the external optical system of the Perkin-Elmer, which consists of a small plane mirror and a concave mirror. At first a preliminary spectral scan was made with the power input to the lamp at the lowest value, dial setting 000, 70 amperes, 26 volts, 1820 watts, and the position of the solar simulator with respect to the plane mirror such that only a small portion at the center of the beam was focused on the slit. A

Table E-18

Comparison of Energy in Wide Wavelength Ranges Between the Sun (Johnson Curve) and the Spectrosun X-25 (Xenon Lamp, 2500 w, Viewed at Different Locations in the Beam and at Different Power Levels (Energy in Milliwatts per cm²)

Range Microns	Center of beam 70 amp first scan	Center of beam 70 amp second scan	Edge of beam 70 amp	Edge of beam 95 amp	Intermediate point between center and edge, 95 amp	Center of beam 95 amp	Center of beam 95 amp with the X-25 filter removed	Solar irradiance (Johnson Curve)
0.25 to .40	12.86	12.78	14.71	14.93	12.55	12.99	10.22	12.6
0.40 to .60	36.75	34.80	36.63	39.37	37.55	36.55	26.78	39.3
0.60 to 1.20	59.36	59.79	54.75	56.13	60.33	59.27	78.61	59.1
1.20 to 2.00	20.46	21.06	18.95	18.31	18.94	21.19	15.84	19.9
2.00 to 2.60	5.67	6.55	9.55	6.05	5.56	5.14	3.84	4.2

Table E-19

Total Absorptance of Typical Spectrally Sensitive Surfaces Where Exposed to High Pressure Xenon Arc, Compared to Absorptance When Exposed to Solar Radiation

	70A CB (1)	70A CB (2)	70A EB	95A EB	95A IB	95A CB	CB 95 No Filter	Solar
Solar Cell	.418	.409	.394	.405	.422	.408	.494	.416
Evap. gold	.192	.187	.206	.213	.195	.193	.151	.199
Cat-o-lac White	.187	.193	.216	.200	.185	.188	.165	.180
Evap. silver	.041	.040	.043	.045	.041	.043	.042	.050
RAE Silver	.119	.116	.125	.130	.120	.121	.101	.126
Seidenberg White	.187	.189	.197	.195	.187	.190	.167	.188
Alzak	.148	.146	.147	.149	.148	.147	.148	.148
Evap. Aluminum	.081	.080	.080	.081	.082	.081	.086	.082
Ti O White	.171	.177	.140	.180	.170	.174	.162	.170
Methyl White	.274	.276	.303	.296	.276	.275	.236	.274

second scan with the same power setting and for the same position in the irradiance plane was made several days later as a check on the repeatability of the readings. The two sets of data were reduced independently, though with reference to the same standard lamp data. Measurements were made at the same low power level for the edge of the beam, by suitably raising the whole solar simulator on its four adjustable legs. Similar sets of readings were taken at the highest possible power level, dial setting 6.86, 95 amperes, 30 volts, 2850 watts, for three positions of the simulator with respect to the focusing optics, so as to sample the spectrum at the center of the beam, the edge of the beam, and a position intermediate between the two. A final scan was made at the center of the beam at 95 amperes current but with the interference filter at the exit port of the solar simulator removed. This would give spectrum of the xenon arc unmodified by the solar spectral match filter.

Some of the more significant results of the computer analysis of the data on these seven series of the spectral scans are presented in Tables E-18 and E-19. In Table E-18 the energy integrated

over wide wavelength bands is given, UV, visible, near IR, IR, distant IR. The unfiltered xenon spectrum is, as is well known, a very poor spectral match to the sun, mainly because of the strong emission lines in the near IR; solar irradiance in the range 0.6 to 1.6 μ is 59.1 mw cm^{-2} , whereas the irradiance of the unfiltered xenon spectrum in the same range is 78.6 mw cm^{-2} . The filtered xenon spectrum is, on the other hand, a rather close spectral match to the Johnson spectrum; much more so than the mercury spectrum, of which energy distribution in the same ranges is shown in Table E-15. There is no clear evidence of any large change in the spectrum due to a change in input power. There is, however, some dependence of the spectrum on the position in the beam. The edge of the beam seems to be relatively stronger in the UV and weaker in the near IR, than the center of the beam and the intermediate position. The computed values of the total absorptance of ten typical surfaces when exposed to the X-25 solar simulator are given in Table E-19. Here again the values are closer to solar absorptance than those listed in Table E-17 for the mercury-xenon lamps. The spectral energy distribution for four of the runs is presented in Figures E-32, E-33, E-34, and E-35. The histograms have been prepared by the same procedure as those of the Hg-Xe arc so that the relative closeness of spectral match can be readily seen. A word of caution must be given, however, based on the experience of those who have used the xenon interference filters for a long time. The filter is located in an area where the energy from the xenon lamp is brought to a sharp focus and is very intense. Since the purpose of the filter is to absorb a great deal of unwanted energy, there is the possibility of extreme temperatures and a consequent deterioration in the transmittance of the filter and in the spectral distribution of the energy.

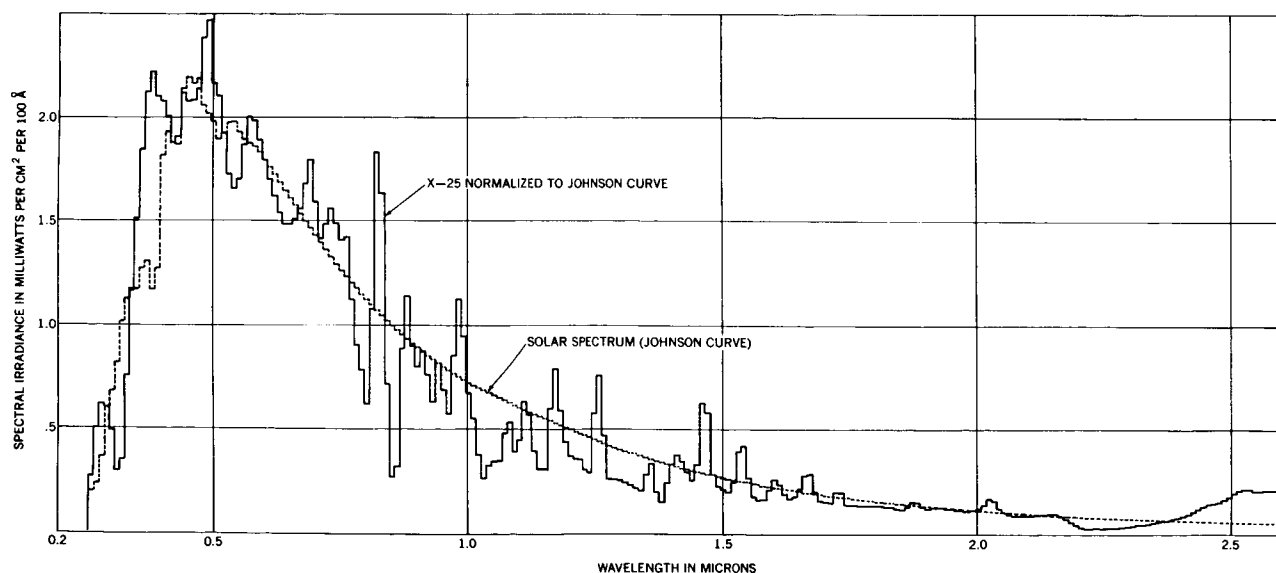


Figure E-32—Filtered xenon source, 2.5 kw, 95 amp. current, viewed at the edge of the beam.

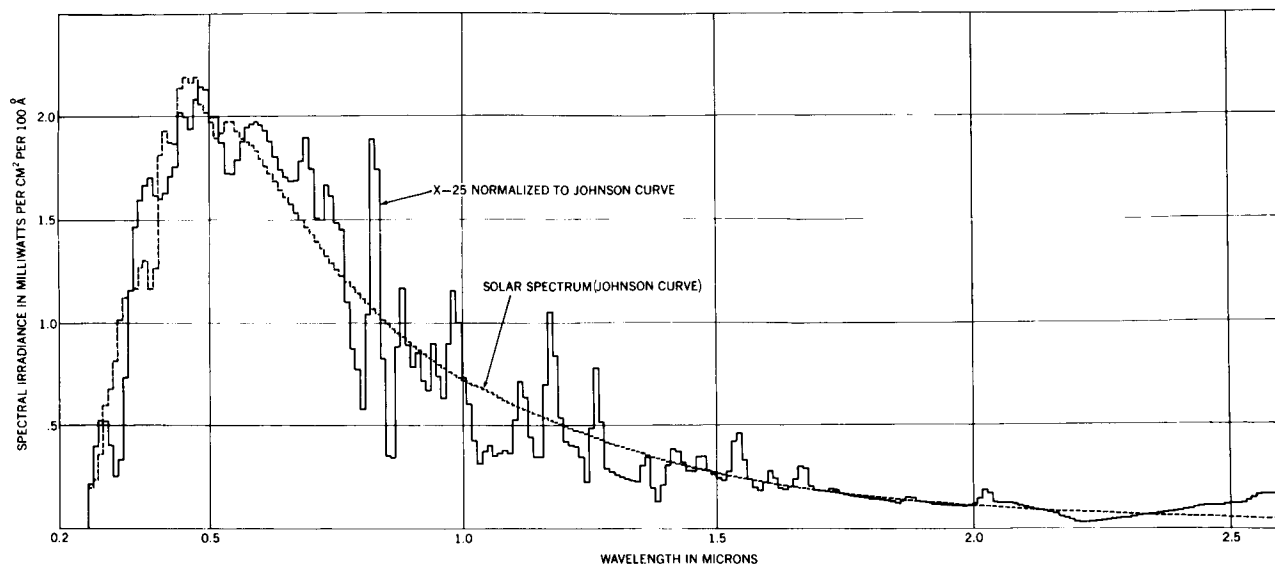


Figure E-33—Filtered xenon source, 2.5 kw, 95 amp. current, viewed at an intermediate point between the center and edge of beam.

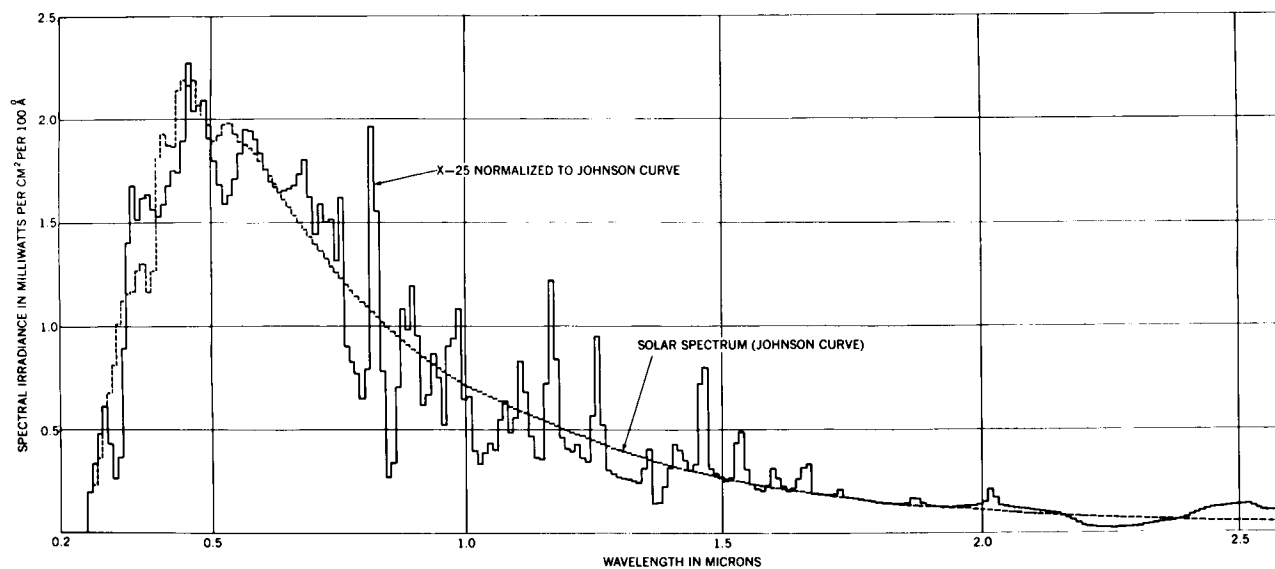


Figure E-34—Filtered xenon source, 2.5 kw, 95 amp. current, viewed at the center of the beam.

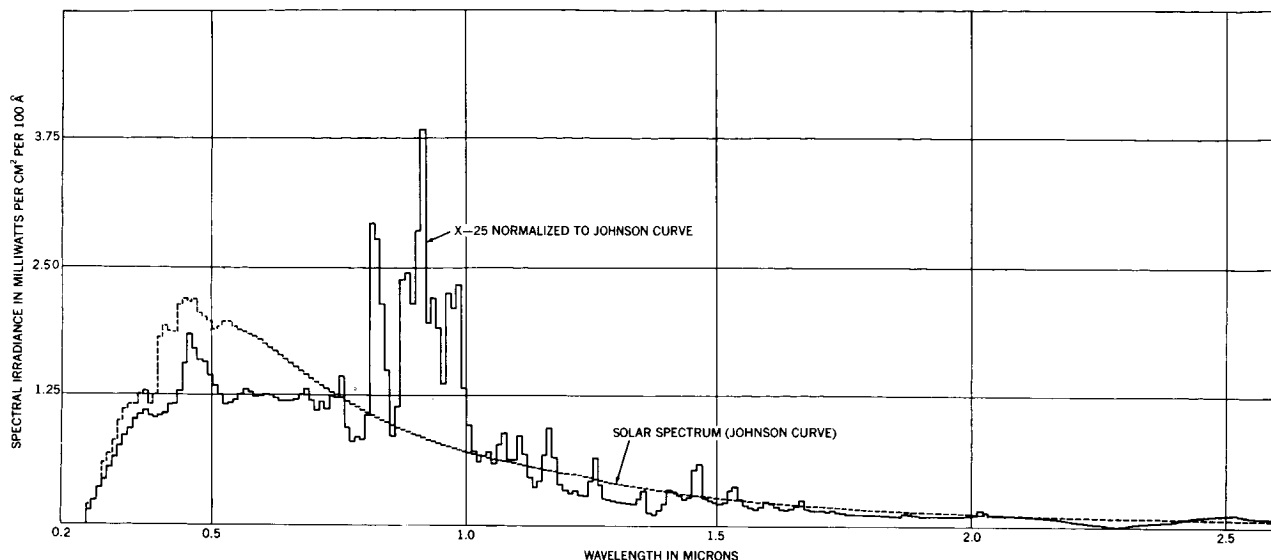


Figure E-35—Xenon source with filter removed, 95 amp current, viewed at the center of the beam.

ACKNOWLEDGMENTS

The work discussed in this report is the result of contributions by several members of the Summer Workshop and GSFC permanent staff besides the authors. The spectral runs on the xenon arc were made by A. Winker and most of the runs on Mercury-Xenon arc were made by E. Reed, D. Henry, and A. McNutt. Considerable help was obtained from J. Crowell for the computer analysis of the data and from A. Winker and J. Riley for setting up the equipment. The Manual Program for the CDC 3100 was written by A. J. Villasenor.

REFERENCES

1. Johnson, F. S., "The Solar Constant," J. Meteor. 11 (6): 431-439, December 1954.
2. Klein, Elias, (Editor), Final Report of the Goddard Summer Workshop Program, X-100-65-407, Page B-63.

PHOTON FLUX OF SUBSTANDARD QUARTZ-IODINE LAMPS IN THE RANGE 2500A TO 8000A

Paul Schoen and Jesselle Mayes

N 67-22775

Due to the short lifetime and great expense of the National Bureau of Standards primary standards of spectral irradiance, it was desirable to calibrate secondary standards for laboratory use. Two different procedures were tried for calibrating secondary standards SW 100 and SW 101 against primary standards EPI 1045 and EPI 1046. The first procedure did not yield consistent results; the second was more satisfactory.

Both the standard and the substandard lamps used were 1000 watt "Quartz-iodine" coiled-coil tungsten lamps produced commercially by General Electric (reference 1). The lamps were calibrated for operation at 8.3 amperes alternating, and were supposed to maintain this calibration for 100 hours. The spectral irradiance values of the standards are given in microwatts/cm²-10A bandwidth vs. wavelength for the source placed 50 cm from the detector. For convenience in future work these values and those of the substandards will be expressed as photons/cm²-sec-10A bandwidth vs. wavelength at 50 cm distance.

The first method of calibration was somewhat similar to that used by the National Bureau of Standards (reference 1) and also to that used in previous summer workshop effort (reference 2). A ratio was found at a given wavelength between the spectral irradiances of the substandard and the standard lamps. This ratio was then multiplied by the calibrated output power of the standard to yield the irradiance of the substandard. Photon flux, f , then found by dividing the irradiance, E , by the energy, hc/λ , of an individual photon:

$$f = \frac{E\lambda}{hc}$$

The output of each source at a given wavelength was measured by dispersing its light with a monochromator and registering with a pen recorder the anode current of a photomultiplier tube attached to the monochromator exit slit. The ratio between the two lamps should then have been independent of the measuring equipment if the equipment was unchanged from lamp to lamp.

Primary and secondary lamps were mounted in pairs on a stand so that they were on a line parallel to the optical bench of the monochromator (see Figure E-36). The monochromator was mounted on ways and could be moved to align with first one source and then the other. The distance between the source and the monochromator entrance slit was maintained by the parallelism of the lamp stand and the optical bench unchanged. A theodolite was used to insure that the two lamp filaments were the same height above the floor, even with the slit. A plane mirror attached to the monochromator was adjusted to fold the light from the source through about 90° into the entrance slit of the monochromator and the horizontal position of the monochromator was set so that the image of the slit fell in the center of the grating. Once the angle of the mirror was set, all that needed to be done to align the optical path from one lamp with the other into the photomultiplier tube was to check that the center of the grating was illuminated.

The monochromator was a 1/2 meter Jarrell Ash grating spectrometer whose slit was opened to 100 microns. The phototube was an RCA 1P28 driven at 700 volts. The anode current was read

by a Keithley micro-micro ammeter and was displayed on a Brush recorder writing at a rate of 2 mm/sec. The recorder printout was marked at 50A intervals by a switching circuit in the Jarrell Ash monochromator.

The current to the lamps was controlled through a system of two variacs and a filament transformer (reference 1).

The monochromator, tube photomultiplier, and lamp stand were located inside a darkroom and controlled remotely, so as to minimize external light and stray reflections.

Data were taken from the recorder printouts at 50A intervals from 2500A to 8000A. Three successive data runs were made on each secondary lamp, followed by the three successive runs on the primary lamp with which it was being compared. For each group of three data points at a given wavelength, an average was taken and the standard deviation was found. The ratios between the primary and secondary averages was calculated, as were their standard deviations. Finally the ratios and the standard deviations for each wavelength were multiplied by the values of the photon flux of the primary standard for the given wavelength as interpolated from the National Bureau of Standards (NBS), values.

All of the above calculations of ratios, standard deviations, and fluxes were performed by the CDC 3100 computer using a program written for this experiment.

As a check on accuracy and repeatability, the entire procedure was repeated with another (NBS) standard lamp to see if the secondary lamp calibrations would be the same.

As a result of the check, we obtained two irradiance curves for each of our substandard lamps differing from each other by approximately 20 percent, although the standard lamps were calibrated to 8 percent in the ultraviolet, and to 3 percent in the visible and the infrared. It is believed that this inaccuracy was due to the movement of the monochromator between measurements. The light from the lamp was not focused on the slit, but entered the monochromator as a narrow pencil. Since the light fell on only a small part of the grating, successive measurements used slightly different parts of the grating. Inhomogeneities in the grating and differences in the light path would cause changes in the phototube signal.

The second method of calibration eliminated movement of the monochromator. The equipment was arranged as shown in Figure E-37. The lamp and monochromator were mounted on an optical bench with the lamp in front of the entrance slit of the monochromator. The light source was not focused on the entrance slit, and therefore, to insure that the grating was filled, a plate of frosted quartz was attached to the entrance slit, effectively causing the monochromator to see an image at the slit. This also reduced the problems encountered due to slight variations in the

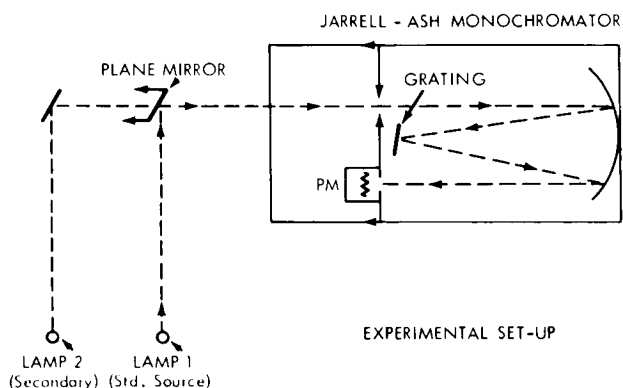


Figure E-36—Experimental set-up No. 1.

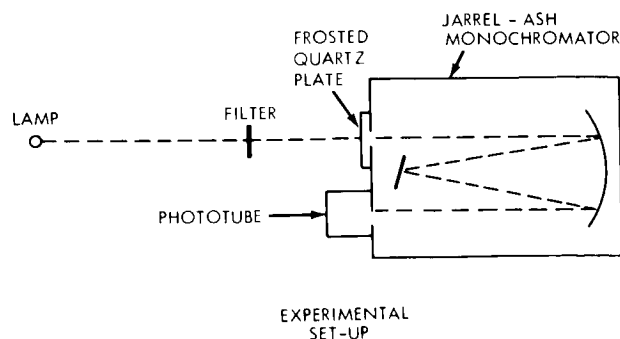


Figure E-37—Experimental set-up No. 2.

Table E-20
Photon Fluxes of Substandards #100 and #101 as Calibrated Against
Standard Lamps EPI 1045 and EPI 1046

λ (A)	Flux in photons/cm ² -sec-10A		% deviation from mean
	#100 from #1045	#100 from #1046	
2500	2.19×10^{12}	2.37×10^{12}	4
2600	4.72	4.91	2
2700	6.22	6.34	1
2800	8.21	8.23	0.1
2900	1.86×10^{13}	1.89×10^{13}	0.8
3000	2.80	2.89	2
3200	5.66	5.85	1
3500	1.44×10^{14}	1.45×10^{14}	0.3
3700	2.30	2.25	1
4000	4.26	4.31	0.6
4500	9.91	9.85	0.3
5000	1.82×10^{15}	1.83×10^{15}	0.3
5500	2.96	3.00	0.7
6000	4.27	4.26	0.2
6500	5.63	5.65	0.2
7000	7.34	7.15	1
7500	1.13×10^{16}	1.07×10^{16}	3
2500	1.96×10^{12}	2.11×10^{12}	4
2600	3.72	3.88	2
2700	6.60	6.73	1
2800	1.10×10^{13}	1.10×10^{13}	0
2900	1.79	1.82	1
3000	2.51	2.58	1
3200	5.35	5.53	2
3500	1.34×10^{14}	1.35×10^{14}	0.4
3700	2.12	2.15	0.7
4000	4.13	4.18	0.6
4500	9.31	9.25	0.2
5000	1.71×10^{15}	1.72×10^{15}	0.3
5500	2.82	2.86	0.7
6000	4.08	4.07	0.1
6500	5.31	5.34	0.3
7000	6.85	6.67	1
7500	8.65	8.16	3

position of the lamp for successive measurements. The quartz plate was masked with tape to form an opening of about 3mm by 15mm, thus lessening the amount of scattered light within the monochromator. The monochromator slit size was set at 15mm by 150 microns. As before, ratios were determined between the substandard and standard lamps.

The 1P28 photomultiplier is most sensitive to light of wavelength 4000A and is rather insensitive at wavelengths longer than 7000A. As a result, the signal from the infrared spectrum of the lamp was small and tended to be overwhelmed by second order ultraviolet light which was seen at the same time by the photomultiplier tube and to which the photomultiplier tube was much more sensitive. To cut out the UV light, a Corning 2-58 filter was placed between the lamp and the

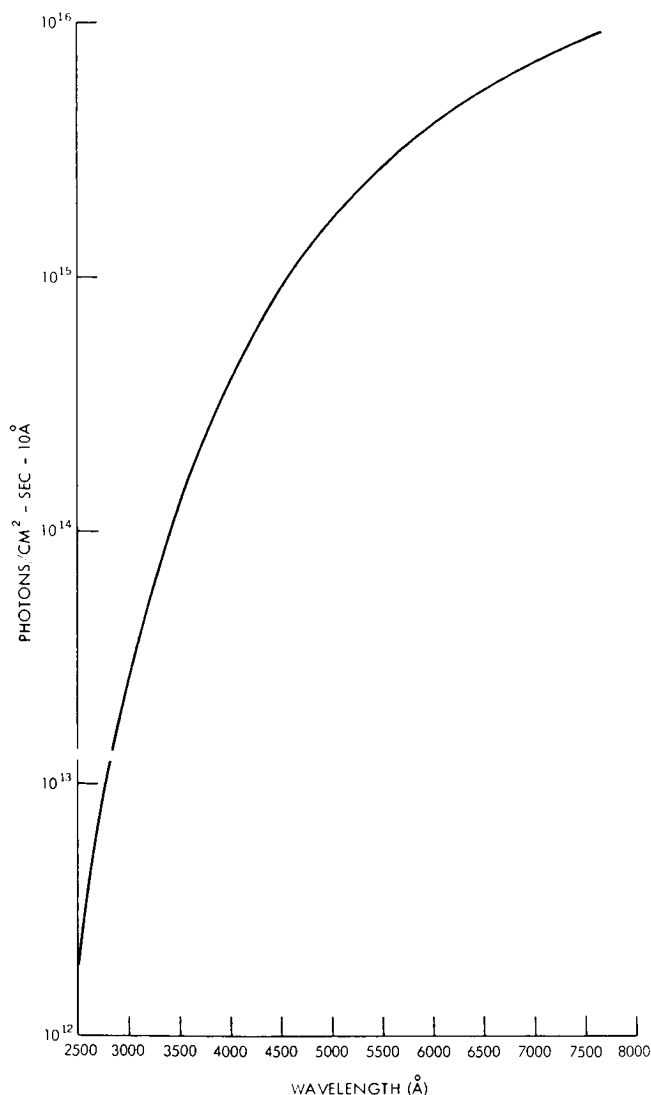


Figure E-38—Photon flux of lamp SW 101 calibrated vs. EPI 1046.

monochromator for readings in the 6600Å to 8000Å range. The high voltage on the photomultiplier tube was set at 900 volts for these readings to increase the signal strength. Use of several combinations of filters revealed that virtually no scattered light was being seen in this spectral region. The signal was so small, however, that the phototube dark current was significant enough in size to affect the ratios. Corrections had to be made for this effect.

The use of combinations of filters revealed that a significant amount of scattered light was being seen in the region 2500Å to 4000Å, in approximately equal amounts from all the wavelengths to which the photomultiplier tube was sensitive. Therefore, for readings made in the 2500Å to 4000Å region, a Corning 7-54 filter was used to reduce, but not eliminate, the scattered light. The scattered light level was then measured by setting the monochromator at 2000Å (to which wavelength the photomultiplier tube is insensitive) and noting that due to scattered visible and I.R. light, the signal was still about ten times the dark current. The photomultiplier high voltage was set at 800 volts for readings in the visible spectrum.

Table E-20 gives the photon flux of the standard lamps at their calibration wavelength, and of the substandard lamps as calibrated against each of the standards. The table also gives the percentage deviation of the two calibrations of each substandard from their mean.

An example of photon flux as a function of wavelength is shown in Figure E-38, which depicts the flux from lamp 101 as calibrated against standard EPI 1045.

REFERENCES

1. Stair, R., Schneider, W. E., and Jackson, J. K., *Journal of Applied Optics*, v.2, p. 15, 1963.
2. Miller, N. J., and Mohr, E. I., in *Final Report of Goddard Summer Workshop Program*, Elias Klein, editor, X-100-65-407, pp. B-47 to B-50.